

Electronic Thesis and Dissertation Repository

12-9-2016 12:00 AM

An Evaluation of the Lithologies and Geochemistry of the Upper Beaver Deposit of the Kirkland Lake Area

Katherine E. Feick
The University of Western Ontario

Supervisor
Dr. Robert Linnen
The University of Western Ontario

Graduate Program in Geology
A thesis submitted in partial fulfillment of the requirements for the degree in Master of Science
© Katherine E. Feick 2016

Follow this and additional works at: <https://ir.lib.uwo.ca/etd>



Part of the [Geochemistry Commons](#), and the [Geology Commons](#)

Recommended Citation

Feick, Katherine E., "An Evaluation of the Lithologies and Geochemistry of the Upper Beaver Deposit of the Kirkland Lake Area" (2016). *Electronic Thesis and Dissertation Repository*. 4336.
<https://ir.lib.uwo.ca/etd/4336>

This Dissertation/Thesis is brought to you for free and open access by Scholarship@Western. It has been accepted for inclusion in Electronic Thesis and Dissertation Repository by an authorized administrator of Scholarship@Western. For more information, please contact wlsadmin@uwo.ca.

Abstract

The Upper Beaver Cu-Au deposit contains a unique style of mineralization in the Larder Lake and Kirkland Lake areas in terms of mineralization, alteration style, and age. This study aims to use company-provided data, supplemented with focused data collection, to evaluate what information can be attained from company-provided geochemical data. The evaluation uses a combination of hand sample, petrographic, geochemical, statistical, and microprobe analytical methods.

Lithochemical analyses indicated that the altered igneous host rock is calc-alkaline in composition and is most likely part of the diorite-monzonite suite. Further, exploratory data analysis of Au and Cu mineralization identified that there are two distinct styles of mineralization in the deposit, including: (1) a Cu-rich style of mineralization and (2) a Mo-rich style. SR-XRF trace element mapping shows that the two styles of mineralization also differ at the microscopic scale.

Keywords

Kirkland Lake, Upper Beaver, Gold, Copper, Geochemistry, Economic geology, Exploration, Abitibi

Acknowledgments

I would like to take this opportunity to thank my thesis supervisor Dr. Robert Linnen for his support and expertise. I would also like to say thank you to everyone at Canadian Malartic Corporation who took me in during two co-op terms during my Undergraduate degree and turned me into a real geologist. I learned so much during those 8 months about core logging, field mapping, and data entry. Your continued guidance and support during my studies has been invaluable. It has been a privilege to have had the opportunity to work with you. A special thank you to Mark Masson, Christal Hanuszczak, Chris Clarke, Chantel Skanes, and Mike Fell for their extensive support and guidance as well as their friendship. Thank you as well to all the friends that I have made over the past two years, especially Liana Stammers and Jessica Stromberg, who I worked closely with during trips to the synchrotron, conferences, and groups meetings.

Thank you to Marc Beauchamp who assisted with microprobe data collection at the University of Western Ontario. I also would like to thank Robert Gordon and Zou Finrock from Sector 20-ID for their time, support, and expertise during data collection at Advanced Light Source. Research described in this work was also collected at Sector 20-ID-B at Advanced Photon Source (APS) of Argonne National Labs. Sector 20 facilities at the Advanced Photon Source, and research at these facilities, are supported by the US Department of Energy - Basic Energy Sciences, the Canadian Light Source and its funding partners, the University of Washington, and the Advanced Photon Source. Use of the Advanced Photon Source, an Office of Science User Facility operated for the U.S. Department of Energy (DOE) Office of Science by Argonne National Laboratory, was supported by the U.S. DOE under Contract No. DE-AC02-06CH11357. Research described in this work was also performed at the Canadian Light Source, which is supported by the Natural Sciences and Engineering Research Council of Canada, the National Research Council Canada, the Canadian Institutes of Health Research, the Province of Saskatchewan, Western Economic Diversification Canada, and the University of Saskatchewan. I would especially like to thank Lisa Van Loon and Erika Bergen from the Canadian Light Source for their expertise, assistance with data collection, interpretation, and helpful suggestions, and for their friendship while performing analysis at both the Advanced Light Source and the Canadian Light Source. This work is also based upon research conducted at the Cornell High

Energy Synchrotron Source (CHESS) which is supported by the National Science Foundation and the National Institutes of Health/National Institute of General Medical Sciences under NSF award DMR-1332208. Arthur Woll and Louisa Smieska were essential in data collection and GeoPIXE analysis. Their help and support both at CHESS and in all communications regarding data analysis after data was collected was instrumental to data interpretation. CLS also provided a Graduate Student/ Post-Doc Travel Support grant for \$1,000 USD for work completed at APS through CLS in October, 2015.

Table of Contents

Abstract	i
Acknowledgments.....	ii
Table of Contents	iv
List of Tables	viii
List of Figures	x
List of Appendices	xviii
1 Chapter 1: Introduction and Background.....	1
1.1 Mining in Kirkland Lake	1
1.2 Regional Geology	2
1.3 Introduction to the Project	5
1.4 Objectives	7
1.5 Previous Work	8
1.6 Deposit Geology	11
1.7 Structural Geology	17
1.8 Mineralization.....	18
1.8.1 Au Mineralization	19
1.8.2 Cu Mineralization	21
1.9 Timing of Mineralization.....	21
1.10 Intrusions and mineralization.....	22
1.11 Alteration	24
2 Chapter 2 Methods	28
2.1 Petrography and Hand Sample Analysis.....	28
2.2 Geochemical Data Sets	30
2.2.1 Compiled CMC Geochemical Dataset.....	31

2.2.2	CMC Surface dataset	35
2.2.3	Past Thesis Datasets	36
2.2.4	Datasets produced for this thesis.....	37
2.2.5	Data Processing.....	39
2.2.6	Exploratory Data Analysis (EDA).....	42
2.3	Spatial Modeling.....	44
2.4	Microprobe Analysis.....	45
2.5	Synchrotron Source X-ray Fluorescence Microprobe Analysis	45
2.5.1	Synchrotron applications in the Earth Sciences.....	46
2.5.2	What is a Synchrotron?.....	46
2.5.3	An Introduction to Hard X-Ray Synchrotron Imaging Techniques.....	48
2.5.4	Data collection at Advanced Photon Source.....	48
2.5.5	Data Collection at Cornell High Energy Synchrotron Source	49
2.5.6	Data Collection at Canadian Light Source.....	52
2.5.7	Data Processing: GeoPIXE.....	52
2.5.8	Element Identification.....	53
3	A Detailed Assessment of Host Rocks of the Upper Beaver Au-Cu Deposit.....	56
3.1	Introduction.....	56
3.1.1	Deposit Geology	57
3.1.2	Lithologies in the Upper Beaver Intrusive Complex	60
3.1.3	Link between Intrusions and Mineralization in the Upper Beaver Deposit 64	
3.2	Geochemical Analysis of Intrusions	65
3.2.1	Available Data	65
3.2.2	Magma Series.....	65
3.2.3	REE Signature of Intrusives.....	70

3.2.4	Comparison to Local Intrusions.....	74
3.2.5	Correlations between Mineralization and Host Rock Lithology	80
3.2.6	Less Common Intrusives.....	84
3.2.7	Sedimentary Sequence	99
3.2.8	Breccia Pipe	113
4	A Detailed Assessment of Trace Element Geochemistry of the Upper Beaver Deposit and An Evaluation of Exploration Vectors for Mineralization.....	119
4.1	Hand Sample Observations.....	119
4.2	Mineralized Zones	120
4.2.1	Zones on the South Side of the Intrusive Complex	121
4.2.2	Zones on the North Side of the Intrusive Complex	131
4.2.3	Petrography.....	135
4.2.4	CMC-Provided Geochemical Database	139
4.2.5	Correlations among Upper Beaver Mineralized Zones	145
4.2.6	Multivariate EDA.....	150
4.2.7	Link between Alteration and Mineralization	162
4.2.8	Surface Geochemistry Survey.....	167
5	Synchrotron source X-ray Fluorescence Microprobe Analysis of Mineralized Thin Sections from the Upper Beaver Deposit.....	175
5.1	Introduction.....	175
5.2	Results.....	175
5.2.1	Ore Minerals in the Upper Beaver deposit	175
5.2.2	Thin Section Selection	176
5.2.3	Mapping at 13.1 and 30.1 keV.....	177
5.2.4	Mapping at different synchrotrons and the effect of step size	178
5.2.5	Trace element Zoning in Mineralized Sulphide Minerals	190

5.2.6	Less Abundant Mineral Phases: A bismuth sulphide mineral, Scheelite, and Ilmenite	195
5.2.7	Au:Ag Ratio	201
6	Discussion	204
6.1	Geochemical analysis of intrusions	204
6.1.1	Evaluation of names.....	207
6.1.2	Interpretation of Less Common Intrusives in the Upper Beaver Intrusive Complex.....	209
6.1.3	Key Characteristics of Sedimentary Sequence and Breccia Lens	214
6.2	Association Between Host rocks and Mineralization	217
6.3	Geochemistry of Mineralization	220
6.3.1	Revised Styles of Mineralization.....	223
6.4	Relationship to Large-Scale Geochemical Trends Among Abitibi Gold Deposits 227	
7	Conclusions	229
	References.....	234

List of Tables

Table 1.1. Indicated and inferred mineral resources for CMC’s five NI43-101 compliant properties.....	6
Table 2.1 Lab and method detection limits for the Upper Beaver geochemical database.....	31
Table 2.2. Detection limits for mineralized dataset	37
Table 2.3. Detection limits for major oxide dataset.....	38
Table 2.4. Elements of interest and their corresponding energy and ROIs for trace element XRF maps acquired at APS. E1 represents the lower limit of the energy peak, while E2 represents the upper limit.....	49
Table 2.5. Characteristic emission lines of select trace elements. Energies highlighted in red were measured during data acquisition at 13.1 KeV, while energies highlighted in blue were measured during data acquisition at higher energies. Energies from “X-ray Data Booklet” .	54
Table 3.1. REE element concentration in samples of mafic syenite, mafic syenite porphyry, crowded syenite, and feldspar porphyry using partial digestion and whole digestion data....	73
Table 3.2. Available data on the age and lithology of local intrusions.....	75
Table 3.3. Information on available published data of local intrusions including where samples are from and the lithologies analyzed	77
Table 3.4. Published REE concentrations for local intrusions. Sample IDs correspond to those in Table 7.....	77
Table 3.5. Summary of the large assay database provided by Canadian Malartic Corporation showing the number of samples, the mean Au grade, and the mean Cu for each lithology after samples without a specific lithology were removed. Concentration of Au greater than 10 g/t with more than 2% of all samples analyzed >2g/t have been bolded	81
Table 4.2. Spearman rank correlation coefficients for Au and Cu in the dataset. Both raw and leveled spearman rank correlation coefficients are shown.	143

Table 4.3. Spearman Rank correlation coefficients for Au in select zones (Lower Porphyry East = “LPE”, Upper Porphyry East = “UPE”, Lower Porphyry West = “LPW”, Upper Porphyry West = “UPW”, and North Contact = “NC”), in the Upper Beaver deposit.....	146
Table 4.4. Pearson Correlations between trace elements used in Principal Component Analysis of data from the Upper Beaver deposit	157
Table 4.5. Eigenvectors showing the relationship between principal components and trace elements	157
Table 4.6. Eigenvalues, percent, and cumulative percent for each principal component.....	158
Table 4.7. Scaled coordinates showing the relationship between each principal component and trace element	158
Table 4.8. Spearman Rank Correlation coefficients for entire CMC land package	168
Table 5.1. Summary of samples analyzed including zone each sample is from, lithology, mineralization style (chalcopyrite = “Cpy”, magnetite = “Mgt”, pyrite = “Py”, visible gold = “VG”), host mineralization, and Au and Cu assays for each sample	176
Table 5.2. Synchrotron source x-ray fluorescence microprobe analysis showing the presence of Bi, W, and Te phases associated with Au mineralization and trace element zoning in pyrite and chalcopyrite grains in each zone in the deposit.....	196
Table 5.3. Synchrotron source x-ray fluorescence microprobe analysis showing the type of Au mineralization and the average Au/Ag ratio in each zone in the deposit. Data from energy scans run at 30.1 keV.	202
Table 5.4. Summary of where each of the main lithologies in the Upper Beaver Intrusive Complex plots on various classification diagrams and proposed names for each rock based on the results of this study	207

List of Figures

Figure 1.1. Location of the Upper Beaver property.....	2
Figure 1.2. Regional geology of the Kirkland Lake and Larder-Lake areas	4
Figure 1.3. Simplified surface geology of the Upper Beaver Property	12
Figure 1.4. Geological model showing major lithological units in the Upper Beaver deposit looking West	13
Figure 1.5. Modified composite cross section of mineralized zones in the Upper Beaver deposit in relation to the major lithological units	14
Figure 1.6. Alteration and mineralization history of the Upper Beaver deposit divided into three main stages of alteration	25
Figure 2.1. The Olympus BX51 microscope with attached Olympus UC30 high resolution digital camera used for petrographic observation	30
Figure 2.2. Percentile box plot showing the distribution of Ni in the deposit among main lithologies as an example of the effects of levelling geochemical data by rock type	41
Figure 2.3. Setup of samples analyzed at CHESS in November, 2015	51
Figure 3.1. Representative photos of the Blake River Group basalts	58
Figure 3.2. Representative lithologies in the Upper Beaver Deposit.....	58
Figure 3.3. Representative lithologies and contacts of the Upper Beaver Intrusive Complex	62
Figure 3.4. Representative photos of A) Feldspar porphyry; B) Spotted Feldspar Porphyry, C) Fine-grained diabase and D) Medium-grained diabase	63
Figure 3.5. Th-Co discrimination diagram showing the classification of select intrusive rocks from the Upper Beaver Intrusive Complex.....	67

Figure 3.6. Tectonic classification diagram for mafic igneous rocks showing the classification of select intrusive rocks from the Upper Beaver Intrusive Complex	69
Figure 3.7. MORB-normalized spider diagram based on Pearce (1983) showing the REE signature of select intrusions from the Upper Beaver Intrusive Complex.....	71
Figure 3.8. Chondrite-normalized spider diagram based on Masuda et al. (1973) showing the REE signature of select intrusions from the Upper Beaver Intrusive Complex	72
Figure 3.9. MORB-normalized spider diagram based on Pearce (1983) for members of the Upper Beaver Intrusive Complex and for intrusions in Gauthier and Lebel as identified	79
Figure 3.10. Chondrite-normalized spider diagram based on Masuda et al., (1973) for members of the Upper Beaver Intrusive Complex and for intrusions in Gauthier and Lebel as identified	80
Figure 3.11. Percentile box plots showing the distribution of Au and Cu in the deposit among the main lithologies.....	83
Figure 3.12. Unusual lithologies in the Upper Beaver deposit.	84
Figure 3.13. Percentile box plots showing the distribution of WDS electron microprobe.....	86
Figure 3.14. Classification of calcic amphiboles	87
Figure 3.15. A) Amphibole pseudomorph after amphibole in sample UWO_2015_27 showing characteristic two cleavages at 60 and 120 degrees; B) Relict dark rim surrounding completely pseudomorphed grain	88
Figure 3.16. Electron photograph showing of mineral phases identified in the opaque rim of a pseudomorphed amphibole	89
Figure 3.17. Backscatter image showing of mineral phases identified in the groundmass of UWO_2015_27.....	90
Figure 3.18. Transmitted cross polarized light photomicrographs of microphyric unit.	91

Figure 3.19. Backscatter image showing the mineral phases identified within an amphibole grain in UWO_2015_26.....	93
Figure 3.20. Backscatter image showing the mineral phases in UWO_2015_26 as identified through EDS microprobe analysis	94
Figure 3.21. Representative photos of Amphibole-rich intrusive.....	95
Figure 3.22. A) Representative hand-sample photo of biotite-rich intrusive	97
Figure 3.23. Backscatter image showing the mineral phases in UWO_2015_48.....	98
Figure 3.24. Backscatter image showing the mineral phases in UWO_2015_48 as identified through microprobe EDS analysis	99
Figure 3.25. Composite cross section of Au mineralization (red zones) in the Upper Beaver deposit in relation to crowded syenite porphyry dikes and the isolated sedimentary sequence (orange) in the Upper Beaver deposit.	100
Figure 3.26 Summary of alteration intensity in UB11_192 based on hand-sample observations	102
Figure 3.27. Sedimentary rocks from the isolated sedimentary sequence	103
Figure 3.28. Wavy deformed beds in graphitic sedimentary rocks	104
Figure 3.29. Photomicrographs of sample UWO_2015_30 showing abundant greenish brown pseudomorphs within a fine-grained quartz-rich matrix.....	106
Figure 3.30. Photomicrographs of sample UWO_2015_30 showing close-up of green pseudomorph.....	106
Figure 3.31. Backscatter image showing the mineral phases identified in the groundmass of UWO_2015_30.....	107
Figure 3.32. Backscatter image showing the mineral phases identified in the green patches in UWO_2015_30.....	108

Figure 3.33. A, B) Upper and lower contact (respectively) between the silty arenite unit and overlying / underlying cherty sedimentary rocks as observed on site.	109
Figure 3.34. Complex intercalated boundary between conglomerate and silty arenite	110
Figure 3.35. Diffuse lower cherty sediment contact in UB_11_190 at 389 m.	111
Figure 3.36. A,B) Cross polarized light photomicrographs of plagioclase and quartz phenocrysts within a fine-grained groundmass in volcanoclastic rocks sample UWO_2015_25; C) Cross polarized light photomicrograph of the edge of a large clast in volcanoclastic rocks unit in UWO_2015_29; D) Photo of typical volcanoclastic rocks unit showing abundant clasts of cherty sedimentary rocks	112
Figure 3.37. Pictures of representative breccias from the Upper Beaver deposit.....	114
Figure 3.38. Two least brecciated samples collected.....	115
Figure 3.39. Petrographic photomicrograph showing cross cutting relationships between chalcopryite, hematite and magnetite.	116
Figure 3.40. Geochemical analysis of brecciated samples from this project compared to available data for relatively unaltered associated igneous intrusions from past projects	117
Figure 3.41. Alteration box plot based on the Ishikawa alteration index (AI) and Chlorite-carbonate-pyrite index (CCPI) showing expected mineralogical changes associated with brecciation.....	118
Figure 4.10. Reflected light photo showing the overprinting relationship between chalcopryite (Cpy), hematite (Hem), and magnetite (Mgt)	123
Figure 4.11. Representative reflected light photomicrographs of mineralization in analyzed thin sections.	137
Figure 4.12. Representative reflected light photomicrographs of gold mineralization in the Upper Beaver deposit.....	138

Figure 4.13. Leapfrog model showing the distribution of Au in the Upper Beaver deposit looking West	141
Figure 4.14. Leapfrog model showing the distribution of Cu in the Upper Beaver deposit looking West.	142
Figure 4.15. Percentile box plots showing the distribution of select trace elements in the deposit arranged by increasing gold grade (10 equal ranges).	145
Figure 4.16. Histogram showing the variation in host rock among and within each mineralized zone in the Upper Beaver deposit.	147
Figure 4.17. (Top) Bivariate Au vs. Ag plot showing the two trends (Ag-rich i.e., $Ag \geq 0.001$) and Ag-poor i.e., $Ag \leq 0.001$) and (Bottom) percentile box plots showing the distribution of select trace elements in each trend.	148
Figure 4.18. Relationship between Au, Cu, Mo, and Ag in select zones in the Upper Beaver Deposit colored by mineralized zone.	149
Figure 4.19. Percentile box plots showing the distribution of select trace elements within in each cluster group	152
Figure 4.20. Au vs. Cu relationship in the Upper Beaver Deposit with colours indicating the respective cluster of each data point	154
Figure 4.21. Distribution of K-Means clusters in the Upper Beaver deposit looking East ..	155
Figure 4.22. PC1 vs. PC2 for the PCA completed on log leveled (by lithology) Au, Cu, S, Ag, Bi, Mo, Ni, Sb, Se, Te, and W.	159
Figure 4.23. PC1 vs. PC3 for the PCA completed on log leveled (by lithology) Au, Cu, S, Ag, Bi, Mo, Ni, Sb, Se, Te, and W	160
Figure 4.24. Binary plots showing the relationships between PC1, PC2, and PC3	161
Figure 4.25. Alteration and mineralization history of the Upper Beaver deposit divided into three main stages of alteration	163

Figure 4.26. Alteration box plot based on the Ishikawa alteration index (AI) and Chlorite-carbonate-pyrite index (CCPI) showing expected mineralogical changes associated with various mineralized samples based on geochemical analysis of samples for this project. ...	164
Figure 4.27. Mean (circle) and median (line) values for Au, Cu, Ag, and Mo based on whether samples are noted to contain different types of alteration minerals.....	167
Figure 4.28. Map highlighting elevated amounts of Au on the Canadian Malartic Corporation property, as identified from the 2013 rock chip survey	170
Figure 4.29. Simplified surface geology of the Upper Beaver Property showing significant major lithological units and local faults, and other surface features of importance	171
Figure 4.30. Gridded maps for select trace elements identifying anomalous surface geochemical signatures for the Upper Beaver Deposit.....	172
Figure 4.31. Gridded maps for major oxides identifying anomalous surface geochemical signatures for the Upper Beaver Deposit	173
Figure 5.1. Maps and associated spectra for Fe K α (top) and Ca K α (middle) at 30.1 keV and 13.1 keV	178
Figure 5.2. (left) RGB image produced for UWO_2015_10 where R=Fe K α , G=Cu K α , and B=Au L α . (right) reflected light photo micrograph showing pyrite (py) grain of interest ...	180
Figure 5.3. RGB image of Au-bearing pyrite grain from UWO_2015_10 where R=Fe K α , G=Cu K α , and B=As K α	181
Figure 5.4. Isolated pyrite grain of interest from UWO_2015_10 mapped at CHESS	182
Figure 5.5. Isolated pyrite grain of interest from UWO_2015_10 mapped at APS.....	183
Figure 5.6. Trace element maps of UWO_2015_10	186
Figure 5.7. Photomicrograph showing the distribution of Au in UWO_2015_10.....	187

Figure 5.8. RGB image showing the distribution of Fe K α , Cu K α , and Au L α in UWO_2015_05	188
Figure 5.9. Energy map showing the distribution of Fe K α , Cu K α , and Au L α in the RGB image on the top left as well as individual energy maps for Fe K α , Cu K α , Au L α , As K α , and Ni.....	189
Figure 5.10. RGB image produced by XRF mapping at CHESS showing the distribution of Mo K α , Fe K α , and Au L α in UWO_2015_08	190
Figure 5.11. RGB image showing the distribution of Fe K α , Co K α , and Au L α in UWO_2015_02	192
Figure 5.12. (upper) Photomicrograph of Ni-rich pyrite grain in sample UWO_2015_04. Au mineralization is observable in may fine fractures in the grain. (lower) SR-XRF energy maps of zoned pyrite grains from UWO_2015_04	193
Figure 5.13. Trace element XRF maps of Au L α , As K α , Fe K α , and Ni K α in UWO_2015_04.....	194
Figure 5.14. (top) Trace element SR-XRF maps of various elements (Au L α ; As K α ; Co K α ; Cu K α ; Fe K α ; and Ni K α) (Bottom) corresponding photomicrograph of pyrite grain analyzed by SR-XRF	195
Figure 5.15. A) RGB image showing the distribution of Fe K α , Bi L α , and Au K α in UWO_2015_02.....	197
Figure 5.16. (A) Photomicrograph of mineralized pyrite grain surrounded by chalcopyrite in KF15	198
Figure 5.17. RGB image showing the distribution of Fe, W, and Cu in UWO_2015_10....	199
Figure 5.18. (Top) SR-XRF energy maps of KF15	200
Figure 5.19 XRF trace element map showing a Au hot spot with the green box representing a sample area that was analyzed to determine the Au:Ag ratio in the particular hot spot.....	201

Figure 6.1. Classification diagrams including TAS Plutonic diagrams by Middlemost, (1994) and Cox et al., (1979) as well as plutonic Rock Classification diagram by Debon and La Fort, (1983).....	205
Figure 6.2. QAP classification diagram showing CIPW normative values for four main members of the Upper Beaver Intrusive Complex	206
Figure 6.3. Alteration box plot based on the Ishikawa alteration index (AI) and Chlorite-carbonate-pyrite index (CCPI) showing alteration trends among select lithologies from the Upper Beaver Intrusive Complex	209
Figure 6.4. QAP classification diagram showing CIPW normative values for select lithology in the Upper Beaver Intrusive Complex	210
Figure 6.5. Alteration box plot based on the Ishikawa alteration index (AI) and Chlorite-carbonate-pyrite index (CCPI) showing alteration trends among select lithologies from the Upper Beaver Intrusive Complex	211
Figure 6.6. Au versus Cu plot for Precambrian intrusion-related and stockwork-disseminated deposits superimposed on geochemical data from the Upper Beaver deposit.....	228

List of Appendices

Appendix A: Hand Sample and Petrographic Description of Collected Samples	248
Appendix B: Detection Limits and Substituted Population Values for the Upper Beaver Dataset.....	301
Appendix C: Summary Statistics for the Upper Beaver Dataset	306
Appendix D: Geochemical Analysis Results for Mineralized Samples in the Upper Beaver Deposit	309
Appendix E: Element Excitation Energies	1
Appendix F: Major Oxide Percents and Calculated CIPW Normative Values	1
Appendix G: APS Standard Operating Procedures	1
Appendix H: GeoPIXE Standard Operating Procedures	11
Appendix I: Microprobe Results.....	30

1 Chapter 1: Introduction and Background

1.1 Mining in Kirkland Lake

Canada is host to some of the most extensive and profitable gold deposits in the world, making it a leader in the global gold market. Many of these deposits are located within the Abitibi Subprovince, a division of the Superior Province, and the largest Archean craton of the Canadian Shield extending for over 500 km E-W from west of Timmins, Ontario to east of Chibougamua, Quebec (Card, 1990; Hodgson et al., 1991; Phillips, 2005). The Abitibi t is one of the world's most prolific gold and base metal producing regions (Benn & Peschler, 2005) with an estimated mineral production of \$120 billion as of 2005 (Thurston et al., 2008).

The town of Kirkland Lake is located within the prolific Southern Abitibi Greenstone Belt, an Archean greenstone belt that also contains prolific economic deposits of gold, zinc, copper, silver, nickel, and PGE's (Poulsen et al., 1992). Gold was first discovered in the Kirkland Lake region in 1906 on the shores of Larder Lake. The region promptly became the site of the first gold rush in northeastern Ontario (Ewert et al., 2011). Production of the first gold mines in Kirkland Lake began in 1910 with the opening of the Gateford and Swastika Mines (Ewert et al., 2011; Kishida and Kerrich, 1987). Gold production in Kirkland Lake was continuous for 90 years, until the closure of the Macassa Mine in 2000 (Isopolatov et al., 2008). The camp produced more than 760 metric tonnes of Au from 25 mines from 1910 to 2002 (Dubé and Gosselin, 2007 and references therein). In 2002, Kirkland Lake Gold Inc. re-opened the Macassa Mine and is has been actively mined since. The Kirkland Lake camp ranks second in Canada, after Timmins, with respect to total ounces of gold produced (Dubé and Gosselin, 2007). The location of the Upper Beaver property is shown in Figure 1.1, below.

Alfred Beauregar first discovered gold on the Upper Beaver property in 1912 (Alexander, 2006). Following discovery, the deposit was exploited as the historic Argonaut Mine, which was in operation between 1919-1920, 1923-1928, and 1965-

1972 (Bernier and Cole, 2012). Following and between periods of production, the property was a target of several surface, shaft, and drilling operations. Past production includes a total of 140,709 oz Au and 11,955,312 pounds of Cu from 526,678 tonnes grading 8.31 g/t Au and 1.03% Cu (Alexander, 2006).

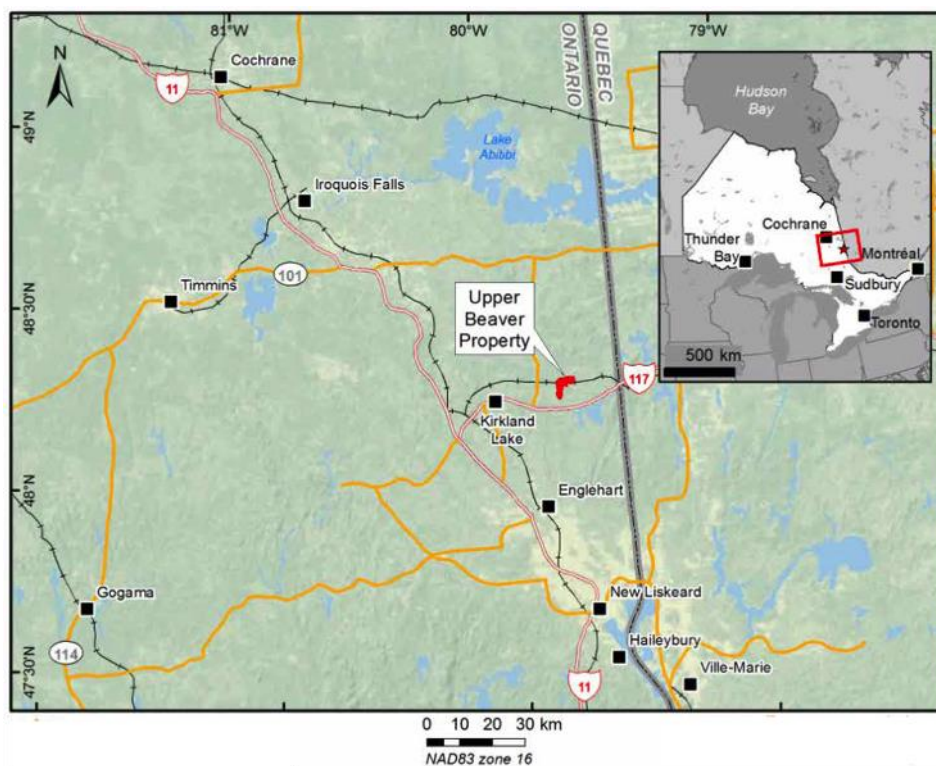


Figure 1.1. Location of the Upper Beaver property. Figure modified after (Bernier and Cole, 2012).

1.2 Regional Geology

The vast majority of gold deposits in metamorphic terranes like the Abitibi Greenstone Belt are related to large first-order, deep-crustal fault zones, although the deposits themselves are not typically directly hosted in the faults. These near-vertical fault zones have complex structural histories, with a strike length of several hundred kilometers and a width of a few hundred to as much as a few thousand meters. They tend to run parallel to sub-parallel to major lithological contacts, which acted as major crustal dewatering conduits during repeated episodes of pressure fluctuations

as seismic events drove fluid migration from the deep-crust (Robert, 2001; Goldfarb et al., 2005; Dubé and Gosselin, 2007).

In the southern Abitibi Greenstone Belt the two major first-order structures that are related to gold deposits include the east-west trending anastomosing zones of high strain: the Porcupine-Destor Deformation Zone (PDDZ) and the Larder-Lake Cadillac Deformation Zone (LLCDZ). These high-strain zones are locally known as “breaks”. Gold deposits mainly occur at jogs or changes in the strike along the second- and third-order structures, which were probably connected to the first-order structures during gold mineralization events (Groves et al., 2003; Goldfarb et al., 2005). Additional less common sites that host gold deposits include fault intersections, areas of regional uplift or anticlines, and zones of competency contrast such as at intrusion margins (Groves et al., 2005). The precise fluid-flow paths, the source of the fluids, and how the fluid evolved as it passed from one part of the system to another, are still unclear and are commonly a topic of debate (Dubé et al., 2015). Similar to other greenstone gold deposits, most of the gold deposits in the Abitibi likely formed during the late stages of orogeny and as such are widely classified under the relatively diverse “orogenic gold” category (Goldfarb et al., 2005). Orogenic gold deposits include epizonal (≤ 6 km, $150\text{-}300^{\circ}\text{C}$), mesozonal (6-12 km, $300\text{-}475^{\circ}\text{C}$), and hypozonal (>12 km, $>475^{\circ}\text{C}$) deposits, whose classification is based on the pressure and temperature conditions of ore formation, as suggested by Bohlke (1982). The term orogenic gold deposit is not universally accepted however as it is commonly used in literature it is also used here. The Kirkland Lake deposits in particular are dominantly classified as mesothermal orogenic lode gold deposits, where mineralization was closely associated with hydrothermal fluid circulation and deposition of gold along major and splay fault and deformation zones, and with gold mineralization being largely hosted within laminated quartz-carbonate fault fill veins (Dubé and Gosselin, 2007). Groves et al., (1998) identified that subduction-related events likely periodically raised the geothermal gradient within hydrated accretionary sequences, initiating and driving long-distance hydrothermal fluid migration from the mantle, resulting in the formation of gold-bearing quartz veins that were emplaced within 15-20 km of the surface.

The Kirkland Lake Gold Camp is situated on the southern limb of the regional Blake River synclinorium, which is truncated in the north by the Destor-Porcupine Break and in the South by the Larder-Lake Cadillac Break and its associated deformation zone (Ewert et al., 2011). Both breaks are east trending and steeply inclined (Kerrich and Watson, 1984). The east-plunging synclinorium extends from the Lake Abitibi batholith to the Round Lake batholith (Kerrich and Watson, 1984).

The Cadillac-Larder Lake Break is considered to have been a major east west thrust fault with associated hydrothermal carbonation that later experienced expansion, creating a basin that was filled with calc-alkaline volcanic and clastic sedimentary rocks of the Timiskaming Group (Dimroth et al., 1983; Ayer et al., 2005). Later compression of this area created parallel and splay faults in the Timiskaming and Lower Tisdale group rocks, such as the Kirkland Lake Main break, along which many of the Kirkland Lake gold deposits were formed, (Figure 1.2; Ewert et al., 2011).

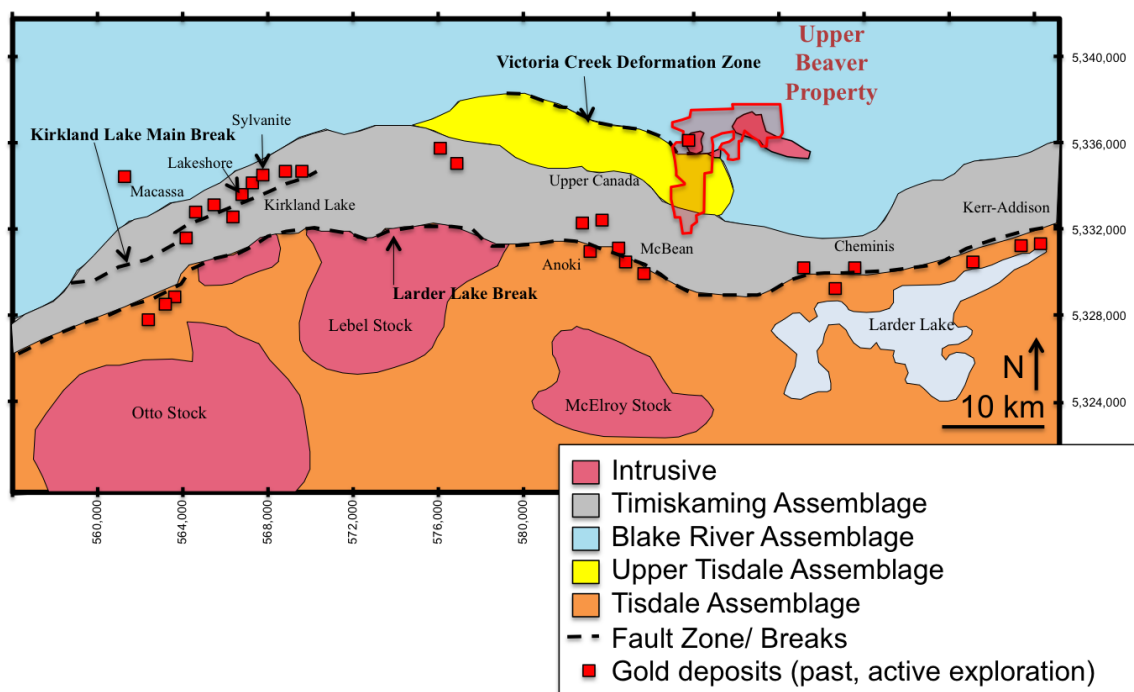


Figure 1.2. Regional geology of the Kirkland Lake and Larder-Lake areas showing the distribution of past and active exploration projects, regional

deformation zones/breaks, and simplified regional geology. Figure modified from Breede et al., (2011).

The Larder Lake-Cadillac Break is up to 600 m wide and is represented by a steeply south-dipping zone of intense ductile deformation and carbonate-chlorite alteration (Wilkinson et al., 1999). Seismic reflection surveys indicate that the LLCB extends to a depth of up to 15 km (Jackson et al., 1990; Cruden and Launeau, 1993). It follows the contact between the 2680-2670 Ma alkalic metavolcanics and clastic metasediments of the Timiskaming Group to the north and the 2705 Ma old mafic metavolcanics and turbidities of the Larder Lake Group to the south (Cruden and Launeau, 1993). North of the break, the Timiskaming Group forms a steeply dipping syncline that lies unconformably over 2701 Ma mafic to felsic metavolcanics of the Blake River Group (Cruden and Launeau, 1993). To the South, the Larder Lake Group rocks are faulted against a north to northeast-dipping sequence of meta-volcanics that are approximately 2747-2701 Ma, which wrap around the Round Lake batholith (2703-2697 Ma) (Cruden and Launeau, 1993; Jensen 1985; Jackson and Fyon, 1991).

In a recent re-interpretation of the break, Bleeker (2015) proposes that synorogenic extension initiated the production of the fault zones, likely in association with upper mantle processes, alkaline magmatism, increased heat flow into the lower crust, and synorogenic basin development. Magmatic and hydrothermal processes produced the gold deposits as a result of this extensional regime. Following deposit development, the deep reaching extensional faults were inverted as thick-skinned thrusts, which effectively uplifted the mineralized hanging wall portion of the faults. Bleeker (2015) uses this process to explain the lack of mineralization in the hanging wall of the Abitibi gold deposits. He also proposes that a combination of extension, mantle-related magmatism, increased heat flow, and the formation of the major faults acted as an engine to drive gold mineralization events.

1.3 Introduction to the Project

Canadian Malartic Corp. (CMC) currently maintains the largest land holdings package in the Kirkland Lake gold camp, consisting of more than 30 properties,

covering an almost contiguous area of approximately 230 km². The properties host 10 gold deposits, including five NI43-101 compliant properties that contain current and historic mineral resources of 2 million ounces (measured and indicated) and 1.8 million ounces (inferred), as outlined in Table 1.1 (Ewert et al., 2010; Ewert et al., 2011; Gamble, 2011; Puritch et al., 2011; Bernier and Cole, 2012).

Table 1.1. Indicated and inferred mineral resources for CMC's five NI43-101 compliant properties

Property	Indicated	Inferred	Reference
Amalgamated	1,145,126 t @ 4.47 g/t	1,530,067 t @ 4.21 g/t	Gamble, 2011
Kirkland	(164,573 oz Au)	(206,991 oz Au)	
Anoki-McBean	1,436,000 t @ 4.69 g/t (216,400 oz Au)	1,558,000 t @ 4.73 g/t (236,800 oz Au)	Ewert et al., 2010
Bidgood	1,464,000 t @ 1.69 g/t (79,000 oz Au)	318,000 t @ 2.02 g/t (21,000 oz of Au)	Puritch et al., 2011
Upper Canada	1,959,000 t @ 2.17 g/t (137,000 oz Au)	4,895,000 t @ 4.02 g/t (633,000 oz Au)	Ewert et al., 2011
Upper Beaver	6,870,000 t @ 6.62 g/t (1,461,000 oz Au)	4,570,000 t @ 4.85 g/t (712,000 oz Au)	Bernier and Cole, 2012
Total	2,057,973 oz Au	1,809,791 oz Au	

CMC's five Kirkland Lake NI43-10 compliant properties (Upper Beaver, Anoki-McBean, Bidgood, Upper Canada, and Amalgamated Kirkland) are located along the Larder Lake-Cadillac deformation zone and are classified as lode gold deposits, where economic concentrations of gold developed from hydrothermal fluids in veining systems of epithermal to mesothermal origin (Ewert et al. 2010). Mineralized zones within these deposits tend to be associated with strongly altered zones, especially those altered by carbonate, silica, and sericite (Ewert et al, 2010; Puritch et al. 2011; Ewert et al. 2011).

The Upper Beaver deposit however, is atypical of the area. Unlike the lode gold deposits in the Larder Lake and Kirkland Lake area, the Upper Beaver deposit consists of abundant gold and copper mineralization, associated with widespread and pervasive magnetite-feldspar-actinolite-epidote-carbonate-sericite alteration. Further, mineralization at the Upper Beaver deposit is not associated with the Larder Lake Cadillac Deformation Zone, which lies roughly 8 km south of the Upper Beaver property, but with a 600 m wide intrusive complex called the Upper Beaver Intrusive

Complex (Bernier and Cole, 2012). The Upper Beaver deposit has a historic production of 140,000 oz. Au and 11.9 million lbs of Cu from 526,678 tonnes grading 8.3 g/t Au and 1% Cu. (Puritch et al., 2012). Further, the most recent NI 43-101 resource published in September 2012 defines an indicated resource of 6,870,000 t @ 0.37% Cu, 6.62 g/t Au and an inferred resource of 4,570,000 t @ 0.32% Cu and 4.85 g/t Au (Bernier and Cole, 2012).

The deposit was historically classified as a volcanogenic exhalative deposit due to the abundance of hydrothermal magnetite and apparently stratabound mineralization in a mafic volcanic-sedimentary sequence (Morris, 1974). Following publication, further work on the deposit identified two types of ore, namely syngenetic or exhalative gold-copper and chalcopyrite-pyrite-magnetite veins, which contributed to deposit model more consistent with greenstone-hosted orogenic Archean gold (Roberts and Morris, 1982), similar to mineralization in the Kirkland Lake gold camp. However, due to the atypical features of the deposit outlined above, the classification has always remained enigmatic. Recent reevaluation of the deposit by Kontak et al. (2008) found that features of the deposit are consistent with a magmatic-hydrothermal origin, but more closely resemble syenite-associated gold deposits or iron oxide copper gold systems as opposed to a strictly lode-gold system. Kontak et al. (2008) concluded that the deposit should be classified as a syenite-associated copper-gold deposit, with some features being more consistent with deposits in the Timmins camp, and with other features more closely resembling an IOCG deposit. Presently, as outlined in the 2012 Technical report on the property, the Upper Beaver deposit is classified as an oxidized, magmatic-hydrothermal, syenite-associated Au-Cu, where the deposit developed syngenetically with an alkaline intrusive body as part of a magmatic-hydrothermal system (Bernier and Cole, 2012).

1.4 Objectives

With the ever-growing massive quantities of geochemical databases, multivariate data analysis methods are becoming increasingly necessary in geological model generation and exploration targeting (Ding and He, 2004). The objectives of this study are to use company-provided data, supplemented with selective core sampling,

to evaluate what information can be attained from company-provided data. The evaluation focuses on documenting and characterizing key lithologies and mineralization signatures in the Upper Beaver deposit. More specific objectives of this project of include:

1. Assess the geochemical signature of intrusions and host rocks (including the sedimentary package and breccia lens) in the Upper Beaver deposit in order to better define the lithologies and to draw conclusions on their genesis and their relationship to mineralization;
2. Assess large-scale geochemical associations with gold mineralization using available company data through exploratory data analysis to better understand spatial variations in mineralization styles; and
3. Utilize synchrotron source x-ray fluorescence microprobe analysis (SR-XRF) to supplement exploratory data analysis of bulk rock geochemical data in order to evaluate the micro-scale spatial relationship between Au mineralization and trace element exploration vectors.

1.5 Previous Work

Previous work on Canadian Malartic Corporation's Kirkland Lake properties includes a detailed technical report that evaluates the economic potential of all CMC's Kirkland Lake properties by Alexander (2006) and two detailed reports specifically focused on assessing mineral resources at Upper Beaver. These reports include the technical report and mineral resource estimate update prepared by Breede, Risto, and Kociumbas, of Watts, Griffs, and McOuat in 2011, and a technical report produced by Bernier and Cole of SRK Consulting in 2012.

Additional work on the Upper Beaver deposit includes a Special Volume CIM publication by Roberts and Morris (1982) on the geological setting of the Upper Beaver Mine, and an open file report by Kontak et al., (2008). Studies by Roberts and Morris (1982) concluded that there are two main types of ore in the deposit, including syngenetic or exhalative gold-copper and chalcopyrite-pyrite-magnetite veins, which were both likely derived syngenetically. The Open File Report by Kontak et al.,

(2008) focused on documenting key features of the Upper Beaver deposit including discussing main lithologies, mineralization and alteration styles, and assessed trace element correlations with Au. It concluded that the deposit is characterized by an Au-Ag-Hg-Te-Bi-Sb association, and the deposit shares similarities with intrusion-related gold deposits, porphyry-type deposits, syenite-associated deposits, and IOCG gold systems.

In addition to published papers, Talisker Exploration Services Inc produced three unpublished external assessment reports on the property including: (1) an assessment on the multi-element drill hole geochemistry of the Canadian Kirkland, Upper Beaver, and Bidgood deposits (Talisker, 2014a); (2) a petrologic and chemical study on igneous rocks from the Canadian Kirkland, Bidgood, and Upper Canada Deposits (Talisker, 2014b); and (3) age-dating using U-Pb zircon analysis of 7 volcanic and intrusive rock samples performed by Dr. Victor Valencia of VU Geoservices Corp located in Tucson AZ and calculated using Isoplot (Talisker, 2014c). Talisker (2014a) concluded that Au mineralization at Upper Beaver had a very strong positive correlation with Ag, Mo, and S, and a moderate positive correlation with Ni, Cu, W, Bi, and Fe. It also concluded that Upper Beaver has a moderate negative correlation with Na. As well, the main findings by Talisker (2014c) concluded that the main mineralizing event at Upper Beaver most likely occurred between 2674-2671 Ma and a late mineral to post mineral intrusive event, which occurred between 2671 to 2665 Ma, followed. They also suggest that the main ore controls included pre- to syn-magmatic faults, dikes, and lithological controls, however they noted that the strong deformation event that produced the shear zones was late to post mineralization. Thus, Talisker (2014c) proposed that mineralization in the Upper Beaver deposit developed prior to mineralization in the Larder Lake and Kirkland Lake gold camps, (Isoplatov et al., 2008).

For the past eight years, the University of Western Ontario (UWO) has also undertaken geologic research work on the Kirkland Properties by successive cooperation with Vault Minerals, Queenston Mining, Osisko Mining Corporation, and Canadian Malartic Corporation. Although the research directive has varied over

the years, a common objective has been maintained; namely to better characterize near-surface and deep mineralization in the Kirkland Gold Camp using optical petrography, stable isotope analysis, electron microscopy, trace element and rock geochemistry methods. Student projects that focus specifically on the Upper Beaver deposit include two projects by students from the University of Western Ontario and one project by a student from the University of Waterloo including: (1) An assessment of the mineralogy, textures, and major and trace element whole-rock geochemistry of gold bearing veins in drill core as it relates to depth across the East and West Porphyry Zones by Griffin (2011); (2) An assessment of the five main lithologies in the deposit in terms of mineral assemblages and trace element signatures of least-altered whole-rock drill core samples by DeAgazio (2012); and (3) An assessment of the alteration assemblages in drill core from the South Contact Zone to define alteration and whole rock geochemical associations with Au mineralization by Feick (2014) from the University of Waterloo. Findings by Griffin (2011) on major and trace element geochemical analysis indicated variable pathfinder element correlations with gold between the East and West Porphyry Zones, possibly related to differences in mineralizing fluid chemistry or more likely the structural level of the deposit on either side of the diabase dyke. Griffin (2011) also concluded that gold typically occurs as inclusions within anhedral chalcopyrite grains that typically have a sieve texture. Inclusions of gold within magnetite and pyrite grains also occurred within several samples. The results of the study by DeAgazio (2012) indicated that all rocks showed some degree of alteration and that there was no difference between oxygen isotopes between fresh and altered samples, suggesting that the alteration system may be more extensive than previously thought. All samples DeAgazio analyzed were enriched in LREEs and depleted in HREEs except for the Tisdale Assemblage, which was more depleted in LREEs relative to chondrite normalized values proposed by Taylor and McLennan, (1985). Finally, the research project completed by Feick (2014) concluded that there were three main alteration assemblages in the strongly altered basalt from the South Contact Zone. These assemblages include early clinocllore \pm hematite \pm goethite \pm magnetite alteration, followed by K-spar \pm albite \pm silica alteration, and late epidote \pm calcite \pm

silica. Overall, evidence from this study suggested that the South Contact Zone is intimately related to the other mineralized zones in the Upper Beaver Deposit and that the localized strong alteration was likely the result of a combination of hydrothermal alteration and contact metamorphism, caused during the intrusion of members of the Upper Beaver Intrusive Complex, specifically a crowded syenite porphyry dike. The underlying volcanoclastic rocks unit may also have acted as an impermeable lower boundary due to competency contrasts between the basalt and the volcanoclastic rocks, and focused fluid circulation in the overlying basalts (Feick, 2014).

This thesis aims to further document the main lithologies in the Upper Beaver deposit that are associated with mineralization in Chapter 3 using company provided data and select hand samples and thin sections. It also aims to statistically assess large amounts of company-provided bulk rock geochemical data in order to draw conclusions on ore genesis and styles of mineralization across the entire Upper Beaver deposit in Chapter 4. Finally, Chapter 5 will focus on assessing samples from all mineralized zones in the deposit using synchrotron source XRF microprobe analysis to provide the necessary mineralogical context to explain the trace element correlations identified in Chapter 4.

1.6 Deposit Geology

The Upper Beaver deposit lies roughly 8 km north of the Larder-Lake Cadillac Break and 30 km east of Kirkland Lake, hosted within a succession of volcanic and volcanoclastic rocks that fill a basinal feature on the northern margin of the Timiskaming basin (Bernier and Cole, 2012). A simplified surface map is provided in Figure 1.3, and a geological model showing the main lithological units, and a composite cross section that shows the distribution of mineralization in the deposit, are provided below in Figures 1.4 and 1.5, respectively. In a recent technical report mineral reserves for the Upper Beaver deposit were reported to be 6,870,000 tonnes

@ 6.62 g/t, or 1,461,000 oz Au, while mineral resources were reported to be 4,570,000 tonnes @ 4.85 g/t, or 712,000 oz Au (Bernier and Cole, 2012).

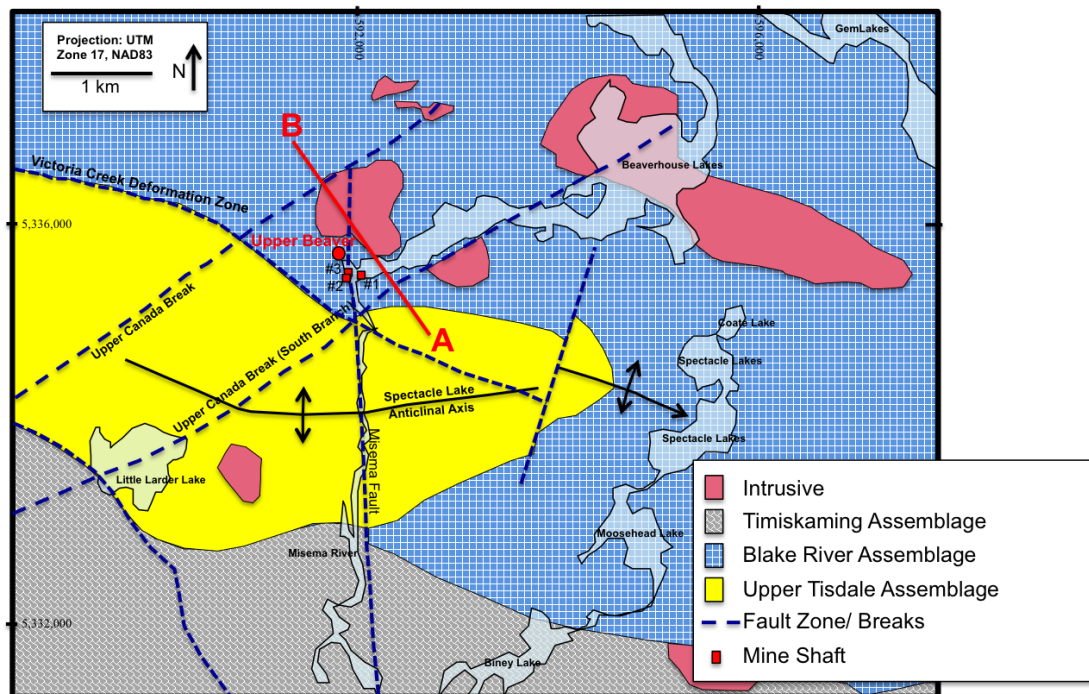


Figure 1.3. Simplified surface geology of the Upper Beaver Property showing the location of the composite cross section provided in Figure 1.5, as well as significant major lithological units and local faults. The Upper Beaver Intrusive Complex is located at the contact between the Blake River and the Upper Tisdale Assemblages, which the Victoria Creek Deformation Zone also in part follows. The Intrusive Complex dips Northwesterly at roughly 60-70 degrees. Figure modified from Alexander, (2006).

The oldest rock unit on the property is part of the 2710-2704 Ma Tisdale Assemblage, which is composed of a variety of volcanic to volcanoclastic rocks, including komatiitic, tholeiitic, and calc-alkaline rocks (Ayer et al., 2005; Bernier and Cole, 2012). Formerly called the Gauthier Group, the Upper Tisdale Assemblage consists mainly of fine-grained, finely bedded, strongly altered and sheared tuff that range in colour from orange to reddish brown to greenish gray. Tuff breccia is also present in this formation, which contains elongated and rounded fine to coarse-grained fragments within a fine-grained ash-rich matrix that is foliated around the fragments.

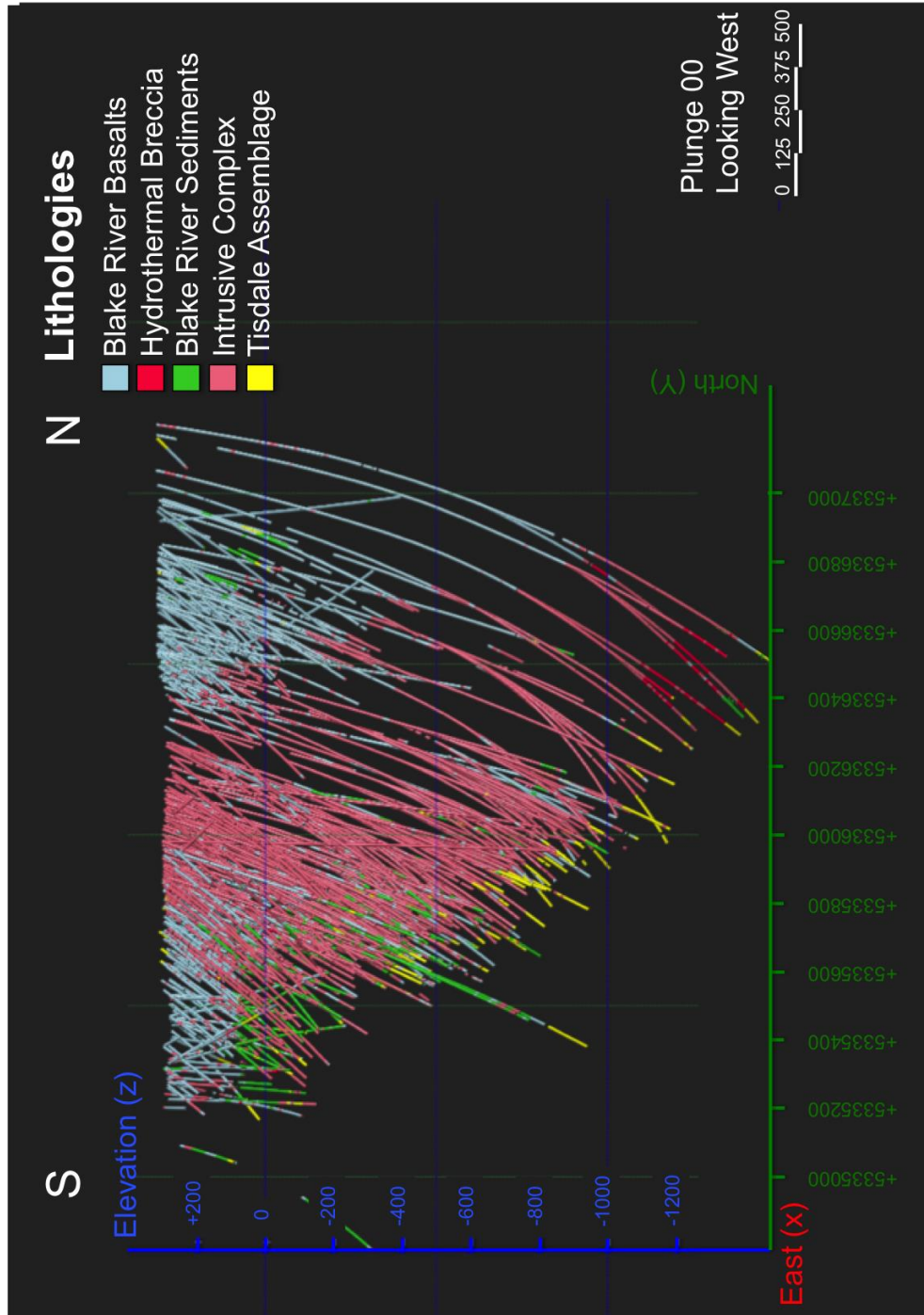


Figure 1.4. Geological model showing major lithological units in the Upper Beaver deposit looking West. Model created in Leapfrog Geo™ software based on logging of 592 drill holes by Canadian Malartic Corporation geologists. Scale and orientation is shown on the bottom right of the figure.

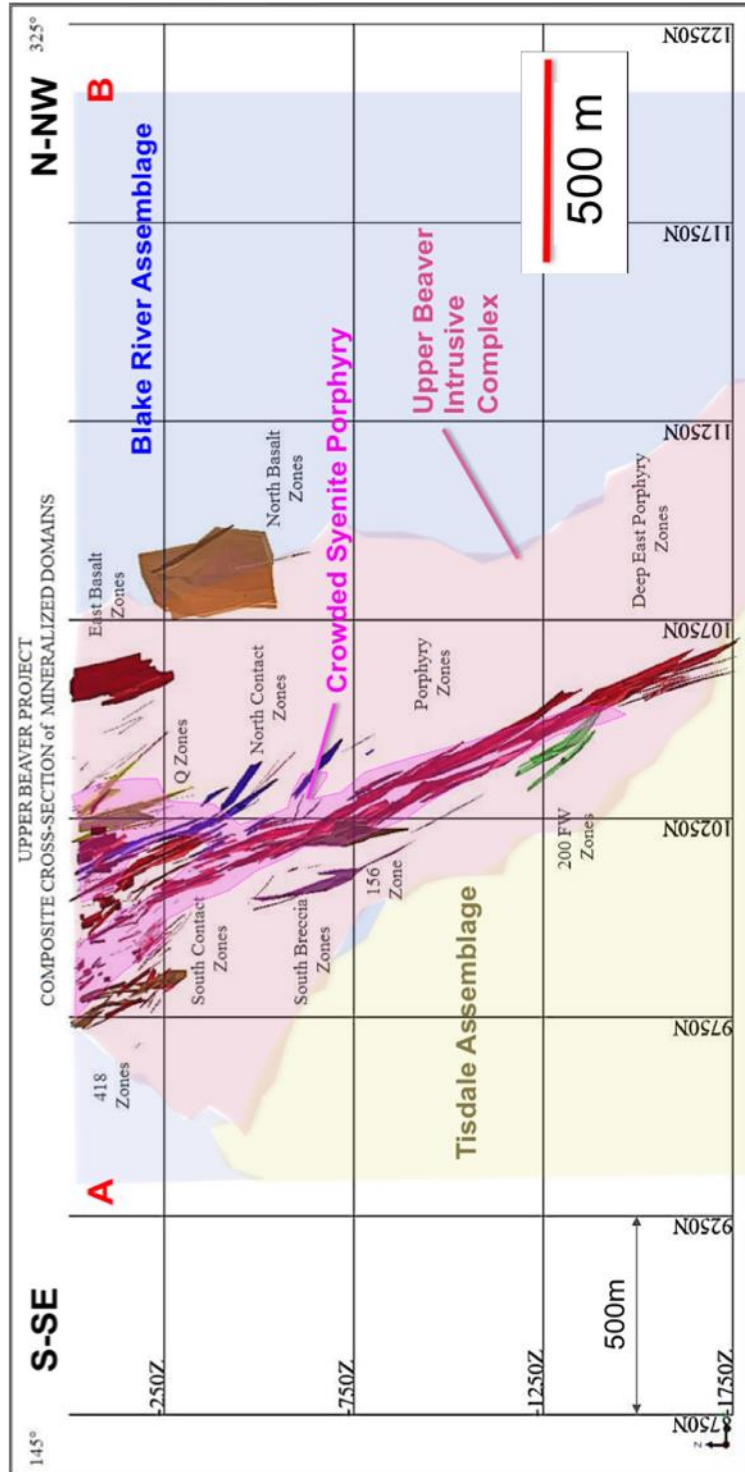


Figure 1.5. Modified composite cross section of mineralized zones in the Upper Beaver deposit in relation to the major lithological units. A and B correspond to Figure 1.3. Original figure provided by Canadian Malartic Corporation. Elevated (z) is shown on the y-axis of the figure from surface while distance is shown along the x-axis according to UTM NAD 85 (Zone 17) gridlines.

The 2701-2696 Ma Blake River Assemblage (formerly called the Kinojevis Group) overlies the Tisdale assemblage and consists of calc-alkaline basalts, tholeiitic mafic volcanics, and rhyolite (Dimroth et al., 1983; Ayer et al., 2005). Together, the two Assemblages record at least two cycles of volcanism, each composed of komatiitic, tholeiitic, and calc-alkaline volcanics (Kishida and Kerrich, 1987). The units themselves are interpreted to represent individual overlapping shield volcanoes with local lenses of sediments intercalated with or capping volcanic cycles (Dimroth et al., 1982; Thurston et al., 2008). Assemblage studies by Goodwin (1980) indicate that the lava flows were likely thick, extensive, and rapid, with large-scale magma outpourings. Goodwin (1980) further argues that the pillows indicate a submarine extrusive environment and the sparse amounts of interflow sediments between flow layers indicate that magmatism occurred at substantial water depths. This is supported by studies by Pearson and Daigneault (2009) who argued that the Blake River Group formed as a subaqueous overlapping and nested caldera complex.

Volcanism and plutonism were terminated by 2,700 Ma as a result of the collision of a large continental mass to the south (Cruden and Laneau, 1993). An extended period of deformation, referred to as D1 deformation, occurred at the end of this collision between 2,687 and 2,680 Ma (Robert, 2001). D1 involved contractional deformation, resulting in early tilting, folding, and local thrusting of supracrustal units as well as the emplacement of diorite-tonalite intrusions (Robert, 2001). A number of upright east-west-trending anticlines and synclines were developed at this time, such as the Blake River synclinorium, which hosts the Kirkland Lake gold camp (Dimroth et al., 1983; Wilkinson et al., 1999). Robert (2001) suggests that in the Noranda district there is evidence that the major fault zones, which would later host gold mineralization, developed and were active during D1, prior to Timiskaming sedimentation.

The termination of D1 marks the beginning of Timiskaming sedimentation (2677-2670 Ma), which produced the Timiskaming Assemblage (Ayer et al., 2005). The Timiskaming Assemblage overlies the older volcanic units unconformably, and consists mainly of clastic alluvial-fluvial sedimentary units, and locally intercalated

high-level alkaline volcanic rocks and their local volcanic equivalents that cross cut the local assemblages (Robert, 2001; Ayer et al., 2005; Isopolatov et al., 2008).

Post D1 activities included an episode of compression, D2, which consisted of regional shortening north-south across the belt and possible sinistral transpression, as suggested by Bleeker and Parish, (1996) and Wilkinson et al., (1999). Structural relationships and age dating can be used to constrain the timing of syenite-associated gold deposit development to between D1 and D2 during the Timiskaming-type sedimentation (Robert, 2001). Local orogenic gold deposits, including the Upper Canada, and the McBean and Anoki deposits east of Kirkland Lake formed during D2, along the Upper Canada deformation zone splay fault and the Larder Lake Cadillac Deformation Zone, respectively (Isopolatov et al., 2008). Isopolatov et al., (2008) suggests that the formation of these deposits is most likely related to a regionally extensive hydrothermal system that was associated with the Larder Lake-Cadillac deformation zone. The D2 transpression event later evolved into the third deformation episode, D3, which involved dextral transverse thrust faults centered along the major fault zones, although mineralization is not associated with this deformation event (Bleeker and Parrish, 1996). Locally deformation was most intense along the Destor-Porcupine Fault Zone and the Cadillac-Larder Lake Fault zone. D4 followed D3 and consisted of northwest-southeast shortening. The Kirkland Lake deposit, which is located off of the '04 break, formed during D4, synchronous with with reverse-dextral movements along the ore-controlling Kirkland Lake fault (Isopolatov et al., 2008). The Kirkland Lake deposit is characterized by sulphide-poor gold- and telluride-rich mineralization with a metal signature of Te-Au, Mo, Pb, Ag, high Au/Ag, and low As) which was interpreted by Isopolatov et al., (2008) to be likely related to a separate hydrothermal system that linked to a deep magmatic fluid source separate from the deposits east of Kirkland Lake.

1.7 Structural Geology

The deposit sits on the north flank the Spectacle Lake anticline, an east to east-southeast trending anticline. The anticline has been described by Alexander (2006) to plunge south-easterly from a well-defined closure eastward on the Lac McVittie lands, and by Jackson and Fyon (1991) as upright and doubly plunging. The Upper Tisdale Assemblage on the property sits in the core of this anticline.

The Larder Lake Cadillac Deformation Zone, which was one of the main controls for gold mineralization in the Archean, is located 8 km south of the Upper Beaver deposit. The deposit is spatially associated with a subtle deformation zone that is roughly subparallel to the Larder Lake Cadillac Break and coincides with a wide zone of sericitic alteration that occurs on the property. This structure, which occurs as a high strain zone at the contact between the Tisdale and Blake River Assemblages, is called the Victoria Creek Deformation Zone, as shown on Figure 1.3. This deformation zone is thought to correlate with the Victoria Creek deposit 5.5 km to the west, where mineralization is hosted in calc-alkaline volcanoclastic rocks of the Upper Tisdale assemblage near the contact with the Lower Blake River basalts (Pflug et al., 1993). The Victoria Creek Deformation Zone likely represents a component of movement related to the Larder Lake Cadillac Deformation Zone (Alexander, 2006). Studies by Roberts and Morris (1982) identified that the deformation zone formed during D0 deformation, which they argue was contemporaneous with volcanism. The lithology contrast at this contact likely played a critical role in focusing fluid migration and was likely intimately related to gold mineralization and intrusion emplacement on the property (Roberts and Morris, 1982; Bernier and Cole, 2012). The exact location of the Victoria Creek Deformation Zone is poorly understood, although for the most part it strikes northwest, dips 065-070 degrees to the northeast, and is typically represented as a broad zone of ductile shearing and strong sericitic alteration (Bernier and Cole, 2012). Dikes and plugs of the Upper Beaver Intrusive Complex likely intruded along, and adjacent to, the Victoria Creek Deformation Zone. As a result, the southern margin of the intrusive-

basalt contact, which includes the Victoria Creek Deformation Zone, is a sheared margin.

Alexander, (2006) also suggested that the intrusions on the property might be spatially related to two splays off of the Larder Lake-Cadillac Deformation Zone, namely the parallel northeast-trending Upper Canada Break and the Upper Canada South Branch. The Upper Canada Break is of particular interest as it hosts the Upper Canada deposit 7 km southwest of the Upper Beaver deposit. If the Upper Canada break is extrapolated along its strike length it tracks roughly 900 m north of the Upper Beaver #3 shaft and if the South Branch is tracks 400 m south of the shaft (Isoplatov et al., 2005; Kontak et al., 2008).

Finally, a younger structure, the North-South Misema fault, consists of a very strong broad mud-clay fault and hosts the barren diabase intrusion on the property along its western margin (Bernier and Cole, 2012). This fault played a role in offsetting the East and West sections of mineralization on the property (Bernier and Cole, 2012).

1.8 Mineralization

Au and Cu mineralization at Upper Beaver is centered on the 600 m wide polyphase intrusive complex referred to as the Upper Beaver Intrusive Complex, consisting of a main igneous body with associated dikes, sills, and apophyses (Bernier and Cole, 2012). Alteration, intrusive breccias, and chilled margins are evidence that the complex intruded as pulses of magma that were replenished by a deep magma chamber (Kontak et al., 2011). Gold and copper mineralization occurs within, proximal to, and outbound of this intrusive complex and is commonly associated with widespread alteration (Bernier and Cole, 2012). Primary hosts for mineralization include the Blake River basalts and members of the polyphase intrusive complex; especially the rocks referred to as mafic syenite and crowded syenite porphyry phases (Bernier and Cole, 2012). The current exploration model for the Upper Beaver deposit is one of oxidized, magmatic-hydrothermal, syenite

associated Au-Cu, where deposit developed syngenetically with an alkaline intrusive body as part of a magmatic-hydrothermal system (Bernier and Cole, 2012).

1.8.1 Au Mineralization

Au mineralization is complex, consisting of a wide range of different mineralization styles, including both vein-style and replacement-style mineralization, as outlined by Masson in a recent technical report (Bernier and Cole; 2012), including:

1. Quartz-calcite-magnetite-chalcopryrite veins ± pyrite ± molybdenite ± visible gold
2. Quartz veins ± chalcopryrite ± pyrite ± molybdenite ± visible gold
3. Calcite veins ± chalcopryrite ± pyrite ± visible gold
4. Quartz-molybdenite-visible gold veins
5. Carbonate-anhydrite veins ± chalcopryrite ± pyrite ± visible gold
6. Disseminated and fracture controlled mineralization
7. Replacement style mineralization – magnetite-epidote-feldspar-hematite-pyrite-chalcopryrite

Au mineralization styles 1-6 occur as steeply dipping zones of multi-generational sheeted and conjugate vein arrays and fracture fillings, while style 7 occurs within areas of intense alteration and is restricted to the South Contact Zone in the deposit. In addition to these styles, gold is rarely seen as coarse disseminations in silicified porphyritic intrusives (Bernier and Cole, 2012).

In general, gold mineralization occurs in veins and altered packages in steeply north to northwest dipping zones along the intrusive-volcanic contact and less often dip shallowly (Bernier and Cole, 2012). Common vein gangue minerals include quartz, calcite, ankerite, and anhydrite. Less abundant gangue minerals include sericite, chlorite, tourmaline, hematite, and magnetite.

The distribution and orientation of subsidiary faults, fractures, and veins, as well as branching and splay elements occur subparallel and perpendicular to regional structures (Alexander, 2006). There are three dominant sets of structure orientations. This includes: (1) east-north striking faults and fractures that dip steeply north; (2) northeast structures that dip steeply southwest; and (3) northwest trending structures that dip steeply northeast (Alexander, 2006).

Three prominent syenite porphyry dikes of the Upper Beaver Intrusive complex occur within the mine workings of the Upper Beaver mine. They have historically, and continue to be, important marker units for geological interpretation (Bernier and Cole, 2012). The porphyry dikes range in width from a few meters to 30 meters thick. They have a strike length of approximately 500 meters down to a depth of more than 2000 meters (Bernier and Cole, 2012).

Multiple sub parallel dikes are observed in the deposit, striking between 025 to 050 degrees and dipping steeply northwest at 60 to 85 degrees (Bernier and Cole, 2012). The dikes are geochemically similar and coalesce down dip and along strike. With decreasing distance to the center of the Upper Beaver Intrusive Complex identification of the individual dikes becomes increasingly more difficult (Bernier and Cole, 2012). They are all are spatially related to mineralization and frequently host mineralization on the property, especially in the porphyry zones. Mineralization is concentrated along dike contacts or is concentrated in the immediate hanging and footwall areas (Bernier and Cole, 2012). From south to north the dikes are named the Botsford, Bregg, and Tully dikes (Bernier and Cole, 2012).

Early production from the upper levels of the mine concentrated on extracting a series of north (000 degrees) to northeast (025 to 055) trending veins that were continuous with depth (Alexander, 2006). East-northeast trending (055-070 degrees) veins were encountered north of the main mine levels and at depth, becoming more common below the 500-ft level, and dominant below the 1000-ft level (Alexander, 2006). Cunningham (1977) describes the vein systems from the mine as being narrow, irregular, and discontinuous with an average width of 0.6 m, an average

height of 30 m, and no longer than 120 m. He further states that the veins tend to terminate abruptly, join with one another, and tend to exhibit a gently curved outline in plan and section. Alexander (2006) attributes the multiple orientations of veins reflect the “complex roll in the geology at the Upper Tisdale contact, combined with potential drag-folding related to faulting, and, fracturing/ remobilization associated with the north trending Misema cross fault in the mine workings that is filled with diabase”.

1.8.2 Cu Mineralization

Abundant copper mineralization is atypical of the Kirkland Lake and Larder Lake regions. The controls on the distribution of copper mineralization in the Upper Beaver deposit remain poorly understood. It can be spatially associated with gold, but often also occurs separately.

1.9 Timing of Mineralization

In a study by Isoplatov et al., (2008) on the geologic and structural setting of gold mineralization in the Kirkland Lake-Larder Lake Gold Belt, they used three generations of post-Timiskaming regional deformation fabrics to constrain the age of mineralization in the Upper Canada, McBean, Anoki, and Kirkland Lake deposits. Their study concluded that the Upper Canada, McBean, and Anoki deposits formed during D2, along with the Kerr-Addison-Chesterville, Omega, and Cheminis deposits, while the Kirkland Lake deposit formed during D4, along a separate hydrothermal system unrelated to mineralization along the syn-D2 deformation zones. Talisker’s (2014c) proposed age of mineralization (2661-2674 Ma), i.e., pre-D2-deformation, in the Upper Beaver deposit is older than that proposed for other local deposits.

This proposed age for mineralization fits the best with the syenite-associated clan of gold deposits, which share a crystallization age of 2680-2672 Ma (Robert, 2001). This group includes the Young-Davidson, Matachewan Consolidated, Ross, Holt-McDermott, Lightning, Beattie, Douay, and Malartic deposits, which share a similar spatial association with major faults and a similar depth of emplacement (Robert,

2001). They also share a similar mineralization style, which consists of disseminated sulphide replacement zones with variably developed stockworks of quartz-carbonate \pm K-feldspar veinlets centered within associated intrusions or along their margins, along satellite dikes and sills, or along faults and lithologic contacts away from intrusions (Robert, 2001).

The Upper Beaver deposit also shares some similarities with Alkaline Cu-Au porphyry to epithermal and IOCG systems. However, Alkaline Cu-Au porphyry to epithermal systems are dominantly Phanerozoic in age with only rare Archean examples (e.g., the Hollinger-McIntyre Au-Cu deposit in the Abitibi, the Boddington Cu-Au deposit in Australia, and the Troilus Au-Cu deposit in the Evans-Frotet greenstone belt in Canada) (Helt et al., 2014). Similarly, although IOCG deposits are recognized to occur in the Archean the lack of IOCG deposits in the Abitibi Greenstone belt make it difficult to compare the deposit with this deposit model. Significant work would need to be performed to unequivocally prove whether Upper Beaver deposit fits this genetic model.

1.10 Intrusions and mineralization

In a recent review of the deposit, Kontak et al., (2011) provided evidence for the overlap of magmatic and hydrothermal activity in the Upper Beaver deposit, indicating an intimate relationship between intrusions and mineralization. This evidence includes a) mafic dikes cross cutting intensely altered volcanic rocks, b) sericite-albite alteration which post dates magnetite alteration, c) mafic syenite dikes cross cutting altered syenite dikes, d) quartz feldspar porphyry cross cuts both felsic syenite and mafic syenite, e) and intense phyllic alteration associated with the quartz feldspar porphyry unit. Kontak et al., (2011) suggests that the relationship between magmatism and mineralization is also supported by sulfur and oxygen isotope studies of mineralization in the deposit. They identify that the $\delta^{34}\text{S}$ signature suggests a uniform or homogenized magmatic sulphur source with $T=400^\circ\text{C}$, while $\delta^{18}\text{O}$

isotopes suggest a uniform reservoir for ^{18}O and a $T=400^\circ\text{C}$, but with a mixed magmatic-metamorphic source.

Intrusion-associated deposits in the Archean Abitibi are associated with a diverse magmatic suite of calc-alkaline to transitional alkaline rocks, including: gabbro, diorite, granodiorite, monzodiorite, syenite, tonalite, trondhjemite, granite, lamprophyre/ albitite, and lithium, cesium, and tantalum pegmatite dikes (Dubé et al., 2015). The wide range in compositions, age of intrusions, and disparate gold events, associated with gold mineralization in the Abitibi led Dubé et al., (2015) to conclude the conditions favorable for gold mineralization were not unique.

Intrusion-associated deposits that are recognized to be associated with oxidized magmatic fluids include alkaline porphyry to epithermal deposits (Jensen and Barton, 2000), syenite-associated deposits (Robert, 2001), and some IOCG deposits (Williams et al., 2005). Oxidized magmatic fluids are thought to suppress sulphide saturation in order to generate gold rich fluids (Richards, 2011 and references therein). The association between IOCG deposits and oxidized igneous intrusions is a current topic of debate, with some authors claiming that a spatial association with igneous intrusions indicates a porphyry or a skarn deposit as opposed to an IOCG deposit (Williams et al., 2005; Hitzman, 2000), and other authors claiming that there is a genetic association (Requia et al., 2003). Alternatively, greenstone-hosted orogenic deposits are not directly associated with intrusive phases. This is a definitive criterion Robert (2001) proposes to separate greenstone-hosted orogenic deposits and syenite-associated deposits into two distinct categories. However, there can be a close spatial association between felsic and intermediate intrusions and orogenic gold deposits in metamorphic belts, which can be problematic in terms of deposit classification. This relationship has been long recognized in the Kirkland Lake gold camp (MacLean, 1954), and the association between the intrusive phases and gold mineralization in the Kirkland Lake deposit is currently being reevaluated (Isoplatov et al., 2008; Dubé et al., 2015; Poulsen and Robert, 2016).

The relationship between oxidized intrusions and gold mineralization is typically attributed to either a structural relationship in which the intrusion acts as a competent trap for mineralizing fluids (Witt, 1992) or as a genetic link between mineralizing fluids and alkaline to calc-alkaline intrusions (Cameron and Hattori, 1987; Robert, 2001). This relationship is especially complex where multiple overprinting styles of mineralization and remobilization, as identified by geochronology and cross cutting relationships occur (Dubé et al., 2015). An example of such a deposit includes the McIntyre Cu-Au-Mo deposit, which has been overprinted by the Hollinger-McIntyre greenstone-hosted quartz carbonate vein system (Dubé and Gosselin, 2007; Bateman et al., 2008).

An important exploration criterion of both porphyry to epithermal and syenite-associated deposits is their common association with multi-phase intrusive complexes, such as the Upper Beaver Intrusive Complex. A recent compilation study on porphyry-type deposits by Sillitoe (2010) suggests that these polyphase intrusions may be essential for porphyry-type deposits as they act as episodic but focused conduits by transferring the bulk of the magmatic fluids from deep parental chambers.

1.11 Alteration

All the rocks in the study area are altered however the prefix meta- has been omitted in this thesis (Bernier and Cole, 2012). Alteration is centered on the polyphase intrusive complex, especially along its sheared margin (Bernier and Cole, 2012). It is present in all lithologies and includes quartz, carbonates (ankerite and calcite), sericite and muscovite, albite, K-feldspar, epidote, chlorite, hematite, magnetite, actinolite, and sulphide minerals. Au mineralization is most closely associated with widespread and pervasive magnetite-feldspar-actinolite-epidote-carbonate-sericite alteration (Bernier and Cole, 2012).

Kontak et al., (2011) proposed that the alteration and mineralization occurred over three main fluid events, as shown in Figure 1.6. Gold mineralization is limited to the second fluid event (Stage II), associated with Bi and Te, as well as pyrite, chalcopyrite, scheelite, hematite and magnetite, and a variety of additional alteration minerals (chlorite, carbonate, epidote, sericite, quartz, tourmaline, and apatite) (Kontak et al., 2011). Studies by Kontak et al. (2011) also indicate that anhydrite formed occurs after the gold mineralization event(s), but free Au can also be hosted within anhydrite and the diagram has thus been modified accordingly.

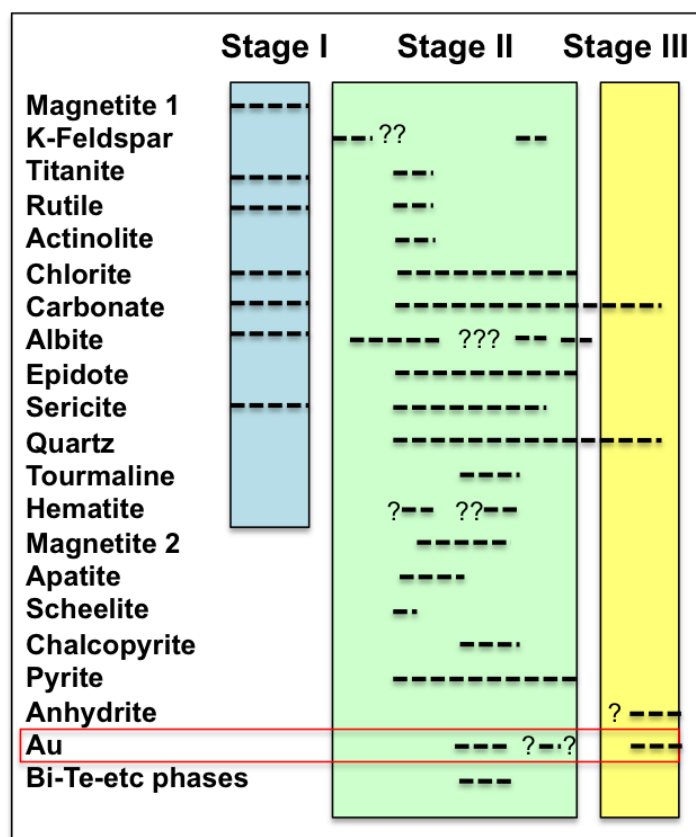


Figure 1.6. Alteration and mineralization history of the Upper Beaver deposit divided into three main stages of alteration (Modified from Kontak, 2011).

Not all alteration assemblages in the deposit are associated with Au and Cu mineralization. Epidote alteration is the most pervasive type of alteration in the deposit, extending throughout the entire paragenetic sequence, and is frequently associated with mineralization. Sodic alteration, on the other hand, in particular

disseminated albite, occurs in all units but is not associated with mineralization. Studies by Kontak et al., (2011) on the deposits paragenesis indicate that this alteration phase may have extended over a long period of time (e.g., early stage in basaltic volcanics). Areas of intense sericitic alteration tend to be most strongly associated with Au mineralization (Kontak et al. 2011).

The presence of magnetite and hematite in the deposit is unusual in the Kirkland Lake camp (Bernier and Cole, 2012). Importantly, there were two successive stages of magnetite and hematite growth in the Upper Beaver deposit (Kontak et al., 2008). Au-Cu mineralization with accompanying Mo, W Bi, Te, etc, postdate early albite-magnetite alteration and is instead associated with the second stage of magnetite growth (Kontak et al., 2011).

Kontak et al., (2011) interpreted the paragenesis of alteration phases in the deposit as follows:

1. There was an early phase of disseminated magnetite alteration within the basic volcanic rocks
2. Massive to semi-massive magnetite, which occurs in all rocks appears early with feldspar ($\text{Na} \gg \text{K}$), is rarely cored by hematite. It is also free of structurally bound titanium suggesting that massive to semi-massive magnetite is hydrothermal in origin (Nadoll et al., 2014)
3. Actinolite alteration is commonly associated with albite and carbonate, and petrographic studies indicate actinolite is much more abundant than initially believed but is difficult to identify in hand sample, due to its fine grain size
4. Epidote, as replacement zones and veins, is extensive and overlaps with early pink albite with hematite dusting and continues through the paragenesis
5. Tourmaline, as disseminations and veins, is generally late in the paragenesis

6. Sericite is most common in syenitic and felsic volcanic rocks, where intense phyllitic zones occur; sericite overlaps with disseminated late Ti-rich magnetite, pink albite, and epidote alteration

Alteration in Upper Beaver is different than alteration assemblages that characterize local deposits. The Kirkland Lake deposit is characterized by strong potassic metasomatism i.e., local sericitization, which Isoplatov et al., (2008) suggests is consistent with epithermal-style deposits related to alkaline magmatism. Alteration is also distinctly different than that in local greenstone-hosted lode gold deposits, which are typically associated with iron carbonate alteration (Dubé et al., 2007). Alteration in local deposits in the Larder Lake Gold Camp include: (1) ankerite and sericite alteration at Amalgamated Kirkland (Gamble, 2011); (2) carbonate alteration with minor zones of sericitization, silicification, and potassic alteration at Bidgood (Puritch et al., 2011); (3) carbonate alteration with mineralized lenses being more strongly altered by ankerite, sericite, albite, chlorite, and fuschite at Anoki (Ewert et al., 2010); (4) sericite, fuschite, and carbonate alteration at McBean (Ewert et al., 2010); and (5) ankerite, sericite, quartz, chlorite, and feldspar alteration at Upper Canada (Ewert et al., 2011).

2 Chapter 2 Methods

A variety of analytical techniques were used to characterize host rocks and mineralization in the Upper Beaver deposit. A total of 50 samples were collected for this deposit from drill core and surface outcrops. In addition to collected samples, a total of 20 thin sections from a thesis project by Feick (2014) were available along with corresponding whole-rock geochemical data. Whole rock geochemical data was also available from DeAgazio (2012) that contained 35 “fresh” samples. Canadian Malartic Corporation also generously provided use of their geochemical databases for drill core and surface outcrops, as described further in section 2.2 below. The following analytical techniques were used: whole rock geochemistry, Leapfrog Geo™ spatial imaging software, ioGAS™ exploratory data analysis software, electron microprobe analysis, and synchrotron-source x-ray fluorescence microprobe analysis. Experimental design moved from the macro to micro scale to better characterize trace element associations with mineralization and host rock geochemistry.

2.1 Petrography and Hand Sample Analysis

Drill holes in the deposit are typically drilled at a 60° dip towards 350°. During the summer of 2015, 50 representative diamond drill core samples of mineralization and select lithological units were collected to be made into polished thin sections and to undergo multi-element geochemical analysis. An additional 20 thin sections from an earlier project by Feick (2014) on one of the mineralized zones in the deposit, the South Contact Zone, were available prior to the start of the project. All samples were photographed and described briefly on site in terms of their host rock, mineralogy, veining, and structural features before being brought to the University of Western Ontario for preparation. All samples were tested with potassium ferro-cyanide (KFC) and hydrochloric acid (HCl) to determine if they contain calcite and/or ankerite. Hand sample and thin section descriptions can be found in Appendix A of this thesis along with a cross section detailing where each sample is from. For igneous rocks,

descriptive terms for grain size are defined as followed: fine-grained represents <1 mm diameter; medium-grained represents 1-5 mm diameter; coarse-grained represents 5-50 mm diameter; and very coarse-grained represents >50 mm in diameter (Winter, 2010). The Wentworth grain-size scale was used for sedimentary rocks, in which grain sizes are defined as follows: mud-sized grains represents <0.0623 mm (subdivided into clay-sized grains <0.0039 mm, and silt-sized grains <0.0226 mm); sand represents <2 mm diameter; and gravel is greater than 2 mm.

Core logs and assay databases were used to identify mineralized intervals that would benefit from complete geochemical and petrographic analysis. Polished thin sections were prepared by Stephen Wood in the Rock Preparation Laboratory at the University of Western Ontario. Twenty samples were collected from mineralized zones in the deposit. Mineralized sample collection aimed at obtaining at least one sample from each mineralized zone and of each different style of mineralization. Samples were collected only where copper mineralization occurred with gold mineralization. Thirty samples were collected as representative lithology samples of the isolated sedimentary sequence, unusual intrusions, and breccia.

Petrographic observation was undertaken at the University of Western Ontario using an Olympus BX51 microscope with a 10x optical eyepiece and five objective lenses (2.5x, 5X, 10X, 20X and 50X). Polished thin sections were analyzed in both reflected and transmitted light using plane-polarized and cross-polarized light. Plane-polarized and cross-polarized transmitted light observation allowed for the identification of distinctive textures, minerals, and alteration, while reflected light allowed for the study of opaque minerals including identification of iron oxide minerals, sulphide minerals, and Au mineralization. Photographs were taken using the Olympus UC30 high-resolution digital camera attached to the microscope, as shown in Figure 2.1.



Figure 2.1. The Olympus BX51 microscope with attached Olympus UC30 high resolution digital camera used for petrographic observation

2.2 Geochemical Data Sets

The purpose of geochemical data analysis is to identify pathfinder elements, or a combination of elements, for mineralization. The term pathfinder is generally used to describe one or more elements that can be used to identify economic mineralization (Levitan et al., 2014). Elements reflect the underlying geological mineralogical, and geochemical characteristics of an ore deposit and can be used to define a target that can be refined with more extensive exploration techniques such as drilling (Grunsky, 2007).

2.2.1 Compiled CMC Geochemical Dataset

Canadian Malartic Corporation provided a dataset consisting of assay results for over 167,000 samples and whole-rock multi-element geochemistry results of over 4,060 samples. Brief summary statistics for the data set (count, max, min, mean, median, standard deviation, interquartile range, and range) are provided in Appendix C. All samples were analyzed between 2005 and 2015, by various labs, as described below.

Assays were obtained using fire assay and gravity methods by Swastika, Accurassay, AGAT, and SGS Laboratories. Samples were first analyzed using fire assays methods with atomic absorption spectroscopy finish on 30-gram subsamples. Samples that returned assay values greater than 1.0 g/t were also analyzing using fire assay with a gravimetric finish.

Whole-rock geochemistry results were obtained by three slightly different methods by different labs. The labs include Laboratoire Exploration in Rouyn Quebec (Labo), which performed aqua-regia mass spectrometry (ICP-MS), AGAT Labs, which used aqua regia digest and an inductively coupled plasma optical emission spectroscopy (ICP-OES) finish, and SGS, which used a two-acid digest followed by an ICP-OES finish. A summary of lab and method detection limits for the geochemical database is provided in Table 2.1. For information on detection limits refer to Appendix B.

Table 2.1 Lab and method detection limits for the Upper Beaver geochemical database

Element Analysis Methods	Unit	Labo-Expert Aqua Regia ICP-MS Finish	AGAT Aqua Regia Digest - Metals Package, ICP- OES finish	AGAT Aqua Regia Digest - Metals Package, ICP- OES finish	SGS Two acid digest, ICP- OES Finish
Number of samples analyzed		765	1271	1631	338
Ag	ppm	0.002	0.20	0.20	2
Al	%	0.01	0.01	0.01	0.01
As	ppm	0.1	1	1	3

Table 2.1 cont. Lab and method detection limits for the Upper Beaver geochemical database

Element Analysis Methods	Unit	Labo-Expert Aqua Regia ICP-MS Finish	AGAT Aqua Regia Digest - Metals Package, ICP- OES finish	AGAT Aqua Regia Digest - Metals Package, ICP- OES finish	SGS Two acid digest, ICP- OES Finish
B	ppm	1	5	5	
Ba	ppm	0.5	1	1	1
Be	ppm	0.1	0.5	0.5	0.5
Bi	ppm	0.02	1	1	5
Ca	%	0.01	0.01	0.01	0.01
Cd	ppm	0.01	0.5	0.5	1
Ce	ppm	0.01	1.00	1.00	
Co	ppm	0.1	0.50	0.50	1
Cr	ppm	0.5	0.5	0.5	1
Cs	ppm	0.02	0.01	0.01	
Cu	ppm	0.01	0.50	0.50	0.5
Cu	%		0.01	0.01	0.01
Cu-OL	%			0.01	
Dy	ppm	0.001	0.05	0.05	
Er	ppm	0.1	0.03	0.03	
Eu	ppm	0.1	0.03	0.03	
Fe	%	0.01	0.01	0.01	0.01
Ga	ppm	0.02	5.00	5.00	
Gd	ppm	0.1	0.05	0.05	
Ge	ppm	0.1			
Hf	ppm	0.1	0.2	0.2	
Hg	ppm		1	1	
Ho	ppm	0.1	0.01	0.01	
In	ppm	0.02	1	1	
K	%	0.01	0.01	0.01	0.01
La	ppm	0.5	1.00	1.00	0.5
Li	ppm	0.1	1	1	1
Lu	ppm	0.1	0.01	0.01	
Mg	%	0.01	0.01	0.01	0.01
Mn	ppm	1	1	1	2
Mo	ppm	0.01	0.50	0.50	1
Na	%	0.001	0.01	0.01	0.01
Nb	ppm	0.1	0.2	0.2	
Nd	ppm	0.02	0.1	0.1	
Ni	ppm	0.1	0.50	0.50	1
P	%		10ppm	10ppm	0.01%

Table 2.1 cont. Lab and method detection limits for the Upper Beaver geochemical database

Element Analysis Methods	Unit	Labo-Expert Aqua Regia ICP-MS Finish	AGAT Aqua Regia Digest - Metals Package, ICP- OES finish	AGAT Aqua Regia Digest - Metals Package, ICP- OES finish	SGS Two acid digest, ICP- OES Finish
Pb	ppm	0.01	0.50	0.50	2
Pr	ppm	0.1			
Re	ppm	0.001			
Rb	ppm	0.1	10.00	10.00	
S	%		0.005	0.005	0.01
Sb	ppm	0.02	1	1	5
Sc	ppm	0.1	0.5	0.5	0.5
Se	ppm	0.1	10	10	
Sm	ppm	0.1	0.03	0.03	
Sn	ppm	0.05	5	5	10
Sr	ppm	0.5	0.5	0.5	0.5
Ta	ppm	0.05	10.00	10.00	
Tb	ppm	0.1	0.01	0.01	
Te	ppm	0.02	10	10	
Th	ppm	0.1	5.00	5.00	
Ti	%		0.01	0.01	0.01
Tl	ppm	0.02	5.00	5.00	
Tm	ppm	0.1	0.01	0.01	
U	ppm	0.1	5.00	5.00	
V	ppm	1	0.50	0.50	2
W	ppm	0.1	1	1	10
Y	ppm	0.01	1.00	1.00	0.5
Yb	ppm	0.1	0.03	0.03	
Zn	ppm	0.1	0.50	0.50	0.5
Zr	ppm	0.1	2 1/2	5	0.5
WtKg	Kg				0.001
Ag-OL	ppm		0.5	0.5	
Au	ppb	0.5			5
Au(R)	ppb				5
Au	g/t				0.03

2.2.1.1 Pre-analysis

Core was initially logged by CMC geologists on site between 2005 and 2016. Different lithologies, styles of mineralization, and major structures are noted in core logs. Potentially mineralized areas are marked, cut, and samples. Half of the cut core is sent to various laboratories to be assayed, while the other half remains on site in the core box for future reference. Core samples were sent to various labs for drying, crushing, splitting, pulverizing and screening. This process breaks the geological material down into a dry pulp. Potential sources of contamination include: (1) contamination from sample handling if jewelry is work; (2) cross contamination introduced during crushing and grinding; (3) contamination introduced from impure reagents used during sample digestion and analysis (Rollinson, 1993).

2.2.1.2 Sample Digestion

Labo, AGAT, and SGS used aqua regia digest to for sample digestion. This technique involves exposing the samples to hot, concentrated acids based on a combination of 2:1 HNO₃:HCl in order to dissolve the target elements. Two acid digest is the weakest of the digestions and does not fully dissolve silicate minerals (Kisser, 2005). As a result, high field strength elements (Ti, Zr, Nb, Hf, Ta, Th, and U) will be partially or wholly resistant to dissolution and analysis will not yield accurate results (Panteeva et al., 2003). SGS recommends this method for samples with organic content or high sulphide content (Two acid digest aqua regia digest, 2015)

2.2.1.3 Aerosol Conversion

After digestion the sample must be converted into an aerosol before it can be introduced into the ICP plasma (typically a partially ionized Ar gas produced in a quartz torch using a 1-2.5 kW radio frequency) for analysis (Olesik, 1991). This involves aspirating a liquid into an aerosol (Olesik, 1991). Following aerosol conversion, the plasma reacts with a heat source, typically 6,000-10,000° K, transforming the plasma into gaseous atoms and subsequently into ionized species

(Wolf, 2005). Benefits of this technique include providing low detection limits and good precision in a short period of time and analyzing multiple elements simultaneously (Rollinson, 1993).

2.2.1.4 Laboratoire Exploration (Labo)

Following aqua regia digestion, Laboratoire Exploration in Rouyn Quebec (Labo) analyzed samples using mass spectrometry (ICP-MS) to assess elemental concentration. In this method, high-temperature ICP (inductively coupled plasma) ions are focused through a pinhole-sized opening into a pumped vacuum and then into a mass spectrometer (Olesik, 1991). The mass spectrometer is a curved tube through which the ions are fired using a very powerful electromagnet, which divides the atoms according to their mass (Rollinson, 1993). Lighter ions are deflected with a smaller radius of curvature than heavy ions and based on where they hit along the tube elemental abundances can be obtained (Rollinson, 1993). In a review of ICP-MS vs. ICP-OES techniques, Olesik, (1991) stated “ICP-MS detection limits are often up to 3 orders of magnitude superior to those in ICP-OES”.

2.2.1.5 AGAT and SGS

Both AGAT and SGS laboratories used inductively coupled plasma optical emission spectroscopy (ICP-OES), also referred to as inductively coupled plasma atomic emission spectroscopy (ICP-AES) to assess the elemental content of the samples. This method involves heating a cloud of sample plasma within a spectrometer to excite the ions and measuring each ion’s ability to absorb electromagnetic radiation (Rollinson, 1993). The wavelength of light absorbed is specific to each element and its intensity is indicative of the concentration of that element within the sample (Rollinson, 1993).

2.2.2 CMC Surface dataset

In 2013 CMC ran a property-wide rock chip sampling survey across their Kirkland Lake Land package, which consists of more than 30 properties and covers an almost contiguous area of approximately 230 km². The properties host 10 gold

deposits that contain current and historic mineral resources of 2.1 million ounces (measured and indicated) and 1.8 million ounces (inferred). This includes five NI43-10 compliant properties: Upper Beaver, Anoki-McBean, Bidgood, Upper Canada, and Amalgamated Kirkland.

The surface sampling program was a rock-chip collection program where pairs of geologists collected rock samples from across the property that were roughly the size of two fists. Geologists were instructed not to take veins and to collect only unweathered rock. Samples were sealed with a zip tie in sample bags in the field immediately after collection with an identification tag inside the bag as well as written on the outside of the bag. GPS coordinates, multi-element results, and all additional notes were reported in GeoticLog™. The overall aim of the survey was to identify any large-scale geochemical trends. Samples were analyzed using aqua regia digest and ICP-AES finish at ALS Global. Au was analyzed using fire assay methods.

2.2.3 Past Thesis Datasets

Additional geochemical data from two student thesis projects on the Upper Beaver deposit were available prior to the start of this project. Projects include: (1) an assessment of the five main lithologies in the deposit in terms of mineral assemblages and trace element signatures by DeAgazio (2012); and (2) an assessment of the alteration assemblages in the South Contact Zone to define alteration and geochemical associations with Au mineralization by Feick (2014). Data from the study by DeAgazio (2012) was obtained from AGAT Laboratories by lithium borate fusion and inductively coupled plasma-emission spectroscopy (ICP-MS) analysis for trace elements and ICP-OES for major oxides. Data from the study by Feick (2014) was obtained by fusion-inductively coupled plasma (FUS-ICP) to generate the percentage of major oxides in each sample and by total digestion inductively coupled plasma (TD-ICP) and instrumental neutron activation analysis (INAA) by Actlabs to determine the concentration of trace elements in each sample.

2.2.4 Datasets produced for this thesis

2.2.4.1 Mineralized Dataset

The 20 samples that were collected from various mineralized zones in the deposit for this study were analyzed by ALS Global using aqua regia digest followed by ICP-AES multi-element analysis. Gold was analyzed first by fire assay and AAS analysis, and when the grade was more than 10 ppm, it was analyzed again using fire assay with a gravimetric finish. Cu was analyzed using ME-ICP. When assays revealed greater than 10,000 ppm Cu, samples were re-analyzed using aqua regia digestion with an ICP or AAS finish. The purpose of multi-element geochemical analysis of mineralized samples was to identify the elements that most strongly correlate with Au in the various mineralized zones and to support mineral phases identified during petrographic analysis. Detection limits for the mineralized dataset are provided in Table 2.2. See Appendix D for full sample geochemistry.

Table 2.2. Detection limits for mineralized dataset

Element	Unit	Detection Limit	Method
Au	ppm	<0.005	Au-AA23
Au	ppm	<0.005	Au-GRA21
Ag	ppm	<0.2	ME-ICP41
Al	%	<0.01	ME-ICP41
As	ppm	<2	ME-ICP41
B	ppm	<10	ME-ICP41
Ba	ppm	<10	ME-ICP41
Be	ppm	<0.5	ME-ICP41
Bi	ppm	<2	ME-ICP41
Ca	%	<0.01	ME-ICP41
Cd	ppm	<0.5	ME-ICP41
Co	ppm	<1	ME-ICP41
Cr	ppm	<1	ME-ICP41
Cu	ppm	<1	ME-ICP41
Fe	%	<0.01	ME-ICP41
Ga	ppm	<10	ME-ICP41
Hg	ppm	<1	ME-ICP41
K	%	<0.01	ME-ICP41
La	ppm	<10	ME-ICP41
Mg	%	<0.01	ME-ICP41
Mn	ppm	<5	ME-ICP41
Mo	ppm	<1	ME-ICP41
Na	%	<0.01	ME-ICP41
Ni	ppm	<1	ME-ICP41
P	ppm	<10	ME-ICP41
Pb	ppm	<2	ME-ICP41
S	%	<0.01	ME-ICP41

Table 2.2 cont. Detection limits for mineralized dataset

Element	Unit	Detection Limit	Method
Sb	ppm	<2	ME-ICP41
Sc	ppm	<1	ME-ICP41
Sr	ppm	<1	ME-ICP41
Th	ppm	<20	ME-ICP41
Ti	%	<0.01	ME-ICP41
Tl	ppm	<10	ME-ICP41
U	ppm	<10	ME-ICP41
V	ppm	<1	ME-ICP41
W	ppm	<10	ME-ICP41
Zn	ppm	<2	ME-ICP41
Cu	%	<0.001	Cu-OG46
Mo	%	<0.001	Mo-OG46
Te	ppm	<10	ME-ICP41

2.2.4.2 Major oxide dataset

All 50 samples that were collected for this thesis were analyzed by ALS Global to determine major oxide concentrations. Samples were analyzed using their preparation package ME-XRF26, which consisted of whole rock digestion followed by lithium borate fusion and XRF analysis. Detection limits for the major oxide dataset are provided in Table 2.3. Results are provided in Appendix D of this thesis.

Table 2.3. Detection limits for major oxide dataset

Element	Unit	Detection Limit	Method
Al ₂ O ₃	%	<0.01	ME-XRF26
BaO	%	<0.01	ME-XRF26
CaO	%	<0.01	ME-XRF26
Cr ₂ O ₃	%	<0.01	ME-XRF26
Fe ₂ O ₃	%	<0.01	ME-XRF26
K ₂ O	%	<0.01	ME-XRF26
MgO	%	<0.01	ME-XRF26
MnO	%	<0.01	ME-XRF26
Na ₂ O	%	<0.01	ME-XRF26
P ₂ O ₅	%	<0.01	ME-XRF26
SO ₃	%	<0.01	ME-XRF26
SiO ₂	%	>100.0	ME-XRF26
SrO	%	<0.01	ME-XRF26
TiO ₂	%	<0.01	ME-XRF26
LOI 1000	%	<0.01	OA-GRA05x

2.2.5 Data Processing

Geochemical trends and associations between elements are not random, but are governed by atomic forces that result in ordered crystalline structures. Compositional data has proven difficult to handle statistically because of the constraint that the components of each rock must sum to 100% (also referred to as closure). This means that the variables (elements) involved occur in constrained space defined by the simplex, a restricted part of real space (Grunsky, 2007). Many significant statisticians such as Aitchison (1990), Pawlowsky-Glahn and Buccianti (2001), Grunsky, 2007, and Filzmoser and Hron, (2008) have developed the concept of Compositional Data Analysis, pointing out the dangers of misinterpreting closed data, such as geochemical compositional data, when treated with “normal” statistical methods. For this reason, analysis in this paper focuses on correlations between elements as opposed to assessing any single element on its own.

Geochemical data was processed to reduce the impact of common problems encountered when evaluating geochemical data, including censored data, offset data groups, and missing values, and to reduce the effects of closure. Processing tools include excel, ioGASTM, and Leapfrog GeoTM; applications specifically developed to interact-with geochemical data.

Pre-processing of the data consisted of compiling multiple multi-element, assay, and lithology databases into one database using drill hole identification numbers and sample intervals. This was followed by the removal of blanks, duplicates, standards, and null values, and the substitution of robust data values below and above detection limits. Substituted values, which are provided in Appendix B, were calculated using the following formulas:

$$D_{ll} = D_l - 1^{n-1}$$

Where: D_l = the reported lower detection limit, n = number of significant figures of the reported lower detection limit, and D_{ll} = the substituted value for results below the detection limit.

$$D_{ul} = D_u + 1^{n-1}$$

Where: D_u = the reported upper detection limit, n = Number of significant figures of the reported above detection limit, and D_{ul} = the substituted value for results above the detection limit.

New columns were also created to aid in analysis including lab, method, mineralized zone name, and lithology. The data was analyzed in both leveled and raw form. Data was logged and leveled using ioGASTM software by the mean to reduce the effects of outliers in the dataset. This technique more clearly highlights elevated elemental concentrations within the deposit by effectively removing the background signature of the rocks (Acme and Bluemel, 2011). This is especially important when assessing correlations between elements such as Ni, Fe, and Co, which naturally occur in higher concentrations in mafic rocks (Rudnick, 1995). Each data point effectively becomes a “times background” since the values were leveled by the mean of each lithology. A value of 1 indicates that the data point is the same value as the mean. An example of the effects of leveling geochemical data by rock type is provided in Figure 2.2. For instance, if the lower detection limit is 10 ppm, the value is replaced with 5 ppm.

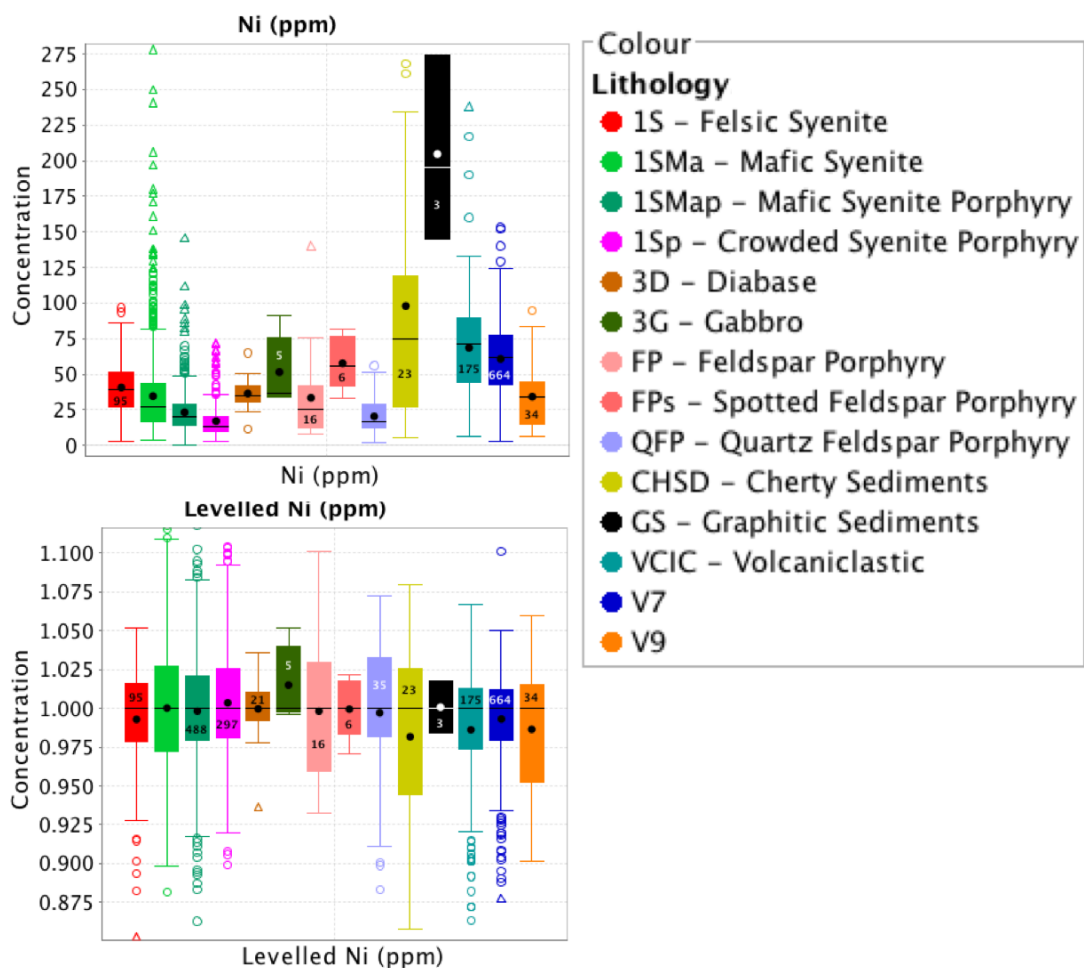


Figure 2.2. Percentile box plot showing the distribution of Ni in the deposit among main lithologies as an example of the effects of levelling geochemical data by rock type. The central portion of the box contains the middle 50% of the data from Q1 (the middle value in the first half of the dataset) to Q3 (the middle value in the second half of the dataset). Upper and lower whiskers contain 5% to 95% of the values in the data set. Outliers are represented by open circles and include the data that is in the top or bottom 5% of the data. The black circle represents the mean Ni content of each lithology and the black line represents the median value for each lithology. By levelling the data, the mean value of all lithologies is brought down to 1.0 so that any data points with a value greater than 0 have a relatively enriched signature for that rock type. This reduces the effects of having naturally Ni-rich groups like the graphitic sedimentary rocks, cherty sedimentary rocks, and mafic rocks. By determining correlations between Au and certain elements from leveled data we can conclude that the correlations are not a function of the rock type, but a function of relative enrichment

2.2.6 Exploratory Data Analysis (EDA)

Exploratory data analysis was performed to identify variables of interest (i.e. trace element exploration vectors for gold mineralization) from a large selection of data. This study focuses on using univariate, bivariate, and multivariate statistical methods to characterize different styles of mineralization within the Upper Beaver deposit.

ioGASTM was used to perform calculations on data, categorize the data points by colour, size, and shape, and to plot correlations between elements. Pre-set diagrams built into the software that were also of use in this study include rock classification diagrams, spider diagrams, histograms, XY plots, scatter matrix, line and probability plots, parallel coordinate plots, pie charts, and ranked variable and attribute maps. EDA consisted of: calculating summary statistics for each element (minimum, maximum, interquartile range, median, mean, mode, skewness and kurtosis); determining correlations between different elements (Pearson and Spearman correlation coefficients, and critical value calculations); and constructing various elemental association plots to show the frequency distribution of elements.

Multivariate methods were of particular importance in this study for identifying the interrelationship between trace elements among different styles of mineralization. Multivariate methods include Principal Component Analysis (PCA) and K-means Cluster Analysis. Cluster analysis uses an algorithm to partition a population of data into smaller sub-populations that may not be readily observable using bivariate analysis methods (Grunsky, 2007). Analysis was performed using ioGASTM's Apache K-Means clustering algorithm. Sub-populations were created by dividing n observations into K -clusters in which each observation is allocated to the cluster with the nearest mean to minimize within group variance and maximize between-group variance (Templ, 2006). This process is iterative, beginning with an initial “guess” of cluster centers until it converges on stable centers based on an initial choice of the number of cluster centers desired (Grunsky, 2007). Values for correlation are used throughout this paper as follows: 0.00-0.19 = very weak correlation; 0.20-0.39 =

weak correlation; 0.40-0.59 = moderate correlation; 0.60-0.79 = strong correlation; and 0.8-1.0 = very strong correlation.

Principal component analysis is a multi-variant technique that aims to describe variables using a new set of variables called principal components (Rollinson, 1993). The first few components will typically account for a large proportion of the variance in the data set and will contain the essential information of the larger set of observed variables (Rollinson, 1993). It aims to reduce the number of variables (Rollinson, 1993) so that in ideal circumstances, each principal component reflects a geological process such as differentiation, alteration, mineralization, and/or weathering (Grunsky, 2007). Principal component analysis was performed using ioGAS™ software. During analysis, a correlation matrix was used, which normalizes the data by centering it and dividing it by the standard deviation.

Data were correlated using the calculation Pearson product moment correlation coefficient (r) and the Spearman rank correlation coefficient (ρ).

Pearson product moment correlation

The Pearson coefficient is a measure of the linear dependence between 2 variables (X,Y) and was calculated using the formula:

$$r_{X,Y} = \frac{cov(X,Y)}{\sigma_X \sigma_Y}$$

Where:

$r_{X,Y}$ = The Pearson correlation coefficient for the populations X and Y

cov = The covariance of populations X and Y

σ_X = The standard deviation of population X

σ_Y = The standard deviation of population Y

Spearman Rank correlation coefficient

The Spearman correlation coefficient is the Pearson correlation coefficient between 2 ranked variables, (X,Y) and is suitable for defining non-linear correlation trends. This method provides a distribution-independent measure of correlation between two variables as it sorts the data first and ranks it and then compares it to another set of ranked data. The Spearman coefficient is calculated with the following formula:

$$\rho = 1 - \frac{6\sum d_i^2}{n(n^2 - 1)}$$

Where

ρ = The Spearman coefficient

d_i = The difference between the ranks x_i and y_i ($x_i - y_i$) for the populations X and Y

n = The number of data pairs

The Spearman rank correlation coefficient is considered the most suitable method for calculating correlations where databases possess numerous outliers or samples have non-linear correlation associations. Similar to the Pearson Correlation, a value of 1 indicates a perfect correlation between elements, while a correlation of 0 indicates no correlation. The values for correlation are used throughout this paper are as follows: 0.00-0.19 = very weak correlation; 0.20-0.39 = weak correlation; 0.40-0.59 = moderate correlation; 0.60-0.79 = strong correlation; and 0.8-1.0 = very strong correlation.

2.3 Spatial Modeling

Leapfrog GeoTM and ioGASTM were used to develop spatial models of the deposit. These spatial models were instrumental in identifying key geochemical patterns and to identify target areas that would benefit from sampling and further analysis. Geochemical modeling and interpolant tools in particular were used to

define trends within the datasets. Similar studies on Archean Abitibi gold deposits that utilize Leapfrog GeoTM as a spatial modeling tool to map main lithological units, alteration zones, and mineralization, include studies by Bogot and Jébrak (2015) on the Beattie syenite deposit, studies by Panneton et al., (2009) on Detour Lake, and studies by Pelletier et al., (2015) on the Rainy River deposit.

2.4 Microprobe Analysis

Microprobe analysis was performed in the Earth and Planetary Materials Analysis Laboratory at the University of Western Ontario in June 2016 using a JEOL JXA-8530F field-emission electron microprobe. The microprobe is equipped with 5 tunable wavelength dispersive spectrometers. Mineral compositions were determined with a voltage of 15 kV, a probe current between 15.3 – 17.4 nA, and a dwell time of 10 seconds. All samples were coated with carbon prior to analysis. Mineral analyses were collected to determine the composition of select amphibole and feldspar grains and to identify associated fine-grained minerals. Both energy-dispersive (EDS) and four wavelength-dispersive (WDS) spectrometers were used. EDS was used to quickly identify mineral species, while WDS was used to more accurately determine the composition of amphiboles and feldspars. Full microprobe results are provided in Appendix I.

2.5 Synchrotron Source X-ray Fluorescence Microprobe Analysis

High-energy synchrotron source x-ray fluorescence microprobe analysis (SR-XRF) was performed on mineralized thin sections to obtain information about trace element zoning and elemental correlation on a sub-microscopic scale. This work was performed to supplement statistical analyses presented in chapter 4, which identified the presence of at least two geochemically distinct styles of mineralization in the Upper Beaver deposit.

2.5.1 Synchrotron applications in the Earth Sciences

Synchrotron light is characterized by high brightness, i.e., photons per second, per unit source size and divergence in a given bandwidth (Balerna and Mobilio, 2015), many orders of magnitude brighter than conventional sources (Aquilanti et al., 2015). Combined with synchrotron light wavelength tenability (Aquilanti et al., 2015), synchrotron light offers new characterization procedures for both research and technological purposes. In the past two decades synchrotron source x-ray fluorescence microprobe analysis (SR-XRF) has succeeded in obtaining small enough beam sizes to allow for fine-detail surface work (Dobsoz, 2012). With this benchmark advancement, SR-XRF has greatly contributed to our understanding of the physio-chemical processes that lead to the formation and weathering of ore deposits (e.g., Brugger et al., 2010; Mumm et al., 2010); hard rock geology and rock mechanics (e.g., Fuisseis et al., 2014); and low temperature geochemistry (e.g., Brown and Sturchio, 2002; Walker et al., 2005; Yang et al., 2014). For this work, synchrotron source x-ray fluorescence microprobe analysis was used to assess trace element vectors for mineralization in an intrusion-associated Au-Cu deposit.

2.5.2 What is a Synchrotron?

Synchrotron radiation is the energy released when charged particles (electrons) change direction as they are accelerated around a vacuum chamber of a storage ring (Margaritondo, 2015). Synchrotrons are able to produce exceptionally intense beams of X-rays, ultra-violet, and infrared light (Aquilanti et al., 2015). They typically consist of 5 major components, including: the linear accelerator, the booster synchrotron, the electron storage ring, insertion device, and the experiment hall. Charged particles (electrons) are first generated in an electrode gun (Nuhn, 2004) and then accelerated by high-voltage alternating electric fields in a linear accelerator (“linac”) until their energy reaches several millions of electron volts, prior to being injected into the booster system (Balerna and Mobilio, 2015). The booster system further accelerates the electrons to nearly the speed of light and then injects them into the storage ring where they circulate for many hours or days (Margaritondo, 2015). For the purposes of this project, third-generation synchrotron storage rings were used,

which are optimized for insertion devices (Nuhn, 2004). Insertion devices consist of magnets or other magnetic systems (Margaritondo, 2015), placed into the straight sections of a storage ring (Aquilanti et al., 2015). Each insertion device, acts as a source of synchrotron light, which is collected by a beamline, processed, and then sent into an experimental chamber (Margaritondo, 2015). Insertion devices help to produce a very bright beam with tunable wavelengths that can be adjusted by altering the field strength (Aquilanti et al., 2015).

This work is based upon research conducted at the Cornell High Energy Synchrotron Source (CHESS), which is supported, by the National Science Foundation and the National Institutes of Health/National Institute of General Medical Sciences under NSF award DMR-1332208. Data collection was performed at Sector F3. Research described in this work was also collected at Sector 20-ID-B at Advanced Photon Source (APS) of Argonne National Labs. Sector 20 facilities at the Advanced Photon Source, and research at these facilities, are supported by the US Department of Energy - Basic Energy Sciences, the Canadian Light Source and its funding partners, the University of Washington, and the Advanced Photon Source. Use of the Advanced Photon Source, an Office of Science User Facility operated for the U.S. Department of Energy (DOE) Office of Science by Argonne National Laboratory, was supported by the U.S. DOE under Contract No. DE-AC02-06CH11357. Research was also performed at the Canadian Light Source, which is supported by the Natural Sciences and Engineering Research Council of Canada, the National Research Council Canada, the Canadian Institutes of Health Research, the Province of Saskatchewan, Western Economic Diversification Canada, and the University of Saskatchewan. There are many benefits to using multiple synchrotrons to perform data analysis. Different configurations are specifically designed to maximize different capabilities including storage ring-generated X-ray beam brightness and flux, which are benchmarks of x-ray beam quality.

2.5.3 An Introduction to Hard X-Ray Synchrotron Imaging Techniques

Synchrotron-sourced hard x-ray imaging techniques were used to produce energy maps that showed the distribution of trace elements in and around mineralized sulphide grains. Using the synchrotron-sourced hard x-rays to excite electrons on the surface of samples and measuring the full-spectrum emitted (i.e., the wavelengths and relative emission strengths of energy released by test materials) XRF element mapping can be performed (Buffiere and Baruchel, 2015). The radiation produced by a synchrotron is of particular interest as its flux is many orders of magnitude higher than conventional X-ray sources allowing weakly emitting or dilute elements to be detected (Sham and Rosenberg, 2007) and can be narrowed to a very small spot size (Aquilanti et al., 2015). This allows for rapid high-resolution full spectrum analysis with the ability to detect elements with ppm-scale detection limits (Sham and Rosenberg, 2007). X-ray fluorescence spectrometry element identification is based on the characteristic energy that is released when individual atoms of different elements are excited by an external energy source (Rollinson, 1993).

2.5.4 Data collection at Advanced Photon Source

Advanced Photon Source (APS) produces the brightest storage ring-generated X-Ray beams in the Northern hemisphere (Lienert et al., 2011). APS operates at 7 GeV and 100 mA (Greig et al., 2011). The storage ring utilizes a third-generation light source to maximize the flux and brilliance of the beam (Lienert et al., 2011). The facility is comprised of 35 discrete sectors, with a total of 42 insertion device lines and 20 bend magnet lines, amounting to 62 operational beamlines (Greig et al., 2011). The typical detector used for at APS is a pixel array (Ross and Kline, 2011).

In the current study, XRF-maps were produced at either 13.1 or 27 keV depending on the elements of interest. Analysis at APS took advantage of the narrow beam and was focused on creating high-resolution maps with a step size between 2 to 10 μm , with larger step sizes only used to locate specific spots of interest. Au and

glass standards were run prior to and at between data collection to ensure data accuracy.

Trace element maps were produced on site by setting specific ROIs (peak energy divided by 30) for elements of interest. A summary of ROIs is provided in Table 2.4. For a full list of element excitation energies, refer to Appendix E. Energy maps are created with the assumption that most, if not all, of the energy measured between E1 and E2 corresponded to the particular element of interest. Full spectrum data can also be uploaded onto the CHESS server to allow for map refinement using GeoPIXE if proper experimental set-up is recorded. Data can be viewed as it is acquired on site or on personal computers using specific data viewing programs. These programs include 1D ScanPlot, 2D ScanPlot, and 2D QScanPlot. See Appendix G for details on APS standard operating procedures used for this project.

Table 2.4. Elements of interest and their corresponding energy and ROIs for trace element XRF maps acquired at APS. E1 represents the lower limit of the energy peak, while E2 represents the upper limit.

Element	Energy line of interest	Peak Energy (eV)	Energy peak ROI	E1	E2
Te	L α	3768	125.6	119	133
Cr	K α	5414.9	180.5	174	188
Fe	K α	6405	213.5	207	221
Co	K α	6930	231	224	238
Ni	K α	7480	249.3	242	256
Cu	K α	8046	268	261	273
W	L α	8398	280	274	282
Zn	K α	8637	288	283	295
Pt	L α	9442	314.7	308	319
Au	L α	9713	323.8	320	331
As	K α	10543	351.4	344	354
Bi	L α	10839	361.3	356	368
Mo	K α	17480	582.7	576	590
Ag	K α	22163	738.8	732	746

2.5.5 Data Collection at Cornell High Energy Synchrotron Source

The Cornell High Energy Synchrotron Source (CHESS) facilities consist of a 780 m wide storage ring that hosts both electrons and positrons in the same ring (Liu, 2014). The storage ring operates with an electron energy of roughly 1.8 to 5.2 GeV

(Liu, 2014). The Cornell Electron-Positron Storage Ring (CESR) is currently the worlds only operating wiggling-dominated storage ring (Palmer et al., 2007).

Data from CHESS was obtained in November, 2015 using the Sector F3 beam line, which utilizes a positron hard bend magnet source. Data was collected with a Maia detector, a 384 element pixel array detector where each pixel functions as a miniature version of a traditional single element detector. Samples can be scanned with count rates larger than 10^7 photons per second with full spectra being obtained in 0.001 seconds (Woll, 2014). The detector collects full spectrum data for analysis and is exceptional for mapping large areas at a high resolution and can be used for XANES mapping and XRF microtomography (Woll, 2014).

The beam is not as bright as that at APS, with a resolution approaching $10\ \mu\text{m}$. XRF-maps were produced at 13.1 and 30.1 keV with a step size of $20\ \mu\text{m}$ at Cornell. Au, Fe, and Bi standards were also run prior to and during data collection to ensure data accuracy and for use as calibration files. All thin sections were loaded onto a device called the RockMaster 3000 to cut down on the time it takes to switch samples. Sample setup was shown in Figure 2.3.

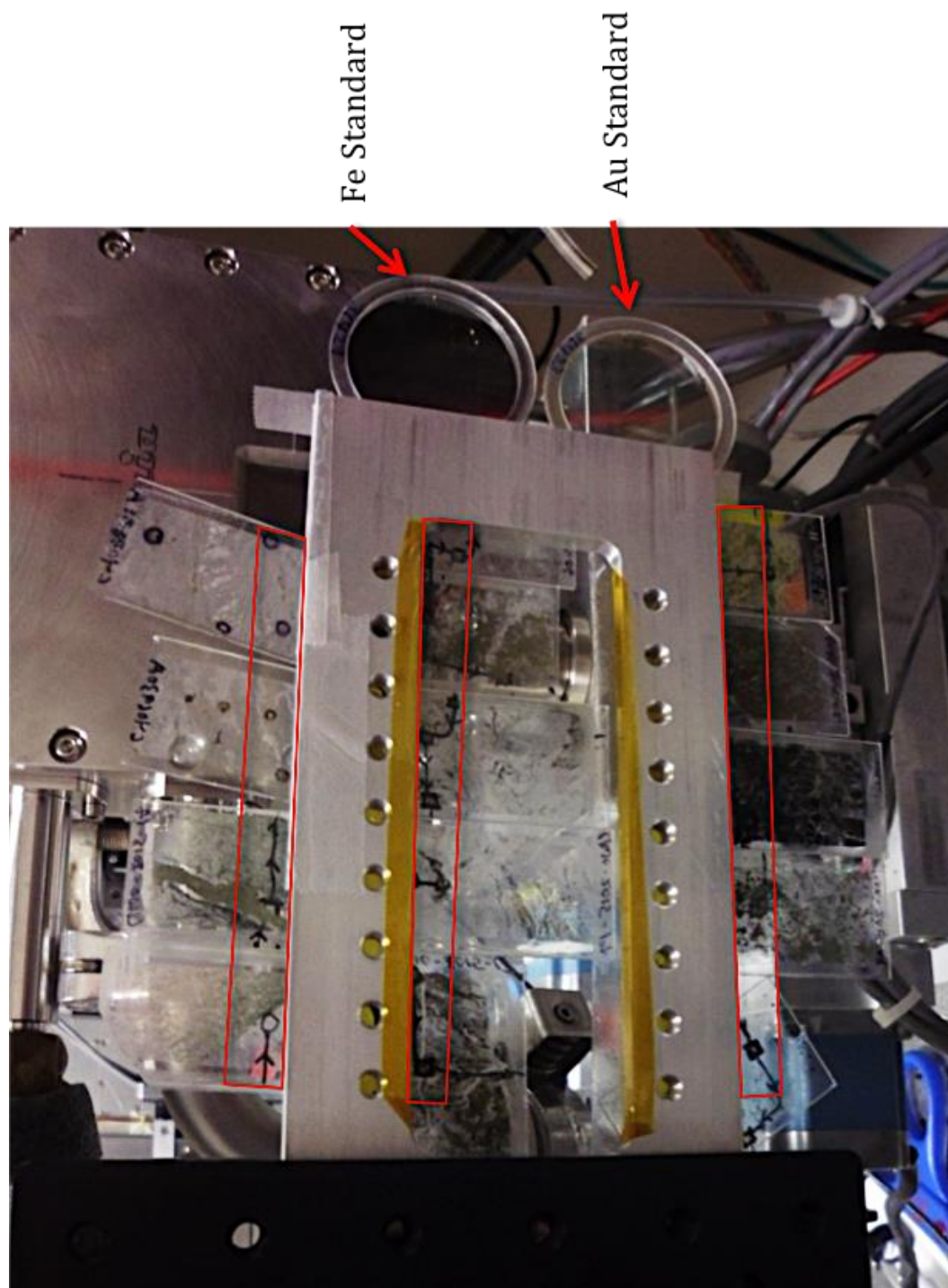


Figure 2.3. Setup of samples analyzed at CHESS in November, 2015. A total of 14 thin sections were mapped, with red boxes highlighting the 3 strips that were mapped. Fe and Au standards were attached to the end of the sample holder so that they could be tested between maps to ensure consistent data quality.

2.5.6 Data Collection at Canadian Light Source

The setup of the Canadian Light Source (CLS) synchrotron operates a 2.9 GeV booster ring, which allows for more stability in the light source (Silzer et al., 2004). Electrons are transferred from the booster to the storage ring using a booster-to-storage ring transfer line, which allows for more tuning flexibility, which permits more beam parameter customization at the injection point (Silzer et al., 2004). The injection system uses a thermionic electron gun and includes a 250 MeV low energy transfer line (LINAC) and a high energy transfer line (Silzer et al., 2004).

Data obtained at CLS was obtained at the Very Sensitive Elemental and Structural Probe Employing Radiation from a Synchrotron (VESPERS) beamline in the experiment hall. This hard X-ray beamline uses a bending magnet source to obtain a spectra range of 6-30 keV (McIntyre et al., 2010) and a spot size of 3-5 μm (Feng et al., 2010). The beamline is set up for both XRF and, although not discussed in this study, XRD capabilities (Feng et al., 2010), Laue and Bragg diffraction and/or XANES data (Dobosz, 2012).

Full spectrum data is collected by using single- and/or four-element Vortex detectors. Following data collection, element maps can be produced by using pre-set ROIs, similar to element map generation at APS. A more detailed analysis of full spectrum data can be performed after data collection by fitting the spectra.

2.5.7 Data Processing: GeoPIXE

Processing of synchrotron X-ray fluorescence data is a dynamic and iterative process that involves correcting images to account for chemical concentration gradients, differential absorption effects, and pileup effects (Ryan et al., 2015). Data processing for this project was achieved using GeoPIXE, a well-established software designed for quantitative particle induced X-ray emission (PIXE) and synchrotron X-ray fluorescence (SR-XRF) trace element imaging and analysis (Pallon et al., 2009; Cohen et al., 2015; Ryan et al., 2015). GeoPIXE automatically accounts for significant non-linear distortion of spectra and provides support for image generation, analysis, and validation (Woll, 2014).

GeoPIXE has built-in routines for data corrections, as described by Pallon et al., (2009), and briefly summarized here. Raw data begins starts as an event-file with coordinates and detector events sorted into a “master spectra”. The spectrum is selected, calibrated, and stored. It must also be “cut” so that the energy range spans all transmitted events without including background noise. The event data is then used to produce an energy map to assist with the next stages of data processing. The event-file is stored using the dynamic analysis (DA) projection for spectral deconvolution, which allows for new PIXE spectra and image reconstruction from event data (Ryan et al., 2015). New PIXE spectra can then be fitted and stored.

Routine data analysis workflow for this project followed five main steps, which are described in detail in Appendix H: (1) energy and charge calibration; (2) spectrum fitting, yields calculation (which takes into account experiment geometry, detector information, and sample information), and individualized DA matrix generation for each sample; (3) production of energy concentration images; (4) image validation; and (5) qualitative and quantitative image analysis.

2.5.8 Element Identification

Element identification from synchrotron data works by using hard x-rays to excite electrons on the surface of samples and measuring the full-spectrum emitted (i.e., the wavelengths and relative emission strengths of energy released by test materials) (Buffiere and Baruchel, 2015). It is based on the characteristic secondary x-ray energy released when individual atoms of different elements are excited by an external energy source (Rollinson, 1993). Dynamic analysis generally includes the fitting of K, L, and M characteristic X-ray lines to a background and the use of primary fitted $K\alpha$, $L\alpha$, or $M\alpha$ line area to determine the elemental concentration (Cohen et al., 2015). Characteristic energies emitted by select trace elements are presented in Table 2.5. For a table of characteristic emission lines for every element, see Appendix E.

Table 2.5. Characteristic emission lines of select trace elements. Energies highlighted in red were measured during data acquisition at 13.1 KeV, while energies highlighted in blue were measured during data acquisition at higher energies. Energies from “X-ray Data Booklet”

Element	K α 1	K α 2	K β 1	L α 1	L α 2	L β 1	L β 2	L γ 1	M α 1
22 Ti	4,510.84	4,504.86	4,931.81	452.20	452.20	458.40			
23 V	4,952.20	4,944.64	5,427.29	511.3	511.3	519.2			
24 Cr	5,414.72	5,405.51	5,946.71	572.8	572.8	582.8			
25 Mn	5,898.75	5,887.69	6,490.45	637.4	637.4	648.8			
26 Fe	6,403.84	6,390.84	7,057.98	705	705	718.5			
27 Co	6,930.32	6,915.30	7,649.43	776.2	776.2	791.4			
28 Ni	7,478.15	7,460.89	8,264.66	851.5	851.5	868.8			
29 Cu	8,047.78	8,027.83	8,905.29	929.7	929.7	949.8			
30 Zn	8,638.86	8,615.78	9,572.00	1,011.70	1,011.70	1,034.70			
33 As	10,543.72	10,507.99	11,726.20	1,282.00	1,282.00	1,317.00			
42 Mo	17,497.34	17,374.30	19,608.30	2,293.16	2,289.85	2,394.81	2,518.30	2,623.50	
47 Ag	22,162.92	21,990.30	24,942.40	2,984.31	2,978.21	3,150.94	3,347.81	3,519.59	
52 Te	27,472.30	27,201.70	30,995.70	3,769.33	3,758.80	4,029.58	4,301.70	4,570.90	
78 Pt	66,832	65,112	75,748	9,442.30	9,361.80	11,070.70	11,250.50	12,942.00	2,050.50
79 Au	68,803.70	66,989.50	77,984	9,713.30	9,628.00	11,442.30	11,584.70	13,381.70	2,122.90
80 Hg	70,819	68,895	80,253	9,988.80	9,897.60	11,822.60	11,924.10	13,830.10	2,195.30
82 Pb	74,969.40	72,804.20	84,936.60	10,551.50	10,449.50	12,613.70	12,622.60	14,764.40	2,345.50
83 Bi	77,107.90	74,814.80	87,343	10,838.80	10,730.91	13,023.50	12,979.90	15,247.70	2,422.60
92 U	98,439	94,665	111,300	13,614.70	13,438.80	17,220.00	16,428.30	20,167.10	3,170.80

An example of full-spectrum data is provided in Figure 2.4. Figure 2.4 includes full spectrum data for the entire region analyzed, as well as for sub regions (as identified). Key characteristic energy lines for elements in the sample have also been identified.

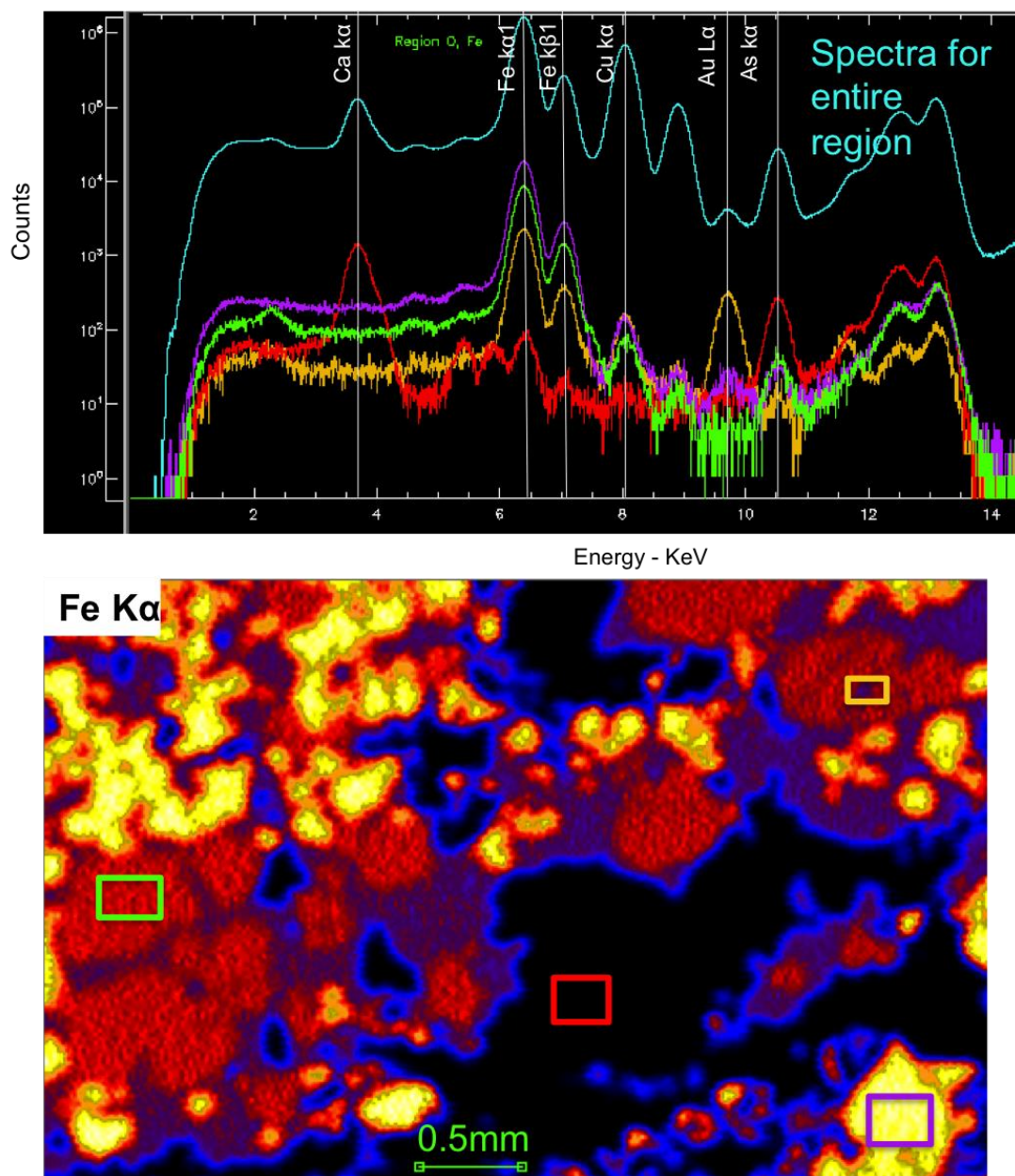


Figure 2.4. (Top) Example of full XRF spectrum data obtained at CHESS including select identified peaks that correspond to elements of interest in the sample for the entire region as well as for sub-regions (as colour coded). (Bottom) Fe $K\alpha$ energy map showing regions of interest included in the spectrum above.

3 A Detailed Assessment of Host Rocks of the Upper Beaver Au-Cu Deposit

3.1 Introduction

Many of the gold deposits in the Archean Abitibi Greenstone Belt are classified as orogenic deposits, where Au mineralization is concentrated along crustal-scale fault zones as a result of hydrothermal fluid circulation (Groves et al., 2003; Goldfarb et al., 2005; Dubé and Gosselin, 2007). However, the source of the gold and the evolution of the mineralizing fluids remain enigmatic (Dubé, 2015). This is further complicated by occurrence of “syenite-associated” or oxidized intrusion-related gold deposits, as proposed by Robert (2001), wherein gold mineralization is genetically associated with calc-alkaline to alkaline intrusions. This association has long been recognized and is typically interpreted as either a structural relationship in which the intrusion acts as a competent trap for mineralizing fluids (Witt, 1992) or as a genetic link between mineralizing fluids and alkaline to calc-alkaline intrusions (Cameron and Hattori, 1987; Robert, 2001).

The Upper Beaver Cu-Au deposit is an anomaly in the Kirkland Lake-Larder Lake areas in terms of mineralization, distance from the Larder Lake-Cadillac break, and alteration style (Kontak et al., 2008; Bernier and Cole, 2012). Because of this, it represents a deposit type that may have gone unexplored for in the past in the Abitibi. The presence of substantial Cu-Au mineralization associated with intrusive phases only 30 km away from the main Kirkland Lake gold camp within the Larder Lake gold camp, underscores the need for a better understanding of the genesis and evolution of intrusion-associated gold deposits in the Abitibi Greenstone Belt.

This chapter aims to better define the host lithologies of the Upper Beaver deposit by geochemically and petrographically classifying intrusive phases by extracting valuable information from a large geochemical company database and from available geochemical data, hand samples, and thin sections from past thesis projects by DeAgazio (2012) and Feick (2014). Additional sampling of breccia and

sedimentary rocks form the deposit followed by whole-rock geochemical analysis was performed to assess the host rocks in order to further characterize the deposit.

3.1.1 Deposit Geology

On the Upper Beaver property, the Blake River Assemblage is represented by medium to dark gray calc-alkaline to tholeiitic, fine-grained mafic volcanics (Bernier and Cole, 2012). Most commonly the basalts occur as flows, although pillowed, hyaloclastitic and glomeroporphyritic mafic basalt have been observed in drill core, as shown in Figure 3.1. The basalt dominantly consists of relict plagioclase, as shown in Figure 3.2a, with lesser amounts of quartz and amphibole. It is typically altered by in patches, stringers, or pervasively, by varying amounts of alteration including chlorite, sericite, epidote, albite/ feldspar, ankerite, calcite, actinolite, magnetite, and hematite, with accompanying pyrite, and chalcocopyrite. Basalt can be so heavily altered that the original mineralogy and rock texture is unrecognizable, as shown in Figure 3.2b.

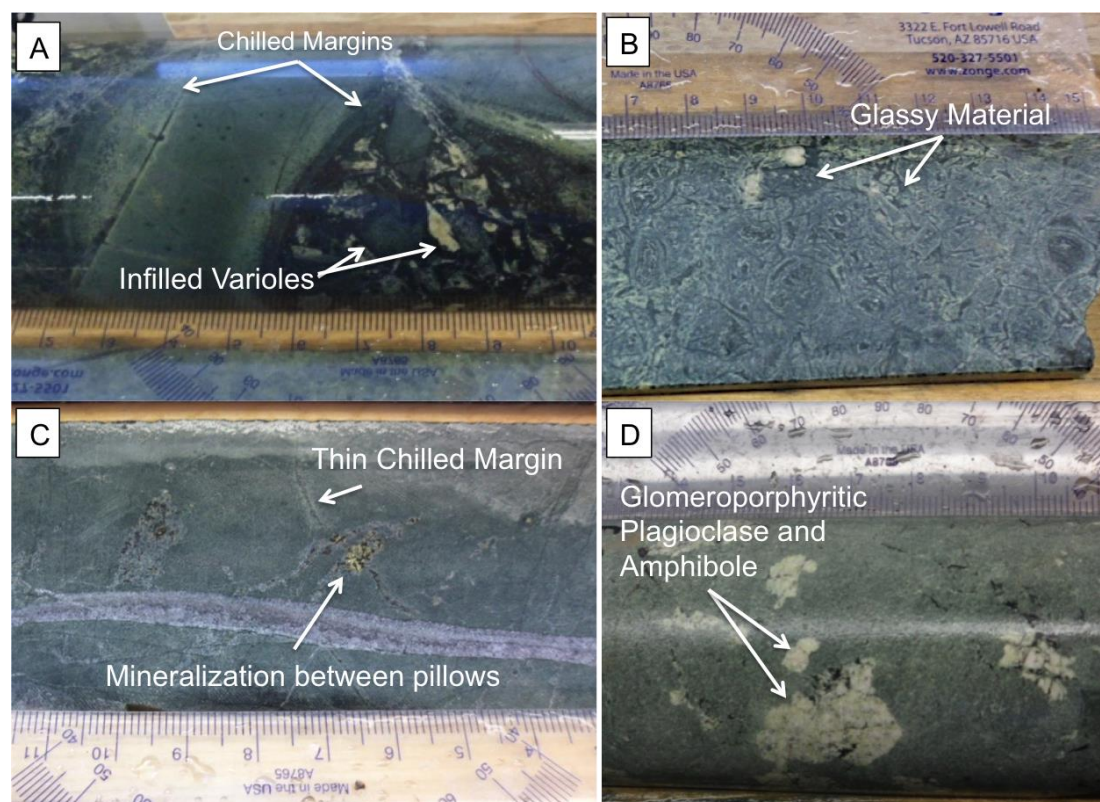


Figure 3.1. Representative photos of the Blake River Group basalts. A) Pillowed basalt from UB10_164 (388 m) showing well defined chilled margins and varioles, infilled by calcite, chlorite, and epidote; B) Hyaloclastitic basalt from UB13_280 (430.6 m) with complex textures resulting from the last-formed interstitial glassy crystals with moderate amounts of epidote and sericite alteration in the basalt surrounding the glassy materials; C) Pillowed basalt from UB14_392 (287 m) showing less well-defined chilled margins than in (A) but showing Au mineralization within chalcopyrite infilling spaces between pillows; and D) Glomeroporphyritic basalt from UB13_311 (35.6 m) showing large clumps of coarse-grained plagioclase and amphiboles within a fine-grained matrix.

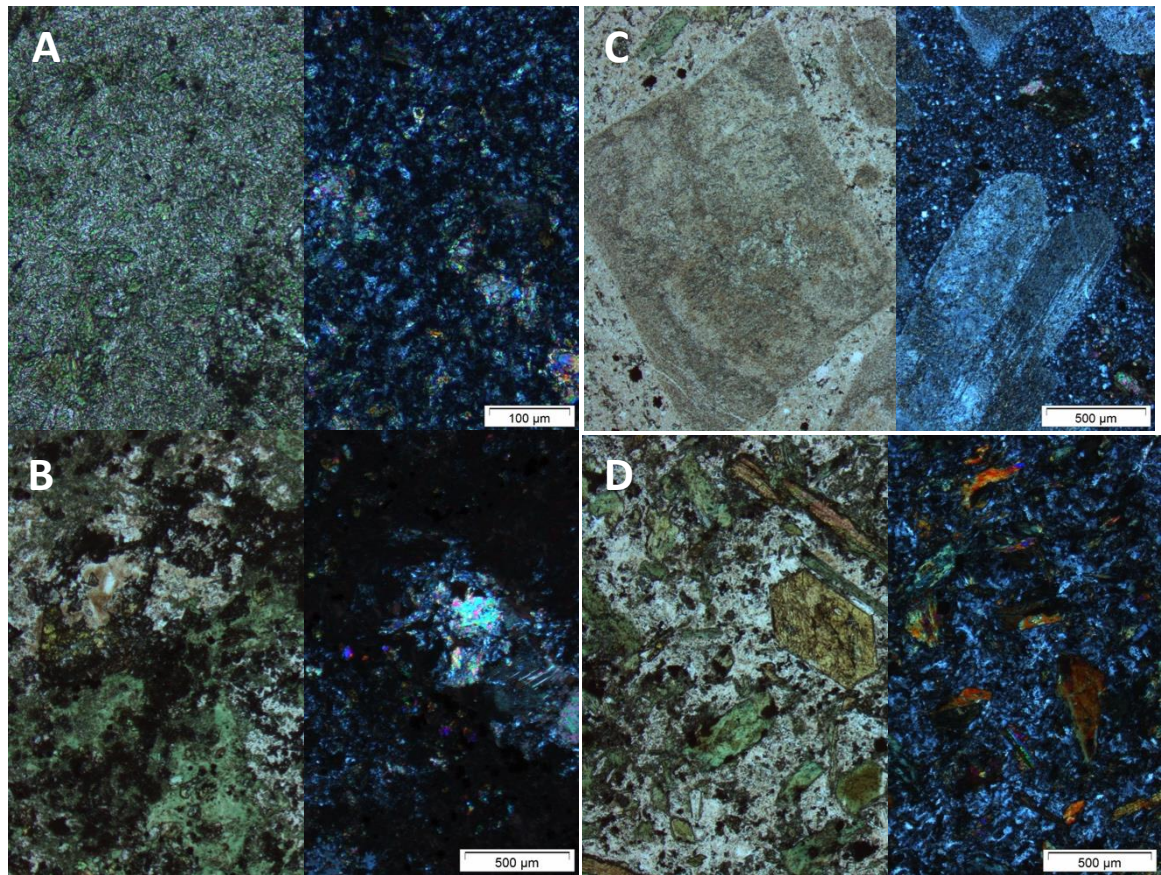


Figure 3.2. Representative lithologies in the Upper Beaver Deposit: A) Relatively fresh basalt (KF03) showing weak alteration by clinocllore, epidote, and calcite, B) Strongly altered basalt defined by strong epidote, hematite, magnetite, chlorite, and sericite alteration (KF11), C) crowded syenite porphyry defined by coarse-grained plagioclase phenocrysts (KF01), and D) mafic syenite defined by coarse-grained amphiboles within a plagioclase-rich matrix (KF17)

An isolated sedimentary sequence occurs within the Blake River Assemblage. It is located near the mine workings of the historic Upper Beaver Mine at a depth of -200 to -500 meter elevations. From top to bottom the sequence consists of fine-grained graphitic sedimentary rocks with associated fine to coarse grained pyrite interlayered with silty arenite, alternating layers of well-rounded clast-supported pebble conglomerate and fine-grained silty arenite, tan to pinkish fine grained cherty sedimentary rocks, and finally a top layer of greenish gray heterolithic volcanoclastic rocks. These sediments were previously interpreted to represent a basin that formed the lowermost boundary for ore in the deposit (Morris, 1974) but diamond drilling has revealed that mineralization is also present outside the sedimentary package.

On the Upper Beaver property, the Timiskaming Assemblage, which consist of trachyte flows, breccias, and agglomerates, (Ayer et al., 2005) is represented by a thin 30-50 m wide unit of conglomerate at surface at the northern margin of the basin on the Upper Beaver property (Alexander, 2006). Local carbonated altered and mineralized zones in the Timiskaming Formation were exploration targets for Mary Ann Gold Mines in 1944-1947 however; gold values were generally low and not economic (Alexander, 2006).

During the Timiskaming a number of high-level calc-alkalic to alkalic intrusions and their local volcanic equivalents were emplaced (Ayer et al., 2005). Local assemblages on the Upper Beaver property are crosscut by many of these intrusives (Bernier and Cole, 2012). These rocks are locally called mafic syenite, felsic syenite, and syenite porphyry based on characteristic textures and minerals across the Kirkland Lake area (Thomson et al., 1950; Ploeger and Crockett, 1980; Watson, 1984). Studies by Corfu et al., (1991), Müller et al., (1991) and Corfu (1993), and references therein, have constrained the age of Timiskaming sedimentation and plutonism in the southern Abitibi belt to be between 2,681-2,676 Ma through detrital zircon, igneous zircon, and titanite-U-Pb dating.

The Upper Beaver property hosts a number of intrusive phases, including rocks identified by Canadian Malartic Geologists as mafic syenite, felsic syenite, and

crowded syenite porphyry. These intrusions comprise the polyphase Upper Beaver Intrusive Complex and are intimately associated with mineralization (Bernier and Cole, 2012). Representative petrographic photos of crowded syenite porphyry and mafic syenite are provided in Figure 7c, and 7d, respectively. A main objective of Chapter 3 is to examine the lithologies that make up this complex based on IUGS classification. Detailed descriptions of the main lithologies in the complex as well as their relationship to original camp names will be provided there, specifically in sections 3.5.1 and 3.6.1. Re-interpreting the lithologies in terms of their geochemistry and mineral content is an essential step towards property evaluating their relationship to gold mineralization. This is of particular importance in the Upper Beaver deposit where mineralization is intimately associated with specific members of the Upper Beaver Intrusive Complex.

The last intrusive phase on the property is the Matatchewan diabase. The diabase dike is a late fine-grained intrusion that trends north south and cuts the deposit roughly in half. It dips steeply to the west at 80 to 85 degrees until approximately 200 to 300 m depth where it changes orientation and dips steeply to the east at 80 to 85 degrees (Bernier and Cole, 2012).

3.1.2 Lithologies in the Upper Beaver Intrusive Complex

Three main lithologies have been identified in the Upper Beaver Intrusive Complex, and in addition three main intrusive types cross cut the complex (Bernier and Cole, 2012). It is important to note that the names used by CMC geologists to identify the rocks are camp terms and are not consistent with the IUGS Classification as defined by Le Bas and Streckeisen, (1991). The CMC geologists are aware that the rocks do not meet the criteria to be classified as “syenites” however, the names have been in use for over a century and as such, they remain in use today (M. Masson, personal communication, 2015). “Camp” names are based on characteristic textures and minerals and are consistent across the Kirkland Lake region (Thomson et al., 1950; Ploeger and Crockett, 1980; Watson, 1984). Representative samples from the Upper Beaver deposit are analyzed in the chapter that follows in order to document the key characteristics of the host rocks in the Cu-Au Upper Beaver Intrusive

Complex using available company data, data from past projects on the deposit by DeAgazio (2012) and Feick (2014), and new data acquired for this project.

Representative photos of the main lithologies in the Upper Beaver Intrusive Complex are provided in Figure 3.3. The rocks that make up the Upper Beaver Intrusive Complex include, from oldest to youngest:

(1) Mafic Syenite: This unit is weakly magnetic and is fine to medium grained green to reddish brown in color. It is the most volumetrically abundant rock in the complex (Bernier and Cole, 2012). It is characterized by up to 15% medium to coarse-grained euhedral amphiboles within a fine-grained plagioclase-rich groundmass with lesser amounts of quartz and trace amounts of rutile, hematite, magnetite, apatite, magnetite, pyrite, and chalcopyrite. Amphiboles are commonly replaced by chlorite, carbonate (dolomite, ankerite, and calcite), and/ or magnetite. Albitic feldspar is commonly replaced by orthoclase and altered to sericite.

(2) Felsic Syenite: this unit is fine-grained, strongly magnetic, and reddish brown to pink in colour. It occurs as narrow dike-like lenses within the broader package of mafic syenite, which it commonly displays gradational contacts with. The unit is characterized by 1-5% fine-grained (<2 mm long) amphiboles within an aphanitic and feldspathic groundmass. It commonly contains variable amounts of pyrite and chalcopyrite.

(3) Crowded Syenite Porphyry: This unit is pink to reddish brown in colour and is characterized by 60-70% densely crowded and tightly packed sodic plagioclase feldspar phenocrysts with rare phenocrysts of K-spar within a fine-grained groundmass. The groundmass consists dominantly of plagioclase with lesser amounts of quartz, hematite, magnetite, and amphiboles, and trace amounts of zircon and rutile. Common alteration products include sericite and chlorite. It contains variable amounts of pyrite, chalcopyrite, and molybdenite. This rock is the intrusive phase that is most intimately associated with gold and copper mineralization at Upper Beaver (Bernier and Cole, 2012).

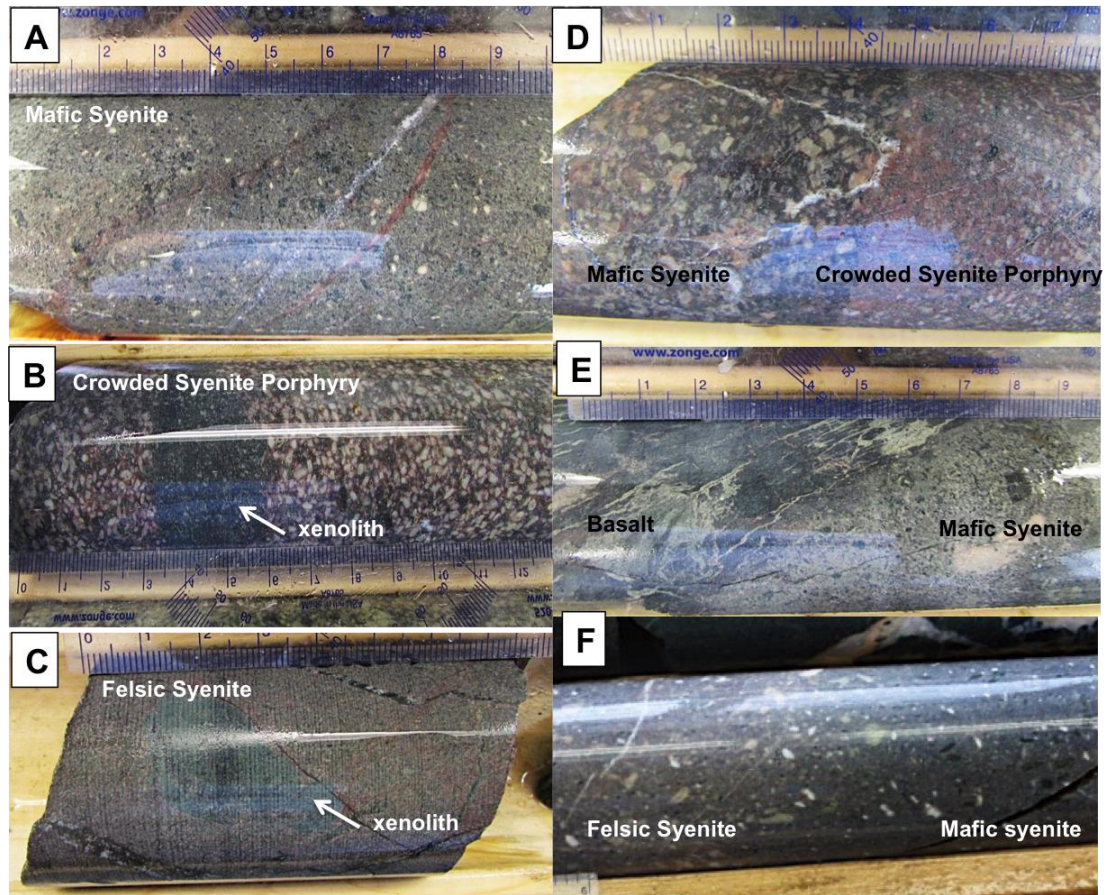


Figure 3.3. Representative lithologies and contacts of the Upper Beaver Intrusive Complex. A) Mafic syenite from UB12_250 (447.5 – 447.7); B) Crowded syenite porphyry with mafic xenoliths from UB10_161, 570 m; C) Felsic syenite with mafic xenoliths from UB10_161, 570 m; D) Sharp contact between mafic syenite and crowded syenite porphyry; E) Sharp contact between mafic syenite and basalt; and F) Gradational contact between felsic syenite and mafic syenite

A number of intrusive phases also crosscut the Upper Beaver Intrusive Complex. Representative photos of these intrusive are provided in Figure 3.4. The intrusive phases that have been identified that cross cut the Upper Beaver Intrusive Complex (Bernier and Cole, 2012) include the following:

(1) Feldspar Porphyry: This unit has an overall pinkish brown color. It consists of 25-50% blocky coarse-grained plagioclase phenocrysts plus 1-5% subhedral medium to coarse-grained amphiboles in a fine-grained feldspathic matrix.

(2) Spotted feldspar porphyry: This unit is characterized by 1-3% blocky subhedral coarse-grained plagioclase phenocrysts in a fine-grained matrix. It is typically hematitized with strong ankerite alteration. Mafic inclusions and xenoliths are relatively common and can reach up to 5 cm in size. This intrusive phase is believed to post-date mineralization in the deposit (Bernier and Cole, 2012).

(3) Matachewan diabase dike: This fine-grained unit is the last intrusive phase on the property. The diabase cross cuts the intrusive complex and mineralization. The diabase intrusion was age-dated using U-Pb zircon ages and yielded an age of $2667.2 \text{ Ma} \pm 1.8 \text{ Ma}$ (Talisker, 2014c). It trends north-south and cuts mineralization in the deposit roughly in half. It dips steeply to the west at 80 to 85 degrees until approximately 200 to 300 m depth where it changes orientation and dips steeply to the east at 80 to 85 degrees (Bernier and Cole, 2012).

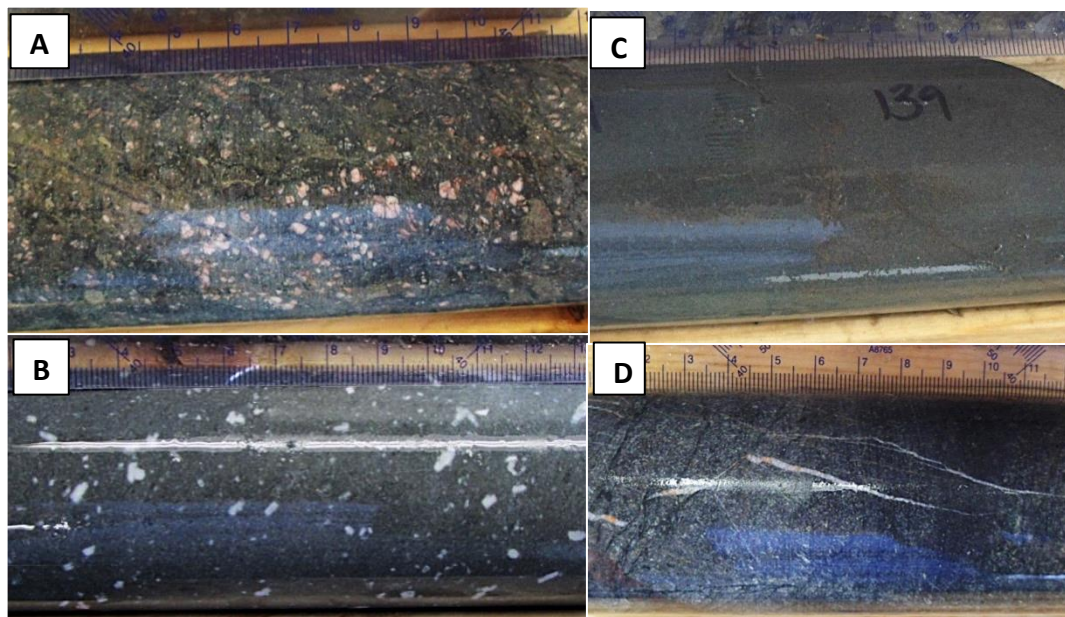


Figure 3.4. Representative photos of A) Feldspar porphyry (UB13_307, 94 m); B) Spotted Feldspar Porphyry (UB11_175, 1086 m), C) Fine-grained diabase (UB08_139) and D) Medium-grained diabase (UB12_250, 272.2 m)

3.1.3 Link between Intrusions and Mineralization in the Upper Beaver Deposit

The link between intrusions and mineralization has long been recognized in the Upper Beaver deposit. Three prominent crowded syenite porphyry intrusions that occur within the mine workings of the Upper Beaver mine have historically, and continue to be especially important marker units for geological interpretation. The intrusions are spatially related to mineralization and frequently host mineralization on the property, especially in the porphyry zones, as shown in Figure 1.5. Mineralization is concentrated along intrusive contacts or in the adjacent rock units. From south to north the dikes are named the Botsford, Bregg, and Tully dikes (Bernier and Cole, 2012).

In a recent review of the deposit, Kontak et al., (2011) interpreted the deposit to be an intrusion-related gold-copper deposit, citing the following as evidence: a) mafic dikes cross cutting intensely altered volcanic rocks, b) sericite-albite alteration which postdates magnetite alteration, c) mafic syenite dikes cross cutting altered felsic syenite dikes, d) quartz feldspar porphyry cross cutting both felsic syenite and mafic syenite, e) and intense phyllic alteration associated with the quartz feldspar porphyry intrusions. Kontak et al., (2011) also stated that the relationship between magmatism and mineralization is supported by sulfur and oxygen isotopes studies of mineralization in the deposit. $\delta^{34}\text{S}$ ($\delta^{34}\text{S} = -13.7$ to $+4\%$ for sulphides associated with mineralization) suggest a uniform or homogenized magmatic S source and $T=400^\circ\text{C}$, whereas $\delta^{18}\text{O}$ isotope data ($\delta^{18}\text{O}_{\text{H}_2\text{O}} = +8$ to 10%) suggests a uniform reservoir for ^{18}O but a mixed magmatic-metamorphic signature, and also a $T=400^\circ\text{C}$ (Kontak et al., 2011). However, this temperature range and ore-fluid composition is not unique for intrusion related deposits. The majority of Late Archean epigenetic gold deposits formed between $325\text{-}400^\circ\text{C}$ and have a globally consistent ore-fluid $\delta^{18}\text{O}$ isotope composition between $6\text{-}13\%$ (Goldfarb et al., 2005). Similarly, the range of $\delta^{34}\text{S}$ isotope values in the Upper Beaver deposit is not unique to intrusion related deposits. $\delta^{34}\text{S}$ isotope measurements on ore-related sulfide minerals in Late Archean epigenetic deposits ranges from 0 to $+10\%$ (Goldfarb et al., 2005), while available sulfur

isotope data for syenite-associated deposits tend to show negative $\delta^{34}\text{S}$ isotope values (Robert, 2001), although there are many exceptions for both groups (Robert, 2001; Goldfarb et al., 2005).

3.2 Geochemical Analysis of Intrusions

3.2.1 Available Data

One of the main goals of this thesis is to extract valuable information from large company-provided geochemical databases. This includes a large dataset consisting of 4026 samples that were analyzed between 2005 and 2015, as described in section 2.2.1, above. All samples from this dataset were analyzed using partial digestion. For this reason, in order to correctly assess the intrusions in the Upper Beaver Intrusive Complex we must compare all results that come from analyzing the large partial digestion database to samples that were analyzed using complete digestion methods. Samples that have undergone complete digestion include data from DeAgazio, (2012) and Feick (2014), which contains 27 samples from the Upper Beaver Intrusive Complex (6 samples each of mafic syenite and mafic syenite porphyry, 8 samples of crowded syenite porphyry, and 7 samples of spotted feldspar porphyry), as well as 6 samples of Tisdale volcanic tuff, 15 samples of basalt from the Blake River Assemblage, and 2 samples of altered volcanoclastic rock from the Blake River Assemblage. Complete digestion data is preferred to partial digestion as partial digestion does not fully dissolve silicate minerals (Kisser, 2005) and as a result high field strength elements, including Ti, Zr, Nb, Hf, Ta, Th, and U, will be partially or wholly resistant to dissolution and analysis will not yield accurate results (Panteeva et al., 2003). Further, due to the widespread alteration in the Larder Lake camp (Powell and Jackson, 1994; Bernier and Cole, 2012) and the inherent mobility of major elements, only select trace elements and REE elements could be used to determine the magma series and host rock composition.

3.2.2 Magma Series

Trace elements were used to determine the magma series of members of the Upper Beaver Intrusive Complex as all rocks in the Upper Beaver deposit are

variably altered (Bernier and Cole, 2012; DeAgazio, 2012). Available data for intrusive rocks from the company-provided geochemical database were plotted on a Th-Co discrimination diagrams and a tectonic classification of mafic igneous rocks diagram. The large dataset is advantageous in that it contains many more samples than were analyzed for the past thesis projects, however all samples were analyzed using partial digestion, which can present problems due to effects of incomplete digestion. For this reason, the results will also be compared to the plotted complete-digestion data. The data set provided by CMC contains the following lithologies: felsic syenite (n=158); mafic syenite (n=1542); mafic syenite porphyry (n=488); brecciated mafic syenite (n=36); brecciated felsic syenite (n=7); crowded syenite porphyry (n=399); feldspar porphyry (n=49); spotted feldspar porphyry (n=6); quartz feldspar porphyry (n=2); and diabase (n=22).

3.2.2.1 Th-Co Discrimination Diagram

Samples were plotted on a Th-Co discrimination diagram to differentiate between calc-alkaline and tholeiitic rocks using relatively immobile elements (Hastie et al., 2007). The diagram uses Th as a proxy for K_2O while Co is used as a proxy for SiO_2 to differentiate between different rock types (Hastie et al., 2007). Data from the CMC-provided partial digestion database was plotted for comparison to data from DeAgazio (2012) and Feick (2014), which contains complete-digestion elemental compositions. Results are provided in Figure 3.5.

The results of plotting both sample sets indicate that the rocks in the Upper Beaver Intrusive Complex are calc-alkaline in composition with minor overlap into the tholeiitic field for mafic syenite and mafic syenite porphyry for incomplete digestion data. On both diagrams crowded syenite porphyry and mafic syenite porphyry plot with compositions similar to dacite-rhyolite rocks, while spotted feldspar porphyry plots with a basaltic andesite-to-andesite composition. Mafic syenite plots with a largely basaltic composition for complete-digestion data. The plot of incomplete-digestion data, however, was very erratic for mafic syenite, with samples having a largely basaltic andesite-to-andesite composition. The considerable scatter is likely due to Th-Co mobility, as neither element is completely immobile

(Hastie et al., 2007). For both sample sets there is more dispersion for Co than for Th. This likely reflects the mobility of Co during metamorphism, which has a limited mobility and is typically retained in Fe-rich minerals including chlorite, Fe-Ti oxides, and amphiboles (Hastie et al., 2007). Ultimately the Th-Co discrimination diagram is useful for differentiating between calc-alkaline and tholeiitic rocks using both partial and complete digestion data, but it cannot be used to differentiate alkaline rocks.

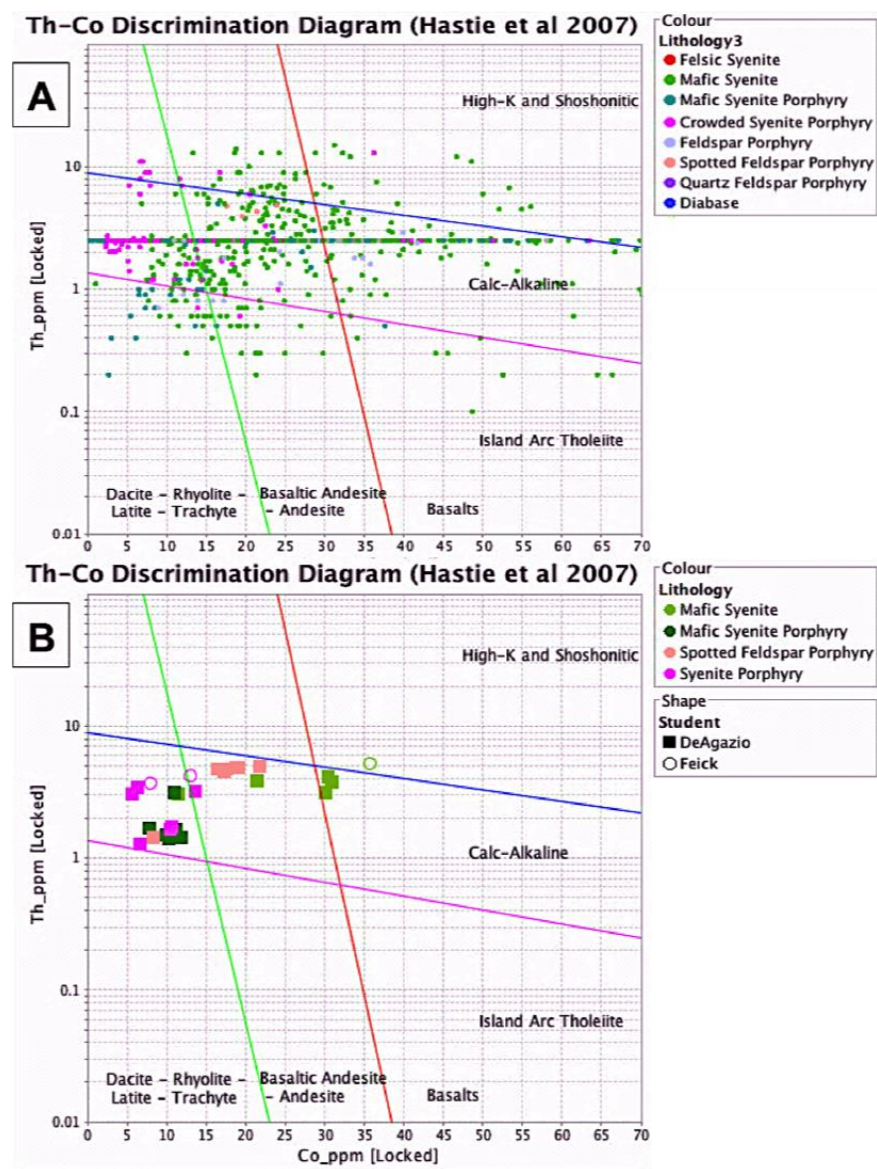


Figure 3.5. Th-Co discrimination diagram showing the classification of select intrusive rocks from the Upper Beaver Intrusive Complex. Data points are colored based on their lithology. (A) Incomplete-digestion geochemical data

provided by Canadian Malartic Corporation; (B) Complete-digestion geochemical data from DeAgazio (2012) and Feick (2014)

3.2.2.2 Tectonic Classification of Mafic Igneous Rocks

Samples were also plotted on a tectonic classification diagram to discriminate between alkaline and calc-alkaline members of the Upper Beaver Intrusive Complex. Results are provided in Figure 3.6.

Plots of partial digestion and complete digestion data are markedly different. While both plots indicate that the rocks are calc-alkaline, samples on the plot that was created using partial-digestion data cluster along the left side of the diagram. This indicates that Nb is likely not being dissolved for samples analyzed using this method and therefore it is not possible to truly differentiate between alkaline and calc-alkaline rocks using incomplete digestion data. However, data from samples that underwent complete digestion can still be used to differentiate between these two rock types as Nb is dissolved using this analytical method. The Y and La data however, is fairly good, with the Y:La ratio remaining relatively consistent between the two datasets. The ratio could potentially serve as a tool to differentiate between different lithologies in the Upper Beaver deposit. Overall, results indicate that the rocks are largely calc-alkaline (arc-type) in composition with some overlap into late-to-post-orogenic intra-continental domains for mafic syenite porphyry. The results ultimately show that the rocks that make up the Upper Beaver Intrusive Complex are calc-alkaline in composition and therefore were not derived from an alkaline source as the name “syenite” suggests.

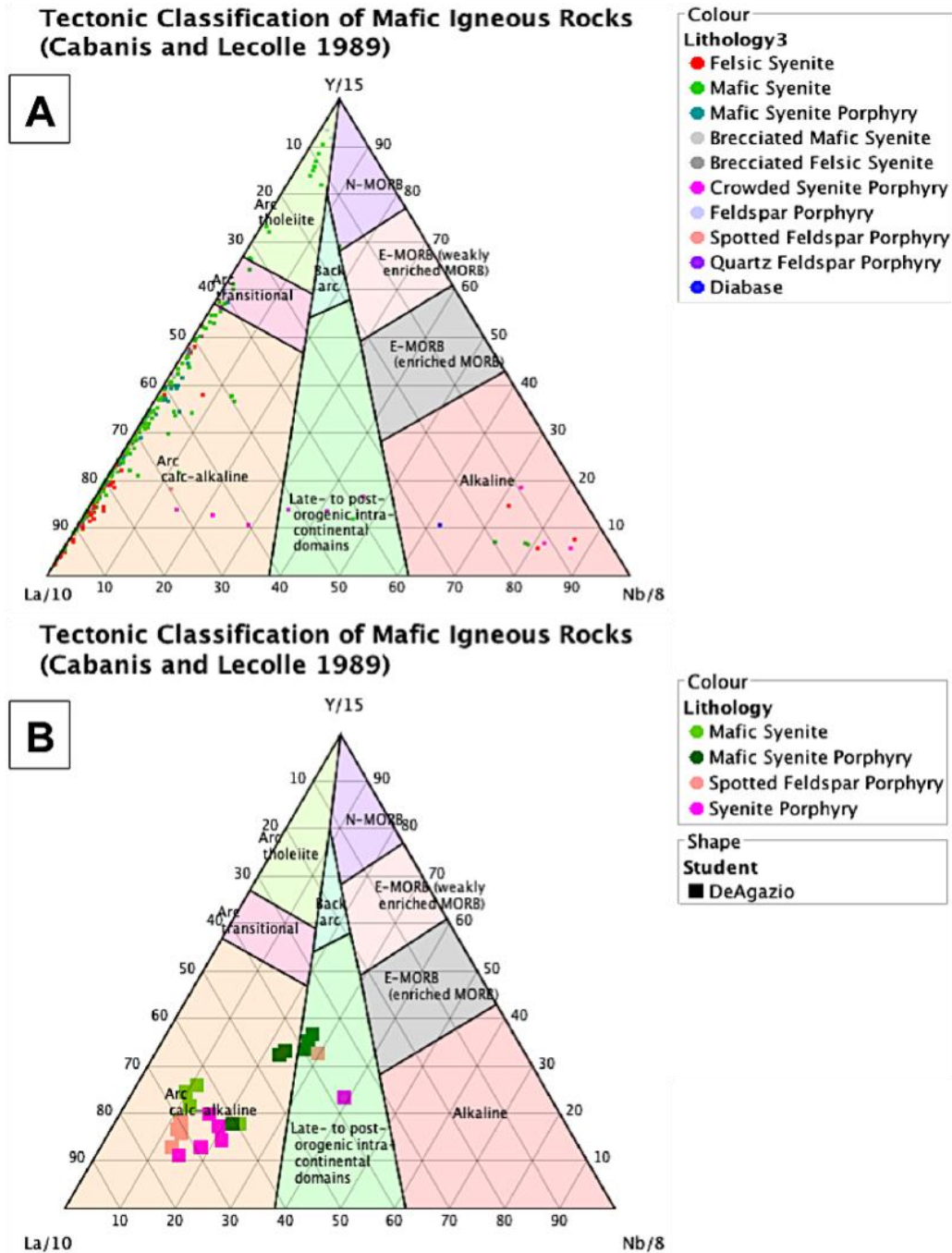
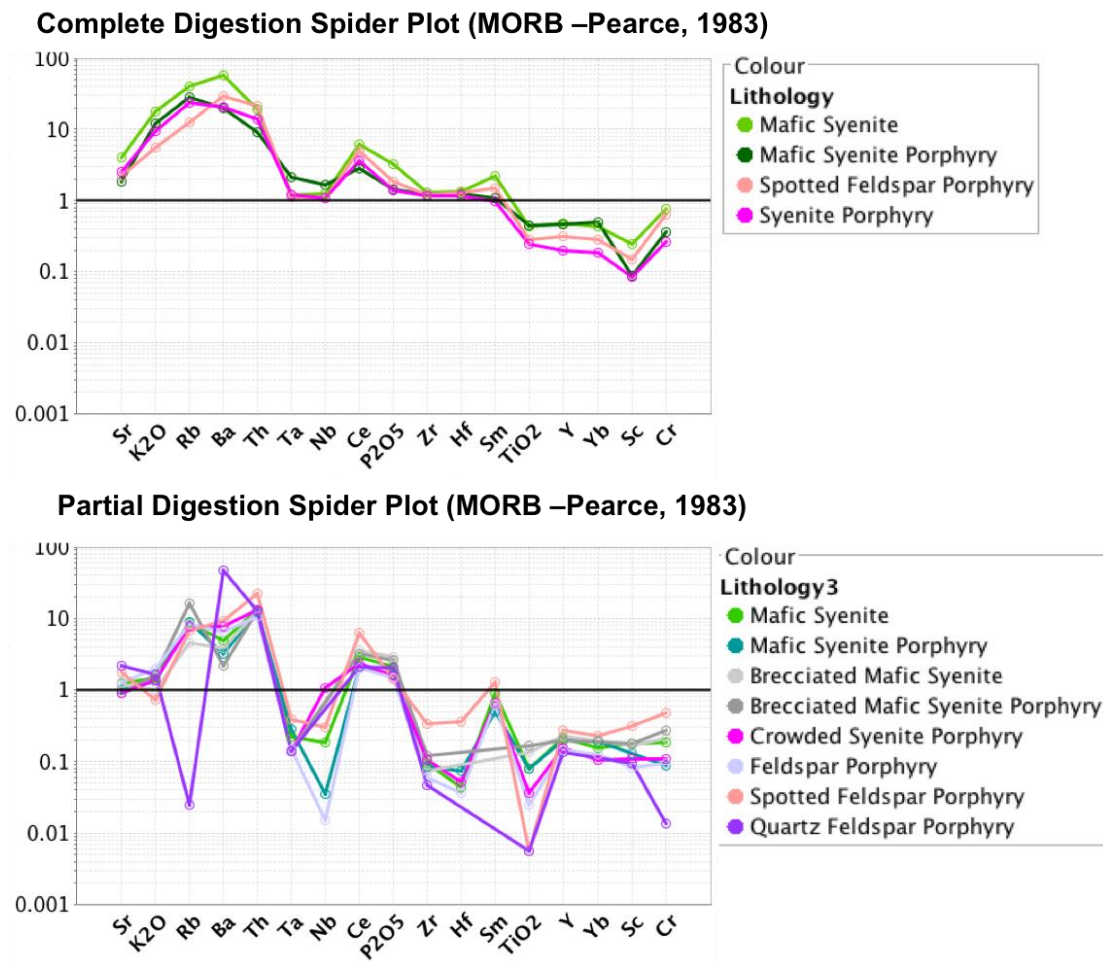


Figure 3.6. Tectonic classification diagram for mafic igneous rocks showing the classification of select intrusive rocks from the Upper Beaver Intrusive Complex. Data points are colored based on their lithology. (A) Incomplete-digestion geochemical data provided by Canadian Malartic Corporation; (B) Complete-digestion geochemical data from DeAgazio (2012) and Feick (2014)

3.2.3 REE Signature of Intrusives

Available REE complete-digestion data was used to determine the main lithologies in the Upper Beaver Intrusive Complex. REEs were plotted on a MORB-normalized spider diagram (Pearce, 1983) and a chondrite-normalized spider diagram (Masuda, 1973) for comparison to the results of Sutcliffe et al., (1993) on plutonism in the Abitibi. Sutcliffe et al., (1993) identified six main intrusive suites in the Abitibi: (1) tholeiitic-calc/alkaline; (2) calc-alkaline tonalite suite; (3) granite-granodiorite suite, (4) diorite-monzonite suite; (5) diorite-syenite suite; and (6) two-mica granite suite. They also put the suites into a petrographic framework where pre- to syn-accretionary magmas produced the tholeiitic and calc-alkaline tonalite suites, while late to post-accretionary magmatic activity produced the diorite-monzonite, granodiorite-granite, and the alkalic diorite-syenite suites. Results are shown for both the complete-digestion dataset and for the partial-digestion dataset in Figure 3.7 and Figure 3.8.



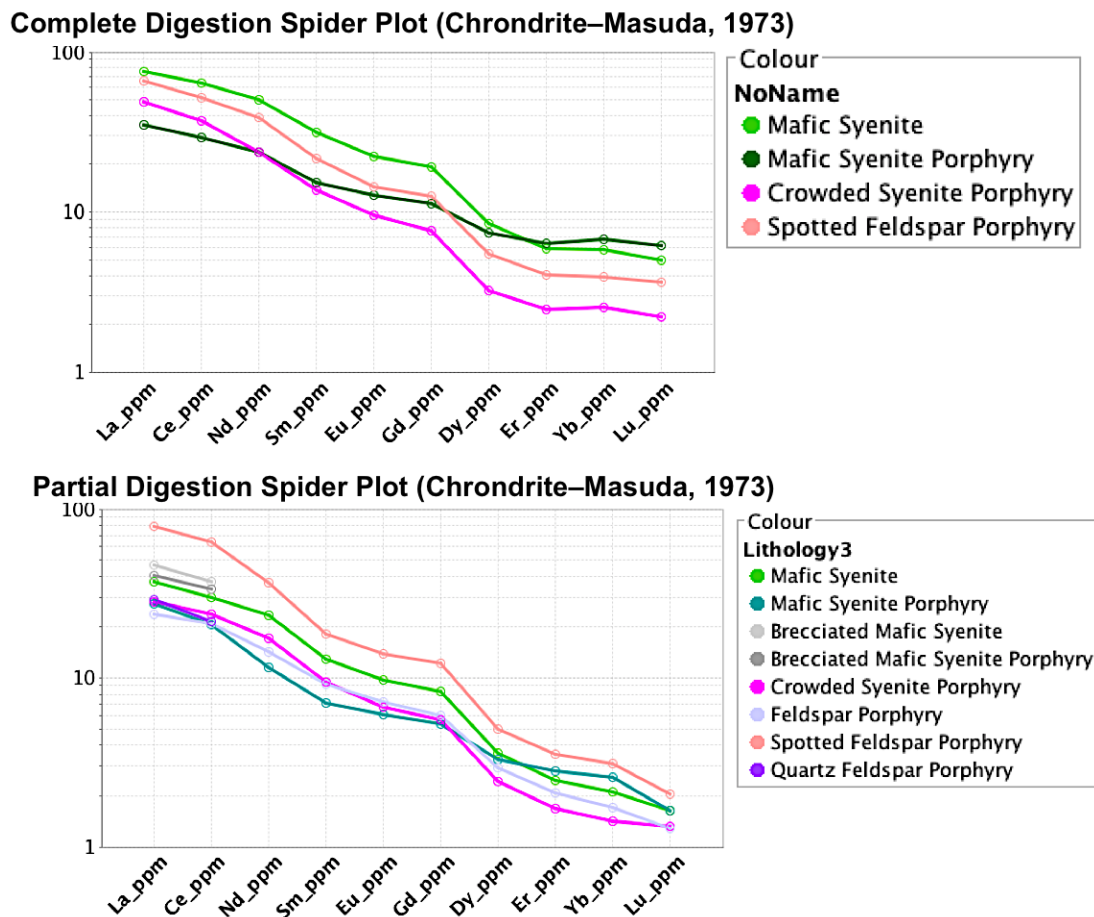


Figure 3.8. Chondrite-normalized spider diagram based on Masuda et al. (1973) showing the REE signature of select intrusions from the Upper Beaver Intrusive Complex. Data that underwent complete digestion (i.e., data from DeAgazio (2012) and Feick (2014) is provided on the upper spider plot, while data from the large company-provided geochemical database that was analyzing using partial digestion is shown on the bottom.

Overall, there are large differences between data that was analyzed using complete-digestion and data analyzed using partial digestion. HFSE's and LILE's analyzed using partial digestion data were highly erratic compared to those analyzed using complete digestion data when plotted on a MORB- normalized spider diagram. Many of these elements analyzed using partial digestion methods plotted on this particular spider diagram had notably lower concentrations than those analyzed using complete digestion methods, likely due to silicate mineral phases being resistant to dissolution (Panteeva et al., 2003). These trends are not prominent on the chondrite-normalized spider diagram, with complete digestion and partial digestion data having

the same overall HFSE and LILE distribution. The ratio of La/Yb is also notably different between the two sample sets however, as identified in Table 3.1, with both La and Yb concentrations being much lower in samples analyzed by partial digestion, possibly due to incomplete dissolution. It is important to note that the analytical method also drastically affects the detection limit of the elements being analyzed for. The detection limit of La and Yb in Feick (2014) is 0.05 ppm for both La and Yb, which were analyzed by INAA. Comparatively, the detection limit for La was 0.5 ppm for data analyzed by LABO and 1.0 ppm for data analyzed by AGAT, and the detection limit for Yb was 0.1 ppm for data analyzed by LABO, and 0.05 ppm for data analyzed by AGAT and SGS. Finally, the HFSE and LILE distribution of samples of mafic syenite porphyry plot with a unique composition. However, this may be due to a relatively small sample size (n=3).

Table 3.1. REE element concentration in samples of mafic syenite, mafic syenite porphyry, crowded syenite, and feldspar porphyry using partial digestion and whole digestion data

	Partial Digestion Data			Whole Digestion Data		
	La	Yb	La/Yb	La	Yb	La/Yb
Mafic Syenite	14.1	0.5	27.2	28.5	1.5	19.6
Mafic Syenite Porphyry	10.4	0.6	16.3	13.3	1.7	7.9
Crowded Syenite Porphyry	10.7	0.4	30.1	18.5	0.6	29.4
Spotted Feldspar Porphyry	29.8	0.8	38.5	25.1	1.0	25.7

The MORB-normalized spider diagram for samples that underwent complete digestion identifies that members of the Upper Beaver Intrusive Complex are characterized by enrichment in lithophile elements (Sr, Ba, and light REE), and a Nb-Ta trough. Additionally, the chondrite-normalized spider diagram identifies that the rocks lack a Eu anomaly and the La/Yb ratio ranges from 7.9 to 29.4 for complete-digestion data.

These features are consistent with the diorite-monzonite and diorite-syenite suites proposed by Sutcliffe et al., (1993). Sutcliffe et al., (1993) identifies that the diorite-monzonite suite is gradational with the diorite-syenite suite. The diorite-syenite suite is more alkaline with members ranging between calc-alkaline and alkaline, while the diorite-monzonite suite is calc-alkaline in composition (Sutcliffe et al., 1993). The calc-alkaline nature of the rocks in the Upper Beaver Intrusive Complex indicate that they fit best with the diorite-monzonite suite.

3.2.4 Comparison to Local Intrusions

An additional factor that may be taken into account to determine the intrusive suite of the lithologies in the Upper Beaver Intrusive Complex is the age of intrusive phases in the complex. Age dating of intrusive phases in the complex indicates that all intrusions are younger than 2.7 Ga. This fits the regional framework defined by Sutcliffe et al., (1993) for members of the diorite-monzonite suite and the diorite-syenite suite, which are typically less than 2.70 Ga years old in the Abitibi.

Local batholiths and stocks include the Round Lake batholith, the Lake Abitibi batholith, and the Lebel, Murdock Creek, and Otto stocks. The bodies occur both north and south of the Larder Lake-Cadillac Deformation Zone (Alexander, 2006). These intrusive bodies have been studied to some extent and authors have determined that the parental magma for the local stocks and batholiths were mantle-derived and possibly subduction-related (Sutcliffe et al., 1990; Cruden, 1993). Unpublished ages for members of the Upper Beaver Intrusive Complex based on age dating by Talisker (2014c) compared to published ages for local intrusions, are provided in Table 3.2.

Table 3.2. Available data on the age and lithology of local intrusions

Intrusion	Lithology	Intrusive Suite	Age (Ma)	Error (\pm Ma)	Reference
Round Lake batholith	trondhjemite-tonalite-granodiorite	Granite-Granodiorite (Sutcliffe et al., 1983)	2703-2679	NA	Jensen (1985) and Jackson and Fyon (1991)
Lake Abitibi batholith	trondhjemite-tonalite-granodiorite	Granite-Granodiorite (Sutcliffe et al., 1983)	2690-2700	NA	Mortensen (1993) Feng and Kerrich, 1990 Jackson and Fyon (1991)
Bidgood quartz porphyry stock	Quartz porphyry		2685	3	Corfu et al., (1991)
Upper Beaver Mafic Syenite	Mafic Syenite		2683.3	1.5	Talisker (2014c)
Lebel	Alkalic intrusives (syenite to mafic syenite)		2680	NA	Corfu (1993)
Otto	Alkalic intrusives (syenite to mafic syenite)	Diorite-syenite (Sutcliffe et al., 1983)	2680	1	Corfu (1989)
Canadian Kirkland Lower foliated tuff	Lower foliated tuff		2675	2.2	Talisker (2014c)
Canadian Kirkland volcanics	Volcanics		2673	3.2	Talisker (2014c)
Murdock Creek	Alkalic intrusives (syenite to mafic syenite)	Diorite-syenite (Sutcliffe et al., 1983)	2672 and 2673	2	Wilkinson et al., (1999)
Upper Beaver Crowded porphyry	Crowded syenite		2671.9	1.8	Talisker (2014c)
Bidgood spotted feldspar porphyry	Spotted feldspar porphyry		2671.7	2.1	Talisker (2014c)
Upper Beaver Spotted feldspar porphyry	Spotted feldspar porphyry		2670.7	3.5	Talisker (2014c)
Upper Beaver Diabase	Diabase		2667.3	1.8	Talisker (2014c)

Sutcliffe et al., (1993) identified that the Round Lake Batholith and the Lake Abitibi Batholith are part of the granite-granodiorite suite. Members of this suite are typically characterized by enriched large ion lithophiles, especially Ba and Sr, and are compositionally similar to the diorite-monzonite suite (Sutcliffe et al., 1993).

With the exception of age dating performed by Jackson and Fyon (1991), all ages reported for the Round Lake Batholith and the Lake Abitibi Batholith are at least 8 Ma older than the oldest intrusions dated in the Upper Beaver Intrusive Complex.

Similarly, Sutcliffe et al., (1993) identified that the Otto Stock and Murdock Creek Intrusions are part of the diorite-syenite suite. Alexander (2006) further suggested that the Lebel Stock is also similar to the Otto Stock and Murdock Creek stocks, which are all alkalic in composition with members ranging from syenite to mafic syenite. The diorite-syenite suite is typically characterized by elevated amounts of large ion lithophile elements, depleted amounts of Ta-Nb, and no significant Eu anomaly (Sutcliffe et al., 1993). Published age dates compared to dating performed by Talisker (2014c) indicates that members of the Upper Beaver Intrusive complex are roughly the same age as local members of the diorite-syenite suite.

REE patterns for members of the Upper Beaver Intrusive Complex were also compared to available data for other intrusions in the area to confirm that intrusions in Upper Beaver are comparable to local intrusions. This includes data from Beakhouse (2011) and from Isopolatov et al., (2005), as summarized in Tables 3.3 and 3.4. Data from Beakhouse (2011) is based on samples from the Lebel stock, while samples from Gauthier were collected from close to the Larder-Lake Cadillac Break near the Anoki and McBean deposits. The Lebel stock is alkalic in composition, and consists largely of syenite (Beakhouse, 2011). The samples from southern Gauthier Township were taken near the Anoki and McBean mines. Local intrusives are identified as calc-alkaline diorities by Ewert et al., (2010) and as syenitic intrusions (by Isopolatov et al., 2008).

Table 3.3. Information on available published data of local intrusions including where samples are from and the lithologies analyzed

Township	Reference	Sample ID	Datum	Easting	Northing	Lithology
Lebel	Beakhouse (2011)	7483	NAD27/17	580671	5335791	Felsic Porphyry
Lebel	Beakhouse (2011)	7541	NAD27/17	577400	5331736	Major Syenite Phase
Lebel	Beakhouse (2011)	7542	NAD27/17	576282	5331692	Major Syenite Phase
Lebel	Beakhouse (2011)	7543	NAD27/17	575910	5331849	Major Syenite Phase
Lebel	Beakhouse (2011)	7544	NAD27/17	574591	5331020	Major Syenite Phase
Lebel	Beakhouse (2011)	7545	NAD27/17	574392	5331363	Major Syenite Phase
Gauthier	Isoplatov et al., (2005)	003VOI0106-1	NAD83/17	589500	5329763	Feldspar Porph
Gauthier	Isoplatov et al., (2005)	003VOI 10115-2	NAD83/17	589682	5329910	Feldspar Porph
Gauthier	Isoplatov et al., (2005)	003VOI0066-2	NAD83/17	589382	5330332	Syenite Porphyry
Gauthier	Isoplatov et al., (2005)	AN08-43-157.4	NAD83/17	586591	5331464	Syenite
Gauthier	Isoplatov et al., (2005)	AN03-53-227.5	NAD83/17	586517	5331416	Syenite

Table 3.4. Published REE concentrations for local intrusions. Sample IDs correspond to those in Table 7

Sample ID	La ppm	Ce ppm	Nd ppm	Sm ppm	Eu ppm	Gd ppm	Dy ppm	Er ppm	Yb ppm	Lu ppm
7483	7.82	16.74	7.96	1.45	0.45	1.01	0.63	0.32	0.31	0.05
7541	74.14	141.53	52.76	8.45	1.96	5.75	3.58	1.70	1.60	0.24
7542	86.33	174.56	73.09	12.01	2.80	7.94	4.80	2.29	2.08	0.30
7543	68.92	150.82	60.68	9.68	2.10	6.30	4.28	2.22	2.08	0.28
7544	67.28	145.52	71.57	12.71	3.28	8.80	4.97	2.04	1.72	0.24
7545	77.77	159.67	72.02	12.12	3.02	8.18	4.62	1.94	1.70	0.26
003VOI0106-1	5.08	13.31	8.61	1.67	0.45	1.13	0.46	0.18	0.14	0.02
003VOI 10115-2	21.75	46.16	22.90	3.99	0.98	2.38	1.08	0.46	0.41	0.06
003VOI0066-2	126.90	264.25	132.60	26.44	7.29	23.41	17.01	7.20	5.43	0.74
AN08-43-157.4	61.66	132.28	67.41	13.00	3.35	10.17	6.52	3.24	3.00	0.45
AN03-53-227.5	26.96	57.22	31.00	6.48	1.83	5.95	4.31	2.38	2.28	0.35

Overall the REE diagrams for samples from Lebel and Gauthier Township show similar patterns, as shown in Figure 3.9 and Figure 3.10. All samples plotted on the MORB-normalized spider plot have a Nb-Ta trough, characteristic of both the monzonite-diorite suites and diorite-syenite suites. Differences in concentrations of enriched lithophile elements (Sr Ba, and LREE) are likely due to their mobility during alteration.

The chondrite normalized spider plot identifies that none of the samples have a Eu anomaly. Further, the La/Yb ratio ranges from 16.6 to 27.1 in the Lebel deposit for felsic porphyry and syenite, respectively, while the ratio ranges from 10.7 for syenite to 15.4 for syenite porphyry to 29.4 for feldspar porphyry in the samples from southern Gauthier Township. The lack of a Eu anomaly and the range in La/Yb values fits with both the diorite-monzonite suite and the diorite-syenite suite as proposed by Sutcliffe et al., (1993). Additionally, these values are similar to those calculated for intrusive rocks from the Upper Beaver deposit.

Overall, although the intrusive rocks from the Lebel stock are identified as being alkalic syenites by Beakhouse (2011) and samples from the southern Gauthier township are cited as being dioritic in composition by Ewert et al., (2010) and syenitic elsewhere (Isopolatov, 2008), they share the same REE signature as rock from the Upper Beaver Intrusive Complex. This may be due to chemical similarities among the diorite-syenite and diorite-monzonite classes, as outlined by Sutcliffe et al., (1993). Further sampling and geochemical analysis of local intrusions may be beneficial for comparison to samples from the Upper Beaver Intrusive Complex.

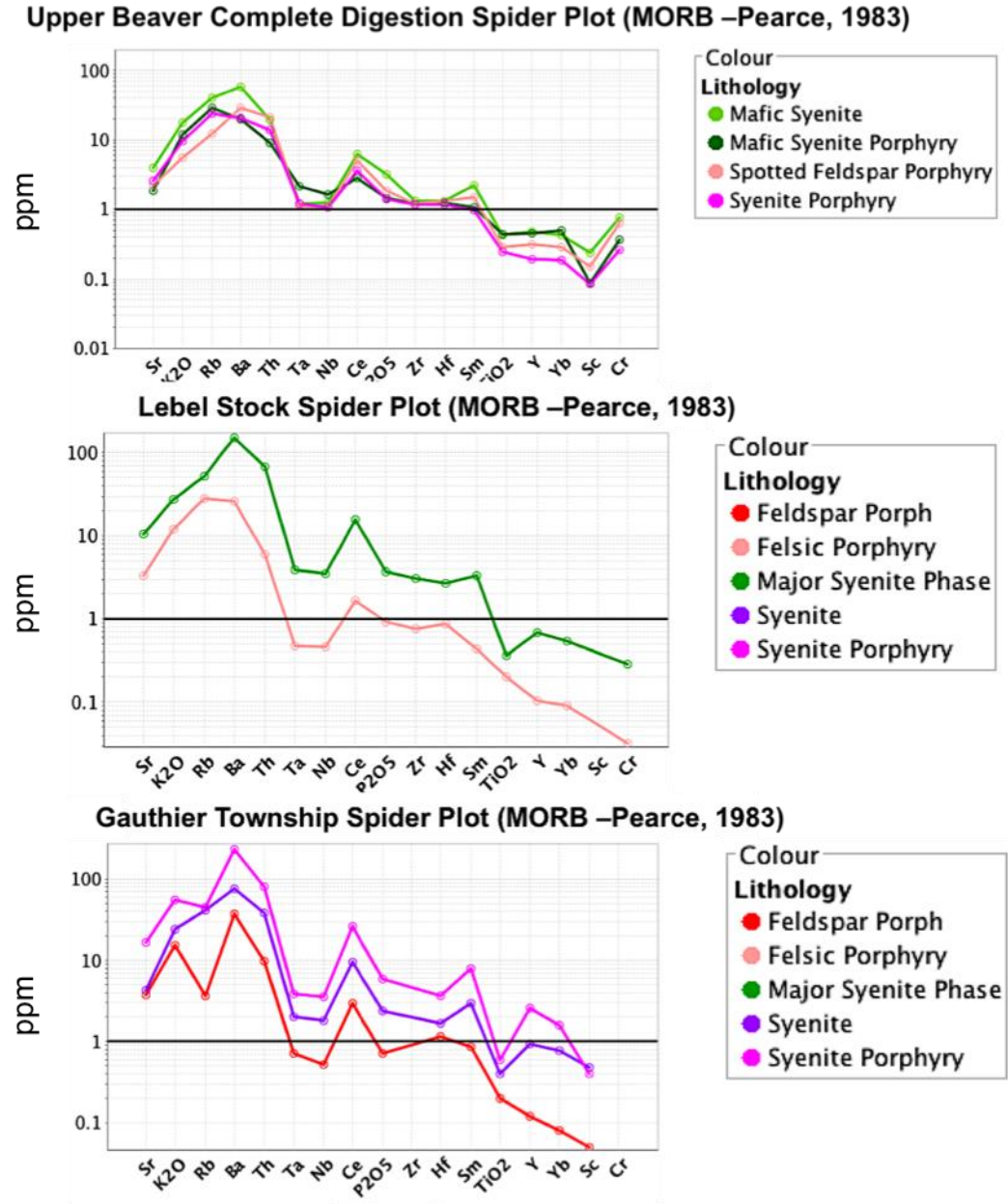


Figure 3.9. MORB-normalized spider diagram based on Pearce (1983) for members of the Upper Beaver Intrusive Complex and for intrusions in Gauthier and Level as identified

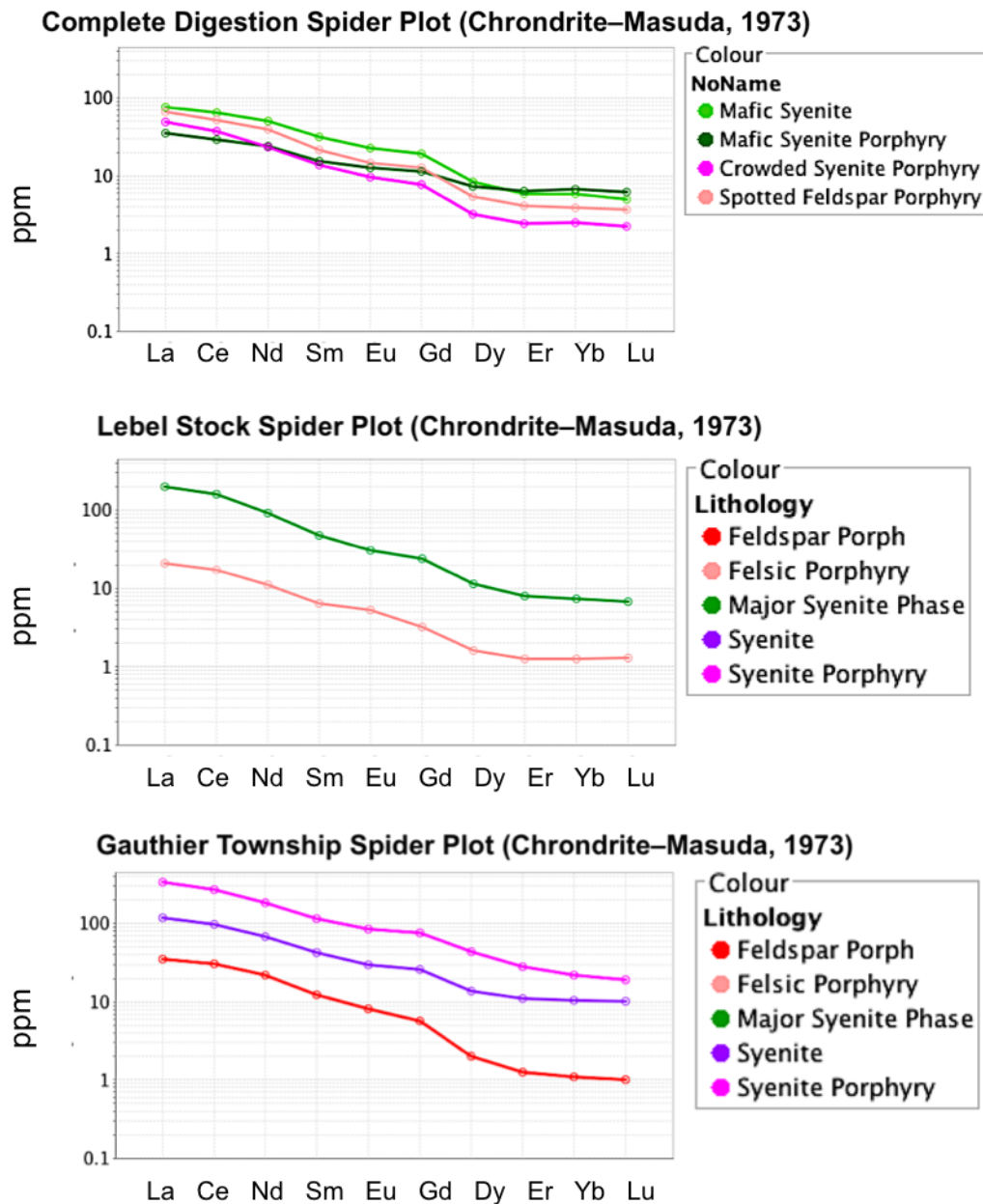


Figure 3.10. Chondrite-normalized spider diagram based on Masuda et al., (1973) for members of the Upper Beaver Intrusive Complex and for intrusions in Gauthier and Lebel as identified

3.2.5 Correlations between Mineralization and Host Rock Lithology

The large Cu-Au Assay dataset provided by Canadian Malartic Corporation was used to identify which lithologies were most intimately associated with mineralization. Lithologies with a sample size of less than 10 and samples that were

classified without a specific lithology (e.g., fault zone samples and quartz carbonate vein zone samples, etc.) were removed from the dataset. The final dataset consisted of 157,580 samples. The data was then filtered to contain samples with a grade over 2 g/t. A summary of the final database is provided in Table 3.5. This corresponds to a grade of 2 g/t that was used in a recent technical report on the property, which was used to define mineralized zones for resource modeling (Bernier and Cole, 2012).

Table 3.5. Summary of the large assay database provided by Canadian Malartic Corporation showing the number of samples, the mean Au grade, and the mean Cu for each lithology after samples without a specific lithology were removed. Concentration of Au greater than 10 g/t with more than 2% of all samples analyzed >2g/t have been bolded

Lithology	Number of samples	Number of samples >2g/t	Mean Au (g/t)	Mean Cu (pct)	% of samples >2g/t
Tisdale Tuff	2769	50	10.40	0.13	1.81
Blake River Basalts	51931	1413	6.62	0.14	2.72
Blake River Basalts (brecciated)	678	30	7.87	0.15	4.42
Agglomerate	138	3	3.21	0.08	2.17
Graphitic sedimentary rocks	195	12	10.08	0.19	6.15
Conglomerate	2159	75	5.45	0.02	3.47
Greywacke/ Silty Arenite	2870	66	8.58	0.10	2.30
Siltstone	199	2	4.12	0.94	1.01
Argillite	448	2	2.91	0.00	0.45
Cherty sedimentary rocks	970	46	4.76	0.06	4.74

Volcaniclastic	4911	145	6.21	0.14	2.95
Felsic Syenite	6970	242	6.97	0.14	3.47
Mafic Syenite	45939	1215	11.04	0.28	2.64
Mafic Syenite Porphyry	11940	381	8.91	0.21	3.19
Brecciated Mafic Syenite	902	54	10.79	0.50	5.99
Brecciated Mafic Syenite Porphyry	29	0			0.00
Crowded Syenite Porphyry	17424	481	11.28	0.19	2.76
Feldspar Porphyry	3483	49	10.15	0.09	1.41
Spotted Feldspar Porphyry	2414	2	2.68	0.10	0.08
Diabase Dike	803	5	6.22	0.16	0.62
Gabbro	396	4	4.20	0.00	1.01
Ultramafic	12	0			0.00

Gold and copper mineralization can be hosted in any lithology in the deposit (Bernier and Cole, 2012). Percentile box plots showing the distribution of Au and Cu among the main lithologies in the deposit is provided in Figure 3.11. Lithologies with the highest mean Au grade include crowded syenite porphyry, mafic syenite, brecciated mafic syenite, feldspar porphyry, and graphitic sedimentary rocks. Lithologies with the highest mean Cu grade include siltstone, brecciated mafic syenite, cherty sedimentary rocks, and brecciated Blake River basalts. Brecciated

mafic syenite porphyry and ultramafics have the lowest Au grades of samples analyzed.

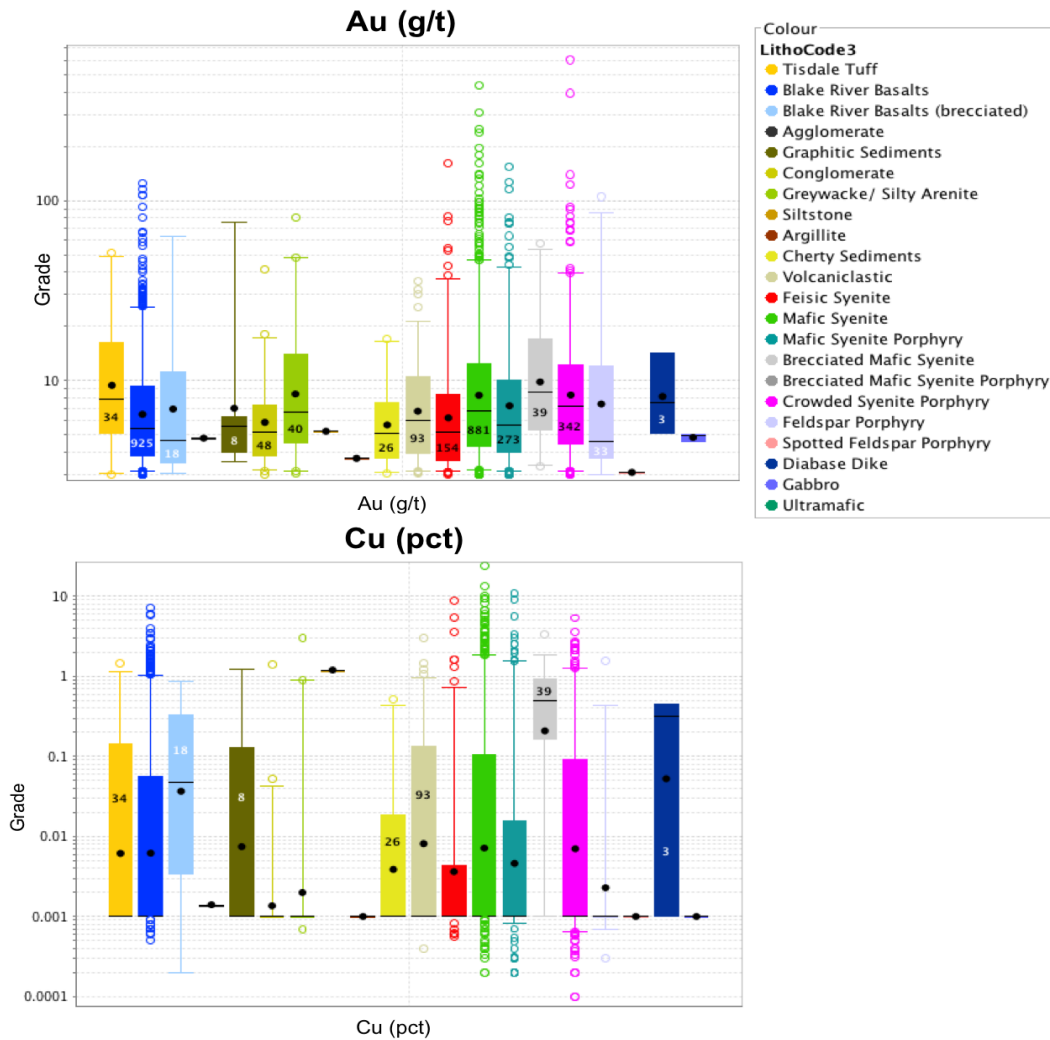


Figure 3.11. Percentile box plots showing the distribution of Au and Cu in the deposit among the main lithologies. The central portion of the box contains the middle 50% of the data from Q1 (the middle value in the first half of the dataset) to Q3 (the middle value in the second half of the dataset). Upper and lower whiskers contain 5% to 95% of the values in the data set. Outliers are represented by open circles and include the data that is in the top or bottom 5% of the data. The black circle represents the mean value for each lithology and the black line represents the median value for each lithology.

3.2.6 Less Common Intrusives

Three variations on typical intrusions are present in the deposit that only occur locally as discontinuous lenses. These include intrusions with a microphyric texture, an amphibole-rich intrusion, and a biotite-rich intrusion. These intrusions are typically grouped together when logged with mafic syenite, to simplify lithology codes. The intrusives are recognized by their distinctive mineralogy and textures. Representative hand-sample photos of the three less common intrusives are shown in Figure 3.12.

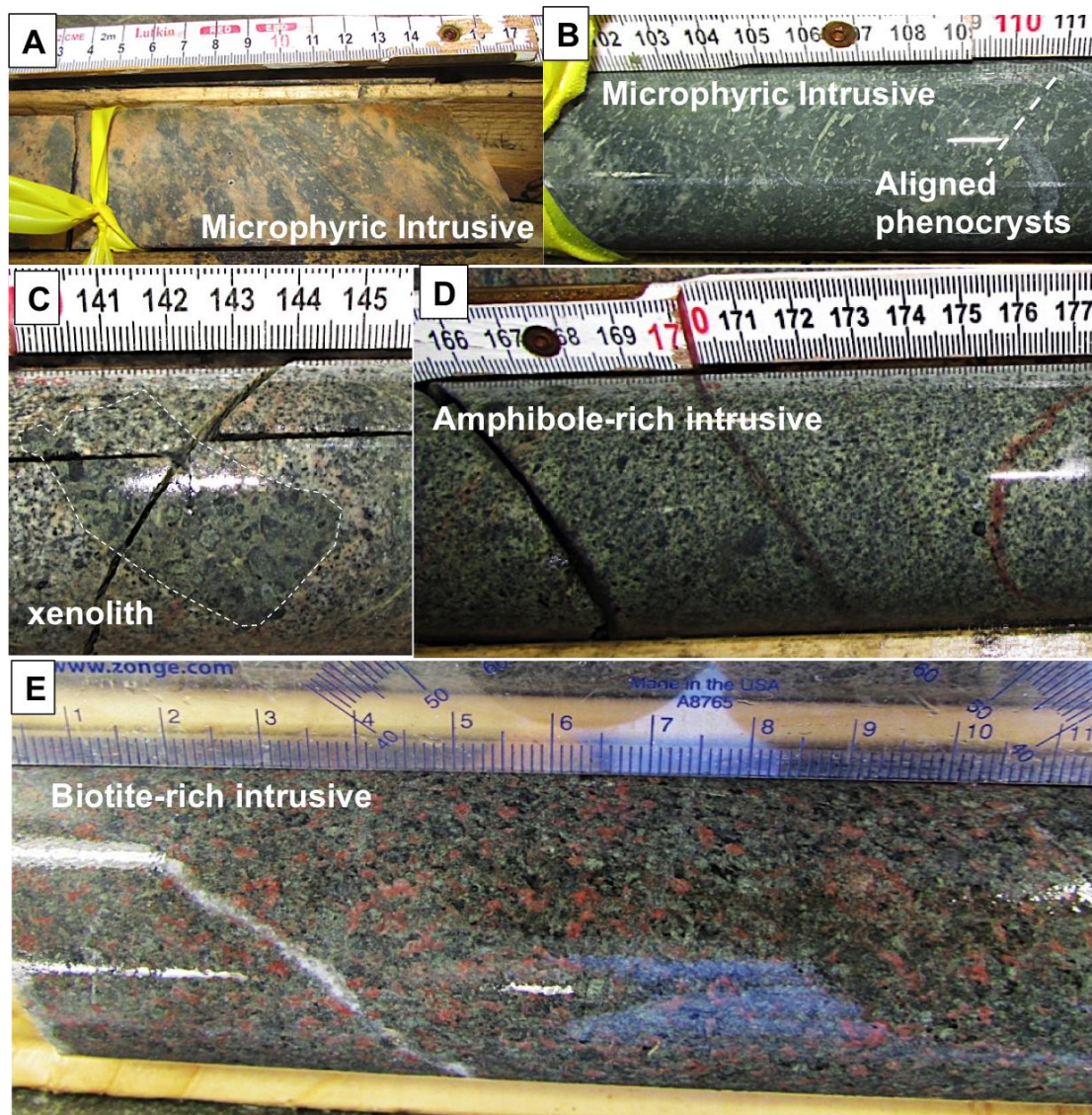


Figure 3.12. Unusual lithologies in the Upper Beaver deposit. A, B) Samples of microphyric intrusives from UB11_175 W4 and UB11_171 W2, respectively; C)

“Xenolithic” inclusion of an amphibole-rich intrusive from UB11_171 845.3-845.5 m; D) Representative photo of amphibole-rich intrusives in the deposit; and E) Representative photo of biotite-rich intrusive from UB13_308, 206.2 m

3.2.6.1 Microprobe WDS Analysis

The mineral composition of amphiboles, biotite (in the biotite-rich intrusive), and feldspars were determined by WDS electron microprobe analysis for the amphibole-rich and biotite-rich intrusives as well as for relatively fresh mafic syenite. Due to the abundance of alteration, WDS data was not collected for the microphyric unit as no relict amphiboles remained. Microprobe analysis was performed on light and dark shades of amphibole and on K-spar and albite to capture the chemical variation and alteration in the minerals. The structural formula of amphiboles was determined using PROBE-AMPH (an amphibole structural formula calculator), and was normalized based on 23 oxygens (Tindle and Webb, 1994) for amphiboles. In general, light shades of amphibole corresponded to more a FeO rich composition, while dark shades were more MgO rich. All amphiboles analyzed were calcic, with $(Ca+Na) \geq 1.34$ and $Na < 0.67$. The composition of amphiboles was also determined for relatively unaltered mafic syenite for comparison to amphiboles in amphibole-rich and biotite-rich intrusives. Mafic syenite contained the least altered amphiboles, with medium and bright shades ranging between potassian magnesio-hastingsite and magnesio-hastingsite because of their high titanium and very high aluminum content. They also contained high amounts of Na_2O , FeO , BaO , and K_2O . Darker shades of amphibole corresponded to actinolitic hornblende and contained much lower amounts of Al_2O_3 , Na_2O , TiO_2 , BaO , and K_2O , and had more Cl and MnO than their brighter counterparts.

The chemical composition of feldspars and biotite were calculated in Excel using a normalization factor of 8 oxygens for feldspars and 11 oxygens for biotite. Results of amphibole analysis are provided in Figure 3.13 and Figure 3.14, and are discussed in detail below.

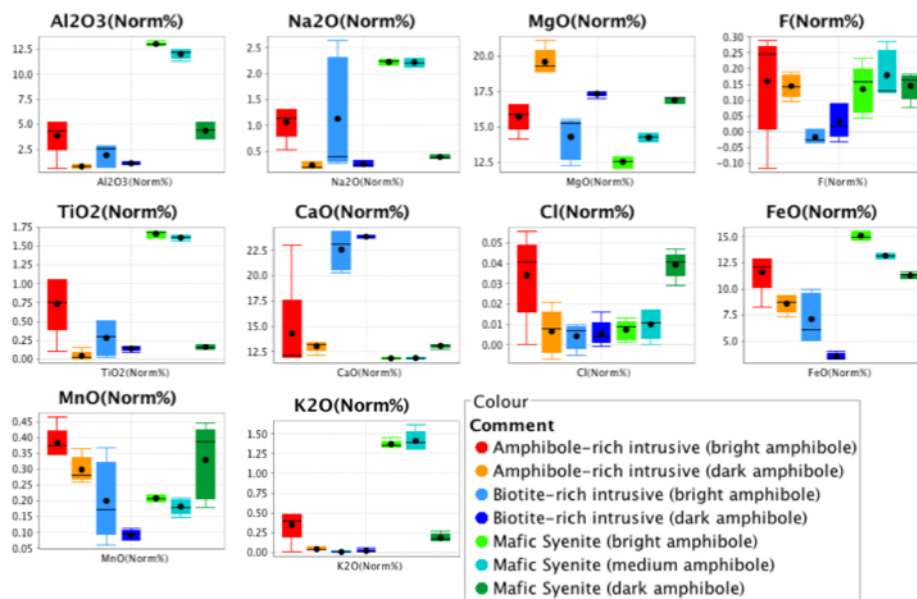


Figure 3.13. Percentile box plots showing the distribution of WDS electron microprobe results based on 5 analysis points per sample group. The central portion of the box contains the middle 50% of the data from Q1 (the middle value in the first half of the dataset) to Q3 (the middle value in the second half of the dataset). Upper and lower whiskers contain 5% to 95% of the values in the dataset. The black circle represents the mean values for each sample group while the black line represents the median value for each sample group

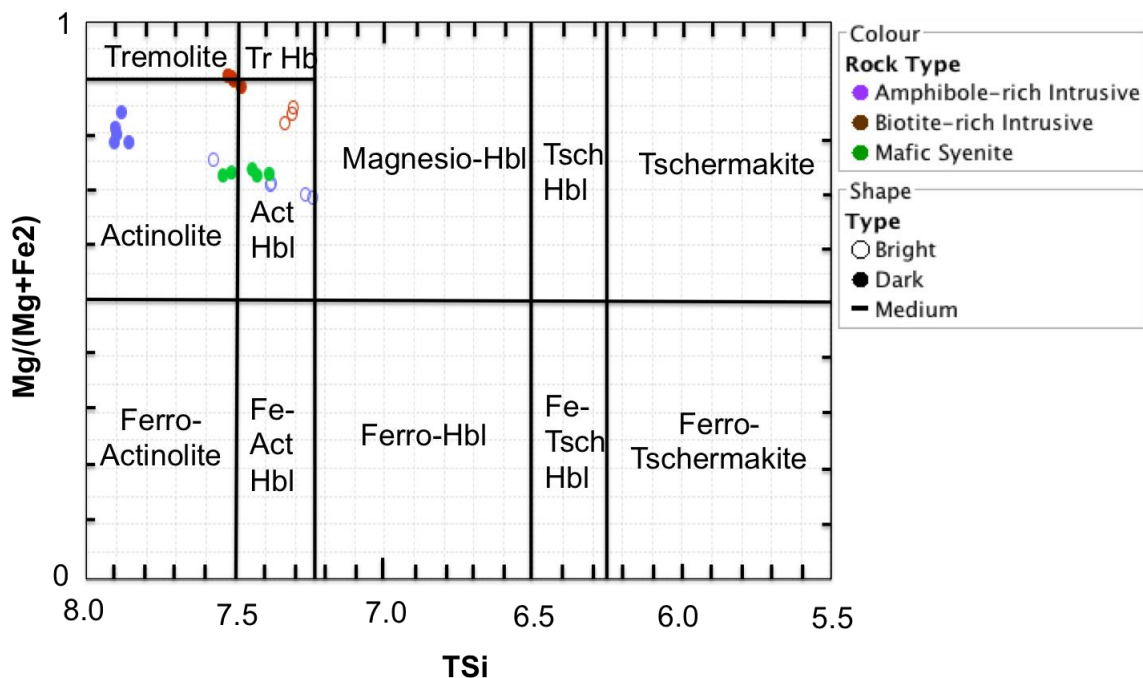


Figure 3.14. Classification of calcic amphiboles in which $(Ca+Na) \geq 1.34$, $Na < 0.67$, $(Na+K) < 0.50$ and $Ti < 0.50$ based on stoichiometric composition (Si vs.. Mg/(Mg+Fe) of amphiboles analyzed by WDS microprobe analysis for select amphiboles based on classification by Leake (1978). Silicic edenite, magnesio-hastingsite and potassian-magnesio-hastingsite are not shown on the diagram

3.2.6.2 Microphyric Intrusive

The microphyric intrusive, referred to as “microphyric mafic syenite” by CMC geologists, is dark green to gray and aphanitic. In hand sample it is characterized by <30% subhedral to euhedral 1-2 mm long light pinkish to yellowish green microphyric phenocrysts in a fine-grained feldspathic groundmass.

In both hand sample and thin section sample UWO_2015_27 appeared to be less altered than sample UWO_2015_28. Petrographic observations of sample UWO_2015_27 revealed that the rock consists of large replaced pseudomorphs, which resemble amphiboles, due to their well-formed cleavages at 60 and 120 degrees, brownish to green color, high relief, and slight pleochroism within a fine-grained feldspathic groundmass. Conversely, sample UWO_2015_28 was much more

strongly altered by albite and sericite and the large replacement pseudomorphs that were observed in UWO_2015_27 were absent in UWO_2015_28. Relict dark rims, as shown in Figure 3.15, were visible where original phenocrysts had been pseudomorphically altered instead. Replacement minerals were too fine grained to identify petrographically and were analyzed by microprobe EDS analysis.

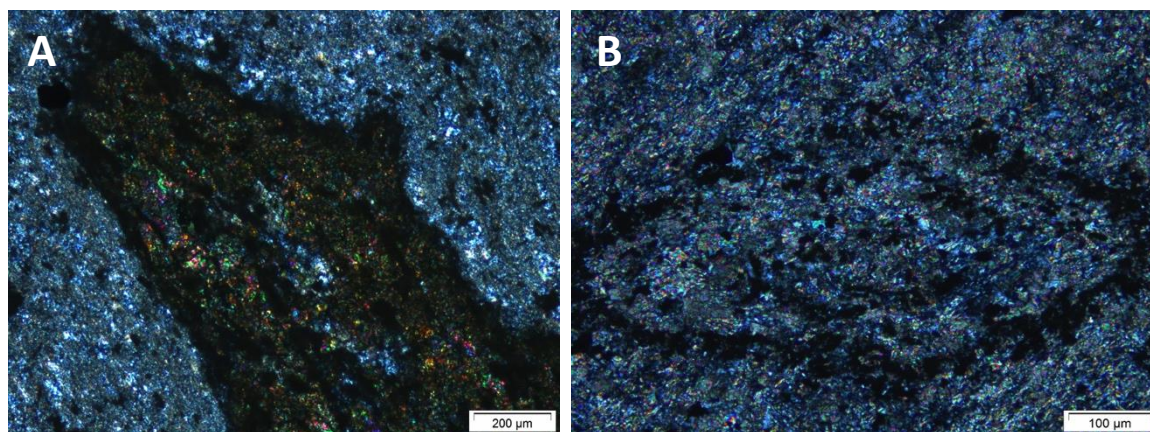


Figure 3.15. A) Amphibole pseudomorph after amphibole in sample UWO_2015_27 showing characteristic two cleavages at 60 and 120 degrees; B) Relict dark rim surrounding completely pseudomorphed grain in sample UWO_2015_28

Microprobe EDS spectra analysis was performed to identify mineralogical and chemical changes between the pseudomorphs in sample UWO_2015_27 and the preserved fine-grained pseudomorph rims in UWO_2015_28. In the less altered sample, UWO_2015_27, pseudomorphs consisted of albite, epidote, titanite, sericite, and chlorite with no identifiable relict amphibole. Similarly, the interior of the pseudomorphs in UWO_2015_28 consisted of dolomite and albite with no relict amphibole remaining.

Pseudomorphs in both samples were surrounded by a thin opaque rim that was unidentifiable petrographically. Microprobe EDS analysis identified that the rim is actually composed of finely inter-grown rutile and quartz (with lesser amounts of albite), as shown in Figure 3.16.

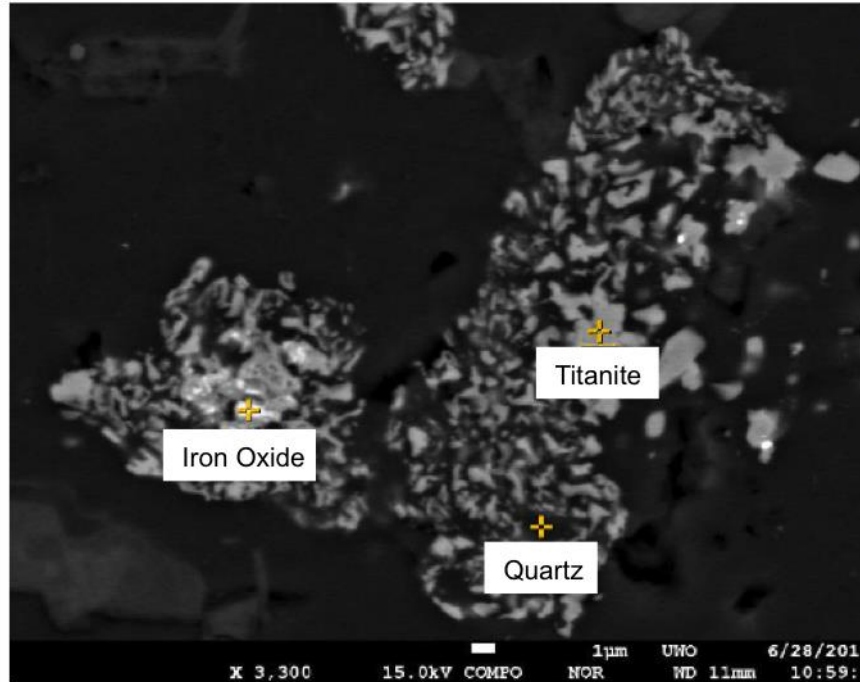


Figure 3.16. Electron photograph showing of mineral phases identified in the opaque rim of a pseudomorphed amphibole. The dark rim is composed of finely inter-grown quartz and titanite with small amounts of iron oxide. Mineral phases identified through EDS microprobe analysis in UWO_2015_28

In both thin sections the groundmass of the rock consisted of fine to medium-grained feldspar, dolomite, and quartz as confirmed by EDS analysis. Feldspar occupied an estimated of 35-45% of the rock. Twinning, where observed, and microprobe EDS analysis revealed that the rock is largely composed of albitic feldspar with no observable potassic feldspar present. Fine to medium-grained quartz occupied roughly 7-10% of the rock. Microprobe EDS analysis identified that quartz and albite were largely inter-grown in the groundmass, as shown in Figure 3.17.

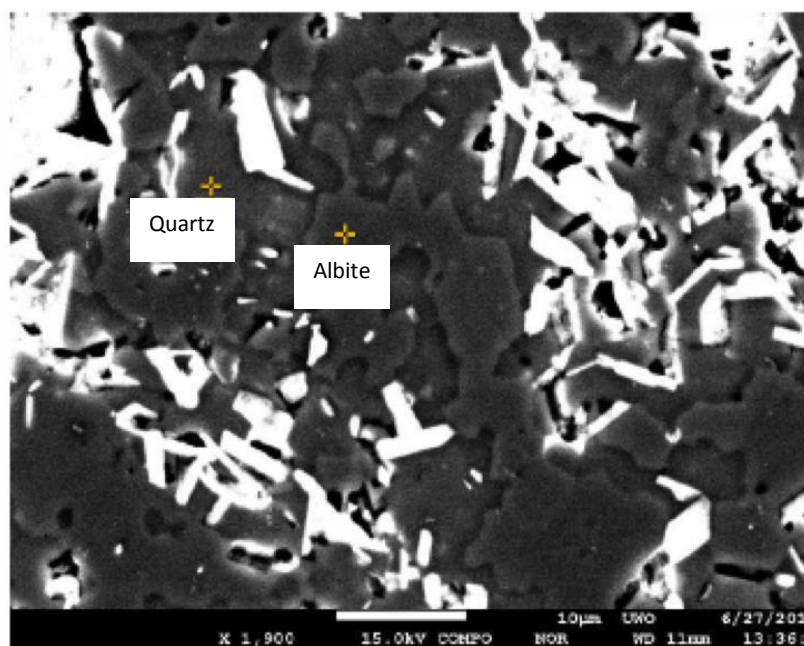


Figure 3.17. Backscatter image showing of mineral phases identified in the groundmass of UWO_2015_27. Mineral phases identified through EDS microprobe analysis. The groundmass of the sample is composed of finely inter-grown quartz and albite. Lighter shades in the figure include a variety of additional minerals, including chlorite, sericite, and dolomite, however contrast has been increased in order to show the subtle differences between quartz and albite.

Hand-sample observations of representative samples of microphyric intrusives from the deposit indicate that the microphyric texture tends to only occur in strongly altered rock. Both collected samples of the microphyric intrusive were strongly altered, giving the rock a patchy appearance in hand sample. The rocks were strongly altered by patchy chlorite, sericite, and pinkish albite, as well as by dolomite. Microprobe EDS analysis confirmed the abundance and composition of alteration minerals. Further, the microphyric pseudomorphs are typically aligned parallel to each other, however some pseudomorphs in the representative samples from other areas of the deposit had a more sporadic orientation.

Oxide minerals in the collected microphyric samples consist of magnetite and hematite. In both samples magnetite and hematite were disseminated throughout the

groundmass. Observations of representative samples from across the deposit indicate that the entire microphyric intrusive unit is typically weakly magnetite and can contain variable amounts of pyrite and chalcopyrite. Further, the microphyric intrusive can host variable amounts of gold and copper mineralization (M. Masson, personal communication, 2015).

Both thin sections had a moderate foliation, defined by the alignment of sericite and chlorite, as shown in Figure 3.18. Pseudomorphs in UWO_2015_28 are also aligned parallel to the foliation.

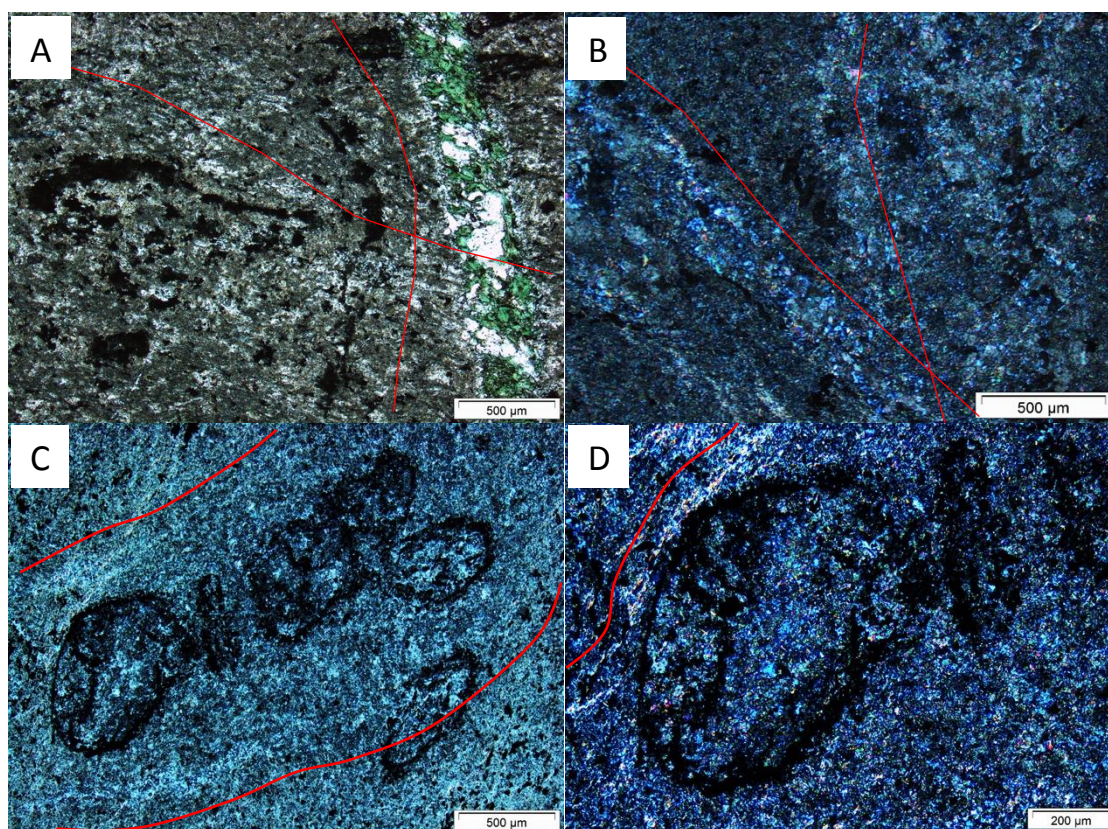


Figure 3.18. Transmitted cross polarized light photomicrographs of microphyric unit. A) Two intersecting planes of foliation in plane polarized light with amphibole pseudomorphs sheared and stretched along with foliation in UWO_2015_27; B) Two intersecting planes of foliation in cross polarized light with pseudomorphs after amphibole stretched and aligned with foliation in UWO_2015_28 in cross polarized light; C) and D) pseudomorphically replaced grain in UWO_2015_28. Note the foliation defined by the parallel alignment of micaceous minerals around the pseudomorphs and the slight stretching of pseudomorphs parallel to foliation highlighted in red.

3.2.6.3 Amphibole-rich Intrusive

The amphibole-rich intrusive unit is greenish yellow to greenish gray in colour and is characterized by roughly 25% coarse-grained (<1 cm wide) amphibole phenocrysts in a fine to medium-grained feldspar-rich groundmass. The amphiboles are relatively euhedral to subhedral, and are zoned with distinctly higher birefringent rims. Fine-to medium- grained feldspar in the groundmass accounts for roughly 25% of the total rock and twinning in larger phenocrysts indicate that they are dominantly plagioclase; although some potassic feldspar may also be present. Fine-grained quartz accounts for only about 5% of the entire rock and larger grains tend to have undulatory extinction. Rutile occurs in trace amounts. The rock has an overall amphibole phyric texture. A representative picture of the rock is provided in Figure 3.19.

Electron microprobe WDS analysis identified that bright shades of amphiboles in the amphibole-rich intrusive unit ranged in composition between Mg-rich magnesio-hornblende, actinolitic hornblende, and actinolite, while darker shades of amphibole corresponded to more Fe-rich amphiboles (actinolite and ferrian-tremolite). Dark-colored amphiboles in this rock type contained more MgO than all other amphiboles analyzed in the sample set, and brighter shades of amphibole contained higher amounts of Cl and MnO than all samples analyzed. Amphibole phenocrysts are moderately altered by chlorite, epidote, and silica, with alteration typically being concentrated in the core of each phenocryst.

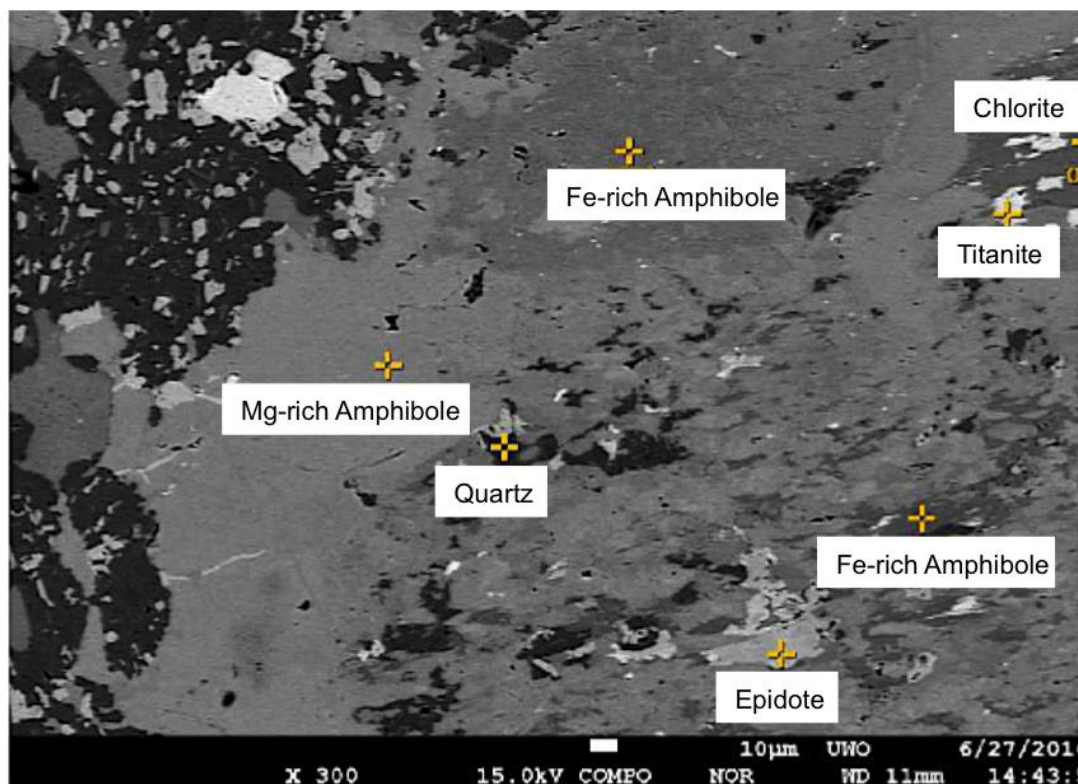


Figure 3.19. Backscatter image showing the mineral phases identified within an amphibole grain in UWO_2015_26. Mineral phases identified through microprobe EDS analysis. The amphibole is zoned with darker spots being enriched in Fe and lighter spots being enriched in Mg. It is altered by chlorite and epidote, and contains small inclusions of titanite.

The groundmass of the rock is composed of fine to medium-grained albite and K-spar with very little accompanying quartz. Microprobe WDS analysis identified that albite and K-spar are both very close to end member, indicating they are likely alteration minerals. Albite is also strongly sericitized throughout the rock, as shown in Figure 3.20. Chlorite is also present throughout the rock. It tends to alter the core of coarse-grained amphiboles and occurs pervasively throughout the groundmass. Late epidote-rich and hematite-calcite rich fracture fills and stringers cross cut all features in the core at irregular angles.

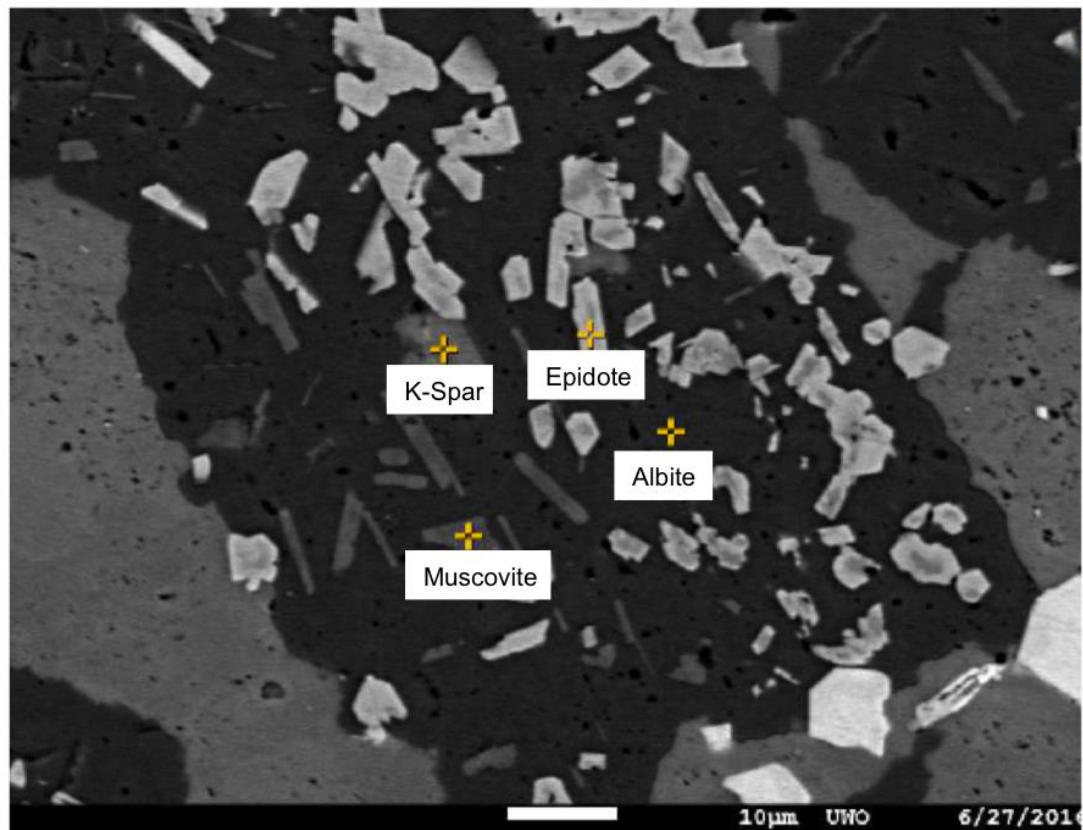


Figure 3.20. Backscatter image showing the mineral phases in UWO_2015_26 as identified through EDS microprobe analysis. Albite is strongly altered by epidote and muscovite, and contains inclusions/ is surrounded by K-spar.

Iron oxide minerals consist of hematite and magnetite, which make up roughly 5% of the rock. Magnetite tends to alter to hematite along its rims and along fractures, as shown in Figure 3.21C. Both magnetite and hematite occur disseminated throughout the groundmass. This gives the rock a moderately magnetic signature. The rock lacks sulphide minerals. Assays from the deposit indicate that the intrusive unit also lacks Au and Cu mineralization.

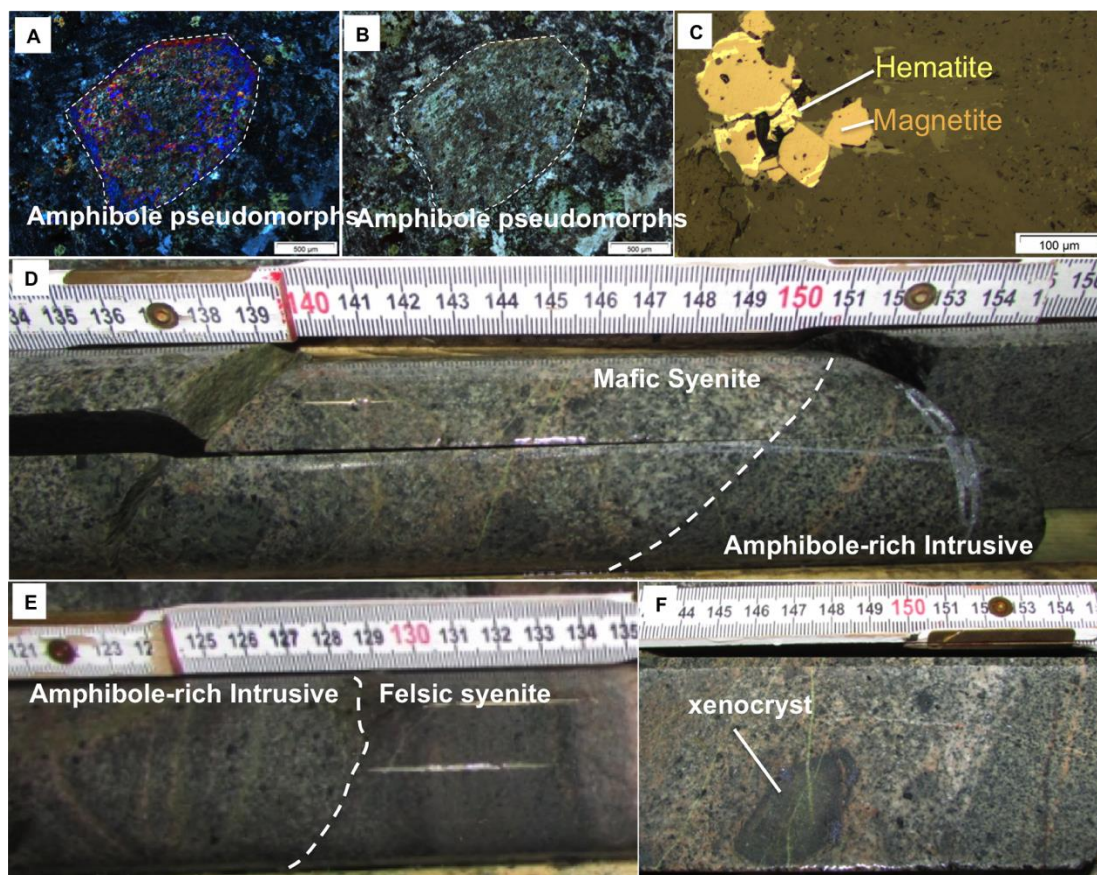


Figure 3.21. Representative photos of Amphibole-rich intrusive. A) Cross polarized light photomicrograph showing amphibole phenocryst with birefringent rims; B) Plane polarized light photomicrograph showing amphibole phenocryst and surrounding chlorite alteration; C) Reflected light photomicrograph of magnetite altering to hematite along grain boundaries and fractures; D) Photo of the sharp upper contact of the amphibole-rich intrusive unit with amphibole-rich xenoliths in the adjacent mafic syenite unit; E) Photo of the sharp lower contact with adjacent “felsic syenite” unit; and F) Large amphibole xenocryst in adjacent mafic syenite unit.

Cross cutting textures indicate that the rock is older than mafic syenite and younger than felsic syenite intrusives. Structural evidence to support this includes the sharp upper contact that the amphibole-rich intrusive shares with an adjacent unit of mafic syenite and its sharp chilled lower contact with felsic syenite, as shown in Figure 3.20D,E, above. Further, the adjacent mafic syenite unit contains xenoliths of the amphibole-rich intrusive as well as xenocrysts of large individual amphibole phenocrysts, indicating that the amphibole-rich intrusive was emplaced prior to the mafic syenite intrusion. Both xenoliths and xenocrysts were moderately well

rounded, indicating possible partial resorption into the adjacent mafic syenite intrusion. Overall, the cross cutting features combined with the preserved portions of amphibole minerals suggest that the mineralogy of the amphibole-rich intrusive reflects a primary igneous mineralogy that has been subsequently metamorphosed as opposed to a metasomatic feature.

3.2.6.4 Biotite-rich Intrusive

The biotite-rich intrusive is a reddish brown coarse-grained rock characterized by 15% 1-2 mm wide flecks of biotite with accompanying 20-30% amphiboles. Electron microprobe analysis identifies that brighter shades of amphibole in the biotite-rich intrusive unit corresponded to actinolitic hornblende and silicic edenite (due to high Na₂O composition), while darker shades of amphibole corresponded to more metamorphic amphiboles with a composition ranging between tremolite, actinolite, and actinolitic hornblende. Amphiboles in this rock-type contained much more CaO than all other samples analyzed.

No other lithology in the deposit contains significant amounts of biotite as a primary phenocryst or alteration product. Microprobe EDS analysis of the biotite-rich intrusive revealed that the composition of the mica has a Mg/Fe ratio of approximately 2.1. Biotite and amphiboles are hosted within a fine- to medium-grained groundmass consisting of roughly 5% quartz and 20% feldspar. The rock has an overall phaneritic texture, as shown in Figure 3.22A.

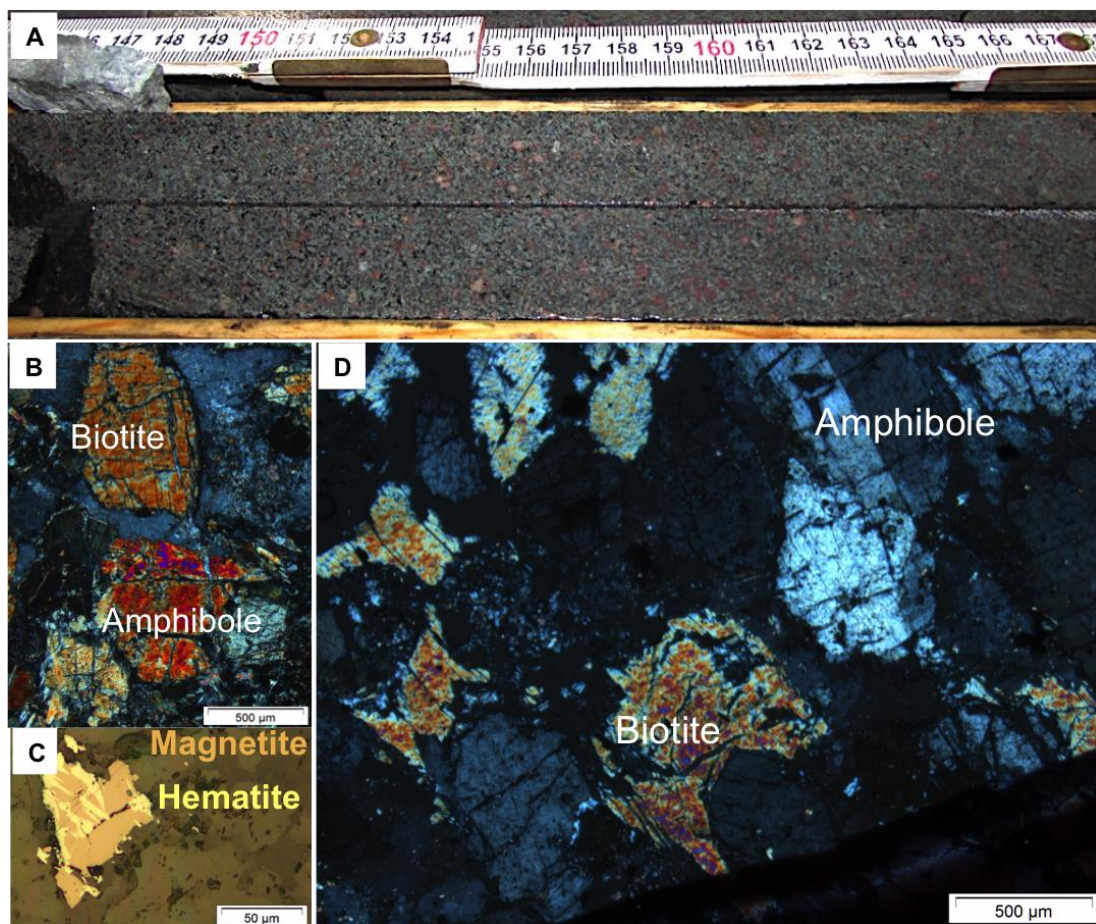


Figure 3.22. A) Representative hand-sample photo of biotite-rich intrusive; B, D) Cross polarized light photomicrograph of amphibole phenocryst in the unit; C) Reflected light photomicrograph of magnetite altering the hematite along fractures

The groundmass of the rock is largely composed of inter-grown medium- to coarse-grained K-spar, biotite, albite, and amphibole, as shown in Figure 3.23. Electron microprobe analysis identifies that the biotite is relatively fresh, with moderate amounts of alteration by K-spar, albite, magnetite, and hematite, as shown in Figure 3.24. Biotite commonly contains numerous small inclusions of subhedral apatite. The rock is moderately altered. Microprobe WDS analysis also identifies that albite and K-spar are very close to end members, indicating that they have a more metamorphic or hydrothermal signature. Other alteration minerals include of roughly 10% actinolite and 10% chlorite, which occur pervasively throughout the rock as well as within amphibole grains, and roughly 5% sericite, which alters albite.

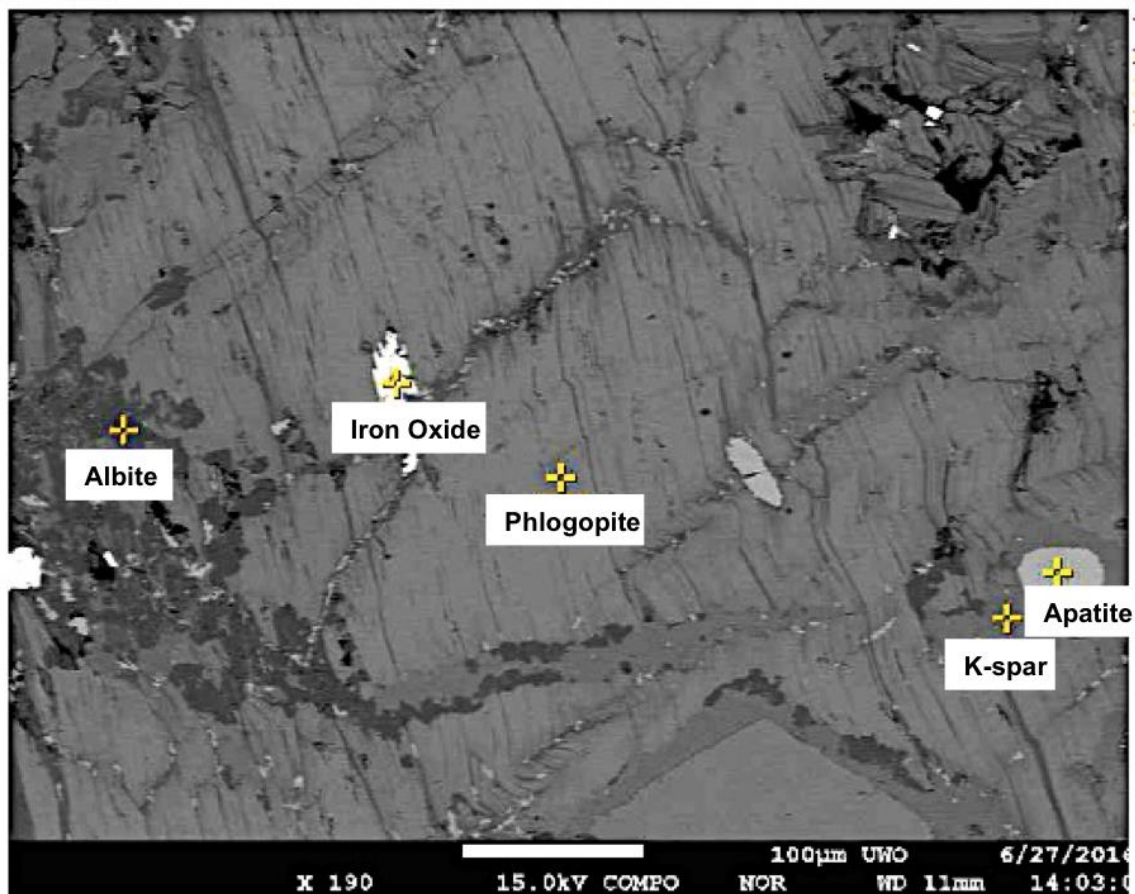


Figure 3.23. Backscatter image showing the mineral phases in UWO_2015_48 as identified through microprobe EDS analysis. Biotite is relatively fresh and contains minor inclusions of albite, K-spar, apatite, and iron oxide

Opaques include disseminated magnetite and hematite, which amount to 3% of the total rock. A late quartz stringer also contains specular hematite. The rock lacks visible pyrite and chalcopyrite. Assays from the deposit indicate that the biotite-rich intrusive also lacks Au and Cu mineralization.

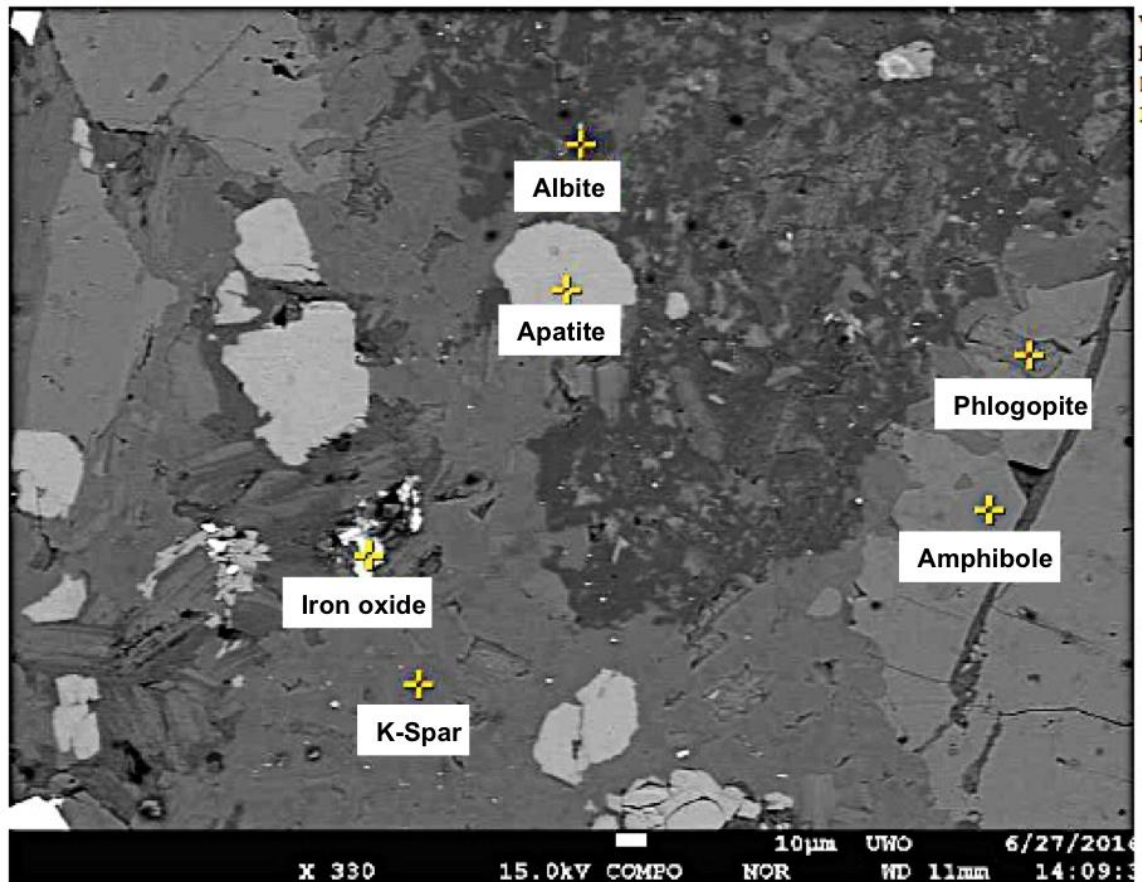


Figure 3.24. Backscatter image showing the mineral phases in UWO_2015_48 as identified through microprobe EDS analysis. The rock consists of phlogopite, amphibole, k-spar and albite with minor amounts of apatite and iron oxide

3.2.7 Sedimentary Sequence

The isolated sedimentary sequence in the Upper Beaver deposit is located on the western side of the diabase dike at approximately -200 to -500 meter elevations below surface and it is roughly 200 to 300 m long with a thickness of 200 to 300 meters (Bernier and Cole, 2012). The sequence is shown in Figure 3.25 as a roughly horizontal sequence to the north, and dipping steeply south closer to the intrusive complex. Morris (1974) originally interpreted the sedimentary package to represent a basin that was in-filled with the Blake River Assemblage. Morris (1974) also interpreted the basin to represent the lowermost boundary of the deposit, with ore being concentrated in the Blake River basalts that overlie the basin. Diamond drilling

however, has revealed that mineralization is also present outside the sedimentary package (Bernier and Cole, 2012).

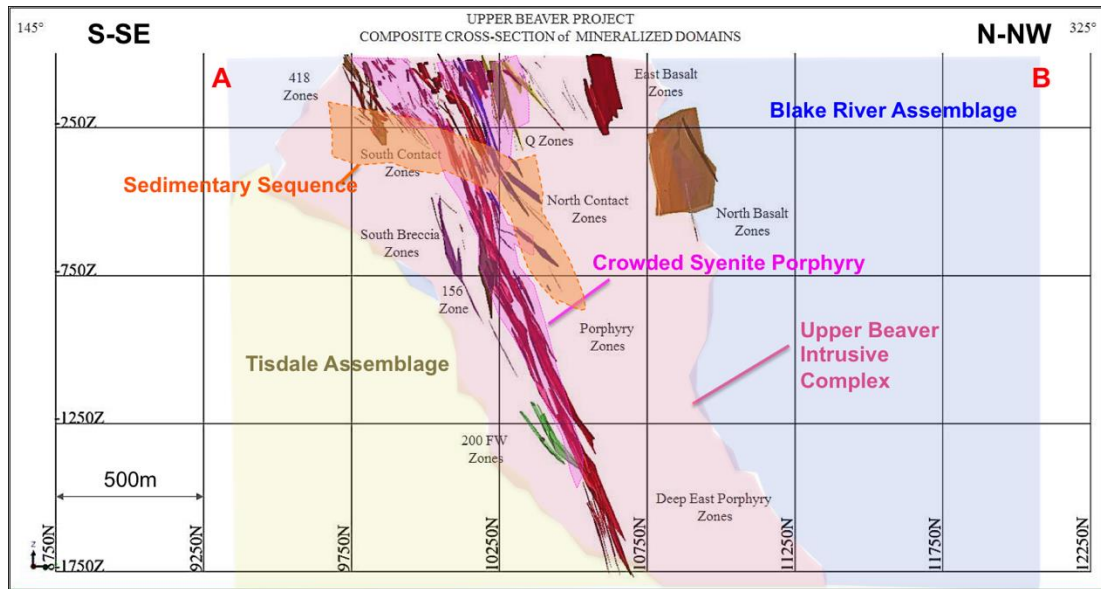


Figure 3.25. Composite cross section of Au mineralization (red zones) in the Upper Beaver deposit in relation to crowded syenite porphyry dikes and the isolated sedimentary sequence (orange) in the Upper Beaver deposit. Modified figure originally provided by Canadian Malartic Corporation.

Volcanic hiatuses, including those that produce sedimentary interface zones, have important exploration implications. They are the ideal settings for both VMS and gold deposits. In fact, the Blake River Group hosts 33 known volcanogenic massive sulphide deposits, including the gold-rich Horne and Bousquet deposits (Pearson and Daigneault, 2009). Important economic implications for isolated sedimentary zones in Abitibi gold deposits such as Upper Beaver include: (1) the ability to use the unit as a marker horizon across large stratigraphically continuous areas; (2) the ability to interpret deposit orientation using younging indicators in the sequence; (3) an indicator of a geochemical or stratigraphic discontinuity deposited during a volcanic hiatus; (4) the ability to define time intervals during which potentially Au-rich VMS mineralization may have occurred, and (5) the ability to define early episodes of hydrothermal activity. Further, given the fact that the hydrothermal systems that give rise to early VMS-style Zn-Cu and Cu-Au mineralization in the Abitibi develop during volcanic hiatuses, combined with the

lower competency of sedimentary units compared to surrounding rock and thus their ability to deform, at surface sedimentary interface zones make reasonable exploration targets for gold mineralization (Thurston et al., 2002; Thurston et al., 2008).

The isolated sedimentary sequence is of particular significance in the deposit as it may have also played a role in concentrating mineralization in the South Contact Zone of the Upper Beaver deposit. A thesis project completed by Feick (2014) emphasized the importance of the isolated sedimentary sequence acting as a relatively impermeable lower barrier for concentrating mineralization in the overlying Blake River Basalts. This lower barrier may have promoted prolonged fluid circulation in the basalts, contributing to the very strong alteration and concentration of gold and copper mineralization that characterizes the South Contact Zone. Relative alteration intensity based on hand-sample observations in 10 cm intervals by Feick (2014), and associated Au and Cu assays are provided in Figure 3.26. An alteration intensity of 3 indicates strong alteration, while an alteration intensity of 0 indicates no alteration by that particular mineral in the analyzed interval. The drill hole studied by Feick (2014) consisted of very strong alteration in the Blake River basalts, which progressively decreased in the underlying volcanoclastic rocks. Mineralization is concentrated near the contact between the altered basalts and the volcanoclastic rocks.

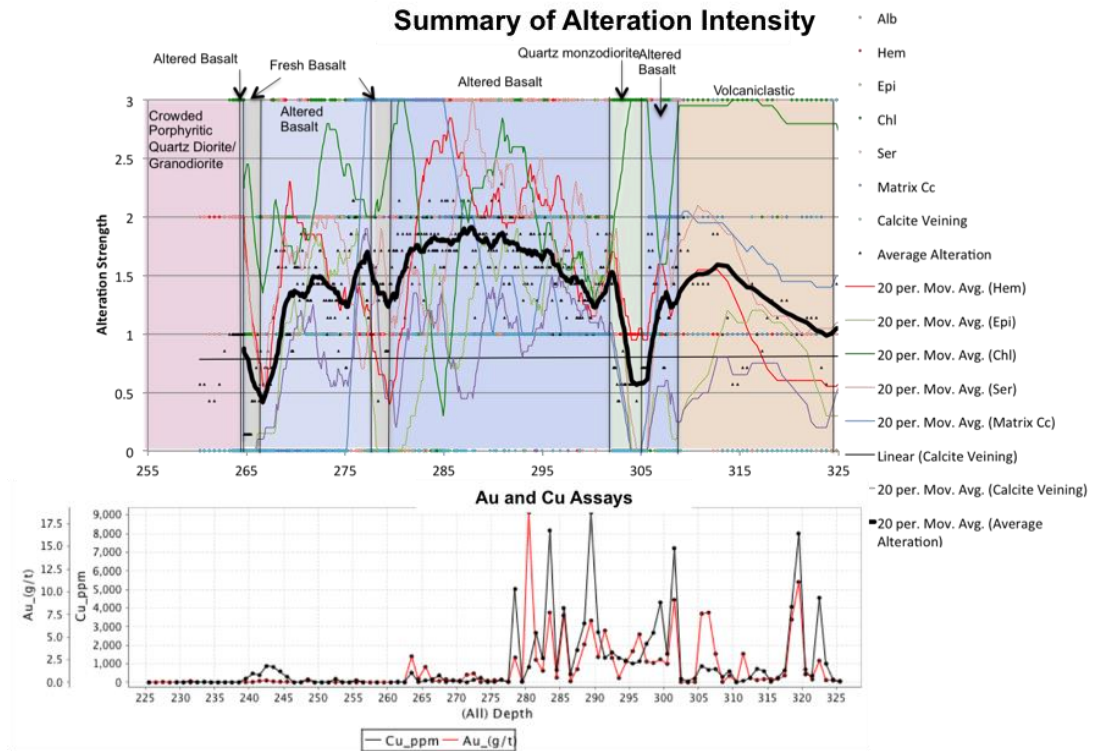


Figure 3.26 Summary of alteration intensity in UB11_192 based on hand-sample observations. Alteration intensity was ranked on a scale of 0 (no alteration) to 3 (very strong alteration) and has been plotted with a 20 point moving average. Alteration intensity was originally recorded in 10 cm intervals. Figure modified from Feick (2014). Assays provided by Canadian Malartic Corporation.

The entire sedimentary sequence consists roughly from bottom to top of graphitic sedimentary rocks, overlain by interbedded conglomerate and siltstone, followed by cherty sedimentary rocks, and finally overlain by a layer of volcaniclastic rocks. Not all lithologies are present in drill holes that cross cut the sequence and boundaries between the units vary from gradational to sharp contacts. Each lithology is described in detail below and representative photos of each lithology have been provided in Figure 3.27. All samples from the sedimentary sequence were taken roughly perpendicular to bedding.

The Wentworth grain-size scale was used for sedimentary rocks, in which grain sizes are defined as follows: mud-sized grains represents <0.0623 mm (subdivided into clay sized grains <0.0039 mm, and silt sized grains <0.0226 mm); sand represents <2 mm diameter; and gravel is greater than 2 mm.

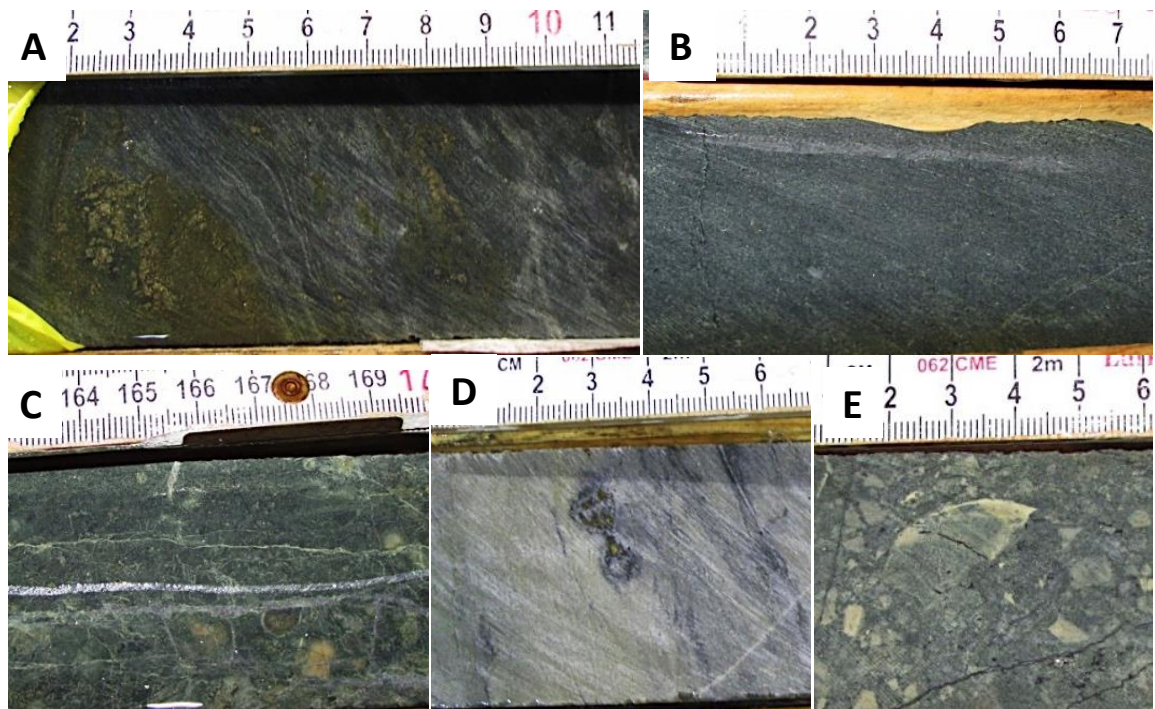


Figure 3.27. Sedimentary rocks from the isolated sedimentary sequence, from lowermost unit to uppermost including (A) graphitic argillite, (B) silty arenite, (C) conglomerate, (D) cherty sedimentary rocks, and (E) volcaniclastic rocks

3.2.7.1 Graphitic Argillite

The graphitic argillite unit is black to dark gray. It is composed dominantly of quartz (37-60%) and calcite (5-10%) that are mud- to sand- sized and that have been deposited in thick massive to well-bedded layers. Layers alternate between darker coarse-grained quartz and calcite beds that are strongly chloritized and sericitized and thin silty to muddy finer-grained beds. Graded bedding can be recognized in sandier layers in both thin section and hand sample. Bedding is roughly perpendicular to the drill axis.

The rock contains abundant chlorite and sericite, with each mineral making up roughly 10% of the rock. Coarser-grained layers tend to be more strongly chloritized. Chlorite and sericite are common low-temperature metamorphic alteration minerals

in pelitic rocks (Winter, 2010), suggesting that these rocks have undergone low-temperature alteration. Variable amounts of chalcopyrite, pyrite, hematite, and magnetite are present within the unit, although pyrite is the dominant opaque present in analyzed samples. Dark chlorite-rich layers tend to contain up to 5 cm wide diagenetic framboidal pyrite grains. Pyrite is a major constituent in this rock unit, making up roughly 9-30% of the thin sections analyzed. Bedding tends to drape over the framboidal grains. Magnetite and hematite are also present in graphitic argillite typically occurring as disseminations throughout the rock, and occupying roughly 1% and 2% of the entire rock, respectively. The presence of magnetite causes the entire unit to become weakly to strongly magnetic in sections. The unit can also host variable amounts of Au mineralization with grades varying between barren to high grade.

Both samples of graphitic sedimentary rock had foliation developed at a 45-degree angle to bedding defined by the parallel alignment of chlorite and sericite minerals. Additional evidence of strain and deformation in both samples include abundant quartz pressure shadows developed around larger sulphide grains. Wavy deformed and folded beds are shown in Figure 3.28.



Figure 3.28. Wavy deformed beds in graphitic sedimentary rocks in UWO_2015_38

The graphitic sedimentary rocks primarily develop at the base of the isolated sedimentary sequence however, locally they can occur as thinner lenses with the other sediment packages. Although the 1-20 m thick unit tends to occur along the bottom of the sedimentary sequence, it is discontinuous across the sedimentary package, typically pinching out and swelling rapidly over short distances and not appearing at all in many of the drill holes (Bernier and Cole, 2012).

3.2.7.2 Silty Arenite

The silty arenite unit is greyish white to grey and is dominantly composed of quartz (40%) with lesser amounts of calcite (5%). Grains are typically silt to sand-sized. In hand sample thin planar bedding can be identified, with beds being no more than a few mm wide. Beds consist of alternating layers of sand-rich and silt-rich layers. Infrequent 1-2 mm wide clasts can also be observed throughout the silty arenite unit. The clasts increased in abundance towards the top of the unit and were dominantly composed of quartz or fragments of cherty sedimentary rocks.

The silty arenite sample is strongly chloritized, as identified by its greenish tinge in hand sample and its ability to be scratched with a fingernail. Additionally, prepared polished thin sections contained approximately 20% coarse-grained green pseudomorphs that are suspected to have originally been amphiboles, due to preserved cleavages at 56 and 124 degrees, prior to chlorite alteration. Representative photomicrographs of the rock are presented in Figure 3.29 and 3.30. There was also approximately 2% fine-grained biotite, identifiable by its distinctive pleochroism and cleavage.

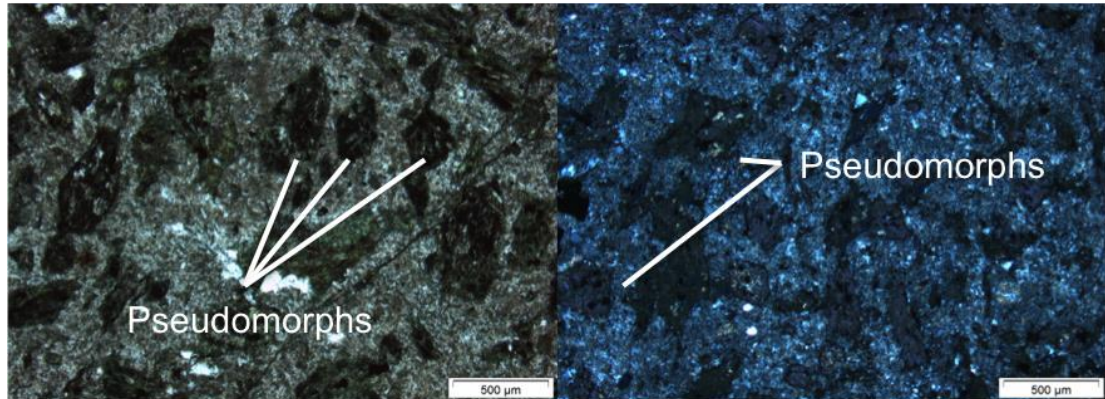


Figure 3.29. Photomicrographs of sample UWO_2015_30 showing abundant greenish brown pseudomorphs within a fine-grained quartz-rich matrix. Photos in plane polarized light (left) and cross polarized light (right).

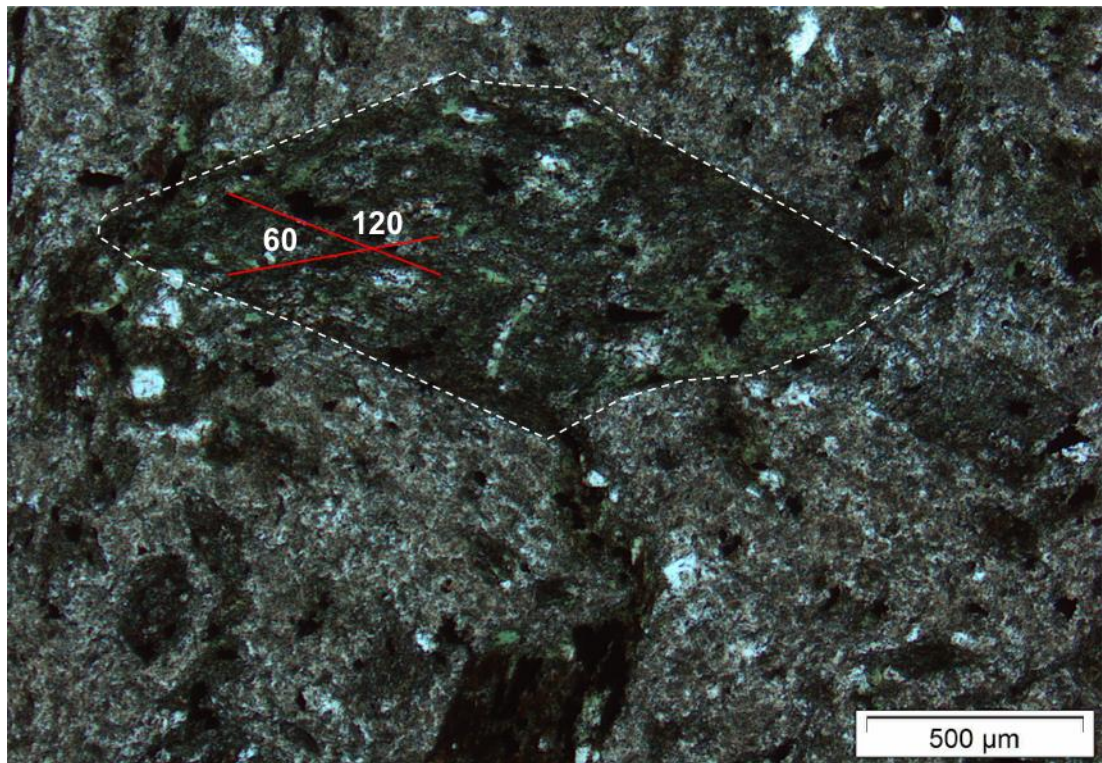


Figure 3.30. Photomicrographs of sample UWO_2015_30 showing close-up of green pseudomorph. Two cleavages are highlighted in red on the figure

Microprobe EDS analysis of the sample revealed that the groundmass is dominantly composed of quartz, with lesser amounts of albite, calcite, chlorite, and apatite, as shown in Figure 3.31. The large weakly pleochroic green grains are very strongly altered and are composed largely of calcite, chlorite, and quartz, with lesser

amounts of rutile, as shown in Figure 3.32. Additionally, the entire rock unit observed on site contained approximately 2% disseminated sieve-textured pyrite and 1% chalcopyrite. Overprinting textures observed petrographically of the sample selected from the silty arenite unit indicate that pyrite formed prior to chalcopyrite.

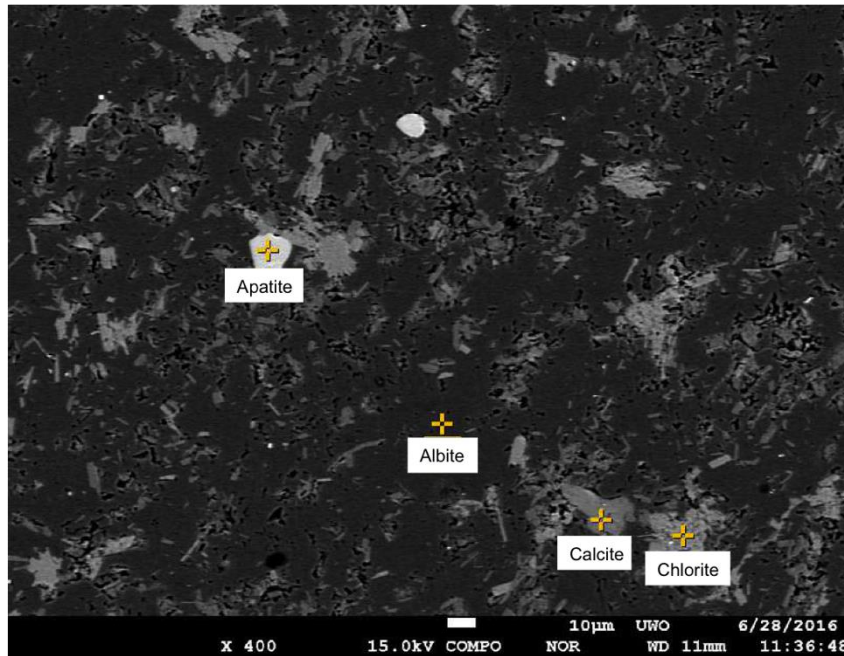


Figure 3.31. Backscatter image showing the mineral phases identified in the groundmass of UWO_2015_30 as identified through microprobe EDS analysis. The groundmass largely consists of quartz with lesser amounts of albite, calcite, chlorite, and apatite.

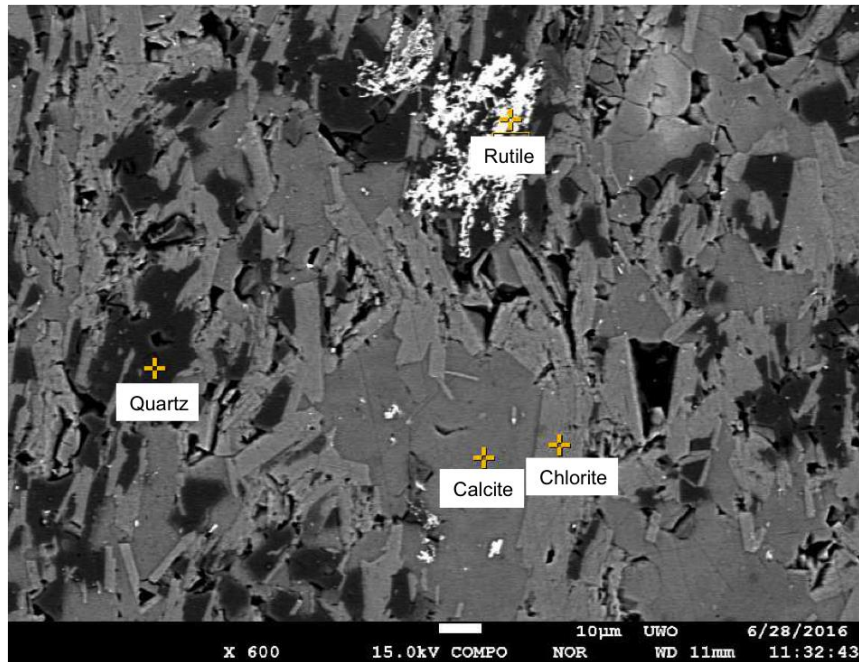


Figure 3.32. Backscatter image showing the mineral phases identified in the green patches in UWO_2015_30, as identified through electron microprobe EDS analysis. The green patch is composed dominantly of chlorite with lesser amounts of calcite and quartz, and minor amounts of rutile

A hand sample was selected from the top of the silty arenite unit where 1-2 mm wide clasts could be seen. The distinctive mineralogy of the sample may be the results of intense alteration or sedimentary contribution from a mafic source. Overlying and underlying the silty arenite unit are layers of cherty sedimentary rocks. Both the upper and lower contacts are roughly perpendicular to the drill axis, as shown in Figure 3.33.

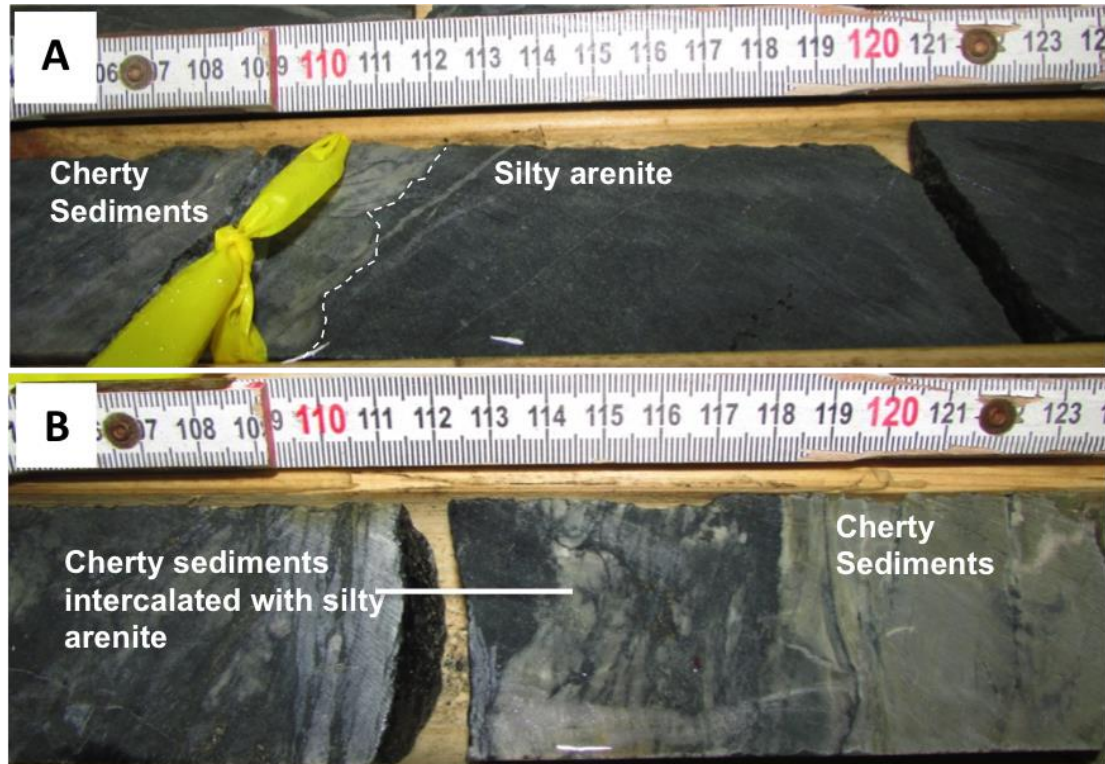


Figure 3.33. A, B) Upper and lower contact (respectively) between the silty arenite unit and overlying / underlying cherty sedimentary rocks as observed on site.

3.2.7.3 Conglomerate

The conglomerate unit is grey to tan and is dominantly composed of polymictic clasts within a clast-supported matrix of quartz (35-40%) and calcite (5-10%). Grains of quartz in the matrix are typically sand-sized. Clasts account for roughly 50-80% of the entire rock and range in size from coarse sand to gravel sized (<1 cm wide).

Clasts range from grey to greyish green to tan. They are typically sub-rounded to sub-angular. Clasts are typically either igneous intrusive in origin (identified by internal coarse-grained quartz and feldspar phenocrysts) or are fine-grained sedimentary clasts of cherty sedimentary rocks.

Original bedding could not be distinguished in thin section, although it was observed in hand sample. Soft sediment deformation and graded bedding can also be recognized in hand-sample. Sharp but intercalated boundaries between the

conglomerate and the underlying silty arenite unit can be seen in sections of the sedimentary sequence, as shown in Figure 3.34.

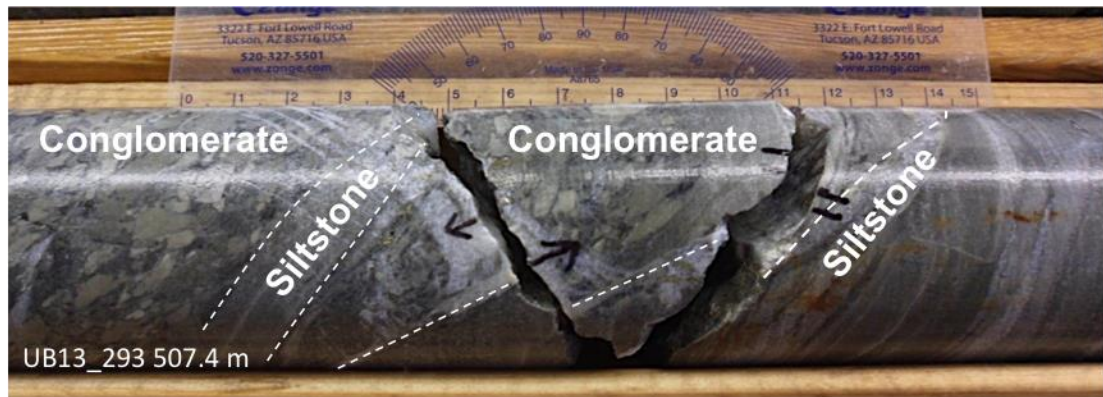


Figure 3.34. Complex intercalated boundary between conglomerate and silty arenite with arrows indicating the direction of movement between units.

The groundmass was typically altered to epidote and/or chlorite, which accounted for up to 3%, and up to 7% of the thin sections analyzed, respectively. Clasts were often sericitized.

Opaques include disseminated chalcopyrite, pyrite, magnetite, and hematite. Clasts were often sulphide-rich, with disseminated pyrite and chalcopyrite occurring internally, while the surrounding matrix was typically magnetite and hematite rich.

Clasts tend to be oriented roughly 45 degrees to the core axis, which may be in part a function of deformation, as many of the clasts also seem to be elongated in this direction.

3.2.7.4 Cherty sedimentary rocks

Cherty sedimentary rocks typically range from light grey to beige to pinkish brown. They are dominantly composed of silt-to sand-sized quartz and calcite grains and accompanying strong pervasive alteration. Alteration includes strong pervasive silicification (chert) as well as strong ankeritization and sericitization. As well, the unit typically has sharp upper contacts and diffuse lower contacts, possibly due to the strong pervasive alteration that accompanies this rock type, as shown in Figure 3.35.



Figure 3.35. Diffuse lower cherty sediment contact in UB_11_190 at 389 m.

Bedding, where observable, is typically 1 mm wide, although thicker layers can be seen with graded bedding indicating that the sequence is upright. In general, cherty sedimentary rocks are overlain by volcanoclastic rocks, although cherty sedimentary rocks are frequently intercalated with volcanoclastic rocks at the same stratigraphic elevation (Bernier and Cole, 2012). This was interpreted to signify that the deposition of cherty sedimentary rocks, at least in the uppermost portion of the sedimentary body, was partly coeval with volcanoclastic rocks (Bernier and Cole, 2012).

Foliation is observed in all four thin sections analyzed dominantly occurring at 60 degrees to bedding, defined by the parallel alignment of chlorite and sericite minerals. Sample UWO_2015_32 had foliation 30 degrees and 60 degrees to bedding, and foliation in sample UWO_2015_37 ranged from 60 to 85 degrees relative to bedding. Late quartz-calcite veins are oriented roughly parallel to foliation. Bedding is visibly faulted where crosscut by stringers in one sample. Opaques consist of variable amounts of disseminated chalcopyrite, pyrite, hematite, and magnetite, including magnetite and hematite minerals.

3.2.7.5 Volcanoclastic rocks

The volcanoclastic rocks overly the sedimentary sequence. They are typically heterolithic and composed of angular to rounded sand to gravel-sized clasts. The matrix surrounding the clasts is typically greyish green to dark green, while clasts range from black to gray to pinkish to white. Clasts occupy between 30% and 80% of the rock. Petrographic observations of the groundmass indicate that matrix

dominantly consists of fine-grained quartz (3-40%) and calcite (7-20%). Bedding is readily identified in both thin section and hand sample.

The clasts are dominantly either igneous (identified by the fine to coarse-grained internal phenocrysts) or sedimentary (dominantly cherty sedimentary rocks with visible bedding up to 3 cm wide). One thin section also contained large phenocrysts of strongly sericitized plagioclase that were roughly 0.5 mm long as well as <0.5 mm wide rounded clasts of quartz, as shown in Figure 3.36.

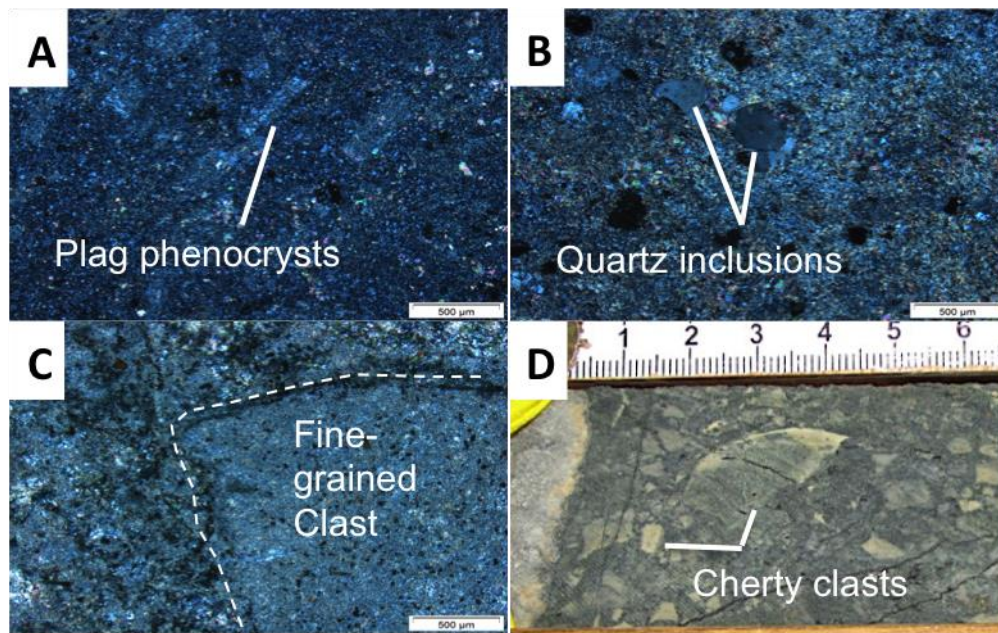


Figure 3.36. A,B) Cross polarized light photomicrographs of plagioclase and quartz phenocrysts within a fine-grained groundmass in volcaniclastic rocks sample UWO_2015_25; C) Cross polarized light photomicrograph of the edge of a large clast in volcaniclastic rocks unit in UWO_2015_29; D) Photo of typical volcaniclastic rocks unit showing abundant clasts of cherty sedimentary rocks

The clasts, phenocrysts, and matrix of the rock can contain varying amounts of carbonate, chlorite, epidote, albite, silica, sericite, pyrite, and chalcopyrite, as well as hematite and magnetite. The unit is frequently altered to the point that clasts in the volcaniclastic rocks appear heterolithic. The unit also contains variable amounts of (between trace and 8%) hematite and/or magnetite fracture fills, and disseminated pyrite, as identified in hand sample and thin section.

The matrix of this rock unit is typically comprised of very fine-grained carbonate and chlorite, although a technical report on the Upper Beaver deposit also states that in areas the matrix can appear to be comprised of finely crystalline material (Bernier and Cole, 2012). This type of matrix was not observed in this study, but may represent a separate unit in the deposit.

Foliation in the volcanoclastic rocks was observed in the two thin sections, developed by the parallel alignment of sericite grains and pyrite-chalcopyrite, as well as parallel quartz-calcite fracture fill veins. The foliation occurred at roughly 60-85 degrees to bedding.

3.2.8 Breccia Pipe

An elongated breccia pipe occurs along the south side of the Upper Beaver Intrusive Complex near its contact with the Blake River Basalts. The pipe extends down to at least 1.5 km and it is steeply dipping with a similar orientation as the mineralized zones. Samples collected for this study include two sets of 3 progressively more brecciated samples from two drill holes that cross cut the brecciated unit, as well as 4 samples from the 200 mineralized Zone, the host lithology of which has been a topic of question for CMC geologists in the past.

Textures, alteration, and clasts in the breccia lens are highly variable. Clasts range in size from <1 mm wide to over 5 cm wide, and from very angular to very rounded. In addition, some clasts have very well defined boundaries, while others have more gradational boundaries. In general, the composition of the breccia clasts is fine to medium-grained plagioclase with minor amounts of quartz and amphiboles, while the matrix is fine-grained and is consists of fractures or stringers of either chlorite and magnetite or coarse-grained calcite. Representative photos of different styles of breccia in the Upper Beaver deposit are provided in Figure 3.37.

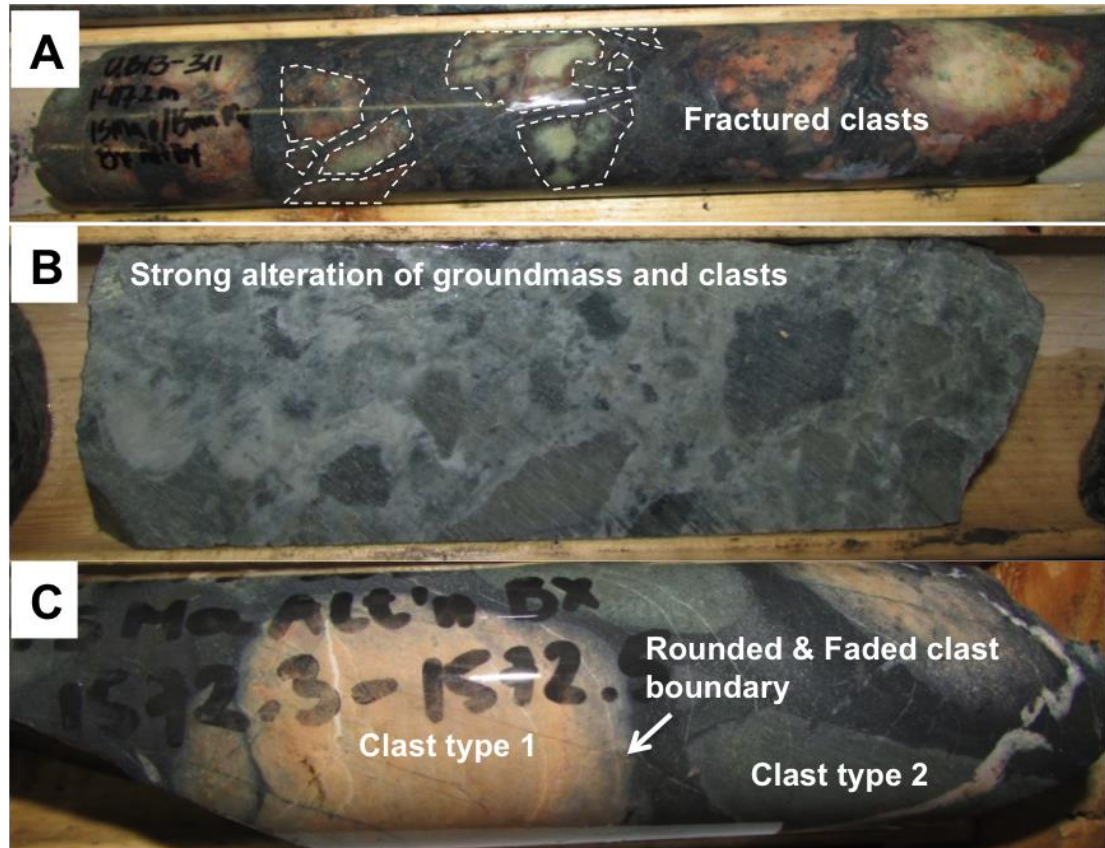


Figure 3.37. Pictures of representative breccias from the Upper Beaver deposit. (A) Mafic syenite breccia from UB13_311 (1472 m) that shows great evidence of fluid-assisted brecciation. Larger clasts are being broken apart. (B) breccia from UB10_161 (162 m) that shows excellent evidence of corrosive wear. Clasts have squiggly boundaries and both the host and the clasts have been altered. (C) breccia from UB13_307 (1572.3 m) that shows the characteristic rounded clasts that are evidence of wear-abrasion brecciation.

Alteration is strong in both the clasts and the matrix, and typically consists of varying amounts of quartz, calcite, epidote, chlorite, sericite, albite, hematite and magnetite. Alteration causes the clasts to be an assortment of colours, including pink, white, lime green, beige, or dark green. Additionally, many of the clasts are zoned with different coloured rims as a result of zoning. For the most part the unit is matrix supported and with no preferential orientation of clasts, however exceptions are present.

Textures in the two least brecciated samples, defined by visible colour contrasts in hand sample, have the appearance of a dull mosaic breccia, as shown in Figure

3.38. However, unlike in the more brecciated samples, these rocks lack or have only minor amounts of the characteristic chlorite or quartz-calcite fractures/ stringers, and these features do not define the boundaries of the fragments. The less brecciated samples also tend to be coarser grained than the more brecciated samples.

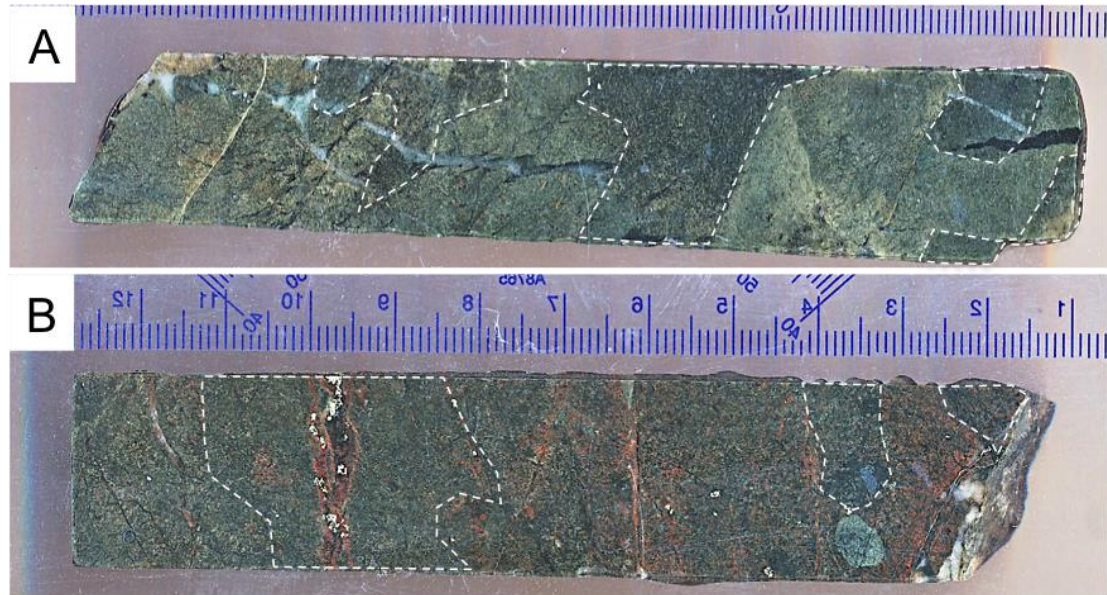


Figure 3.38. Two least brecciated samples collected. Samples include UWO_2015_42 (top) and UWO_2015_45 (bottom).

Preserved ~1 mm wide amphibole phenocrysts were observable in almost all representative samples from the deposit, in both the clasts and groundmass, indicating that the texture is primarily developed within sections of mafic syenite intrusions, and mafic syenite porphyry intrusions.

Most of the breccia hand samples observed contained trace amounts of disseminated pyrite, chalcopyrite, and hematite (rarely specular hematite), although most contained magnetite. When present, pyrite and chalcopyrite occurred in both the matrix and in the clasts. Many thin sections analyzed contained magnetite altering to hematite, typically in the form of a magnetite core surrounded by a hematite rim. Additionally, one of the brecciated samples contained aligned hematite and magnetite laths that are overgrown by chalcopyrite and pyrite, as shown in Figure 3.39. The aligned crystals are present in other areas of the deposit as well. Overprinting textures

suggest that magnetite formed first, followed by chalcopyrite and pyrite. Magnetite commonly alters to hematite.

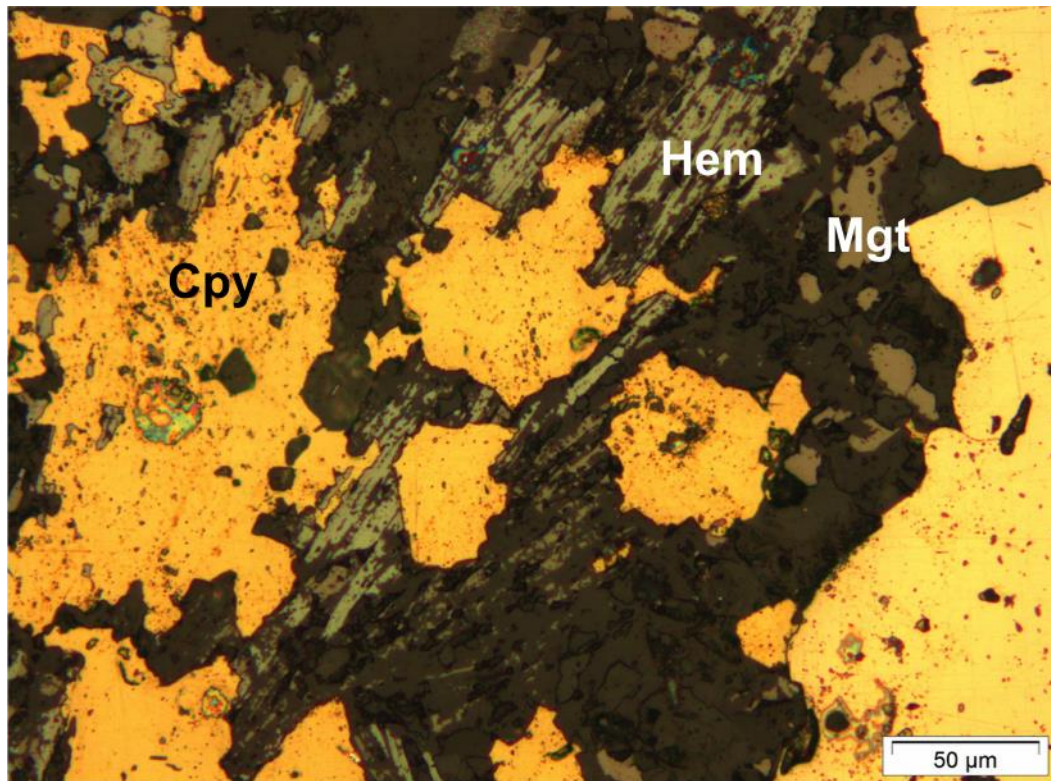


Figure 3.39. Petrographic photomicrograph showing cross cutting relationships between chalcopyrite, hematite and magnetite.

Geochemical analysis of brecciated samples compared to available data for relatively unaltered associated igneous intrusions identified a number of interesting trends. Brecciated samples tend to have much a much lower SiO_2 content and a much higher Fe_2O_3 MgO and TiO_2 content than relatively unaltered samples from DeAgazio (2012) and Feick (2014), as shown in Figure 3.40. The much lower concentration of SiO_2 is consistent with strong chlorite alteration, as observed petrographically, while the elevated Fe_2O_3 and MgO content of the brecciated rocks are consistent with the strong and magnetite and chlorite alteration. Interestingly the concentration of CaO in the brecciated samples is not exceptionally different than their unbrecciated equivalents.

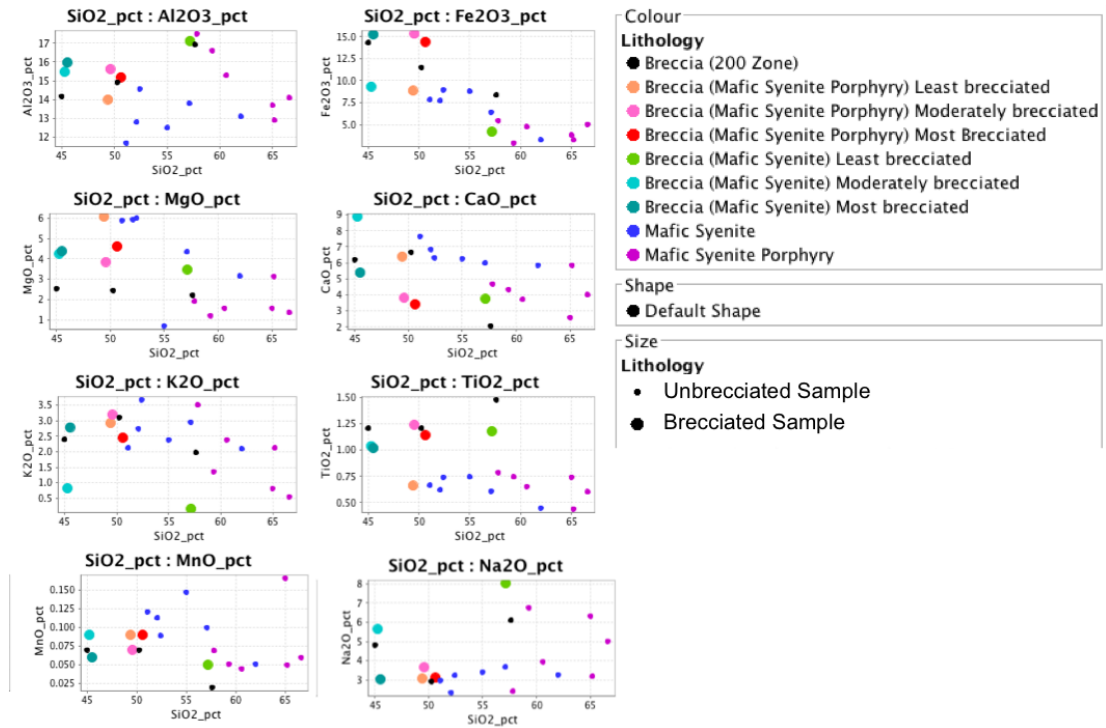


Figure 3.40. Geochemical analysis of brecciated samples from this project compared to available data for relatively unaltered associated igneous intrusions from past thesis projects by DeAgazio (2012) and Feick (2014).

The geochemical composition of each sample was also plotted on an alteration box plot, as defined by Large (2001) using the chlorite-carbonate-pyrite index (CCPI) and the Ishikawa alteration index (AI), to determine the likely mineralogical changes that occur during brecciation. The results are shown in Figure 3.41. Results indicate that the progressively more altered brecciated mafic syenite porphyry samples trend towards increasing amounts of chlorite-pyrite alteration, relative to their unaltered equivalents. Similarly, samples of brecciated mafic syenite trend towards increasing amounts of epidote-calcite and then chlorite-pyrite alteration relative to their unaltered equivalents. These trends are consistent with the petrographic and hand-sample observations.

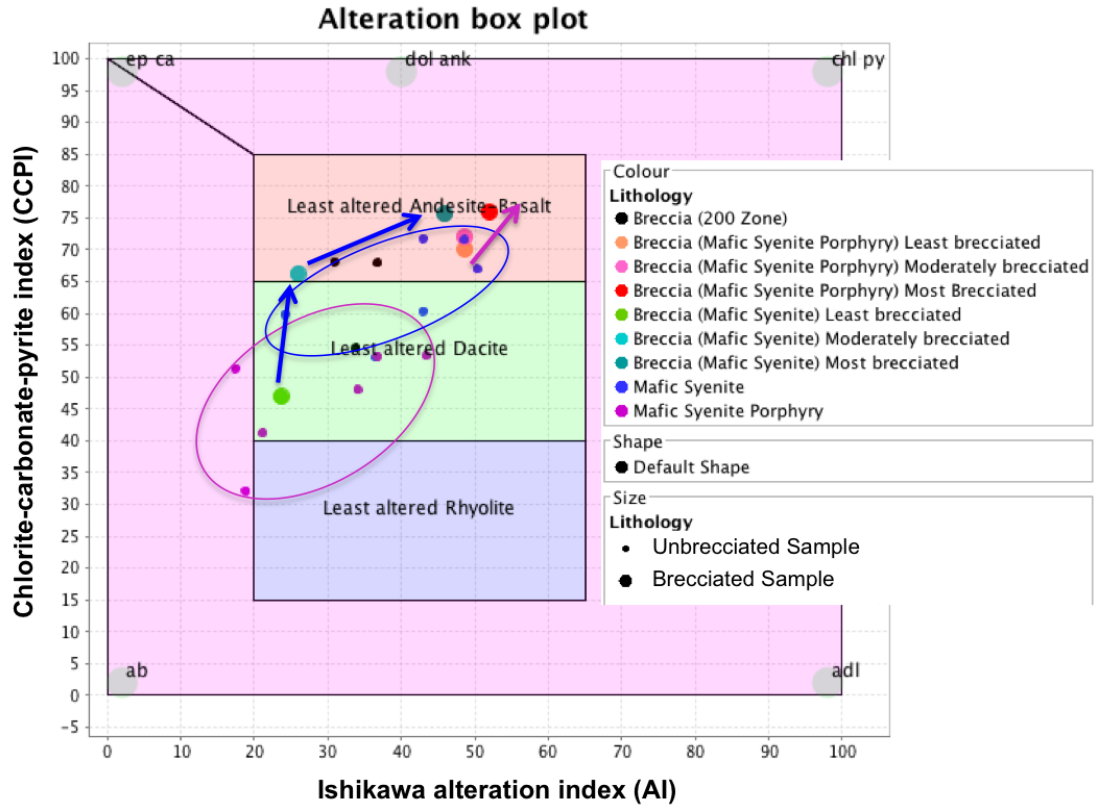


Figure 3.41. Alteration box plot based on the Ishikawa alteration index (AI) and Chlorite-carbonate-pyrite index (CCPI) as suggested by Large et al., (2001) showing expected mineralogical changes associated with brecciation based on geochemical analysis of samples for this project compared to available data from past thesis projects on the Upper Beaver deposit by DeAgazio (2012) and Feick (2012). “ep ca” = Epidote and calcite, “dol ank” = dolomite and ankerite, “chl py” = chlorite and pyrite, “ab” = albite, “il” = sericite; and “adi” = andalucite.

4 A Detailed Assessment of Trace Element Geochemistry of the Upper Beaver Deposit and An Evaluation of Exploration Vectors for Mineralization

4.1 Hand Sample Observations

Twenty mineralized samples were collected from the mineralized zones in the deposit. The aim of sample collection was to obtain representative samples of different styles of mineralization in different host rocks, from each major mineralized zone in the deposit. All collected hand-samples underwent multi-element analysis performed by ALS Global. Refer to 2.2.4.1 for details on geochemical analysis of these samples. Details on samples collected are summarized in Table 4.1, and further details on mineralized zones in the deposit are provided below. Additional information about each sample is provided in Appendix A of this thesis along with a cross section detailing where each sample is from.

Table 4.1. Summary of mineralized samples selected for analysis including: the drill hole and depth each sample is from; the mineralized zone (Q-Zone = “Q”, Syenite Breccia Zone = “SB”, 200-Zone = “200” North Contact Zone = “NC”, Lower Porphyry East Zone = “LPE”, Upper Porphyry East Zone = “UPE”, Lower Porphyry West Zone = “LPW”, Upper Porphyry West Zone = “UPW”, East Basalt Zone = “EB”, and North Basalt Zone = “NB”); host lithology (lith); minerals associated with mineralization (chalcopyrite = “Cpy”, pyrite = “Py”, magnetite = “Mgt” and visible gold = “VG”); host type (disseminated = “D”, vein = “V”, fracture fill = “F”); and the Au/ Cu grade of each sample as determined by multi-element analysis of collected hand-samples.

Sample ID	Hole ID	Sample Depth (m)	Zone	Lith	Mineralization	Host Type	Au Assay (g/t)	Cu Assay (ppt)
UWO_2015_01	UB07_76	332.6	Q	Basalt	Cpy, Py, Mgt	Calcite ± Quartz + Weak Ankerite D	1.01	0.318
UWO_2015_02	UB08_127	999.3	SB	Mafic syenite	Cpy, Py, VG, Mgt	Quartz Calcite D	168	0.942
UWO_2015_03	UB08_139	1000.8	LPE	Mafic syenite	Cpy, Py, Mgt	Quartz-Calcite V	128	3.53
UWO_2015_04	UB08_139	1001.2	LPE	Mafic syenite	Cpy, Py, Mgt	Quartz-Calcite V	86.8	0.595
UWO_2015_05	UB09_100 WI	856.3	UPW	Quartz-Carbonate vein zone	Mgt, Cpy, VG	Quartz-Calcite V	126	3.86
UWP_2015_06	UB11_170 W3	1016.6	UPW	Altered crowded syenite porphyry	VG	Anhydrite-Ankerite V	71.4	0.01

Table 4.1 cont. Summary of mineralized samples selected for analysis

Sample ID	Hole ID	Sample Depth (m)	Zone	Lith	Mineralization	Host	Au Assay (g/t)	Cu Assay (pct)
UWO_2015_07	UB11_170 W3	1017.5	UPW	Altered crowded syenite porphyry	Cpy, VG	Anhydrite-Ankerite V	87.8	6.92
UWO_2015_08	UB11_184	93.5	Q	Basalt	Mo, VG	Quartz-Calcite V	268	0.0154
UWO_2015_09	UB11_204	192.2	Q	Basalt	Cpy, Py, Mgt, VG	Quartz-Calcite V	232	4.67
UWO_2015_10	UB12_200 W3	1582.2	200	Mafic syenite	Cpy, Py, Mgt, VG	Quartz-Calcite D	28.4	7.82
UWO_2015_11	UB12_230	557.9	LPW	Mafic syenite	Cpy, Py, Mgt, VG	Quartz-Calcite V	51.3	0.995
UWO_2015_12	UB12_75W 3	603	UPE	Mafic syenite	Mo, Mgt, Py, Cpy	Quartz-Calcite V	129.5	0.0308
UWO_2015_13	UB13_284	165	EB	Basalt	Py, Cpy, Mgt, VG	Quartz-Calcite V	39.9	3.59
UWO_2015_14	UB13_310 A	378.8	NB	Basalt	Cpy, Mgt, VG	Quartz-Calcite V	1.7	5.31
UWO_2015_15	UB14_334	142.3	NC	Altered crowded syenite porphyry	Mgt, VG	Quartz FF	31.8	0.0202
UWO_2015_16	UB14_337	205.3	UPE	Altered Basalt	Mo, Py, VG	Quartz-Calcite V	25.8	0.0145
UWO_2015_17	UB14_337	205.6	UPE	Altered Basalt	Mo/Py/VG	Quartz-Calcite V	25.8	0.0145
UWO_2015_18	UB14_353	98.9	NC	Pillowed Basalt	Cpy, Py, Mgt, VG	Quartz-Calcite (and weak ankerite) V	42	0.404
UWO_2015_19	UB14_355	207.0	NC	Crowded syenite porphyry	Mgt, Py, VG	Quartz-Ankerite FF	21.8	0.0212
UWO_2015_50	UB10_170 W2	1028	LPW	Mafic syenite	Py, Cpy, VG, Mgt	Quartz-Calcite V	146.5	1.865

4.2 Mineralized Zones

The Upper Beaver deposit can be divided into nine main mineralized zones that vary in length, grade, metal ratios, and alteration including: Lower and Upper East and West Porphyry Zones, North Contact Zone, Q Zone, South Contact Zone, Syenite Breccia Zone, 200 Zone, 156 Zone, North Basalt Zone, and East Basalt Zone (M. Masson, personal communications, 2015). The division of zones is strongly dependent on morphology and each zone can be further subdivided based on mineralization style and location (M. Masson, personal communications, 2015).

There is a large variation in space and time between the different types of mineralization on the property (Bernier and Cole, 2012). Only gold mineralization was considered for defining mineralized zones for resource modeling in the recently published N43-101 report (Bernier and Cole, 2012).

4.2.1 Zones on the South Side of the Intrusive Complex

The relative location of all mineralized zones is presented in Figure 1.5 in Chapter 1. Ore zones have been well defined on the south side of the intrusive complex, with most ore zones being intimately associated with crowded syenite porphyry stocks, as described below.

4.2.1.1 Shallow Mineralized Zones

Shallow mineralized zones (zones that are <400 m in depth) occur along the boundaries of three crowded porphyry intrusions. All of the shallow zones are dominantly hosted within the Blake River Assemblage basalts.

(1) South Contact Zone: The south contact zone is hosted by strongly altered mafic volcanics and volcanoclastic conglomerate with variable amounts of silica, calcite, ankerite, epidote, magnetite, hematite, sericite, potassic feldspar, chalcopryrite, pyrite, and visible gold (Feick, 2014). It lies below and to the south of the mine workings in the Upper Tisdale contact area. Mineralization in the South Contact Zone consists of replacement style mineralization where gold and copper are dominantly hosted within patches of quartz and calcite as opposed to veins (Bernier and Cole, 2012). Multi-stage deformation and fluid circulation at the contact between the Lower Blake River and Tisdale assemblages, which includes the Victoria Creek Deformation Zone, the intrusion of the crowded feldspar porphyry dike, and the progressive deformation prior to, during, and postdating the emplacement of the crowded feldspar porphyry dike likely played an important role in the development of the south contact zone (Bernier and Cole, 2012). The South Contact Zone contains an indicated mineral resource of 401,000 tonnes of Au at 2.89 g/t and 0.15 % Cu equivalent, to 37,000 Oz Au and 1,347,000 pounds of Cu; and an inferred 369,000 tonnes of Au at

3.08 g/t, and 0.17% Cu, equivalent to 37,000 Oz Au and 1,367,000 pounds Cu (Bernier and Cole, 2012).

Samples analyzed from the South Contact Zone were collected in 2013 for an undergraduate thesis project by Feick (2014) on alteration and mineralization in the South Contact Zone. Samples are variably mineralized and altered by chlorite, sericite, epidote, albite, k-spar, hematite and magnetite. Of particular interest to this study are samples KF05, KF07, and KF15, which contain visible gold hosted within pyrite grains or along pyrite grain boundaries enclosed in chalcopyrite. Sulphide minerals in all three samples are hosted within calcite ± epidote patches within very strongly altered basalt, with additional K-feldspar, sericite, chlorite, magnetite, hematite, and leucoxene surrounding mineralized patches.

(2) **North Contact Zone:** The North Contact Zone occurs at the basalt/ syenite contact area (Bernier and Cole, 2012). The North Contact Zone contains an indicated mineral resource of 742,000 tonnes of Au at 2.84 g/t and 0.26 % Cu equivalent, to 68,000 Oz Au and 4,256,000 pounds of Cu; and an inferred 804,000 tonnes of Au at 3.36 g/t, and 0.23% Cu, equivalent to 87,000 Oz Au and 4,100,000 pounds Cu (Bernier and Cole, 2012).

Two samples were analyzed from the North Contact Zone. Both samples consisted of fracture fill mineralization and were hosted within crowded syenite porphyry in 1 cm thick quartz-calcite veins. Minor amounts of hematite and pyrite are present in one of the samples, but they are not associated with Au mineralization. The other sample contains hematite, magnetite, and chalcopyrite, and in this sample Au mineralization associated with magnetite, as shown in Figure 4.1. Textural relationships, as shown in Figure 4.2, indicate that Au formed after hematite and magnetite.

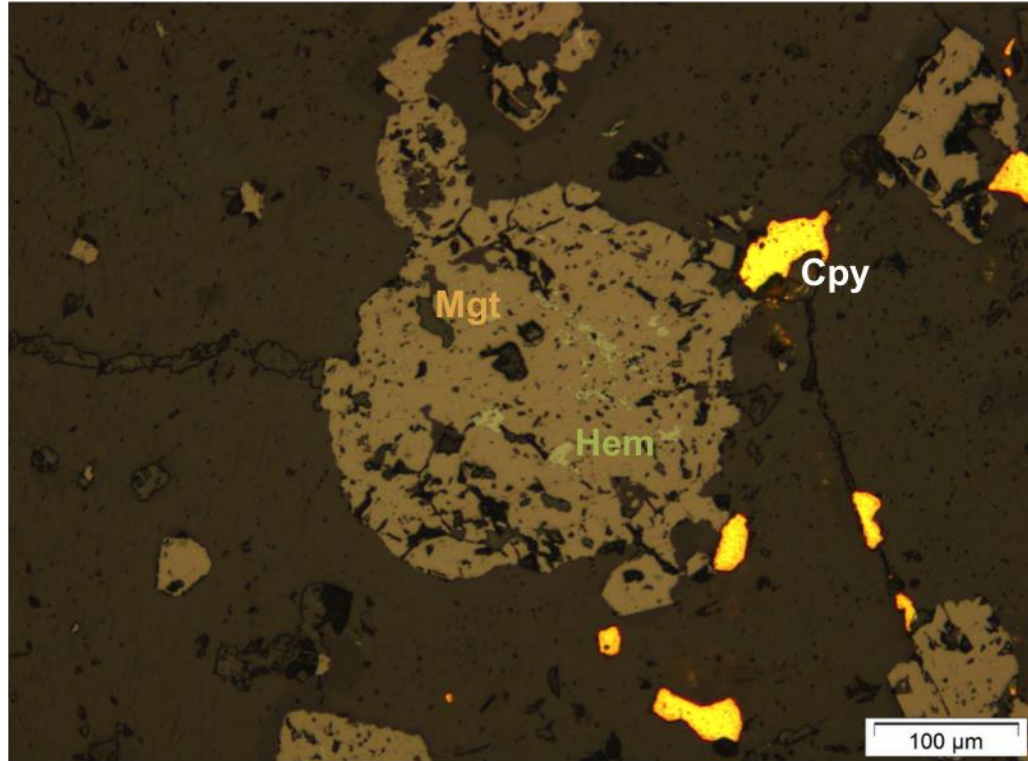


Figure 4.1. Reflected light photo showing the overprinting relationship between chalcopyrite (Cpy), hematite (Hem), and magnetite (Mgt) in UWO_2015_19 from the North Contact Zone

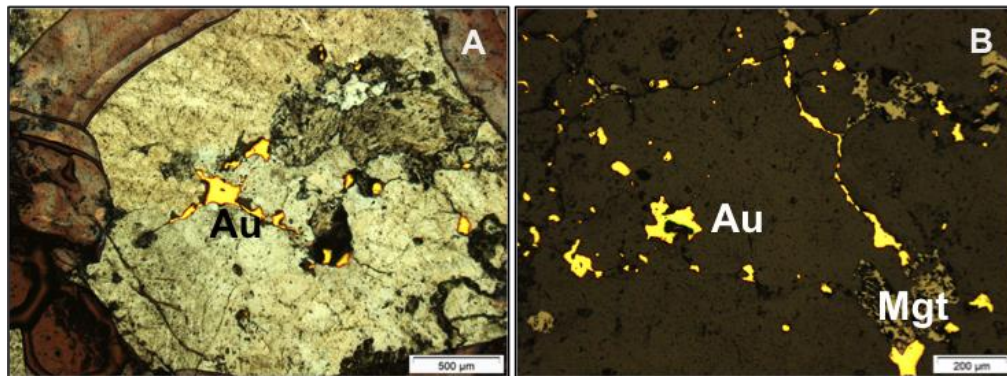


Figure 4.2. Reflective light photos of Au mineralization from the North Contact Zone: A) Free / fracture fill Au (sample UWO_2015_15), and b) Free/ fracture fill Au and magnetite (UWO_2015_19). Identified minerals include gold (Au) and magnetite (Mgt)

(3) Q Zone: Mineralization in the Q Zone occurs along the boundaries with crowded porphyry dikes (Bernier and Cole, 2012). Alteration in the Q Zone is similar to that seen in the South Contact Zone, but it is not as intense (M. Masson, personal

communications, 2015). The Q Zone contains an indicated mineral resource of 377,000 tonnes of Au at 3.29 g/t and 0.35 % Cu equivalent, to 40,000 Oz Au and 2,946,000 pounds of Cu; and an inferred 496,000 tonnes of Au at 3.50 g/t, and 0.21% Cu, equivalent to 56,000 Oz Au and 2,305,000 pounds Cu (Bernier and Cole, 2012).

Three samples were analyzed from the Q Zone. Mineralized samples were highly variable as shown in Figure 4.3. One sample contained very small Au and chalcopyrite inclusions within a large subhedral pyrite, with small amounts of chalcopyrite occurring separately as well. A second sample contained Au inclusions within molybdenite and free Au, and the final sample analyzed from the Q-zone contained blocky early pyrite with Au nucleated along grain boundaries and enveloped in chalcopyrite. All three samples also contained magnetite and hematite intergrowth.

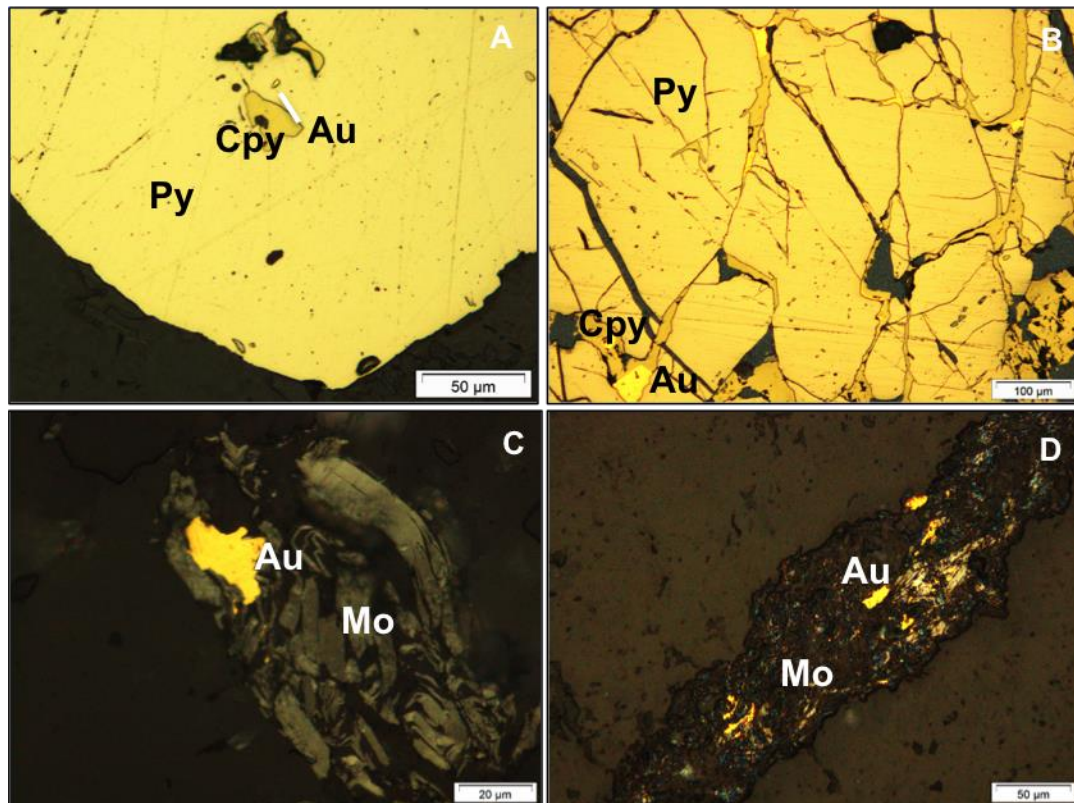


Figure 4.3. Reflective light photos of mineralization from the Q-Zone. A) Au and chalcopyrite hosted in a pyrite grain (sample UWO_2015_01 from Q1). B) Au, pyrite, and magnetite hosted within chalcopyrite (sample UWO_2015_09 from Q1). C) and D) Au hosted in molybdenite (sample UWO_2015_08 from Q2).

Identified minerals include gold (Au), chalcopyrite (Cpy), pyrite (Py), and molybdenite (Mo).

4.2.1.2 Deeper Porphyry Zones

The Porphyry Zones are steeply dipping mineralized zones that developed footwall to a series of large crowded feldspar porphyry intrusions. Zones are continuous to at least 2 km depth, and mineralization remains open at depth (Bernier and Cole, 2012). Mineralization is subparallel to the dikes, occurring within, at the contact of, and just outside of the intrusions, but the location of the zone suggests that the dike and mineralized fluids may have shared the same brittle-ductile deformation corridor measuring up to 300 m in width (M. Masson, personal communication, 2015).

Mineralization primarily occurs within a series of sheeted veins that range from a few mm to >1 m in width within a broad alteration envelope. The alteration envelope varies greatly in intensity and assemblage, although is generally phyllitic in composition (sericite - chlorite \pm hematite \pm quartz \pm calcite \pm albite \pm ankerite \pm epidote) (M. Masson, personal communications, 2015). There is also locally developed fracture controlled and disseminated mineralization throughout the zone (M. Masson, personal communications, 2015).

The Porphyry zones can be subdivided into Upper, Middle, and Lower zones, which coalesce and diverge along strike and up dip. However, they are more commonly separated into Upper and Lower East Porphyry Zone and West Porphyry zones. East and West zones are separate by a 30-40 m thick, west-dipping, north-trending late-stage diabase dike (Bernier and Cole, 2012). The Porphyry East Zone contains an indicated mineral resource of 2,906,000 tonnes of Au at 7.60 g/t and 0.25 % Cu equivalent (expressed as a gold equivalent), to 710,000 Oz Au and 15,796,000 pounds of Cu; and an inferred 1,471,000 tonnes of Au at 6.28 g/t, and 0.21% Cu, equivalent to 297,000 Oz Au and 6,726,000 pounds Cu (Bernier and Cole, 2012). The Porphyry West Zone contains an indicated mineral resource of 1,924,000 tonnes

of Au at 8.60 g/t and 0.65 % Cu equivalent, to 532,000 Oz Au and 27,522,000 pounds of Cu; and an inferred 874,000 tonnes of Au at 6.06 g/t, and 0.66% Cu, equivalent to 170,000 Oz Au and 12,770,000 pounds Cu (Bernier and Cole, 2012).

Collectively the porphyry zones strike northeast at 320-330°, dip northwesterly at 60-70°, and plunge 50-60° northeast (Breede et al., 2011). Mineralization remains open at depth but exhibit a strong vertical continuity down plunge with a vertical: horizontal aspect ratio of more than 3:1 (M. Masson, personal communication, 2015).

Ten samples were analyzed from the porphyry zones to capture the variation within the vertically extensive zones. Samples collected from the Porphyry Zones contain variable amounts of gold enclosed within chalcopyrite or pyrite, associated with molybdenite, or as free gold as shown in Figures 4.4-4.7. One sample, UWO_2015_04, contained Au in both pyrite and chalcopyrite, as well as free gold. Magnetite altered to hematite along its grain boundaries occurred two of the three samples (not in the molybdenite-rich samples). Textures typically indicate that there was an early phase of magnetite growth, followed by pyrite then chalcopyrite. Three samples, UWO_2015_12, UWO_2015_16, and UWO_2015_17, contained molybdenite associated with Au mineralization. These thin sections were also unusual because they contained abundant hematite but lacked magnetite. Pyrite and chalcopyrite, if present, occurred in very small amounts. Two samples, UWO_2015_06 and UWO_2015_07 from the Upper West Porphyry Zone were taken from a 4 m wide anhydrite vein. Au mineralization in both samples occurred either within chalcopyrite or as free Au.

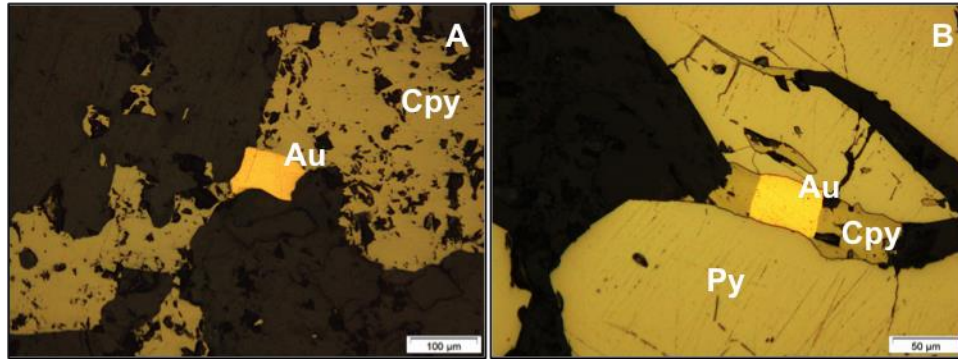


Figure 4.4. Reflective light photos of mineralization from the Lower East Porphyry Zone. A) Au hosted within chalcopyrite (sample UWO_2015_03). B) and C) Au and chalcopyrite trapped between pyrite grains (sample UWO_2015_04). Identified minerals include gold (Au), chalcopyrite (Cpy), and pyrite (Py).

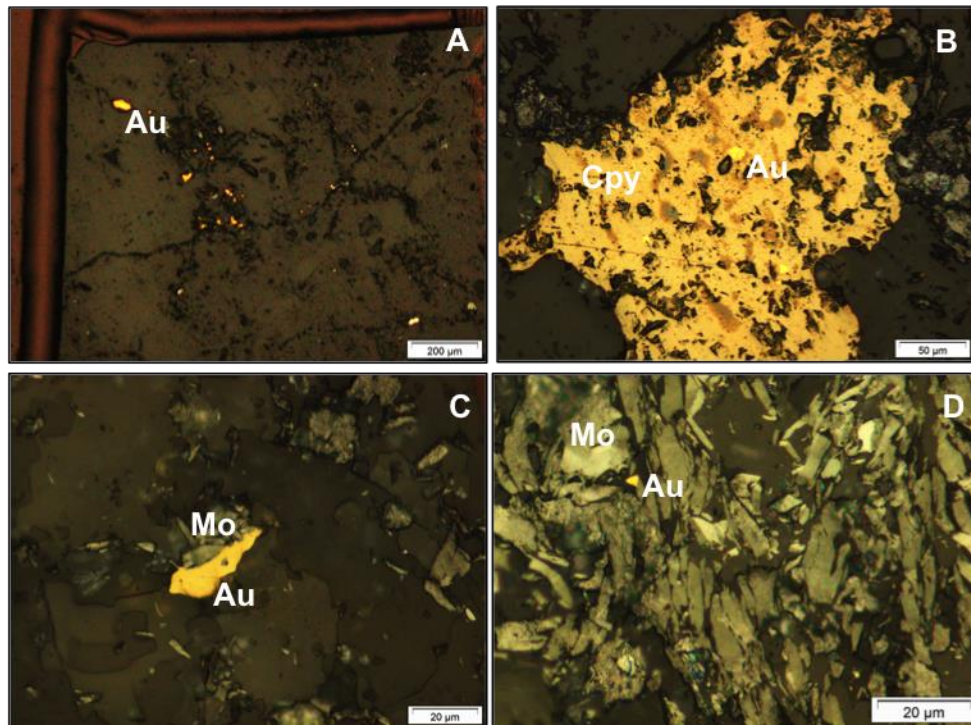


Figure 4.5. Reflective light photos of mineralization from the Upper East Porphyry Zone. A) Free Au (sample UWO_2015_12). B) Au hosted within chalcopyrite (sample UWO_2015_16). C) and D) Au hosted within molybdenite (sample UWO_2015_17).

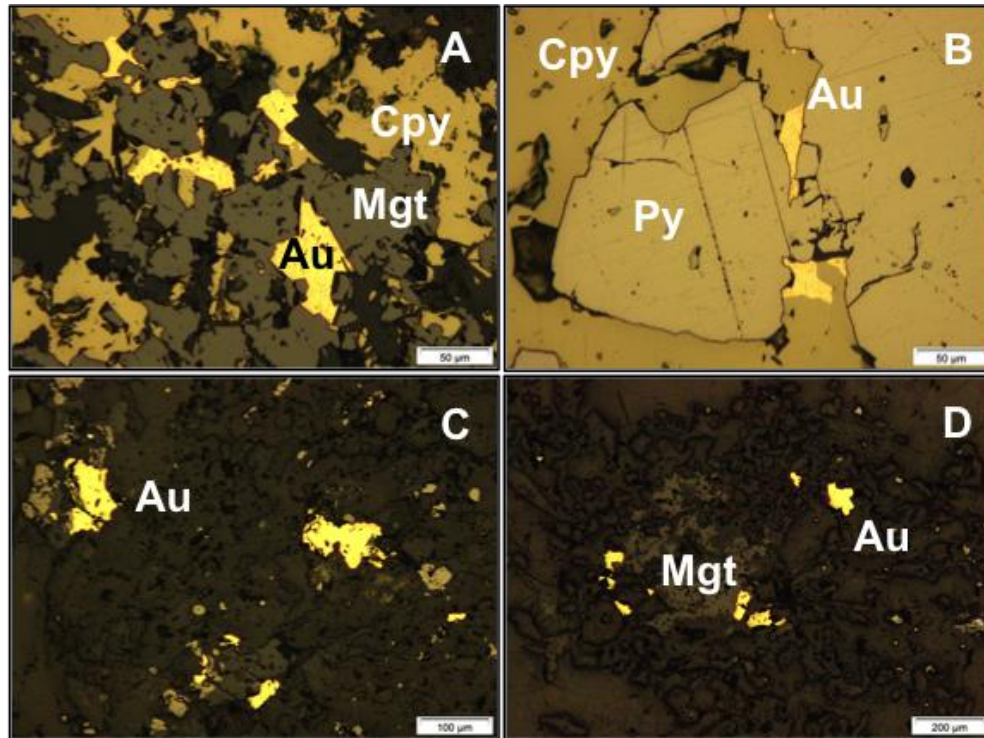


Figure 4.6. Reflective light photos of mineralization from the Upper West Porphyry Zone. A) Au hosted within magnetite and chalcopyrite and B) Au hosted between pyrite grains hosted within chalcopyrite (sample UWO_2015_05). C) and D) Free Au with magnetite in an anhydrite vein (sample UWO_2015_06). Identified minerals include gold (Au), chalcopyrite (Cpy), pyrite (Py), and magnetite (Mgt).

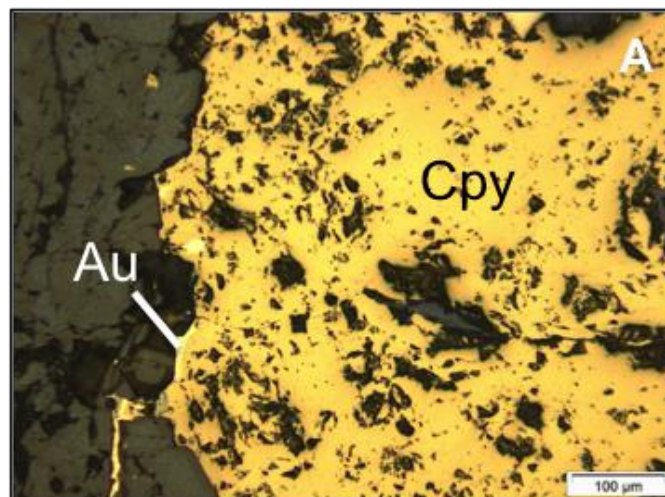


Figure 4.7. Reflective light photos of Au mineralization from the Lower West Porphyry Zone showing Au along chalcopyrite (Cpy) grain margins

4.2.1.3 Additional Zones

Additional less continuous zones in the deposit include the 200 Zone and the Syenite Breccia Zone, which are hosted within the brecciated lens along the Southern side of the intrusive complex and the 156 Zone.

200 Zone and Syenite Breccia Zone: Mineralization in the breccia lens is dominated by hematite and magnetite, which form the matrix between brecciated fragments with little to no accompanying sulphide mineralization, which can host Au mineralization. Two ore zones are hosted by the breccia lens: the 200 Zone and the Syenite Breccia Zone, but elsewhere the breccia is generally not mineralized. The breccia texture is developed within the mafic syenite and syenite porphyry intrusions, as recognized in hand-sample by preserved phenocrysts. The crowded porphyry dike, which is intimately associated with Au mineralization in the deposit, is not brecciated.

The 200 Zone contains an indicated mineral resource of 355,000 tonnes of Au at 4.96 g/t and 0.50 % Cu equivalent, to 57,000 Oz Au and 3,891,000 pounds of Cu; and an inferred 313,000 tonnes of Au at 4.27 g/t, and 0.74% Cu, equivalent to 43,000 Oz Au and 5,073,000 pounds Cu (Bernier and Cole, 2012).

The Syenite Breccia Zone contains an indicated mineral resource of 161,000 tonnes of Au at 3.35 g/t and 0.004 % Cu equivalent, to 17,000 Oz Au and 143,000 pounds of Cu; and an inferred 240,000 tonnes of Au at 2.92 g/t, and 0.03% Cu, equivalent to 23,000 Oz Au and 177,000 pounds Cu (Bernier and Cole, 2012).

One drill core sample was collected from mineralized veins in each zone. The sample from the 200 Zone, UWO_2015_10, is composed almost entirely of magnetite, pyrite, and chalcopyrite (87%). Magnetite laths are infilled by calcite, pyrite, and chalcopyrite in the space between the laths. Au is present along the margins of pyrite and magnetite grains and is typically enclosed within chalcopyrite. The sample from the Syenite Breccia Zone, UWO_2015_02, on the other hand was dominantly composed of pyrite and chalcopyrite and contained very large globs of

Au within chalcopyrite and a bismuth sulphide mineral. Textures in both thin sections indicate that magnetite and hematite formed first, followed by pyrite and then chalcopyrite and a bismuth sulphide mineral, which are associated with the Au mineralization, as shown in Figure 4.8 A and B.

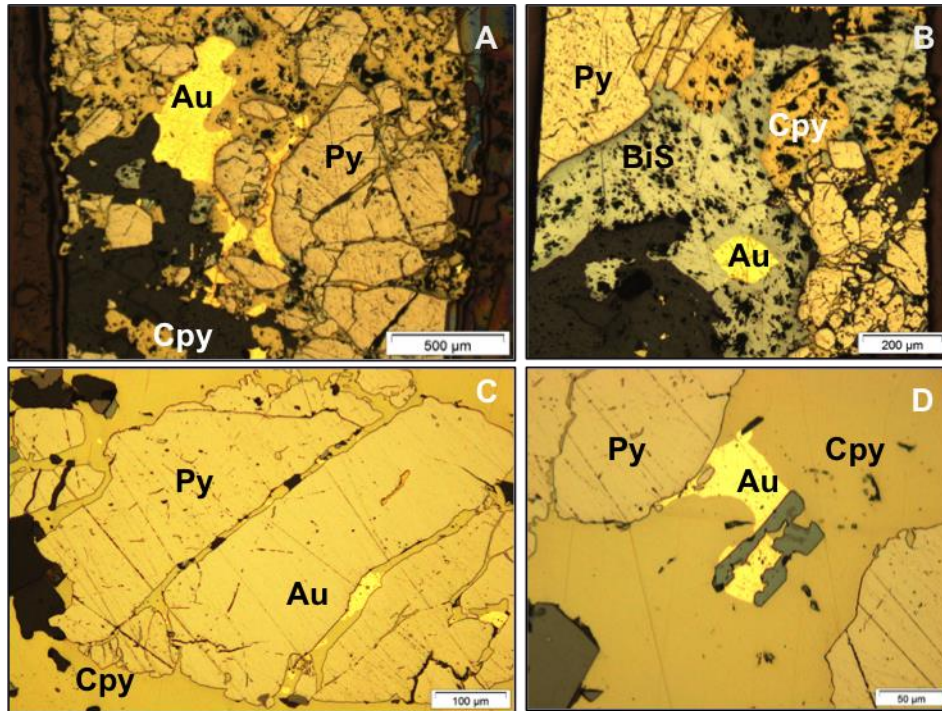


Figure 4.8. Reflective light photos of mineralization from 200 and Syenite Breccia Zones showing gold (Au), chalcopyrite (Cpy), pyrite (Py), and a bismuth sulphide mineral (BiS). A) Au and pyrite hosted within chalcopyrite and B) Au hosted within a bismuth sulphide mineral (sample UWO_2015_02 from the Syenite Breccia Zone). C) Au along the margins of a pyrite grain within chalcopyrite and D) Au hosted with magnetite and pyrite within chalcopyrite (sample UWO_2015_10 from the 200 Zone)

156 Zone: The 156 Zone consists of quartz-Au veining (\pm Mo) at 700 m depth and below. The zone has a unique orientation in the deposit. It is roughly vertical as opposed to steeply dipping, and it is oriented at 003° as opposed to 050° like the other zones in the deposit (M. Masson, personal communications, 2015).

Unfortunately no samples were collected from the 156 Zone for this project.

4.2.2 Zones on the North Side of the Intrusive Complex

Mineralization is not as abundant on the north side of the intrusive complex. Two zones have been defined.

East and North Basalt Zones: The East and North Basalt Zones, which are hosted in basalt at the northern contact of the Upper Beaver Intrusive Complex, likely developed due to shearing along the contact of the intrusion (M. Masson, personal communications, 2015). Both zones are roughly parallel to the intrusion and occur within 200 m of it (M. Masson, personal communications, 2015). Au mineralization is characterized by a series of fractures and stringers with chalcopyrite and magnetite. The fracture system that hosts the mineralization strikes east-northeast and dips steeply to the north (M. Masson, personal communications, 2015). The two zones may be able to be connected but mineral resources have not yet been completely defined within the zones. The emplacement of the North Basalt Zone is believed to have been at least in part controlled by the Upper Canada Break, folded primary volcanic stratigraphy, and the intrusion of the syenite complex (Bernier and Cole, 2012). Mineralization varies between the zones but dominantly consists of pyrite and chalcopyrite, as well as hematite and magnetite, similar to the bulk of mineralization in the southern zones. Representative pictures of gold mineralization in the East and North Basalt Zones is shown in Figure 4.9.

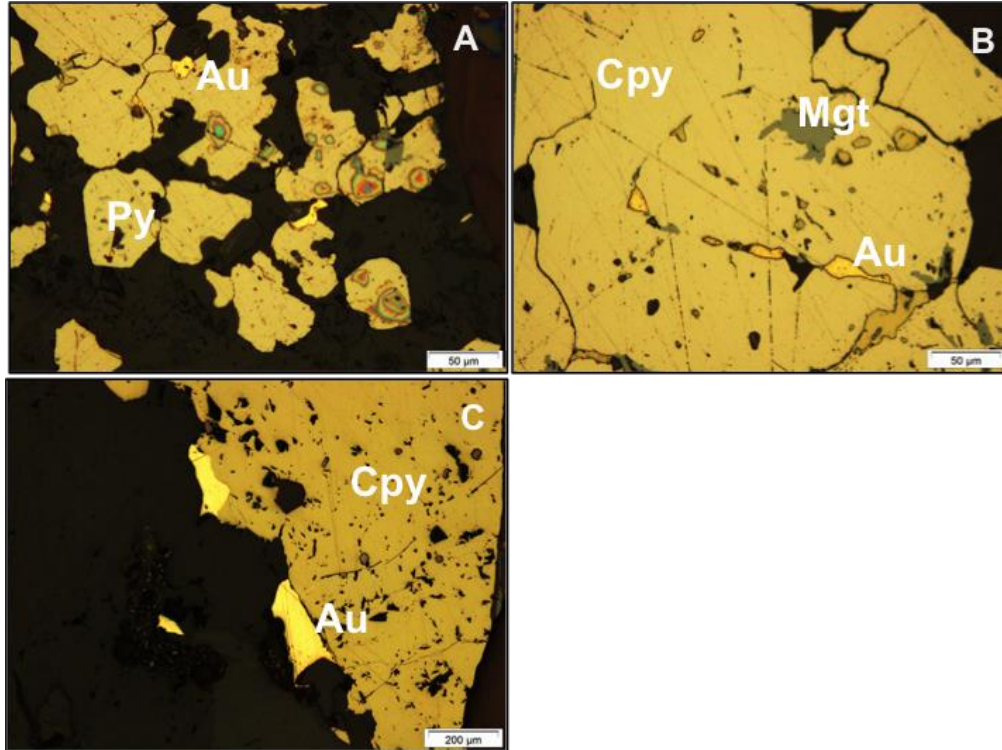


Figure 4.9. Reflective light photos of mineralization from East and North Basalt Zones. A) Au along pyrite grain margins and B) Au hosted with chalcopyrite and magnetite within pyrite (sample UWO_2015_13 from the East Basalt Zone), and C) Au along the margins of a chalcopyrite grain (sample UWO_2015_14 from the North Basalt Zone). Identified minerals include gold (Au), pyrite (Py), chalcopyrite (Cpy), and magnetite (mgt).

One sample was collected from each zone. Mineralization varies between the zones but dominantly consists of pyrite and chalcopyrite, as well as hematite and magnetite, similar to the bulk of mineralization in the southern zones. Textural relationships define a similar paragenesis as well, with magnetite forming first, followed by pyrite, chalcopyrite, and Au mineralization. Both collected samples were associated with chlorite alteration.

The sample from the East basalt zone, UWO_2015_13, contained Au hosted within or at the margins of pyrite. Pyrite also contained inclusions of magnetite and chalcopyrite. Textural relationships indicate that the sieve-textured pyrite formed first, followed by sieve-textured chalcopyrite, and finally by hematite and magnetite.

Mineralization is hosted within a very laminated and folded vein that occurs 30 degrees to the core axis.

The sample from the North Basalt Zone, UWO_2015_14, contained Au mineralization along the margins of chalcopyrite grains and as thin fracture fills within sieve-textured chalcopyrite grains. Au mineralization occurs within a cm-thick chalcopyrite vein that is rimmed by tiny grains of disseminated hematite and magnetite as well as fine-grained and chalcopyrite. Textural relationships indicate that magnetite formed first, followed by chalcopyrite as shown in Figure 4.10. Mineralization occurs within irregular chalcopyrite-dominated quartz-carbonate veins oriented approximately 20 degrees to the core axis. The sample lacks pyrite.

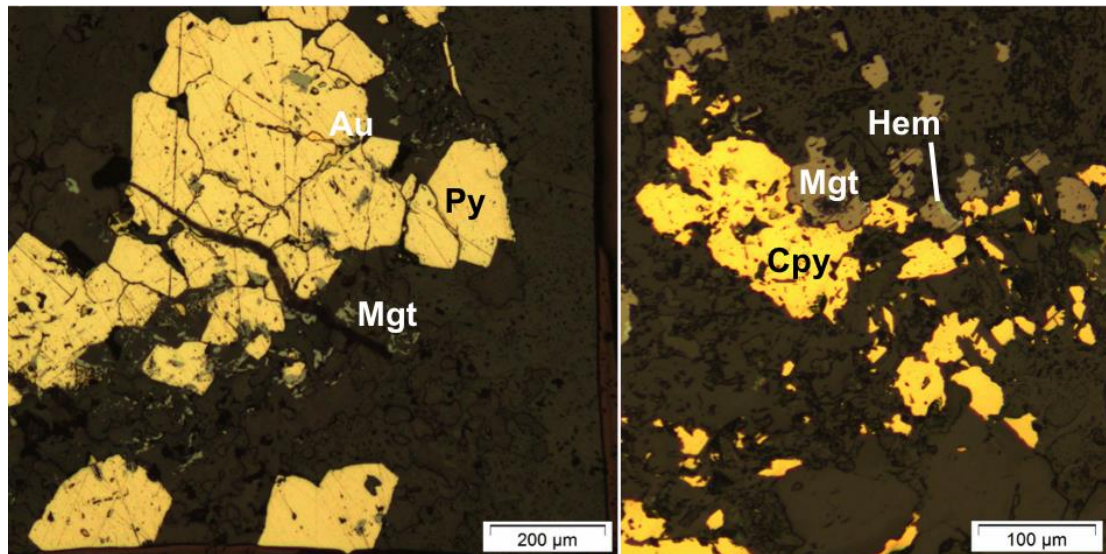


Figure 4.10. Reflected light photo showing the overprinting relationship between gold (Au), chalcopyrite (Cpy), hematite (Hem), and magnetite (Mgt) in UWO_2015_13 and UWO_2015_14 from the East and North Basalt Zones, respectively.

4.2.2.1 Host Rock and Alteration as identified in Hand Sample

In the Upper Beaver deposit, Au and Cu mineralization occur as veins or disseminations throughout their host rock. Mineralization is recognized to be associated with a range of alteration products, including widespread pervasive magnetite-feldspar (albite and K-spar)-actinolite-epidote-carbonate-sericite alteration (Bernier and Cole, 2012). Alteration minerals were recorded for each hand-sample collected to identify differences in alteration signature among samples collected from the various mineralized zones. A magnet, potassium ferro-cyanide (KFC), and hydrochloric acid (HCl), were used to identify the presence of magnetite, ankerite, and calcite, respectively, in hand sample. Other alteration minerals were determined by their characteristic colour, hardness, and streak in hand sample.

Collected samples of basalt are medium to dark grey with variable amounts of alteration. They dominantly consist of fine-grained plagioclase and quartz with lesser amounts of quartz and amphibole. Alteration included chlorite, sericite, epidote, albite, actinolite, and carbonate alteration minerals in this rock type. Responses to the application of KFC and HCl indicate that the 8 collected samples of basalt are typically non- to weakly- ankeritized and are typically calcitic. Five of the 8 samples were magnetic and contained variable amounts of chalcopyrite and pyrite, while the remaining three samples were non-magnetic and contained molybdenite.

Collected samples of mafic syenite, which is the most volumetrically abundant rock in the Upper Beaver Intrusive Complex, are fine to medium grained and greenish to reddish brown in colour. The unit is characterized by medium to coarse-grained euhedral amphiboles within a relatively fine-grained groundmass. The most common alteration products in mafic syenite are chlorite and sericite, although a range of alteration products can occur. The host rock of samples, UWO_2015_02 and UWO_2015_11, was very strongly altered mafic syenite, however, the rock was so altered and mineralized that it was difficult to identify the protolith in hand sample. Inspection of core surrounding the strongly altered and mineralized section of rock

and relic phenocrysts of coarse-grained amphiboles indicate that the host rock in both cases was most likely mafic syenite. None of the 6 collected samples of mafic syenite responded to the application of KFC, indicating that the rock does not contain ankerite. Additionally, 3 of the 6 samples contained calcite, as determined by their response to the application of HCl. All six samples were magnetic, and contained variable amounts of magnetite and pyrite. One sample also contained molybdenite.

Samples were also collected of mineralized crowded syenite porphyry, which is characterized by up to 60% medium-to coarse-grained crowded and tightly packed feldspar phenocrysts in a fine-grained plagioclase-rich groundmass with lesser amounts of quartz and amphiboles. Sericite and chlorite were the most common alteration products in this rock type. Four samples were collected from the mineralized crowded syenite porphyry unit, three of which responded to the application of KFC and not HCl, indicating the rock contains ankerite and not calcite, while the remaining sample that did not respond to KFC but responded to HCl, indicating that they are calcitic. Two of the four samples contained magnetite (one of these samples also contained pyrite) while the remaining two samples were non-magnetic. The two non-magnetic samples were from an anhydrite vein within the wider package of crowded syenite porphyry. One of these samples also contained chalcopyrite and pyrite.

4.2.3 Petrography

Hand samples were collected from veins and mineralized patches that ranged in width from mm wide to meters wide intervals. Thin sections were made from offcuts of the collected hand-samples. Offcuts were either made of the mineralized veins or of disseminated mineralized patches. Although varying in abundance, the mineralogy of the veins and patches of mineralization consisted dominantly of quartz and carbonates, with lesser amounts of chlorite and sericite, and minor amounts of magnetite and/or hematite, epidote, feldspar, and amphibole. Trace elements included zircon and rutile, which were observed in almost every sample. The two samples (UWO_2015_06 and UWO_2015_07) that were taken from a thick anhydrite vein were largely composed of anhydrite. Refer to Appendix A of this thesis for a full

description of thin sections as well as a cross section detailing where in the deposit each sample is from.

Feldspars, where observed, commonly exhibited a strongly turbid texture, which is described as “dustings” of clay or sericite within the larger grains due to alteration (Jensen and Barton, 2000). As well, many of the larger quartz and feldspar grains had undulose extinction. A weak foliation was observed in most samples, defined by the roughly parallel alignment of sulfide-rich stringers and chlorite and/or sericite in the groundmass. Quartz pressure shadows were identified in many samples as well, often occurring around pyrite grains due to the re-precipitation of quartz in low-pressure areas. This is a characteristic texture of low-grade metamorphism.

Mineralization frequently consisted of magnetite altering to hematite and sieve-textured magnetite and hematite, as well as pyrite, chalcopyrite, and molybdenite. Most samples showed evidence for initial growth of magnetite, followed by sieve-textured pyrite and chalcopyrite. Magnetite was commonly altered to hematite. Representative photos of iron oxide minerals and sulphide minerals in the Upper Beaver deposit are provided in Figure 4.11.

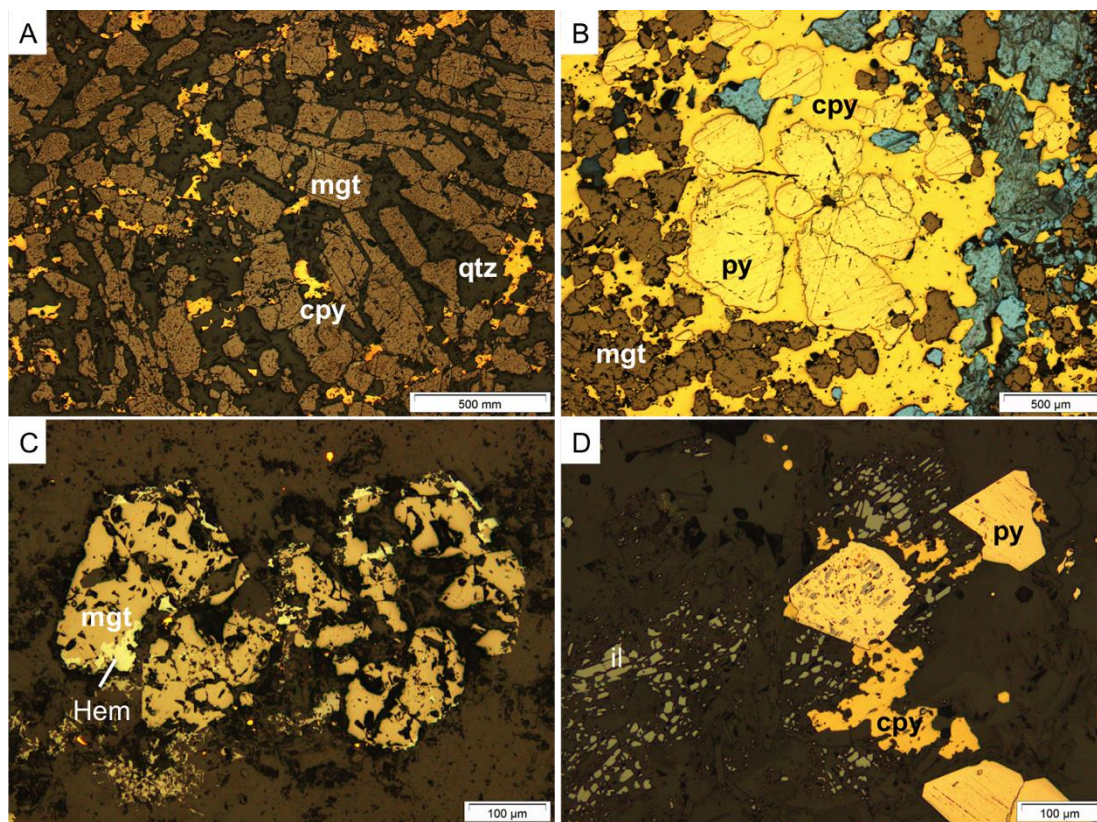


Figure 4.11. Representative reflected light photomicrographs of mineralization in analyzed thin sections. A) magnetite (mgt) overprinted by chalcopyrite (cpy) hosted within a quartz and calcite rich vein in UWO_2015_10; B) magnetite (mgt) with later pyrite (py) overprinted by chalcopyrite (cpy) within a quartz and calcite-rich vein in UWO_2015_10; C) magnetite (mgt) altering to hematite (hem) along grain boundaries hosted within a quartz and calcite rich vein in UWO_2015_12; and D) ilmenite (il) overgrown by pyrite (py) and later chalcopyrite (cpy) within a quartz-calcite vein in UWO_2015_04.

In analyzed samples, gold globs ranged in size from <10 microns to coarse (>500 microns), and frequently occurred with chalcopyrite grains. Less commonly gold occurred with pyrite, magnetite, a bismuth sulphide mineral, and molybdenite, or as free gold. Representative reflected light photomicrographs are provided in Figure 4.12. Two or more styles of Au mineralization were present in nearly every thin section analyzed.

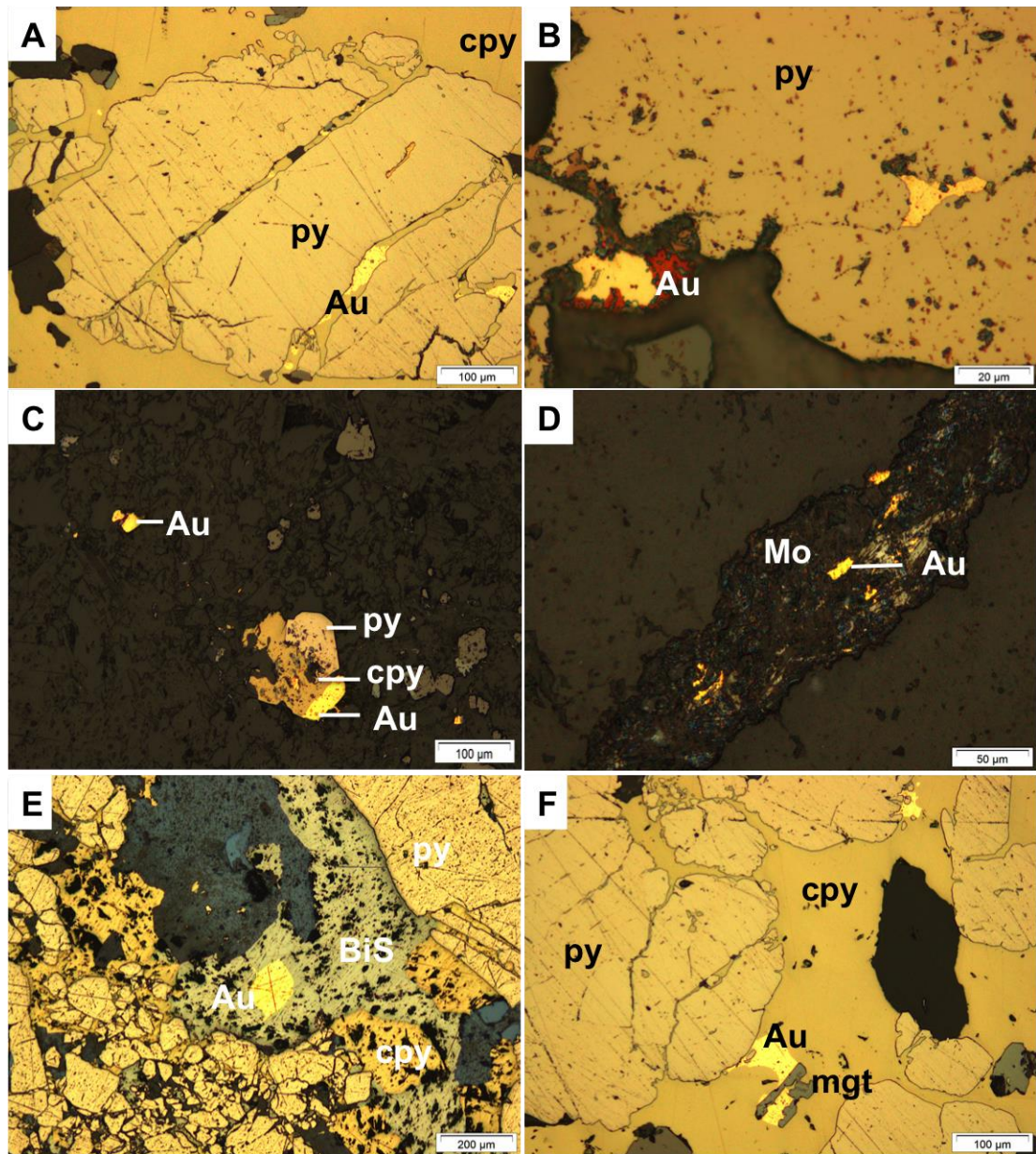


Figure 4.12. Representative reflected light photomicrographs of gold mineralization in the Upper Beaver deposit. A) Au with chalcopyrite (cpy) along pyrite (py) fractures in UWO_2015_10; B) Au hosted within fractures in pyrite (py) in KF15; C) Au nucleated along chalcopyrite (cpy) mineralization and as free gold (Au) hosted within an anhydrite vein in UWO_2015_07; D) Au hosted within molybdenite (Mo) vein in UWO_2015_08; E) Au hosted within a bismuth sulphide (BiS) mineral in UWO_2015_02, Au is also hosted directly in chalcopyrite (cpy) elsewhere in the slide; and F) Au nucleated along magnetite mineralization and pyrite (py) grain margins hosted within chalcopyrite (cpy).

4.2.4 CMC-Provided Geochemical Database

With the use of modern chemical analytical techniques, such as inductively coupled mass spectrometry, large geochemical datasets can be produced rapidly at low costs (Levitan et al., 2014). The increasing number of large datasets promotes the use of Exploratory Data Analysis (EDA) to identify the interrelationships between variables (elements). The overall goal of exploratory analysis is to use the relationships between variables to provide an understanding of underlying geochemical processes (Grunsky, 2007). EDA can be used to identify trends in soil geochemistry (e.g., Levitan et al., 2014 and Templ et al., 2006); in lake and stream sediments (e.g., Rukhlov et al., 2009); in organic materials (e.g., Heberlein and Dunn, 2011); in whole-rock samples (e.g., Wang et al., 2015); in regional survey data (e.g., Harris et al., 1999; Grunsky, 2007; Grunsky, 2013); and in global databases to compare deposit styles (e.g., Grunsky, 2015). EDA commonly incorporates a variety of methods including univariate methods (probability QQ plots and fractals), statistical classification and mathematical ratios (CIPW normative mineral classification and alteration indices), statistical multivariate methods (clustering, regression, principal component analysis, scatter plots, selective querying, geochemical classifications, and geochemical classification versus mapped lithology) and geostatistical (factoral kriging) techniques (Harris et al., 1999). For this work, values for correlation are as follows: 0.00-0.19 = very weak correlation; 0.20-0.39 = weak correlation; 0.40-0.59 = moderate correlation; 0.60-0.79 = strong correlation; and 0.8-1.0 = very strong correlation.

Canadian Malartic Corporation provided a dataset consisting of Au-Cu assay results for over 167,000 samples for their Upper Beaver project. Of this sample set, 4,060 samples also had multi-element geochemistry results, which were used to better characterize trace element associations with gold and copper mineralization. All samples were analyzed between 2005 and 2015, by various labs using aqua regia digestion or two-acid digestion followed by either mass spectrometry or inductively coupled plasma optical emission spectroscopy. Refer to section 2.2.1 for a more detailed description on multi-element analytical methods.

Gold assays were obtained by fire assay with atomic absorption spectroscopy finish, and gravity methods (when grades returned by fire assay analysis were greater than 1.0 g/t) by Swastika, Accurassay, AGAT, and SGS Laboratories (Bernier and Cole, 2012). Copper assays were attained using aqua regia digestion and fire assay methods (Bernier and Cole, 2012). Assays greater than 1 percent Cu were re-analyzed using a smaller charge (Bernier and Cole, 2012).

Gold and copper mineralization is centered on the southern margin of the Upper Beaver Intrusive Complex (Bernier and Cole, 2012). In general, gold mineralization occurs in veins and altered packages in steeply dipping (southeast) zones along the intrusive-volcanic contact and less often they dip shallowly. Refer to section 1.8 for a more detailed description of gold mineralization, including detailed descriptions of mineralized zones. The overall distribution of gold mineralization in the Upper Beaver deposit is shown in Figure 4.13.

Copper mineralization is atypical of the Kirkland Lake District. The Upper Beaver deposit is the only local deposit that contains significant amounts of copper mineralization. However, the controls on the distribution of copper mineralization in the deposit remain poorly understood. In the Upper Beaver deposit copper can be spatially associated with gold, and is abundant within the mineralized zones in the deposit, but it also commonly also occurs separately. Copper is especially abundant in shallow mineralized zones along the south side of the intrusive complex. The distribution of copper mineralization in the Upper Beaver deposit is shown in Figure 4.14. Samples were collected only where copper mineralization occurred with gold mineralization because zones were defined for resource modeling based on where gold mineralization occurred (Bernier and Cole, 2012).

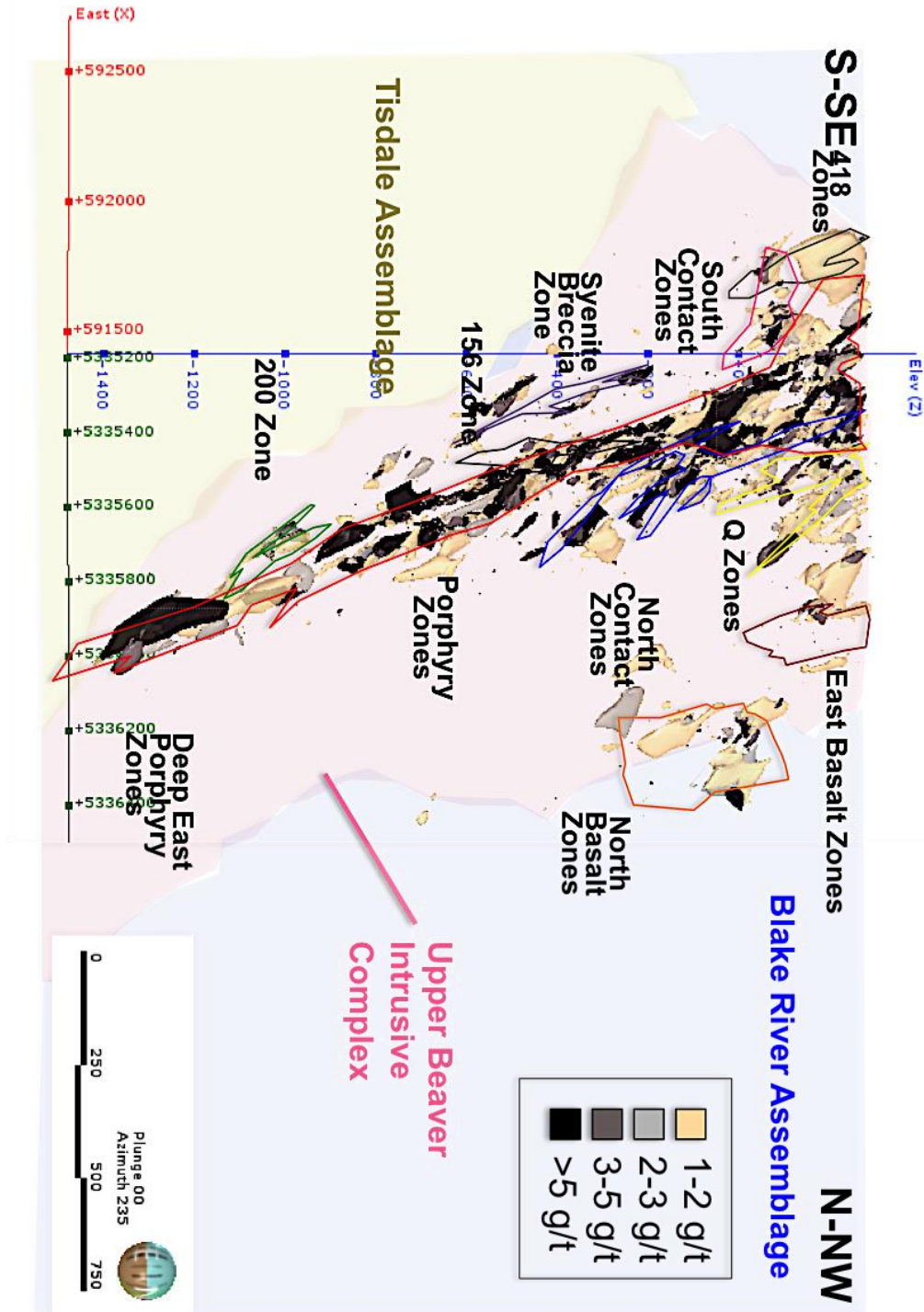


Figure 4.13. Leapfrog model showing the distribution of Au in the Upper Beaver deposit looking West. Model built using Leapfrog’s Geological Models tool. A trend of 58,0,0 and a spherical interpolate was applied to Au assays to define mineralized zones. Only values greater than 3 g/t are included in the model. Values were not automatically clipped.

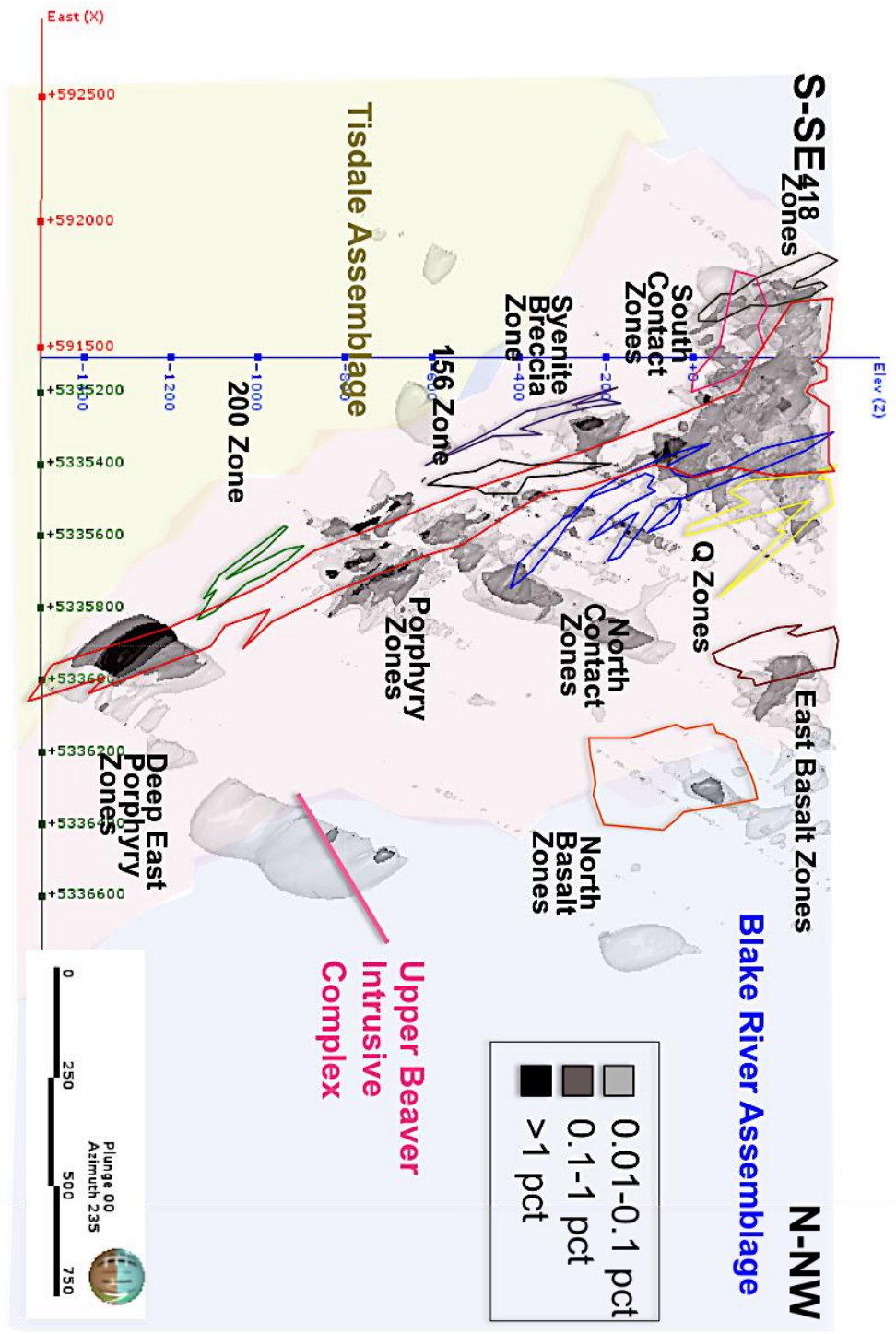


Figure 4.14. Leapfrog model showing the distribution of Cu in the Upper Beaver deposit looking West. Model built using Leapfrog’s Geological Models tool. A trend of 58,0,0 and a spherical interpolate was applied to the Cu assays to define the mineralized zones. Values were not automatically clipped. Cu mineralization is much more widespread than Au mineralization.

Trace element correlations were calculated using Spearman Rank Correlation methods to define the strength of association between two variables measured on a ranked scale (Rollinson, 1993). Data was analyzed in both leveled by lithology (according to the methods described in Section 2.2.5) and raw form. Analysis of the raw data using Spearman Rank Correlation, as shown in Table 4.2, reveals that in the Upper Beaver deposit Au is moderately correlated with Mo, Ag, Cu, and S, and is weakly correlated with Bi, W, Ni, Se, and Sb. Raw data for Cu suggests that it is moderately associated with Ag, Au, S, and Co, and is weakly associated with Bi, Ni, Se, Te, As, Sb and W. A significant trend is that Mo and Cu are not correlated, however, with the exception of Ag, they are the elements that most closely correlate with Au.

Table 4.2. Spearman rank correlation coefficients for Au and Cu in the dataset. Both raw and leveled spearman rank correlation coefficients are shown.

Spearman	Raw data		Leveled data	
	Au (g/t)	Cu (pct)	Au (g/t)	Cu (pct)
N=4319				
Au (g/t)	1	0.52	1	0.43
Cu (pct)	0.52	1	0.43	1
S_pct	0.5	0.45	0.47	0.36
Ag_ppm	0.55	0.58	0.52	0.49
As_ppm	-0.02	0.21	-0.065	0.096
B_ppm	0.034	0.14	0.039	0.1
Bi_ppm	0.35	0.22	0.32	0.18
Co_ppm	0.084	0.42	0.16	0.39
Cr_ppm	-0.056	0.042	-0.017	-0.023
Hg_ppm	-0.015	0.15	0.049	0.12
Mo_ppm	0.55	0.23	0.51	0.16
Ni_ppm	0.2	0.24	0.29	0.13
Pb_ppm	0.077	0.15	0.095	0.076
Sb_ppm	0.28	0.2	0.24	0.19
Se_ppm	0.32	0.34	0.3	0.27
Sn_ppm	0.12	0.053	0.13	0.02
Te_ppm	0.21	0.27	0.21	0.2
U_ppm	0.18	0.21	0.09	0.083
V_ppm	-0.015	0.0021	0.063	-0.077
W_ppm	0.32	0.19	0.29	0.13
Zn_ppm	-0.0059	0.12	-0.021	0.044

The bulk rock geochemical data was divided into 10 groups based on equal percentile bins for Au grade (i.e., 0-10%, 10-20%, ... 90-100%). The trace element content of each percentile bins was then plotted to define the overall relationship between trace element data in each percentile bin (i.e., mean, median, outliers) compared to gold content. Larger increases in the mean value of each percentile with increasing gold content indicates a stronger correlation between gold and the trace element plotted. Results are shown in Figure 4.15. Overall results show large increases in the Cu, Ag, and Mo content of each percentile bin with increasing gold content, and lesser increases in Ni, Sb, and W. Further, Te, Se, and Bi are relatively depleted where Au grades are lowest (with the exception of outliers in the dataset). Results confirm that the calculated Spearman Rank Correlation coefficients accurately represent trace element associations with Au grade for trace elements plotted.

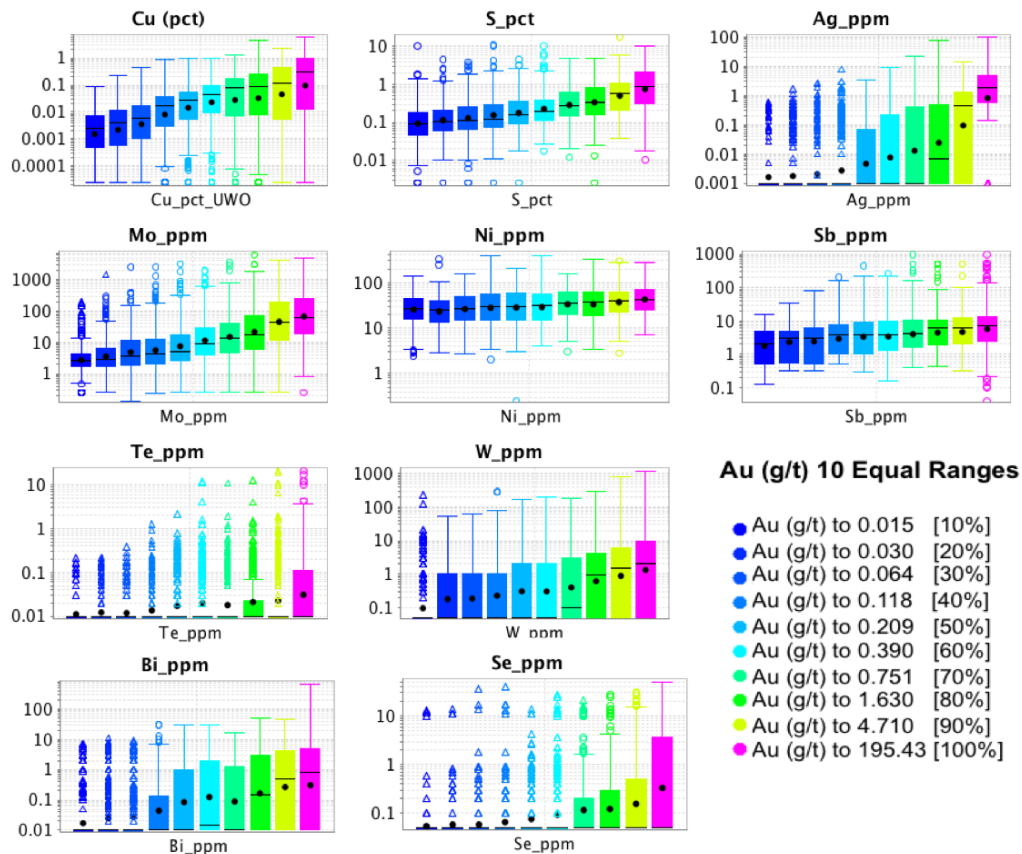


Figure 4.15. Percentile box plots showing the distribution of select trace elements in the deposit arranged by increasing gold grade (10 equal ranges). The central portion of the box contains the middle 50% of the data from Q1 (the middle value in the first half of the dataset) to Q3 (the middle value in the second half of the dataset). Upper and lower whiskers contain 5% to 95% of the values in the dataset. Outliers are represented by open circles and include the data that is in the top or bottom 5% of the data. The black circle represents the mean value for each Au group while the black line represents the median value for each gold group.

4.2.5 Correlations among Upper Beaver Mineralized Zones

Following the analysis of the entire CMC-compiled data set, the bulk rock geochemistry was assessed for each defined mineralized zone to capture the full complexity and signature of each zone. Refer to section 1.8 for detailed descriptions of each mineralized zone. The degree of enrichment of different metals associated with Au mineralization reflects magma chemistry, proximity of peripheral mineralized zones to intrusions, and local conditions of ore formation (Thompson et al., 1999). Each mineralized zone in the deposit has different trace element correlations, as shown in Table 4.3, which may reflect differences in gold mineralization, host rock, alteration, timing, structures, fluid properties, and temperature-pressure relationships (Thompson et al., 1999). Correlations are only shown for the Porphyry Zones and the North Contact Zone due to the limited number of samples analyzed for full trace element geochemistry from other zones in the deposit. Mineralization in the Porphyry Zones occurs footwall to a series of large crowded syenite porphyry intrusions. Zones are continuous to at least 2 km depth, and mineralization remains open. Porphyry Zones are characterized by an alteration envelope that varies widely in intensity and assemblage, although it is generally phyllitic in composition (sericite – chlorite ± hematite ± quartz ± calcite ± albite ± ankerite ± epidote) (Bernier and Cole, 2012). Comparatively, the shallow mineralized zones, which include the South Contact Zone, North Contact Zone, and the Q Zone occur along the boundaries of three crowded syenite porphyry intrusions to a depth of about 300 m. The shallow zones are largely hosted within the Blake River Assemblage Basalts as well as within members of the Upper Beaver Intrusive

Complex (Bernier and Cole, 2012). Alteration in the shallow mineralized zones includes variable amounts of silica \pm calcite \pm ankerite \pm epidote \pm magnetite \pm hematite \pm sericite \pm chlorite \pm potassic feldspar (Bernier and Cole, 2012).

Correlations within the Syenite Breccia Zone, 200 Zone, Q zone, and the South Contact Zone are not shown here as less than 7 samples were available in the bulk rock geochemistry dataset provided by Canadian Malartic Corporation. The original division of zones by CMC was strongly dependent on the morphology of the zones and as such, they could be further subdivided based on mineralization style and location (M.Masson, Personal communication, 2015). Most zones on the property contain multiple styles of mineralization. In addition, the host rock for each zone is variable, as shown in Figure 4.16.

Table 4.3. Spearman Rank correlation coefficients for Au in select zones (Lower Porphyry East = “LPE”, Upper Porphyry East = “UPE”, Lower Porphyry West = “LPW”, Upper Porphyry West = “UPW”, and North Contact = “NC”), in the Upper Beaver deposit

Zone	LPE	UPE	LPW	UPW	NC
Group size (n)	175	171	73	134	72
Cu_pct	0.26	0.11	0.77	0.78	0.58
As (ppm)	0.1	-0.13	0.35	0.36	0.15
Ag (ppm)	0.71	0.61	0.84	0.86	0.34
Bi (ppm)	0.13	0.35	0.027	-0.015	0.12
Co (ppm)	0.046	0.11	0.27	0.22	0.12
Cr (ppm)	-0.19	-0.0066	0.04	-0.13	-0.048
Mo (ppm)	0.34	0.32	0.33	0.66	0.47
Ni (ppm)	0.34	0.23	0.28	0.56	0.22
Sn (ppm)	-0.027	0.019	-0.19	-0.19	-0.19
Sb (ppm)	-0.045	0.064	0.15	0.14	0.27
Se (ppm)	0.18	0.16	0.54	0.53	0.2
Te (ppm)	0.22	0.12	-0.18	0.15	0.23
V (ppm)	0.086	0.11	-0.0027	0.26	-0.18
W (ppm)	0.078	0.0048	0.39	0.31	0.19
Zn (ppm)	-0.029	-0.17	-0.25	0.31	-0.024
S (pct)	0.42	0.26	0.74	0.8	0.72
K(pct)	-0.25	-0.09	0.095	-0.093	0.088
Fe (pct)	0.14	0.093	0.44	0.61	0.2
Mg (pct)	-0.073	0.053	-0.28	-0.1	-0.38
Ca (pct)	0.12	0.28	0.11	-0.057	0.069
Na (pct)	-0.1	-0.093	-0.36	-0.26	-0.32

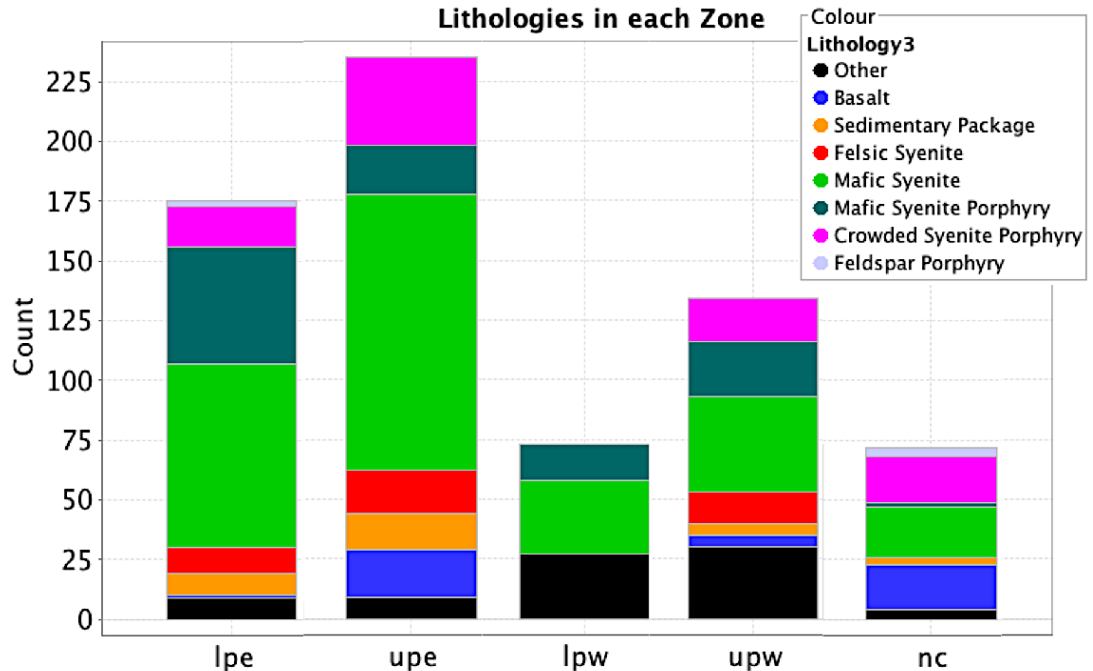


Figure 4.16. Histogram showing the variation in host rock among and within each mineralized zone in the Upper Beaver deposit.

Analysis of the Porphyry Zones and the North Contact Zone revealed significant trends. In all zones, Au mineralization is intimately correlated with Ag, with correlation strengths ranging from strong to very strong in all zones except the North Contact Zone where the Ag is only weakly correlated with Au. No other element has such a consistently strong correlation with Au. Available geochemical data was plotted to show overall trends in the ratio of Au:Ag in the deposit, as shown in Figure 4.17. Trends indicate that the ratio is highly variable. The median Au:Ag ratio of the entire dataset is 24. Two distinctive groups can be observed on the Au:Ag plot, a Ag poor group (n=191) (i.e., $Ag \leq 0.001$) and an Ag rich group (n=4013) (i.e., $Ag \geq 0.001$). This trend was observed in the datasets from 4 separate labs and is not a function of analysis method or detection limits. In general, the Ag-rich trend has a higher Au and Cu grade than the Ag-poor trend.

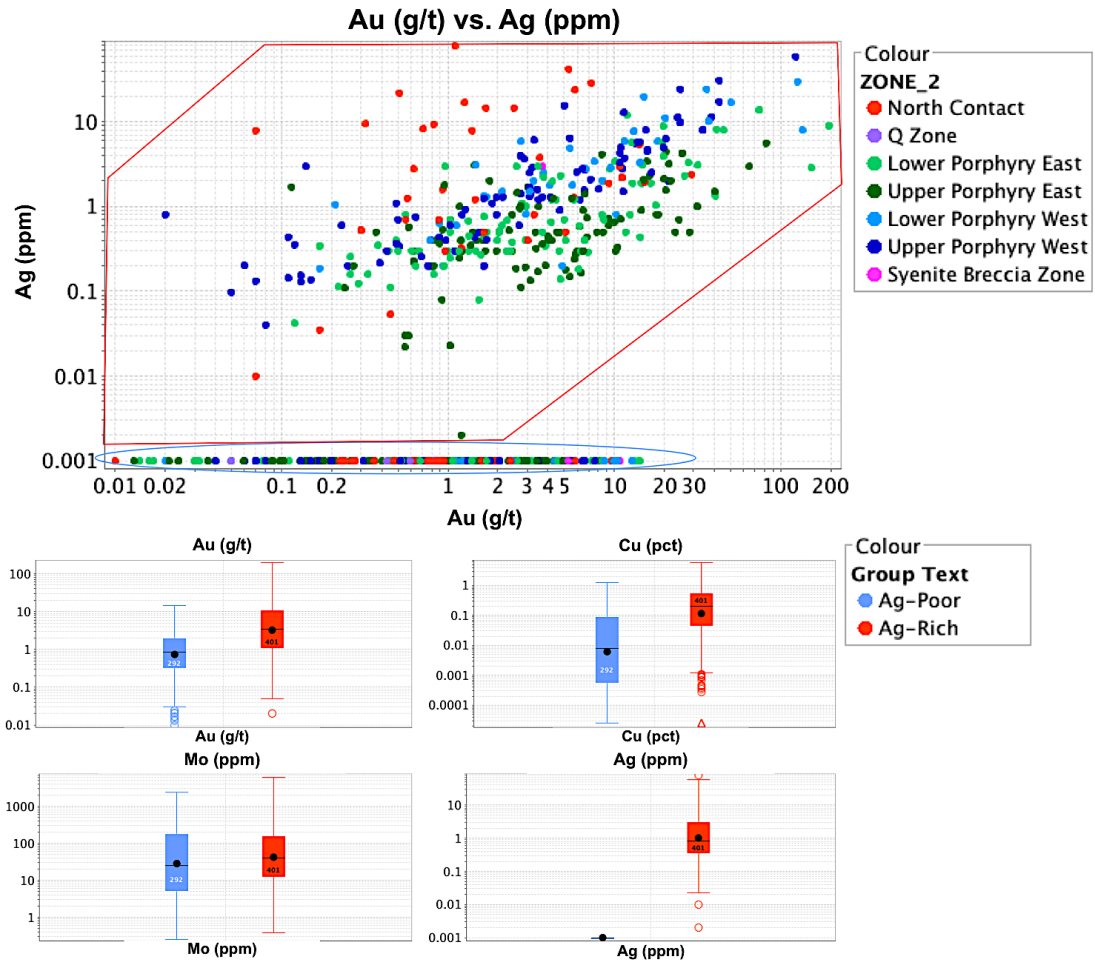


Figure 4.17. (Top) Bivariate Au vs. Ag plot showing the two trends (Ag-rich i.e., $Ag \geq 0.001$) and Ag-poor i.e., $Ag \leq 0.001$) and (Bottom) percentile box plots showing the distribution of select trace elements in each trend. The central portion of the box contains the middle 50% of the data from Q1 (the middle value in the first half of the dataset) to Q3 (the middle value in the second half of the dataset). Upper and lower whiskers contain 5 to 95% of the values in the dataset. Outliers are represented by open circles and include data that is in the top or bottom 5% of the data. The black circle represents the mean value for each zone and the black line represents the median value for each zone

Bulk rock geochemistry comparisons between Au, Cu, and Mo from mineralized zones highlight a number of significant trends, as shown in Figure 4.18. A Cu:Au plot identifies three distinct groups in the dataset: (1) a Au-Cu trend, which has a steeper slope than the other trends; (2) a Au-Mo trend; and (3) a Cu poor trend that correlates with the Ag-poor trend. Approximately three quarters of the total data has the Cu-rich signature ($n=3001$) while the remaining quarter has the Mo-rich Cu-poor

signature (n=1012). Further, data that correlates with the Au-Mo rich trend has a significantly higher Au:Ag ratio than that which correlates with the Au-Cu trend. Zones can also be divided using this relationship. Data from the Upper Porphyry East and the Q Zones tend to be largely defined by an Au-Mo signature, while data from the Porphyry West, Lower Porphyry East, and the North Contact Zone tend to be largely defined by an Au-Cu signature.

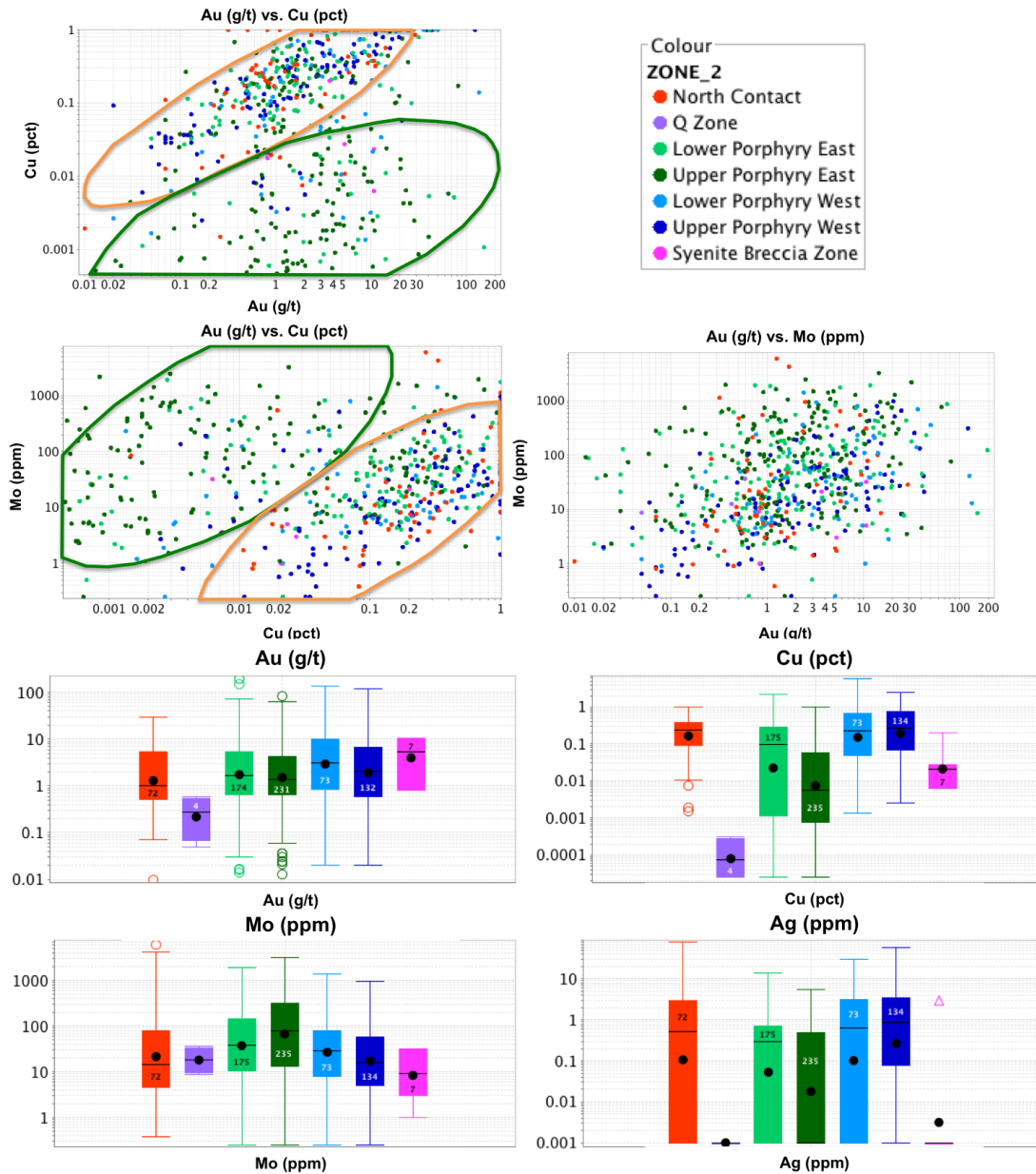


Figure 4.18. Relationship between Au, Cu, Mo, and Ag in select zones in the Upper Beaver Deposit colored by mineralized zone. (Top) bivariate box plots

showing the association between Au and Cu on the left and Au and Mo on the right. (Bottom) percentile box plots showing the distribution of select trace elements in the deposit among the main mineralized zones. The central portion of the box contains the middle 50% of the data from Q1 (the middle value in the first half of the dataset) to Q3 (the middle value in the second half of the dataset). Upper and lower whiskers contain 5 to 95% of the values in the dataset. Outliers are represented by open circles and include data that is in the top or bottom 5% of the data. The black circle represents the mean value for each zone and the black line represents the median value for each zone

Correlations with all other elements, including Bi, Te, W, Sb, and Fe from the mineralized zones were much more variable. W had a weak correlation with Au in the Upper and Lower Porphyry West Zones with $p=0.31$ and 0.39 , respectively, and a very weak correlation with Au in the North Contact Zone ($p=0.19$). Bi correlated weakly with Au mineralization in the Upper Porphyry East Zone ($p=0.35$), and correlated very poorly in the remainder of the zones. An association between Au and Te was less apparent, with weak Spearman Rank correlations in the North Contact ($p=0.23$) and in the Lower Porphyry East Zones ($p=0.22$). This trend is significant as mineralization in Kirkland Lake 30 km to the east is strongly correlated with tellurium (Isoplatov et al., 2008). Au also correlated weakly with As in the Upper and Lower Porphyry West Zones, with Spearman Rank values of 0.36 , and 0.35 , respectively.

Unexpected correlations were also identified by Spearman Rank correlations. Co correlated weakly and Se correlated moderately well with Au in the Upper and Lower Porphyry West Zones, and Ni correlated weakly with Au in all but the Upper Porphyry West Zone (where it correlated moderately well). Other elements that are weakly correlated with Au mineralization in isolated zones in the deposit include: Sb in the North Contact Zone ($p=0.27$); Zn in the Upper Porphyry West zone ($p=0.31$); and V in the Upper Porphyry West Zone (0.26).

4.2.6 Multivariate EDA

Because the lithology and alteration style alone cannot be used to explain the variability in mineralization, multivariate EDA was performed to identify anomalies, populations within the data, and element associations. Multivariate EDA consisted of

cluster analysis, followed by principal component analysis to analyze the relationship between multiple elements at the same time. Both methods are robust and identify complex relationships in the data in simple ways (e.g., Grunsky, 2007; Rollinson, 1993; Templ, 2006). Principal component analysis was performed after cluster analysis to validate the clustering algorithm (Levitan et al., 2014). Typically, in statistical studies on ore deposits a log 10-transformation is applied to produce normally distributed data and to solve for the effects of closure (e.g., Aitchison, 1990; Pawlowsky-Glahn, 2001; Levitan et al., 2014). However, this is only a valid approach for a single population of data, which rarely occurs in geological materials (McQueen, 2007). Reimann and Filzmoser (2000) have shown since few geochemical variables follow a log-normal distribution, each variable should be considered for transformation and for different transformations prior to analysis. Even after applying a log-transformation, the compositional nature of geochemical data typically remains inherent in the data (Filzmoser and Hron, 2008). For this reason, while no transformations were applied to the dataset prior to cluster analysis, the data was leveled about the median of each lithology prior to PCA to confirm that trends were statically robust in order to fully compare the interrelationship between different geochemical variables.

4.2.6.1 Cluster Analysis

A Cluster analysis was performed on the dataset using the raw data for Au, Cu, Mo, and Ag to divide the large dataset into discrete sub-populations that reflect different geochemical groups. The aim of this analysis was to define a number of clusters where the members of each group are as similar to each other as possible and the differences between each cluster are as large as possible. Cluster analysis does not require that data be normally distributed (i.e., log-transformed) however it is recommended if the data is highly skewed (Templ et al., 2008). Cluster analysis was performed using the K-means cluster analysis tool in ioGASTM, which creates populations by dividing n observations into K-clusters in which each observation is allocated to the cluster with the nearest mean to minimize within group variance and

maximize between-group variance (Templ, 2006). This process is iterative, beginning with an initial “guess” of cluster centers until it converges on stable centers based on an initial choice of the number of cluster centers desired (Grunsky, 2007). Results from cluster analysis for select trace elements have been provided in Figure 4.19.

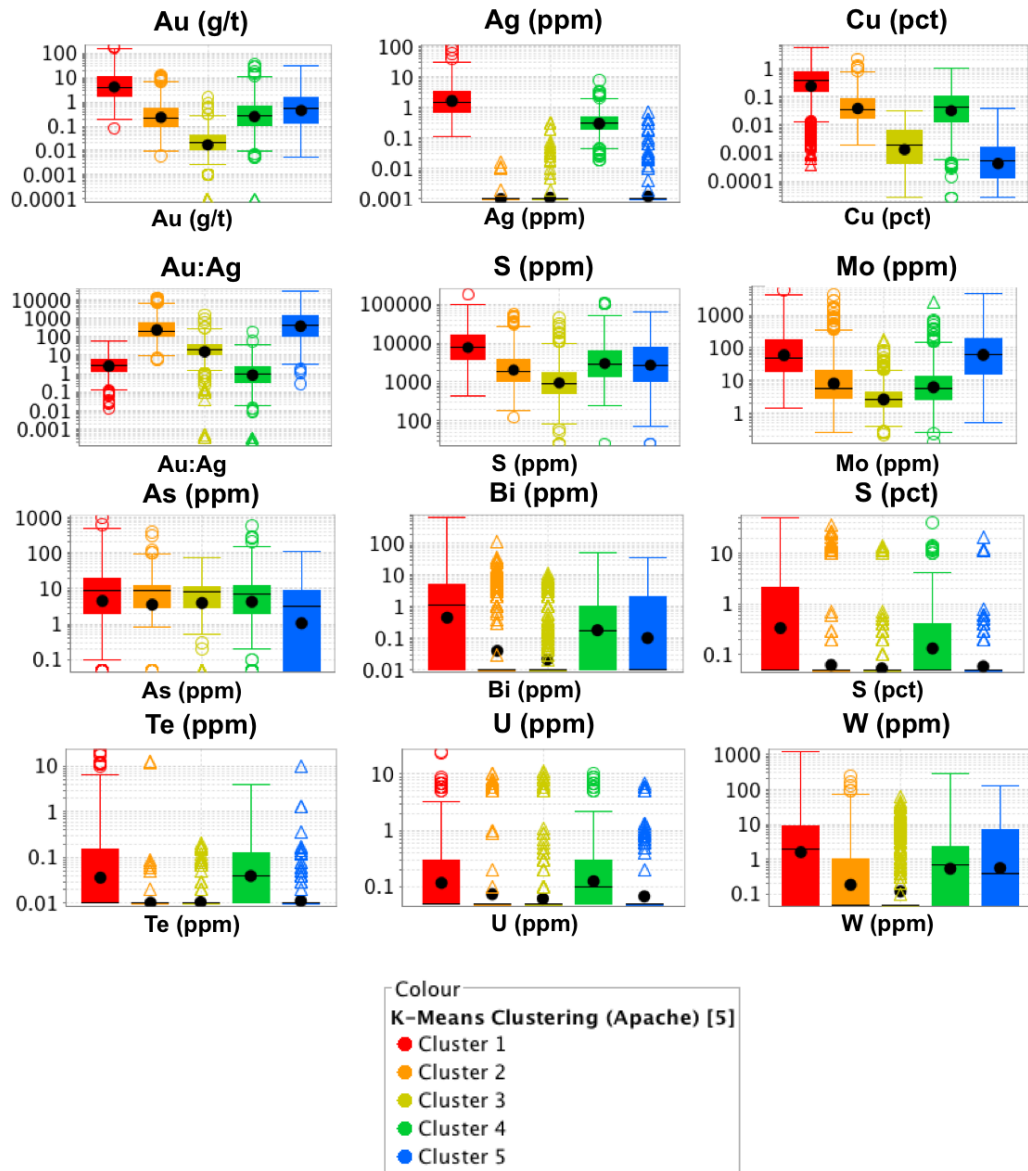


Figure 4.19. Percentile box plots showing the distribution of select trace elements within in each cluster group. The central portion of the box contains the middle 50% of the data from Q1 (the middle value in the first half of the dataset) to Q3 (the middle value in the second half of the dataset). Upper and lower whiskers contain 5% to 95% of the values in the dataset. Outliers are represented by open circles and include data that is in the top of bottom 5% of

the data. The black circle represents the mean value for each cluster group and the black line represents the median value for each cluster group

Cluster analysis was optimized when the dataset was divided into five distinct sub-populations, each with characteristic trace element associations. Cluster 1, which is the cluster with the highest Au grade is associated with Mo and Cu, as well as elevated amounts of Se, Te, U, and Bi. Cluster 1 has the second lowest Au:Ag ratio, with a mean of 2.54 and a median of 2.68. Cluster 2 is associated with strong enrichments in Cu with minimal enrichments in Mo and no enrichment in Ag. This group appears to have a high Au:Ag ratio with a mean Au:Ag ratio of 205 and a median ratio of 230, but this reflects the lack of Ag mineralization within the group. It also has minor enrichments in W but lacks any enrichment in Bi, Se, Te, and U. Cluster 3 is associated with the lowest Au grades in the dataset. It lacks any significant enrichment in any trace element group. Similar to group 2, this cluster appears to have a high Au:Ag ratio but this just reflects the lack of associated Ag mineralization. Cluster 3 has a mean Au:Ag ratio of 20 and a median of 15. This group is also the only one without W enrichment. Cluster 4 contains strong enrichments in Cu, Au, and Ag, and also has enrichments in Bi, Se, Te, Y, and W. Due to the elevated amounts of Ag the Ag:Ag ratio is very low with a mean value for the group of 0.82 and a median of 0.88. Finally, cluster 5 is associated with enrichments in Au and Mo and lacks enrichments in Cu. This group has the highest Au:Ag ratio with a mean of 363 and a median of 433, and is associated with lower amounts of As, and high amounts of Bi and W.

When the data is coloured by cluster and plotted on a Au:Cu plot, as shown in Figure 4.20, significant trends are apparent. Cluster 3 represents the data points with low amounts of Au, Cu and Mo, while cluster 1 represents high-grade data with high Cu and relatively high Mo. Cluster 2 and 4 represent the data with high Au and Cu and low Mo, while Cluster 5 has high Au and Mo and low Cu.

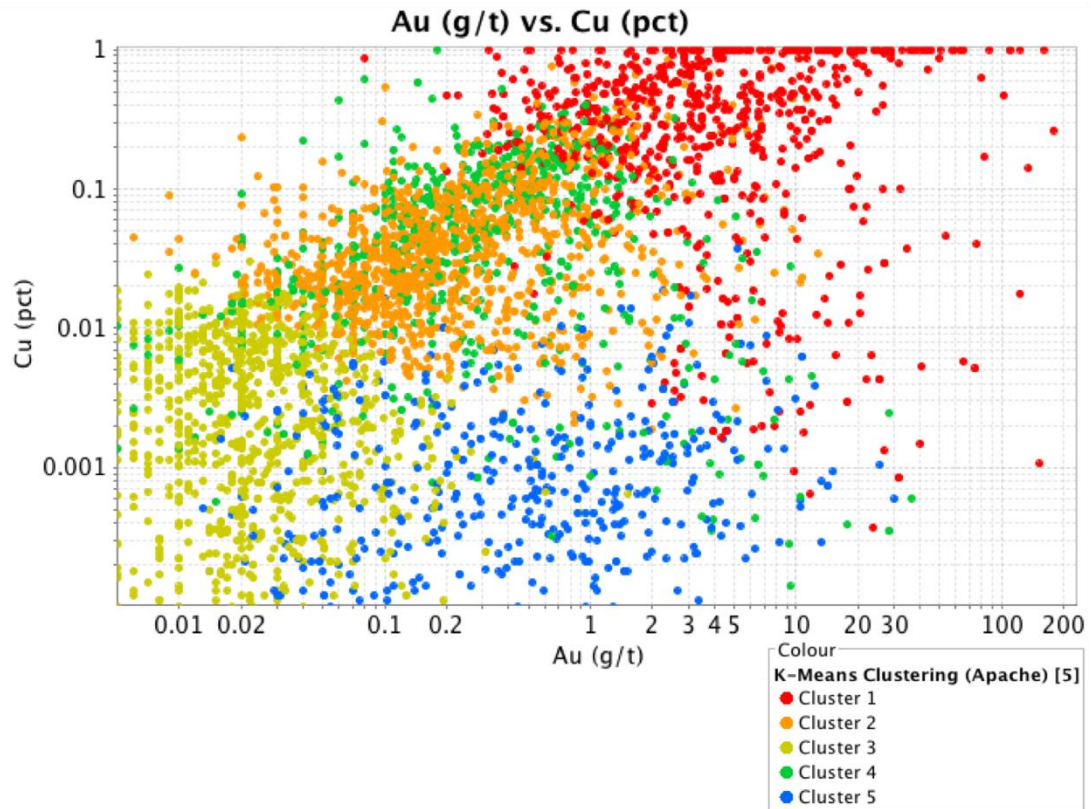


Figure 4.20. Au vs. Cu relationship in the Upper Beaver Deposit with colours indicating the respective cluster of each data point

Geochemical Clusters were also mapped in 3D using Leapfrog GeoTM, as shown in Figure 4.21, to identify spatial changes in the geochemical signature of the zones. The 3D model identifies that the mineralized zones are not defined by only one cluster. This is especially clear in the porphyry zones. The Porphyry East Zones are characterized by Cluster 3 and 5, with Cluster 1 becoming the dominant geochemical signature with depth. The Porphyry West Zones are better characterized by Cluster 3 and 4, with Cluster 1 becoming dominant with depth. The shallow mineralized zones are characterized by Cluster 1, with the remaining clusters being variable.

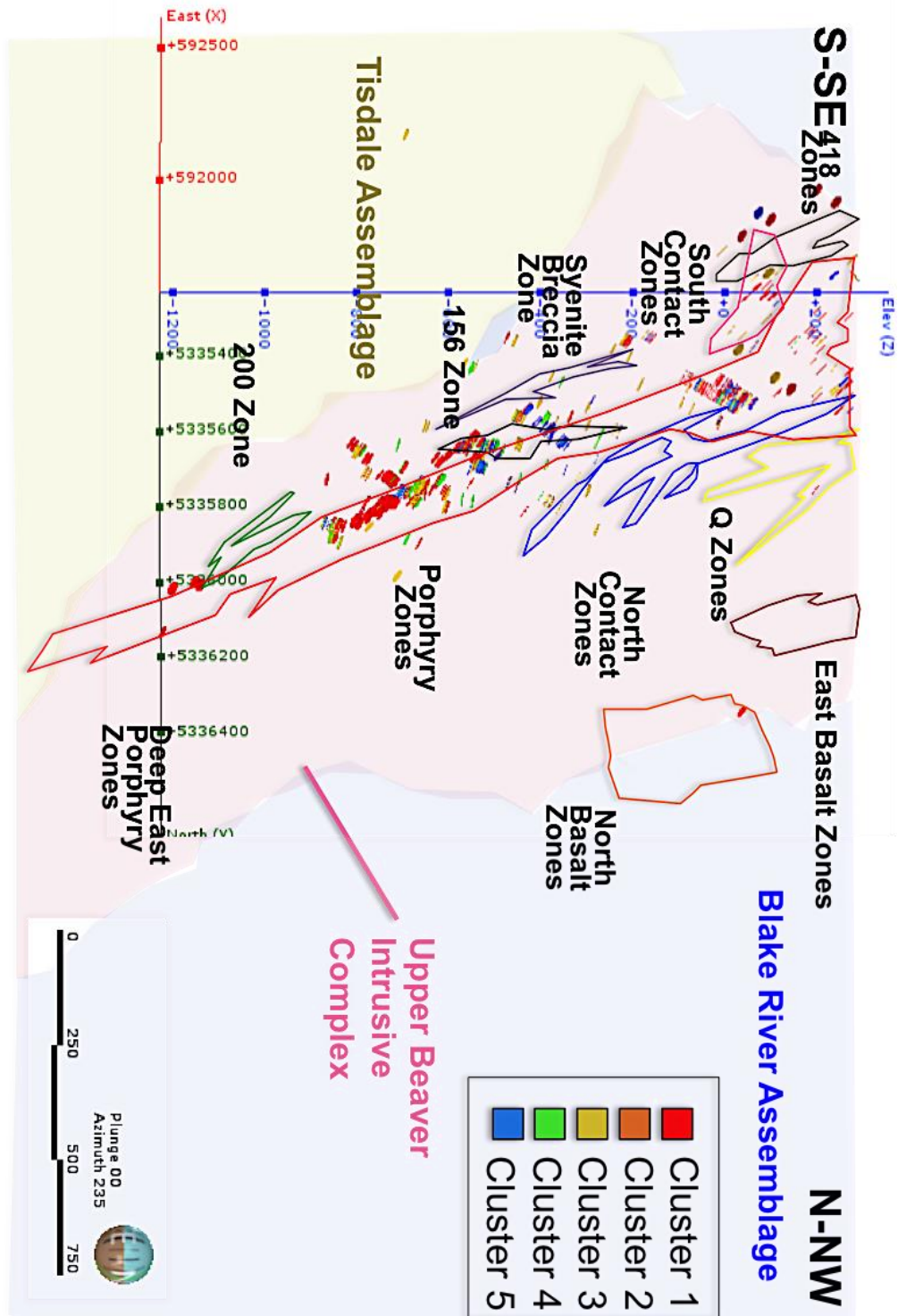


Figure 4.21. Distribution of K-Means clusters in the Upper Beaver deposit looking East. Larger data points are the clusters while the different zones are outlined by the coloured lines (coloured lines that define zones were used to

make it easy to differentiate between different zones and do not reflect different clusters)

4.2.6.2 Principal Component Analysis

Principal Component Analysis (PCA) was performed after clustering to validate the clustering algorithm. This multivariate analysis method is a widely used technique (e.g., Templ et al., 2006 and references therein; Grunsky 2007; Rukhlov et al., 2009; Grunsky, 2013; Levitan et al., 2014) for assessing the interrelationships between multiple variables by defining principal components that reflect the dimensions with the largest variance so that patterns can be detected more clearly (Rollinson, 1993). Refer to Ding and He (2004) for a detailed review on the mathematical and statistical relationship between K-means cluster analysis and PCA. PCA was completed on the lithology-leveled and raw form dataset to identify trends between Au, Cu, S, Ag, Bi, Mo, Ni, Sb, Se, Te, and W. Analysis used a correlation matrix with 11 principal components, although the first three components captured the majority of variance in the data. No transformations were applied to the dataset prior to analysis other than the leveling of data by the median of each rock type. Because analysis was performed using different labs and because not all labs analyzed for the same elements, only samples that were analyzed for every element of interest were used during PCA. A total of 2,819 data points were used in this analysis. Results from principal component analysis are provided below and include the following information for select trace elements: Pearson Correlation coefficients (Table 4.4); eigenvectors (Table 4.5); eigenvalues (Table 4.6); Scaled coordinates (Table 4.7); PC1 vs. PC2 (Figure 4.22); and PC1 vs. PC3 (Figure 4.23).

Table 4.4. Pearson Correlations between trace elements used in Principal Component Analysis of data from the Upper Beaver deposit

Correlation	Au (g/t)	Cu (ppm)	S (ppm)	Ag (ppm)	Bi (ppm)	Mo (ppm)	Ni (ppm)	Sb (ppm)	Se (ppm)	Te (ppm)	W (ppm)
Au g/t	1.00	0.45	0.51	0.62	0.31	0.52	0.26	0.32	0.24	0.09	0.29
Cu ppm	0.45	1.00	0.37	0.52	0.15	0.16	0.10	0.19	0.20	0.07	0.12
S ppm	0.51	0.37	1.00	0.47	0.25	0.41	0.27	0.30	0.25	0.10	0.27
Ag ppm	0.62	0.52	0.47	1.00	0.26	0.31	0.17	0.25	0.29	0.15	0.27
Bi ppm	0.31	0.15	0.25	0.26	1.00	0.26	0.11	0.49	0.23	0.18	0.44
Mo ppm	0.52	0.16	0.41	0.31	0.26	1.00	0.32	0.21	0.19	0.08	0.30
Ni ppm	0.26	0.10	0.27	0.17	0.11	0.32	1.00	-0.03	0.16	0.07	0.14
Sb ppm	0.32	0.19	0.30	0.25	0.49	0.21	-0.03	1.00	0.12	0.08	0.28
Se ppm	0.24	0.20	0.25	0.29	0.23	0.19	0.16	0.12	1.00	0.24	0.26
Te ppm	0.09	0.07	0.10	0.15	0.18	0.08	0.07	0.08	0.24	1.00	0.19
W ppm	0.29	0.12	0.27	0.27	0.44	0.30	0.14	0.28	0.26	0.19	1.00

Table 4.5. Eigenvectors showing the relationship between principal components and trace elements

Eigenvectors	PC1	PC2	PC3	PC4	PC5	PC6	PC7	PC8	PC9	PC10	PC11
Au (g/t)	0.41	-0.24	-0.11	-0.08	0.12	-0.19	0.03	-0.26	0.24	0.08	0.76
Cu (ppm)	0.29	-0.34	-0.33	0.35	-0.02	0.22	-0.27	-0.11	-0.66	-0.05	-0.02
S (ppm)	0.37	-0.19	-0.02	-0.08	0.04	0.05	0.24	0.80	0.04	-0.34	0.03
Ag (ppm)	0.38	-0.24	-0.18	0.25	0.04	-0.10	-0.19	-0.11	0.58	0.11	-0.54
Bi (ppm)	0.30	0.49	-0.11	-0.17	-0.04	0.30	-0.14	-0.29	0.10	-0.65	-0.02
Mo (ppm)	0.32	-0.11	0.24	-0.40	0.15	-0.46	0.32	-0.29	-0.36	-0.08	-0.34
Ni (ppm)	0.19	-0.26	0.59	-0.29	0.01	0.61	-0.19	-0.05	0.04	0.23	-0.03
Sb (ppm)	0.27	0.39	-0.43	-0.19	0.10	0.31	0.36	0.05	-0.07	0.56	-0.08
Se (ppm)	0.25	0.12	0.30	0.43	-0.69	0.01	0.39	-0.10	-0.01	0.05	0.05
Te (ppm)	0.14	0.31	0.37	0.55	0.66	0.00	0.08	0.02	-0.05	0.02	0.05
W (ppm)	0.29	0.40	0.15	-0.10	-0.20	-0.37	-0.62	0.28	-0.14	0.26	0.05

Table 4.6. Eigenvalues, percent, and cumulative percent for each principal component

	Eigenvalues	Percent	Cumulative %
PC1	3.686	33.51	33.51
PC2	1.312	11.93	45.44
PC3	1.137	10.33	55.78
PC4	1.056	9.599	65.37
PC5	0.7351	6.683	72.06
PC6	0.6601	6.001	78.06
PC7	0.6487	5.897	83.96
PC8	0.5543	5.039	88.99
PC9	0.4613	4.194	93.19
PC10	0.4335	3.941	97.13
PC11	0.3158	2.871	100

Table 4.7. Scaled coordinates showing the relationship between each principal component and trace element

Scaled Coordinates	PC1	PC2	PC3	PC4	PC5	PC6	PC7	PC8	PC9	PC10	PC11
Au (g/t)	0.79	-0.27	-0.11	-0.08	0.10	-0.15	0.02	-0.19	0.17	0.05	0.43
Cu (ppm)	0.55	-0.39	-0.35	0.36	-0.02	0.18	-0.22	-0.08	-0.45	-0.03	-0.01
S (ppm)	0.71	-0.22	-0.02	-0.08	0.03	0.04	0.19	0.60	0.02	-0.22	0.02
Ag (ppm)	0.73	-0.27	-0.19	0.25	0.04	-0.08	-0.15	-0.08	0.40	0.07	-0.30
Bi (ppm)	0.58	0.56	-0.11	-0.17	-0.04	0.24	-0.11	-0.22	0.07	-0.43	-0.01
Mo (ppm)	0.62	-0.12	0.26	-0.41	0.13	-0.37	0.26	-0.21	-0.24	-0.05	-0.19
Ni (ppm)	0.37	-0.29	0.62	-0.30	0.01	0.50	-0.16	-0.04	0.03	0.15	-0.02
Sb (ppm)	0.51	0.44	-0.45	-0.20	0.08	0.25	0.29	0.04	-0.05	0.37	-0.04
Se (ppm)	0.47	0.14	0.32	0.44	-0.59	0.00	0.32	-0.08	0.00	0.03	0.03
Te (ppm)	0.27	0.36	0.40	0.57	0.56	0.00	0.07	0.02	-0.04	0.01	0.03
W (ppm)	0.56	0.45	0.16	-0.11	-0.17	-0.30	-0.50	0.21	-0.09	0.17	0.03

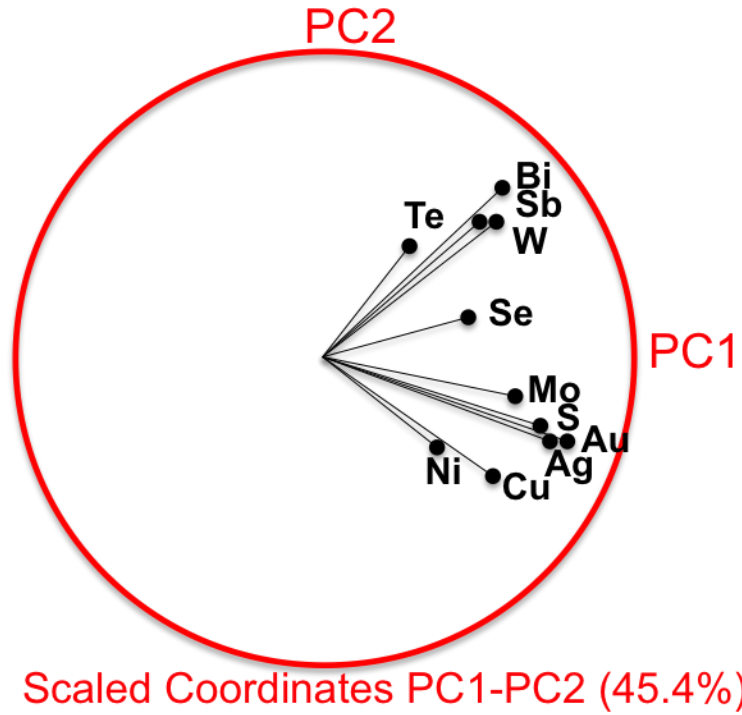


Figure 4.22. PC1 vs. PC2 for the PCA completed on log leveled (by lithology) Au, Cu, S, Ag, Bi, Mo, Ni, Sb, Se, Te, and W. +PC1 and -PC2 controls the distribution of Au, Cu, Mo, S, Ag, Ni, and Se, while +PC1 and +PC2 control the distribution of Bi, Sb, W, and Te.

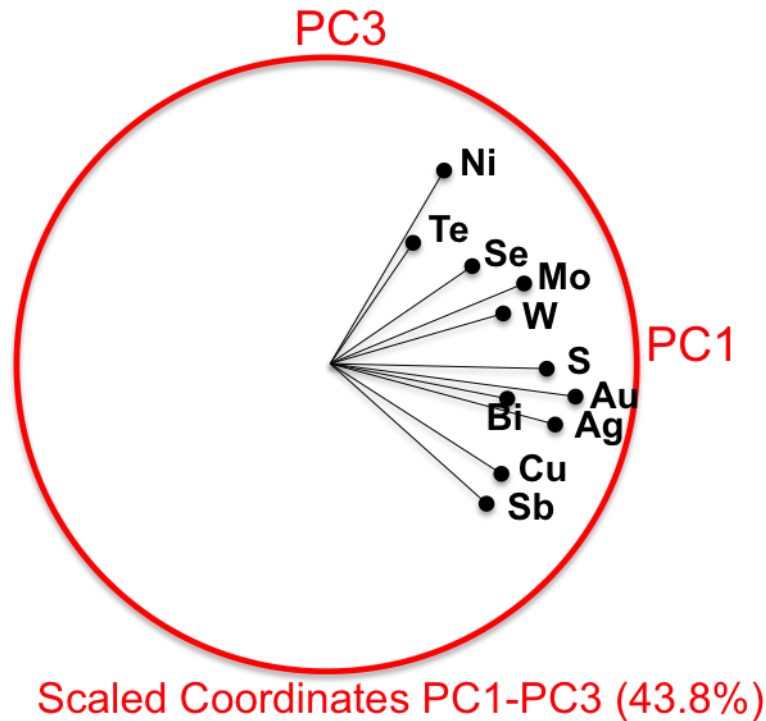


Figure 4.23. PC1 vs. PC3 for the PCA completed on log leveled (by lithology) Au, Cu, S, Ag, Bi, Mo, Ni, Sb, Se, Te, and W. +PC3 and +PC1 controls the distribution of Ni, Te, Se, Mo and W, while +PC1 and –PC3 controls the distribution of S, Bi, Au, Ag, Cu, and Sb.

The first three principal components control the distribution of 56% of the data. Trends indicate:

- (1) +PC1 and –PC2 controls the distribution of Au, Cu, Mo, S, Ag, Ni, and Se, while +PC1 and +PC2 control the distribution of Bi, Sb, W, and Te; and
- (2) +PC3 and +PC1 controls the distribution of Ni, Te, Se, Mo and W, while +PC1 and –PC3 controls the distribution of S, Bi, Au, Ag, Cu, and Sb.

Figure 4.24 is coloured by leveled Au, Cu, and Mo (as identified), and indicates that for PC1 vs. PC2 Au and Cu have almost identical distributions while Mo is more randomly distributed. Plots of PC1 vs. PC3 show similar but not the same distribution for Au and Cu, with the distribution of both elements more strongly controlled by PC1, while Mo is more controlled by PC3.

These results are similar but not identical to those identified by Cluster Analysis. Differences are expected due to the differences in trace elements selected for either analysis. Cluster 1 provides the same trends as PC1 vs. PC2, where enrichments in Mo and Cu are more associated with enrichments in Au, Ag, S, but identify that the distribution of Bi, Te and W may be controlled by another factor. Similarly, PC1 vs. PC3 separates enrichments in Mo and Cu, similar to Cluster 5, 2 and 4. Cluster 5 is enriched in Mo relative to Cu and is associated with enrichments in W, while Clusters 2 and 4 are associated with enrichments in Cu relative to Mo and are associated with S, Au, and Ag. Both trends are enriched in Bi, although PCA identifies that Bi enrichments are more closely associated with Cu enrichments.

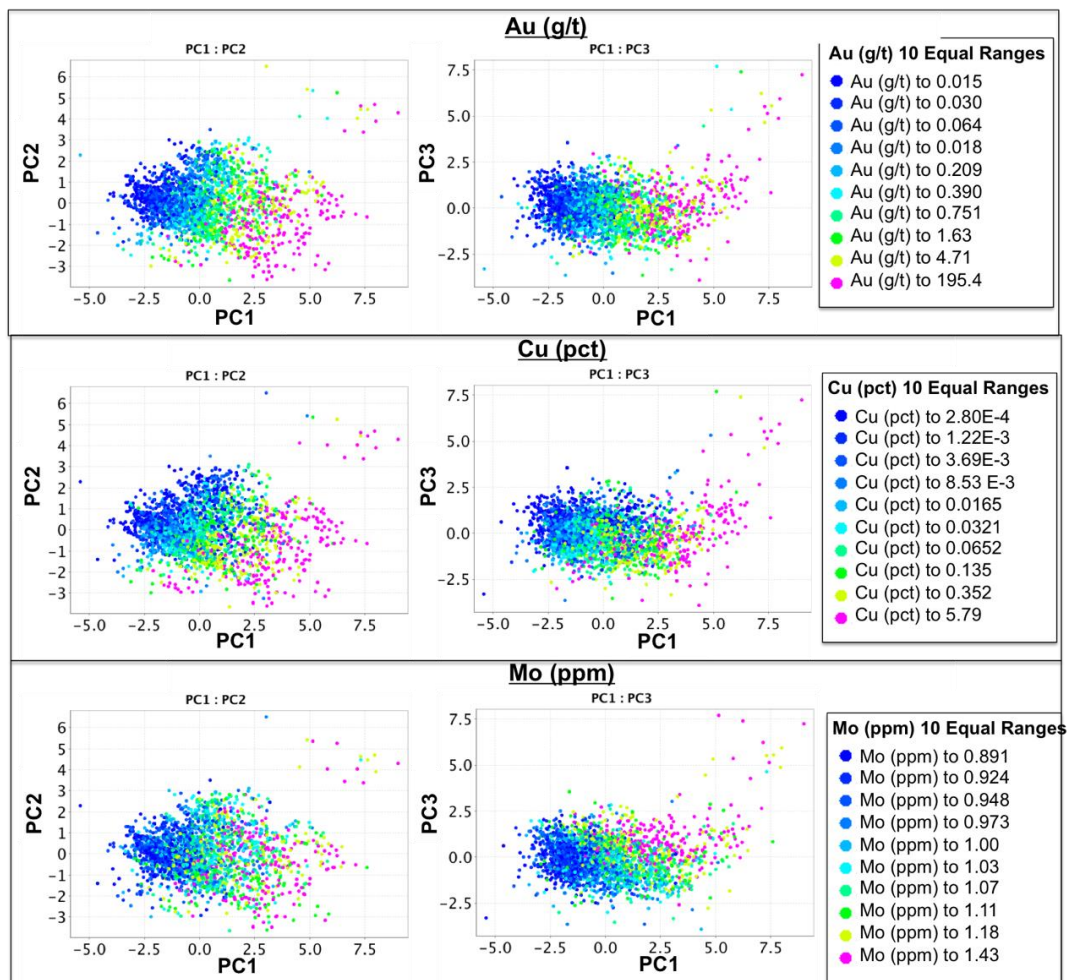


Figure 4.24. Binary plots showing the relationships between PC1, PC2, and PC3 coloured by levelled (median lithology) Au, Cu, and Mo. PC1 vs. PC3 best defines the Cu-enriched trend and the Mo-enriched trend

4.2.7 Link between Alteration and Mineralization

Mineralization in the Upper Beaver deposit is complex, commonly consisting of many overprinting alteration minerals. Alteration is centered on the polyphase intrusive complex, especially along its sheared margin, which is strongly sericitized (Bernier and Cole, 2012). All lithologies can be altered by silica, carbonates (ankerite and calcite), sericite and muscovite, albite, K-feldspar, epidote, chlorite, hematite, magnetite, actinolite, and sulphide phases, however, in a technical report on the property Bernier and Cole (2012) state that mineralization is most closely associated with widespread and pervasive magnetite-feldspar-actinolite-epidote-carbonate-sericite alteration.

In previous studies by Kontak et al., (2011), on the alteration and mineralization paragenesis of the deposit, evidence has been presented for extended three phase mineral paragenesis, as shown in Figure 4.25. Widespread alteration is thought to have developed during Stage I and Stage II, while Stage III was limited to just carbonate and quartz alteration. Gold mineralization is limited to the second phase of mineral growth, associated with Bi and Te, as well as pyrite and chalcopyrite, scheelite, hematite and magnetite, as well as a variety of additional alteration minerals (chlorite, carbonate, epidote, sericite, quartz, tourmaline, and apatite). The presence of Au mineralization within anhydrite veins indicates that mineralization also occurred during, or was partially remobilized during Stage III alteration. This has been reflected in the modified figure (Figure 4.25).

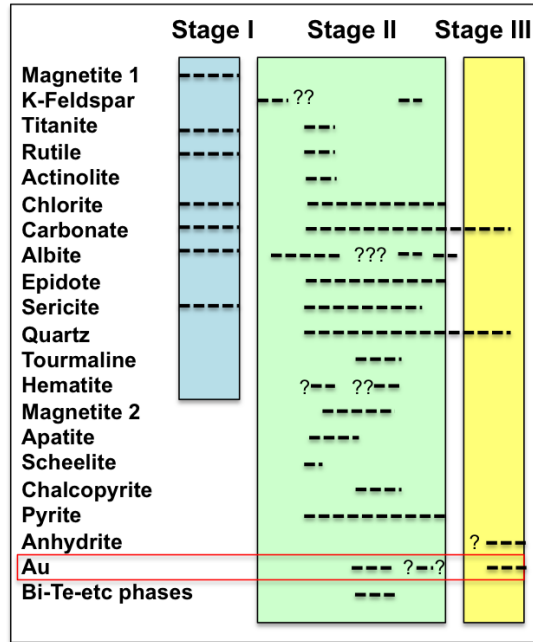


Figure 4.25. Alteration and mineralization history of the Upper Beaver deposit divided into three main stages of alteration (Modified from Kontak, 2011).

4.2.7.1 Alteration in Collected Mineralized Samples

Collected samples from the various mineralized zones in the deposit were plotted on an alteration box plot as defined by Large et al., (2001) to identify which alteration assemblage best characterizes the different styles of mineralization (Figure 4.26). Results suggest a trend where samples that contain molybdenite are relatively less altered than samples that contain chalcopyrite, pyrite, and magnetite. Samples that contain a combination of chalcopyrite, pyrite, and magnetite, are moderately to strongly altered by epidote and calcite or dolomite and ankerite. In general, samples that contain chalcopyrite and magnetite without pyrite are typically more altered by dolomite/ankerite, and the one sample that contains magnetite without accompanying pyrite and chalcopyrite is moderately albitized.

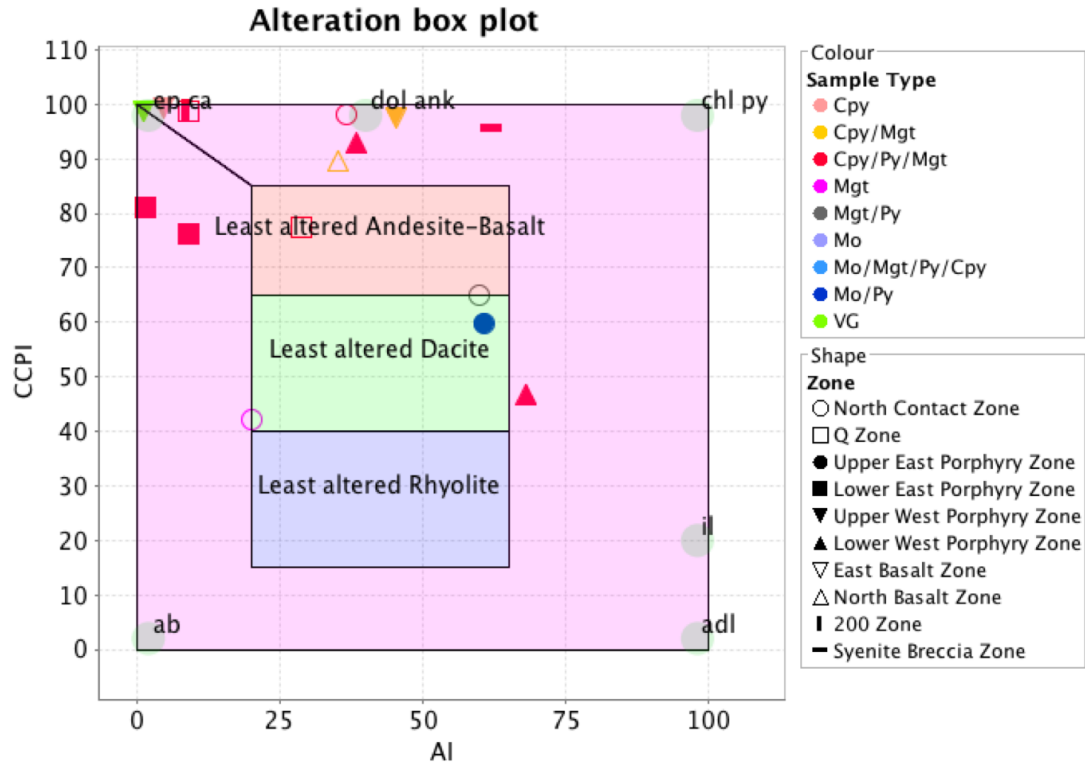


Figure 4.26. Alteration box plot based on the Ishikawa alteration index (AI) and Chlorite-carbonate-pyrite index (CCPI) as suggested by Large et al., (2001) showing expected mineralogical changes associated with various mineralized samples based on geochemical analysis of samples for this project. Samples have been colored based on their mineralogy and their shape reflects the zone each sample is from. “ep ca” = Epidote and calcite, “dol ank” = dolomite and ankerite, “chl py” = chlorite and pyrite, “ab” = albite, “il” = sericite; and “adl” = andalucite.

4.2.7.2 Alteration Database

This study uses a descriptive database provided by Canadian Malartic Corporation to link different styles of mineralization with specific alteration minerals. Plots showing how the mean and median value of select trace elements (Au, Ag, Cu, and Mo) are affected by each alteration mineral are provided in Figure 4.27. Analysis of the descriptive alteration database is not as robust as geochemical analysis as it is purely based on qualitative observations. However, interesting trends worth noting do occur.

Although intense alteration is commonly associated with gold and copper mineralization in the Upper Beaver deposit (Bernier and Cole. 2012), not all alteration assemblages in the deposit are associated with Au and Cu mineralization. Epidote alteration is the most pervasive type of alteration in the deposit, extending throughout the entire paragenetic sequence, and is frequently associated with mineralization (M.Masson, Personal communication, 2015). However, the mean and median values for Au, Ag, Cu, and Mo, are not as drastically affected by the presence of epidote alteration. This may be because epidote is noted to occur in 1068 of the 4319 samples (25%) that have undergone geochemical analysis.

Similarly, sodic alteration, in particular disseminated albite, occurs in all units but is not associated with mineralization (Kontak et al., 2011). Studies on the deposits paragenesis by Kontak et al., (2011) indicate that this alteration phase may have extended over a long period of time (e.g., early stage in basaltic volcanics), leading to a relatively weak or an absence of an association between Au and albite. A total of 657 samples out of 4319 were noted to contain albite alteration (15%), This contradicts the results of the study by Kontak et al., (2011) and suggests that albite alteration is not often noted in core logs. Figure 4.27 identifies that the mean and median values of Cu mineralization in particular are elevated in samples that are noted to contain elevated amounts of albite. Comparatively, samples that are noted to contain elevated amounts of K-spar have higher mean and median values for Au, Cu, and Mo. Elevated amounts of K-spar are only noted in 340 samples from the dataset (8%).

Kontak et al., (2011) also concluded that areas of intense sericitic alteration tend to be most strongly associated with Au mineralization. This result is consistent with observations presented in the technical report published by Bernier and Cole (2012), who note that the sheared southern margin of the polyphase Upper Beaver Intrusive Complex, along which gold mineralization occurs, is strongly sericitized. However, assessment of the alteration database identifies only weak enrichments in the mean and median values for Au and Cu associated with sericite alteration. This may be a result of the relatively high number of samples (1855) that were identified to be

altered by sericite (43%) in the alteration database. In fact sericite is the most commonly identified alteration mineral in the descriptive database.

Assessment of the database indicates that all mineralization styles are strongly correlated with magnetite and moderately correlated with silica alteration. Kontak et al., (2011) noted two phases of magnetite development in their study on alteration in the Upper Beaver deposit. They identify that early magnetite tends to contain higher Ti relative to late magnetite and that Au and Cu mineralization with accompanying W Bi, Te, etc, post dates the early albite-magnetite alteration and be associated with the second stage of magnetite growth (Kontak et al., 2011). The association between Cu, Au, Ag, and magnetite is consistent with petrographic observations in this study. Correlations between Mo and magnetite however, are not.

Mean and median values for Mo mineralization are also associated with elevated amounts of hematite, which agrees with petrographic observations. Mean and median values for Cu, Au, and Ag do not appear to be affected by whether or not hematite is noted in the sample.

Alteration styles that do not coincide with changes in the mean and median values for Au, Cu, Ag, and Mo include chlorite, and ankerite. Although samples noted to have ankerite alteration have drastically lower mean and median values for Mo mineralization.

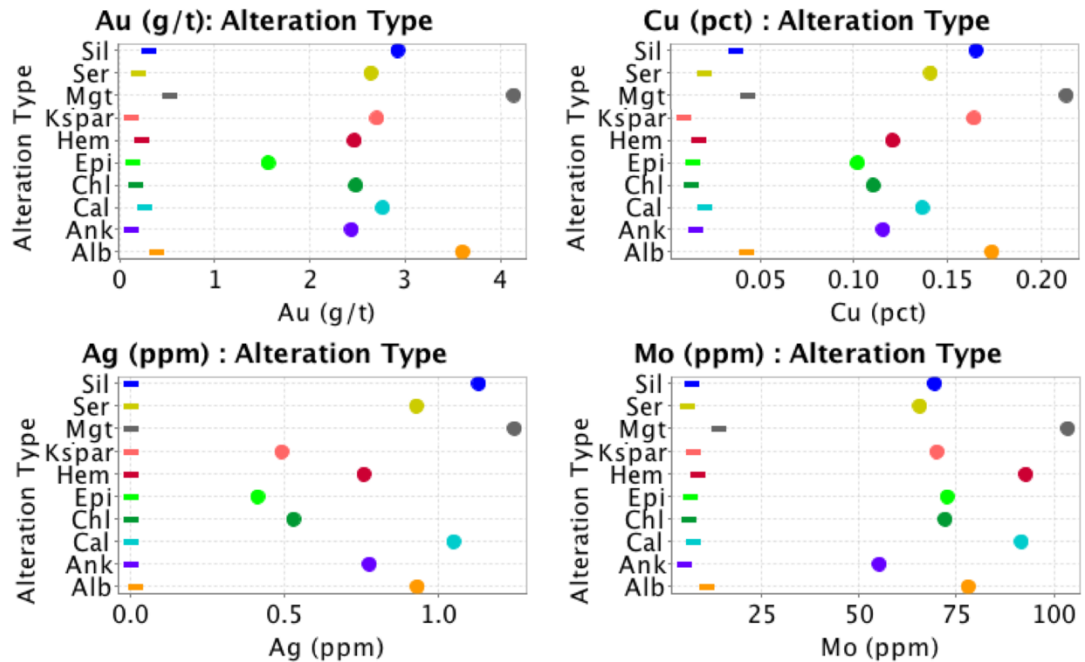


Figure 4.27. Mean (circle) and median (line) values for Au, Cu, Ag, and Mo based on whether samples are noted to contain different types of alteration minerals (Sil = silica; Ser = sericite; Mgt = magnetite; Kspar = K-spar; Hem = hematite; Epi = epidote; Chl = chlorite; Cal = calcite; Ank = ankerite; Alb = albite) based on the descriptive alteration database provided by CMC.

4.2.8 Surface Geochemistry Survey

4.2.8.1 Geochemical trends across the entire land package

In 2013 CMC ran a property-wide rock chip sampling survey across their Kirkland Lake Land package, which consists of more than 30 properties and covers an almost contiguous area of approximately 230 km². The properties host 10 gold deposits that contain current and historic mineral resources of 2.1 million ounces (measured and indicated) and 1.8 million ounces (inferred) (Ewert et al., 2010; Ewert et al., 2011; Gamble, 2011; Puritch et al., 2011; Bernier and Cole, 2012). This includes five NI43-10 compliant properties: Upper Beaver, Anoki-McBean, Bidgood, Upper Canada, and Amalgamated Kirkland. All five deposits are described in detail in technical reports by Ewert et al., (2010) (Anoki-McBean); Puritch et al., (2011)

(Bidgood); Ewert et al., (2011) (Upper Canada); and Gamble (2011) (Amalgamated Kirkland). In general, all five deposits are characterized by greenstone-hosted lode gold mineralization where gold is hosted in hydrothermal vein systems of epithermal or mesothermal origin (Ewert et al., 2010; Puritch et al., 2011; Ewert et al., 2011; and Gamble, 2011), whereas mineralization at Upper Beaver is intrusion-associated (Bernier and Cole, 2012).

In an attempt to find geochemical vectors that correlate with Au mineralization across the entire land package, Spearman Rank analysis was used. Spearman Rank correlation coefficients identify that across the camp the elements that most strongly correlate with Au mineralization are S, Ag, As, and W, as shown in Table 4.8. However, all correlations with gold are relatively weak with S having the highest correlation at $p=0.39$ indicating that using only one element as a geochemical indicator for mineralization across the Larder-Lake gold camp would be problematic for finding areas of elevated Au.

Table 4.8. Spearman Rank Correlation coefficients for entire CMC land package

Spearman	Au	Cu	Mo	Ag	As	Bi	S	Sb	U	V	W
n	(ppm)	(pct)	(ppm)	(ppm)	(ppm)	(ppm)	(ppm)	(ppm)	(ppm)	(ppm)	(ppm)
Au (ppm)	1.00	0.12	0.13	0.29	0.27	-0.13	0.39	0.06	0.12	0.02	0.27
Cu (pct)	0.12	1.00	-0.01	0.08	0.13	0.02	0.15	0.08	-0.02	0.60	0.08
Mo (ppm)	0.13	-0.01	1.00	-0.07	0.12	0.20	0.13	0.03	0.13	-0.04	-0.19
Ag (ppm)	0.29	0.08	-0.07	1.00	0.04	-0.20	0.10	0.26	0.24	0.03	0.26
As (ppm)	0.27	0.13	0.12	0.04	1.00	0.03	0.37	0.11	-0.05	0.10	0.02
Bi (ppm)	-0.13	0.02	0.20	-0.20	0.03	1.00	0.03	0.02	0.08	0.09	-0.27
S (ppm)	0.39	0.15	0.13	0.10	0.37	0.03	1.00	0.06	0.00	0.08	0.13
Sb (ppm)	0.06	0.08	0.03	0.26	0.11	0.02	0.06	1.00	0.05	0.07	0.05
U (ppm)	0.12	-0.02	0.13	0.24	-0.05	0.08	0.00	0.05	1.00	0.00	0.13
V (ppm)	0.02	0.60	-0.04	0.03	0.10	0.09	0.08	0.07	0.00	1.00	0.07
W (ppm)	0.27	0.08	-0.19	0.26	0.02	-0.27	0.13	0.05	0.13	0.07	1.00

To identify geochemical vectors for Au mineralization for the Upper Beaver deposit surface lithology-leveled data from the surface exploration survey was also plotted in ioGASTM using the display gridded data function. Leveled data was used to ensure that geochemical enrichments and depletions were a function of the mineralization signature as opposed to the rock type. The grid was made using a “maximum of cell” pre-gridding operation for a cell size of 64.8 and a search radius of 6. A minimum smoothing radius of 1 was applied to the data. Further, unequal bins (30/60/80/90/95/98/99/100%) with a shading direction of S and a shading brightness of 5 were used to highlight elevated areas of select geochemical indicators for mineralization. Results are provided in Figure 4.28.

Gridded maps of the area immediately surrounding the Upper Beaver deposit, as shown in Figure 4.29, 4.30, and 4.31, indicate that at surface the deposit is characterized by elevated amounts of Cu, Mo, and W where there are the highest concentrations of Au, and by Ag, As, Sb, and U where there are moderate concentrations of Au. The strong enrichment in Mo and W is restricted to only where the Upper Beaver Intrusive Complex outcrops, with no enrichments where other intrusives outcrop, suggesting these enrichments reflect the mineralizing fluid chemistry as opposed to the host rock chemistry and may serve as an exploration vector when evaluating the mineralization potential of other intrusive bodies. Elevated Cu, U, Sb, and Ag correlate more weakly with the outcropping Upper Beaver Intrusive Complex, but are also elevated elsewhere on the property where Au mineralization does not occur. Elevated amounts of leveled As correlate strongly with outcropping intrusive phases surrounding and including the Upper Beaver Intrusive Complex, suggesting the intrusions immediately surrounding the Upper Beaver deposit are relatively As-enriched compared to the bulk composition of intrusions across CMC property.

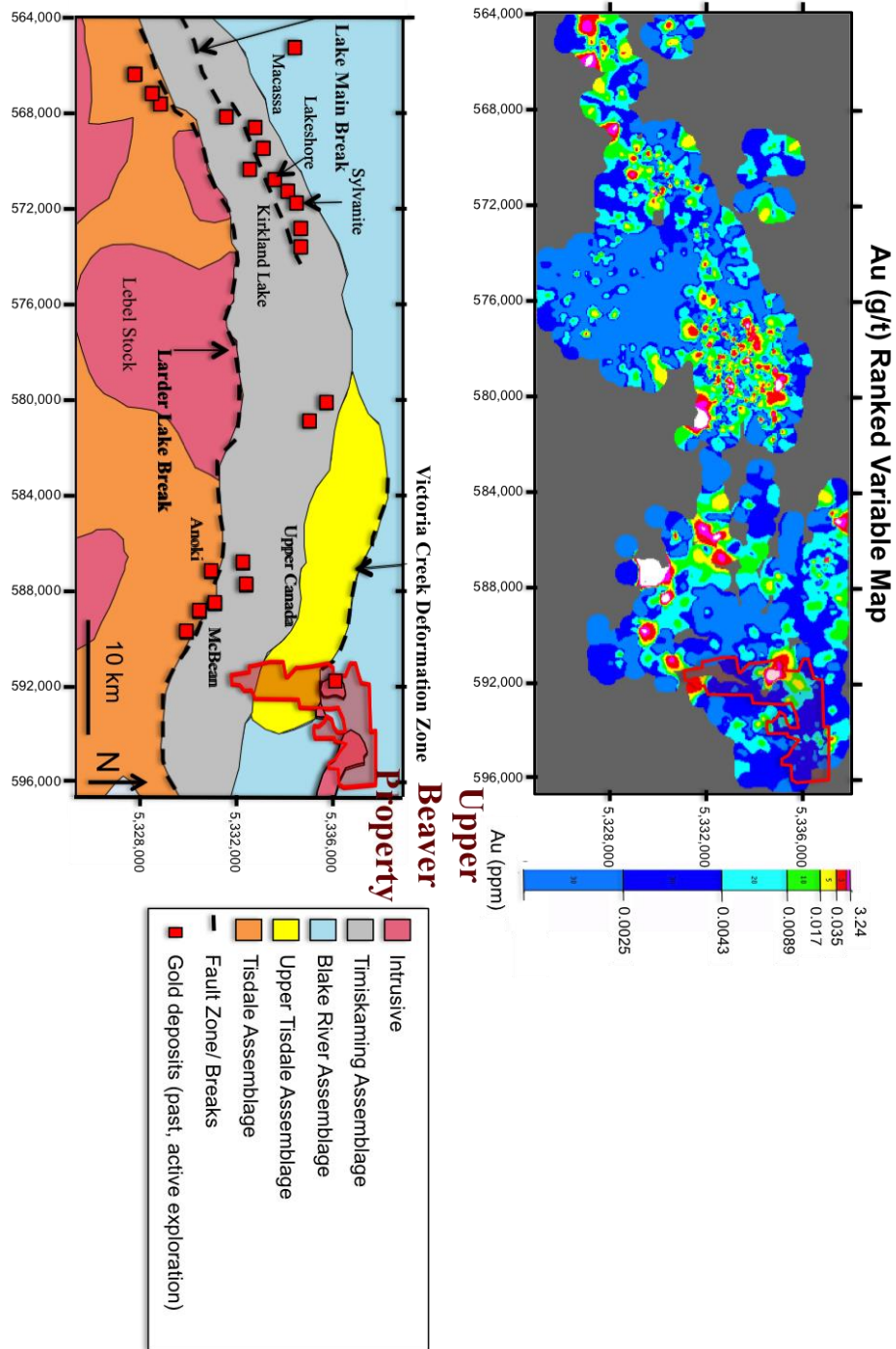


Figure 4.28. Map highlighting elevated amounts of Au on the Canadian Malartic Corporation property, as identified from the 2013 rock chip survey with past and producing mines, exploration projects, and deformation zones superimposed on the image. Bottom portion of figure modified from Breede et al., (2011)

Gridded maps of lithology-leveled concentrations of major oxides, as shown in Figure 4.30 and 4.31 identify that elevated concentrations of K₂O correlate with Au mineralization. No other major oxide is elevated around the deposit. It is important however, to note that samples were analyzed using aqua regia digest and not full fusion so only partial major oxides were attained. This is why SiO₂ analyses were not returned. Rough estimated values for SiO₂ were calculated using 100% minus the sum of all other major oxides (in percent). Elevated concentrations of K₂O also occur along the strike of the Upper Canada Break. MnO, CaO, and Al₂O₃ also correlate along strike with the Upper Canada Break. Elevated amounts of Na₂O relative to other Tisdale sediments characterize the outcropping Upper Tisdale sediments at surface. Similarly, elevated amounts of Fe₂O₃ occur in the Blake River Assemblage at the contact between the Upper Tisdale and the Blake River Assemblage.

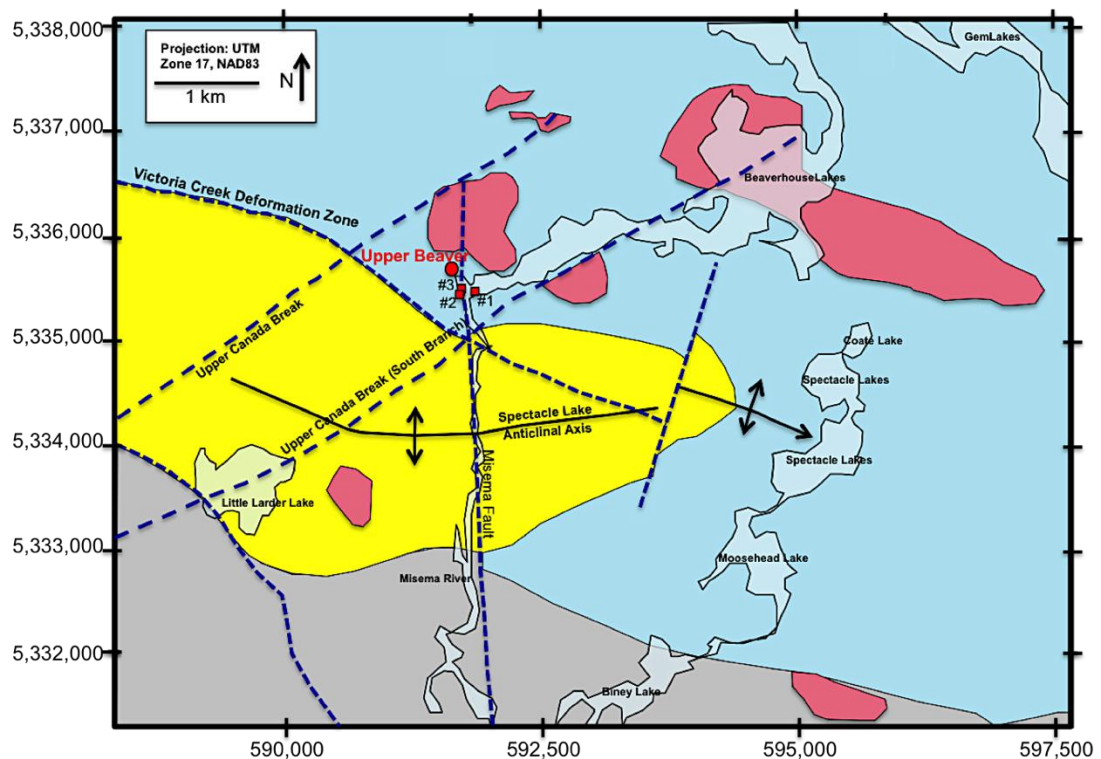


Figure 4.29. Simplified surface geology of the Upper Beaver Property showing significant major lithological units and local faults, and other surface features of importance for reference in Figures 82 and 83. The Intrusive Complex dips Northwesterly at roughly 60-70 degrees. Figure modified from Alexander, (2006).

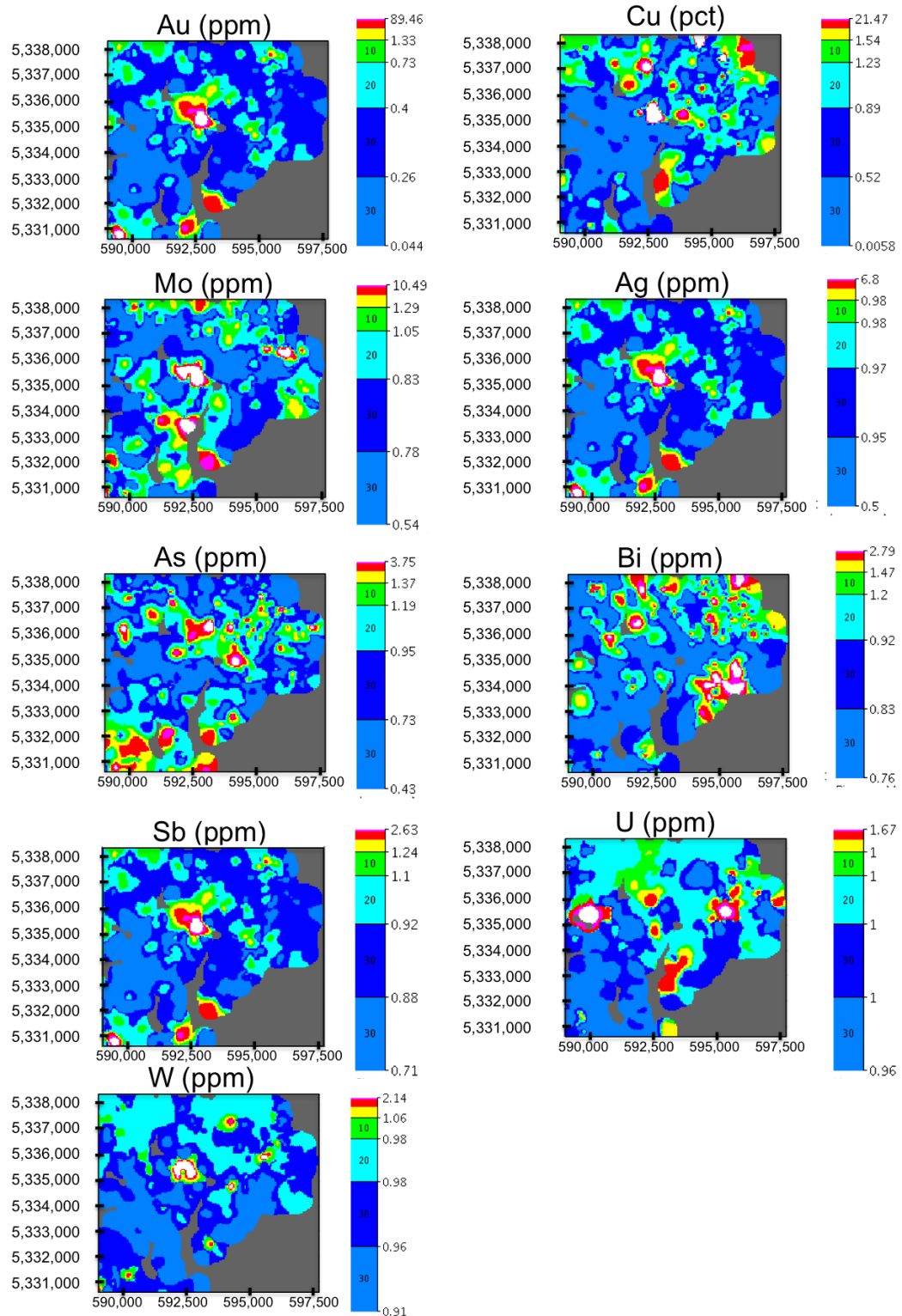


Figure 4.30. Gridded maps for select trace elements identifying anomalous surface geochemical signatures for the Upper Beaver Deposit, as identified from the 2013 rock chip survey. Regional geology map modified from Alexander, 2006

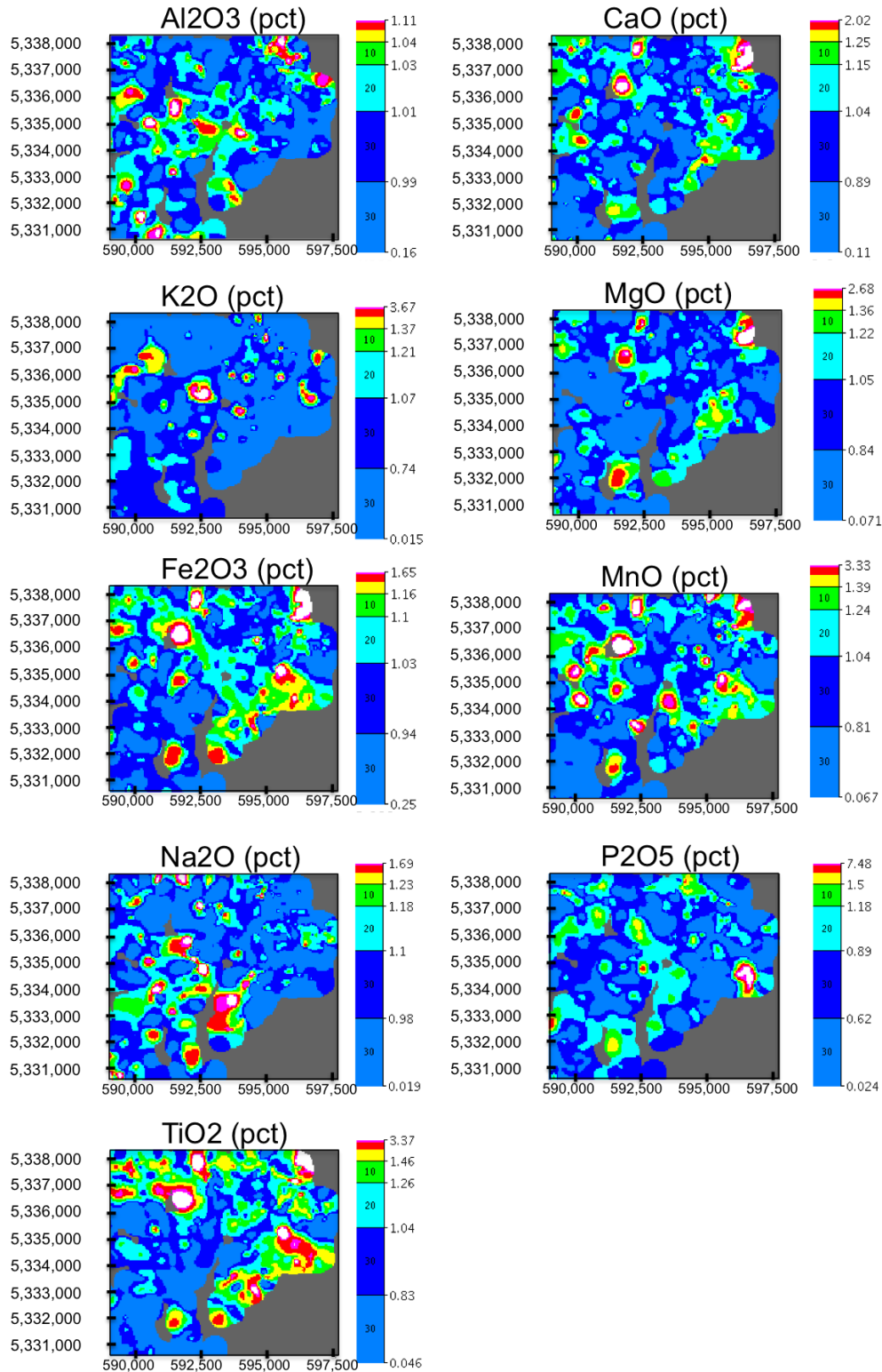


Figure 4.31. Gridded maps for major oxides identifying anomalous surface geochemical signatures for the Upper Beaver Deposit, as identified from the 2013 rock chip survey. Regional geology map modified from Alexander, 2006

Overall, both Spearman Rank Correlation coefficients and gridded maps of lithology-leveled trace and major elements indicate that using only one element as a geochemical indicator for mineralization across the Larder Lake gold camp would be problematic for finding areas of elevated Au. Gold itself remains the best geochemical indicator for Au mineralization. However, trace elements and major oxide data can be used to highlight different geological processes that may aid in identifying potentially prospective exploration targets.

5 Synchrotron source X-ray Fluorescence Microprobe Analysis of Mineralized Thin Sections from the Upper Beaver Deposit

5.1 Introduction

High-energy synchrotron source x-ray fluorescence microprobe analysis (SR-XRF) was performed on mineralized thin sections to obtain information about trace element zoning and elemental correlation on a sub-microscopic scale. This work was performed to supplement statistical analyses presented in chapter 4, which identified the presence of at least two geochemically distinct styles of mineralization (Cu-Au and Mo-Au mineralization) in the Upper Beaver deposit. SR-XRF was an ideal analytical tool as it allowed for analysis of the spatial relationship between Au mineralization and trace element exploration vectors, namely Cu, Mo, Ag, Bi, Te, and W and their associated mineral phases. It was also used to discern if fine-scale differences such as the Au:Ag ratio and Co, Ni, and As zoning within sulphides differed between the different styles of mineralization. By moving from the macro to micro scale large-scale bulk-rock geochemical changes could be linked to specific mineral phases and assemblages that otherwise would have not been distinguishable.

5.2 Results

5.2.1 Ore Minerals in the Upper Beaver deposit

Minerals associated with Au in the Upper Beaver deposit include magnetite, pyrite, chalcopyrite, and molybdenite. Petrographic observations of overprinting textures in mineralized thin sections, as outlined in Chapter 4 and in Appendix A, identified that most samples showed evidence that magnetite formed first, followed by pyrite and then chalcopyrite. In analyzed samples, gold globs ranged in size from <10 microns to coarse (>500 microns). Although mineral abundance varied between samples, fine-scaled synchrotron XRF mapping confirmed gold's close association with both chalcopyrite and molybdenite. Most frequently Au was observed along the rim of pyrite grains or within grain fractures, which were then surrounded by chalcopyrite. Less commonly, gold occurs either in chalcopyrite, along the rim of

magnetite surrounded by chalcopyrite, within a bismuth sulphide mineral, as free gold, or in association with molybdenite.

5.2.2 Thin Section Selection

Thin sections analyzed for this project were collected as representative samples of different styles and textures of mineralization from across the mineralized zones in the Upper Beaver deposit. A total of 15 mineralized thin sections were analyzed using SR-XRF methods, including at least one thin section from each ore zone in the deposit. An additional three thin sections were analyzed from an undergraduate thesis project on the South Contact Zone by Feick (2014). Key characteristics of samples analyzed are provided in Table 5.1. Samples were collected from a variety of host rocks throughout the deposit, including mafic syenite, altered crowded syenite porphyry, and basalt, to determine if the trace element geochemistry was a function of the host rock.

Table 5.1. Summary of samples analyzed including zone each sample is from, lithology, mineralization style (chalcopyrite = “Cpy”, magnetite = “Mgt”, pyrite = “Py”, visible gold = “VG”), host mineralization, and Au and Cu assays for each sample

Sample ID	Zone	Lithology	Mineralization	Host	Au Assay (g/t)	Cu Assay (pct)
KF05	South Contact	Strongly Altered Basalt	Cpy, Mgt, Py, VG	Alteration Patch	210	0.0404
KF07	South Contact	Strongly Altered Basalt	Cpy, Mgt, Py, VG	Alteration Patch	959	0.0111
KF15	South Contact	Strongly Altered Basalt	Cpy, Mgt, Py, VG	Alteration Patch	2010	0.0791
UWO_2015_02	Syenite Breccia	Mafic syenite	Cpy, Py, VG, Mgt	Quartz-Calcite	168	0.942
UWO_2015_04	Lower Porphyry East	Mafic syenite	Cpy, Py, Mgt	Quartz-Calcite	86.8	0.595
UWO_2015_05	Upper Porphyry West	Quartz-Carbonate vein zone	Mgt, Cpy, VG	Quartz-Calcite	126	3.86
UWO_2015_06	Upper Porphyry West	Altered crowded syenite porphyry	VG	Anhydrite-Ankerite	71.4	0.01
UWO_2015_07	Upper Porphyry West	Altered crowded syenite porphyry	Cpy, VG	Anhydrite-Ankerite	87.8	6.92
UWO_2015_08	Q	Basalt	Mo, VG	Quartz-Calcite	268	0.0154

Table 5.1 cont. Summary of samples analyzed including zone each sample is from, lithology, mineralization style (chalcopyrite = “Cpy”, magnetite = “Mgt”, pyrite = “Py”, visible gold = “VG”), host mineralization, and Au and Cu assays for each sample

Sample ID	Zone	Lithology	Mineralization	Host	Au Assay (g/t)	Cu Assay (pct)
UWO_2015_10	200	Mafic syenite	Cpy, Py, Mgt, VG	Quartz- Calcite	28.4	7.82
UWO_2015_11	Lower Porphyry West	Mafic syenite	Cpy, Py, Mgt, VG	Quartz- Calcite	51.3	0.995
UWO_2015_13	Each Basalt	Basalt	Py, Cpy, Mgt, VG	Quartz- Calcite	39.9	3.59
UWO_2015_14	North Basalt	Basalt	Cpy, Mgt, VG	Quartz- Calcite	1.7	5.31
UWO_2015_15	North Contact	Altered Crowded Syenite Porphyry	Mgt, VG	Quartz (Host responds to acid, FF/Veinlets do not)	31.8	0.0202
UWO_2015_17	Upper Porphyry East	Altered Basalt	Mo/Py/VG	Quartz- Calcite	25.8	0.0145

5.2.3 Mapping at 13.1 and 30.1 keV

SR-XRF was a critical tool used for evaluating the effectiveness of trace elements associated with both styles of mineralization, as it provided the necessary context to explain why the correlation exists. Trace elements of interest included elements that correlate most strongly with Au in the Upper Beaver bulk rock geochemistry dataset. Elements of particular interest include Cu, Ag, Mo, W, As, Bi, and Te, as cluster analysis and/or principal component analysis identified variations in these elements between Mo-rich and Cu-rich mineralization. Scans were run at 13.1 keV and 30.1 keV in order to capture the full array of trace elements associated with mineralization.

Running maps at 13.1 keV, just above the gold $L\alpha$ edge allows for full spectrum data to be collected for elements with lower excitation energies, creating high resolution maps for elements with lower emission energies, as shown in Figure 5.1. Mapping at energies just above the Au $L\alpha$ provides sufficient spectral resolution and count rates to be collected for elements with lower excitation energies while

minimizing background noise (Steele et al., 2000). Maps were then re-run at a significantly higher energy (30.1 keV) to collect full spectrum data for elements with higher excitation energies including Ag and Mo. At higher energies the response of elements with low excitation energies is diluted, affecting the overall resolution of maps produced. Delicate element zoning, such as in the Fe $K\alpha$ map produced at 13.1 keV, shown on the right in Figure 5.1, is not observed in the map produced at 30.1 keV.

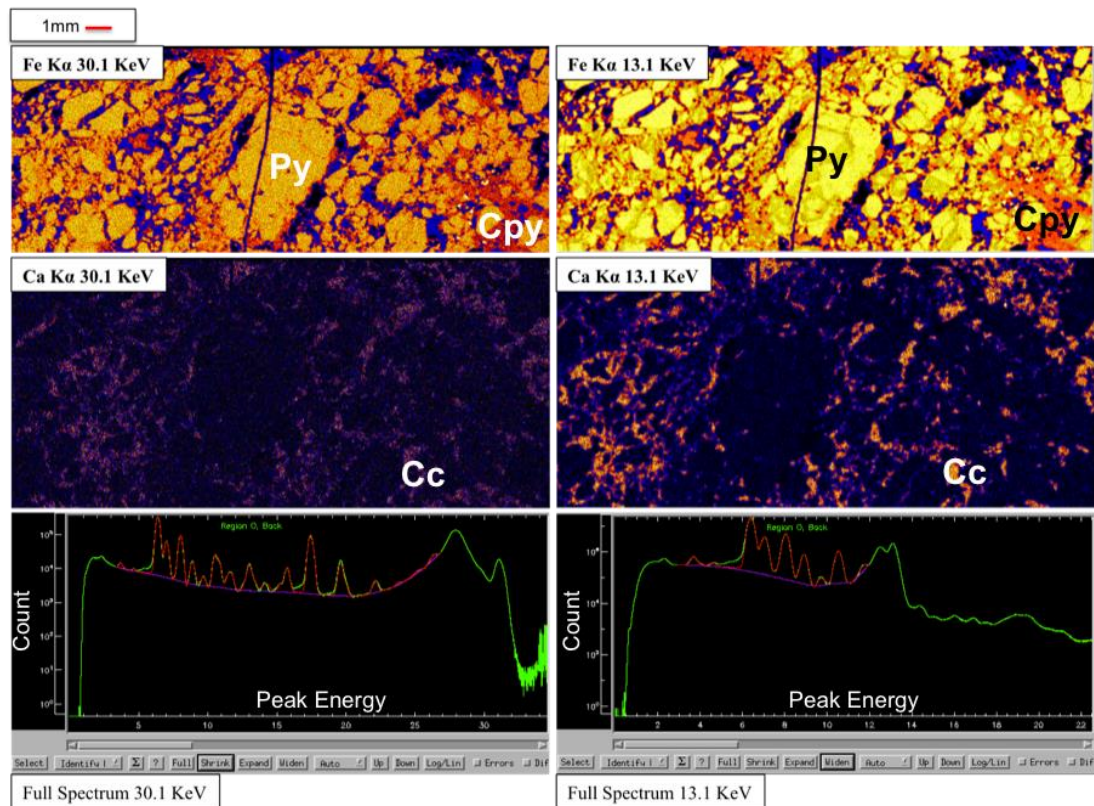


Figure 5.1. Maps and associated spectra for Fe $K\alpha$ (top) and Ca $K\alpha$ (middle) at 30.1 keV and 13.1 keV for UWO_2015_02 at CHESS. “Cpy” = chalcopyrite, “Py” = pyrite, “Cc” = calcite.

5.2.4 Mapping at different synchrotrons and the effect of step size

There are many benefits to mapping at different synchrotrons; many of which result from variations in synchrotron facility setup as each synchrotron facility is set

up with different capabilities. One such capability is the bright X-ray beams produced at APS (Lienert et al., 2011). Brightness is a measure of photons per second, per unit source size and divergence in a given bandwidth (Balerna and Mobilio, 2015). In fact, APS produces the brightest storage ring-generated X-ray beams in the Northern hemisphere, allowing users to use beams as small as 2 μm (Lienert et al., 2011). Comparatively, XRF mapping at the CHESS synchrotron is set up to produce beams as small as 10 μm but takes advantage of a Maia detector to produce high-quality energy maps in short periods of time (Woll, 2014). The Maia detector is a 384-element pixel array detector where each pixel functions as a miniature version of a traditional single element detector. Samples can be scanned with count rates larger than 10^7 photons per second with full spectra being obtained in 0.001 seconds (Woll, 2014). The detector is exceptional for mapping large areas at a high resolution and can be used for XANES mapping and XRF microtomography (Woll, 2014). CLS is set up differently as well. The Very Sensitive Elemental and Structural Probe Employing Radiation From a Synchrotron (VESPERS) beamline can obtain a spot size as small as 3-5 μm , similar to that obtainable at APS (Feng et al., 2010). Further, the beamline is set up for combined X-ray fluorescence (XRF) and X-ray powder diffraction (XRD) capabilities (Feng et al., 2010).

As an example of the effects that mapping at different synchrotrons and the effects that step size have on the detection of trace element maps, an auriferous pyrite grain surrounded by chalcopyrite from UWO_2015_10 was selected as a case-example. Trace element maps were initially produced at CHESS in November 2015 as part of a scan that encompassed a roughly 1 mm wide strip across five thin sections. The scan was completed at 13.1 keV with a dwell time of 400 ms, and a step size of 20 μm . After data collection was complete the energy map was spliced to separate each thin section into an isolated image. The entire image for thin section UWO_2015_10 is shown in Figure 5.2 with a small white box surrounding the pyrite grain of interest.

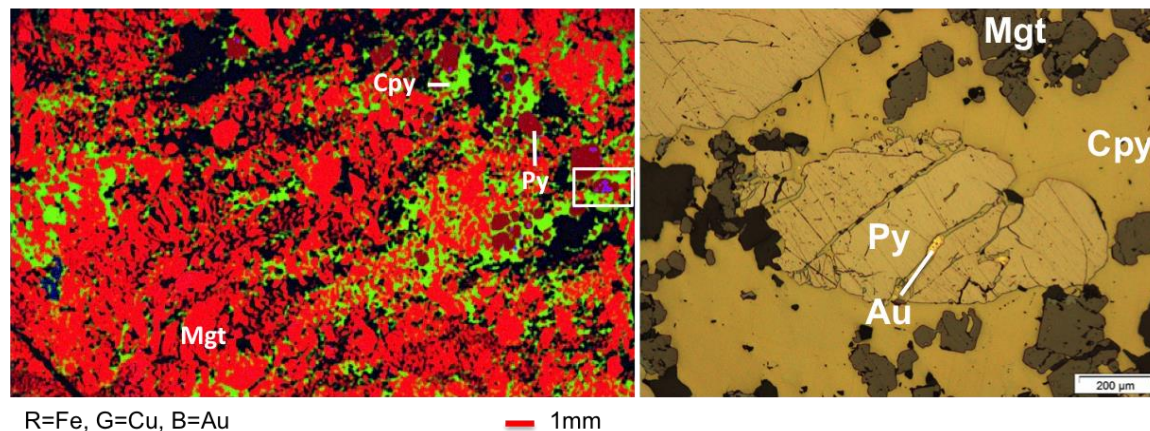


Figure 5.2. (left) RGB image produced for UWO_2015_10 where R=Fe $K\alpha$, G=Cu $K\alpha$, and B=Au $L\alpha$. The map was produced with a 20 μm step size at 13.1 keV with a dwell time of 400 ms. (right) reflected light photo micrograph showing pyrite (py) grain of interest with Au infilling fractures in the grain and surrounded by chalcopyrite (cpy), which also contains magnetite (mgt). Maps were produced at 13.1 keV at CHESS. “Mgt” = magnetite, “Cpy” = chalcopyrite, “Py” = pyrite, “Au” = gold.

The map of thin section UWO_2015_10 was then trimmed to isolate the pyrite grain of interest. A major advantage to analyzing data collected at CHESS is that data is automatically uploaded onto the CHESS server so that it can be analyzed using a program called GeoPIXE. GeoPIXE is a revolutionary data processing software designed for quantitative particle induced X-ray emission and synchrotron X-ray fluorescence trace element imaging and analysis (Pallon et al., 2009; Cohen et al., 2015; Ryan et al., 2015). It allows users to interact with full spectrum data acquired at synchrotron facilities by providing fundamental parameters for quantitative composition analysis and by allowing the user to select and verify an elements presence based on K-, L-, and M-line energy peaks (Cohen et al., 2015). The ultimate goal of GeoPIXE data analysis for this project was to produce a fit that describes all the elements in the sample and to use this to generate refined XRF maps and to determine spatial elemental concentrations from raw XRF spectrum data. GeoPIXE also has a number of functions that allow users to interact with data, including the ability to produce RGB images to show the relative distribution of three trace elements in one figure. An example is provided in Figure 5.3. For the purposes of this

exercise, the RGB image was produced for Fe, Cu, and As, respectively to demonstrate the elevated amounts of As present in the rim of pyrite grain.

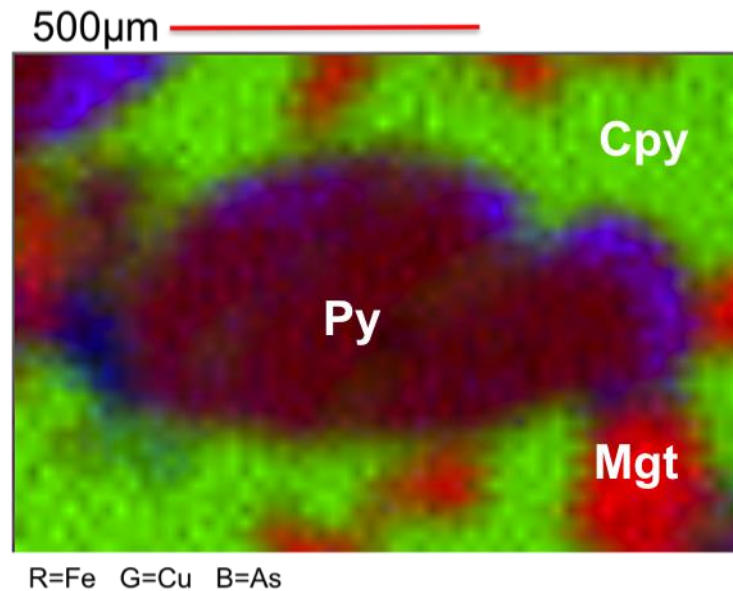


Figure 5.3. RGB image of Au-bearing pyrite grain from UWO_2015_10 where R=Fe $K\alpha$, G=Cu $K\alpha$, and B=As $K\alpha$. The RGB image makes it easy to observe the As-rich upper rim of the pyrite grain. Map was produced based on results of mapping at 13.1 keV at CHESS. See Figure 5.2 (right) for a petrographic photo of the Au-bearing pyrite grain. “Mgt” = magnetite, “Cpy” = chalcopyrite, “Py” = pyrite.

Data can also be exported as individual energy (trace element) maps using refined full spectra data once appropriate trace elements have been “fit” to the curve. An example of energy maps produced for the pyrite grain of interest are provided in Figure 5.4.

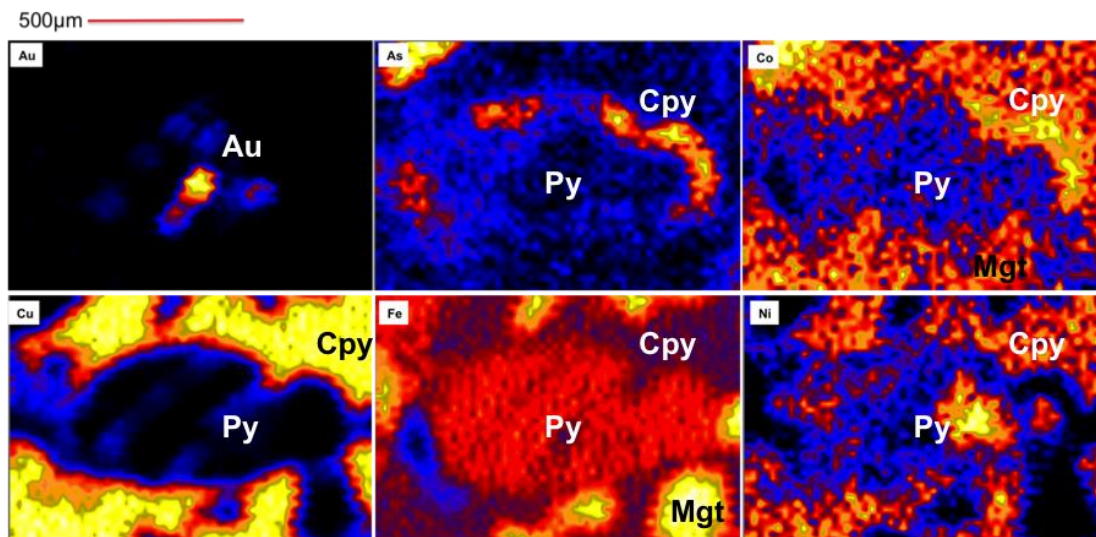


Figure 5.4. Isolated pyrite grain of interest from UWO_2015_10 mapped at CHESS with a 20µm step size showing energy maps for various trace elements of interest (Au L α ; As K α ; Co K α ; Cu K α ; Fe K α ; Ni K α). Maps were produced at 13.1 keV at CHESS. See Figure 5.3 (right) for a petrographic photo of the Au-bearing pyrite grain. “Mgt” = magnetite, “Cpy” = chalcopyrite, “Py” = pyrite, “Au” = gold.

Data collected at APS was focused specifically on the pyrite grain of interest as opposed to mapping a large section of the slide. The grain of interest was located and a map was produced at 27 keV using a step size of 4 µm and a dwell time of 300 ms. Trace elements of interest are selected and ROIs are used to produce energy maps, as described in Section 2.5.4, above. Mapping sequentially at CHESS and then at APS took advantage of the relatively quick scanning techniques at CHESS producing scans that were several cm’s across to isolate areas of interest, which were then followed-up with very fine-scale mapping at APS taking advantage of the beams brightness. Maps from APS are provided in Figure 5.5.

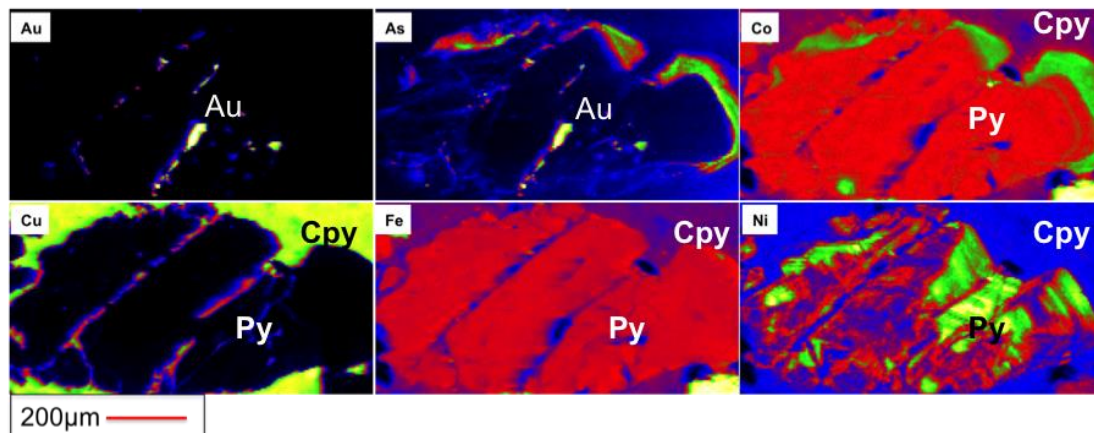


Figure 5.5. Isolated pyrite grain of interest from UWO_2015_10 mapped at APS with a 5 μ m step size showing energy maps for various trace elements of interest (Au L α ; As K α ; Co K α ; Cu K α ; Fe K α ; Ni K α). Maps were produced at 13.1 keV at APS. See Figure 5.3 (right) for a petrographic photo of the Au-bearing pyrite grain. “Mgt” = magnetite, “Cpy” = chalcopyrite, “Py” = pyrite, “Au” = gold.

Although both maps show roughly the same features there are large differences in the resolution of the images. APS produces the brightest storage ring-generated X-Ray beams in the Northern hemisphere, which allows the user to complete analysis at a finer step size (down to 2 μ m) (Lienert et al., 2011). For comparison, at CHESS the beam is not as bright as at APS, and has a resolution approaching 10 μ m. This has a large effect on mapping of small areas, as the step size dramatically alters the quality of data resolution with larger grain sizes producing progressively fuzzier images. Maps produced at CHESS were created using a step size of 20 μ m, which was ideal for collecting data for large areas in a relatively short period of time, and maps produced at APS were produced using a step size of 5 μ m. For the most part major zoning features can still be observed in both maps, however, in smaller grains these delicate zoning features are often unidentifiable at such a large step size.

Using a finer step size to produce element maps also has a downside. Mapping with such a small step size dramatically slows down the amount of time it takes to create maps. The large map that Figure 5.5 was cut from was 1400 mm² and was produced in 4 hours and 42 minutes, while the map produced at CHESS was 9,900 mm² and was produced in only 3 hours. This is also a function of the detector used.

At CHESS a Maia detector was used, which is a 384-element pixel array detector capable of achieving count rates of over 10^7 photons per second and full spectra in roughly 0.001 seconds (Woll, 2014).

Au and As maps produced at APS also had greater peak overlap effects. The effects of peak overlap can be problematic when producing trace element energy maps. For instance, overlap between the Au $K\alpha_1$ and As $L\alpha_1$ lines, which occur at 9713 (ROI = 324) and 10,543 (ROI = 351), respectively, can result in false positives in energy maps produced. At APS this effect was reduced by producing maps from energy peaks with ROIs that were limited between 334 to 354 for As (equivalent to 9600-9930 eV) and between 320 and 331 for Au (equivalent to 10,020 – 10,620 eV). This reduced the effects of the peak overlap between As and Au. Further, differentiation between conflicting element peaks was performed by setting the beam energy 10 eV above the energy peak of interest and then 10 eV below peak. For instance, for Au a beam energy of 10, 553 eV would excite Au $K\alpha$ electrons and would cause Au to release characteristic secondary x-ray energy, while a beam energy of 10,533 would not be enough to excite the Au $K\alpha$ electrons. If energy were recorded below the Au $K\alpha$ energy line then it would indicate that the energy recorded is not caused by the emission of Au $K\alpha$ x-rays and may be due to energy released from As $L\alpha$ x-rays.

5.2.4.1 Cu-Au Mineralization

The geochemically distinct Cu-enriched group of Au mineralization was associated with a distinctly lower Au:Ag ratio and was associated with enriched U and As, as described in Chapter 4. A total of 12 of the 15 thin sections analyzed contained chalcopyrite that was associated with Au, as well as with variable amounts of magnetite (\pm hematite) and pyrite. Au was frequently observed as inclusions within fractures in pyrite or magnetite, which were then surrounded by chalcopyrite. Chalcopyrite also frequently hosted isolated gold globs. Less often Au was observed as free gold. Two representative samples are described in detail below as representative examples of Cu-associated mineralization.

The first sample, UWO_2015_10 from the 200-Zone was the most magnetite-rich sample analyzed. It consisted dominantly of brecciated magnetite with chalcopyrite and pyrite infilling the space between magnetite and hematite grains. Textures indicate that pyrite formed prior to chalcopyrite. Au mineralization is present in both pyrite and the chalcopyrite, or it occurs along magnetite grain boundaries and is surrounded by chalcopyrite. This relationship is shown in the RGB image (R=Fe, G=Cu, B=Au) in Figure 5.6, and in the photomicrograph in Figure 5.7.

Pyrites also contain notable As zoning with As-poor cores and As-rich rims, as shown in Figure 5.6, with no notable As enrichment along fractures that host Au mineralization. There is no trace element zoning in either chalcopyrite or magnetite. The breccia host surrounding mineralization is also very Ca-rich.

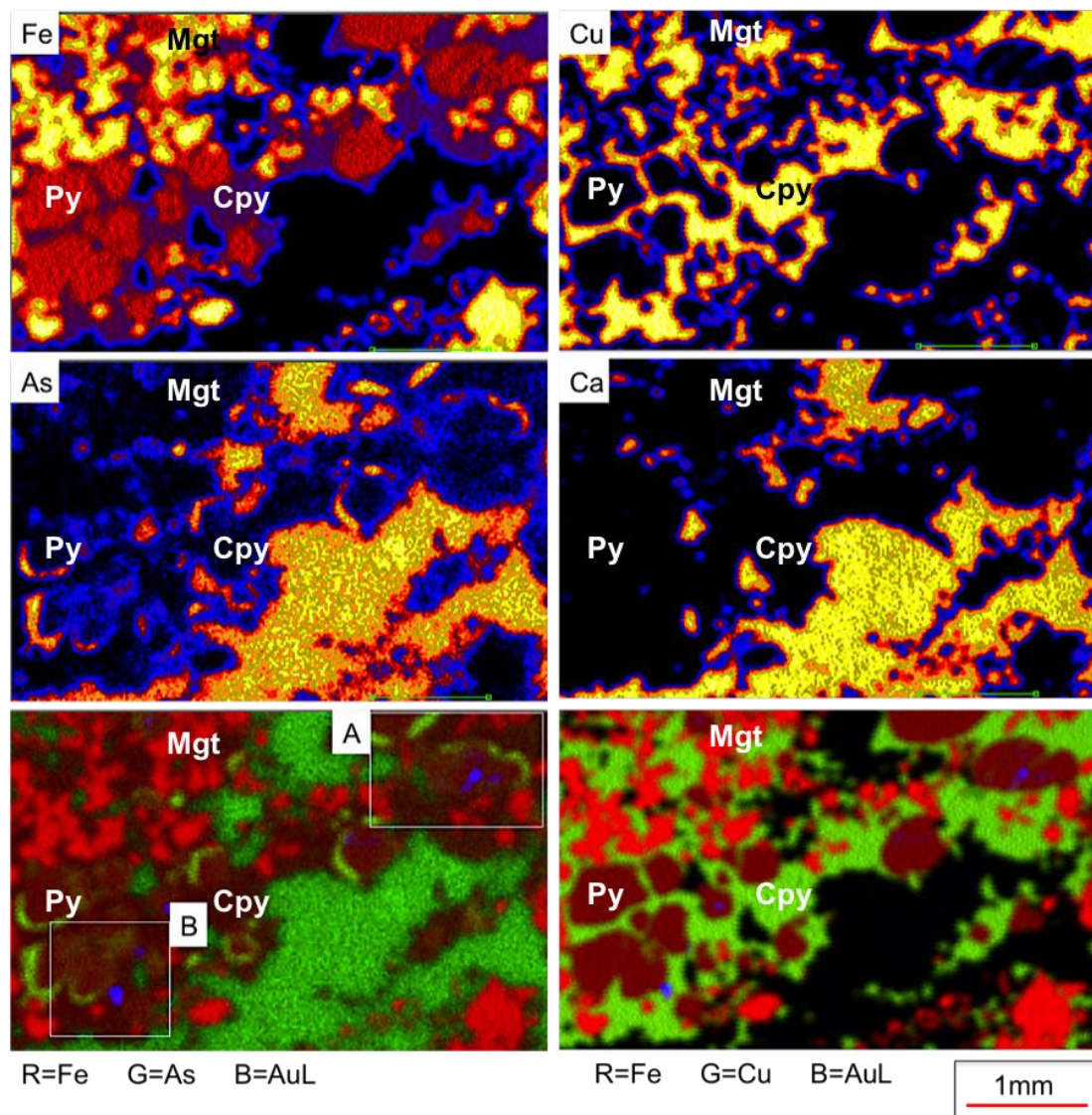


Figure 5.6. Trace element maps of UWO_2015_10 showing (from top left to bottom right) trace element maps of Fe $K\alpha$, Cu $K\alpha$, As $K\alpha$, and Ca $K\alpha$, as well as two RGB images to show the associations between different trace elements (Fe $K\alpha$, As $K\alpha$, and Au $L\alpha$ on the left and Fe $K\alpha$, Cu $K\alpha$, and Au $L\alpha$ on the right). Maps were produced using a 20 μm step size. Box A and B in the energy map on the bottom right corner correlate with A and B in Figure 5.7, below. Maps were produced at 13.1 keV at CHESS. “Mgt” = magnetite, “Cpy” = chalcopyrite, “Py” = pyrite, “Au” = gold.

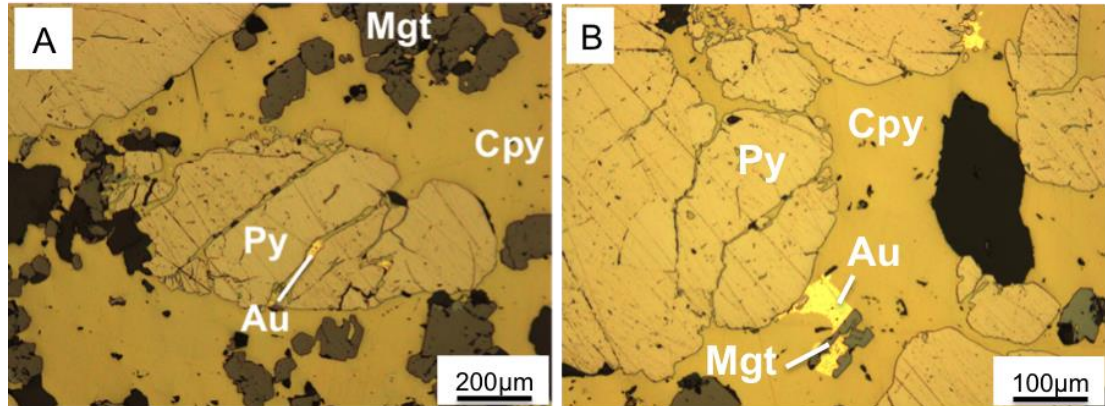


Figure 5.7. Photomicrograph showing the distribution of Au in UWO_2015_10, corresponding to Box A and B in Figure 5.6. “Mgt” = magnetite, “Cpy” = chalcopyrite, “Py” = pyrite, and “Au” = gold.

The second representative sample selected is UWO_2015_05 from the Upper Porphyry West Zone, which also contained abundant hematite, magnetite, pyrite, and chalcopyrite. Interestingly, Au mineralization was localized at the boundary between the large zones of magnetite (with lesser hematite) and chalcopyrite (with lesser pyrite), with additional small amounts of Au occurring in the massive chalcopyrite, as shown in Figure 5.8. Petrographic observations reveal that in this sample Au can be hosted directly within chalcopyrite or it can nucleate on magnetite grain boundaries enclosed within chalcopyrite. Au mineralization has no associations with pyrite in this thin section. Textures indicate that magnetite (+hematite) formed first, followed by pyrite and then chalcopyrite. Synchrotron source x-ray fluorescence microprobe analysis identifies that there is no trace element zoning (Ni, Co, or As) in either pyrite or chalcopyrite.

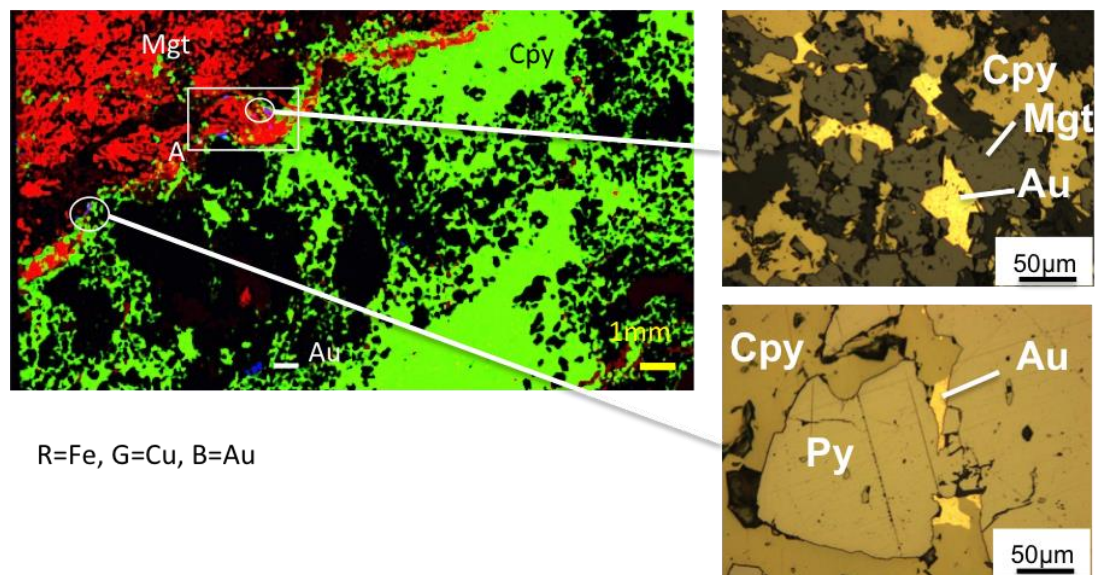


Figure 5.8. RGB image showing the distribution of Fe $K\alpha$, Cu $K\alpha$, and Au $L\alpha$ in UWO_2015_05 based on synchrotron XRF Mapping at CHESS with associated photomicrographs of mineralization on the right side of the figure. “Cpy” = chalcopyrite, “Mgt” = magnetite, “Au” = gold, and “Py” = pyrite.

The large energy map was trimmed to isolate a Au-bearing region of interest identified as A in the white box in Figure 5.8, above. This area corresponds to the energy maps presented in Figure 5.9. The region is characterized by a wave shaped section of magnetite that is surrounded and in part infilled by chalcopyrite mineralization. Au in both Au-rich hot spots shown in Figure 5.9 consists of Au nucleated on magnetite grain margins, and then surrounded by chalcopyrite. No notable zoning in terms of Ni, Co, or As is present.

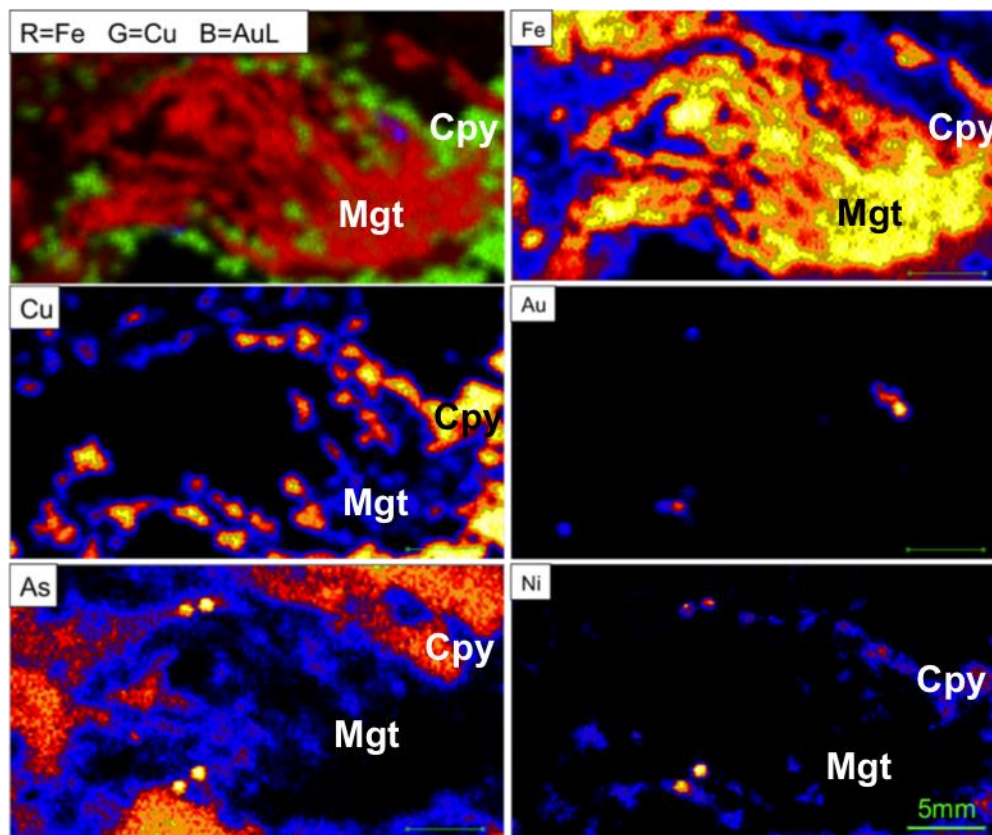


Figure 5.9. Energy map showing the distribution of Fe $K\alpha$, Cu $K\alpha$, and Au $L\alpha$ in the RGB image on the top left, as well as individual energy maps for Fe $K\alpha$, Cu $K\alpha$, Au $L\alpha$, As $K\alpha$, and Ni $K\alpha$ for UWO_2015_05. Maps were produced at 13.1 keV at CHESS. “Cpy” = chalcopyrite, “Mgt” = magnetite.

5.2.4.2 Mo-Au Mineralization

Molybdenum-associated Au mineralization is characterized by a distinctly higher bulk rock Au:Ag ratio and strong enrichments in W, as well as low As. Au typically occurs directly associated with molybdenite or as free Au. Less often small amounts of chalcopyrite are present, and Au can be hosted directly within it. Of the 15 samples analyzed at the synchrotron, 2 contained molybdenum-associated Au mineralization.

Sample UWO_2015_08 from the Q Zone was selected as a representative sample for this type of mineralization. It was the most Mo-rich sample analyzed. Au occurred as fine particle of free Au in close spatial association with Mo mineralization, or as fine particles within strands of molybdenite. Additionally, the

sample lacked chalcopyrite, pyrite, and magnetite mineralization, but contained small amounts of hematite. A Au-rich area of the thin section is presented in Figure 5.10. The RGB image shows the occurrence of Mo, Fe, and Au in the slide. It should be noted that enriched amounts of Fe are due to chlorite alteration, not pyrite or chalcopyrite. No trace element zoning (Ni, Co, As) was observed in the sample.

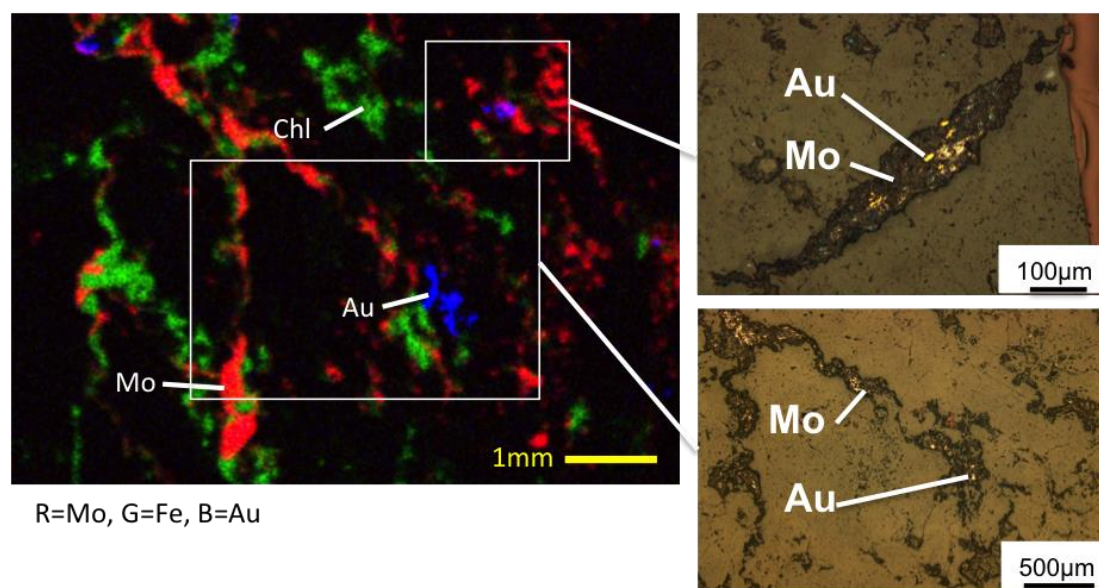


Figure 5.10. RGB image produced by XRF mapping at CHESS showing the distribution of Mo $K\alpha$, Fe $K\alpha$, and Au $L\alpha$ in UWO_2015_08 based on synchrotron XRF Mapping with molybdenite (Mo), gold (Au), and chlorite (Chl) identified on synchrotron XRF map

5.2.5 Trace element Zoning in Mineralized Sulphide Minerals

Ni and Co zoning was observed in pyrite grains in many of the samples analyzed by SR-XRF methods. Two thin sections from the South Contact Zone, as well as one thin section from each of the Syenite Breccia, Lower Porphyry East, and the 200 Zone had well-defined trace element zoning in pyrite. Less often As zoning also occurs, in some cases associated with trace amounts of finely disseminated Au. Trace element zoning may also occur in other zones from the deposit however it is only observable when the step size is relatively small. Mapping between 2-10 μm is ideal for detecting the delicate zoning.

Trace element zoning only occurs within a subset of pyrite grains from the Upper Beaver deposit, and where observed in this study, zoned grains were typically associated with Cu-enriched style Au mineralization. Pyrite is typically sieve-textured. Au typically occurs within fracture fills in pyrite grains, or along pyrite grain boundaries, which are in turn surrounded by chalcopyrite. Additionally, although in most deposits zoning typically includes both Ni and Co zoning within pyrite, in the Upper Beaver deposit Ni and Co are not always co-enriched. Sample UWO_2015_02 contains only Co-enriched zones whereas sample UWO_2015_04 contains only Ni-enriched zoning.

Three samples are described in detail below as representative examples of trace element zoning in the Upper Beaver deposit. They include sample UWO_2015_10 from the 200 mineralized zone, which is characterized by both Ni and Co zoning, as well as samples UWO_2015_02 and UWO_2015_04 from the Syenite Breccia and Lower Porphyry East Zones, respectively. Sample KF05 was described in detail in section 5.5.4.3 above.

Sample UWO_2015_02 from the Syenite Breccia Zone is almost entirely composed of pyrite with lesser amounts of chalcopyrite. The sample contains abundant Au mineralization, which is hosted in both chalcopyrite and bismuth-sulphide. SR-XRF analysis reveals the presence of at least 3 phases of pyrite mineralization, with early and late pyrite lacking Co-enrichment, and the middle phase having strong Co enrichment, as shown in Figure 5.11. The delicate zoning within the pyrite grains is not observable in reflected light, and was only detected through SR-XRF analysis. Textural relationships identified in the thin section reveal that an initial period of magnetite growth, which was followed by multiple phases of pyrite growth (previously described) with varying amounts of Co enrichment, followed by chalcopyrite, bismuth-sulphide, and Au precipitation.

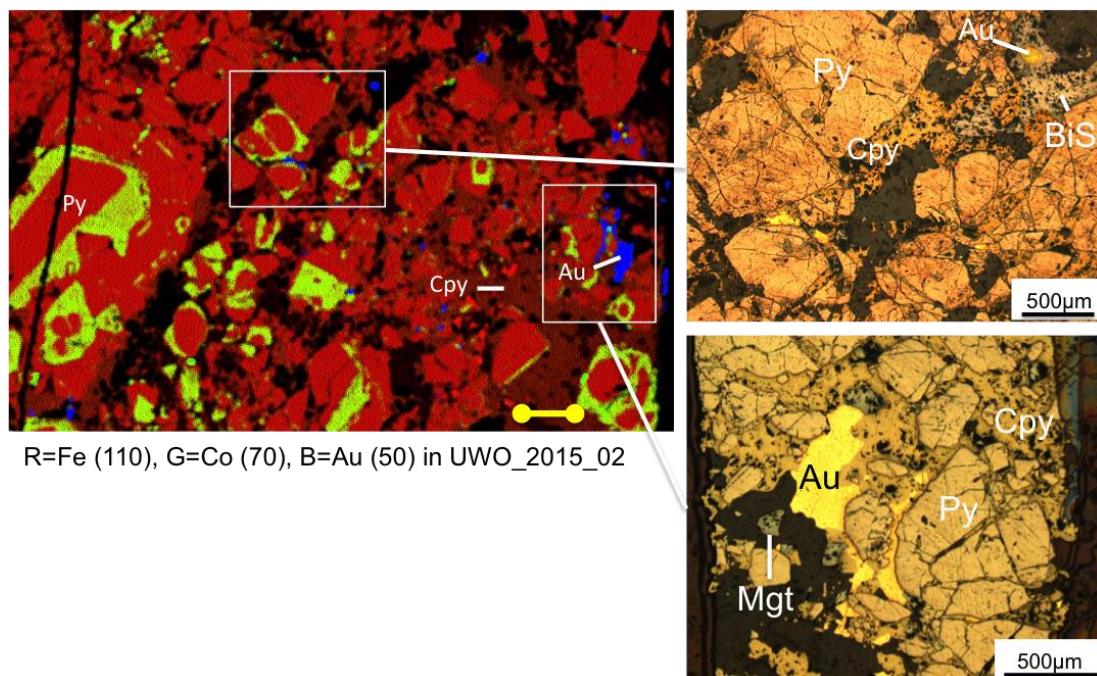


Figure 5.11. RGB image showing the distribution of Fe $K\alpha$, Co $K\alpha$, and Au $L\alpha$ in UWO_2015_02 based on synchrotron XRF energy mapping at 13.1 keV with a step size of 20 μm , and a dwell time of 300 ms performed at CHESS. Associated corresponding photomicrographs are presented along the left side of the figure. “Py” = pyrite “Au” = gold, “Cpy = chalcopyrite, “mgt = magnetite, and “BiS” = bismuth sulphide.

Sample UWO_2015_04 is from the Lower Porphyry East zone. Mineralization consists of pyrite, chalcopyrite, hematite and magnetite. Au is hosted in both chalcopyrite and pyrite minerals in the sample and is not directly associated with magnetite and hematite. The pyrite grain of interest was first mapped at CHESS in November 2015. Mapping revealed a delicate Ni-rich core which hosted abundant fracture fill Au mineralization. Follow-up mapping was performed at APS in March, 2016 to more clearly defined the Ni halo in the core of the grain using a step size of 3 μm . The results of the mapping performed at CHESS is presented in Figure 5.12.

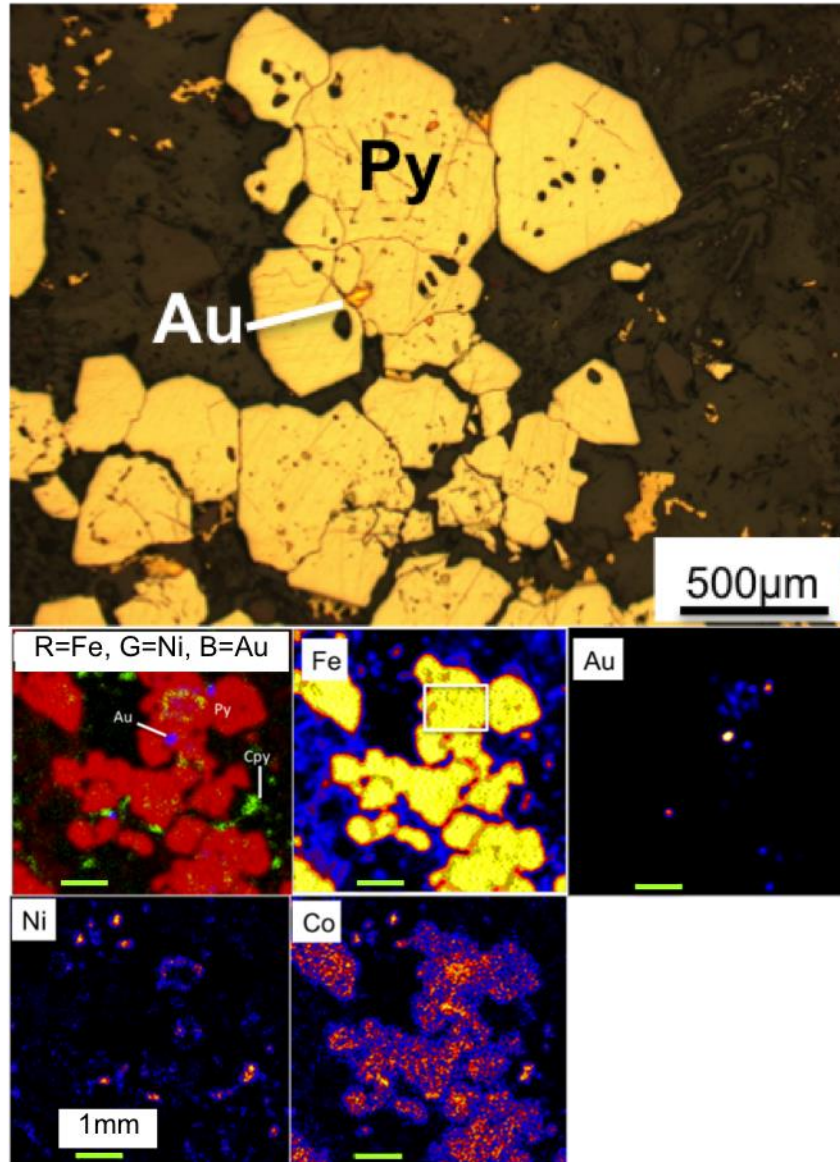


Figure 5.12. (upper) Photomicrograph of Ni-rich pyrite grain in sample UWO_2015_04. Au mineralization is observable in many fine fractures in the grain. (lower) SR-XRF energy maps of zoned pyrite grains from UWO_2015_04. Maps include a RGB map showing the distribution of Fe $K\alpha$, Ni $K\alpha$, and Au $L\alpha$. Maps also include specific energy maps for Fe $K\alpha$, Au $L\alpha$, Ni $K\alpha$, and Co $K\alpha$. Mapping revealed a delicate core of Ni in the clump of pyrite grains in the upper half of the image. “Au” = gold, “Py” = pyrite.

Follow-up mapping performed at APS in March 2016, used a much finer step size ($3\mu\text{m}$). Results are shown in Figure 5.13. Mapping concentrated on the Ni-rich core of the pyrite grain, which also contains the bulk of the Au mineralization. Mapping with a $3\mu\text{m}$ step size revealed that Au enrichments dominantly occur along

fractures in the Ni(+As) enriched core of the pyrite grain. It also revealed that the fracture-fill Au is intimately associated with elevated amounts of As.

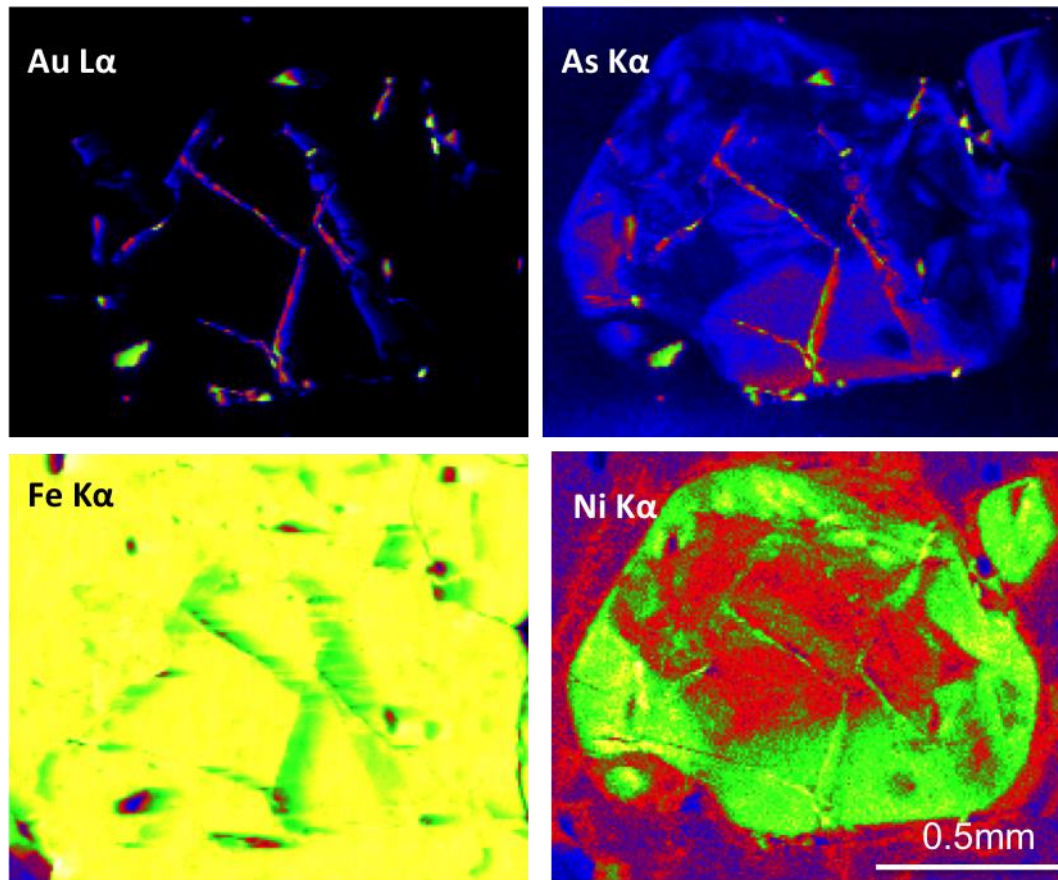


Figure 5.13. Trace element XRF maps of Au La, As Ka, Fe Ka, and Ni Ka in UWO_2015_04 collected from APS using a step size of 3 μm

Mapping of a mineralized pyrite grain in UWO_2015_10 identified a patchy Ni-rich core, surrounded by a Co and As rich upper rim. Similar to UWO_2015_04, Au mineralization dominantly occurs in fracture fills within the pyrite and is associated with elevated amounts of As. Results are presented in Figure 5.14. Pyrite is enclosed within chalcopyrite.

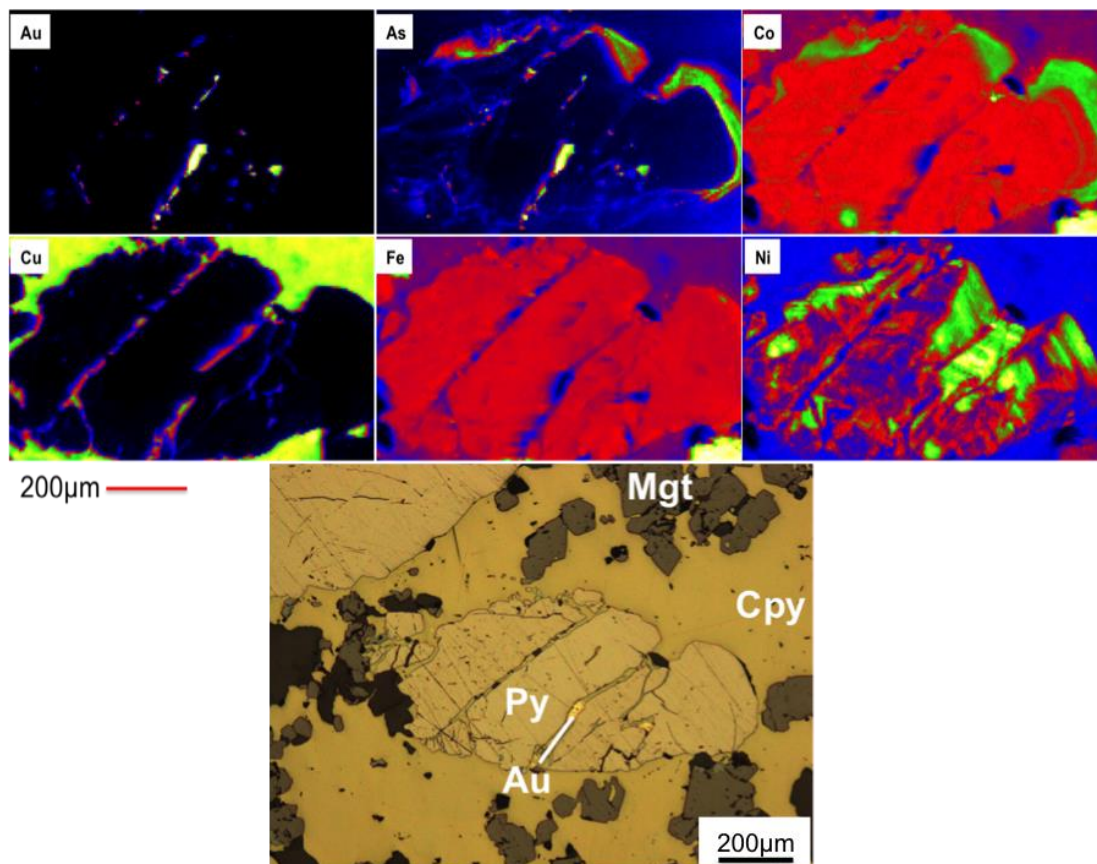


Figure 5.14. (top) Trace element SR-XRF maps of various elements (Au $L\alpha$; As $K\alpha$; Co $K\alpha$; Cu $K\alpha$; Fe $K\alpha$; and Ni $K\alpha$) in UWO_2015_04 collected from APS using a step size of 4 μm , a dwell time of 300 ms, and an energy of 13.1 keV. Mapping performed at APS. (Bottom) corresponding photomicrograph of pyrite grain analyzed by SR-XRF. “Mgt” = magnetite, “Py” = pyrite, “Au” = gold, and “Cpy” = chalcopyrite.

5.2.6 Less Abundant Mineral Phases: A bismuth sulphide mineral, Scheelite, and Ilmenite

Bulk rock geochemical analysis revealed variable correlations with other elements, including Bi, Te, and W among the different mineralized zones in the deposit. For this reason, Bi, Te, and W were of particular interest when performing SR-XRF analysis. To aid with trace element identification, synchrotron source x-ray fluorescence microprobe analysis was performed at both 13.1 keV and 30.1 keV to

ensure that K-emission lines were collected for all elements of interest. A summary of the samples containing these phases is provided in Table 5.2.

Table 5.2. Synchrotron source x-ray fluorescence microprobe analysis showing the presence of Bi, W, and Te phases associated with Au mineralization and trace element zoning in pyrite and chalcopyrite grains in each zone in the deposit

SampleID	Zone	Type of Au	Bi mineral?	W mineral?	Ni and/or Co Zoning?
KF05	South Contact	Cpy, Mgt, Py, Au	No	No	Ni and Co
KF07	South Contact	Cpy, Mgt, Py, Au	No	No	No
KF15	South Contact	Cpy, Mgt, Py, Au	Yes	No	Ni and Co
UWO_2015_02	Syenite Breccia	Cpy-Py-Mgt	Yes	No	Co
UWO_2015_04	Lower Porphyry East	Cpy-Py-Mgt	No	No	Ni
UWO_2015_05	Upper Porphyry West	Cpy-Py-Mgt	No	No	No
UWO_2015_06	Upper Porphyry West	Anhydrite	No	No	No
UWO_2015_07	Upper Porphyry West	Anhydrite	No	No	No
UWO_2015_08	Q	Mo	No	No	No
UWO_2015_10	200	Cpy-Py-Mgt	No	Yes	Ni and Co
UWO_2015_11	Lower Porphyry West	Cpy-Py-Mgt	No	No	No
UWO_2015_13	Each Basalt	Cpy-Py-Mgt	No	No	No
UWO_2015_14	North Basalt	Cpy-Py-Mgt	No	No	No
UWO_2015_15	North Contact	Cpy-Py-Mgt	No	No	No
UWO_2015_17	Upper Porphyry East	Mo	No	No	No

Unfortunately, no Te-rich minerals were identified in SR-XRF maps, however both Bi-, and W-rich minerals, including a bismuth sulphide mineral, and scheelite, were observed. Additionally, one thin section contained ilmenite that was enclosed within magnetite, as described in detail below. All three minerals occurred in rocks with a Cu-enriched mineralization style, and did not occur in association with Mo-enriched mineralization.

Sample UWO_2015_02 and KF15 both contained the bismuth sulphide mineral. The RGB image, reflected light photomicrograph, and energy maps presented in Figure 5.15 show the close association between Bi and Au in UWO_2015_02. In this sample Au is directly hosted within the bismuth sulphide mineral. Au is also hosted within chalcopyrite elsewhere in the sample.

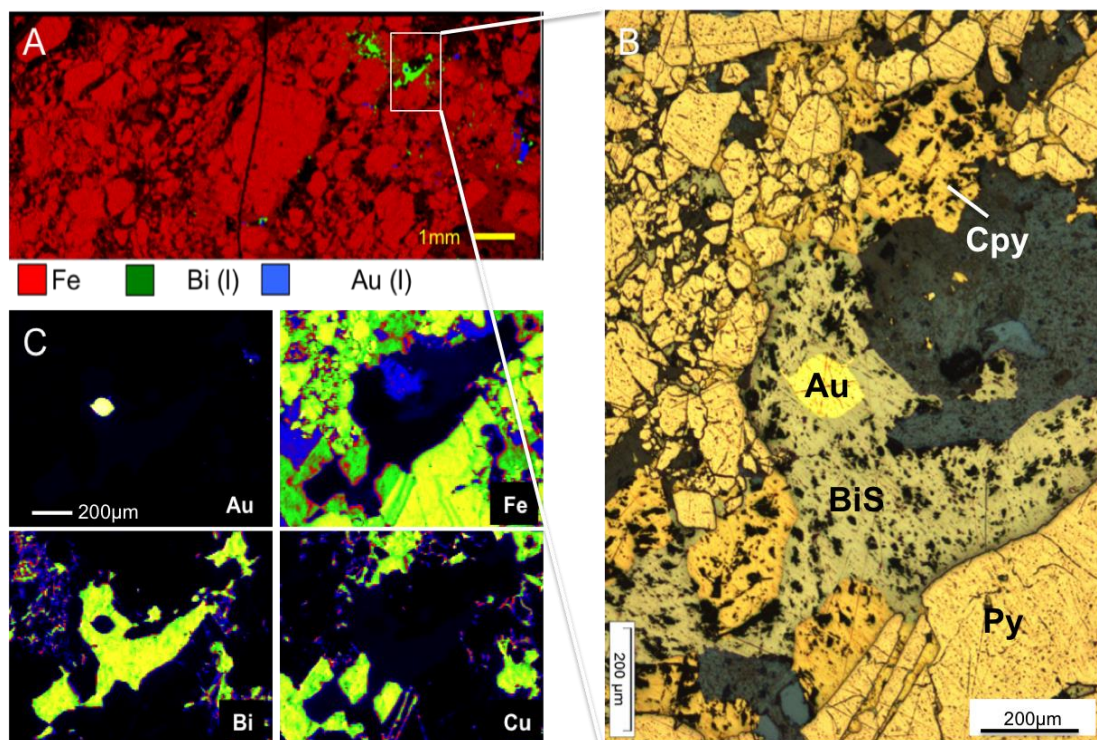


Figure 5.15. A) RGB image showing the distribution of Fe $K\alpha$, Bi $L\alpha$, and Au $K\alpha$ in UWO_2015_02 based on synchrotron XRF Mapping from Cornell with a step size of $20\mu\text{m}$; B) Reflective light photomicrograph of auriferous a bismuth sulphide mineral grain; and C) Trace element XRF maps of Au $L\alpha$, Fe $K\alpha$, Bi $L\alpha$, and Cu $K\alpha$ collected from APS using a step size of $10\mu\text{m}$. “Cpy” = chalcopyrite, “Au” = gold, “BiS” = bismuth sulphide, and “Py” = pyrite.

Sample KF15 also contained a bismuth sulphide mineral. Unlike in UWO_2015_02, Bi does not host Au mineralization in KF15 however, small amounts of Au are associated with a bismuth sulphide mineral in the upper portion of the pyrite grain, and additional zones of Au enrichment are present in the lower section of the grain, as shown in Figure 5.16. SR-XRF mapping also reveals strong trace element zoning, consisting of a Co rich rim, surrounded by a Ni-rich inner layer. Other pyrite grains close to the grain of interest also have well defined internal As- and Ni enrichments.

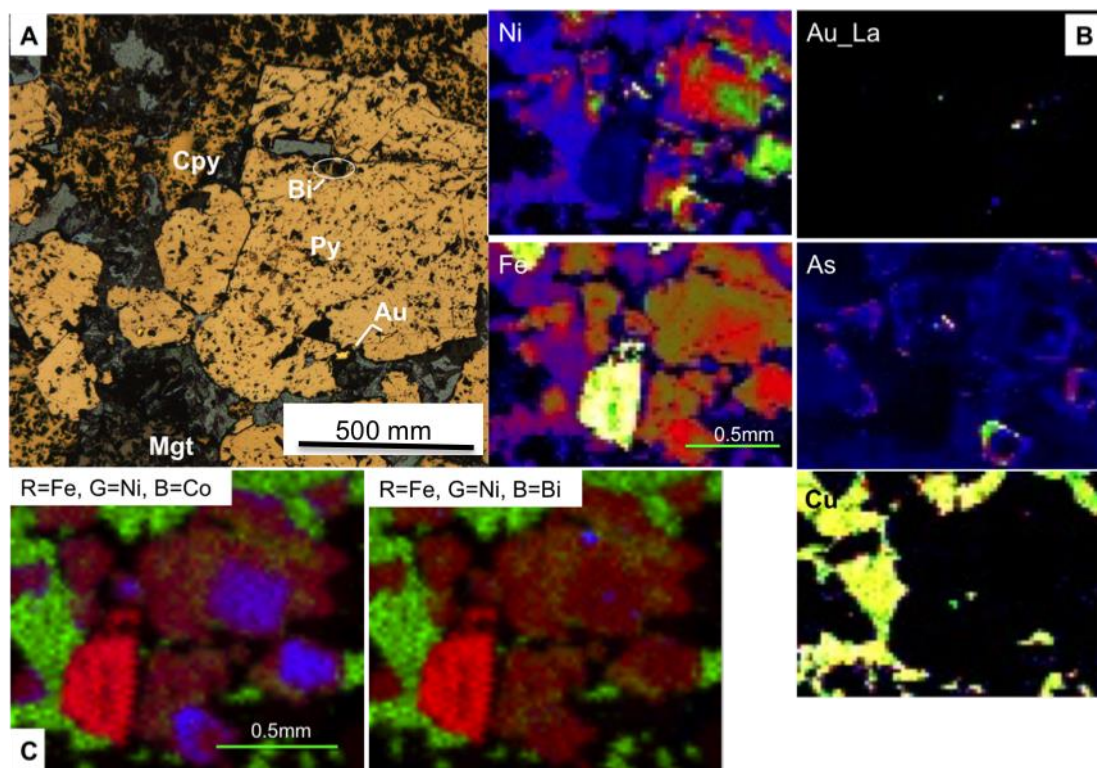


Figure 5.16. (A) Photomicrograph of mineralized pyrite grain surrounded by chalcopyrite in KF15; (B) Corresponding energy maps produced by SR-XRF mapping at ALS in 2014 of Ni K α ; Au L α ; Fe K α ; As K α and Cu K α ; (C) Corresponding RGB images (left: Fe K α ; Ni K α ; Co K α ; right: Fe K α ; Ni K α ; Bi L α) produced by SR-SRF mapping at CHESS in November 2015. “Cpy” = chalcopyrite, “Bi” = bismuth mineral, “Py” = pyrite, “Au” = gold, and “Mgt” = magnetite.

Sample UWO_2015_10 from the 200 Zone contained a ~1 mm wide W-rich mineral (scheelite), as shown in figure 5.17. The RGB image shows that the scheelite is surrounded by chalcopyrite and magnetite. Au mineralization is not hosted within scheelite, however the presence of both scheelite and Au in the same thin section suggests a possible spatial relationship between both mineral phases. This is supported by bulk rock geochemistry, which revealed that four of the twenty mineralized samples contained elevated concentrations of W. Sample UWO_2015_10 had the second highest concentration of W in the dataset.

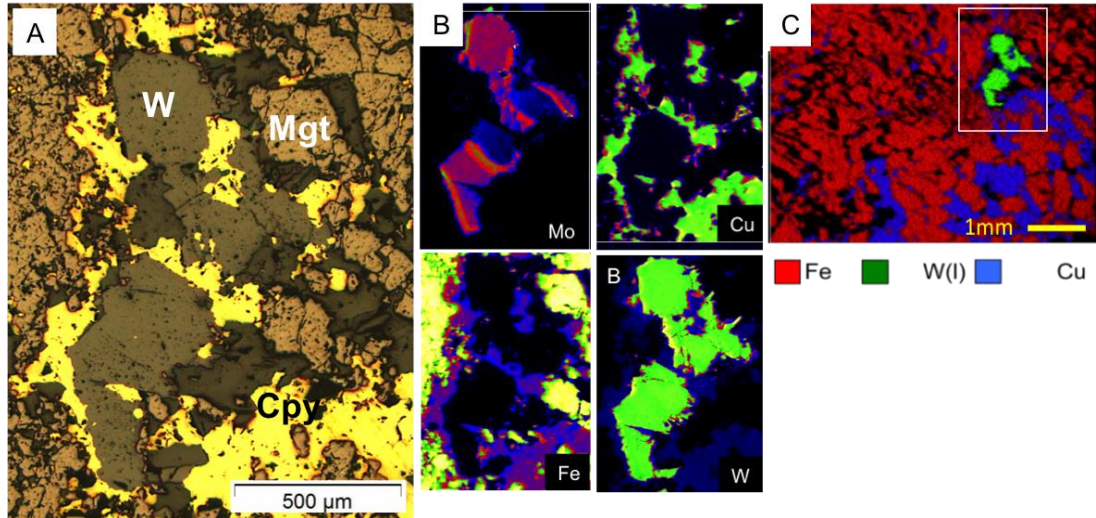


Figure 5.17. RGB image showing the distribution of Fe, W, and Cu in UWO_2015_10 based on synchrotron XRF Mapping from Cornell with a step size of 20µm; B) Trace element XRF maps of W $L\alpha$, Cu $K\alpha$, Fe $K\alpha$, Mo $L\alpha$, and Ag $K\alpha$ collected from APS using a step size of 4 µm. “W” = tungsten mineral, “mgt” = magnetite, and “Cpy” = chalcopyrite.

Thin section KF15 also contained long ilmenite blades within the core of magnetite, as shown in Figure 5.18. Chalcopyrite frequently occurred along with the magnetite and ilmenite clusters.

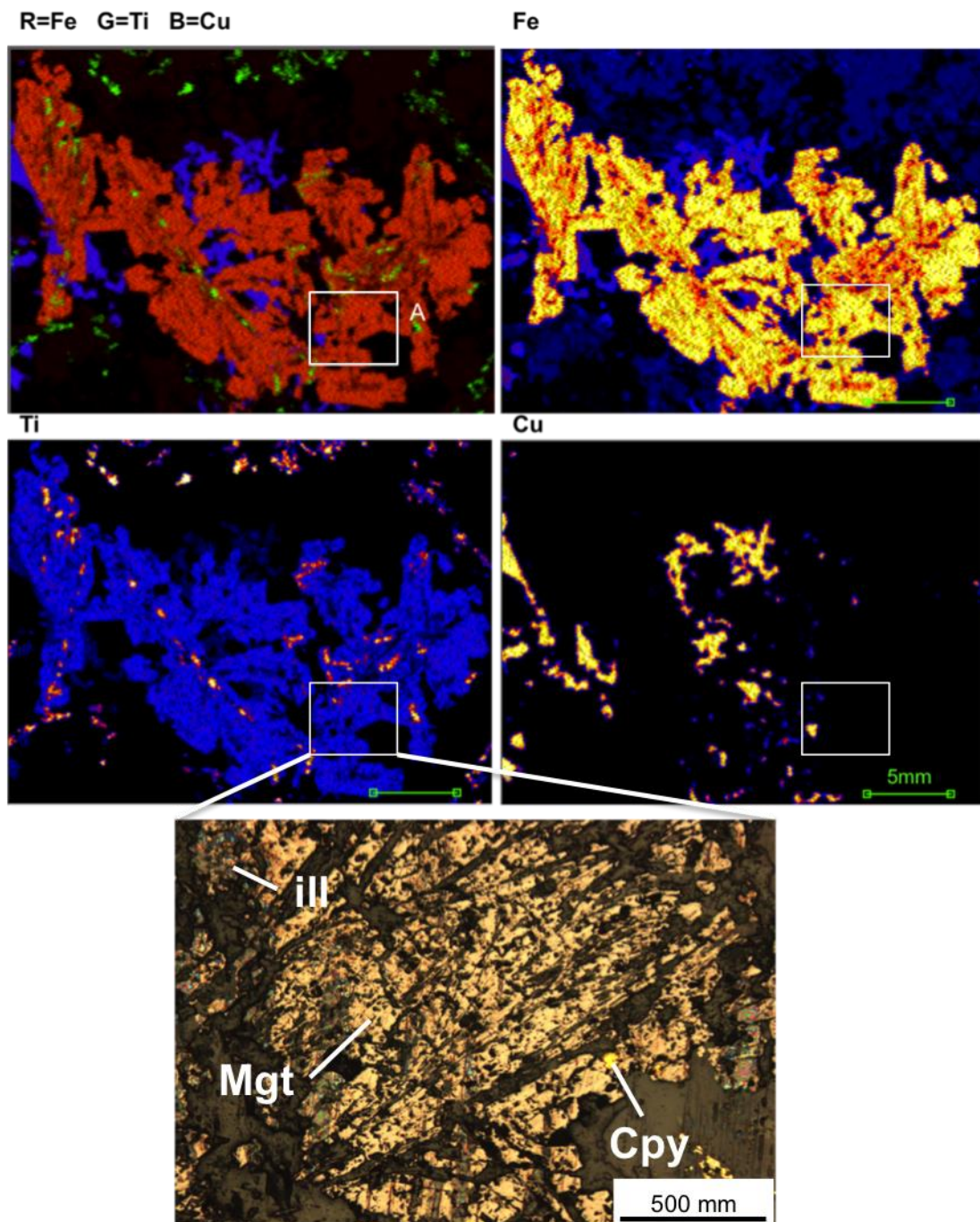


Figure 5.18. (Top) SR-XRF energy maps of KF15 produced at CHESS in 2015 including an RGB map of Fe $K\alpha$, Ti $K\alpha$, and Cu $K\alpha$, as well as separate energy maps of Fe $K\alpha$; Ti $K\alpha$; and Cu $K\alpha$, with a step size of 20 μm at 13.1 keV with the white box on the RGB image corresponding to the area that the photomicrograph (bottom) was taken. “ill” = illite, “mgt” = magnetite, and “Cpy” = chalcopyrite.

5.2.7 Au:Ag Ratio

Geochemical data analyzed in chapter 4 identified a significant trend where samples with a Cu-Au rich signature has a significantly lower Au:Ag ratio than samples with a Mo-Au rich signature. For comparison purposes, Au:Ag ratios were calculated for both Au-rich hot spots (i.e., gold globs) and for larger cm-sized regions containing multiple gold globs to determine if small-scale regions in different thin sections were characterized by the same trend that is observed in bulk rock geochemistry analysis. Data was collected at 31.1 KeV for this portion of the experiment, allowing us to compare Au $L\alpha$ measurements with Ag $K\alpha$ measurements. An example of a typical gold-rich hot spot from which data was collected is shown in Figure 5.19.

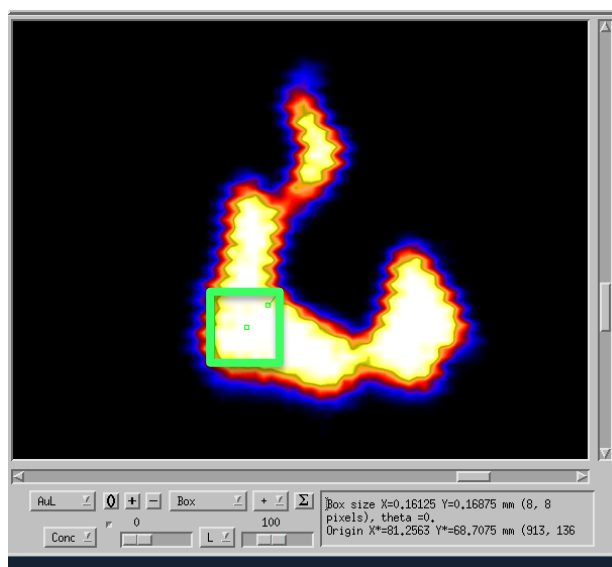


Figure 5.19 XRF trace element map showing a Au hot spot with the green box representing a sample area that was analyzed to determine the Au:Ag ratio in the particular hot spot

The results of Au:Ag ratio calculations are summarized in Table 5.3. This analysis method took advantage of GeoPIXE's ability to obtain quantifiable elemental concentrations by normalizing full spectrum data using standards with known elemental concentrations to calibrate results. For the purposes of this analysis, a Au standard on 6.3 μm mylar was used.

Table 5.3. Synchrotron source x-ray fluorescence microprobe analysis showing the type of Au mineralization and the average Au/Ag ratio in each zone in the deposit. Data from energy scans run at 30.1 keV.

Sample ID	Zone	Type of Mineralization	Au:Ag on Au-rich hot spots			Large Region/ Full Slide Au:Ag
			n spots with Ag	n spots without Ag	Average	
UWO_2015_02	Syenite Breccia	CpyPyMgt	4	1	3.76	4.64
UWO_2015_04	Lower Porphyry East	CpyPyMgt	2	3	7.76	20.45
UWO_2015_05	Upper Porphyry West	CpyPyMgt	2	3	3.41	4.36
UWO_2015_06	Upper Porphyry West	Anhydrite	0	0	low Ag	low Ag
UWO_2015_07	Upper Porphyry West	Anhydrite	0	5	low Ag	low Ag
UWO_2015_08	Q	Mo	0	5	low Ag	65.33
UWO_2015_10	200	CpyPyMgt	2	3	2.16	0.042
UWO_2015_11	Lower Porphyry West	CpyPyMgt	2	3	1.71	0.26
UWO_2015_13	Each Basalt	CpyPyMgt	2	3	2.72	0.091
UWO_2015_14	North Basalt	CpyPyMgt	5	0	3.08	0.056
UWO_2015_15	North Contact	CpyPyMgt	2	3	22.84	0.069
UWO_2015_17	Upper Porphyry East	Mo	0	1	low Ag	low Ag

Overall, synchrotron source x-ray fluorescence microprobe analysis of Au-rich hot spots/ globs revealed the same wide range in Au:Ag ratios as bulk-rock geochemistry with Mo-rich samples having a higher Au:Ag ratio than Cu-rich samples. Au:Ag ratios ranged from very low (more Ag than Au) to very high (too large to report for areas with low Ag). The highest ratios occurred in areas with low Ag, specifically in the Mo-rich samples from the Q Zone, Upper Porphyry East Zone, as well as in the Lower Porphyry East Zone. No ratio could be reported for the anhydrite-bearing Au samples from the Upper Porphyry West Zone because both samples contained little to no Ag, indicating a likely high Au:Ag ratio. Interestingly the sample from the North Contact Zone contained the highest average Au:Ag ratio

for Au-rich hot spots but had a very low average for the entire slide. Sample UWO_2015_15 consists of abundant of free Au. Of the 5 hot-spots tested only 2 contained quantifiable amounts of Ag. If these 2 spots were the only ones to contain Ag, with the rest of the Au-rich regions in the slide containing only Au, then this bias may have caused the unusually high Au:Ag average for the hot spots. The lowest ratios occurred in the North Basalt and the East Basalt Zones, as well as in the 200 Zone.

6 Discussion

6.1 Geochemical analysis of intrusions

In an attempt to classify the rocks into chemically definable groups TAS and plutonic rock classification diagrams were used to plot least altered sample data from DeAgazio (2012) and Feick (2014) as shown in Figure 6.1. It is important to note that although these rocks are called syenites throughout the Kirkland Lake area, none of the intrusive phases from the Upper Beaver Intrusive Complex plot in the syenite field of the classification diagram. These results agree with the findings of Canadian Malartic Corporation geologists, who recognize that the rocks are not syenites, but to be consistent with past work on the property, use camp names for the rocks (M. Masson, personal communication, 2015).

On all three classification diagrams the rock identified as crowded syenite porphyry by CMC geologists plot with a granodiorite to quartz diorite composition. The rock identified as mafic syenite plots with a monzodiorite, quartz monzodiorite, and with a dioritic to gabbroic composition depending on the diagram used. The porphyritic variety of mafic syenite plots with a granodiorite, quartz monzodiorite, and quartz diorite to diorite depending on the diagram used. Finally, the spotted feldspar porphyry plots with a dioritic composition on both TAS diagrams, and a tonalitic composition on the Plutonic Rock Classification diagram. A summary of these results are presented in Table 5.4.

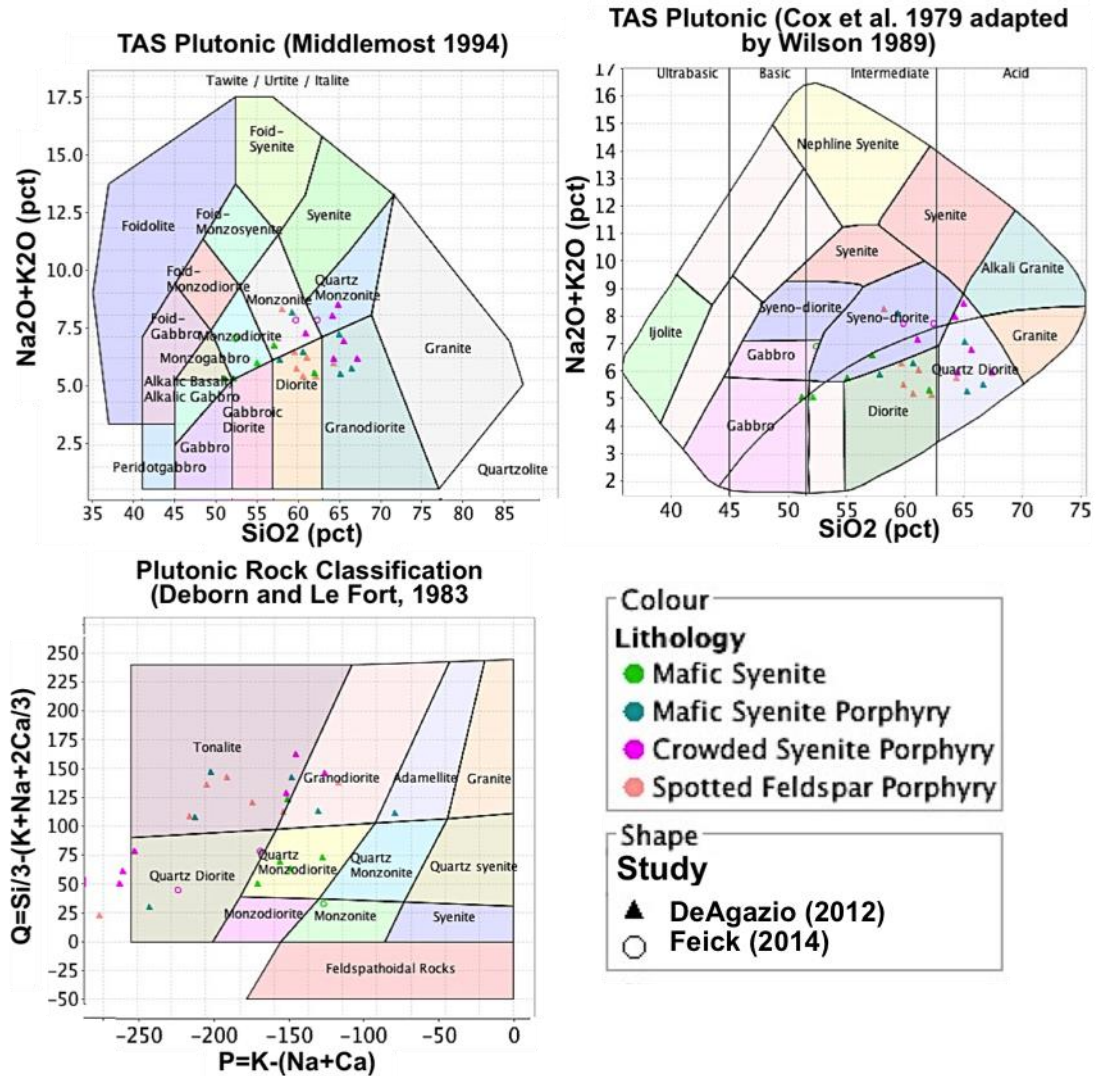


Figure 6.1. Classification diagrams including TAS Plutonic diagrams by Middlemost, (1994) and Cox et al., (1979) as well as plutonic Rock Classification diagram by Debon and La Fort, (1983) (parameters calculated as oxide percentages converted to milliequivalents), with the composition of the four main members of the Upper Beaver Intrusive Complex. Data points are colored based on their lithology. Geochemical data provided by past thesis projects on the Upper Beaver deposit by DeAgazio (2012) and Feick (2014).

Geochemical data from Feick (2014) and DeAgazio (2012) were used to calculate CIPW normative values. Calculated values were then plotted on a QAP diagram to confirm classification diagram results, as shown in Figure 6.2. Calculated CIPW normative values are included in Appendix F.

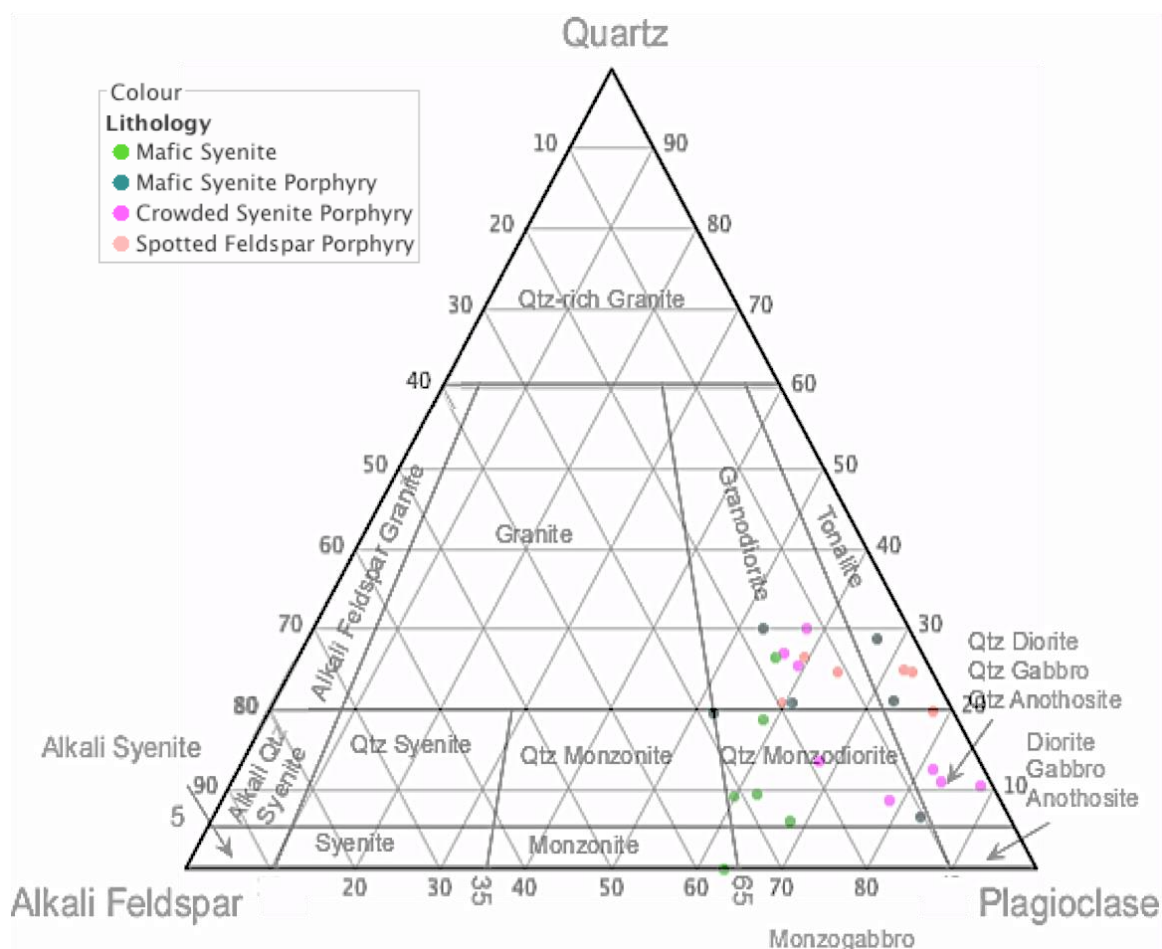


Figure 6.2. QAP classification diagram showing CIPW normative values for four main members of the Upper Beaver Intrusive Complex. Data points are colored based on their lithology. Geochemical data provided by past thesis projects on the Upper Beaver deposit by DeAgazio (2012) and Feick (2014).

Results of the normative values plotted on the QAP diagram agree strongly with those from the classification diagrams. Crowded syenite porphyry plots with a composition between granodiorite to quartz diorite. Mafic syenite plots with a quartz monzodiorite composition, while mafic syenite porphyry plots with the composition of granodiorite or tonalite. Spotted feldspar porphyry however, plots with a composition between granodiorite and tonalite, which is different than the results from the classification diagrams where it plotted with a dioritic composition. A summary of where each rock type plots on the classification diagrams is provided in Table 5.4.

Table 5.4. Summary of where each of the main lithologies in the Upper Beaver Intrusive Complex plots on various classification diagrams and proposed names for each rock based on the results of this study

CMC Rock Type	Mafic Syenite	Mafic Syenite Porphyry	Crowded Syenite Porphyry	Spotted Feldspar Porphyry
TAS Plutonic (Middlemost 1994)	Monzogabbro, Monzodiorite, Monzonite	Diorite, Granodiorite	Monzonite, Quartz monzonite, Granodiorite	Diorite
TAS Plutonic (Cox et al. 1979 adapted by Wilson 1989)	Gabbro, Syenodiorite, Diorite	Diorite, Syenodiorite, Quartz diorite	Syeno-diorite, Quartz diorite	Diorite
Plutonic Rock Classification (Debon and Le Fort, 1983)	Quartz monzodiorite	Tonalite, Granodiorite	Quartz diorite, Granodiorite	Tonalite
QAP Classification based on calculated CIPW Normative Values	Quartz monzodiorite, Granodiorite	Granodiorite, Tonalite	Quartz Diorite, Quartz monzodiorite, Granodiorite	Granodiorite, Tonalite
Proposed Name based on results of this study	Quartz monzodiorite	Porphyritic granodiorite	Crowded Porphyritic quartz diorite/ granodiorite	Spotted diorite

6.1.1 Evaluation of names

Trends revealed by REE analysis of members of the Upper Beaver Intrusive Complex (section 3.2.3-3.2.4) indicated that intrusive phases most likely have a syenite-diorite composition. However, plotted calculated CIPW normative values indicate that the rocks do not plot with that composition. Mafic syenite plots with a quartz monzodiorite composition, however Sutcliffe et al., (1993) identifies that the diorite-monzodiorite suite of samples in the Abitibi are typically older than 2.7 Ga and age dating by Talisker (2014c) identifies that mafic syenite in the Upper Beaver deposit is younger than 2.7 Ga. Further, samples of mafic syenite porphyry plot with a granodioritic composition, although in section 3.2.3-3.2.4, REE trends, namely the Nb-Ta trough as well as the lack of an Eu anomaly and a La/Yb ratio of roughly 27.2, indicate that the rock is not a granodiorite. Additionally, local granodiorites range in age between roughly 2.703-2.690 Ga (Jensen, 1985; Jackson and Fyon, 1991; Mortensen, 1993; Feng and Kerrich, 1990) while intrusions in the Upper Beaver Intrusive Complex range in age from 2685-2665 ± 3.5 Ma (Talisker, 2014c). In addition, local intrusions, including Lebel, Otto, and Murdock Creek Stocks contain intrusives identified as syenite and mafic syenite (Corfu, 1993; Corfu, 1989; Wilkinson et al., 1999), are a similar age to intrusions in the Upper Beaver Intrusive Complex (Corfu, 1993; Corfu, 1989; Wilkinson et al., 1999), and are classified as

members of the syenite-diorite suite proposed by Sutcliffe et al., (1993). Overall results suggest that samples from DeAgazio (2012) and Feick (2014) are relatively enriched in quartz compared to original unaltered equivalents.

The discrepancy between expected lithological names and the names proposed by discrimination diagrams and calculated CIPW normative values likely results from alteration. All of the rocks in the Upper Beaver Intrusive Complex are altered to some extent (Bernier and Cole, 2012; DeAgazio, 2012) with alteration being centered along the southern margin of the intrusive complex, especially along its sheared margin (Bernier and Cole, 2012). It is present in all lithologies and includes silica, carbonates (ankerite and calcite), sericite and muscovite, albite, K-feldspar, epidote, chlorite, hematite, magnetite, actinolite, and sulphide minerals. Au mineralization in particular is most closely associated with widespread and pervasive magnetite-feldspar-actinolite-epidote-carbonate-sericite alteration (Bernier and Cole, 2012).

Samples from DeAgazio (2012) and Feick (2014) were also plotted on an alteration box plot to identify alteration trends, as shown in Figure 6.3. Samples plotted with a wide range in Chlorite-carbonate-pyrite index (CCPI) and Ishikawa alteration index (AI) values indicating variable alteration by different alteration minerals, although most rocks plot in the least altered boxes. The least altered boxes that samples plot in agree with where samples plotted on the Th-Co discrimination diagram with crowded syenite porphyry and mafic syenite porphyry plotting between rhyolite and dacite, and mafic syenite plotting with a least altered basaltic composition. Conversely, spotted feldspar porphyry plotted with a dacitic composition, although the Th-Co discrimination diagram identified that it should plot with a composition similar to a basaltic andesite or andesite.

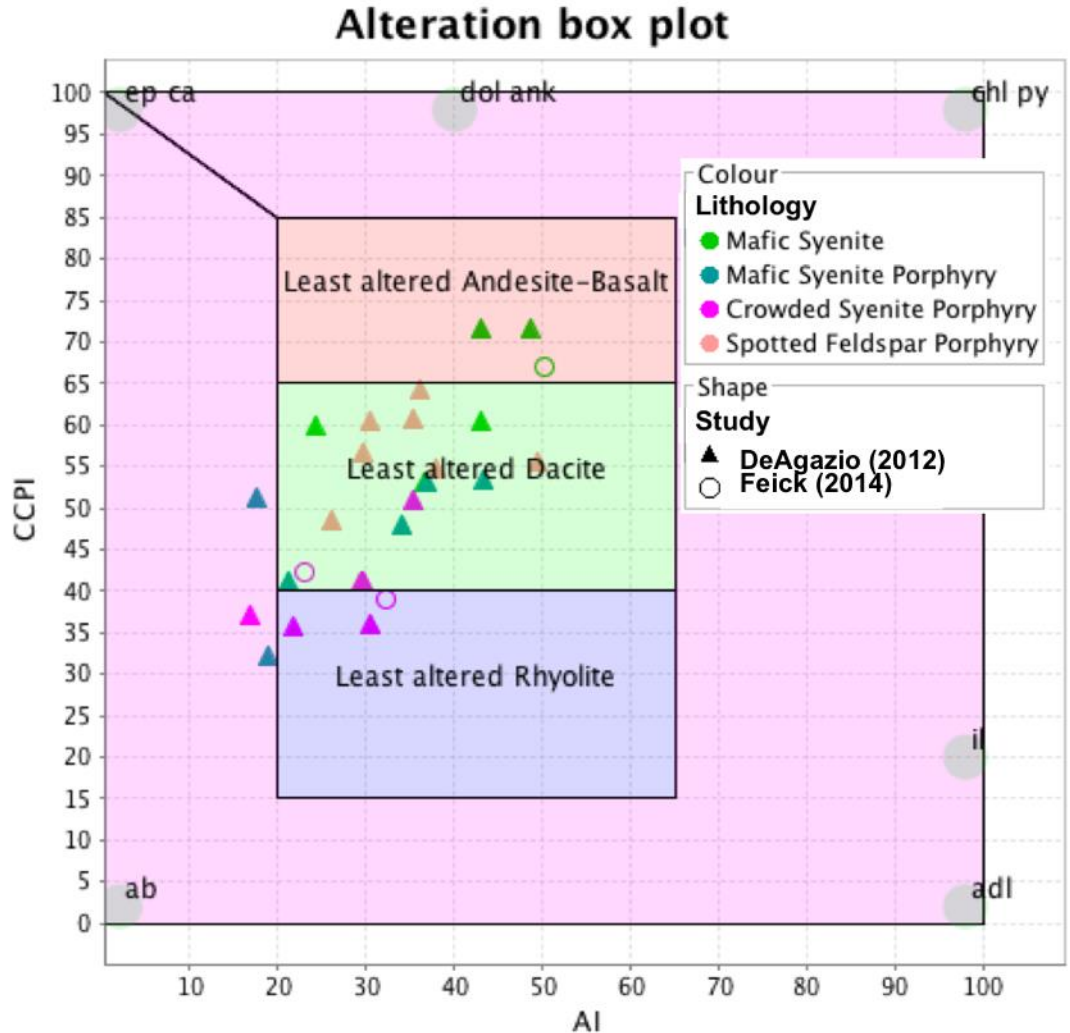


Figure 6.3. Alteration box plot based on the Ishikawa alteration index (AI) and Chlorite-carbonate-pyrite index (CCPI) as suggested by Large et al., (2001) showing alteration trends among select lithologies from the Upper Beaver Intrusive Complex. Data points are colored based on their lithology. Geochemical data provided by DeAgazio (2012) and Feick (2014). “ep ca” = Epidote and calcite, “dol ank” = dolomite and ankerite, “chl py” = chlorite and pyrite, “ab” = albite, “il” = sericite; and “adl” = andalucite.

6.1.2 Interpretation of Less Common Intrusives in the Upper Beaver Intrusive Complex

Bulk rock major oxide geochemical analysis was performed on the unusual intrusions to compare their geochemical composition to the main intrusions in the Upper Beaver Intrusive Complex. Bulk rock geochemistry was also used to calculate CIPW normative values for comparison to the CIPW normative values of the main

intrusive phases in the complex. The results of this comparison are presented in Figure 6.4, and discussed in detail below.

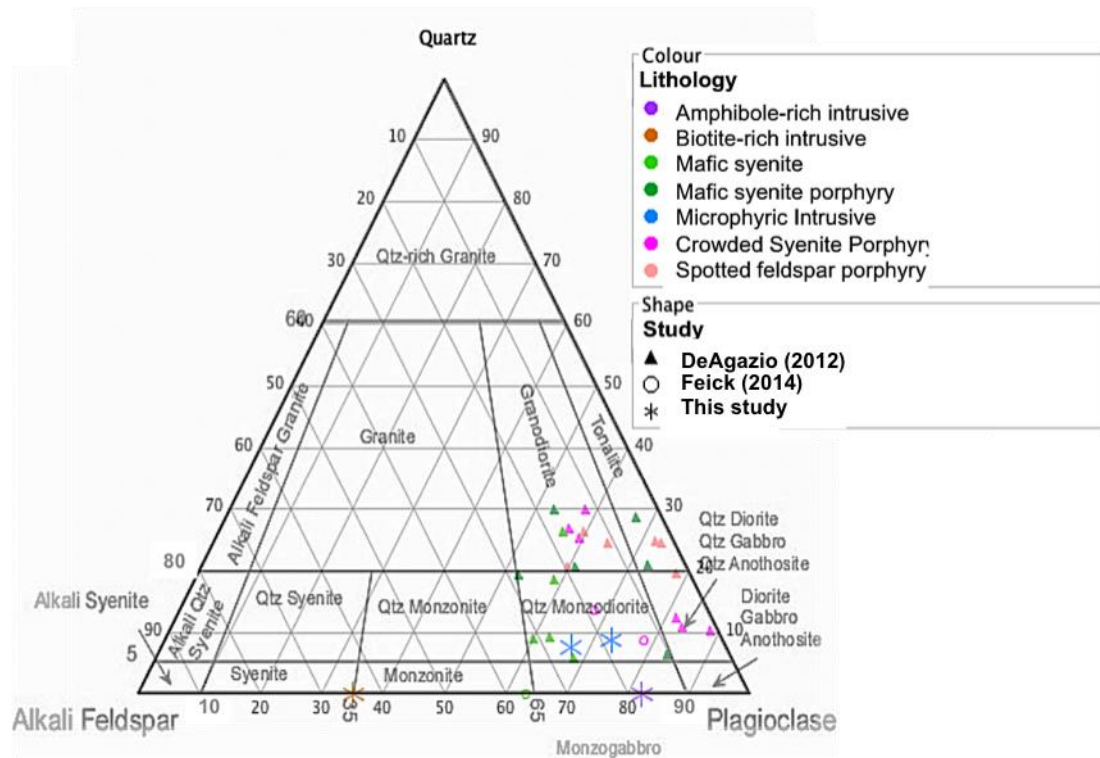


Figure 6.4. QAP classification diagram showing CIPW normative values for select lithology in the Upper Beaver Intrusive Complex. Data points are colored based on their lithology. Geochemical data includes results from this study and data provided by past thesis projects on the Upper Beaver deposit by DeAgazio (2012) and Feick (2014).

Bulk rock geochemistry was also plotted on an alteration box plot, as shown in Figure 6.5. The alteration box plot, as developed by Large et al., (2001) is used to characterize different alteration trends, namely as a way to measure the intensity of sericite, chlorite, carbonate, and pyrite replacement of sodic feldspars and glass, during hydrothermal alteration proximal to volcanic-hosted massive sulphide-related orebodies. This is an important step when trying to assess if the distinctive mineralogy of the three intrusions is the result of alteration (and in particular which alteration assemblage), or a primary feature.

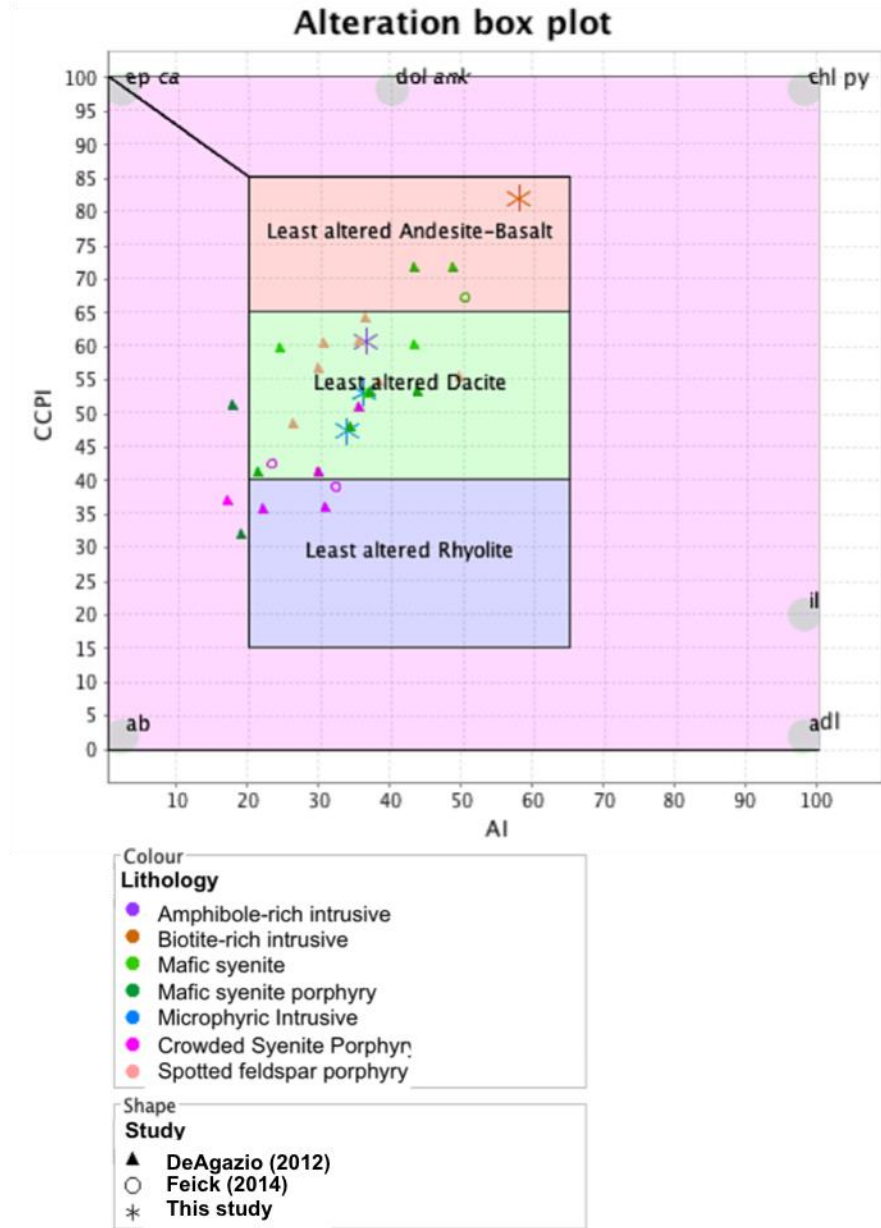


Figure 6.5. Alteration box plot based on the Ishikawa alteration index (AI) and Chlorite-carbonate-pyrite index (CCPI) as suggested by Large et al., (2001) showing alteration trends among select lithologies from the Upper Beaver Intrusive Complex. Data points are colored based on their lithology. Geochemical data provided by past thesis projects on the Upper Beaver deposit by DeAgazio (2012) and Feick (2014).

6.1.2.1 Biotite- and amphibole-rich Intrusives

Both the biotite- and amphibole-rich intrusives have a distinctive mineralogy in the Upper Beaver deposit, characterized by the presence of coarse-grained biotite

with amphiboles in the biotite-rich diorite and the presence of coarse porphyritic amphiboles in the amphibole-rich diorite. Based on petrographic, microprobe, and geochemical analyses it is most likely that the distinctive mineralogy reflects a primary igneous mineralogy that has been subsequently metamorphosed as opposed to an alteration feature. The amphibole-rich intrusive contains amphiboles that range from Fe-rich magnesio-hornblende, to actinolitic hornblende, to actinolite and ferrian-tremolite to Mg-rich actinolite based on the classification of amphiboles proposed by Leake (1978) using WDS microprobe data. Additional alteration minerals include variable amounts of relatively pure albite and K-spar, as well as sericite, chlorite, and late epidote, hematite, and calcite.

Structural evidence also supports this conclusion, namely: (1) the sharp upper contact with the adjacent mafic syenite intrusion as well as (2) the presence of amphibole-rich diorite xenoliths and very coarse-grained amphibole xenocrysts in the adjacent mafic syenite intrusion; and (3) the chilled lower contact between the amphibole-rich intrusion and felsic syenite. Geochemical analysis of the amphibole-rich intrusive, shown in Figure 6.4, identifies that the rock plots as a monzogabbro due to its low quartz content, however due to the abundance of alteration minerals and the mobility of major oxide elements during alteration, this naming scheme likely does not accurately identify the parent rock. Samples were also plotted on an alteration box plot, as described by Large et al., (2001) to compare with relatively unaltered intrusive rocks in the Upper Beaver Intrusive Complex (Figure 6.5). The rock plots in the relatively unaltered basalt portion of the alteration box plot, similar to unaltered samples of mafic syenite, however it trends more towards chlorite pyrite alteration than all other sampled intrusive rocks in the deposit. Chlorite and sericite alteration were observed petrographically and through EDS microprobe analysis.

Similarly, the distinctive mineralogy of the biotite-rich intrusive is likely also a primary feature as opposed to an alteration/ metasomatic feature. Microprobe analysis revealed that the coarse-grained biotite is relatively fresh with minor amounts of alteration (K-spar, albite, hematite and magnetite). Additional alteration minerals in the rocks include variable amounts of sericite and chlorite. Results from

plotting the composition of the sample from the biotite-rich intrusive on the alteration box plot defined by Large et al., (2001) (Figure 6.5) indicates that it has higher AI and CCPI values than any other intrusive phase analyzed, consistent with strong chlorite alteration. However, strong chlorite alteration is not consistent with petrographic or microprobe EDS analysis. Similar to the amphibole-rich intrusive, the biotite-rich intrusive contains significantly less quartz than the other intrusions in the deposit (Figure 6.4). This low quartz content combined with the rocks abundant K-spar results in the rock plotting between a syenite and a monzonite, however, due to the alteration in the rock and the mobility of major elements, this classification is likely does not accurately represent the parent rock.

6.1.2.2 Microphyric Intrusive

Structural, textural, and geochemical evidence indicate that the microphyric texture is the result of alteration of portions of the mafic syenite intrusive. Structural evidence includes the gradational contacts that the microphyric unit has with adjacent mafic syenite intrusives. Textural evidence includes the subparallel alignment of phenocrysts with foliation in sample UWO_2015_28, as well as the abundance of alteration minerals, i.e., the completely pseudomorphically replaced amphiboles and the abundance of inter-grown quartz and albite in the groundmass in both thin sections.

Bulk rock geochemistry was used to calculate CIPW normalized values, which were then plotted on a QAP diagram to determine the distinctive mineralogy of the rock is an alteration feature or a primary feature. The microphyric intrusive plots with the composition of a mafic syenite, as shown in Figure 6.4.

Bulk rock geochemistry for the two microphyric samples were also plotted with other intrusive rocks from the Upper Beaver deposit on an alteration box plot, as developed by Large et al., (2001) to determine if the distinctive mineralogy is the result of a particular alteration assemblage. Results identify that the microphyric mafic syenite intrusive is characterized by lower Chlorite-carbonate-pyrite index (CCPI) and Ishikawa alteration index (AI) values relative to samples of microphyric

diorite, indicating a trend towards albitic alteration (Figure 6.5) associated with the development of the microphyric texture. These result agrees with petrographic and microprobe analyses, which both identified that the rock is strongly albitized.

6.1.3 Key Characteristics of Sedimentary Sequence and Breccia Lens

6.1.3.1 Interpretation and significance of the Isolated Sedimentary Sequence

The isolated sedimentary sequence provides valuable information about the depositional environment of the Blake River Assemblage as well as providing information regarding the deposits orientation. The lithologies and the relatively horizontal geometry of the Upper Beaver isolated sedimentary sequence fit the description by Thurston et al., (2008) of a sedimentary interface zone in the Archean Abitibi Belt. Thurston et al., (2008) describes these zones as being discontinuously deposited during localized gaps of 2 to 27 million years between volcanic episodes in the Abitibi and consist of up to 350 m of chemical and minor clastic sedimentary rocks, including: iron formation; chert breccia; heterolithic debris flow; sandstone and/or argillite; and conglomerate. Thurston et al., (2008) also suggests that these zones develop at the top of mafic to felsic volcanic cycles, or at geochemical transitions in volcanic units of greenstone belts worldwide. This fits with interpretations by Dimroth et al., (1982; 1983) and Thurston et al., (2008) that the Blake River Assemblage consists of over-lapping shield volcanoes with local lenses of sediments intercalated with or capping volcanic cycles. The presence of graphitic argillite at the bottom of the sequence in the Upper Beaver deposit indicates that it likely developed at a geochemical discontinuity in the volcanic stratigraphy (Thurston et al., 2008). This interpretation of the sedimentary sequence accounts for why the sediments are horizontal with younging indicators pointing up as opposed to steeply dipping like the local Tisdale Assemblage and accounts for the lack of thrust features in the unit, which would be expected if the unit was related to Tisdale sedimentation. The orientation of the sequence also suggests that the local stratigraphy has not been overturned.

Variations in the thickness of the sedimentary interface zone and the abundance of cherty sedimentary rocks and graphitic argillite, suggest that both the condensed section model, as described by Catuneau (2002) and the rock-water exchange model, as described by Krapez et al., (2003), respectively likely contributed to the formation of the Upper Beaver sedimentary sequence. Both models involve negligible rates of sedimentation on the near-shore, the shelf, or the abyssal environment, which will affect the lithologies produced. Based on the lithologies that make up the sequence in the Upper Beaver deposit, it likely dominantly developed in a basinal setting as opposed to a deep marine setting due to (1) the presence of both iron formation marine units and associated terrigenous sedimentary rocks, (2) the presence of thin-bedded turbidities which are typically deposited in distal settings, (3) the presence of conglomerates suggesting multiple cycles of downslope movement of previously deposited iron formation, and (4) a lack of shale units typical of deep-marine settings. This result agrees with studies by Roberts and Morris (1982) on the geological setting of the Upper Beaver deposit, which also concluded that the sedimentary sequence most likely formed in a basinal environment. Roberts and Morris (1982) identify that the sediments were most likely sourced from the east, based on grain size and unit thicknesses, however more extensive studies on recent drilling is needed to confirm this source.

Siever (1992) and Thurston et al., (2008) have proposed two alternative mechanisms for the formation of cherty sediments in sedimentary interface zones. Siever, (1992) proposed that they develop from the interaction of silica-saturated seawater and the rock at low temperatures, where the rock is replaced from the top down, while Thurston et al., (2008) argues that they formed by the interaction of silica-and metal rich seawater circulating through sub adjacent volcanic rocks thereby replacing the existing units. It is likely that a combination of these features contributed to the formation of Upper Beaver's sedimentary interface zone.

6.1.3.2 Interpretation and Significance of Upper Beaver's Breccia Lens

Upper Beaver's breccia lens provides information about periodic pressure releases in the deposit. Textures within the two least-brecciated samples indicate that there was likely an initial magmatic breccia that prior to the main stage of brecciation. Magmatic brecciated fragments were identified in two relatively "unbrecciated" samples taken from the deposit through color contrasts in the rock, without the accompanying matrix of chlorite, magnetite, quartz, and calcite that define the brecciated fragments deeper in the lens. Magmatic breccias are produced by the mechanical fragmentation and incorporation of wall rocks by intrusive magma and that they typically consist of angular to sub-rounded fragments cemented by an igneous matrix (Sillitoe, 1985). This is consistent with the shape of the brecciated fragments in analyzed samples. Permeability contrasts between the magmatic breccias and their unbrecciated counterparts could have contributed to the concentration of hydrothermal fluids from subsequent pressure releases along the pre-existing breccias structure, producing hydrothermal-magmatic breccia. Geochemical analysis of the two sets of progressively more brecciated samples compared to available data for the relatively unaltered igneous intrusion is consistent with the strong chlorite-pyrite and epidote-calcite alteration observed in samples analyzed and in the representative breccia samples from the deposit observed on site.

Textures in the strongly brecciated rock indicate that the Upper Beaver breccia lens most likely formed in response to high-pressure fluctuations with abundant associated fluids. These textures include fluid-assisted brecciation, wear abrasion, and corrosive wear, as described by Jébrak, (1997). Evidence of fluid-rock interactions, which typically result from pressure variations in the system, can be observed in almost all strongly altered of the representative samples from the breccia lens. This process occurs as a result of the in-situ fracturing of larger clasts into smaller clasts creating small closely fitting angular clasts (Jébrak, 1997). Most of the breccia samples from the Upper Beaver deposit showed evidence of repeated episodes of this style of brecciation, with larger clasts broken into smaller fragments,

which are in turn also broken. Jébrak (1997) suggests that this is a common characteristic of breccias in ore deposits. Futher, Laznicka, (2006) identifies that breccias in ore deposits typically have a steep pipe-like to irregular shape and gradually fade with depth as a result of increase clast-matrix/cement ratios. The steep orientation of the breccia lens in the Upper Beaver deposit also supports the evidence from the isolated sedimentary sequence that suggests that the deposit is upright and has not been significantly reoriented.

The large range in particle size and the abundance of well rounded breccia fragments observed in almost all of the representative samples from the Upper Beaver deposit is particularly characteristic of wear abrasion brecciation according to criteria proposed by Jébrak, (1997). This brecciation process typically involves the rotation of breccia fragments in surrounding media (Jébrak, 1997). Jébrak (1997) suggests that dissolution and re-crystallization of the rock under pressure also adds to the textural complexity of the boundaries of the fragments and contributes to the rounded and sometimes gradual clast boundaries. Lastly, the strong alteration of both the clasts and the matrix indicates that corrosive wear has occurred, as described by Jébrak, (1997). They suggest that this process is intimately related to the degree of equilibrium between the composition of both the fluid and the rocks.

6.2 Association Between Host rocks and Mineralization

The assay database provided by CMC, which consisted of 157,580 samples was filtered to contain only samples from major lithologies with a grade over 2 g/t. Analysis of the remaining set of data confirmed that Au and Cu mineralization can occur in all of the main lithologies in the Upper Beaver deposit. Additionally, analysis confirmed that although gold and copper are recognized to occur together in the deposit, they are also recognized to frequently also occur separately. Lithologies with the highest mean Au grade largely include members of the Upper Beaver Intrusive Complex, such as crowded syenite porphyry and mafic syenite, as well as brecciated mafic syenite and feldspar porphyry. Comparatively, lithologies with the highest mean Cu grade on the other hand include brecciated mafic syenite, cherty sedimentary rocks, and brecciated Blake River basalts.

The spatial association between members of the Upper Beaver Intrusive Complex, namely crowded syenite porphyry intrusions and gold mineralization has long been recognized. Three prominent syenite porphyry dikes of the Upper Beaver Intrusive complex occur within the mine workings of the Upper Beaver mine. They have historically, and continue to be, important marker units for geological interpretation with gold grades increasing along, adjacent to, or just outside of the intrusive contact (Bernier and Cole, 2012). To detect more subtle changes in ore mineralization style more geochemical indicators are necessary.

To constrain the appropriate timing of Au mineralization in the deposit Talisker (2014c) performed age dating on different intrusive rocks in the deposit. They defined four main intrusive events: (1) Pre-mineral intrusive event associated with the emplacement of felsic syenite at 2683 ± 1.5 Ma; (2) Coeval intrusive event with mineralization associated with the emplacement of crowded syenite porphyry at 2671.9 ± 1.8 Ma; (3) Late intrusive event (relative to mineralization) associated with the emplacement of spotted feldspar porphyry intrusives at $2670.7 \text{ Ma} \pm 3.5 \text{ Ma}$; and (4) Post mineral event associated with the emplacement of diabase at 2667.3 ± 1.8 Ma.

Samples were taken from the unusual intrusions in the deposit in order to better define the lithologies and to draw conclusions on their genesis and their relationship to mineralization. Analysis of the sample taken from the amphibole-rich intrusive and hand-sample observations of the intrusion performed on site from drill core indicates that it intruded early relative to mafic syenite and late relative to felsic syenite. Structural evidence includes: (1) the sharp upper contact with the adjacent mafic syenite intrusion as well as (2) the presence of amphibole-rich diorite xenoliths and very coarse-grained amphibole xenocrysts in the adjacent mafic syenite intrusion; and (3) the chilled lower contact between the amphibole-rich intrusion and felsic syenite. This relative timing of mineralization indicates that the amphibole-rich intrusive has the potential to host Au and Cu mineralization, since the mafic syenite intrusive intruded prior to the crowded syenite intrusives (Bernier and Cole, 2012). However, assays and hand-sample observation have not yet revealed the presence of

mineralization within the amphibole-rich intrusive. Analysis of the biotite-rich intrusive margins was inconclusive and the relative age of the unit cannot be identified without further analysis. Assays and hand-sample observations of the biotite-rich intrusive however, indicate that this unit also lacks Au and Cu mineralization.

Structural, textural, and geochemical evidence indicates that the microphyric texture of the microphyric intrusive is the result of strong albite alteration of mafic syenite. Conclusions on the age of alteration of the unit cannot be made without further analysis. However, assays identify that both mafic syenite and microphyric mafic syenite can contain Au and Cu mineralization.

Conversely, structural evidence including younging indicators within the sedimentary interface zone and surrounding basalts, and the orientation of the zone indicate that the interface zone is likely older than any of the intrusive phases in the deposit, predating mineralization. Although the sedimentary interface zone is older than mineralization, studies by Feick (2014) indicate that it may have acted as a relatively impermeable lower boundary and assisted with concentrating mineralization in the overlying basalts, contributing to the formation of the South Contact Zone by promoting prolonged fluid circulation. Both Au and Cu mineralization can occur within the sedimentary interface zone in varying amounts.

Au and Cu mineralization also occur within a steeply dipping breccia lens in the Upper Beaver deposit. Textures indicate that the breccia originated as a magmatic breccia which then developed into a hydrothermal breccia. Because the breccia texture overprints portions of the mafic syenite and mafic syenite porphyry intrusions, the hydrothermal brecciation event must have occurred late or after the intrusions occurred. Further, the presence of Au and Cu mineralization within portions of the hydrothermal breccia lens suggest that Au and Cu mineralization occurred late or after the brecciation event. Three deposits that are similar in terms of mineralization signature (i.e., abundant Au and Cu mineralization) to the Upper Beaver deposit in the Abitibi gold deposits are the Hollinger-McIntyre mine in

Timmins, the Troilus mine near Chibougamu, and the Côté gold deposit near Gogama. In all three deposits, Cu-Au mineralization is centered on magmatic-hydrothermal breccia bodies and their associated intrusive bodies (felsic porphyry, metadiorite, and diorite/ tonalite, respectively for the three deposits) (Mason and Melnik, 1986; Carles, 2000; Katz et al., 2015). The intimate relationship between breccias and mineralization suggests that breccias in Archean Cu-Au deposits can play a critical role in concentrating ore mineralization and may be a useful exploration vector. The breccia lens in the Upper Beaver deposit also hosts two isolated lenses of mineralization called the 200 Zone and the Syenite Breccia Zone. However, in the Upper Beaver deposit mineralization is concentrated outside the lens, largely along the contacts of crowded syenite porphyry.

6.3 Geochemistry of Mineralization

Most studies on Au mineralization in the Abitibi greenstone belt utilize bivariate analyses to identify trace elements that correlate with mineralization. Reviews on ore deposit models and classification systems, such as reviews by Groves et al., (1998), Lang and Baker, (2001), Robert, (2001), Goldfarb et al., (2005), Dubé et al., (2007), Robert et al., (2007), Richerds (2011), and Dubé et al, (2015), typically use the results from these studies to propose standard arrays of trace elements that are associated with mineralization for each deposit type. However, bivariate analysis of Au and Cu assays from the Upper Beaver deposit fail to recognize subtle changes in the style of mineralization, which is particularly necessary in the Upper Beaver deposit since it contains many different vein types as well as disseminated mineralization. Recently studies have also focused on using multielement statistical analysis of mass amounts of bulk rock data from many different deposits to classify different deposit types based on geochemical signature. An example of such a study includes a study by Grunsky et al., (2015), which presented a new approach to characterize and classify mineral deposits using whole rock geochemistry. Their study was based on statistical analysis (centered-log ratio transformations, principal component analysis, multi-dimensional scaling, and linear discriminant analysis) of 24 elements (Fe, Co, Ni, Re, Pd, Pt, Cu, Ag, Au, Zn, Cd, In, Tl, Pb, Hg, As, Sb, Bi,

Te, Mo, W, Sn La and U) from various mineral deposits, including many deposits from the Abitibi. The study required that all samples must first be normalized using Ore Samples Normalized to Average Crustal Abundance (OSNACA) methods to properly characterize ore samples based on “enrichment vectors”.

This study aims to evaluate the mineralization signature of the Upper Beaver deposit in a different way. By using EDA, namely cluster and principal component analysis methods, different styles of mineralization and associated trace element exploration vectors can be determined for the Upper Beaver deposit. The ultimate goal of EDA analysis was to detect multivariate trends or structures in the data that standard methods lack the ability to identify, in order to provide insight into the geochemical/geological processes that formed the deposit. EDA was supplemented by synchrotron source XRF mapping to identify which mineral phases were responsible for the different trace element associations with Au mineralization. Combining EDA and synchrotron-source XRF mapping has distinct advantages over traditional methods of assessing trace element associations with mineralization, namely EDA identifies more subtle geochemical signatures, and SR-XRF identifies the mineral phases responsible for these trends, which may not have been identifiable using standard methods.

Spearman rank coefficients of the entire geochemical dataset indicates that Au correlates moderately well with Ag, Mo, Cu, and S and is weakly correlated with Bi, W, Ni, Se and Sb. Cu correlates moderately well with Ag, Au, S, and Co, and is weakly correlated with Bi, Ni, Se, Te, As, Sb, and W. Trace element correlations with Au in mineralized zones is more variable. In general, Au has a relatively consistent moderate correlation with Ag, and a moderate to strong correlation with Cu, Mo, and S in all zones, and correlations with As, Co, Ni, Sb, Se, Te, V, W, and Zn vary between zones. The Au:Ag ratio in the deposit is also variable throughout the deposit with an average of 24. While most mineralization in the deposit contains variable amounts of Ag, there is an additional group that completely lacks Ag and is strongly Cu depleted relative to mineralization in the deposit.

Overall cluster analysis and PCA identified two geochemically distinct groups of Au mineralization. EDA revealed that the Mo-rich group had a distinctly higher Au:Ag ratio and the Cu-rich group had a distinctly lower Au:Ag ratio. This trend was also supported by the results of SR-XRF microprobe analysis of Au-rich hot spots/Au-globs, which revealed that the Mo-rich samples have a higher Au:Ag ratio (Au:Ag <10:1) than Cu-rich samples (Au:Ag >10:1). Au:Ag ratios ranged from very low (more Ag than Au) to very high (too large to report for areas with low Ag).

The two groups of mineralization also had distinct trace element associations. The Mo-rich group was associated with enrichments in W and relative depletions in As, and the Cu-rich group was associated with enriched U. Bi, Te, and Se correlated with both groups, depending on analysis methods used.

Although W was not identified to be associated with Cu-rich mineralization using EDA, one sample that was characterized by this style of mineralization contained scheelite, as identified by SR-XRF. No Mo-rich samples contained scheelite however this may be due to the limited number of Mo-enriched samples analyzed by SR-XRF. Bulk rock geochemistry supports these findings as all three Mo-enriched samples lack enrichments in W.

SR-XRF analysis also identified a close spatial and temporal association between Bi and Au in the Cu-enriched style of mineralization, with Au locally hosted directly within a bismuth sulphide mineral in one sample. No Mo-enriched samples were identified to contain bismuth minerals however this may be due to the limited number of samples with the Mo-enriched style of Au mineralization analyzed by SR-XRF. In a recent study on the deposit, Kontak et al., (2011) also noted both Bi-and W-mineral phases in ore samples from the Upper Beaver deposit. The results of their study identified that both these mineral phases overlap with at least an early phase of Au mineralization.

SR-XRF mapping also identified distinctive trace element (Ni, Co, and As) zoning in a subset of pyrite grains associated with the Cu-enriched style of Au mineralization. In fact, almost half of the 12 Cu-enriched samples had trace element

zoning. Geochemical correlations between Au and As, Co, and Ni were noted in various ore zones in the deposit as highlighted in Chapter 4. For instance, the Lower Porphyry West and Upper Porphyry West Zones have weak Spearman rank correlations with As (0.35 and 0.36, respectively) and Co (0.27 and 0.22, respectively), and the Lower Porphyry East, Upper Porphyry East, Lower Porphyry West, Upper Porphyry West, and North Contact Zones all have weak to moderate correlations with Ni (0.34, 0.23, 0.28, 0.56, 0.22, respectively).

6.3.1 Revised Styles of Mineralization

A main objective of this study was to assess the large-scale geochemical association with gold mineralization using available company data through exploratory data analysis in order to better understand the spatial variations in mineralization. Prior to the start of the study, mineralization in the deposit was grouped into 7 distinct categories as identified in a Technical report on the property (Bernier and Cole, 2012). This includes:

- 1) Quartz – calcite – magnetite - chalcopyrite ± pyrite ± visible gold veins
- 2) Quartz ± chalcopyrite ± pyrite ± visible gold
- 3) Calcite ± chalcopyrite ± pyrite ± visible gold
- 4) Quartz – molybdenite ± visible gold veins
- 5) Disseminated and fracture controlled mineralization chalcopyrite – pyrite – visible gold
- 6) Carbonate – anhydrite veins ± chalcopyrite ± visible gold
- 7) Visible gold in fractured and silicified porphyry

These categories were reassessed in this thesis to determine if the division of mineralization styles was supported by bulk-rock geochemistry. Due to similarities in geochemical signature as determined by principal component and cluster analysis, and the presence of multiple styles of mineralization in the same thin section mineralization, results suggest that styles 1, 2, and 3 should be grouped together to form a general quartz-carbonate ± magnetite ± pyrite ± chalcopyrite ± visible Au category. This style of mineralization corresponds to the Cu-Au style of

mineralization defined using bulk rock geochemistry and EDA, and consists of Au hosted dominantly in chalcopyrite along pyrite grain boundaries, and also includes less-common occurrences of Au hosted within magnetite and within pyrite. Au in pyrite was only observed in thin sections collected for this study from the Q Zone, however, in a MSc. thesis by Sarah Griffin (2011) the presence of gold in pyrite also occurred deeper in the deposit in the East and West Porphyry Zones suggesting that although it is less common it has a widespread occurrence. Geochemical associations between Au and Cu reveal that this style of mineralization is the dominant form of mineralization in the deposit.

Results also indicate that Category 4, which consists of quartz-molybdenite-visible gold mineralization, should remain a separate category due to its unique geochemical signature as determined through principal component and cluster analysis, and due to its distinctive Cu-poor, Mo-enriched nature and its distinct spatial distribution in the deposit. This style of mineralization dominantly consists of Au hosted within molybdenite or free Au, located near molybdenite stringers and is similar to mineralization in the rest of the Kirkland-Lake and the Larder-Lake gold camps. Mineralization typically occurs in either relatively fresh quartz veins with trace to abundant thin lenses of purplish molybdenite stringers or in mm to cm wide molybdenite slips. Samples analyzed in this study included only vein-type mineralization. Another distinctive characteristic of this style of mineralization includes its co-spatial association with small grains of hematite without magnetite. This could perhaps be attributed to reflect higher oxygen fugacities associated with molybdenite mineralization compared to Au-Cu rich mineralization. Sulphate minerals however were not found in collected hand samples or thin sections. Molybdenite-style mineralization is abundant in the East Porphyry Zones and the Q Zone.

An additional three styles of mineralization are recognized that were not distinguished using geochemistry, namely fracture-fill, carbonate-anhydrite \pm chalcopyrite \pm pyrite \pm visible gold, and replacement style mineralization. These styles are likely less common variations of the first two styles of mineralization.

Fracture-fill mineralization includes both Cu-Au and Mo-Au styles of mineralization, and depending on the associated minerals can be separated into the two categories defined by bulk-rock geochemistry and EDA.

Carbonate-anhydrite \pm chalcopyrite \pm pyrite \pm visible gold mineralization should also remain a distinct style of mineralization, due to the occurrence of sulphate minerals as opposed to sulphide minerals. This group consists of Au associated with magnetite, free Au, and Au hosted within chalcopyrite, all within thick veins of anhydrite. Anhydrite veins are typically fresh and unaltered with only minor amounts of magnetite and chlorite alteration and variable amounts of ankerite alteration. They are also not overprinted by quartz veins. For this reason, they are typically interpreted to be relatively late-veins in the deposit.

The semi-massive vein that the two anhydrite-rich samples were taken from had sharp contacts oriented 95 degrees to the core axis. The lowermost portion of the vein contained chalcopyrite stringers oriented 80-90 degrees to the core axis, indicating that this vein may be a fracture fill vein as opposed to an extensional vein, and the uppermost portion lacked pyrite and chalcopyrite. Samples were taken roughly 1 m apart. The vein extends 4 m in length, and assays indicate that although the entire vein is mineralized (ranging from 13.2 g/t Au and 184 ppm Cu), the central portion of the vein contains the highest amounts of Au and Cu mineralization (47.78 g/t Au and 2.04% Cu, respectively). Along the lower margin of the vein in the host rock there are also high assays for Au and Cu mineralization. An unusual feature of this group is the presence of molybdenite within anhydrite veins as well, although the molybdenite in the anhydrite veins is not associated with Au mineralization.

Anhydrite is common in intrusion-associated ore deposits and a number of authors have suggested various reasons for the coexistence of sulphide and sulphate phases, including Cameron and Hattori, (1987), Jensen and Barton (2000), Lang and Baker, (2001), Rye (2004), Evans et al., (2010), and Richards (2011); although the topic is still debated. In the two samples analyzed from an anhydrite vein, the rock contains an average of 79.6 g/t of Au, and elevated concentrations of Mo with sample

UWO_2015_06 containing 1165 ppm Mo and sample UWO_2015_07 containing 228 ppm Mo. Sample UWO_2015_07 also contained 6.92% Cu, whereas sample UWO_2015_06 contained 100 ppm Cu, the lowest of all 20 samples analyzed. Overall the cause of Au mineralization within an anhydrite vein in the Upper Beaver deposit is still unclear. Mineralization in sample UWO_2015_07 is further described in Chapter 5.

Replacement style mineralization could be grouped in with the chalcopyrite-pyrite style of mineralization, or it could remain separate due to its restricted spatial distribution in the deposit. In fact, mineralization in the south Contact Zone somewhat resembles mineralization in the Detour Lake gold deposit, which occurs above a Chert Marker Horizon. Mineralization in both cases is concentrated either within or above a sedimentary marker horizon, possibly in response to permeability contrasts. In the case of Detour Lake, mineralization is hosted directly within the horizon in shear-hosted and extensional vein arrays and consists of 17.26 million ounces of Au within 445.9 million tonnes of rock grading 1.2 g/t Au (Oliver et al., 2012). In the case of Upper Beaver, mineralization is more disseminated throughout the strongly altered rock, with the highest grades occurring where mineralized lenses cross cut disseminated style mineralization. Zones are difficult to define, at times appearing roughly horizontal and in other instances occurring as steeply dipping lenses. Competency contrasts have an especially clear impact on mineralization in the South Contact Zone where mineralization occurs as a laterally extensive lens within the Blake River Group and only extends a few meters into the underlying volcanoclastic unit before fading into roughly fresh rock. The mineralized zone is hosted within strongly altered Blake River Basalts characterized by intense alteration, referred to as “Dogs Breakfast” alteration among geologists on site.

This reduces the list to 4 main styles of mineralization, with the first 2 being the dominant forms within the Upper Beaver deposit, and an additional two less common variations of the first two. The list includes:

1. Quartz-carbonate-chalcopyrite ± magnetite ± pyrite ± molybdenite ± visible Au
2. Quartz-molybdenite-visible gold
3. Carbonate-anhydrite ± chalcopyrite ± pyrite ± visible gold
4. Replacement style mineralization – magnetite-epidote-feldspar-hematite-pyrite-chalcopyrite

6.4 Relationship to Large-Scale Geochemical Trends Among Abitibi Gold Deposits

In a recent paper by Dubé et al. (2015) they plot Au versus Cu for a number of Archean Au deposits. Results from the analysis of mineralization in the Upper Beaver deposit compared to the findings of Dubé et al., (2015) has been provided in Figure 6.6. Dubé et al. (2015) interpreted deposits that have a strong correlation between Au and Cu to be dominated by pre-main deformation deposits (e.g., Côté, Westwood, Troilus, and McIntyre) while the low-Cu deposit are interpreted to be syn- to late- main deformation (e.g., McBean, Anoki, Upper Canada, Bidgood, Amalgamated Kirkland, Kirkland Lake, Camflo, and Canadian Malartic). Upper Beavers Cu-rich trend, correlates with the trend defined by Dubé et al. (2015) as being characteristic of pre-main deformation deposits, similar to syenite-associated gold deposits, as defined by Robert (2001). This includes all mineralization defined by Clusters 1, 2, and 4. Similarly, Upper Beaver's Mo-rich trend is characterized by the same low-Cu trend that Dubé et al. (2015) suggests is characteristic of deposits that formed contemporaneous with syn- to late- main stage deformation. This includes all mineralization defined by Cluster 5.

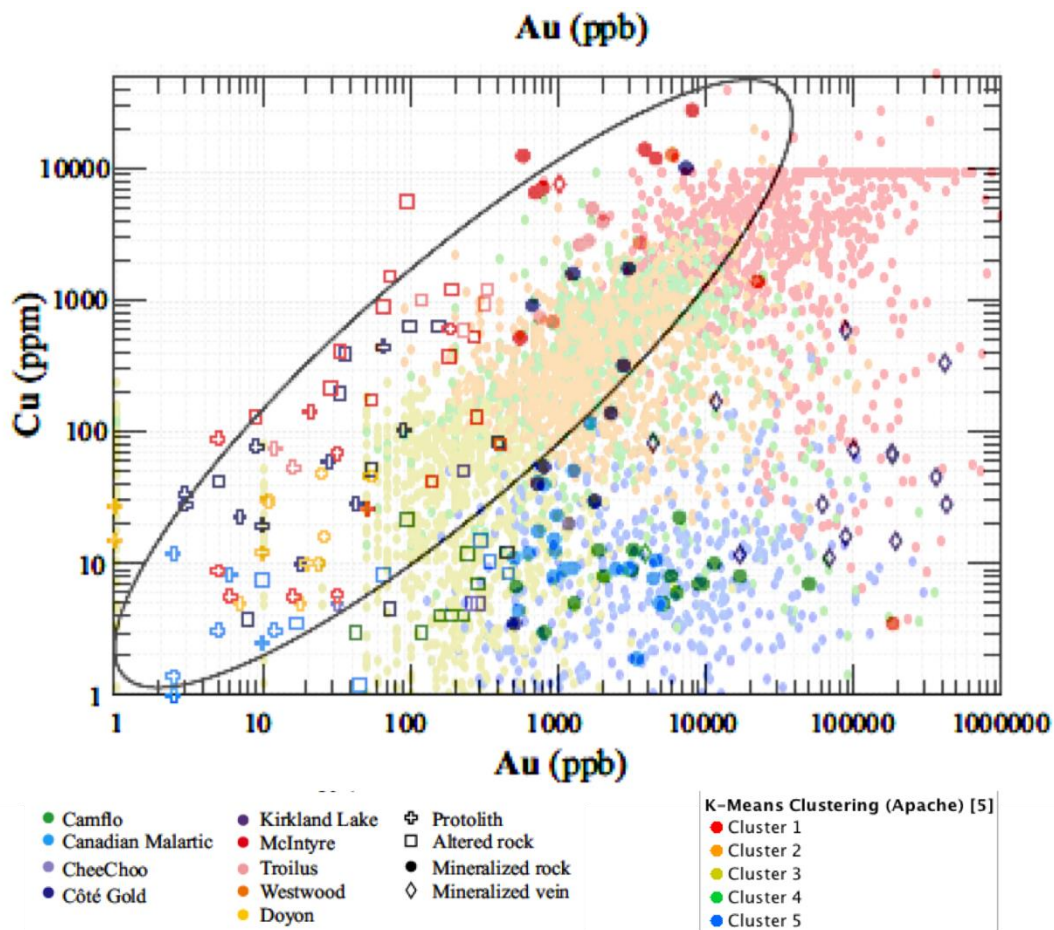


Figure 6.6. Au versus Cu plot for Precambrian intrusion-related and stockwork-disseminated deposits superimposed on geochemical data from the Upper Beaver deposit. Ellipse outlines data that has a good correlation between Au and Cu. Figure modified from Dubé et al., (2015).

7 Conclusions

The Upper Beaver deposit contains an unusual style of mineralization for the Kirkland Lake – Larder Lake area. Mineralization, which includes both gold and copper, is centered on an intrusive complex 8 km north of the Larder Lake Cadillac Break (Bernier and Cole, 2012). Unlike local deposits, mineralization in Upper Beaver is associated with widespread pervasive magnetite, feldspar, actinolite, epidote, carbonate, and sericite alteration. Further, mineralization in the Upper Beaver deposit occurred during D1 deformation, while mineralization in local deposits in the Larder Lake area formed during D2 deformation, and the Kirkland Lake deposit formed during D4. The deposit is classified as a magmatic-hydrothermal, syenite associated Au-Cu deposit, where mineralization developed syngenetically with an alkaline intrusive body (Bernier and Cole, 2012). This aim of this study was to use company-provided data, supplemented with selective core sampling, to evaluate what information can be attained from company-provided geochemical data. Evaluation focused on documenting and characterizing key lithologies and assessing the various mineralization signatures in the Upper Beaver deposit using hand-sample observations, petrography, microprobe, geochemistry, exploratory data analysis, and synchrotron-source microprobe XRF analyses. The study aimed to move from the macro (km-wide) scale by assessing the geochemical signature of host-rocks to micro-scale by assessing the specific mineral phases associated with mineralization.

With the ever-growing massive quantities of geochemical databases, multivariate data analysis methods are becoming increasingly necessary in geological model generation and exploration targeting (Ding and He, 2004). The objectives of this study were to use company-provided data, supplemented with selective core sampling, to evaluate what information can be attained from company-provided data. The evaluation focuses on documenting and characterizing key lithologies and mineralization signatures in the Upper Beaver deposit. More specific objectives of this project included:

1. Assess the geochemical signature of intrusions and host rocks (including the sedimentary package and breccia lens) in the Upper Beaver deposit in order to better define the lithologies and to draw conclusions on their genesis and their relationship to mineralization;
2. Assess large-scale geochemical associations with gold mineralization using available company data through exploratory data analysis to better understand spatial variations in mineralization styles; and
3. Utilize synchrotron source x-ray fluorescence microprobe analysis (SR-XRF) to supplement exploratory data analysis of bulk rock geochemical data in order to evaluate the micro-scale spatial relationship between Au mineralization and trace element exploration vectors.

Major oxide and trace element geochemical analyses were used to try to classify the igneous host rocks of the Upper Beaver deposit. Since aqua regia digestion followed by ICP-MS and ICP-OES were used to attain the geochemical composition of rocks, resistant minerals such as silica were not fully dissolved. For this reason, typical classification diagrams and calculated CIPW normative values plotted on QAP classification diagrams could not be used to conclusively determine the proper classification of host rocks. Data from Feick (2014) and DeAgazio (2012), which was analyzed using full-digestion methods, was also plotted on classification diagrams. Results indicate that mafic syenite is similar in composition to quartz monzodiorite, mafic syenite porphyry is similar to granodiorite, crowded syenite porphyry is similar to quartz diorite or granodiorite, and spotted feldspar is similar in composition to diorite. Further, geochemical classification diagrams indicate that the intrusive rocks that make up the Upper Beaver Intrusive Complex are largely calc-alkaline in composition. The rocks were also compared to local assemblages as defined by Sutcliffe et al., (1993) using REE trends plotted on MORB- and chondrite-normalized spider diagrams. Results indicate that the host rocks are most similar to the diorite-syenite class.

Less common intrusive rocks were also exemplified. This includes the biotite- and amphibole-rich intrusive and the microphyric intrusive. Hand-sample, petrographic,

microprobe, and geochemical analyses identify that the distinctive mineralogy of the biotite- and amphibole-rich intrusives reflect a primary igneous mineralogy that has been subsequently metamorphosed as opposed to an alteration feature. Conversely, analysis of the microphyric-textured intrusive indicates that its distinctive mineralogy is likely the result of alteration of mafic syenite (albitization), namely due to the pseudomorphic replacement of coarse-grained amphiboles.

Samples from an isolated sedimentary sequence in the Blake River Assemblage that occurs within the Upper Beaver deposit were also examined. The sequence most likely represents a roughly 300 m thick sedimentary interface zone that was deposited during a volcanic hiatus. Younging indicators in the sequence reveal that the stratigraphy is upright. The sequence may have potential use as a marker horizon across the deposit. Variations in the thickness of the sedimentary interface zone and the abundance of cherty sedimentary rocks and graphitic argillite, suggest that both the condensed section model, as described by Catuneau (2002) and the rock-water exchange model, as described by Krapez et al., (2003) likely contributed to the formation of the Upper Beaver sedimentary sequence. Both models involve negligible rates of sedimentation on the near-shore, the shelf, or the abyssal environment

Finally, samples of a steeply dipping breccia lens were examined. The steep orientation of the breccia lens supports the evidence from the isolated sedimentary sequence that suggests that the deposit is upright and has not been significantly reoriented. The breccia texture overprints sections of mafic syenite and mafic syenite porphyry intrusions. Textures indicate that a primary magmatic breccia developed into a magmatic-hydrothermal breccia due to fluid fluctuations. Geochemical analysis of the two sets of progressively more brecciated samples compared to available data for the relatively unaltered igneous intrusion is consistent with the strong chlorite-pyrite and epidote-calcite alteration observed in samples analyzed and in the representative breccia samples from the deposit observed on site. Two mineralized zones occur in the breccia lens while the rest of the breccia is largely unmineralized.

The geochemical signature of gold and copper mineralization was also examined using exploratory data analysis (EDA) methods, a tool not typically applied by industry when evaluating mineral deposits. The goal of EDA was to use statistical methods to assess if mineralization is consistent throughout the deposit and to identify multivariate vectors for mineralization. EDA was favorable to standard bivariate analytical methods as it allowed for the more detailed evaluation of a complex deposit with multiple styles of mineralization. Analysis revealed that there are at least two geochemically distinct types of mineralization present in the deposit. Spearman rank coefficients of the entire geochemical dataset indicates Au correlates best with Ag, Mo, Cu, S, Bi, Se, and W, with weaker correlations with Te and Ni. Cu correlates best with Ag, Au, S, Co, and Se with weaker correlations with Te, Mo, Bi, As, U, Sb, and W. Analysis of trace element correlations with Au in mineralized zones indicates that correlations between Au and trace elements vary between zones in the deposit. Ag consistently has a strong correlation with Au, and Cu, Mo, and S consistently have moderate to strong correlations with Au. More variable correlations exist for As, Co, Ni, Sb, Se, Te, V, W, and Zn.

Cluster analysis and principal component analysis were used to investigate multivariate trace element correlations with mineralization. Both methods indicated that there are at least two geochemically distinct styles of mineralization in the Upper Beaver deposit including a Cu-rich style and a Mo-rich style of Au mineralization. The Mo-rich group was associated with a distinctly higher Au:Ag ratio and strong enrichments in W, as well as with low As. The Cu-rich group was associated with a distinctly lower Au:Ag ratio and was associated with enriched U. Both groups were associated with enriched amounts of Bi. Te and Se correlated with both groups, depending on analysis methods used. Synchrotron-sourced microprobe XRF analysis identified that the Cu-rich style of mineralization is associated with pyrites that are zoned with Ni, Co, and As. This style of mineralization can also be intimately associated with bismuth-sulphide minerals and scheelite. Gold-rich host spots were also analyzed using SR-XRF methods. Results agreed with bulk-rock geochemical trends and identified that the Cu-rich group has a lower Au:Ag ratio (typically less

than 10:1) while the Mo-rich group has a higher Au:Ag ratio (typically greater than 10:1).

The results of this study suggest four main styles of mineralization in the Upper Beaver deposit, with the first two being dominant mineralization styles that were defined using geochemistry, and the last two being less common variations on the first two that were observed in hand sample but that were not definable using geochemistry. Mineralization styles include:

1. Quartz-carbonate-chalcopyrite ± magnetite ± pyrite ± molybdenite ± visible Au
2. Quartz-molybdenite-visible gold
3. Carbonate-anhydrite ± chalcopyrite ± pyrite ± visible gold
4. Replacement style mineralization – magnetite-epidote-feldspar-hematite-pyrite-chalcopyrite

The Cu-rich style of mineralization shares similarities with that proposed by Dubé et al. (2015), which they suggest is dominated by pre-main deformation deposits (e.g., Côté, Westwood, Troilus, and McIntyre). Similarly, the Mo-rich style of mineralization resembles the low-Cu group of deposits defined by Dubé et al., (2015), which they suggest is characteristic of syn- to late- main deformation deposits (e.g., McBean, Anoki, Upper Canada, Bidgood, Amalgamated Kirkland, Kirkland Lake, Camflo, and Canadian Malartic).

References

- Aitchison, J. (1990). Relative variation diagrams for describing patterns of compositional variability, *Mathematical geology*, 22, 487-511
- Alexander, D. 2006. Technical Report on the Mineral Properties of Queenston Mining Inc. in the Kirkland Lake Gold Camp.
- Aquilanti, G., Vaccari, L., Plaisier, J. R., and Goldoni, A. (2013). Chapter 3: Instrumentation at synchrotron radiation beamlines. *In: Synchrotron radiation, basics, methods, and applications*, (ed.) S. Mobilio et al, 65-104.
- Ayer, J. A., Thurston, P. C., Bateman, R., Dubé, B., Gibson, H. L., Hamilton, M. A., Hathway, B., Hocker, S.M., Houlié, M. G., Hydak, G., Isopotalov, V. O., Lafrance, B., Leshner, C. M., MacDonald, P. J., Péloquin, A. S., Piercey., S. J., Reed, L. E. and Thompson, P. H. 2005. Overview of Results from the Greenstone Architecture Project Discover Abitibi Initiative; Ontario Geological Survey, Open File Report 6154, 146p.
- Balerna, A., and Mobilio, S. (2015). Chapter 1: Introduction to synchrotron radiation. *In: Synchrotron radiation, basics, methods, and applications*, (ed.) S. Mobilio et al, 3-28.
- Bernier, S. B., and Cole, G. (2012). Technical report on the upper beaver gold-copper project, Ontario, Canada. Sudbury, ON: SRK Consulting Inc (Canada). Retrieved from <http://www.CanadianMalarticCorporation.com/fr/files/2013/01/qmi-upper-beaver-tech-report-121105.pdf>
- Bleeker, W., and Parrish, R. (1996). Stratigraphy and U-Pb zircon geochronology of Kidd Creek: Implications for the formation of giant volcanogenic massive sulphide deposits and the tectonic history of the Abitibi greenstone belt. *Can. J. Earth Sci.*, 33, 1213-1231.
- Bleeker, W. (2015). Synorogenic gold mineralization in granite-greenstone terranes: the deep connections between extension, major faults, synorogenic clastic basins, magmatism, thrust inversion, and long-term preservation, *In: Targeted Geoscience Initiative 4: Contributions to the Understanding of Precambrian Lode Gold Deposits and Implications for Exploration*, (ed.) B Dubé and P. Mercier-Langevin; Geological Survey of Canada, Open File 7852, p. 24-47
- Breede, K., Risto, R. W., and Kociumbas, M. W. (2011). Technical report and mineral resource estimate for the Upper Beaver Property, Ontario for Queenston Mining Inc, *Watts, Griffis and McQuat Consulting Geologists and Engineers*.

- Brown, G. E., Sturchio, N. C. (2002). An overview of synchrotron radiation applications to low temperature geochemistry and environmental science. *The Mineralogical society of America*, 49, 1-115
- Brugger, J., Pring, A., Reith, F., Ryan, C., Etschmann, B., Liu, W., O'Neill, B., Ngothai, Y. (2010). Probing ore deposits formation: New insights and challenges from synchrotron and neutron studies. *Radiation Physics and Chemistry*, 79, 151-161.
- Cameron, E., and Hattori, K. (1987). Archean gold mineralization and oxidized hydrothermal fluids. *Economic Geology*, 82, 1177-1191.
- Card, K. D. (1990). A review of the Superior Province of the Canadian Shield, product of Archean accretion. *Precambrian Research*. 48, 99-156
- Cohen, D. D., Crawford, J., Siegele, R. (2015). K, L, and M shell datasets for PIXE spectrum fitting and analysis, *Nuclear instruments and methods in particle research B*, 363, 7-18.
- Corfu, F., Jackson, S. L., Sutcliffe, R. H. (1991). U-Pb ages and tectonic significance of late Archean alkali magmatism and non marine sedimentation: Timiskaming Group, southern Abitibi Belt, Ontario. *Canadian journal of earth sciences*, 28, 489-501.
- Cruden, A. R., and Launeau, P. (1993). Structure, magnetic fabric and emplacement of the Archean Lebel stock SW Abitibi greenstone belt. *Journal of structural geology*, 16, 677-691.
- Cunningham, L. J., (1977). A geological report on the Upper Beaver mine, Gauthier and McVittie Townships, Ontario, for Upper Canada Resources, 43. Pp + 6 plates.
- DeAgazio, J. (2012). Geochemical and isotopic characterization of fresh and altered lithological equivalents as an exploration vector surrounding the Upper Beaver Deposit, Kirkland Lake, Ontario. BSc Thesis, Earth Sciences Department, University of Western Ontario, London, Ontario
- Dimroth, E., Imreh, L., Goulet, N., and Rocheleau, M. (1982). Evolution of the south-central segment of the Archean Abitibi Belt, Quebec. Part I: Stratigraphy and paleogeographic model. *Canadian Journal of Earth Sciences*, 19, 9, 1729-1758.
- Dimroth, E., Imreh, L., Goulet, N., and Rocheleau, M. (1983). Evolution of the south-central segment of the Archean Abitibi Belt, Quebec. Part II: Tectonic evolution and geochemical model. *Canadian Journal of Earth Sciences*, 20, 9, 1374-1388.

- Dobosz, A. N. (2012). Characterization of Carlin-type auriferous arsenian pyrite from the goldstrike property using EMP, SIMS, and VESPERs synchrotron u-XRF: Constrains to ore deposition mechanisms, MSc Thesis, Department of Geological Sciences and Geological Engineering, Queen's University, Kingston, Ontario
- Dubé, B., and Gosselin, P., 2007, Greenstone-hosted quartz-carbonate vein deposits, in Goodfellow, W.D., ed., *Mineral Deposits of Canada: A Synthesis of Major Deposit- Types, District Metallogeny, the Evolution of Geological Provinces, and Exploration Methods*: Geological Association of Canada, Mineral Deposits Division, Special Publication, v.5, p. 49-73.
- Dubé, B., Mercier-Langevin, P., Castonguay, S., McNicoll, V. J., Bleeker, W., Lawley, C. J. M., De Souza, S., Jackson, S. E., Dupuis, C., Gao, J.-F., Bécu, V., Pilote, P., Goutier, J., Beakhouse, G. P., Yergeau, D., Oswald, W., Janvier, V., Fontaine, A., Pelletier, M., Beauchamp, A.-M., Katz, L. R., Kontak, D. J., Tóth, Z., Lafrance, B., Gourcerol, B., Thruston, P. C., Creaser, R. A., Enkin, R. J., El Goumi, N., Grunsky, E. C., Schneider, D. A., Kelly, C. J., and Lauzière, K. (2015). Precambrian lode gold deposits – a summary of TGI-4 contributions to the understanding of lode gold deposits, with an emphasis on implications for exploration, *In: Targeted Geoscience Initiative 4: Contributions to the Understanding of Precambrian Lode Gold Deposits and Implications for Exploration*, (ed.) B. Dubé and P. Mercier-Langevin; Geological Survey of Canada, Open File 7852, p. 1-24.
- Evans, K. A., Powell, R., Holland, J. B. (2010). Internally consistent data for sulphur-bearing phases and application to the construction of pseudosections for mafic greenschist facies rocks in Na₂O-CaO-K₂O-FeO-MgO-Al₂O₃-SiO₂-CO₂-O-S-H₂O. *Journal of metamorphic geology*, 28, 667-687
- Ewert, W. D., Armstrong, T., Yassa, A., and Puritch, E. (2010). Technical report and resources estimate for the McBean and Anoki gold deposits of the Kirkland Lake gold project Lebel Township, Kirkland Lake north-eastern Ontario, Canada. Brampton, ON: PandE Mining Consultants Inc (Canada). Retrieved from <http://www.CanadianMalarticCorporation.com/fr/files/2013/01/kl-anoki-mcbean-43-101.pdf>
- Ewert, W. D., Puritch, E., Burga, D., and Armstrong, T. (2011). Technical report and resources estimate for the Upper Canada gold deposit of the Kirkland Lake gold project Gauthier Township, Kirkland Lake north-eastern Ontario, Canada. Brampton, ON: PandE Mining Consultants Inc (Canada). Retrieved from <http://www.CanadianMalarticCorporation.com/fr/files/2013/01/qmi-upper-canada-ni43-101.pdf>
- Feick, K. (2014). Alteration in UB11_192 from the South Contact Zone of the Upper Beaver Gold-Copper Deposit, BSc Thesis, Earth Sciences Department, University of Waterloo, Waterloo, Ontario

- Feng, R., Dolton, W., Igaraashi, R., Wright, G., Bradford, M., and McIntyre, S. (2010). Commissioning of the VESPERs Beamline at the Canadian Light Source, *The 10th International Conference on Synchrotron Radiation Instrumentation*, 315-318.
- Filzmoser, P., Hron, K. (2008). Correlation analysis for compositional data, *Mathematical Geosciences*, 41, 905-919
- Fraser, R. J. (1993). The Lac Troilus gold-copper deposit, northwestern Quebec: A possible Archean porphyry system. *Economic Geology*, 88, 6, 1685-1699.
- Fusseis, F., Xiao, X., Schrank, C., De Carlo, F. (2014). A brief guide to synchrotron radiation-based microtomography in (structural) geology and rock mechanics, *Journal of Structural Geology*, 65, 1-16.
- Gamble, D. (2011). *Technical report and resources at Amalgamated Kirkland property Teck Township – Larder Lake mining division*. Retrieved from <http://www.osisko.com/fr/files/2013/01/qmi-ak-ni43-101.pdf>
- Gao, J.-F., Jackson, S. E., Dubé, B., Kontak, D. J., and De Souza, S. (2015). Genesis of the Canadian Malartic, Côté Gold, and Musselwhite gold deposits: Insights from LA-ICP-MS element mapping of pyrite, *In: Targeted Geoscience Initiative 4: Contributions to the Understanding of Precambrian Lode Gold Deposits and Implications for Exploration*, (ed.) B. Dubé and P. Langevin; Geological Survey of Canada, Open File 7842, p. 157-175
- Goldfarb, R. J., Baker, T. Dubé, B. Groves, D. I. Hart, C. J. R. Gosselin, P. (2005). Distribution, character, and genesis of gold deposits in metamorphic terranes. *Economic Geology*, 100th Anniversary Volume, 407-450.
- Goodwin, A., and Smith, I. (1980). Chemical discontinuities in Archean metavolcanic terrains and the development of Archean Crust. *Precambrian Research*, 10, 301-311.
- Greig, R. E., Gibson, J. M., Mills, D. M., Ruzicka, W. G., Young, L., Zholents, A. (2011). Status of the Advanced Photon Source, *Nuclear Insights and Methods in Physics Research A*, 649, 1-2
- Griffin, S. (2011). Determining a genetic relationship of gold bearing veins from Upper Beaver Property, Kirkland Lake, Ontario, MSc Thesis, Earth Sciences Department, University of Western Ontario, London, Ontario
- Groves, D. I., Goldfarb, R. J., Robert, F., Hart, C. J. R. (2003). Gold deposits in metamorphic belts: Overview of current understanding, outstanding problems, future research, and exploration significance. *Economic Geology*, 98, 1-29

- Groves, D. I. Goldfarb, R. J. Gebre-Mariam, M. Hagemann, S. G. Robert, F. (1998). Orogenic gold deposits: A proposed classification in the context of their crustal distribution and relationship to other gold deposit types. *Ore Geology Reviews*, 13, 7-27.
- Grunsky, E. C. (2007). The interpretation of regional geochemical survey data. *Advances in Regional-scale Geochemical Methods, Part 8*.
- Grunsky, E. C. (2013). Predicting Archean volcanogenic massive sulphide deposit potential from lithochemistry: application to the Abitibi Greenstone Belt. *Geochemistry: Exploration, Environment, Analysis*, 13, 317-336.
- Grunsky, E. C., Dubé, B., Hageman, S., and Brauhart, C. W. (2015). A global database of gold deposits: quantification or multi-element signatures, *In: Targeted Geoscience Initiative 4: Contributions to the Understanding of Precambrian Lode Gold Deposits and Implications for Exploration*, (ed.) B. Dubé and P. Mercier-Langevin; Geological Survey of Canada, Open File 7852, p. 271-285.
- Hagemann, S. F., and Cassidy, K. F. (2000). Archean orogenic lode gold deposits, *In: Hagemann, S. F., Brown, P. E. (eds.) Gold in 2000. Society of economic geologists, Reviews in Economic Geology*, 14, 9-68.
- Harris, J. R., Wilkinson, L., Grunsky, E., Heather, K., Ayer, J. (1999). Techniques for analysis and visualization of lithochemical data with applications to the Swayze greenstone belt, Ontario, *Journal of Geochemical Exploration*, 67, 301-334.
- Hastie, A. R., Kerr, A. C., Pearce, J. A., and Mitchell, S. F. (2007). Classification of altered volcanic island arc rocks using immobile trace elements: Development of the Th-Co discrimination diagram, *Journal of petrology*, 48, 12, 2341-2357
- Hart, C. (2007). Reduced intrusion-related gold systems, *in Goodfellow, W. D., ed., Mineral deposits of Canada: A synthesis of major deposit types, district metallogeny, the evolution of geological provinces, and exploration methods. Geological Association of Canada, Mineral deposits division, Special publication No. 5, 95-112*
- Heberlein, D., R., and Dunn, C. E. (2011). The application of surface organic materials as sample media over deeply buried mineralization at the Kwanika Central Zone, North-Central British Columbia, Geoscience BC Report 2011-3
- Helt, K. M., Williams-Jones, A. E., Clark, J. R., Wing, B. A., Wares, R. P. (2014). Constraints on the genesis of the Archean oxidized, intrusion-related Canadian Malartic gold deposit, Quebec, Canada. *Economic Geology*, v.109, 713-735.

- Hodgson, C.J., Hamilton, J.V., and Guimond, R.P., 1991, Relationship between gold deposits and the tectonic framework of the Abitibi Greenstone Belt in the Kirkland Lake- Larder Lake area: Ontario Geoscience Research Grant Program: Ontario Geological Survey Open File Report, v. 227, p. 1-60
- Ispolatov, V., Lafrance, B., Dubé, B., Hamilton, M., and Creaser, R. 2005. Geology, Structure, and Gold Mineralization, Kirkland Lake and Larder Lake area (Gauthier and Teck Townships): Discover Abitibi Initiative; Ontario Geological Survey, Open File Report 6159, 170p.
- Ispolatov, V., Lafrance, B., Dubé, B., Creaser, R., and Hamilton, M. (2008). Geologic and structural setting of gold mineralization in the Kirkland Lake-Larder Lake Gold Belt, Ontario. *Economic Geology*, 103, 1309-1340.
- Jackson, S. L., Sutcliffe, R. H., Ludden, J. N., Hubert, C., Green, A. G., Milkereit, B., Mayrand, L., West, G. F., Verpaelst, P. (1990). Southern Abitibi greenstone belt: Archean crustal structure from seismic-reflection profiles. *Geology*, 18, 1086-1090.
- Jackson, S., and Fyon, J. (1991). The Western Abitibi Subprovince in Ontario. *Precambrian Geology Section, Ontario Geological Survey, Special Volume 4. Part 1.*, 404-482.
- Jébrak, M. (1997). Hydrothermal breccias in vein-type ore deposits: A review of mechanisms, morphology, and size distribution. *Ore Geology Reviews*. Volume 12, Issue 3., 111-134
- Jensen, L., and Langford, F. (1985). *Geology and Petrogenesis of the Archean Abitibi Belt in the Kirkland Lake area, Ontario* (Vol. Miscellaneous Paper 123). Toronto, Ontario: Ministry of Natural Resources.
- Jensen, E., and Barton, M. (2000). Gold deposits related to alkaline magmatism. *SEG Reviews*. Volume 13. Chapter 8. 279-314.
- Katz, L. R., Kontak, D. J., Dubé, B., and McNicoll, VJ. (2015). The Archean Côte Gold intrusion-related Au(-Cu) deposit, Ontario: A large-tonnage, low-grade deposit centered on a magmatic-hydrothermal breccia, *In: Targeted Geoscience Initiative 4: Contributions to the Understanding of Precambrian Lode Gold Deposits and Implications for Exploration*, (ed.) B. Dubé and P. Mercier-Langevin; Geological Survey of Canada, Open File 7852, p. 139-155.
- Kerrich, R., and Watson, G. (1984). The Macassa Mine Archean Lode Gold Deposit, Kirkland Lake, Ontario: Geology, Patterns of Alteration and Hydrothermal Regimes. *Economic Geology*, 79, 1104-1130.

- Kerrich, R. and Kishida, A. (1987). Hydrothermal alteration zoning and gold concentration at the Kerr-Addison lode gold deposit, Kirkland Lake, Ontario. *Economic geology*, 82, 649-690.
- Kisser, M. I. (2005). Digestion of solid matrices Part 1: Digestion with aqua regia report of evaluation study, *Horizontal- 18*, 1-38
- Kontak, D., Dubé, B., and Benham, W. (2008). The Upper Beaver project, Kirkland Lake area: Investigation of a syenite-associated copper-gold deposit with magnetite-epidote-feldspar alteration in Summary of Field Work and Other Activities 2008, Ontario Geological Survey, Open File Report 6226, p. 12-1 to 12-12.
- Kontak, D., Dubé, B., Kyser, T. K. (2011). Geological, petrological and geochemical observations of an Archean syenite-associated Au-Cu deposit, Kirkland Lake, Ontario: A temporal or genetic relationship, Presentation at GAC-MAC 2011 in Ottawa, ON.
- Krapež, B., Barley, M. E., and Pickard, A. L. (2003). Hydrothermal and resedimented origins of the precursor sediments to banded iron formations: sedimentological evidence from the Early Paleoproterozoic Brockman Supersequence of Western Australia. *Sedimentology*, 50, 979-1011
- Lang, J. R., and Baker, T. (2001). Intrusion-related gold systems: the present level of understanding. *Mineralium Deposita*, 36, 477-489
- Large, R. R., Gemmell, J. B., Paulick, H., and Houston, D. L. (2001). The alteration box plot: An approach to understanding the relationship between alteration and mineralogy and lithochemistry associated with volcanic-hosted massive sulphide deposits, *Economic Geology*, 96, 957-971.
- Laznicka, P. (2006). *Giant metallic deposits: Future sources of industrial metals* (Vol. 1, Chapter 8: Volcano-sedimentary orogens). Berlin: Springer science business media.
- Leake, B. E. (1978). Nomenclature of amphiboles. *Canadian Mineralogist*, 16, 501-520
- Le Bas, M. J., and Streckeisen, A. L. (1991). The IUGS systematics of igneous rocks, *Journal of geological society*, 148, 825-833
- Levitan, D. M., Zipper, C. E., Donovan, P., Schreiber, M. E., Seal II, R. R., Engle, M. A., Chermak, J. A., Bodnar, R. J., Johnson, D. K., Ayllor Jr. J. G. (2014). Statistical analysis of soil geochemical data to identify pathfinders associated with mineral deposits: An example from the Coles Hill uranium deposit, Virginia, USA. *Journal of Geochemical Exploration*, 154, 238-251

- Lienert, U., Li, S. F., Hefferan, C. M., Lind, J., Suter, R. M., Bernier, J. V., Barton, N. R., Brandes M. C., Mills, M. J., Miller, M.P., Jakobsen, B., and Pantleon, W. (2011). High-energy diffraction microscopy at the Advanced Photon Source, *Advanced Materials Analysis, Part II*, 63, 7, 70- 77
- Liu, X. (2014). Cornell electron storage ring (CESR) South arc upgrade. Presentation
- Mair, J. L., Farmer, G. L., Groves, D. I., Hart, J. R., Goldfarb, R. J. (2011). Petrogenesis of postcollisional magmatism at Scheelite Dome, Yukon, Canada: Evidence for a Lithospheric mantle source for magmas associated with intrusion-related gold systems. *Economic geology*, 106, 451-480.
- Martin, R. (2012). Syenite-hosted gold mineralization and hydrothermal alteration at the Young-Davidson deposit, Matachewan, Ontario. Retrieved November 23, 2014, from <https://uwspace.uwaterloo.ca/handle/10012/6677>.
- Mason, R., Melnik, N., Edmunds, C.F., Hall, D. J., Jones, R., Mountain, B. (1986). The McIntyre-Hollinger investigation, Timmins, Ontario: A gold dominated porphyry copper system. Canada Geological Survey Paper, 86-1B, p. 577-583.
- Margaritondo, G. (2015). Chapter 2: Characteristics and properties of synchrotron radiation. *In: Synchrotron radiation, basics, methods, and applications*, (ed.) S. Mobilio et al, 29-63.
- McIntyre, S. N., Sherry, N., Suominen Fuller, M.m Feng, R., Kotzer, T. (2010). X-ray fluorescence spectroscopy and mapping using excitation from white and broad bypass synchrotron radiation, *Journal of analytical atomic spectrometry*, 25, 1381-1389.
- McQueen, K., G. (2008). Identifying Geochemical Anomalies, Technical Report, Australian National University.
- Morris, J. H. 1974. The geology of the Upper Beaver Mine, Gauthier Township, Ontario; unpublished MSc thesis, University of Waterloo, Waterloo, Ontario, 117p.
- Müller, W., Donaldson, J., Dufresne, D., and Rocheleau, M. (1991). The Duparquet Formation: Sdimentation in a late Archean successor basin, Abitibi greenstone belt, Quebec, Canada. *Can. J. Earch Sci.*, 28, 1394-1406.
- Mumm, A. S., Brugger, J. Zhao, C., Schacht, U. (2010). Fluids in geological processes – the present state and future outlook, *Journal of geochemical exploration*, 106, 1-7.
- Nadoll, P., Angerer, T., Mauk, J. L., French, D., Walshe, J. (2014). The chemistry of hydrothermal magnetite: a review, *Ore geology reviews*, 61, 1-32

- Nuhn, H-D. (2004). From storage rings to free electron lasers for hard X-rays, *Journal of physics: Condensed matter*, 16, 33
- Olesik, J. (1991). Elemental Analysis using – An evaluation and assessment of remaining problems. *American Chemical Society*, 12-21.
- Oliver, J., Ayer, J., Dubé, B., Aubertin, R., Burson, M., Panneton, G., Friedman, R., Hamilton, M. (2012). Structure, stratigraphy, U-Pb Geochronology and alteration characteristics of gold mineralization at the Detour Lake Gold Deposit, Ontario, Canada. *Exploration and Mining Geology*, 20, 1-30
- Pallon, J., Ryan, C. G., Marrero, N. A., Elfman, M., Kristiansson, P., Nilsson, E. J. C., Nilsson, C. (2009). STIM evaluation in GeoPIXE to complement the quantitative dynamic analysis, *Nuclear instruments and methods in physics research B*, 267, 2080-2084
- Palmer, M. A., Ehrlichman, M., Hartill, D., Helms, R., Rice, D., Rubin, D., Sagan, D., Schächter, L., Shanks, J., Tigner, M., Urban, J. (2007). Plans for utilizing the Cornell electron storage ring as a test accelerator for ILC damping ring research and development, *Proceedings of PAC07, Albuquerque, New Mexico, USA*, 42-44
- Panneton, G. Aubertin, R., Donovan, P. (2009). Detour Lake: Discovery of a world class gold deposit in Ontario, Canada. 2009 NewGenGold Conference, 23-24 November 2009
- Panteeva, S. V., Gladkochoub, D. P., Donskaya, T. V., Markova, V. V., Sandimirova, G. P. (2003). Determination of 24 trace elements in felsic rocks by inductively coupled plasma mass spectrometry after lithium metaborate fusion, *Spectrochimica Acta Part B*, 58, 341-350
- Pawłowsky-Glahn, V., and Buccianti, A. (2001). Visualization and modeling of sub-populations of compositional data: statistical methods illustrated by means of geochemical data from fumarolic fluids, *International journal of earth sciences*, 91, 357-368
- Pearson, V., and Daigneault, R. (2009). An Archean megacaldera complex: The Blake River Group, Abitibi greenstone belt, *Precambrian Research*, 168, 66-82
- Pelletier, M., Mercier-Langevin, P., Dubé, B., Crick, D., Tolman, J., McNicoll, V. J., Jackson, S. E., Beakhouse, G. P. (2015). The Rainy River “atypical” Archean Au deposit, western Wabigoon Subprovince, Ontario, *In: Targeted Geoscience Initiative 4: Contributions to the understanding of Precambrian Lode Gold Deposits and Implications for Exploration*, (ed.) B. Dubé and P. Mercier-Langevin; Geological Survey of Canada, Open File 7852, p. 193-207

- Pflug, K. A., Killeen, P. G., and Mqenifumbo, C. J. (1993). Application of borehole geophysics to gold exploration. *In: Proceedings of Exploration 97: Fourth decennial international conference on mineral exploration*, ed: Gubins, A. G., 717-720.
- Phillips, P., 2005, Excitement in the Abitibi greenstone belt: *Canadian Mining Journal*, v. 2, p. 1- 2.
- Ploeger, F. R., and Crockett, J. H. (1982). Relationship of gold to syenite intrusive rocks in Kirkland Lake, *Canadian Institute of Mining and Metals*, Special volume 24, 69-82
- Poulsen, H., Robert, F. (2016). SC1: Geology of granite-greenstone terranes and their mineral deposits, AME BC mineral exploration roundup, course notes.
- Poulsen, K. H., Card, K. D., and Franklin, J. M. (1992). Archean tectonic and metallogenic evolution of the Superior Province of the Canadian Shield, *Precambrian Research*, 58, 25-54.
- Puritch, E., Yassa, A., Armstrong, T., and Burga, D. (2011). Technical report and resources estimate for the Lebel gold deposit of the Kirkland Lake gold project Lebel Township, Kirkland Lake north-eastern Ontario, Canada. Brampton, ON: PandE Mining Consultants Inc (Canada). Retrieved from <http://www.CanadianMalarticCorporation.com/fr/files/2013/01/qmi-bidgood-ni43-101.pdf>
- Reimann, C., and Fizmoser, P. (2000). Normal and lognormal data distribution in geochemistry: death of a myth. Consequences for the statistical treatment of geochemical and environmental data. *Environmental Geology*, 39, 1001-1014.
- Requia, K., Stein, H., Fontboté, L., and Chiaradia, M. (2003). Re-Os and Pb-Pb geochronology in the Archean Salobo iron oxide copper-gold deposit, Carajás mineral province, northern Brazil. *Mineralium Deposita*, 38, 727-738.
- Richards, J. P. (2011). Magmatic to hydrothermal metal fluxes in convergent and collided margins. *Ore Geology Reviews*, 40, 1-26.
- Robert, F. (1997). A preliminary geological model for syenite-associated disseminated gold deposits in the Abitibi belt, Ontario and Quebec. GSC Current Research Canadian Shield, 201-210. Retrieved June 23, 2014
- Robert, F., and Poulsen, K. H. (1997). World-class archean gold deposits in Canada: An overview. *Australian journal of earth sciences*, (44), 329-351. Retrieved from <http://journals1.scholarsportal.info.proxy.lib.uwaterloo.ca/tmp/6416057644267145911.pdf>

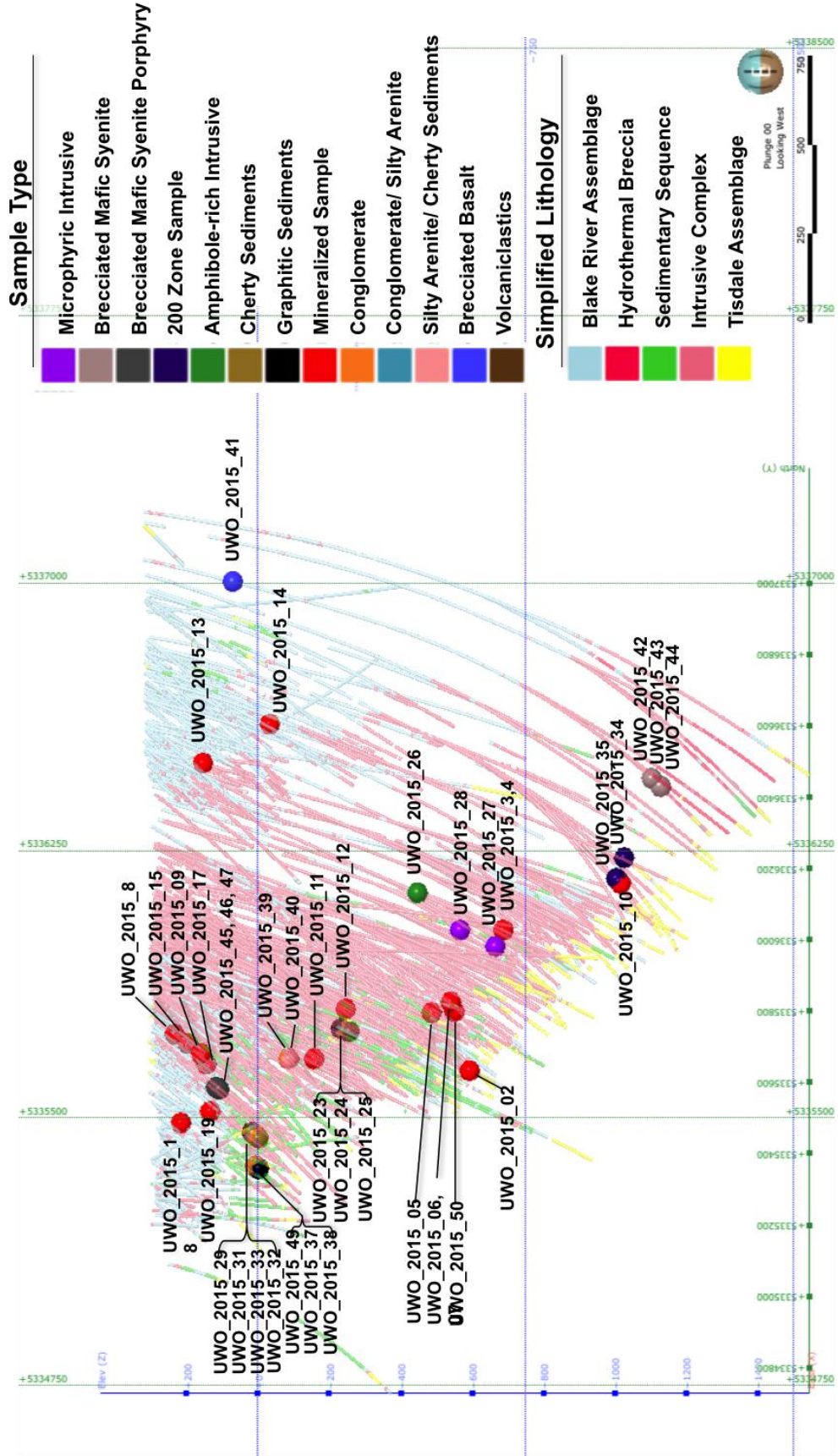
- Robert, F. (2001). Syenite-associated disseminated gold deposits in the Abitibi greenstone belt, Canada. *Mineralium Deposita*, 36, 503-516.
- Roberts, G. R., Morris, J. H. (1982). The geological setting of the Upper Beaver Mine, Kirkland Lake District, Ontario: Copper-gold deposit in mafic volcanic rocks, *Canadian Institute of Mining, Metallurgy and Petroleum*, Special Volume 24, 73 – 82.
- Rollinson, H. (1993). Chapter 1. Geochemical data. In *Using geochemical data: Evaluation, presentation, interpretation* (pp.13-14). Harlow, Essex: Longman Group UK Limited.
- Ross, S., Kline, D. (2011). Developments in X-ray detectors at Advanced Photon Source, *Nuclear Instruments and Methods in Physics Research A*, 649, 73-74.
- Rudnick, R. L. (1995). Making continental crust, *Nature*, 378, 571-578
- Rukhlov, A. S., Han, T., Nelson, J., Hickin, A. S., Ferri, F. (2009). Carlin-type geochemical signal in lake and stream sediments from the Kechika trough, north-central British Columbia. In: *Geological Fieldwork 2014*, British Columbia Ministry of Energy and Mines, British Columbia Geological Survey Paper 2015-1, pp. 165-188
- Ryan, C. G., Laird, J. S., Fisher, L. A., Kirkham, R., Moorhead, G. F. (2015). Improved dynamic analysis method for quantitative PIXE and SR-XRF element imaging of complex materials, *Nuclear instruments and methods in physics research B*, 363, 42-47.
- Rye, R. O. (2004). A review of the stable-isotope geochemistry of sulfate minerals in selected igneous environments and related hydrothermal systems. *Chemical Geology*, 215, 5-36.
- Sham, T- K., and Rosenberg, R. A. (2007). Time-resolved synchrotron radiation excited optical luminescence: Light-emission properties of silicon-based nanostructures. *ChemPhysChem*, 8, 2557-2567.
- Siever, R. (1992). The silica cycle in the Precambrian. *Geochimica et Cosmochimica Acta*, 56, 3265-3272
- Sillitoe, R. H. (1985). Ore-related breccia in volcanoplutonic arcs. *Economic Geology*, 80, 1467-1514
- Sillitoe, R. H. (2010). Porphyry copper systems. *Economic Geology*, 105, 3-41
- Silzer, R. M., Berg, R., Bergstron, J., Dallin, L., Shen, X., Vogt, J. M. (2004). Injection system for the Canadian Light Source, *Proceedings of EPAC, Lucerne, Switzerland*, 2272-2274.

- Steele, I. M., Cabri, L. K., Gaspar, G. C., Marquez, M. A., Vasconcellos, M. A. Z. (2000). Comparative analysis of sulfides for gold using SR-XRF and SIMS, *The Canadian Mineralogist*, 38, 1-10
- Talisker, 2014a. Analysis of multi-element exploration geochemistry for Kirkland Lake, Ontario. Unpublished manuscript.
- Talisker, 2014b. Comments on the petrochemical features of igneous rocks from Canadian Kirkland, Bidgood, and Upper Canada Au systems. Unpublished manuscript.
- Talisker, 2014c. Comments on the results from 7 new U-Pb ages from the Kirkland Lake gold district Talisker Exploration Services Inc. Unpublished manuscript.
- Taylor, S. R., and McLennan, S. M. (1985). The continental crust: Its composition and evolution. Blackwell, Oxford, 312 pp.
- Templ, M., Filzmoser, P., Reimann, C. (2006). Cluster analysis applied to regional data: Problems and possibilities, Research Paper CS-2006-5 for Institut F. Statistik u. Wahrscheinlichkeitstheorie
- Tesfaye, G. (1990). Ore microscope and geochemical characteristics of gold-telluride's-sulfide mineralization in the Macassa Gold Mine, Abitibi Belt, Canada. *Mineralium Deposita*, 27, 66-71. Retrieved November 23, 2014, from <http://link.springer.com/article10.1007/BF00196083#page-1>
- Thompson, J. F. H., Sillitoe, R. H., Baker, T., Lang, J. R., Mortensen, J. K. (1999). Intrusion-related gold deposits associated with tungsten-tin provinces. *Mineralium Deposita*, 34, 323-334
- Thomson, J. (1950). Geology of Teck Township and teh Kenogami Lake Area, Kirkland Lake Gold Belt. *Ontario Department of Mines Annual Report for 1984, Part 5, V. 57*, 1-53
- Thurston, P. C. (2002). Autochthonous development of Superior Province greenstone belts? *Precambrian research*, 115, 11-36
- Thurston, P. C., Ayer, J. A., Coutier, J., and Hamilton, M. A. (2008). Depositional gaps in Abitibi greenstone belt stratigraphy: A key to exploration for syngenetic mineralization. *Economic Geology*, 103, 1097-1134.
- Tindle, A. G., and Webb, P. C. (1994). PROBE-AMPH- a spreadsheet program to classify microprobe-derived amphibole analyses. *Journal of Computers and Geoscience*, 20, 7-8, 1201-1228
- Two acid digest aqua regia digest. (2015). Retrieved July 1, 2015, from http://www.sgs.com/en/Mining/Analytical-Services/Geochemistry/Digestion-and-Fusion/Two-Acid-Digest-and-Aqua_Regia-Digest.aspx

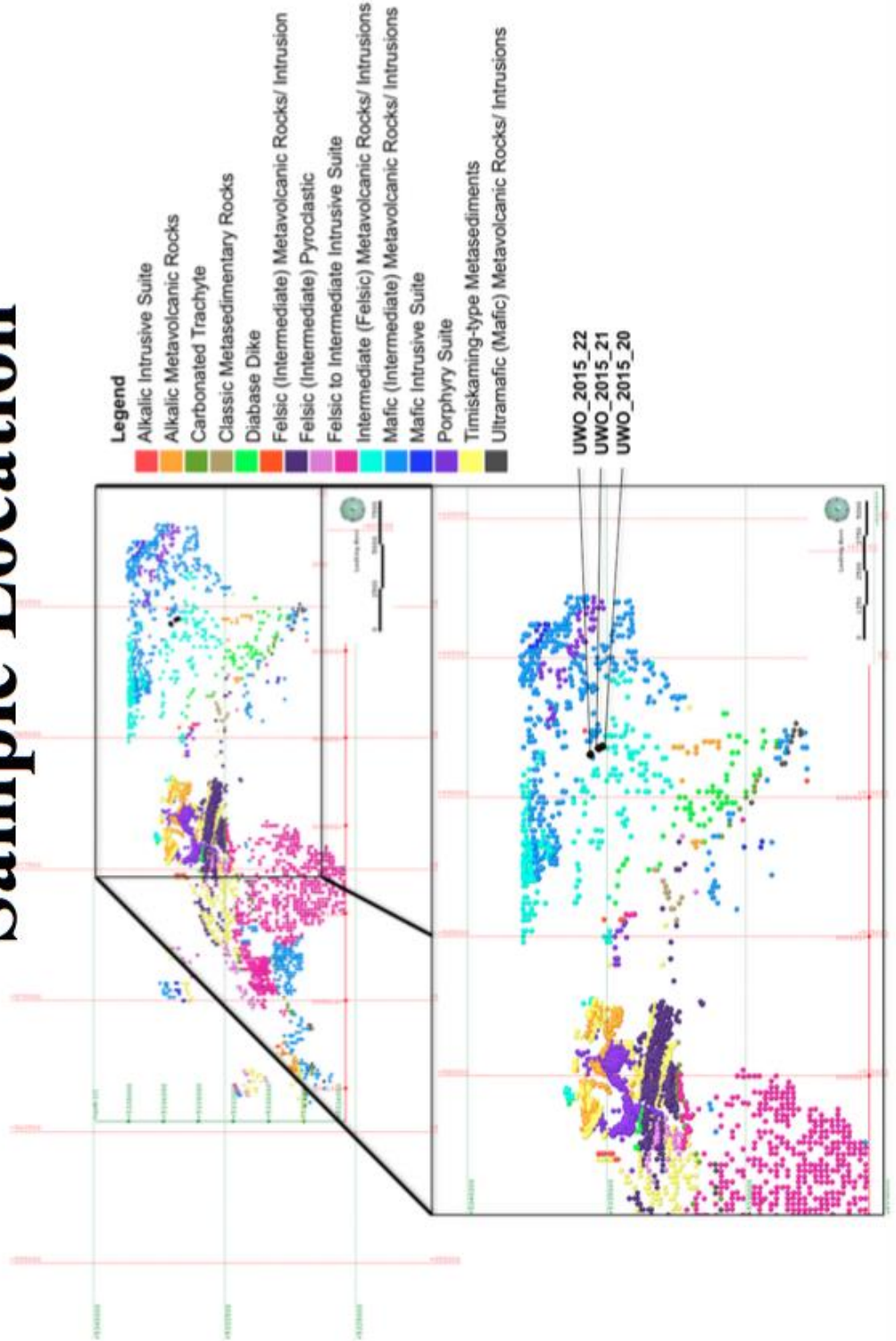
- Valencia, V. A., Eastoe, C., Ruiz, J., Ochoa-Landlin L., Geherls, G., Gonzales-Leon, C., Barra, F., Espinoza, E. (2008). Hydrothermal evolution of the porphyry copper deposit at La Caridad, Sonora, Mexico, and the relationship with a neighboring high-sulfidation epithermal deposit. *Economic Geology*, 103, 473-491.
- Walker, S. R., Jamieson, H. E., Lanzirotti, A., Andrade, C. F., Hall, G. E. M. (2005). The speciation of arsenic in iron oxides in mine wastes from the Giant Gold Mine, N. W. T.: Application of synchrotron micro-XRD and micro-XANES at the grain scale, *The Canadian Mineralogist*, 43, 1205-1224.
- Wang, C., Carranza, E. J. M., Zhang, S., Zhang, J., Liu, X., Zhang, D., Sun, X., and Duan, C. (2013). Characterization of primary geochemical haloes for gold exploration at the Huanxiangwa gold deposit, China, *Journal of Geochemical Exploration*, 124, 40-58
- Wilkinson, L., Cruden, A. R., and Krough, T. E. (1999) Timing and kinematics of post-Timiskaming deformation within the Larder Lake - Cadillac deformation zone, southwest Abitibi greenstone belt, Ontario, Canada. *Canadian journal of earth sciences*, 36, 627-648.
- Williams, P. J., Barton, M. D., Johnson, D. A., Fontboté, L., De Haller, A., Mark, G., Oliver, N. H. S., and Marschik, R. (2005). Iron oxide copper-gold deposits: Geology, space-time distribution, and possible modes of origin. *Economic Geology*, 100th anniversary volume, 371-405.
- Winter, J. D. (2010). *Principles of igneous and metamorphic petrology* (2nd ed.). New Jersey: Pearson Education.
- Witt, W. K. (1992). Porphyry intrusions and albitites in the Bardoc-Kalgoorlie area, Western Australia, and their role in Archean epigenetic gold mineralization. *Canadian Journal of Earth Sciences*, 29, 1609-1622.
- Wolf, R. E. (2005). Introduction to ICP-MS. Retrieved July 1, 2015, from <http://crustal.usgs.gov/laboratories/icpms/intro.html>
- Woll, A. (2014). CHESS workshop on XRF mapping: GeoPIXE and the Maia detector. Presentation.
- “X-ray Data Booklet” Pub-490 Rev. 2, from the Technical Information Department, Lawrence Berkeley Laboratory, 1 Cyclotron Road, Berkeley, California 94720.
- Xu, W. Y., Pan, F. C., Qu, X. M., Hou, Z. Q., Yang, Z. S., Chen, W. S., Yang, D., and Chi, Y. H. (2009). Xiongkun, Tibet: A telescoped system of veinlet-disseminated Cu(Au) mineralization and late vein-style Au(Ag)-polymetallic mineralization in a continental collision zone. *Ore Geology Reviews*, 36, 174-193.

Yang, J., Liu, J., Dynes, J. J., Reak, D., Regier, T., Wang, J., Zhu, S., Shi, J., Tse, J. S. (2014). Speciation and distribution of copper in a mining soil using multiple synchrotron-based bulk and microscopic techniques. *Environ Sci Pollut Res*, 21, 2943-2954

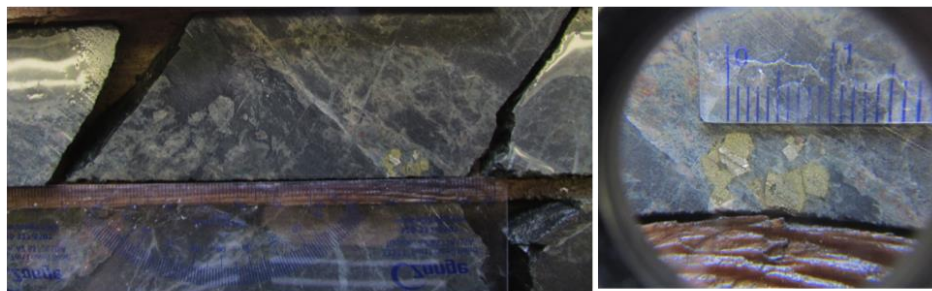
Appendix A: Hand Sample and Petrographic Description of Collected Samples



Sample Location



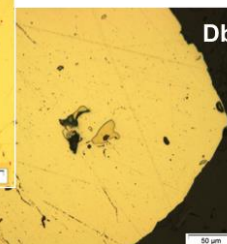
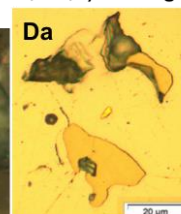
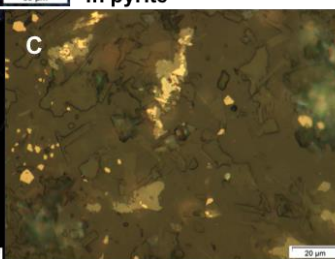
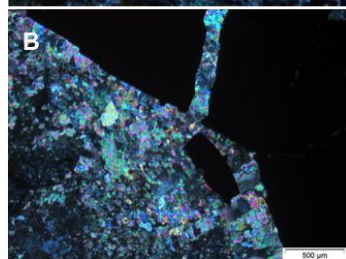
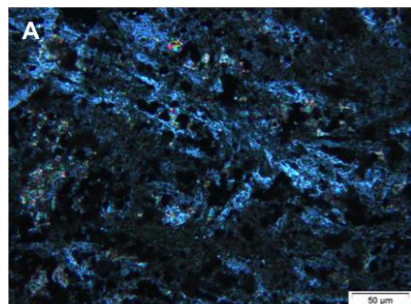
UWO_2015_01 (Q Zone Mineralized Sample)



Sample ID	UWO_2015_01
Hole ID	UB07_76
Sample Interval (m)	332.6-332.7
Lithology	Basalt
Mineralization	Cpy/Py/VG/Mgt
Host	Calcite +/- Quartz +Weak Ankerite
Zone	Q-Zone
Au Assay (g/t)	1.01
Cu Assay (pct)	0.318
Angle of mineralization	40 dtca

Hand Sample Description: Sample is hosted within a fine grained mafic basalt unit that is variably altered by chlorite, sericite, and hematite. There are a fair number of quartz veins within the core box (an interval of about 4m). The thicker veins tend to contain abundant chalcopyrite while the thinner ones are typically unmineralized. The Sample itself is from a small patch of large 3-5mm wide euhedral pyrite grains, one of which appears to contain a thin blade of visible gold roughly 1mm long. The pyrite grains don't appear to be from a vein, but are from a zone of fractures that are filled with magnetite and/or chlorite that occur at 40 degrees to the core axis. Deeper in the hole there are chalcopyrite-calcite veins which also occur at 40 degrees to the core axis.

Thin section Description: The groundmass consists of varying amounts of plagioclase (35%), quartz (15%), calcite (15%), and opaques (hematite and magnetite) with accompanying chlorite, and sericite alteration. There are trace amounts of rutile and zircon. The majority of the minerals are very fine grained. Mineralization consists of 10% pyrite, 2% chalcopyrite, 15% magnetite, and 5% hematite. Au mineralization is hosted in a cluster of euhedral pyrite grains that range in size from 1mm-5mm wide. Pyrite grains contain small amounts of chalcopyrite and one very tiny spec of Au. Quartz, plagioclase, and calcite grains may reach up to 0.5mm in grain size around the pyrite cluster. Chalcopyrite and pyrite are sieve-textured and contain tiny inclusions of hematite and magnetite. Pyrite contained inclusions of chalcopyrite, indicating the pyrite likely formed first, followed by the chalcopyrite and iron oxides.



A) Representative picture of the groundmass, B) Change in grain size beside sulphides, C) Hematite and magnetite intergrowths, Da,b) Small grain of Au in pyrite

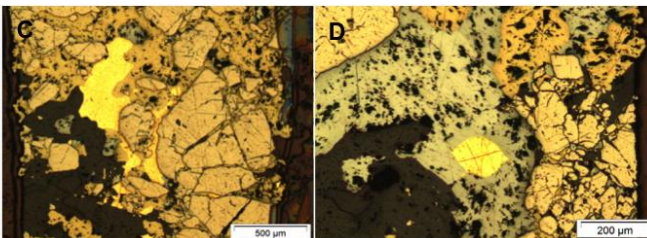
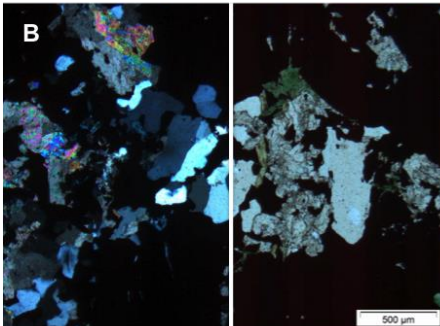
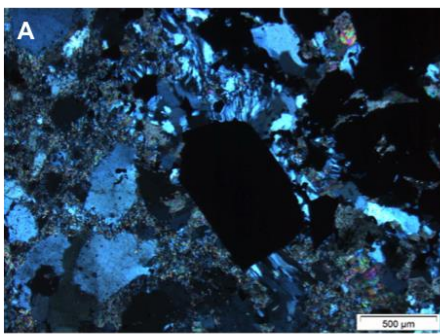
UWO_2015_02 (Syenite Breccia Zone Mineralized Sample)



Sample ID	UWO_2015_02
Hole ID	UB08_127
Sample Interval (m)	999.3-999.4
Lithology	Mafic Syenite
Mineralization	Py/Cpy/VG/Mgt
Host	Quartz-Calcite
Zone	Syenite Breccia Zone
Au Assay (g/t)	168
Cu Assay (pct)	0.942
Angle of mineralization	50 dtca

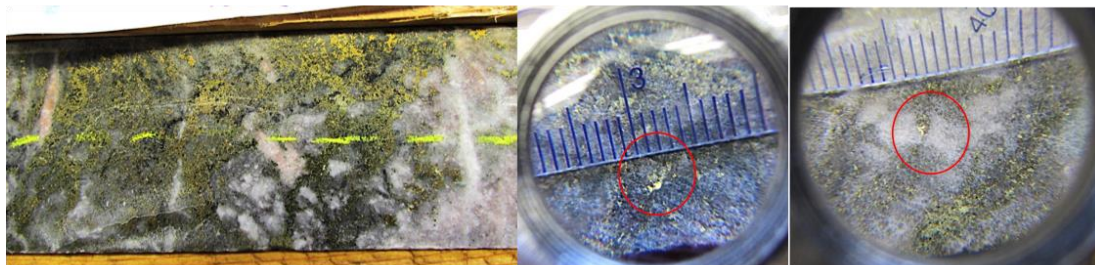
Hand Sample Description: The host rock is unidentifiable due to alteration. Core logs identify the rock as being an "altered and mineralized unit", however the interval before and after this unit are identified to be mafic syenite and due to lack of observable lithology contrasts it is fair to assume that this unit could be the same rock type. The host rock is very strongly altered by sericite, hematite, and chlorite. As well, some of the fractures contain magnetite but for the most part the rock is not magnetic. There are very few quartz-calcite stringers in this interval of core (two thin ones and a few very fine ones). The interval that the sample is from contains abundant pyrite and chalcopyrite mineralization. The core is red (oxidized hematite) and contains abundant black magnetite patches. The host isn't a typical quartz-calcite vein, but is more of a sulphide rich vein with irregular margins that on average are ~ 50 degrees to core axis. Pyrite grains are euhedral and range from fine to fairly coarse grained. Chalcopyrite splashes occur irregularly throughout the interval, for the most part being concentrated between the pyrite grains. Fine grained gold is disseminated throughout the sulphide vein. The gold doesn't strictly occur within the pyrite or chalcopyrite grains, but rather tends to occur at pyrite grain margins.

A) Pressure shadows around sulphide grain, Ba,b) Representative picture of the groundmass in cpl and ppl, respectively, C) Au in chalcopyrite, D) Au in magnetite



Thin Section Description: The thin section consists of 80% opaques (sulphides and oxides) within a coarse grained quartz (7%)-calcite (20%)-chlorite(3%) matrix. In a number of areas there are intensely deformed quartz grains. There are trace amounts of rutile and zircon. The remainder of the sample consists of 33% pyrite, 33% chalcopyrite, %2 magnetite, and 2% hematite. The pyrite is sieve textured and contains chalcopyrite, hematite, and magnetite. Chalcopyrite likely formed after pyrite, slightly earlier than hematite and magnetite, and it is also sieve textured, containing inclusions of magnetite, and hematite.

UWO_2015_03 (Lower East Porphyry Zone Mineralized Sample)

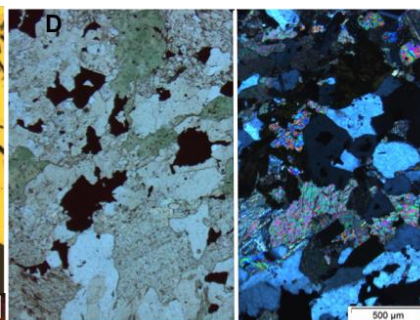
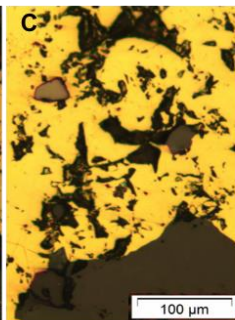
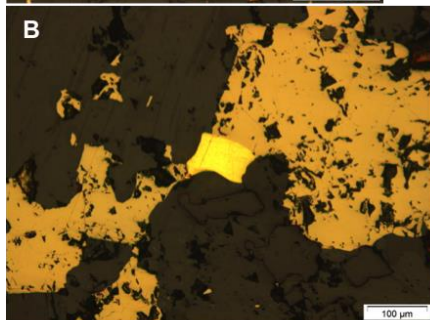
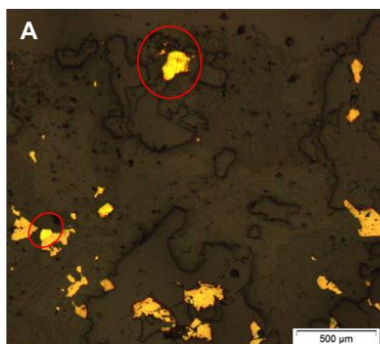


Sample ID	UWO_2015_03
Hole ID	UB08_139
Sample Interval (m)	1000.8-1000.9
Lithology	Mafic Syenite
Mineralization	Cpy/Py/Mgt
Host	Quartz-Calcite
Zone	Lower East Porphyry Zone
Au Assay (g/t)	128
Cu Assay (pct)	3.53
Angle of mineralization	30 dtca

Hand Sample Description: This is the shallower sample from a high grade interval in hole UB08_139. In this interval, there is abundant chalcopyrite occurring in a network-like pattern. Trace fine grained pyrite mineralization also occurs in this interval. Magnetite and chlorite fracture fills are overprinted by the chalcopyrite mineralization. Trace amounts of fine grained visible gold can be seen throughout the chalcopyrite. One large spec of gold (~3mm long) can be seen when the sample is cut.

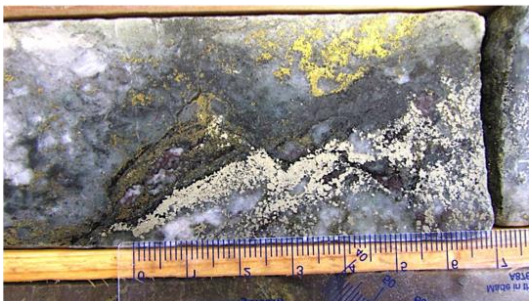
The core is so highly silicified in this interval it is difficult to tell that it was originally mafic syenite. There is also weak chlorite alteration within and outside of the sample interval. The matrix seems to be composed dominantly of coarse grained quartz and feldspar crystals.

Thin Section Description: The matrix consists dominantly of fine to coarse grained 36% quartz and 36% calcite with minor amounts of chlorite (5%), and plagioclase (3%). There are trace amounts of rutile and zircon. Opaques make up 20% of the thin section. They include 3% hematite, 1% magnetite, and 16% chalcopyrite. Chalcopyrite is sieve textured and contains inclusions of hematite, magnetite, pyrite, and gold. Gold is also found as free gold. It is difficult to say whether the chalcopyrite or the iron oxides formed first.



A) Free Au, B) Au in chalcopyrite, C) Magnetite and hematite in chalcopyrite, D) Representative picture of groundmass in ppl and cpl

UWO_2015_04 (Lower East Porphyry Zone Mineralized Sample)

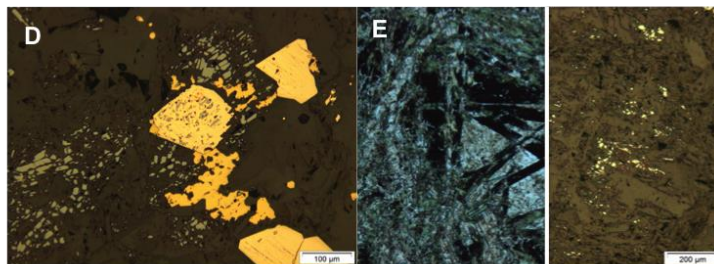
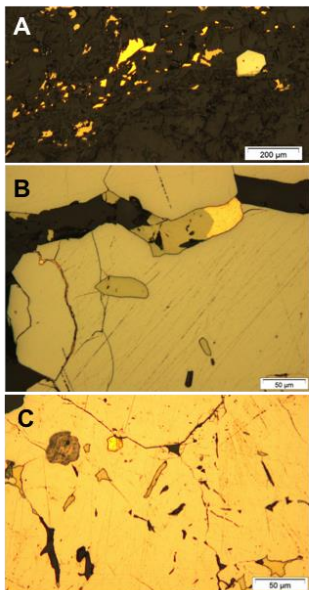


Sample ID	UWO_2015_04
Hole ID	UB08_139
Sample Interval (m)	1001.2-1001.3
Lithology	Mafic Syenite
Mineralization	Cpy/Py/Mgt
Host	Quartz-Calcite
Zone	Lower East Porphyry Zone
Au Assay (g/t)	86.8
Cu Assay (pct)	0.595
Angle of mineralization	35 dtca

Hand Sample Description: This is the deeper sample from hole UB08_139. This sample is from a slightly lower grade interval than shallower sample from the same hole. There is abundant pyrite and chalcopyrite mineralization throughout this interval, although they occur in separate bands in the rock. The bands are separated by a fracture fill/ 1cm thick vein of chlorite and magnetite. Pyrite grains euhedral to subhedral, fine to coarse grained (typically 2mm wide), and are hosted within a coarse grained strongly altered quartz-rich matrix. Core logs identify that the host was originally mafic syenite. Strong hematite alteration also occurs in fractures. It is overprinted by the pyrite mineralization. The margins of pyrite grains are full of lighter shade/ more yellowish coloured mineralization. It is possibly gold, arsenopyrite, or another type of mineralization, although microscopic analysis is necessary to determine the actual type of mineralization. A large spec of visible gold is seen with chalcopyrite rich section once core is cut. Overprinting relationships suggest that the pyrite mineralization occurred after the chalcopyrite mineralization. The thin section will be made of the pyrite rich portion of the rock to compare it to the chalcopyrite rich mineralization from the previous sample.

Thin Section Description: The matrix of the sample dominantly consists of quartz (22%) and calcite (30%) with minor plagioclase (3%), and chlorite (15%). There are trace amounts of rutile and zircon in the thin section. Opaques make up 30% of the thin section. Opaques consist of 15% pyrite, 10% chalcopyrite, 2% magnetite, and 3% hematite. Gold occurs in chalcopyrite pyrite, and as free gold. Both pyrite and chalcopyrite are sieve textured and contain inclusions of magnetite and hematite. Pyrite also contains inclusions of chalcopyrite. In some cases it seems like the magnetite and hematite formed first and were overgrown by pyrite and chalcopyrite, while in other cases it seems like the hematite and chalcopyrite are overprinting the sulphides.

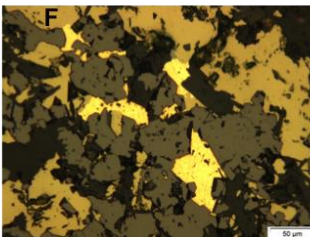
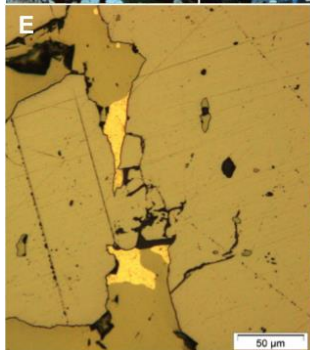
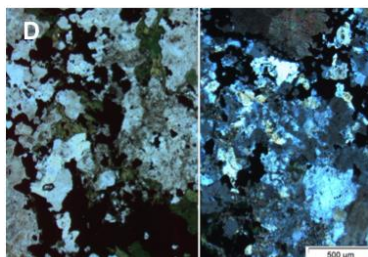
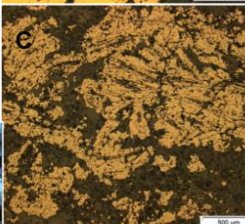
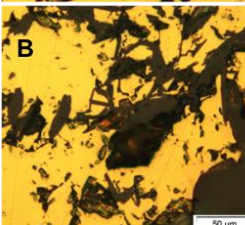
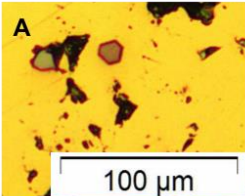
A) Free Au, B) Au in chalcopyrite, C) Au in pyrite, D) Magnetite and hematite laths overgrown by pyrite and chalcopyrite, E) Magnetite laths in plane polarized and reflected light



UWO_2015_05 (Upper West Porphyry Zone Mineralized Sample)



Sample ID	UWO_2015_05
Hole ID	UB09_100W1
Sample Interval (m)	856.3-856.4
Lithology	Quartz-Carbonate vein zone
Mineralization	Mgt/Cpy/VG
Host	Quartz-Calcite
Zone	Upper West Porphyry Zone
Au Assay (g/t)	126
Cu Assay (pct)	3.86
Angle of mineralization	45 dtca



A) Euhedral magnetite and hematite in chalcopyrite, B) Interesting texture in chalcopyrite, C) Hematite and magnetite laths, D) Representative picture of groundmass in ppl and cpl, E) Au in chalcopyrite, and F) Au in magnetite

Hand Sample Description: The mineralized interval is hosted within a fine grained mafic rock that has been altered by sericite, chlorite, and magnetite. Greater than 5cm wide mineralized veins of chalcopyrite and magnetite and abundant (up to 3cm wide) quartz-calcite veins at irregular orientations commonly hosting chalcopyrite mineralization, occur throughout the core box (~4m long). The sample is from a thick quartz-calcite vein that has a 10cm wide top section of magnetite and a 15cm bottom section of chalcopyrite and quartz. Visible gold occurs as tiny specs within the quartz-rich sections of the vein. it also occurs as larger flecks within the chalcopyrite mineralization.

Thin section Description: The groundmass of the sample consists of coarse grained quartz (15%) and calcite (15%) with minor amounts of chlorite (6%). There are trace amounts of rutile in the thin section. The sample consists of 20% magnetite, 40% chalcopyrite, and 3% pyrite and 3% hematite. Magnetite in the sample is subhedral and blocky to lath-shaped and is sieve textured, with tiny inclusions of chalcopyrite, and pyrite. Chalcopyrite is also sieve textured and contains inclusions of hematite, and magnetite. Textural relationships suggest that the oxides formed first, followed by the sulphides, likely followed by another episode of oxide growth. Au is found as inclusions within chalcopyrite and as free gold.

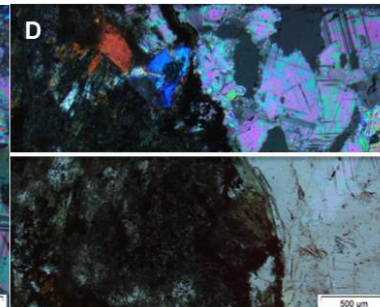
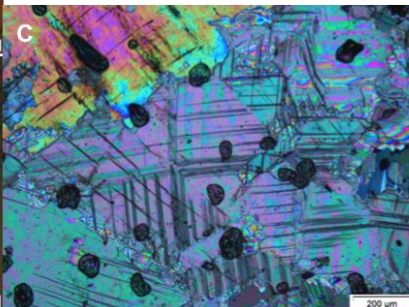
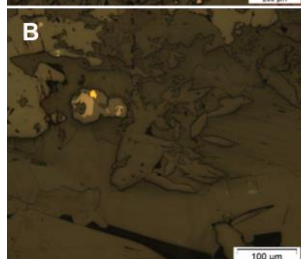
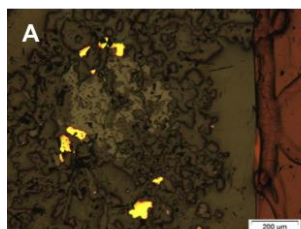
UWO_2015_06 (Upper West Porphyry Zone Mineralized Sample)



Sample ID	UWP_2015_06
Hole ID	UB11_170W3
Sample Interval (m)	1016.6-1016.7
Lithology	Altered Crowded Syenite Porphyry
Mineralization	VG
Host	Anhydrite-Ankerite
Zone	Upper Porphyry West Zone
Au Assay (g/t)	71.4
Cu Assay (pct)	0.01
Angle of mineralization	95 dtca

Hand Sample Description: Shallower sample of a large mineralized anhydrite vein from UB11_170 W3. The anhydrite vein spans almost the entire length of the core box except for the last ~30 cm, making it roughly 3.7m wide. The vein is overprinted by mineralization, but not by quartz veins, indicating that the vein is fairly late. The top of the vein contains clear anhydrite with small patches of magnetite and chlorite alteration and with free visible gold specks. There is no chalcopyrite or pyrite mineralization near this sample interval. The anhydrite is fairly coarse grained and is very soft. It reacts to KFC and not HCl, indicating that there is some ankerite within the vein, and no calcite.

Thin Section Description: The sample dominantly consists of 61% coarse grained anhydrite with minor amounts of fine grained chlorite (10%), rutile (1%), ankerite (10%), and zircon (1%). Sulphides include fine grained hematite (3%), magnetite (6%), and trace amounts of chalcopyrite and Au.

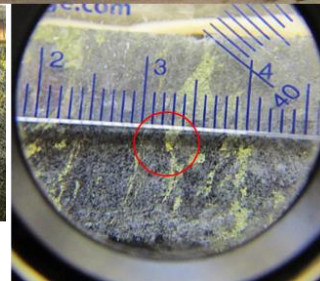
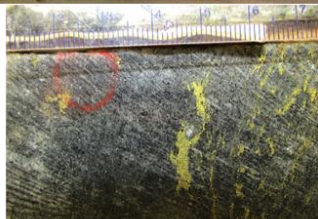


A) Chalcopyrite and magnetite, B) Au and magnetite, C) Zircon in anhydrite, D) Representative picture of the groundmass in cpl and ppl

UWO_2015_07 (Upper West Porphyry Zone Mineralized Sample)



Sample ID	UWO_2015_07
Hole ID	UB11_170W3
Sample Interval (m)	1017.5-1017.6
Lithology	Altered Crowded Syenite Porphyry
Mineralization	Cpy/VG
Host	Anhydrite-Ankerite
Zone	Upper Porphyry West Zone
Au Assay (g/t)	87.8
Cu Assay (pct)	6.92
Angle of mineralization	95 dtca

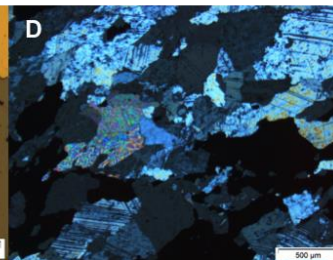
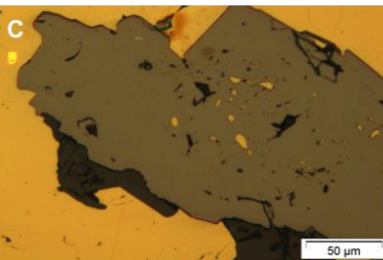
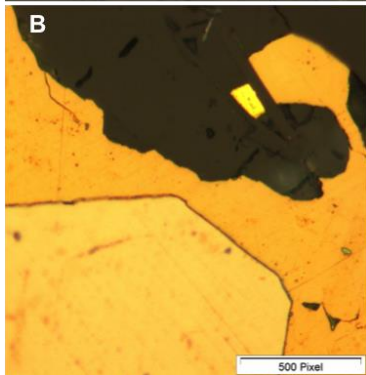
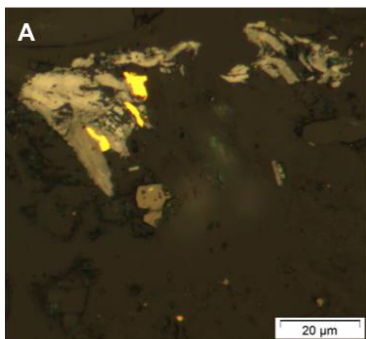


Hand Sample Description: Deeper sample of a large mineralized anhydrite vein from UB11_170 W3. This sample is from the deeper end of the vein that contains chalcopyrite and gold mineralization. Chalcopyrite stringers occur at approximately 90 degrees to the core axis. Visible gold occurs as free specks in the anhydrite and also as larger flecks in the chalcopyrite stringers. The anhydrite host is the same as the previous sample, i.e., fairly coarse grained and very soft. It also reacts to KFC and not HCl, indicating that there is some ankerite within the vein, and no calcite.

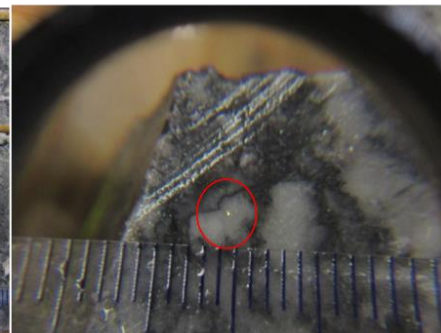
Thin section Description: The groundmass of the sample is composed of 5% ankerite, 5% quartz, and 69% anhydrite. There are also approximately 1% zircon and trace amounts of rutile in the sample as well. Opaques take up 20% of the thin section. These include 15% chalcopyrite, 2% pyrite, 2% magnetite, and 1% hematite. There are also trace amounts of molybdenum. Hematite and magnetite are finely sieve textured and contain inclusions of chalcopyrite. Textural relationships between the sulphides and oxides show that magnetite and hematite likely formed first, followed by pyrite, and then chalcopyrite.

Au mineralization occurs with the hematite-magnetite laths, as free Au, and as inclusions in chalcopyrite.

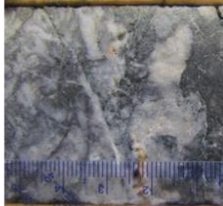
A) Au in molybdenum, B) free Au, C) Au in chalcopyrite, D) Representative picture of the groundmass



UWO_2015_08 (Q Zone Mineralized Sample)



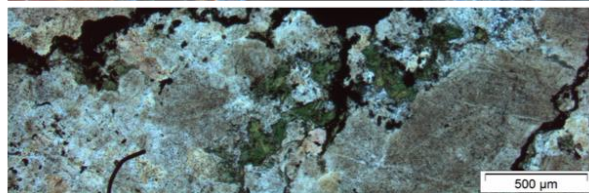
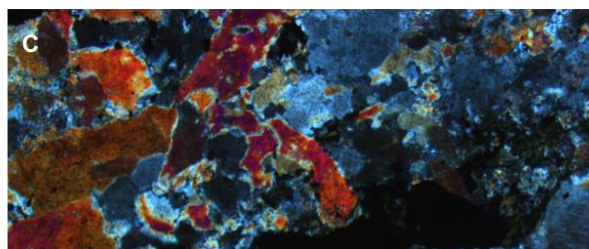
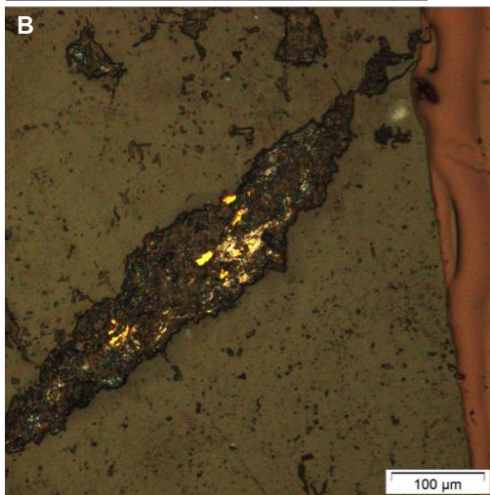
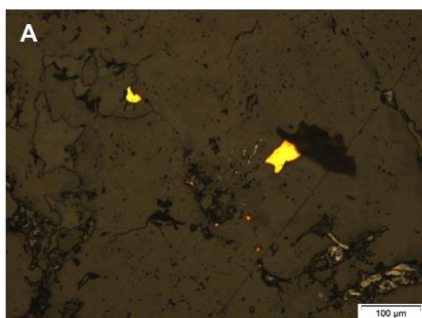
Sample ID	UWO_2015_08
Hole ID	UB11_184
Sample Interval (m)	93.5-93.6
Lithology	Basalt
Mineralization	Mo-VG
Host	Quartz-Calcite
Zone	Q-Zone
Au Assay (g/t)	268
Cu Assay (pct)	0.0154
Angle of mineralization	45 dtca



A) Free Au, B) Au in molybdenum, C)
Representative picture of the groundmass
in cpl and ppl

Hand Sample Description: This sample is from an approximately 30 cm wide molybdenum rich vein within a fine grained mafic host. Above the vein the host is strongly sericitized and chloritized with small patches of epidote and hematite. There are also hematized stringers within the host which are ~1mm to ~1cm wide that cut the core at irregular angles (typically 90, 75, or 45 degrees to core axis). The top contact of the vein with the fine grained mafic host is strongly sericitized, causing it to be greenish yellow in colour. The lower contact between the vein and the mafic host is notable different. The host is instead quite pink in colour, and appear to be strongly sericitized and hematized. The vein's contacts are both 45 degrees to core axis. The vein itself consists of ankerite, quartz, molybdenum, and chlorite all mottled together. The chlorite and molybdenum occur as irregular fractures and wiggly thin veinlets within the vein. The sample contains a tiny spec of free visible gold within a quartz patch.

Thin section Description: The sample consists dominantly of coarse 35% calcite and 30% anhydrite?, and 20% quartz, with minor amounts of chlorite (5%) and zircon (2%) as well as trace amounts of rutile. Opaques in the sample consist of 10% molybdenum, which hosts Au mineralization, and trace amounts of hematite. Free Au is also present.



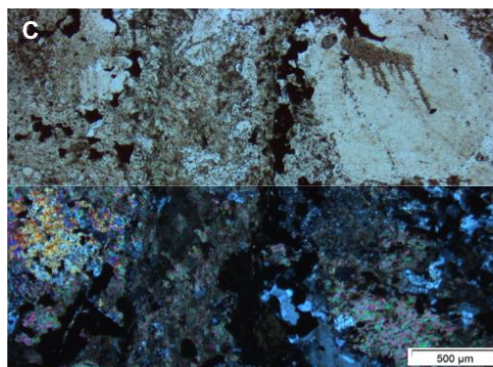
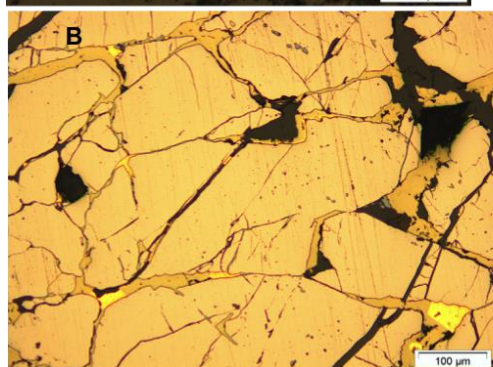
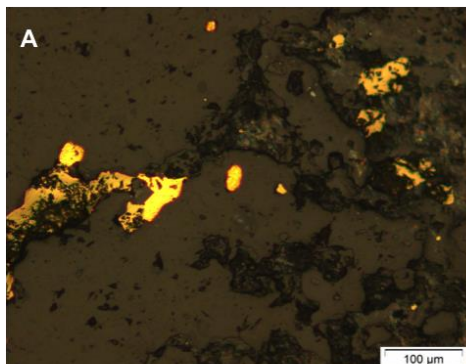
UWO_2015_09 (Q Zone Mineralized Sample)



Sample ID	UWO_2015_09
Hole ID	UB11_204
Sample Interval (m)	192.2-192.3
Lithology	Basalt
Mineralization	Cpy/Py/Mgt/VG
Host	Quartz-Calcite
Zone	Q-Zone
Au Assay (g/t)	232
Cu Assay (pct)	4.67
Angle of mineralization	80 dtca

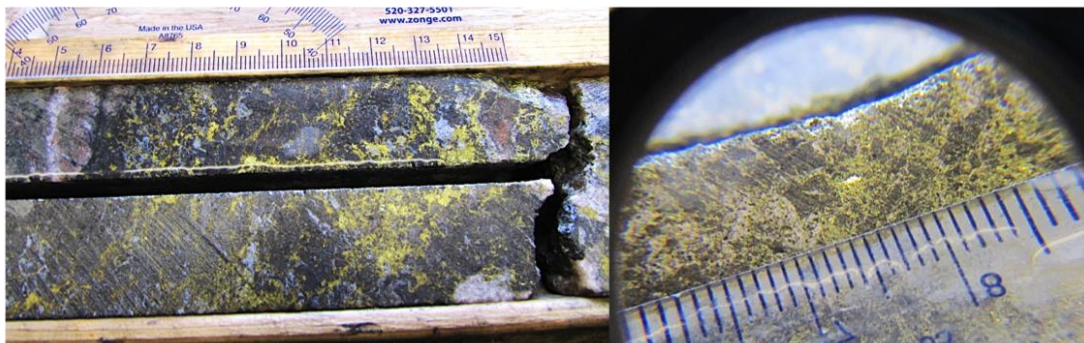
Hand Sample Description: The core box has two ~30 cm wide quartz-calcite veins within a fine grained mafic host. Veins occur at ~45 degrees to core axis and are composed of quartz, calcite, chlorite, and sulphides (dominantly chalcopryite) with trace pyrite and no magnetite. A tiny blade of visible gold can be seen within the chalcopryite (easiest to see on the weathered surface of the core). Chalcopryite occurs as a network throughout the vein at the same angle to the core axis as the vein margins. The mafic host is strongly chloritized and contains abundant <1cm wide stringers and veins throughout. Many of the thin stringers and veins contain trace amounts of chalcopryite.

A) Free Au and Au on margins of chalcopryite,
B) Au in chalcopryite, C) Representative picture
of the groundmass in ppl and cpl

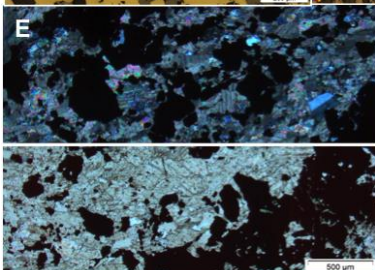
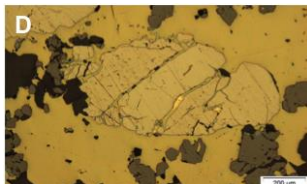
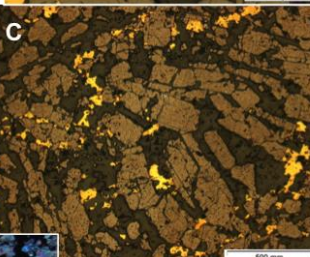
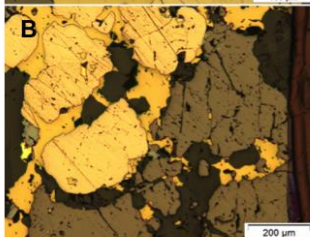
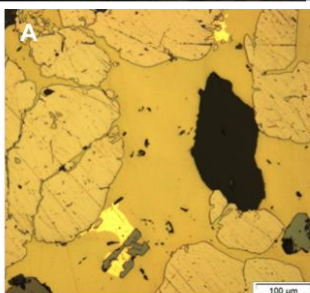


Thin Section Description: The host is coarse grained and is made up of 38% strained quartz and 38% calcite, as well as 4% chlorite. There are also trace amounts of rutile and zircon. Opaques consist of 13% sieve-textured chalcopryite, 2% hematite, 2% magnetite, and 3% sub-to euhedral pyrite. Both the pyrite and the chalcopryite are strongly sieve textured and contain inclusions of hematite, and magnetite. Hematite and magnetite are needle shaped to blockly. Textures in thin section identify that pyrite likely formed first, followed by chalcopryite, and then followed by magnetite, hematite, and Au. Au occurs as inclusions along pyrite grain margins enclosed in chalcopryite and also along chalcopryite grain margins. More than one generation of oxide growth may have occurred.

UWO_2015_10 (200-Zone Mineralized Sample)



Sample ID	UWO_2015_10
Hole ID	UB12_200W3
Sample Interval (m)	1582.2-1582.3
Lithology	Mafic Syenite
Mineralization	Cpy/Py/Mgt/VG
Host	Quartz-Calcite
Zone	200-Zone
Au Assay (g/t)	28.4
Cu Assay (pct)	7.82
Angle of mineralization	30 dtca

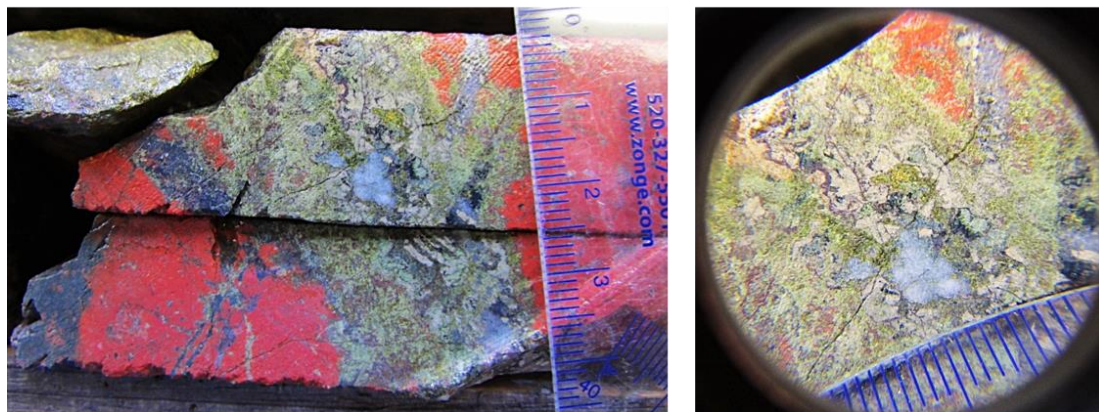


A-D) Au in chalcopyrite nucleate on either magnetite or pyrite grain margins, E) Representative picture of the groundmass in cpl and ppl

Hand Sample Description: The host rock is most likely mafic syenite although due to alteration it is hard to tell for certain. The host is variably altered by hematite and K-spar. There are also abundant magnetite +/- chalcopyrite rich fractures & veins throughout the core box. The sample interval is a ~10cm thick vein of chalcopyrite and magnetite with minimal quartz and calcite. The vein is very strongly magnetic and contains trace amounts of pyrite and a 2mm long blade of gold within the chalcopyrite mineralization. Vein contacts are roughly 75 degrees to core axis. Above the vein the host is strongly sericitized, while below it is strongly albitized. Further down hole at 1584m the core has a 5m thick fracture network that creates a brecciated pattern with chalcopyrite and magnetite surrounding a magnetite & K-spar altered host rock. A similar chalcopyrite-magnetite rich vein occurs a few 10s of centimeters below it but sample interval did not contain a high gold grade.

Thin Section Description: The sample is dominantly composed of magnetite, with only 15% calcite, 2% quartz, 3% chlorite, 1% plagioclase, 1% epidote, and 1% amphibole. There are also trace amounts of zircon and rutile in the sample as well. Magnetite appears to have been forced apart by the calcite. The remainder of the sample consists of 50% magnetite, 30% chalcopyrite, 5% pyrite and 2% hematite. Textural relationships indicate that pyrite formed first, followed by magnetite, hematite, chalcopyrite, and Au. All opaques are sieve-textured and contain inclusions of one another.

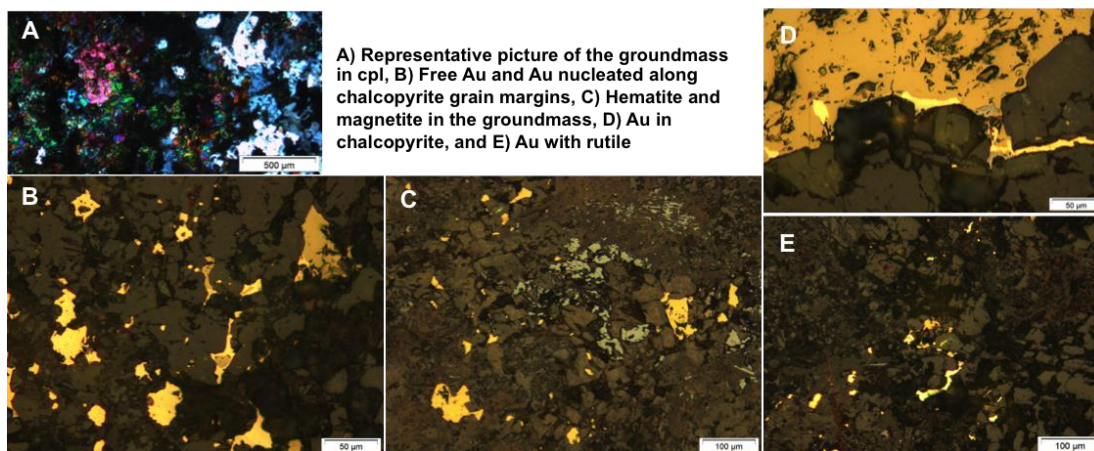
UWO_2015_11 (Lower West Porphyry Zone Mineralized Sample)



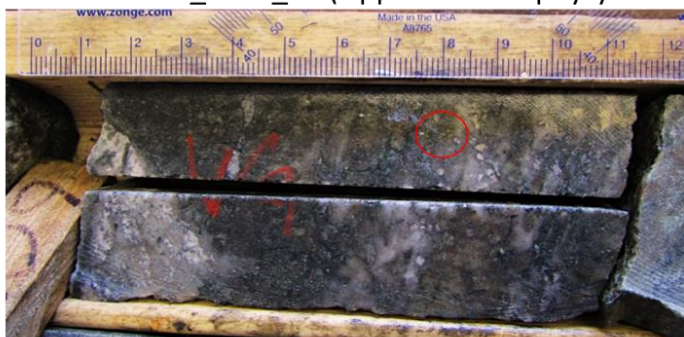
Sample ID	UWO_2015_11
Hole ID	UB12_230
Sample Interval (m)	557.9-558
Lithology	Mafic Syenite
Mineralization	Cpy/Py/Mgt/VG
Host	Quartz-Calcite
Zone	Lower Porphyry West Zone
Au Assay (g/t)	51.3
Cu Assay (pct)	0.995
Angle of mineralization	60 dtca

Hand Sample Description: The mafic syenite host is strongly altered by andalucite, causing it to appear very bright red. Mineralization is hosted within a quartz-calcite vein that is also full of epidote. The vein is altered sericite and chlorite alteration products in patches. The vein also contains magnetite, and deep red hematite fracture fills. Mineralization within the vein consists of chalcopyrite, pyrite, and a thin blade of visible gold in fractures in the vein. The host vein is just about 10cm below a large 1.75m long fault (highly fractured and ground up core with grain sizes ranging from dust sized to pebble sized). There is a similar vein at the top margin of the fault as well.

Thin Section Description: The groundmass of the sample consists of 55% epidote, 3% chlorite, 15% quartz, 5% calcite, 1% plagioclase, 10% very fine grained hematite/ Fe staining, and 1% zircon and rutile. Mineralization consists of 2% hematite, 2% pyrite, and 6% chalcopyrite. Chalcopyrite is sieve textured and contains inclusions of hematite, magnetite. Textural relationships are unclear; sometimes it looks like the oxides formed first, but other times it looks like the sulphides formed first. Au mineralization nucleates on the outer margin of chalcopyrite grains and occurs as free Au in the sample. Free Au occurs near rutile grains.



UWO_2015_12 (Upper East Porphyry Zone Mineralized Sample)

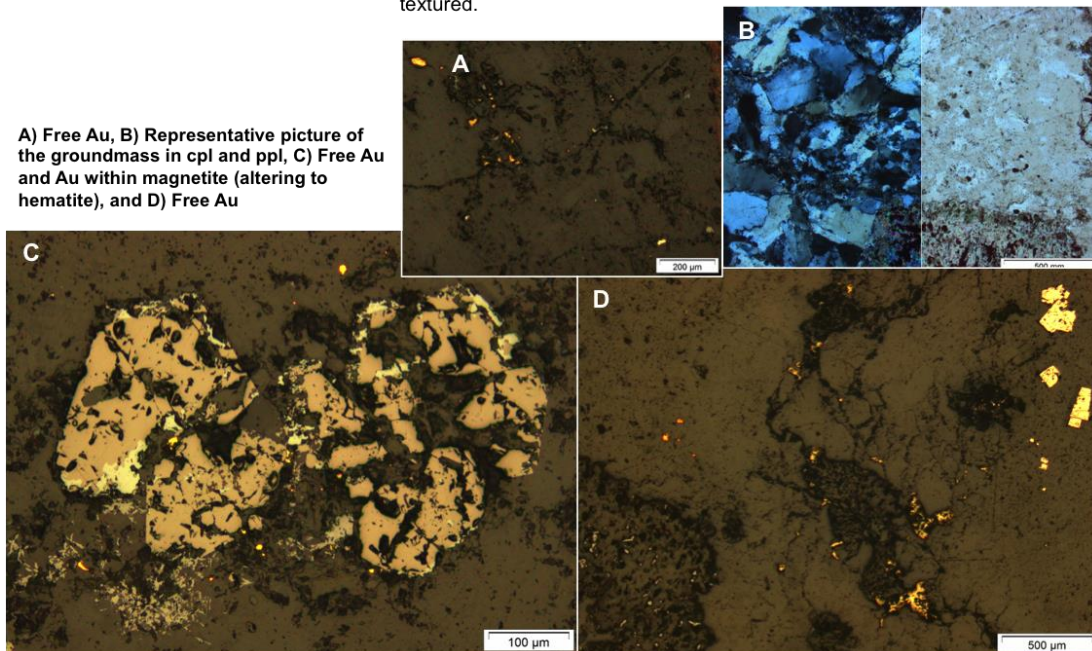


Sample ID	UWO_2015_12
Hole ID	UB12_75W3
Sample Interval (m)	603-603.1
Lithology	Mafic Syenite
Mineralization	Mo/Mgt/Py/Cpy
Host	Quartz-Calcite
Zone	Upper Porphyry East Zone
Au Assay (g/t)	129.5
Cu Assay (pct)	0.0308
Angle of mineralization	NA

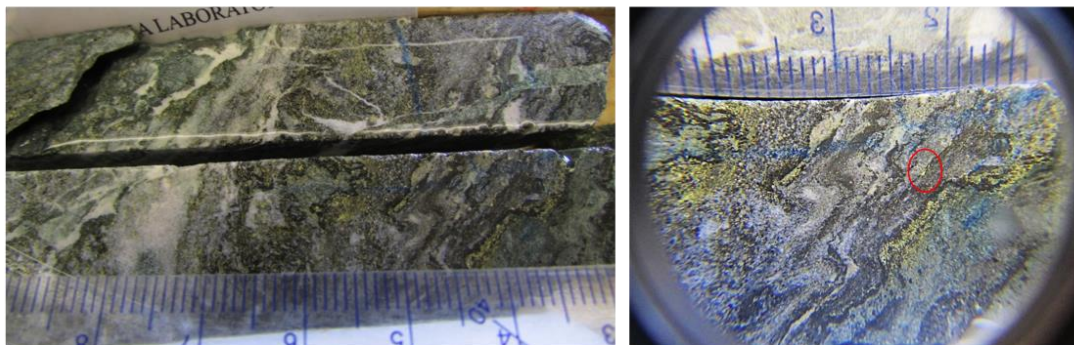
Hand Sample Description: The host looks like strongly sericitized, chloritized, and silicified crowded porphyritic quartz diorite/ granodiorite, although the core logs identify that the interval is mafic syenite. The mineralization isn't hosted in a specific vein, but rather in a patch of silica alteration. The host also contains small patches of epidote alteration. There are trace amounts of pyrite and chalcopyrite throughout. The pyrite is roughly euhedral and fine grained. There are also molybdenum rich fractures throughout the core.

Thin section description: The sample consists of deformed 70% quartz, as well as 12% calcite, 6% chlorite, 1% rutile and 1% zircon. Opaques include 1% magnetite, 2% hematite, 2% pyrite, and 5% chalcopyrite. Au occurs with hematite and magnetite and as free Au in the sample. Textural relationships indicate that pyrite formed before chalcopyrite, and that hematite and magnetite formed together, but do not indicate if pyrite and chalcopyrite or magnetite and hematite formed first. All sulphides and oxides are sieve textured.

A) Free Au, B) Representative picture of the groundmass in cpl and ppl, C) Free Au and Au within magnetite (altering to hematite), and D) Free Au



UWO_2015_13 (East Basalt Zone Mineralized Sample)

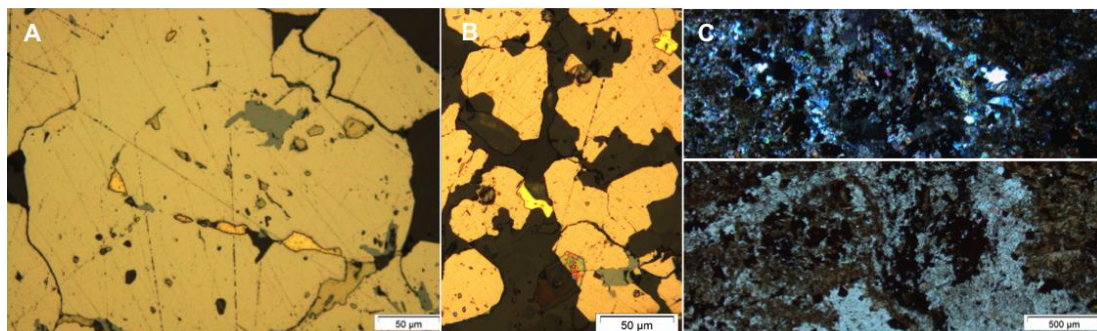


Sample ID	UWO_2015_13
Hole ID	UB13_284
Sample Interval (m)	165-165.1
Lithology	Basalt
Mineralization	Py/Cpy/Mgt/VG
Host	Quartz-Calcite
Zone	East Basalt Zone
Au Assay (g/t)	39.9
Cu Assay (pct)	3.59
Angle of mineralization	30 dtca

Hand Sample Description: The host rock is a fine grained mafic unit. The mineralization occurs in a vein of quartz, calcite, sericite, and chlorite, and has magnetite fracture fills. Mineralization seems to be concentrated within a vein that runs at approximately 30 degrees to the core axis and that consists of mm-wide stringy quartz, calcite, chlorite, sericite, and magnetite bands that occur at same angle as the vein margins. There are also abundant fine grained pyrite grains and really fine pinpricks of unidentifiable sulphides throughout the vein. Due to the colour of the vein there is possible molybdenum in the core as well although it is not obvious without a microscope. Visible gold occurs in the quartz rich patches in the rock.

Thin Section Description: Host minerals include 5% anhydrite, 32% calcite, 3% chlorite, 2% hornblende, 1% zircon, and 7% quartz. There are also trace amounts of rutile and zircon. The sample has a fair amount of iron staining. Sample consists of 25% pyrite, 25% chalcopyrite, 2% hematite, and 2% magnetite. Textural relationships indicate that the sieve-textured pyrite formed first, followed by sieve-textured chalcopyrite, then magnetite and hematite. Hematite and magnetite are irregularly shaped to needle shaped.

A) Au in pyrite, B) Au on pyrite grain boundaries, C) Representative picture of the groundmass in cpl and ppl



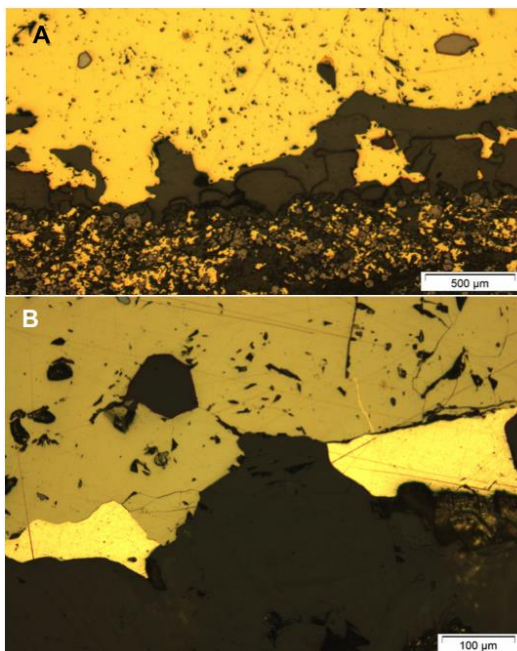
UWO_2015_14 (North Basalt Zone Mineralized Sample)



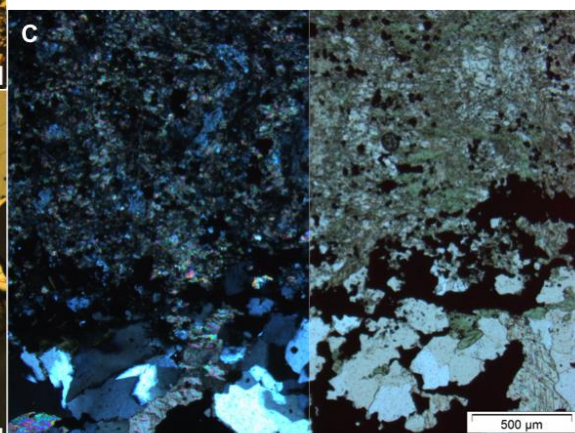
Sample ID	UWO_2015_14
Hole ID	UB13_310A
Sample Interval (m)	378.8-378.9
Lithology	Basalt
Mineralization	Cpy/Mgt/VG
Host	Quartz-Calcite
Zone	North Basalt Zone
Au Assay (g/t)	1.7
Cu Assay (pct)	5.31
Angle of mineralization	20 dtca

Hand Sample Description: The host is a magnetic and chloritized fine grained basalt. Sulphides tend to occur in abundant small networks of veinlets or in fractures in the host. The interval also contains purplish quartz veins (possibly molybdenum rich). There doesn't seem to be any pyrite within the core box.

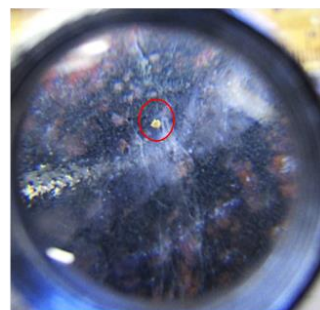
Thin Section Description: The host is composed of fine grained 20% quartz, 30% calcite, and 15% chlorite. There is also 1% zircon and rutile. Grain size increases to coarse grained close to the mineralized vein. The remaining 35% of the sample consists of opaques, which include 8% magnetite, 2% hematite, and 20% sieve-textured chalcopyrite. Textural relationships indicate multiple generations of oxide growth, with hematite and magnetite forming before chalcopyrite and also after it.



A) Hematite and magnetite in massive chalcopyrite vein with fine grained chalcopyrite and iron oxides outside the vein, B) Au in and along the margins of chalcopyrite, and C) Representative picture of the groundmass in cpl and ppl



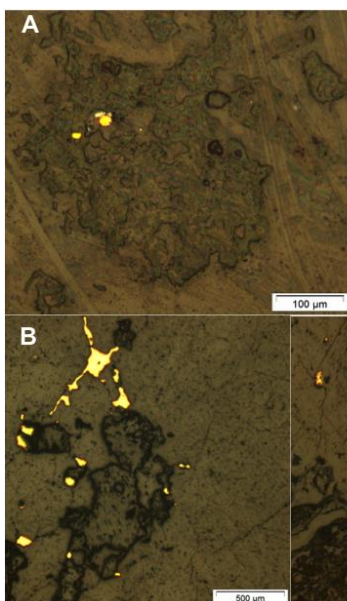
UWO_2015_15 (North Contact Zone Mineralized Sample)



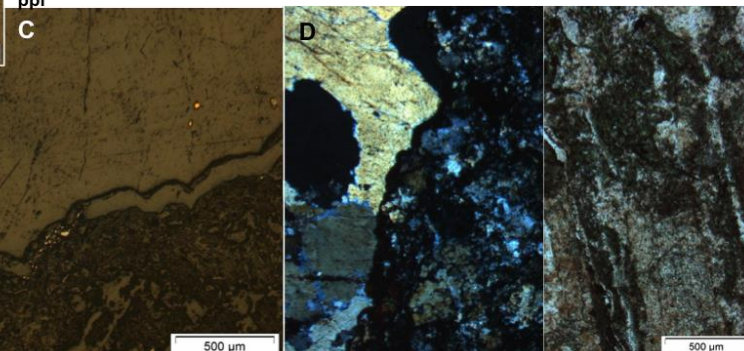
Sample ID	UWO_2015_15
Hole ID	UB14_334
Sample Interval (m)	142.3-142.4
Lithology	Altered Crowded Syenite Porphyry
Mineralization	Mgt/VG
Host	Quartz (Host responds to acid, FF/Veinlets do not)
Zone	North Contact Zone
Au Assay (g/t)	31.8
Cu Assay (pct)	0.0202
Angle of mineralization	45 dtca

Hand Sample Description: The host rock is a crowded syenite porphyry. Mineralization occurs within a ~1 cm wide vein of quartz surrounded by an up to 2cm wide halo of chlorite and magnetite. The vein cuts the core at roughly 50 degrees to the core axis. There are no visible sulphides in the vein however, there is a tiny spec of visible gold within the quartz vein near the chlorite/ magnetite rich halo. An earlier magnetite-pyrite fracture fill is cut by the vein.

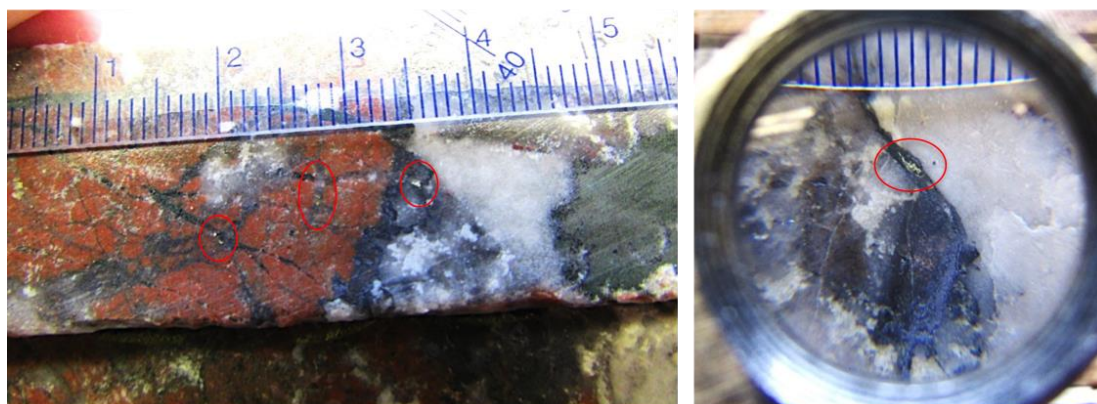
Thin section description: The rock consists of fine to coarse-grained minerals including 10% chlorite, 45% plagioclase, 25% quartz, and 10% calcite, as well as trace amounts of rutile and zircon. The rock is dominantly a mix of plagioclase, chlorite, and calcite with minor amounts of quartz. The remainder of the quartz % comes from a coarse-grained quartz-rich vein that runs through the sample. This vein hosts the majority of the Au mineralization in the sample. Opaques in the sample consist of 4% hematite, <1% pyrite, and Au. Au occurs as fracture-fill mineralization and as free-Au



A-C) Free and fracture-fill Au, D) representative picture of the groundmass in cpl and ppl



UWO_2015_16 (Upper East Porphyry Zone Mineralized Sample)

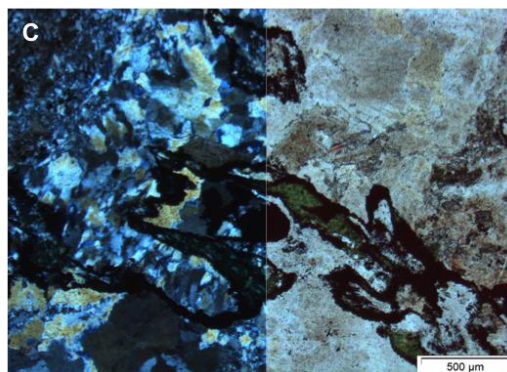
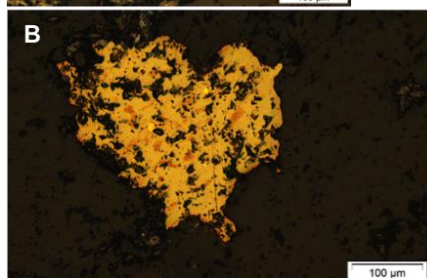
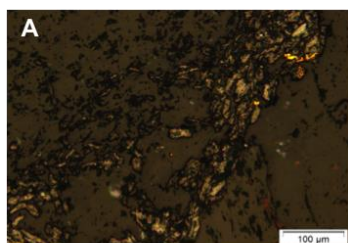


Sample ID	UWO_2015_16
Hole ID	UB14_337
Sample Interval (m)	205.3-205.4
Lithology	Altered Basalt
Mineralization	Mo/Py/VG
Host	Quartz-Calcite
Zone	Upper East Porphyry Zone
Au Assay (g/t)	25.8
Cu Assay (pct)	0.0145
Angle of mineralization	70 dtca

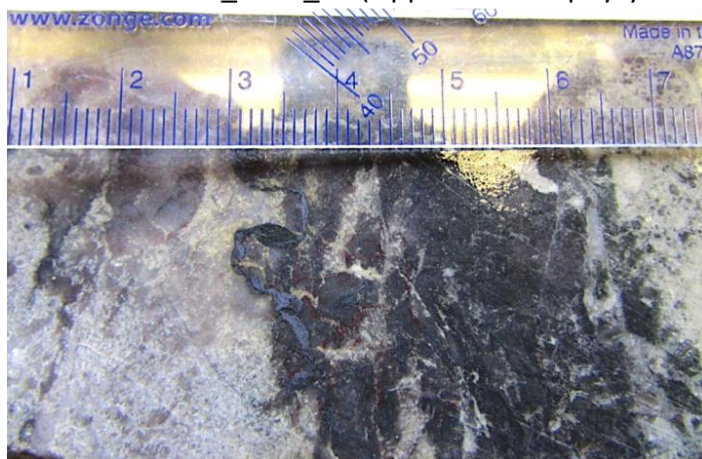
Hand Sample Description: This sample is the shallower sample from a high grade interval in hole UB14_337. The sample is of a molybdenum and quartz rich vein and fracture fill within a fine grained mafic host that is strongly altered by hematite. The sample contains tiny flecks of gold within the quartz fracture fills in the strongly hematized host as well as in the main quartz vein. Molybdenum occurs as thin squiggly fracture fills within the host rock. There is also a large patch of chlorite alteration within lower section of the vein however it lacks visible mineralization. Finally, there are small ankerite patches throughout the entire vein.

A) Au in molybdenum, B) Au in chalcopyrite, C) Representative picture of the groundmass in cpl and ppl

Thin Section Description: The groundmass is made of dominantly quartz (50%) and calcite (36%) and ranges in size from fine grained to coarse grained. Grains are all anhedral. There are also trace amounts of zircon and rutile. Chlorite is present as well (5%), and is closely associated with the molybdenum stringers. Mineralization in the thin section consists of chalcopyrite, hematite, and molybdenum. In this slide, Au is associated with the chalcopyrite or the molybdenite, or occurs as free Au. Cu is present in very minor amounts (1%) in the slide, while hematite occupies approximately 3% of the slide, and molybdenum occupies ~ 5%.



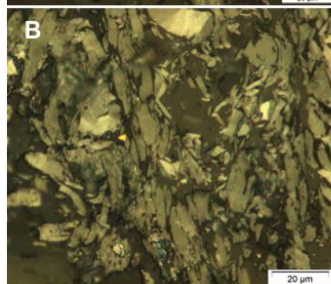
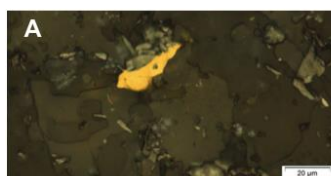
UWO_2015_17 (Upper East Porphyry Zone Mineralized Zone)



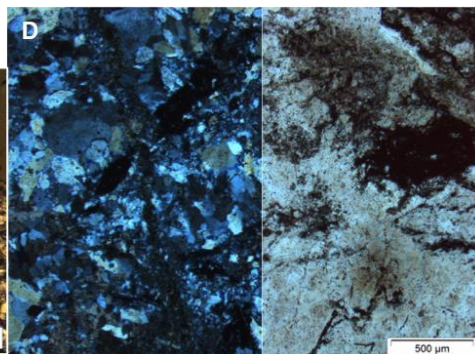
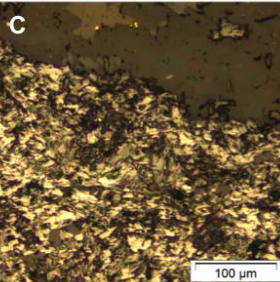
Sample ID	UWO_2015_17
Hole ID	UB15_337
Sample Interval (m)	205.6-205.7
Lithology	Altered Basalt
Mineralization	Mo/Py/VG
Host	Quartz-Calcite
Zone	Upper Porphyry East Zone
Au Assay (g/t)	25.8
Cu Assay (pct)	0.0145
Angle of mineralization	70 dtca

Hand Sample Description: This sample is the deeper sample from a high grade interval in hole UB14_337. The host is a fine grained mafic unit which hosts a quartz, calcite, ankerite, molybdenum, chlorite, and hematite rich vein. The fine grained visible gold occurs within a thin molybdenum rich band near the vein margin with no other associated visible sulphides. There is an additional tiny spec of visible gold a few cm's away in the quartz-rich vein which appears to be unassociated with visible molybdenum or sulphides.

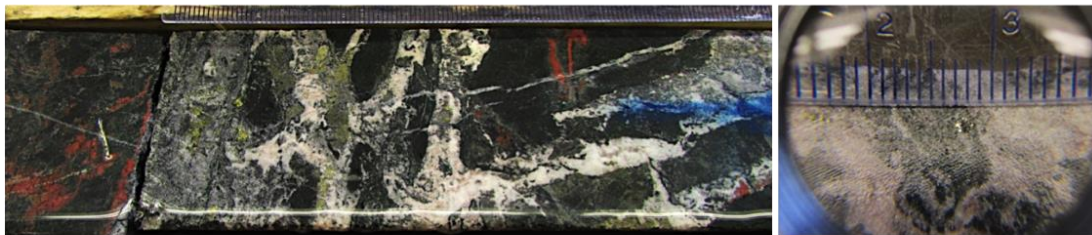
Thin Section Description: The rock is dominantly composed of fine to coarse grained quartz (50%) and calcite (35%) with minor (2%) anhydrite and 1% chlorite. There are also trace amounts of rutile and zircon. Opaques include molybdenite (8%), hematite (2%), pyrite (1%), and chalcopyrite (2%). Au mineralization is associated with molybdenum and was not found as inclusions within pyrite or chalcopyrite grains



A, B) Au in molybdenum, C) Free Au, D) Representative picture of the groundmass in cpl and ppl



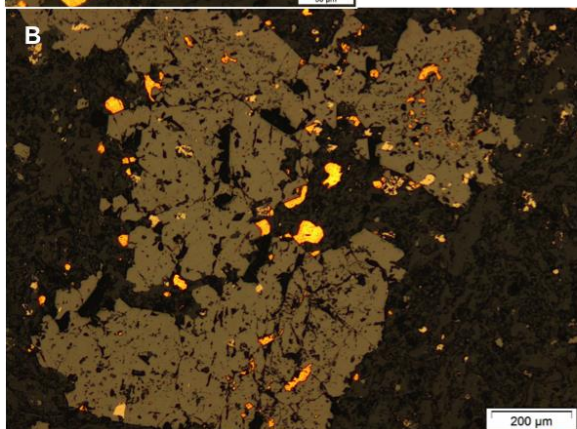
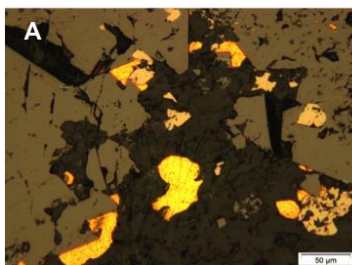
UWO_2015_18 (North Contact/ South Contact Zone Mineralized Sample)



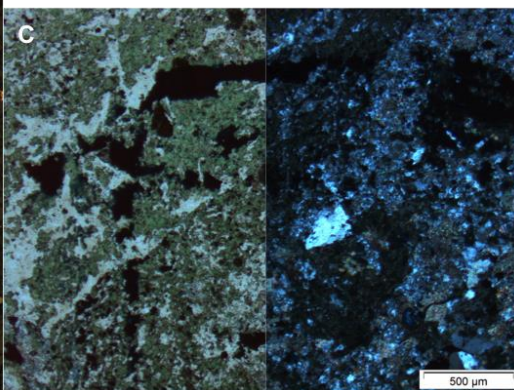
Sample ID	UWO_2015_18
Hole ID	UB14_353
Sample Interval (m)	98.85-95
Lithology	Pillowed Basalt
Mineralization	Cpy/Py/Mgt/VG
Host	Quartz-Calcite (and weak ankerite)
Zone	North Contact Zone
Au Assay (g/t)	42
Cu Assay (pct)	0.404
Angle of mineralization	80 dtca

Hand Sample Description: The parent rock is a fine grained mafic volcanics which hosts a mineralized vein. The vein that contains the mineralization is brecciated with homolithic clasts of the fine grained mafic host/ magnetite patches in a quartz rich matrix. The clasts are elongated (<5cm long and <1cm wide) and are oriented in various directions. Some clasts have been almost completely altered to magnetite. Vein contains small patches of strong pinkish red K-spar alteration and the mafic volcanics surrounding the vein also contain this type of alteration. The vein itself occurs at 45 degrees to core axis. Pyrite mineralization and trace chalcocopyrite mineralization is concentrated along the edges of the homolithic clasts within the quartz matrix. Trace visible gold occurs as tiny fine grain flecks in both the quartz rich sections and within the pyrite. The vein contains mostly pyrite alteration however in ~20 cm there is another vein that dominantly contains chalcocopyrite. This vein cuts the vein at 90 degrees to the core axis and consists of chalcocopyrite, magnetite, and quartz bands. The entire box (~4m) contains abundant quartz-calcite+/- chlorite stringers throughout at 45 or 90 degrees to core axis and some of them (but not all of them) are mineralized.

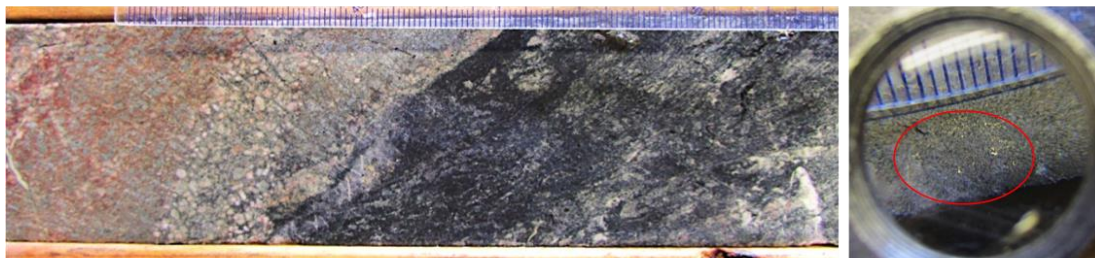
Thin Section Description: Opaques in the thin section include 5% pyrite, 3% chalcocopyrite, 10% magnetite, and 2% hematite. The remainder of the slide is composed of 30% chlorite, 10% anhydrite, 20% quartz, 19% calcite, and 3% biotite. There are also trace amounts of zircon, rutile, and trace amounts of garnet. Textural relationships show that there was an early generation of pyrite growth, followed by hematite and magnetite growth, and finally by a second phase of sulphide growth. All opaques are sieve-textured.



A,B) Free Au and Au nucleated on magnetite grain margins, C) Representative picture of the groundmass in ppl and cpl



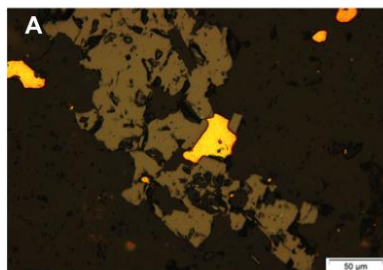
UWO_2015_19 (North Contact Zone Mineralized Sample)



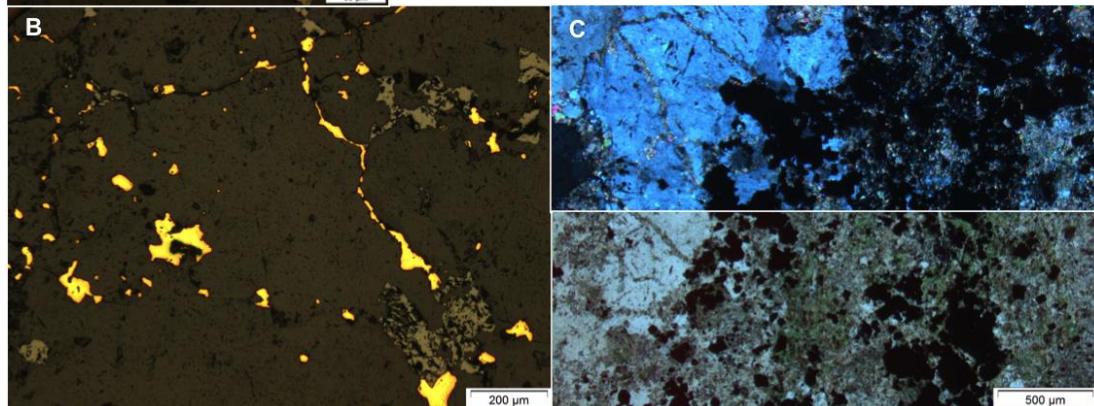
Sample ID	UWO_2015_19
Hole ID	UB14_355
Sample Interval (m)	207-207.1
Lithology	Crowded syenite porphyry
Mineralization	Mgt/Py/VG
Host	Quartz-Ankerite
Zone	North Contact Zone
Au Assay (g/t)	21.8
Cu Assay (pct)	0.0212
Angle of mineralization	45 dtca

Hand Sample Description: The parent rock is an altered crowded syenite porphyry that has been bleached by sericite and hematite alteration. The sample is from a thin ~1cm wide quartz vein that has magnetite along its margins in a 1mm-5mm wide rim. This rim also contains euhedral pyrite with trace free gold along the rims of the pyrite grains. Down hole the rock becomes more chloritized while above it's more sericitized. The entire box has abundant unmineralized (to trace amounts of mineralization) quartz-calcite stringers that typically occur at 45 degrees to core axis.

Thin Section Description: The sample is composed of 10% chlorite, 30% fine to very coarse grained quartz, 37% calcite, 1% biotite 2% anhydrite, trace zircon, and 20% opaques. There are also trace amounts of rutile and zircon. Opaques include 2% fracture fill Au, 1% hematite, 2% chalcopryite, 15% magnetite. Chalcopryite, hematite, and magnetite are sieve-textured. Textural relationships show that hematite and magnetite formed prior to Au and chalcopryite.



A) Au in magnetite, and B) Free Au, C) Representative picture of the groundmass in cpl and ppl



UWO_2015_20 (Surface sample of Tisdale cherty sediments)

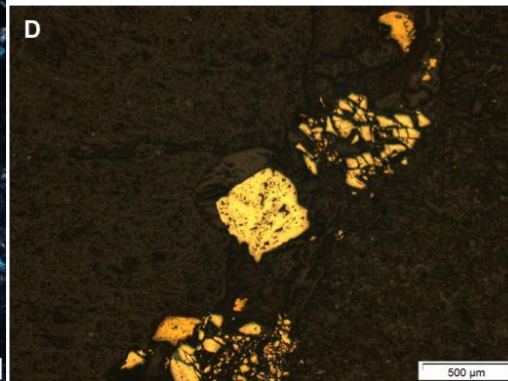
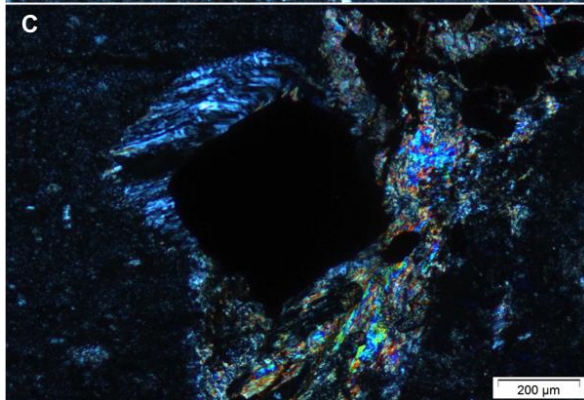
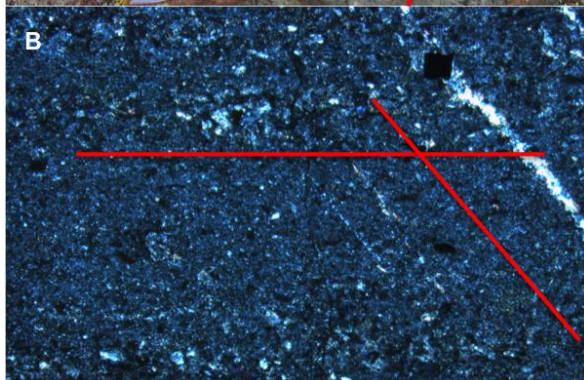
Sample ID	UWO_2015_20
Hole ID	Surface sample. (519817; 5335170)
Sample Interval (m)	NA
Lithology	Upper Tisdale cherty sediments

Hand Sample Description: Upper Tisdale sample taken from the Victoria Creek Deformation Zone, a few meters from the contact with the Blake River Group rocks. Sample consists of well-interbedded layers of cherty sediments and greywacke. The bedding as seen in outcrop is nearly vertically dipping and there is abundant evidence of soft sediment deformation and faulting. There are trace amounts of euhedral pyrite throughout the rock.

Thin Section Description: The rock is relatively fine grained and consists dominantly of quartz and calcite with abundant chlorite and sericite alteration. Coarse grains are all anhedral. Zircon is present in trace amounts. Original bedding can be seen in thin layers ~1mm-10mm wide. Late strain caused quartz +/- calcite veins to develop. These veins cross original bedding at ~80 degrees.

The rock is composed of 59% quartz, 30% calcite, 7% sericite, 3% chlorite, and 1% sulphides.

The rock contains ~1% euhedral to anhedral and sieve- textured pyrite ~0.25 mm wide as well as trace amounts of chalcopyrite, which is only present in the quartz stringers. Quartz pressure shadows are present around the pyrite



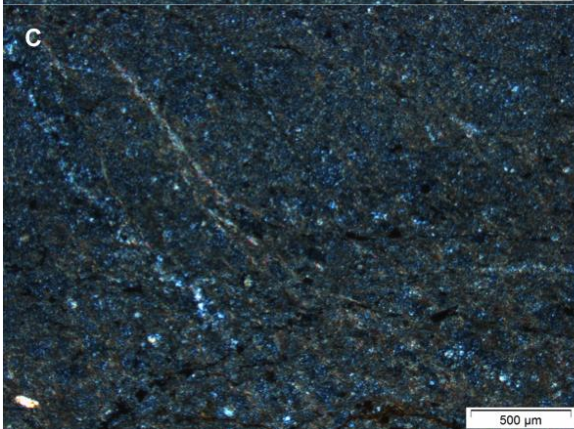
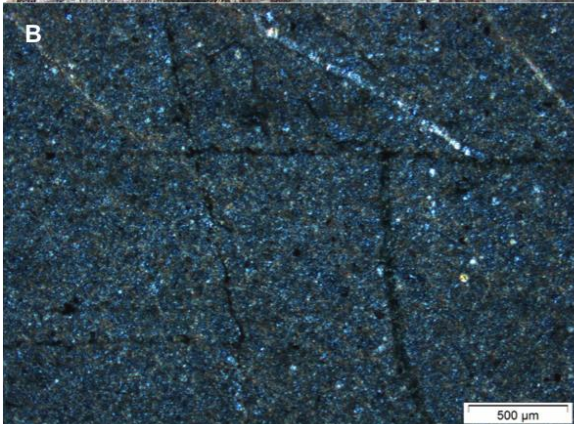
a) Outcrop photo with bedding planes in red, B) Representative picture of the groundmass with horizontal bedding planes and foliation identified, C) Pressure shadows around sulphide grain, D) Mineralization following foliation

UWO_2015_21 (Surface sample of Tisdale Cherty Sediments)

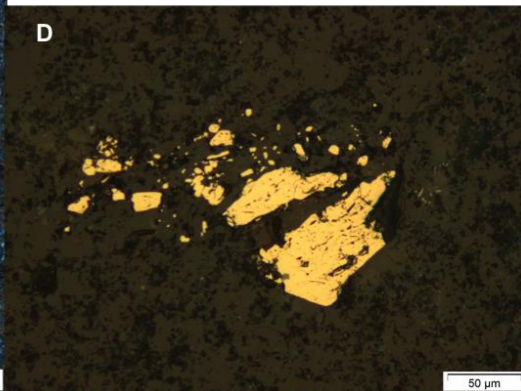
Sample ID	UWO_2015_21
Hole ID	Surface sample. (591756; 5335298)
Sample Interval (m)	NA
Lithology	Upper Tisdale cherty sediments

Description: Upper Tisdale sample taken from the Victoria Creek Deformation Zone, a few meters from the contact with the Blake River Group rocks. Sample is nearly identical to the first sample visually and consists of well-interbedded layers of cherty sediments and greywacke. The bedding as seen in outcrop is nearly vertically dipping and strikes 320 degrees. There is abundant evidence of soft sediment deformation and faulting. There are trace amounts of euhedral pyrite throughout the rock.

Thin Section Description: The rock is relatively fine grained and consists dominantly of quartz and calcite with abundant chlorite and sericite alteration. Coarser grains are well rounded. Zircon is present in trace amounts. Original bedding can be seen in thin layers ~1cm wide. A foliation is defined by the parallel alignment of sericite and chlorite grains and occurs roughly 60 degrees to the bedding. Irregularly oriented quartz-calcite veins are also present in minor amounts. Graded bedding can be easily identified in the sample. Overall, the rock is composed of 65% quartz, 20% calcite, 12% sericite, 3% chlorite, and 1% sulphides. Opaques include roughly 1% euhedral to anhedral and sieve- textured pyrite ~0.25 mm wide as well as trace amounts of fine-grained magnetite and hematite.



A) Outcrop photo of sample location, B) Horizontal bedding and oblique foliation, C) Change in grain size grading up, D) Mineralization in the sample



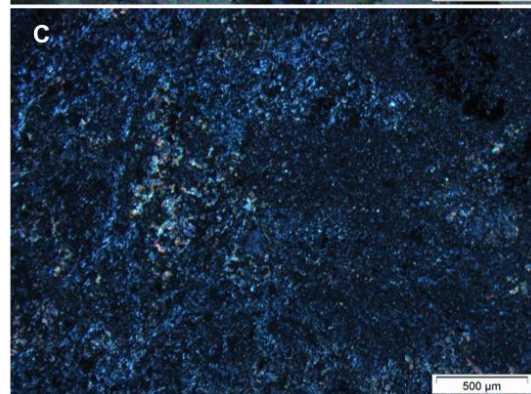
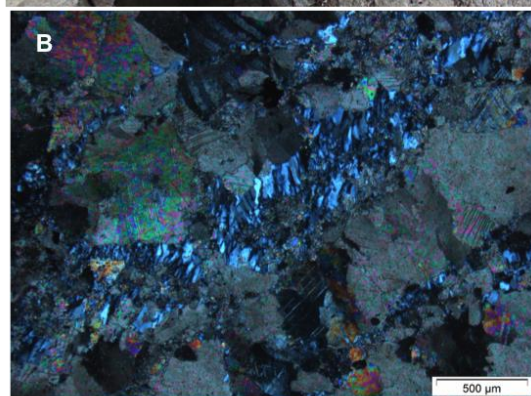
UWO_2015_22 (Surface sample of Tisdale metagreywacke)

Sample ID	UWO_2015_22
Hole ID	Surface sample. (519530; 5335595)
Sample Interval (m)	NA
Lithology	Upper Tisdale greywacke

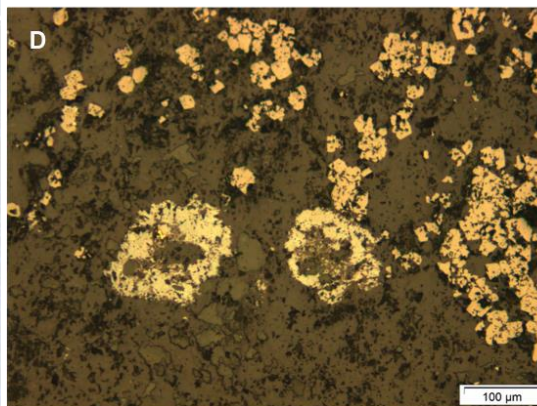
Hand Sample Description: Upper Tisdale sample taken from the Victoria Creek Deformation Zone, a few meters away from the Blake River Group rocks. Sample is crystalline metagreywacke with a sugary texture. Bedding at the outcrop is nearly vertically dipping. Additionally, trace amounts of pyrite can be seen throughout the sample.

Thin Section Description: The sample consists dominantly of coarse grained calcite and fine grained quartz. All grains are anhedral. Most of the quartz occurs in aligned bands in the rock and shows evidence of high amounts of strain. The rock consists of approximately 75% calcite and 25% quartz.

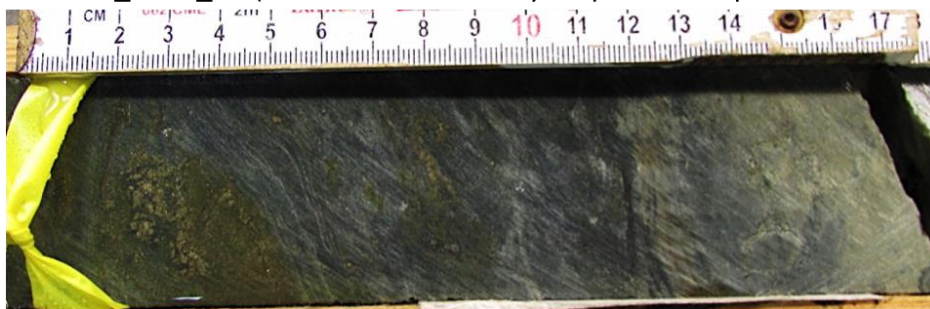
The sample also contains trace amounts of fine-grained (0.1mm) anhedral pyrite, chalcopyrite, and magnetite and trace amounts of zircon.



A) Outcrop photo of sample location, B) Deformed quartz band, C) Horizontal bedding and foliation at roughly 60 degrees, D) Hematite, magnetite, and chalcopyrite in sample



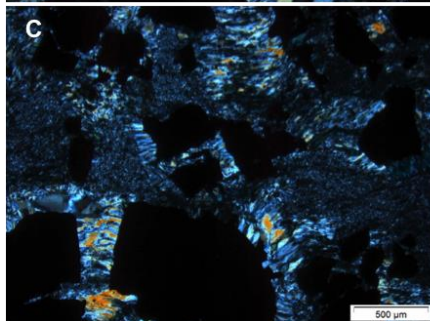
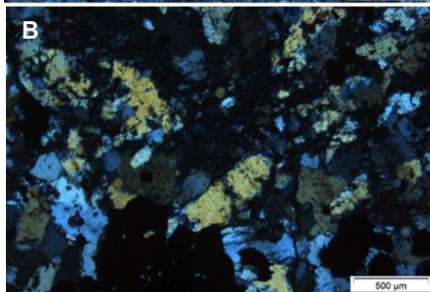
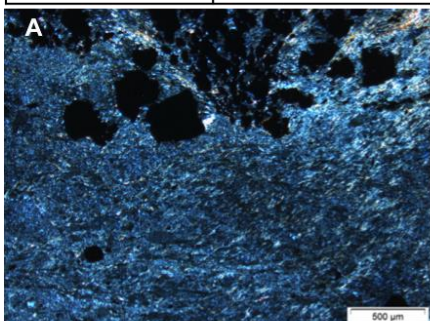
UWO_2015_23 (Isolated Sedimentary Sequence Graphitic Sediments Sample)



Sample ID	UWO_2015_23
Hole ID	UB07_116W1
Sample Interval (m)	581.8-581.9
Lithology	Graphitic sediments

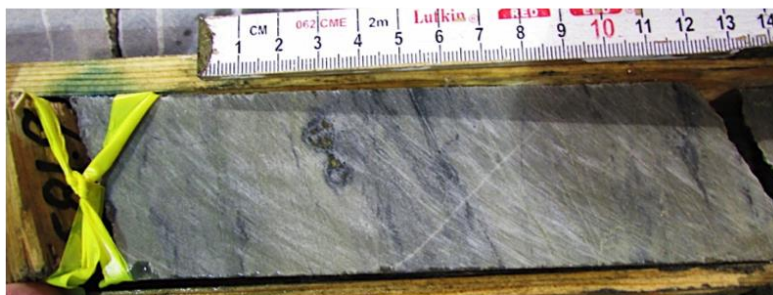
Hand Sample Description: Sample of graphitic sediment. Sample interval is dark grey to beige-green in colour and consists of layered fine-grained sediments. Layers range in size from less than 1mm in width up to 5mm in width. Abundant diagenetic pyrite nodules occur within the layers. All minerals in the rock are very fine grained except for the pyrite nodules which range in size from fine grained up to 1cm wide. Layers are oriented roughly 45 degrees to the core axis. Darker layers contain more graphite while lighter layers are more sericite altered and resemble fine layers of cherty sediments. Pyrite seems to occur in dark graphite-rich bands that are up to 5cm wide.

Thin Section Description: The rock is fine to coarse grained layered quartz and calcite with abundant chlorite and sericite alteration. Thin bedding can be distinguished by changes in grain size, and a foliation is developed by the parallel alignment of sericite and chlorite grains roughly 45 degrees to the bedding. Approximately 30% of the rock is composed of sulphides in bands. Sulphides include both chalcopyrite (5%) and pyrite (25%). Textures indicate that the pyrite formed first, followed by chalcopyrite. Both minerals are sieve-textured. There is also roughly 2% hematite and 1% magnetite, which formed within the sieve textured pyrite as well as outside of it. Quartz pressure shadows are well developed around sulphide grains in sections of the groundmass. The portion of the rock that contains the sulphide bands is strongly chloritized is coarse grained, while the portion that does not host the sulphides is dominantly fine grained and strongly sericitized. Overall, the rock is approximately 30% sulphides, 2% hematite, 1% magnetite, 37% quartz, 10% sericite, 10% chlorite, and 10% calcite.



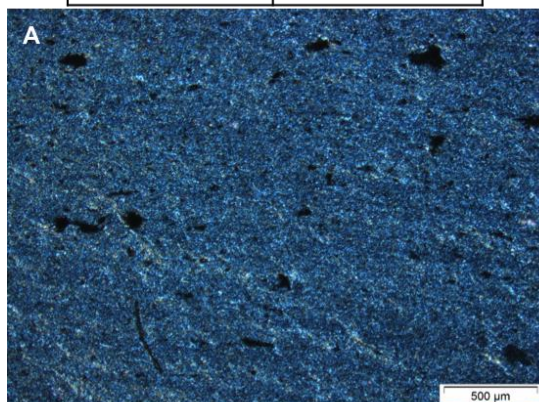
A) Fine-grained section of groundmass, B) coarse grained section of groundmass, C) Pressure shadows around large sulphide grains

UWO_2015_24 (Isolated Sedimentary Sequence Cherty Sediments Sample)



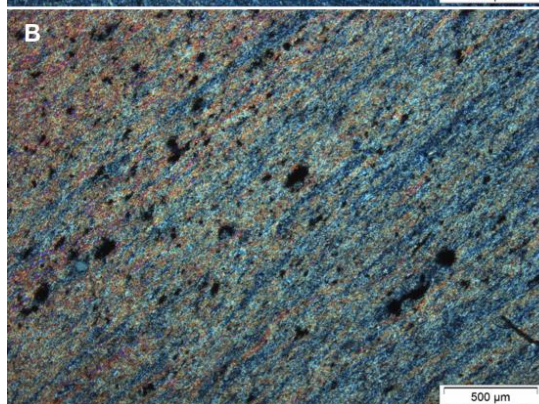
Sample ID	UWO_2015_24
Hole ID	UB07_116W1
Sample Interval (m)	581.9-582
Lithology	Cherty sediments

Hand Sample Description: Sample of cherty sediment. Tan in colour and very fine grained. The rock contains many sand-sized fragments surrounded by fine cherty grains. In places it almost looks like it may have originally been a sandstone with the cherty texture being an alteration feature, but it's hard to say for certain. Unit is has no distinct bedding but foliation/ chlorite rich thin bands occur at roughly 20 degrees to the core axis.

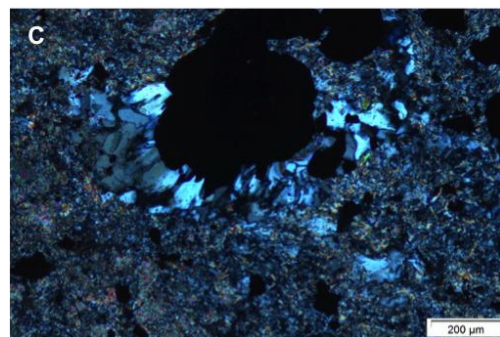


Thin Section Description: The rock is very fine grained and consists dominantly of quartz and calcite with abundant sericite and lesser amounts of chlorite alteration. The parallel alignment of sericite and chlorite grains creates a very strong foliation in the rock. Original bedding is very difficult to see, but where it is visible the foliation occurs at roughly 60 degrees to it. Quartz pressure shadows are developed around sulphide grains.

The rock is composed of 55% quartz, 7% calcite, 30% sericite, 5% chlorite, and 3% sulphides.



The rock contains roughly 1% euhedral to anhedral and sieve- textured pyrite 0.25 mm wide, 1% irregularly shaped chalcopryite grains <0.25mm wide, and 1% magnetite and hematite. Complex overprinting relationships between pyrite and chalcopryite suggest they formed at roughly the same time. Sieve textured pyrite also contains inclusions of chalcopryite.



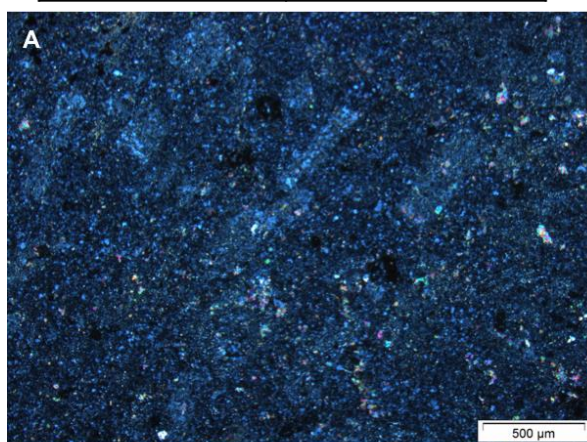
A) Horizontal bedding and oblique foliation, B) Strong foliation in the sample, C) Pressure shadows around large sulphide grain

UWO_2015_25 (Isolated Sedimentary Sequence Volcaniclastic Sample)

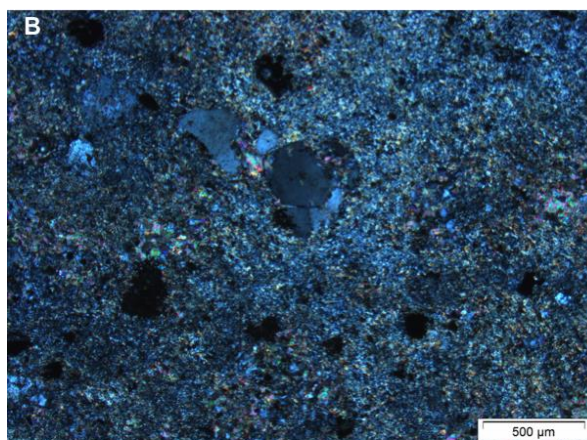


Sample ID	UWO_2015_25
Hole ID	UB07_116W1
Sample Interval (m)	608.3-608.4
Lithology	Volcaniclastic

Hand Sample Description: Highly altered unit of volcaniclastics, altered by chlorite, hematite, albite, and sericite. The groundmass as well as many of the clasts have been completely replaced. No bedding can be seen and clasts do not seem to be oriented in any particular direction. The clasts range in size from 0.5-2 cm across and can only be seen in sections due to the strong alteration. There is also a huge pyrite nodule on the back side of the core. The groundmass is strongly magnetic.



Thin Section Description: The rock dominantly consists of fine grained quartz and calcite with altered coarse grained phenocrysts. Phenocrysts make up approximately 30% of the slide and are include plagioclase laths and lesser amounts of anhedral quartz. The coarse-grained plagioclase phenocrysts are up to 1 mm long and have a "fuzzy" appearance, likely caused by sericite alteration. Original bedding planes can be discerned from the orientation of the larger phenocrysts. A foliation has developed ~60-85 degrees to the bedding plane and is defined by the orientation of the sulphides, sericite, and calcite. Original phenocrysts are much easier to identify in reflected light.



The total composition of the rock is roughly 22% plagioclase, 40% quartz, 20% calcite, 7% sericite, 2% zircon, and 8% opaques. Opaques include 1% pyrite and chalcopryrite (combined), 6% magnetite, and 1% hematite. Magnetite frequently is altered to hematite along grain rims. Completely replaced isolated grains of hematite are also present, sometimes with chalcopryrite occurring in the center of the grains.

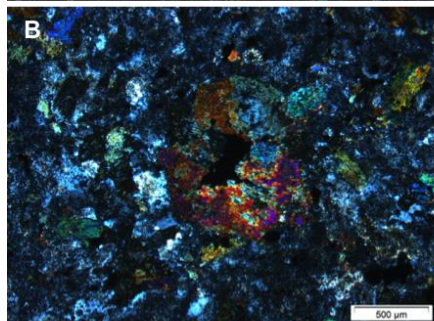
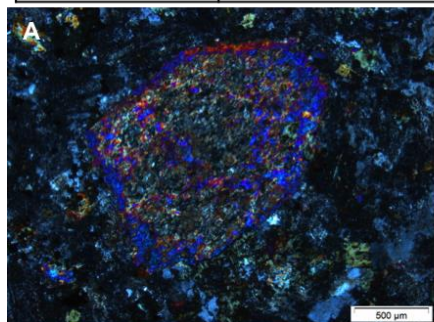
A,B) Coarse grained plagioclase and quartz phenocrysts, respectively, in a fine-grained groundmass

UWO_2015_26 (Amphibolite Dike)



Sample ID	UWO_2015_26
Hole ID	UB11_171
Sample Interval (m)	845.3-845.5
Lithology	Amphibole-rich intrusive

Hand Sample Description: The description says the rock unit has been classified as a mafic syenite (Mafic Syenite) with large amphibole phenocrysts. The large amphiboles range in size from fine grained to nearly 1cm wide. The contact with the more clearly Mafic Syenite unit is at roughly 845.5m and although the boundary is distinct, it is also somewhat gradual. Bits of the amphibolite have been broken off and occur as inclusions within the previous unit. The unit itself is greenish yellow to greenish gray in colour with large amphibole phenocrysts in a fine to coarse grained feldspar-rich groundmass that contains variable amounts of alteration by pervasive chlorite, epidote fracture-fill/ stringers, and late finally hematitic fracture-fill that cross cuts all features in the rock. The hematitic fractures are also calcitic. The unit is non to moderately magnetic. No pyrite or chalcocopyrite is visible but there are large mafic clasts in the upper Mafic Syenite unit with purplish moly along their margins (See photos). The bottom contact of the dike is at 848.4m. This contact is more of a chilled margin with a much more hematized and vein riddled syenite dike.



Thin Section Description: The rock consists of large amphibole phenocrysts and chlorite within a fine to coarse grained matrix. Amphiboles are frequently zoned with more birefringent rims. Their interiors are more heavily altered than their rims by what appears to be fine grained chlorite and/or serpentine. The matrix consists of fine to coarse grained heavily altered and deformed quartz and feldspar. The feldspar is heavily sericitized, giving it a fuzzy appearance and a brownish colour in plane polarized light and the quartz is has undulatory extinction. All grains, with the exception of the amphiboles, are highly anhedral. Late thin coarse-grained quartz veins run through the rock. Overall the rock is approximately 25% amphibole, 20% chlorite, 25% plagioclase, 5% quartz, 20% sericite, and 5% opaques. There are trace amounts of rutile in the sample as well. Opaques include magnetite (altering to hematite).

A) Large zones amphibole phenocryst, B) Representative picture of groundmass



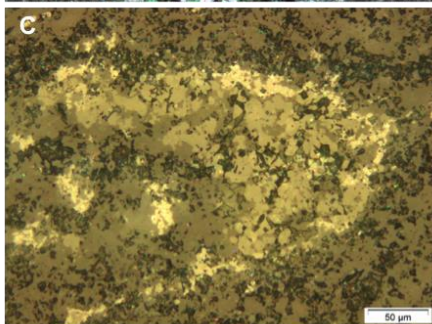
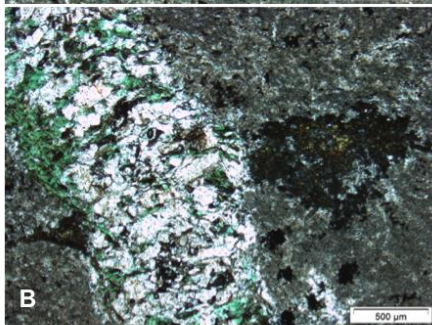
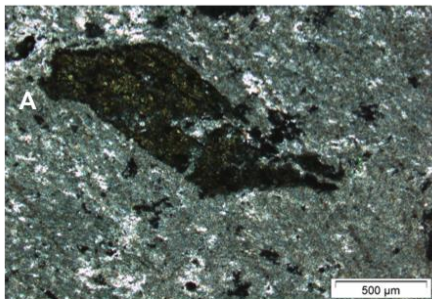
UWO_2015_27 (Microphyric Mafic Syenite Sample)



Sample ID	UWO_2015_27
Hole ID	UB11_171W2
Sample Interval (m)	1110-1110.2
Lithology	1SMa (mp)

Hand Sample Description: The host rock is greenish grey in colour with strong patchy chlorite and sericite alteration to the point that the rock almost has an almost brecciated texture in places. The microphyric texture tends to occur in patches for roughly 20 cm before the texture becomes pervasive. Each microphyric phenocryst has an almost clear core with an opaque yellowish rim. Additionally, each phenocryst is oriented roughly 45 degrees to the core axis.

Thin Section Description: The rock consists of up to 1cm long amphiboles within a fine grained plagioclase rich matrix. Amphiboles were identified by their characteristic cleavage planes at 60 and 120 degrees and their brown green to brown pleochroic colour in plane polarized light. Most of the amphiboles in the slide are highly altered and sieve-textured. Some of the amphiboles contain tiny amounts of pyrite at their core. The groundmass is dominantly very fine grained and it is strongly sericitized and chloritized. Overall the rock consists of 15% amphibole, 30% plagioclase, 7% quartz, 28% chlorite 15% sericite, 5% opaques, and trace amounts of zircon. Thin quartz-calcite veinlets run through the sample (40% calcite, 20% quartz, 20% chlorite) and are up to 5mm wide. Parallel alignment of chlorite and amphiboles creates a foliation in the rock, oblique to the direction of quartz-calcite veinlets. Opaques include 1% pyrite, and 4% hematite and magnetite, frequently occurring around amphibole phenocrysts.



A,B) Relatively competent and strongly altered amphibole phenocrysts, respectively, C) Hematite and magnetite around amphibole phenocryst, and D) Strong foliation in sample destroying amphibole phenocryst

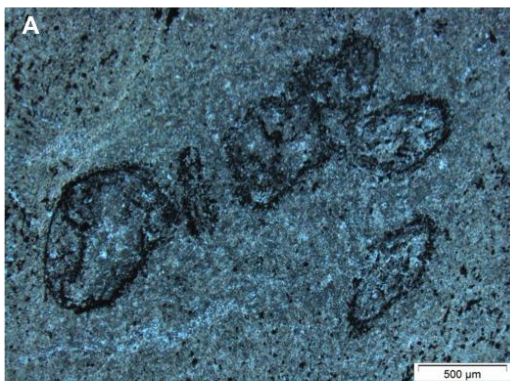


UWO_2015_28 (Microphyric Mafic Syenite Sample)

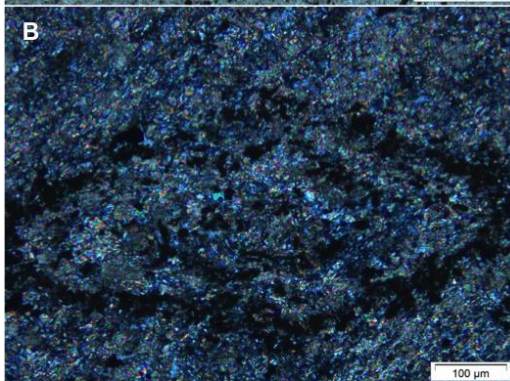


Hand Sample Description: The core box interval starts at 944.2 and there are a few microphyric phenocrysts. The microphyric texture increases towards the end of the interval and by 947.9 the texture is quite distinct. The host rock is fine grained, likely feldspathic, and is fairly dark gray with patches of pinkish alteration. The microphyric phenocrysts appear to be composed of some pinkish tan mineral in long blades. Each phenocryst is more pinkish in the center of the grain, with a very fine yellow rim along the grain boundaries. The rock almost looks like the phenocrysts were originally mafic coffin shaped amphiboles that were replaced by some sort of feldspar or muscovite, although the phenocrysts could also be feldspars. The phenocrysts are very abundant and occupy almost 20-30% of the rock in places. Unlike in the other microphyric sample, the blades of microphyric crystals do not appear to have any sort of orientation, nor are the alteration patches in any sort of orientation.

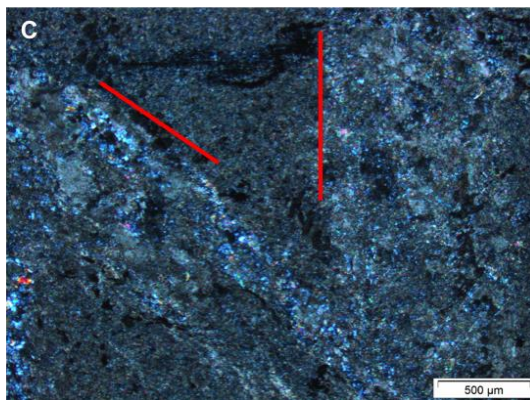
Sample ID	UWO_2015_28
Hole ID	UB11_175W4
Sample Interval (m)	947.9-948
Lithology	1SMa (mp)



Thin Section Description: The sample dominantly consists of fine-grained quartz, calcite, sericite, plagioclase, and opaques with larger phenocrysts of what may have originally been plagioclase or an amphibole completely replaced. The hexagonal grain shape of the replaced phenocrysts suggests that the grains were likely amphiboles. Overall the rock is roughly 45% plagioclase, 15% quartz, 30% sericite and 10% opaques. Opaques include 9% fine grained magnetite and 1% fine grained hematite as well as rare chalcopyrite.



Stringers define two episodes of deformation, occurring roughly 60 degrees from each other. Large phenocrysts are not aligned with either direction, but fine-grained plagioclase and micas in the groundmass can be aligned with either foliation.



A,B) Replaced phenocrysts, C) multiple directions of strain highlighted in red

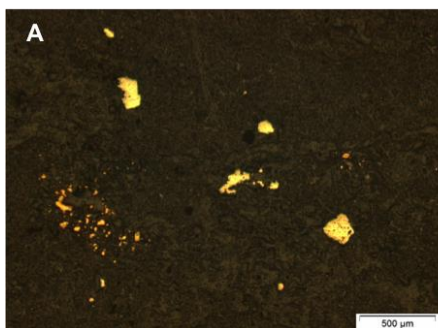
UWO_2015_29 (Isolated Sedimentary Sequence Volcaniclastics Sample)



Sample ID	UWO_2015_29
Hole ID	UB11_190
Sample Interval (m)	381.7-381.8
Lithology	Volcaniclastics

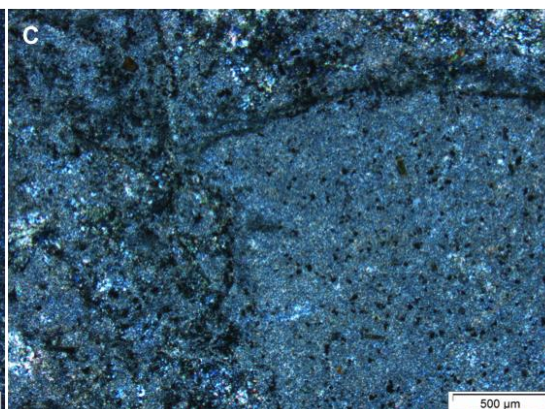
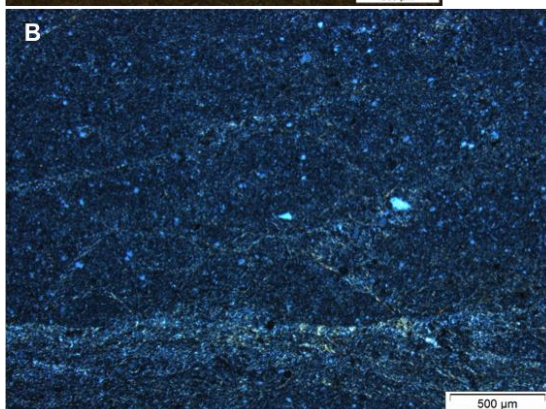
Hand Sample Description: The rock is a greenish grey unit, and is composed of mud to sand sized grains. It has been strongly altered by chlorite. It has angular clasts in a matrix-supported matrix that range in size from roughly 1mm wide to 3cm wide. Clasts are mostly quartz-rich, although many of them have been replaced by sericite or a cherty material. The clasts are for the most part well rounded and lack a clear orientation. Additionally, no bedding can be seen, possibly as the result of a flow or a slump event. Trace euhedral pyrite can be seen scattered throughout the rock.

A) Chalcopyrite and pyrite in groundmass, B) horizontal bedding and foliation roughly 60 degrees to it, and C) Large quartz rich clasts

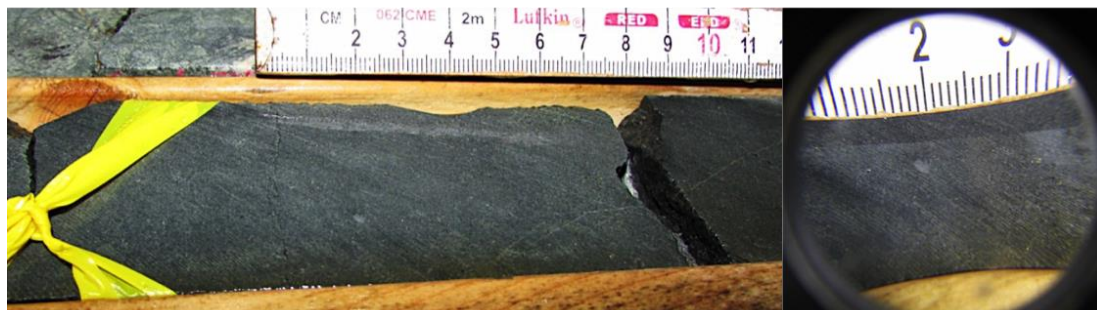


Thin Section Description: The rock is composed of roughly 80% clasts in a fine-grained and chloritized groundmass. Components that make up the groundmass include 3% biotite, 5% chlorite, 3% quartz, and 7% calcite. There are also 3% opaques in the rock, that occur in both the groundmass and the clasts. Clasts dominantly appear to be of cherty sediments (composed of quartz with lesser amounts of calcite), which are subrounded to subangular, range in size from 1mm to 3cm wide, and larger clasts have visible bedding. The original bedding of the rock can somewhat be seen, although the bedding is wavy. Thin late chlorite, biotite, and opaques occur in fractures throughout the clasts and groundmass and are oriented roughly 60 degrees to the bedding.

Opaques include euhedral to highly anhedral pyrite with trace amounts of chalcopyrite. The grain size of the opaques is roughly 0.1mm.

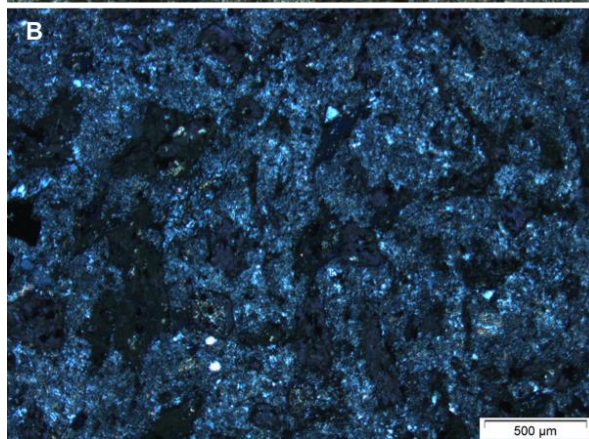
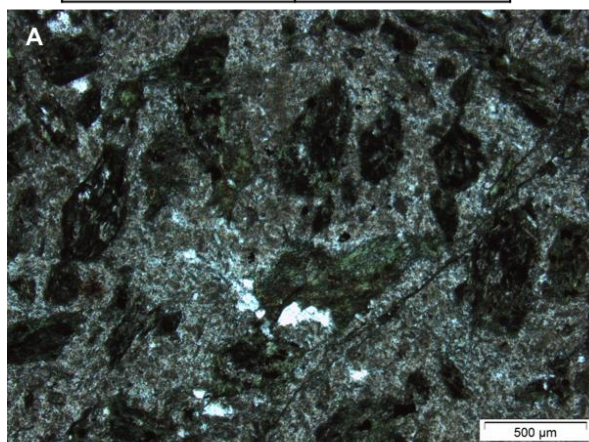


UWO_2015_30 (Isolated Sedimentary Sequence Silty Arenite Sample)



Sample ID	UWO_2015_30
Hole ID	UB11_190
Sample Interval (m)	382.2-382.3
Lithology	Silty arenite

Hand Sample Description: The rock is medium dark gray in colour and composed of sand to fine sand sized grains. It has also been strongly altered by chlorite. Within the rock, a few 1-2mm wide original clasts can be seen. These occur very infrequently but increase towards the top of the unit where the sample is from. The clasts are composed of quartz and possibly sericite or chert with a fine reaction rim. Original bedding cannot be seen in the rock but the upper contact with the overlying cherty sediments unit is roughly 45 degrees to the core axis. Trace amounts of disseminated <1mm wide grains of pyrite can be seen throughout the unit. There are also a few late quartz veinlets/ fracture fills throughout the rock unit that are most abundant at the top of the silty arenite unit. These occur at 45 degrees to the core axis.



Thin Section Description: The rock is a bit unusual as it contains a surprising amount of euhedral amphiboles that are strongly chloritized within a very fine-grained and felty groundmass consisting of quartz and calcite. The rock has a bimodal size distribution and can be said to have a porphyritic texture. Overall, the rock is approximately 20% amphibole, 30% chlorite, 40% quartz, 5% calcite, 2% biotite, and 3% opaques. No bedding can be seen in the rock. It looks more like a sample of amphibole-rich mafic syenite. Opaques include 2% sieve-textured pyrite and 1% chalcocopyrite. Textures indicate that pyrite formed first.

A,B) Amphibole and chlorite phenocrysts in a fine-grained groundmass

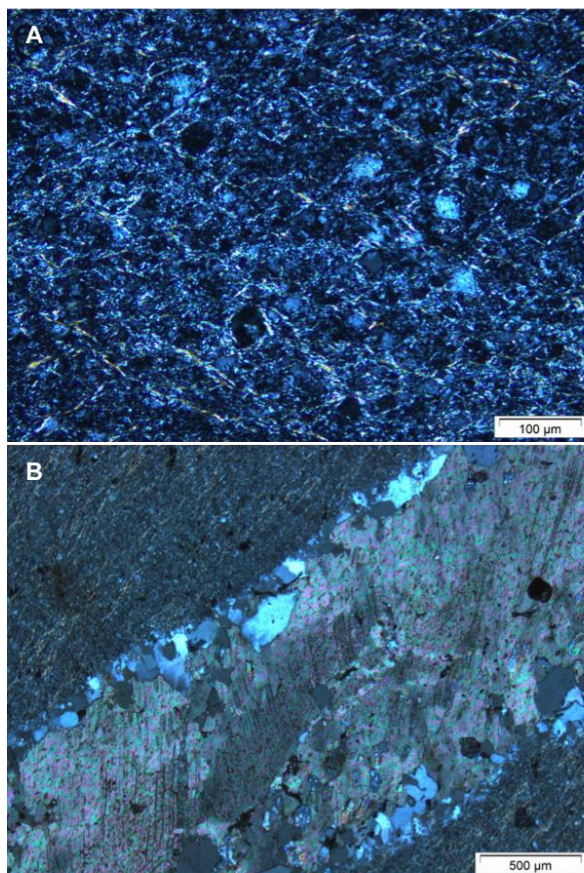
UWO_2015_31 (Isolated Sedimentary Sequence Cherty Sediments Sample)



Sample ID	UWO_2015_31
Hole ID	UB11_190
Sample Interval (m)	389-389.2
Lithology	Cherty Sediments

Hand Sample Description: Very fine grained tan cherty sediment package with cherty layers (not necessarily bedding) that occur at roughly 10-20 degrees to the core axis. The unit is strongly sericitized with variable amounts of epidote alteration that occurs dominantly as stringers. In addition, there are very thin quartz veins throughout. Within these veins as well as disseminated throughout the unit there is trace amounts of very fine grained pyrite. Where the rock is less "cherty" you can see sandy layers with grains that have a sugary texture.

Thin Section Description: The rock is dominantly composed of very fine grained quartz and calcite with lesser amounts of sericite and opaques that are oriented either parallel with bedding or 60 degrees to bedding. Late quartz-calcite veins cut through the rock and mainly contain a core of coarse grained calcite and a rim of medium grained to coarse grained quartz. Vein minerals are anhedral. The rock consists of roughly 85% quartz, 11% calcite, 11% sericite, and 3% zircon.



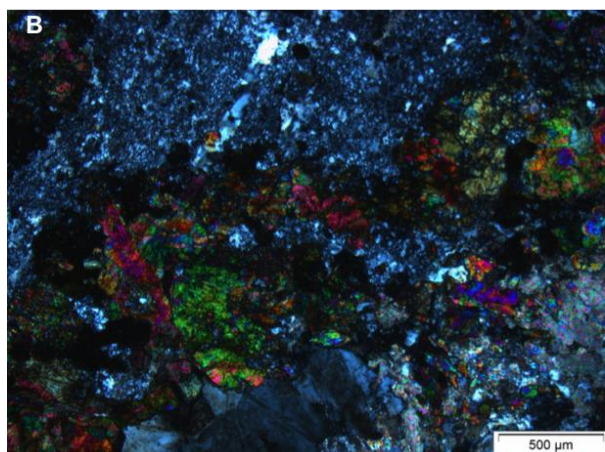
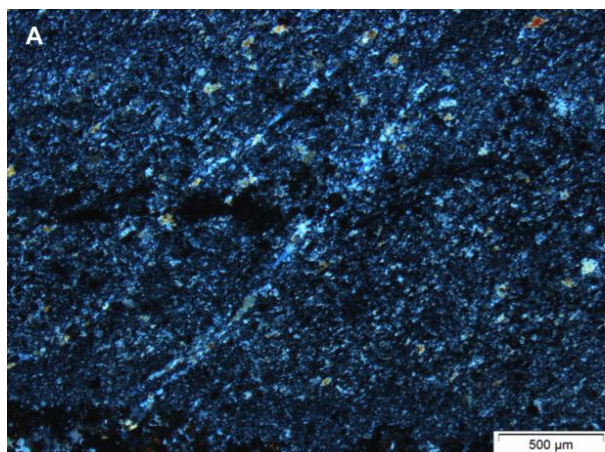
A) Quartz-rich matrix with strong foliation defined by mica planes, B) Coarse-grained calcite grain with fine grained quartz along vein margins

UWO_2015_32 (Isolated Sedimentary Sequence Cherty Sediments Sample)



Sample ID	UWO_2015_32
Hole ID	UB11_190
Sample Interval (m)	409.3-409.4
Lithology	Cherty Sediments

Hand Sample Description: Pinker unit of very fine grained cherty sediments with abundant sericite and hematite or albite alteration. The grain size ranges from fine sand to non-visible grains. More cherty layers alternate with less cherty layers and occur roughly perpendicular to the core axis in very mm-wide to 2cm-wide thin layers. The layers that contain the most cherty sediments are roughly wavy. Late coarse grained quartz stringers and fine veinlets occur throughout, as do trace amounts of fine grained euhedral pyrite, especially associated with the fracture fill. Late epidote and chlorite fracture fill are also present, as are patches of chlorite that are surrounded by epidote.



Thin Section Description: Like the previous sample, this sample dominantly consists of quartz and calcite with late stringers. This sample is slightly coarser grained than the previous, although still dominantly consists of fine grains. Original bedding can be discerned, and is cut by foliation and stringers, which occur at 30 to 60 degrees to the foliation or as irregular patches. Veins are much coarser grained in this sample and are dominated by epidote with lesser amounts of quartz and calcite. Vein grains are anhedral to subhedral in shape. The margins of the veins are dominated by anhedral quartz. The sample is roughly composed of 30% epidote, 42% quartz, 20% calcite, 5% sericite, 2% zircon and 1% opaques. Opaques consist of very fine grained euhedral pyrite, chalcopyrite, and magnetite altering to hematite. Opaques reside in the rock as veins lack sulphides and oxides.

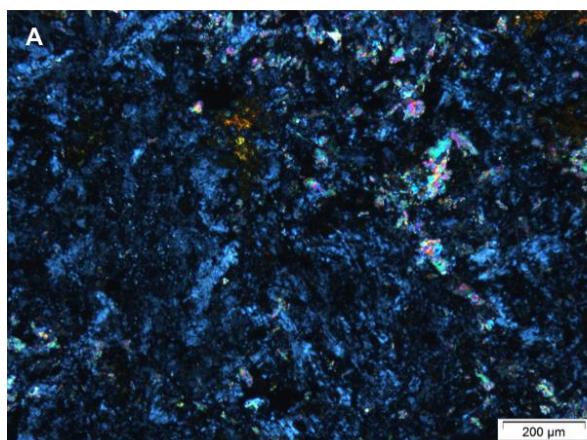
A) Horizontal bedding with oblique foliation,
B) Epidote-rich vein

UWO_2015_33 (Isolated Sedimentary Sequence Conglomerate Sample)

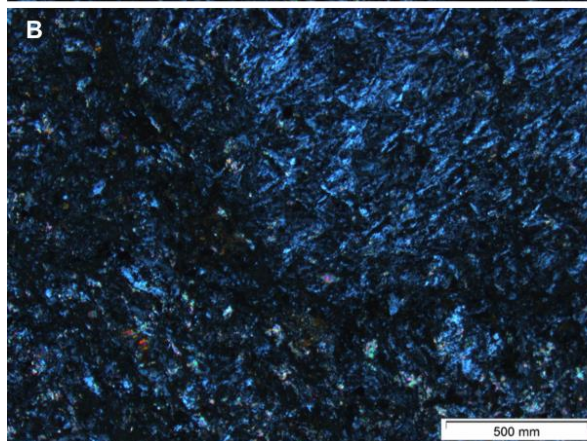


Sample ID	UWO_2015_33
Hole ID	UB11_190
Sample Interval (m)	401.6-401.8
Lithology	Conglomerate

Hand Sample Description: This sample is from a unit of clast-supported conglomerate with a fine grained and strongly chloritized groundmass. The clasts range in size from 1mm to 1cm and bedding can be seen, occurring roughly 45 degrees to the core axis. The bedding seems to almost resemble graded bedding in places, and the larger clasts tend to be aligned parallel with the bedding layers. The Clasts are heterolithic and are composed of quartz, feldspar, and rock fragments. Finally, trace fine pyrite is disseminated throughout.



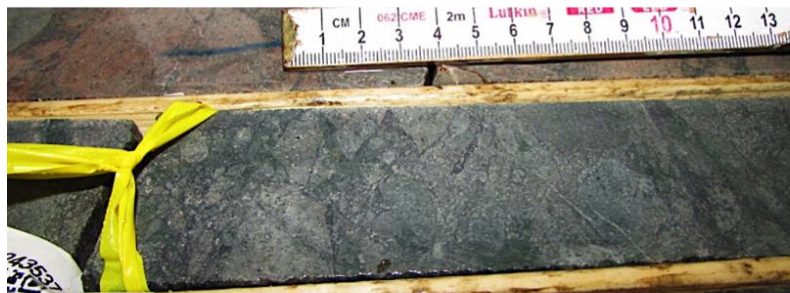
Thin Section Description: The sample consists of roughly 70% clasts in a clast-supported conglomerate. The clasts are well rounded and consist dominantly of fine to medium grained plagioclase (unoriented) with varying amounts of alteration and opaques. The groundmass is composed of roughly 10% calcite, 5% quartz, and 3% opaques. Roughly 7% of the rock is overprinted by patches of medium- to coarse-grained epidote and 5% is altered by sericite (especially the plagioclase phenocrysts). With the exception of the plagioclase, all grains are roughly anhedral in shape and fine to medium grained. Original bedding cannot be discerned in the sample.



Opaques occupy ~3% of the sample and consist of 0.1mm wide subhedral to sieve-textured pyrite grains with trace amounts of chalcopyrite.

A, B) Representative pictures of the coarse-grained clasts and the surrounding fine-grained matrix

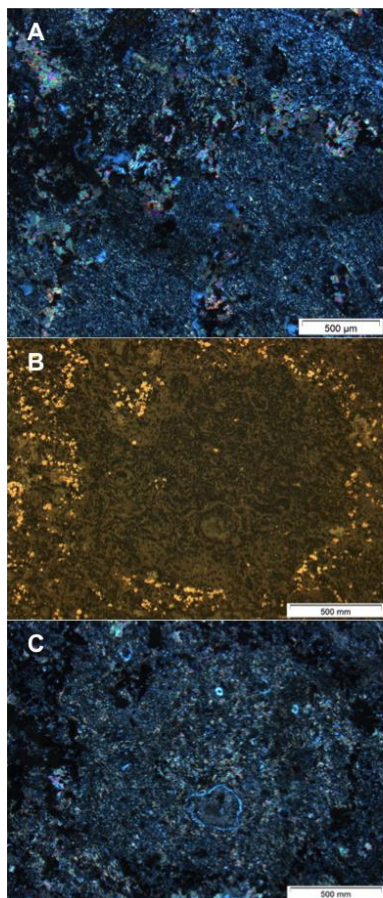
UWO_2015_34 (200 Zone Sample)



Sample ID	UWO_2015_34
Hole ID	UB12_200W2
Sample Interval (m)	1545.6-1545.7
Lithology	200 Zone

Hand Sample Description: 200 zone sample of either volcanoclastic or hydrothermal breccia. The core is highly altered by chlorite and it completely masks the groundmass. In the sample interval the "clasts" range from 0.5cm to 4cm across and appear to be composed of pinkish rock fragments, although the contents of the clasts are so fine grained that it's difficult to say for certain. Most clasts are rimmed by a thin fine grained black mineral that occurs in <1mm wide bands around the clasts. These bands are highly magnetic and are mostly likely dominantly composed of magnetite. Clasts range from being rounded to being very angular and there is no sorting whatsoever into beds or by grain size. The clasts seem to be more sericitized relative to the highly chloritized groundmass. One of the clasts in particular contains abundant magnetite. Speckles of leucoxene (?) overprints both the matrix and the ground mass. Within the entire core box the clast size can be quite large, up to 6-7cm long. The description of the sample interval is representative of the entire box, however there are sections that contain more abundant pinkish or tan clasts than sample interval. Overall, the clast:matrix ratio is ~ 1:2 (sample interval is more like 3:1) however it's highly variable.

Thin Section Description: The rock is highly altered, consisting dominantly of sericite and/or calcite (25%), and chlorite (20%), as well as deformed quartz (10%) and plagioclase (30%). Minor phases include epidote (3%) and anhydrite (5%). Clasts are very fine grained and pinkish in plane polarized light and consist of sericite or calcite, with minor amounts of anhydrite and magnetite, or of very fine grained plagioclase and quartz where less altered. The matrix surrounding the clasts on the other hand is highly chloritized, giving it a uniform greenish colour in plane polarized light, or is clear and colourless with green patches and composed dominantly of medium-grained calcite and fine-grained chlorite. Other phases that make up the matrix include very fine grained plagioclase and quartz, as well as opaques, epidote, and calcite. Opaques in the groundmass include pyrite, chalcocopyrite, magnetite, and hematite. Textural relationships indicate that hematite and magnetite formed first, followed by chalcocopyrite and pyrite. 2% pyrite, trace chalcocopyrite, trace hematite, and 5% magnetite.



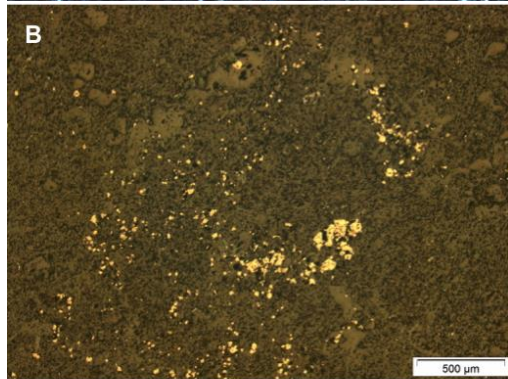
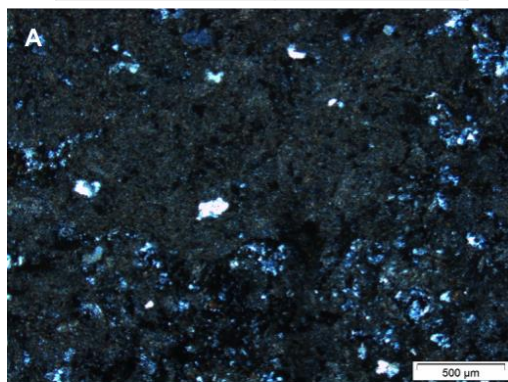
A) Representative picture of the groundmass, B,C) Large clasts in a fine-grained matrix surrounded by fine-grained magnetite

UWO_2015_35 (200 Zone Sample)



Sample ID	UWO_2015_35
Hole ID	UB11_200W3
Sample Interval (m)	1563.4-1563.5
Lithology	200 Zone

Hand Sample Description: The original rock type / groundmass cannot be discerned due to its strong alteration. The groundmass is moderately to strongly magnetic and is highly chloritized. "Clasts" are rounded and range in size from mm wide to 4cm across and contain abundant sericite and albite-hematite alteration. These clasts are pinkish to tan in colour and many contain mm-wide highly magnetic black blobs. Alteration within the clasts seems to occur in bands within the larger clasts (parallel to grain boundaries) and is more random in smaller clasts. Once again clasts are not particularly well sorted but they do appear to be oriented roughly 20 degrees to the core axis. The description of the sample interval is more or less representative of the entire box, which consists of abundant clasts within a highly chloritized groundmass. The Clast : matrix ratio is roughly 2:1 throughout. There is late chalcopyrite fracture fill throughout, sometimes occurring with magnetite. There is also trace amounts of chalcopyrite throughout the clasts.



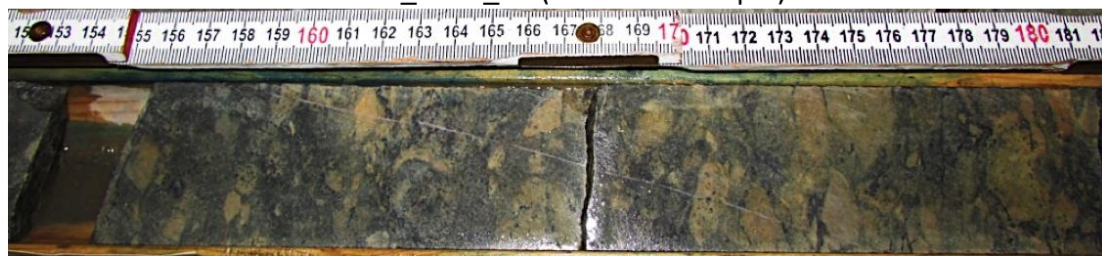
A) Large clasts in a quartz-rich matrix in cross polarized light and B) Magnetite and hematite surrounding a clast

Thin Section Description: The rock is highly altered, consisting dominantly of sericite and/or calcite (35%), and chlorite (20%), as well as deformed quartz (7%) and plagioclase (30%).

"Clasts" are very fine grained and pinkish in plane polarized light and consist of sericite with minor amounts of magnetite, or of very fine grained plagioclase and quartz where less altered. The matrix surrounding the clasts on the other hand is highly chloritized, giving it a uniform greenish colour in plane polarized light.

Opaques in the groundmass include pyrite, chalcopyrite, magnetite, and hematite. Textural relationships indicate that hematite and magnetite formed first, followed by chalcopyrite and pyrite. 1% pyrite, 1% chalcopyrite, 1% hematite, and 5% magnetite.

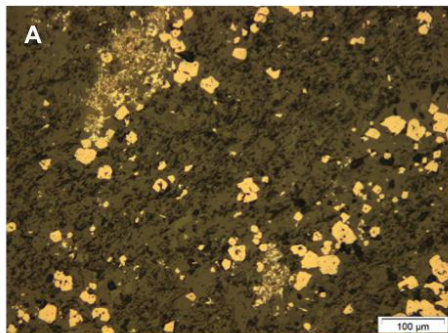
UWO_2015_36 (200 Zone Sample)



Sample ID	UWO_2015_36
Hole ID	UB11_200W3
Sample Interval (m)	1574.6-1574.8
Lithology	200 Zone

Hand Sample Description: The groundmass is fine grained, strongly magnetic, and is bleached a greyish beige colour. The clasts are greyish pinkish tan and clast edges range from being rounded to subangular. The clast size ranges from 1mm to roughly 3cm across. There are a few very thin quartz fracture fills throughout the box as well. Both the clasts and the groundmass contain plagioclase and coffin-shaped amphiboles. Clasts appear to be oriented roughly 90 degrees to the core axis. Late fracture fills appear to work their way into the larger "clasts", breaking them apart. trace fine grained pyrite is associated with these late thin quartz fracture fillings.

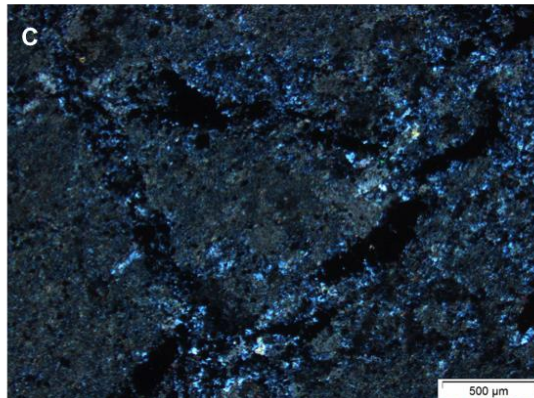
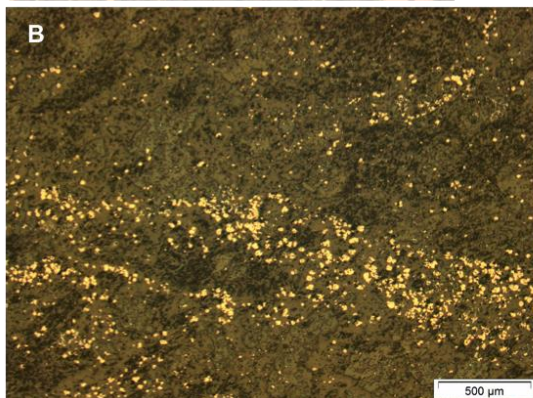
A,B) Hematite and magnetite in bands in the sample, C) Clasts in a quartz-rich matrix



Thin Section Description: The rock is highly altered, consisting dominantly of sericite (40%), and chlorite (5%), as well as deformed quartz (10%) and plagioclase (35%).

"Clasts" are very fine grained and pinkish in plane polarized light and consist of sericite with minor amounts of magnetite, although the majority of magnetite occurs in the chloritized matrix that surrounds the clasts. The matrix surrounding the clasts is more quartz rich and coarser grained. Late coarse grained quartz-calcite veinlets cross cut the rock, giving it a further brecciated appearance.

Opauques in the groundmass include 7% magnetite, 3% hematite, and trace amounts of chalcopyrite.



UWO_2015_37 (Isolated Sedimentary Sequence Cherty Sediments Sample)



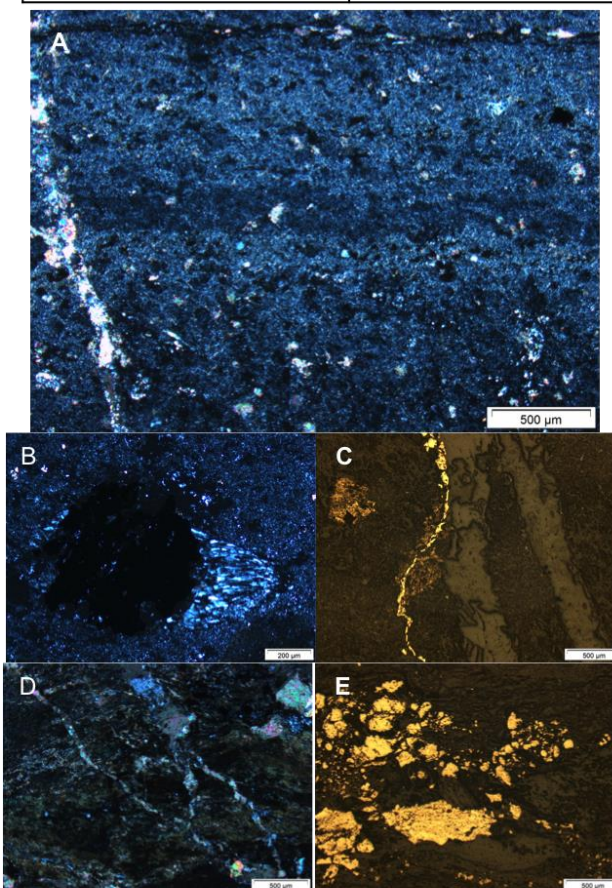
Sample ID	UWO_2015_37
Hole ID	UB12_212
Sample Interval (m)	438.15-438.4
Lithology	Cherty sediments

Hand Sample Description: Irregular interval of cherty sediments that is oriented perpendicular to the typical bedding of the rest of the rock. This section of core consists of alternating layers of fine grained mugs with sand sized layers. The lower unit contact with the underlying unit (which is at 438.5) is perpendicular to the core axis while this section is more parallel to the core axis. The unexpected orientation may be the result of soft sediment deformation. Silty layers may also be a function of alteration - can still see a few larger sand sized clasts but these could also be inclusions. Trace amounts of pyrite are present within the unit. This includes both fracture-fill pyrite as well as diagenetic pyrite.

Thin Section Description: The rock consists dominantly of alternating light and dark layers composed of very fine quartz and calcite. Larger grains of calcite are also present. There is also a 3mm wide band of what appears to be serpentine that is parallel with the bedding. Late quartz-calcite veins cross cut the beds and serpentine layer at roughly 60-85 degrees, creating a foliation in the rock. Pressure shadows occur around sulphide grains, parallel to the foliation in the rock. Bedding layers are also faulted around the veins.

Overall, the rock is composed of 15% serpentine, 57% quartz, and 25% calcite.

The remaining 3% of the rock consists of anhedral pyrite, which is concentrated in the serpentine-rich layer or in the quartz-calcite veinlets. Pyrite ranges in size from very fine grained to nearly 0.5mm.



A) Horizontal bedding, B) Pressure shadows developed around sulphide grain, C) Sulphide surrounding vein, D,E) Serpentine-rich vein in plane polarized light and reflected light, respectively

UWO_2015_38 (Isolated Sedimentary Sequence Graphitic Sediments Sample)

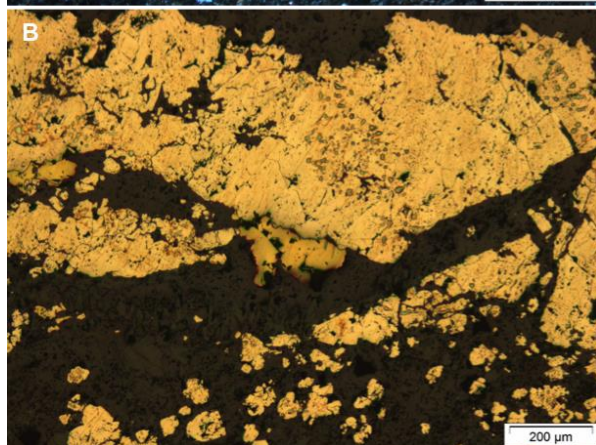
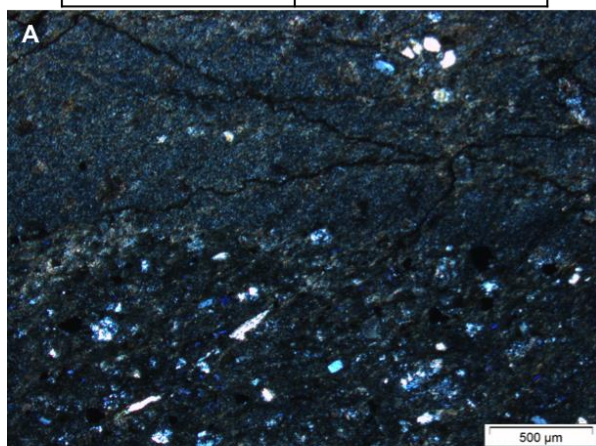


Sample ID	UWO_2015_38
Hole ID	UB12_212
Sample Interval (m)	442.3-442.4
Lithology	Graphitic sediments

Hand Sample Description: Sample of graphitic sediments interlayered with fine bands of muddy siltstone. Layers are wispy and <1mm wide, they occur at roughly 45 degrees to the core axis. Some of the thicker graphite-rich layers contain pyrite nodules that range in size from being very fine grained to 0.5cm wide and they have no distinct crystal shape.

Thin Section Description: The rock is fine to coarse grained layered quartz and calcite with abundant sericite and lesser amounts of chlorite alteration. Thick bedding can be distinguished by changes in grain size, and a foliation is developed by the parallel alignment of sericite and chlorite grains roughly 45 degrees to the bedding. The sample consists of two coarse grained lenses within a dominantly fine-grained rock. The coarse grained lenses are dominantly composed of coarse-grained quartz and are more chloritized than the rest of the rock. One of the lenses contains the sulphide grains. Quartz pressure shadows are well developed around sulphide grains in coarse-grained sections of the rock.

Overall, the rock is approximately 60% quartz, 5% calcite, 5% chlorite, 20% sericite, and 10% opaques. Opaques include 9% sieve-textured anhedral pyrite grains and 1% irregularly shaped chalcopryrite grains. Textural relationships indicate that pyrite formed first, followed by chalcopryrite. Trace amounts of hematite and magnetite are also present.



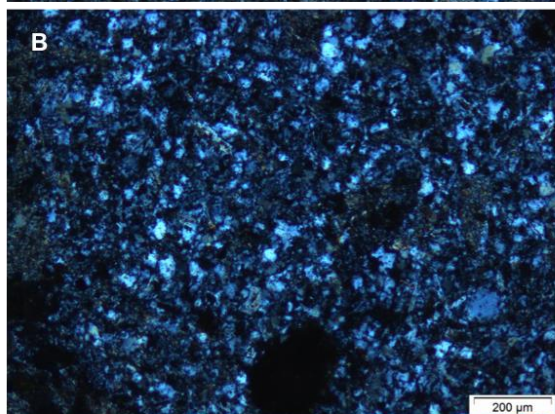
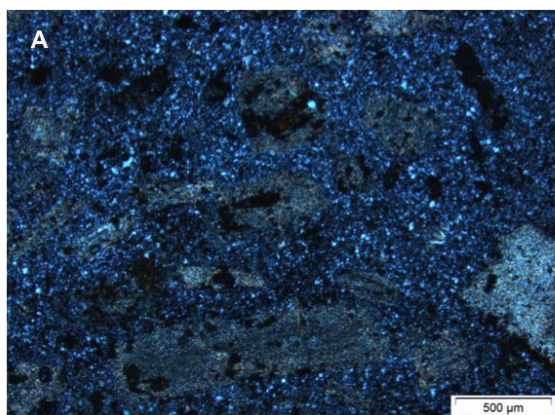
A) Fine and coarse grained layering in the rock, B) Sieve-textured pyrite and chalcopryrite

UWO_2015_39 (Isolated Sedimentary Sequence Conglomerate Sample)



Sample ID	UWO_2015_39
Hole ID	UB12_221
Sample Interval (m)	543.8-543.9
Lithology	Conglomerate

Hand Sample Description: Conglomeritic unit containing abundant clast-supported 0.5-1cm wide clasts deposited in what appears to be beds. There are alternating layers of larger and smaller clasts with possible graded bedding but difficult to say for certain. Clasts are rounded and not particularly oriented. They are composed of quartz, feldspar, and very small mafic fragments. The unit has variable alteration (sericite, chlorite). There seems to be a possible large clast near the top of the unit that is 10cm long with a very sharp contact. This large grain is very sericitized, and almost looks like a piece of cherty sediment. The top portion where the sample is from is more tanish yellow in colour due to sericite alteration while below it, it is more chlorite and hematite/albite altered. The contact with very altered cherty sediments unit above (at 343.4-.6) is gradational and is roughly 80 degrees to the core axis



Thin Section Analysis: The consists of 50% clasts in a matrix-supported conglomerate. Original bedding cannot be discerned. Clasts include coarse-grained quartz phenocrysts, which display undulatory extinction, and coarse-grained feldspar phenocrysts that have a velvety texture, likely due to sericitic replacement. These clasts are irregularly oriented throughout the matrix. Other clasts are rock fragments and are composed dominantly of medium grained quartz or very fine grained muds, giving the clasts a dark greenish gray colour. Clasts are sub-rounded and up to 1cm wide. Surrounding the clasts the matrix is composed of roughly 35% fine-grained quartz and 10% fine-grained calcite. 3% of the matrix also consists of coarse grained epidote and 2% consists of anhedral 0.1mm wide grains of pyrite and trace amounts of inter-grown hematite and magnetite. Opaques overprint both the matrix and the clasts.

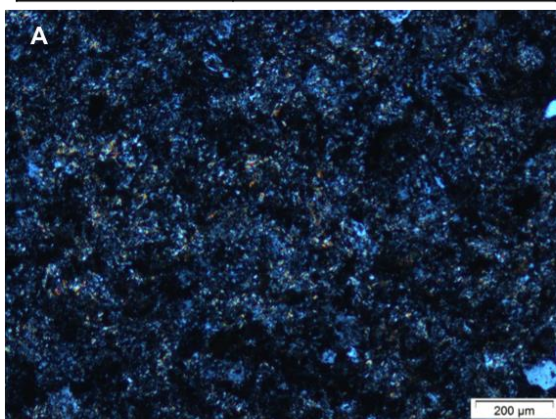
A,B) Coarse grained clasts in a fine-grained quartz-rich groundmass

UWO_2015_40 (Isolated Sedimentary Sequence Conglomerate/ Cherty Sediments Sample)

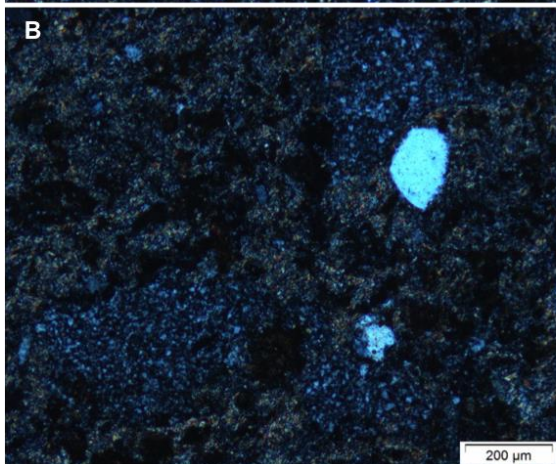


Sample ID	UWO_2015_40
Hole ID	UB12_221
Sample Interval (m)	546.1-546.2
Lithology	Conglomerate/ cherty sediments

Hand Sample Description: The unit can be considered to be partly composed of cherty sediments and partly composed of sand-sized to fine-sand sized fragments. The bedding is very distinct and occurs at roughly 80 degrees to the core axis. This very thin mm-wide bedding contains partly oriented grains and seems to be graded (see pictures) with younging direction pointing up drill. There is trace amounts of very fine grained mineralization within the core.



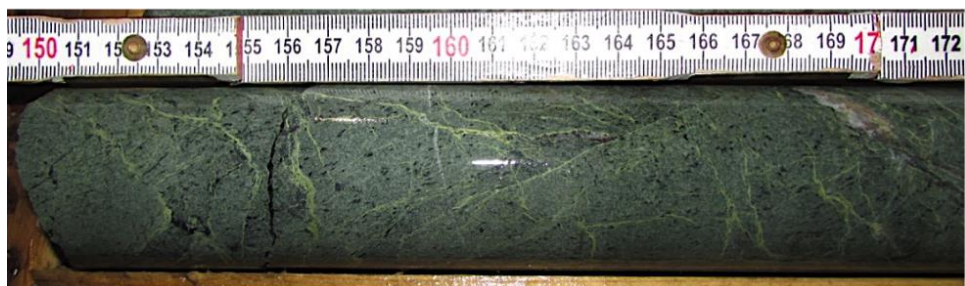
Thin Section Description: The rock consists of 40% fine grained quartz, 40% fine grained calcite, 3% coarse-grained quartz, which has undulose extinction, 5% medium-grained epidote, and 2% opaques. All grains are anhedral in shape. An additional 10% of the rock is composed of well-rounded clasts of sandstone. Original bedding is difficult to distinguish as calcite rich bands are wavy and may have follow a foliation as opposed to bedding structures. Very thin vein occur in the sample and are dominantly composed of quartz and calcite. Trace amounts of zircon also occur in the sample.



Opaques include 1% subhedral to sieve-textured pyrite (0.1mm wide), 1% sieve-textured magnetite, rarely inter-grown with trace amounts of hematite, and trace chalcopyrite.

A) fine-grained quartz-calcite matrix and foliated bedding, B) Quartzite clasts

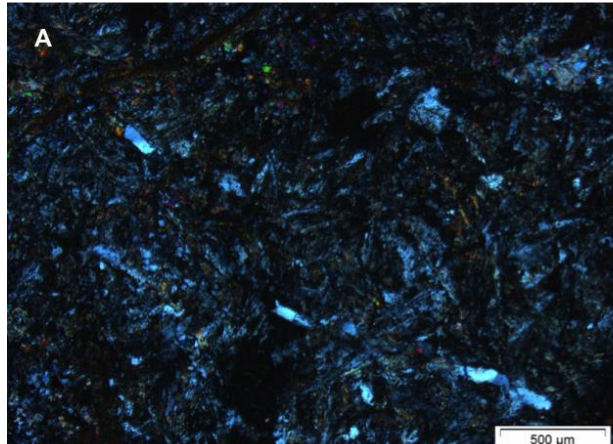
UWO_2015_41 (Basalt Crackle Breccia)



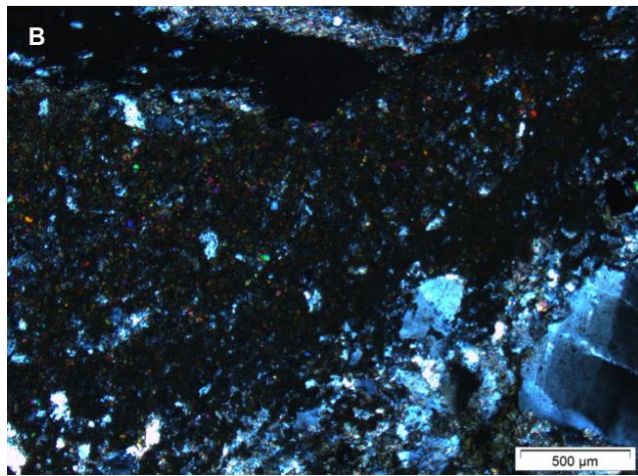
Sample ID	UWO_2015_41
Hole ID	UB13_328
Sample Interval (m)	265.5-265.7
Lithology	Crackle breccia (Basalt)

A) Representative photo of the plagioclase-rich pillows, B) Epidote-rich pillow margin

Hand Sample Description: Sample of fine grained pillow basalt that has been brecciated. It looks like epidote and sericite, and later quartz and hematite fracture fill/ stringers break the pillows apart creating a brecciated appearance. The core is weakly magnetic and contains trace amounts of pyrite that seems to be especially abundant within the quartz-hematite stringers/ fracture fillings. There are also roughly 1-5% black grains throughout the basalt, that could be composed of chlorite or a mafic mineral. These grains are roughly lath shaped and are oriented more or less 60 degrees to the core axis.



Thin Section Description: The sample consists 80% pillows, which are composed of irregularly oriented plagioclase needles with ~5% fine-grained quartz. Grain size decreases near pillow margins. The space between pillows occupies ~20% of the sample and consist of coarse-grained quartz (which has undulose extinction), and fine grained calcite, epidote, and rust.



Approximately 20% of the sample is chlorite, which occurs in clumps or disseminated throughout the pillows and the space between pillows. Overall, the rock is ~58% plagioclase, 10% quartz, 20% chlorite, 5% epidote, and 5% calcite.

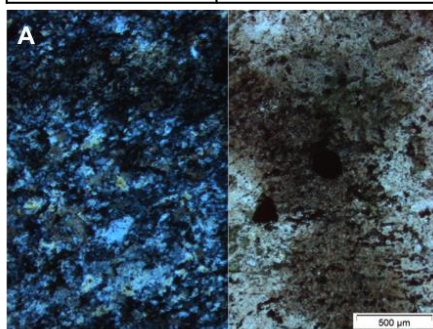
Opauques occupy ~2% of the sample and consist of 1% anhedral to sieve-textured pyrite with 1% sieve-textured chalcopyrite. Grain size ranges from very fine grained to ~0.1mm.

UWO_2015_42 (Hydrothermal Breccia Sample)

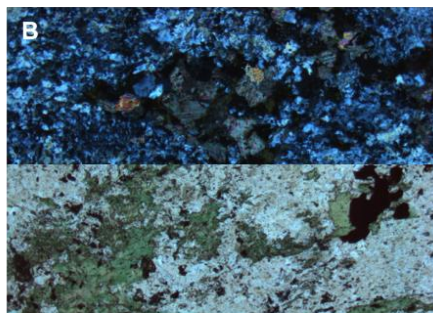


Sample ID	UWO_2015_42
Hole ID	UB14_328W2
Sample Interval (m)	1596.3-1596.5
Lithology	Hydrothermal breccia (Mafic Syenite)

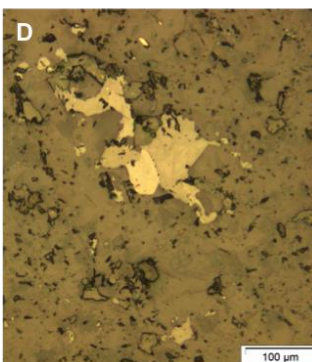
Hand Sample Description: Shallowest sample of the mafic syenite breccia package. This sample is much less brecciated in appearance than the deeper two samples and is classified as just "mafic syenite" in the logs. The rock is fine to medium grained and is greenish-brown in colour. It contains abundant plagioclase phenocrysts and mafic phenocrysts (up to 15% amphiboles) that are visible with a hand lens. It is also strongly magnetic and is variably altered by chlorite and hematite. It contains trace to 1% sub to anhedral pyrite grains. The box that the sample is from (as well as the sample itself) contain about 1% late quartz-calcite-chlorite fracture fills and stringers that are oriented at various angles.



Thin Section Description: The rock is strained and altered and consists dominantly of medium to rare coarse-grained weakly aligned plagioclase laths (45%) and strained quartz (10%), with chlorite (15%), and calcite or sericite (20%) alteration. Hornblende makes up ~1-2% of the sample but is highly corroded. Trace zircon and biotite are present. The rock is relatively unbrecciated compared to the other two samples from the brecciated zone, but brecciation is beginning with chlorite and opaques filling the space between angular proto clasts. The groundmass is overall pinkish in colour in plane polarized light.

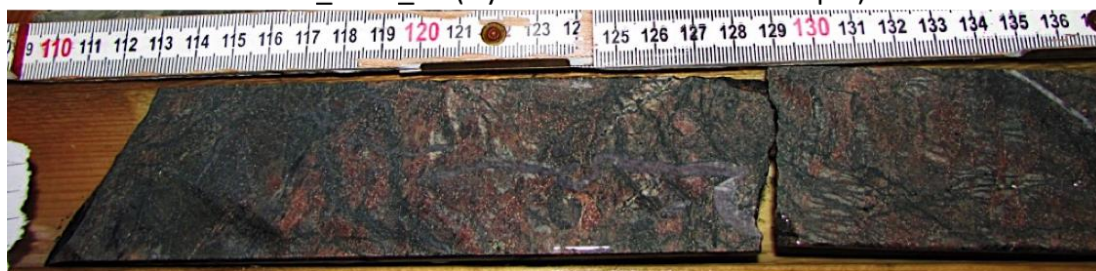


Opaques include 5% coarse grained euhedral pyrite, and fine-grained magnetite (3%) and hematite (trace). Hematite and magnetite often occur as thin long stringers between clasts. Pyrite is often surrounded by chlorite.



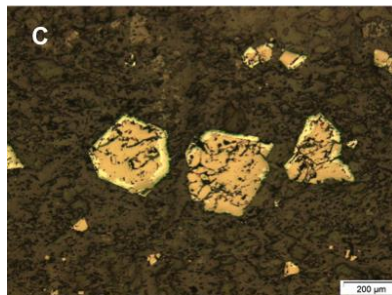
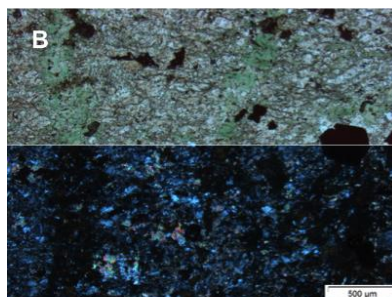
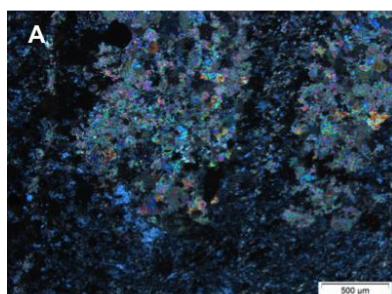
A) Brown syn-breccia alteration rind in cpl and ppl, B) Representative photo of the groundmass in cpl and ppl, C) Hematite-magnetite stringer, D) hematite-magnetite intergrowth

UWO_2015_43 (Hydrothermal Breccia Sample)



Sample ID	UWO_2015_43
Hole ID	UB14_328W2
Sample Interval (m)	1628.2-1628.4
Lithology	Hydrothermal breccia (Mafic Syenite)

Hand Sample Description: Sample of mafic syenite breccia. The sample is greenish gray to reddish to pinkish in colour, is highly altered by varying amounts of chlorite, sericite, hematite-albite, and is strongly magnetic. Each "clast" looks like it's composed of a different rock type (mainly due to colour), making the rock appear to be heterolithic. The clasts are sub rounded and range in size from 1mm to more than 3cm long. In areas, the clasts show a preferential orientation while in other areas they lack this. The clasts also typically have a reaction rim surrounding them and for the most part are typically fine grained and strongly altered. Tiny little plagioclase and amphibole phenocrysts can be seen throughout the core in the groundmass and in the clasts themselves. Late quartz & hematite fracture fillings cut through the core, breaking up some of the larger clasts. These late quartz stringers contain trace amounts of chalcopyrite and the groundmass also contains trace amounts of chalcopyrite. Larger clasts are broken up by chlorite stringers/ bits of fine grained groundmass giving it a fluid-assisted fracture texture.



Thin Section Description: The rock is much more altered, sheared, and more fine-grained than the previous sample but the host rock remains the same. It is composed dominantly of oriented fine grained plagioclase (40%) and quartz (10%) with abundant alteration consisting dominantly of chlorite (13%), coarse grained calcite (15%), and sericite or calcite (10%). Alteration products range in size from being fine grained to coarse grained in the sample. The clasts are dominantly composed of fine-grained altered plagioclase/ quartz although rarely it consists of coarse-grained calcite. The matrix between clasts is typically fine-grained and composed of chlorite and opaques, or is composed of calcite. Medium-grained hornblende accounts for ~3% of the thin section, but is heavily altered and in sections appears to be elongated. Trace amounts of rutile and 1% of zircon is present in the slide as well. Opaques include pyrite and magnetite (altering to hematite). Pyrite accounts for ~5% of the thin section, and occurs as stringers throughout the sample. Magnetite and hematite are more widespread, with magnetite accounting for ~3% of the slide and hematite about 1%.

A) Coarse-grained calcite clasts in a quartz-rich matrix, B) Representative picture of the rock in ppl and cpl, C) Magnetite altering to hematite

UWO_2015_44 (Hydrothermal Breccia Sample)

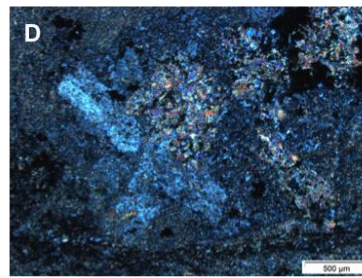
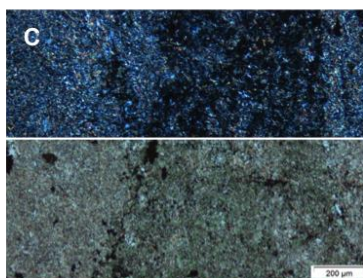
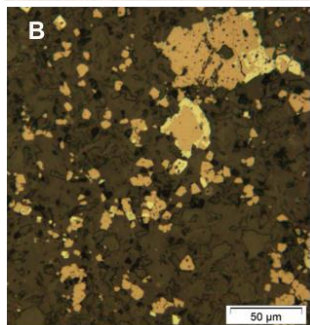
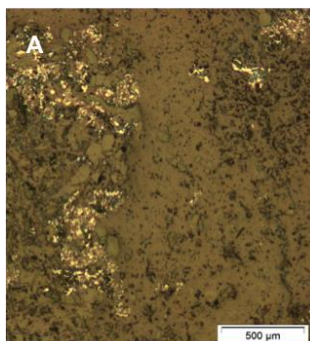


Sample ID	UWO_2015_44
Hole ID	UB14_328W2
Sample Interval (m)	1632.5-1632.7
Lithology	Hydrothermal breccia (Mafic Syenite)

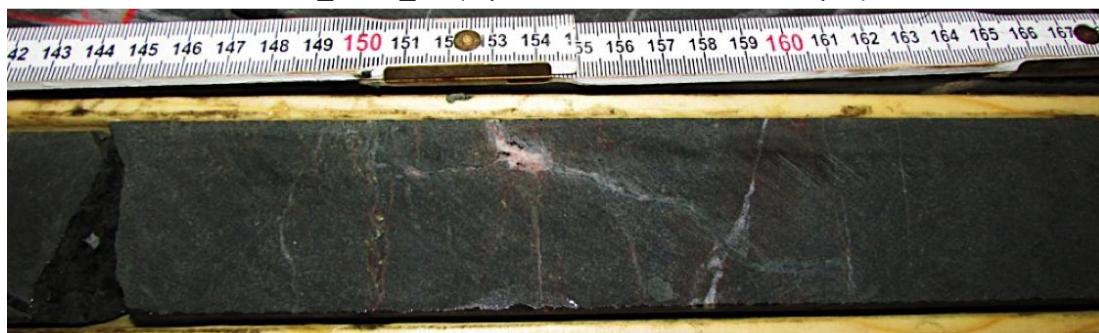
Hand Sample Description: Sample of strongly brecciated mafic syenite, taken a little bit deeper than the first two samples from this hole. This sample has very strong chlorite and sericite alteration, causing it to be greenish gray in colour. The clasts range in composition with some appearing reddish brown to pink and felsic in appearance to others appearing fine grained and dark black/green. Tiny crystals of mafic phenocrysts (amphibole) and plagioclase phenocrysts can be seen in both the host rock and in the matrix surrounding the clasts. Late hematite fracture fill and late quartz fracture fill cuts through the core, in some cases breaking apart pieces of the host rock and including them within the veins (see pictures). Trace to 1% amounts of pyrite can be seen throughout the groundmass of the sample, infilling the cracks between the clasts and sometimes occurring within the clasts themselves. Larger clasts are broken up by chlorite stringers/ bits of groundmass, giving it a fluid-assisted fracture texture.

A) Wormy hematite-magnetite intergrowths, B) Zoned hematite and magnetite, C) representative picture of the groundmass in cpl and ppl, D) coarse-grained plagioclase in the fine-grained groundmass

Thin Section Description: The rock is much more altered, sheared, and more fine-grained than the previous two samples but the host rock remains the same. It is composed dominantly of oriented fine grained plagioclase (40%) and quartz (7%) with abundant alteration consisting dominantly of fine grained sericite or calcite (28%), and chlorite (15%). The clasts are dominantly composed of fine-grained altered plagioclase/ quartz and are lighter in colour (more birefringent due to more sericite) than the groundmass in cross polarized light. Some of the clasts consist of highly altered coarse grained plagioclase and calcite. The matrix between clasts is fine-grained and composed of chlorite with lesser amounts of plagioclase, quartz, sericite, and opaques. Medium-grained hornblende accounts for ~3% of the thin section, but is heavily altered and in sections appears to be elongated. Trace amounts of rutile and 1% of zircon is present in the slide as well. Opaques include wormy or zoned magnetite altering to hematite, completely replaced hematite grains, and unaltered magnetite grains. Zoned phases typically have a core of magnetite and a rim of hematite. Magnetite and hematite are widespread and disseminated throughout the sample, with magnetite accounting for ~5% of the slide and hematite about 2%.



UWO_2015_45 (Hydrothermal Breccia Sample)



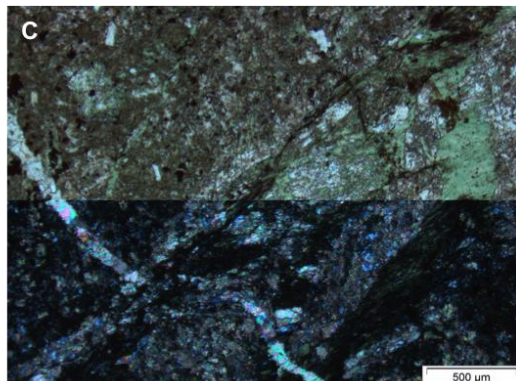
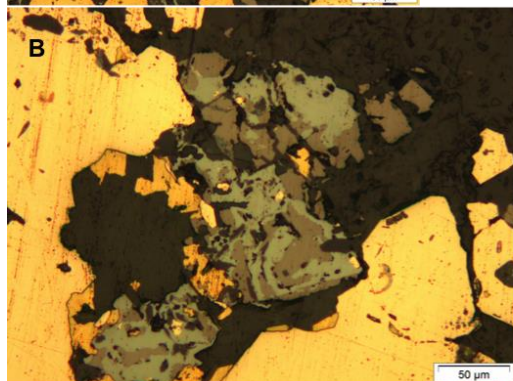
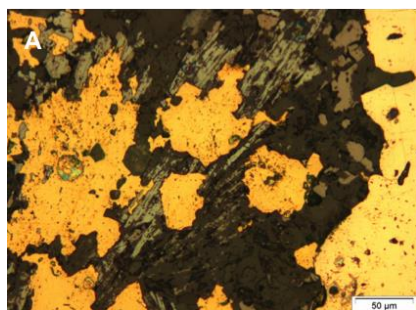
Sample ID	UWO_2015_45
Hole ID	UB14_396
Sample Interval (m)	255.4-255.7
Lithology	Hydrothermal breccia (porphyritic mafic syenite)

Hand Sample Description: Sample of porphyritic mafic syenite that is relatively "fresh" compared to the next two brecciated samples from the same drill hole. The sample is variably altered by sericite and chlorite and as such has a greenish gray to yellowish gray colour. The core is not magnetic. Bands of alteration are present, which causes the rock to begin to look brecciated. The sample contains abundant fine grained amphiboles and plagioclase phenocrysts that can be seen with a hand lens, and lacks any visibly sulphides. Late quartz fracture fill occurs throughout the core at various angles, but gives the rocks a blocky appearance. There is also less abundant late chlorite fracture fill.

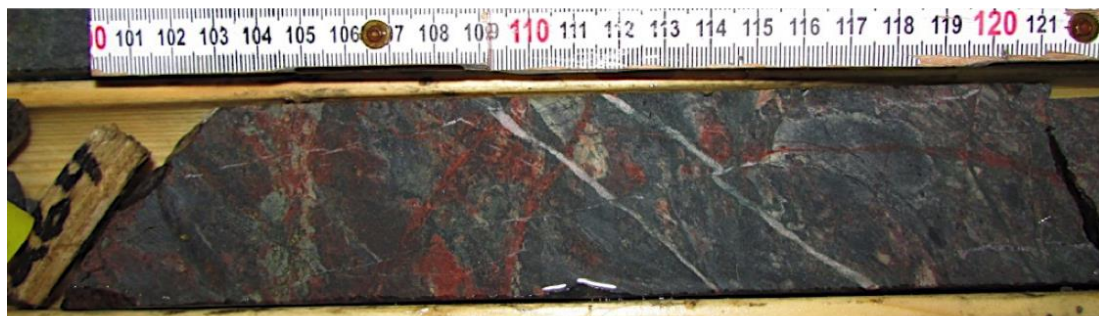
A) Radial hematite-magnetite laths overgrown by pyrite, B) Swirl-shaped texture created by magnetite altering to hematite, C) representative picture of the groundmass in ppl and cpl

Thin Section Description: The sample is overall heavily altered and composed of fine grained laths of plagioclase (40%) with lesser amounts of quartz (10%), chlorite (20%), sericite (15%), and opaques. There is ~1% biotite and 2% heavily corroded and occasionally elongated hornblende in the rock. The rock is beginning to develop a brecciated texture due to abundant chlorite or calcite stringers running at irregular angles throughout the rock. There are less common larger phenocrysts in the rock of quartz and plagioclase.

Opaques include pyrite (3%), chalcopyrite (4%), hematite (2%), and magnetite (3%). Textural relationships indicate that the hematite and the magnetite formed first, followed by the sieve-textured pyrite and then chalcopyrite. In the slide there are semi-radial laths of magnetite altering to hematite



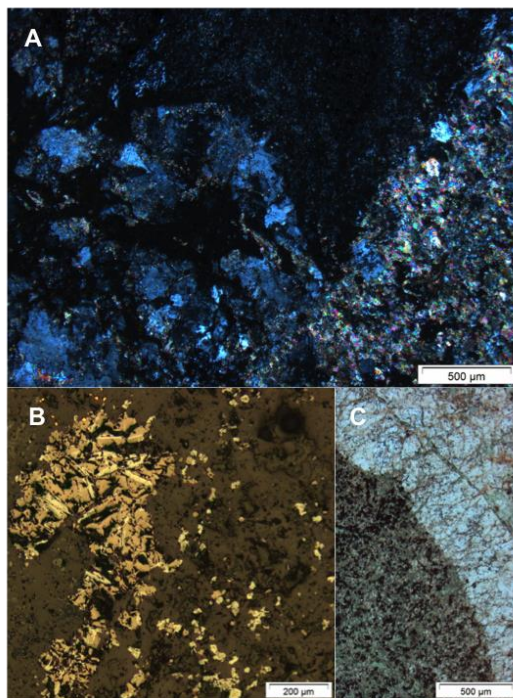
UWO_2015_46 (Hydrothermal Breccia Sample)



Sample ID	UWO_2015_46
Hole ID	UB14_396
Sample Interval (m)	264-264.1
Lithology	Hydrothermal breccia (porphyritic mafic syenite)

Hand Sample Description: First sample of strongly altered and brecciated porphyritic mafic syenite. The unit contains variable amounts of sericite, hematite, chlorite, magnetite, and leucoxene. Most of the clasts appear to be felsic and range in size from 0.5cm to 3cm across. On the far side of the core, not seen in the photograph above, there is one large mafic clast that is broken up by quartz stringers. Most of the clasts are angular with the exception of the "mafic" clast which is well rounded. The rock contains abundant phenocrysts of mafic amphiboles and plagioclase in both the groundmass and within the clasts. Further, quartz, chlorite, and magnetite fracture fill riddles the core and appears to break up fragments of the host rock. Euhedral to subhedral pyrite is associated with these fractures and also occur within the clasts. Larger clasts are broken up by the fractures, giving the rock a fluid-assisted fracture texture.

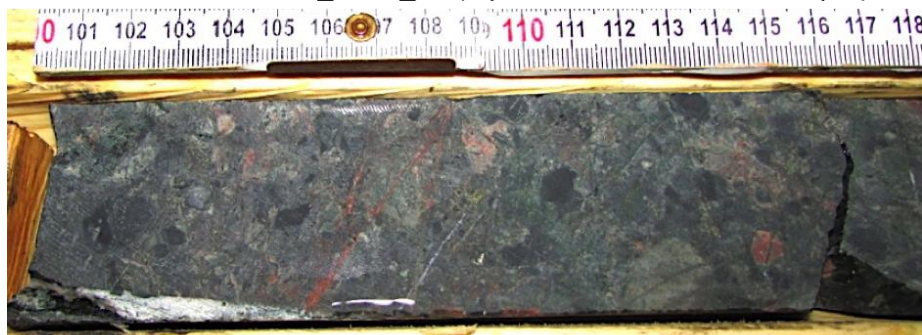
A) Representative picture of darker clasts in a quartz and calcite rich matrix, B) radial hematite overgrown by hematite, C) Opaque-rich chloritized clast margin



Thin Section Description: The sample is more heavily altered than the previous sample and is finer grained. It's composed of cm-wide clasts of plagioclase, quartz, and sericite or calcite, and chlorite with local coarser-grained patches (60%) which are pinkish green in plane polarized light, surrounded by a matrix of opaques and chlorite (10%) or coarse grained calcite (10%). There are trace amounts of rutile in the sample, as well as roughly 4% heavily corroded and occasionally elongated hornblende in the rock. There are patches of epidote (2%) alteration as well.

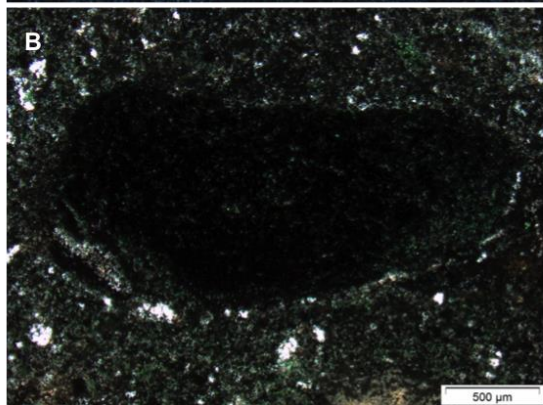
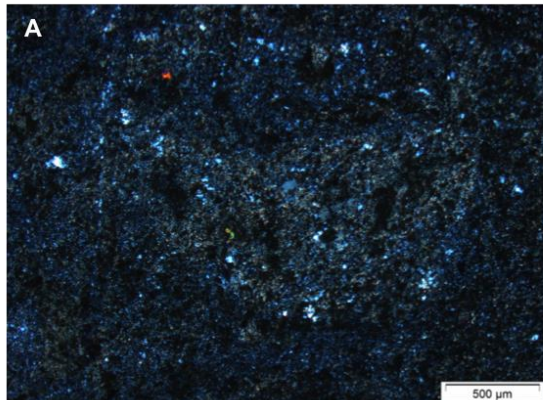
Opagues include 1% chalcopryite, as well as hematite (5%), and magnetite (7%). In the slide there are semi-radial laths of hematite and magnetite. Magnetite and hematite tends to form clusters surrounding clasts or occur as disseminations within clasts. Textural relationships indicate that the hematite and the magnetite formed first, followed by the chalcopryite.

UWO_2015_47 (Hydrothermal Breccia Sample)



Sample ID	UWO_2015_47
Hole ID	UB14_396
Sample Interval (m)	267-267.2
Lithology	Hydrothermal breccia (porphyritic mafic syenite)

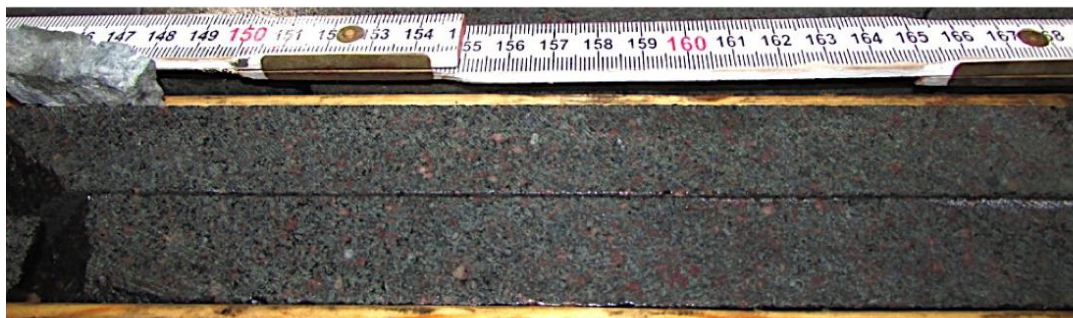
Hand Sample Description: Second sample of strongly altered brecciated porphyritic mafic syenite that looks incredibly different than last sample. This sample contains abundant sericite and chlorite alteration that bleaches the core a greenish gray colour. The core is also very magnetic. There are abundant mafic clasts within this bleached groundmass, as well as a number of felsic clasts that are well rounded. The rock looks heterolithic. Clast boundaries are somewhat squiggly in appearance and are less well defined than in the last sample, making it look more like a chemical reaction front as opposed to a strictly physical fracture system. Late quartz-hematite stringers occur throughout the core at various angles which is in turn cross cut by late chlorite fractures. The core still has the speckled leucoxene or sericitized plagioclase grains that were seen in the past 2 samples, but it is less abundant in this sample. Abundant coffin-shaped mafic amphiboles phenocrysts as well as lath shaped plagioclase grains occur throughout both the ground mass and the clasts. The core does not have any visible sulphides



A) Calcite-rich clast and B) Dark opaque-rich clast

Thin Section Description: The rock is very fine grained and dominantly composed of chlorite (37%), quartz (18%), calcite (18%), and plagioclase (17%). Clasts are roughly cm-sizes and are rimmed by opaques and chlorite, while the groundmass is composed of fine grained quartz and plagioclase. Clasts are variable in composition, typically consisting of fine grained calcite, calcite and chlorite, dark fine-grained chlorite, or plagioclase and quartz. Roughly 2% of the sample is hornblende, 1% is zircon, and 7% is opaques. Opaques include fine-grained intergrown and separate magnetite (2%) and hematite (1%), as well as 2% sieve-textured 0.1-0.3mm wide chalcocopyrite.

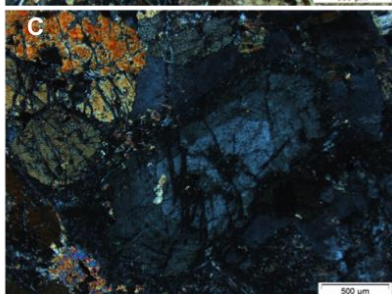
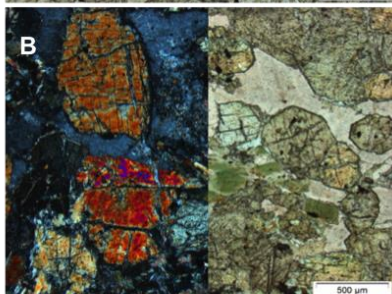
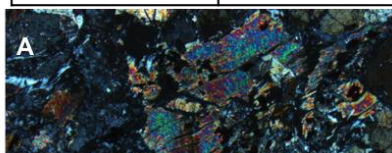
UWO_2015_48 (Biotite Dike Sample)



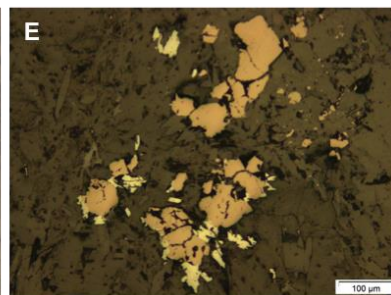
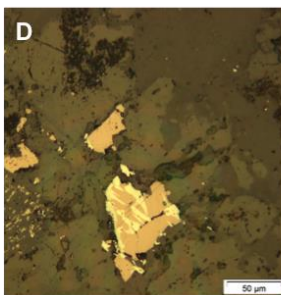
Sample ID	UWO_2015_48
Hole ID	UB13_308
Sample Interval (m)	202.5-202.7
Lithology	Biotite dike

Hand Sample Description: Core logs identify that the rock unit is a biotite-rich mafic syenite (1SMa). The rock is reddish brown in colour with abundant 1-2mm wide biotite (15%), plagioclase (25%), and amphibole(40%) phenocrysts. The groundmass is strongly hematized and chloritized and makes up roughly 20% of the sample. A late quartz stringer contains specular hematite but the dike itself lacks any sulphides.

Thin Section Description: The rock is coarse grained, consisting of 20% amphiboles, 15% biotite, 5% quartz, 25% feldspar, 10% actinolite, 10% chlorite, 5% sericite, 7% serpentine, 3% opaques, and trace zircon. Overall the rock is highly altered with chlorite, sericite, and serpentine as alteration products. Opaques include magnetite and hematite



A) Representative picture of the groundmass in cpl and ppl, B) Amphiboles phenocrysts in cpl and ppl, C) Zoned plagioclase phenocryst, D,E) Zoned and isolated hematite and magnetite



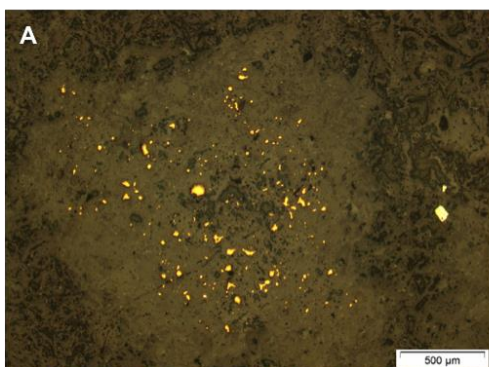
UWO_2015_49 (Isolated Sedimentary Sequence Conglomerate Sample)



Sample ID	UWO_2015_49
Hole ID	UB12_212
Sample Interval (m)	427.1-427.3
Lithology	Conglomerate

Hand Sample Description: Unit of conglomerate. In this sample clasts are very abundant (80%) and range in size from 1mm-5mm across. With a hand lens it is possible to identify that the rock is clast-supported. Clasts are composed of quartz, feldspar, and rock fragments. The groundmass is very fine grained and appears to be dominantly replaced by chlorite. No bedding or clast orientation can be seen. Additionally, scattered disseminated pyrite occurs throughout.

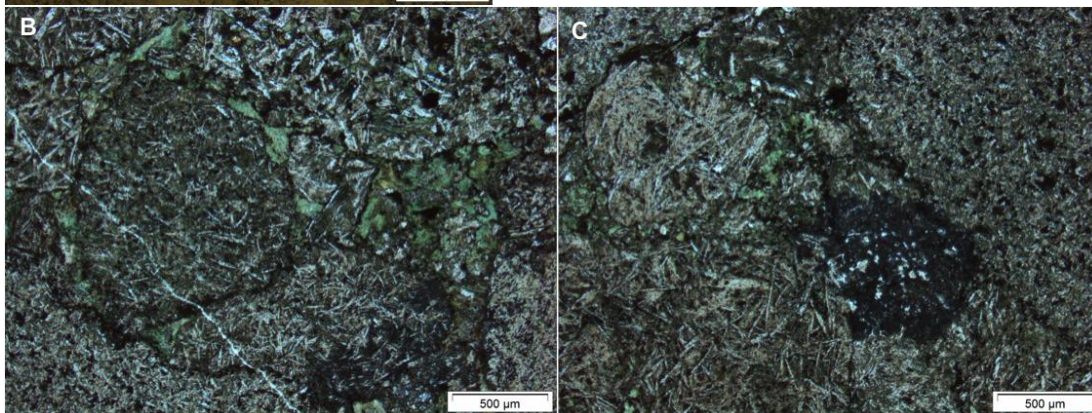
A) Chalcopyrite within a clast, B,C) Representative pictures of the rock including clasts within a chloritized groundmass



Thin Section Description: The sample consists of roughly 80% clasts in a clast-supported conglomerate. The clasts are well rounded and consist dominantly of fine to medium grained plagioclase (unoriented) with varying amounts of alteration and opaques.

The groundmass is composed of roughly 5% calcite, 2% quartz, 3% opaques, and roughly 7% chlorite. With the exception of the plagioclase, all grains are roughly anhedral in shape and fine to medium grained. Original bedding cannot be discerned in the sample.

Opaques occupy ~3% of the sample and consist of 2% subhedral to sieve-textured pyrite grains that dominantly occur within the matrix and 1% chalcopyrite that occurs with the pyrite or disseminated within clasts.



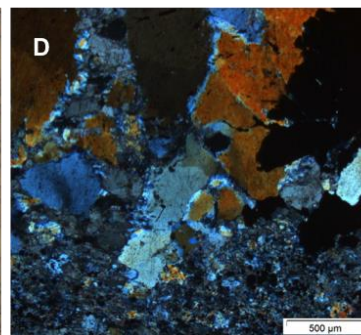
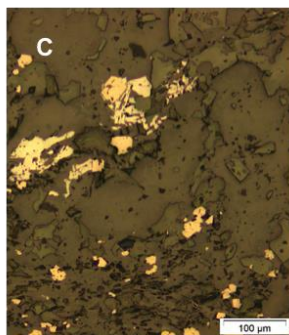
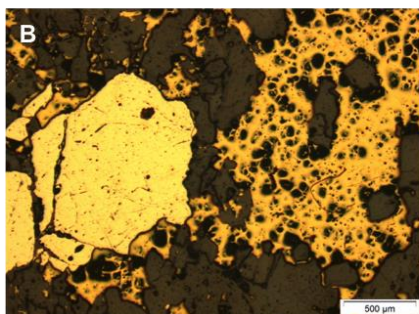
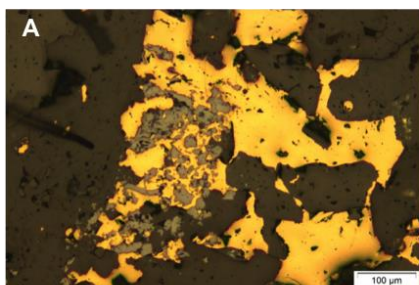
UWO_2015_50 (Mineralized Sample)



Sample ID	UWO_2015_50
Hole ID	UB10_170W2
Sample Interval (m)	1028-1029.3
Lithology	Mafic Syenite
Mineralization	Py/Cpy/VG/Mgt
Host	Quartz-Calcite
Zone	Lower Porphyry West Zone
Au Assay (g/t)	146.5
Cu Assay (pct)	1.865
Angle of mineralization	50 dtca

Hand Sample Description: Sample of a mineralized vein in mafic syenite. The vein is roughly 10cm wide and occurs at roughly 30 degrees to the core axis. The vein contains both anhydrite and calcite (lots of anhydrite, a little calcite) as well as abundant pyrite and magnetite with small amounts of chalcopyrite and visible gold. The pyrite grains are roughly subhedral to euhedral and are 1mm-1cm wide. Fine grained chalcopyrite and pyrite riddle the core infilling fractures below the vein. The host rock surrounding the vein is magnetized and chloritized, causing it to appear greenish gray in colour. A meter or so below the sample interval the core becomes strongly bleached

Thin section Description: The rock is composed of fine to coarse grained quartz (30%), calcite (40%), and opaques (30%). Quartz and calcite are anhedral in shape. There are also trace amounts of zircon, rutile, and plagioclase. Grain size is dominantly fine-grained, except for in the cm-size vein where grain size reaches up to 0.5cm in width. Opaques consist of inter-grown hematite and magnetite, as well as euhedral to sieve-textured pyrite and sieve-textured chalcopyrite. Chalcopyrite occupies roughly 5% of the slide, while pyrite occupies 3%, and hematite occupies 2%. Magnetite is very abundant and takes up 20% of the rock. Textures indicate that magnetite and hematite growth was followed by sulphide growth, and then by a second phase of oxide growth.



A) Magnetite within sieve-textured chalcopyrite, B) Chalcopyrite growth after pyrite, C) Hematite and magnetite, and D) Representative picture of the fine-grained groundmass and the coarse-grained vein

**Appendix B: Detection Limits and Substituted Population Values for the Upper
Beaver Dataset**

Table A-1. Detection limits and substituted population values in Upper Beaver dataset

Element	Detection Vale	No. Records Altered	Count %	Substituted Population Value
Ag ppm	< 0.002	34	0.8	0.001
	<0.2	2329	57.4	0.001
	<1	2	0.05	0.001
	<2	277	6.8	0.001
	>10	10	0.2	10.1
	>100	1	0.02	100.1
	N.A.	4	0.1	null
Al pct	<0.01	1	0.02	0.005
	N.A.	4	0.1	null
As ppm	<0.1	40	1	0.05
	<1	559	13.8	0.05
	<3	92	2.3	0.05
	N.A.	4	0.1	null
B ppm	<1	20	0.5	0.5
	<5	1729	46.2	0.5
Ba ppm	<0.5	4	0.1	0.25
	<1	39	1	0.25
	N.A.	4	0.1	null
Be ppm	<0.1	169	4.2	0.05
	<0.5	2713	66.9	0.05
	N.A.	4	0.1	null
Bi ppm	<0.02	7	0.2	0.01
	<1	2183	53.8	0.01
	<5	301	7.4	0.01
	N.A.	4	0.1	null
Ca pct	<0.01	1	0.02	0.005
	N.A.	4	0.1	null
Cd ppm	<0.01	289	8	0.005
	<0.5	2318	64.3	0.005
	<1	318	8.8	0.005
	N.A.	4	0.1	null
Ce ppm	<1	55	1.5	0.5
Co ppm	<0.5	1	0.02	0.25
	N.A.	4	0.1	null
Cr ppm	<0.5	2	0.05	0.25
	N.A.	4	0.1	null
Cs ppm	<0.02	195	29.3	0.01
Dy ppm				

Table A-1 Cont. Detection limits and substituted population values in Upper Beaver dataset

Element	Detection Vale	No. Records Altered	Count %	Substituted Population Value
Eu ppm	<0.1	46	6.9	0.05
Er ppm				
Fe pct	<0.01	1	0.02	0.005
	>15	1	0.02	15.1
	N.A.	4	0.1	null
Ga ppm	<5	1111	29.7	2.5
Gd ppm				
Ge ppm	<0.1	419	57.2	0.05
Hf ppm	<0.1	347	52.1	0.05
Hg ppm	<1	2380	77.3	0.5
Ho ppm	<0.1	217	32.6	0.05
In ppm	<0.02	335	9	0.01
	<1	1994	53.3	0.01
K pct	<0.01	156	3.8	0.005
	N.A.	4	0.1	null
La ppm	<0.5	22	0.5	0.25
	<1	59	1.5	0.25
	N.A.	4	0.1	null
Li ppm	<0.1	2	0.05	0.05
	<1	87	2.1	0.05
	N.A.	4	0.1	null
Lu ppm	<0.1	549	82.4	0.05
Mg pct	<0.01	2	0.05	0.005
	N.A.	4	0.1	null
Mn ppm	<1	1	0.03	0.5
	N.A.	4	0.1	null
Mo ppm	<0.5	73	1.8	0.25
	<1	42	1	0.25
	<2	1	0.02	0.25
	N.A.	4	0.1	null
Na pct	<0.001	3	0.07	0.0005
	<0.01	138	3.4	0.0005
	N.A.	4	0.1	null
Nb ppm	<0.1	484	62	0.05
Nd ppm				
Ni ppm	<0.5	1	0.03	0.25
	N.A.	4	0.1	null
P ppm	<10	1	0.03	5
P pct	N.A.	4	0.1	null

Table A-1 Cont. Detection limits and substituted population values in Upper Beaver dataset

Element	Detection Vale	No. Records Altered	Count %	Substituted Population Value
Pb ppm	<0.01	1	0.02	0.005
	<0.5	543	13.4	0.005
	<2	158	3.9	0.005
	N.A.	4	0.1	null
Pr ppm				
Rb ppm	<0.1	1	0.03	0.05
	<10	853	22.8	0.05
Re ppm	<0.001	171	25.8	0.0005
S pct	<0.005	9	0.3	0.0025
	>5	12	0.4	5.1
	>10	4	0.1	10.1
	N.A.	4	0.1	null
Sb ppm	<1	652	16.1	0.5
	<5	162	4	0.5
	>500	6	0.1	500.1
	N.A.	4	0.1	null
Sc ppm	<0.5	6	0.1	0.25
	N.A.	4	0.1	null
Se ppm	<0.1	137	3.7	0.05
	<10	2933	78.4	0.05
Sm ppm				
Sn ppm	<0.05	26	0.6	0.025
	<1	2	0.05	0.025
	<5	1552	38.2	0.025
	<10	312	7.7	0.025
	N.A.	4	0.1	null
Sr ppm	<0.5	2	0.05	0.25
	>1000	1	0.02	1000.1
	N.A.	4	0.1	null
Ta ppm	<0.05	636	17	0.025
	<10	3074	82.1	0.025
Tb ppm	<0.1	219	20.9	0.05
	<10	371	35.3	0.05
Te ppm	<0.02	71	2.1	0.01
	<10	2681	79.8	0.01
Th ppm	<5	2892	77.3	2.5
Ti pct	<0.01	1226	36.1	0.005
	N.A.	4	0.1	null

Table A-1 Cont. Detection limits and substituted population values in Upper Beaver dataset

Element	Detection Vale	No. Records Altered	Count %	Substituted Population Value
Tl ppm	<0.02	261	7	0.01
	<0.5	2	0.05	0.01
	<5	1889	50.2	0.01
Tm ppm	<0.1	330	49.5	0.05
U ppm	<0.1	62	1.7	0.05
	<5	2931	78.3	0.05
V ppm	<0.5	1	0.02	0.25
	<1	2	0.05	0.25
	N.A.	4	0.1	null
W ppm	<0.1	28	0.8	0.05
	<1	1542	42.8	0.05
	<10	275	7.6	0.05
	>200	16	0.4	200.1
	N.A.	4	0.1	null
Y ppm	<1	1	0.02	0.5
	N.A.	4	0.1	null
Yb ppm				
Zn ppm	<0.1	9	0.2	0.05
	N.A.	4	0.1	null
Zr ppm	<5	946	23.3	2.5
	N.A.	4	0.1	null
AuBest g/t				
Cu ppm	<0.5	180	4.4	0.25
	>10000	136	3.4	10000.1
	N.A.	4	0.1	null
Cu pct	37675	1	0.03	null

Appendix C: Summary Statistics for the Upper Beaver Dataset

Table A-2. Summary statistics of the Upper Beaver dataset

Element	Count Numeric	Max	Min	Mean	Median	Standard Deviation	Interqu- artile Range	Range
Al2O3 pct	4317	0.01	11.85	2.95	2.66	1.70	2.23	11.84
CaO pct	4317	0.01	22.39	4.72	4.32	2.39	2.88	22.38
FeO pct	4317	0.01	39.88	5.71	4.86	3.85	4.38	39.88
Fe2O3 pct	4317	0.01	44.32	6.35	5.40	4.28	4.87	44.31
K2O pct	4317	0.01	0.76	0.19	0.16	0.14	0.19	0.75
MgO pct	4317	0.01	13.91	2.75	2.26	1.74	2.45	13.90
MnO pct	4317	0.00	0.72	0.07	0.06	0.04	0.05	0.72
Na2O pct	4317	0.00	0.31	0.06	0.05	0.04	0.04	0.31
P2O5 pct	3595	0.00	0.96	0.20	0.19	0.12	0.12	0.95
TiO2 pct	3595	0.01	1.67	0.18	0.08	0.22	0.29	1.66
SiO2 pct	4319	11.96	100.00	76.88	79.28	10.76	15.01	88.04
Ag ppm	4319	0.00	100.10	0.68	0.00	3.09	0.30	100.10
As ppm	4317	0.05	972.00	11.63	8.00	30.70	9.00	971.95
B ppm	4008	0.50	119.00	4.70	3.00	7.15	6.50	118.50
Ba ppm	4319	0.25	2410.00	81.38	38.00	152.48	64.00	2409.75
Bi ppm	4317	0.01	672.00	1.90	0.01	11.88	0.99	671.99
Be ppm	4317	0.05	4.90	0.24	0.05	0.36	0.25	4.85
Cd ppm	4317	0.01	4.20	0.09	0.01	0.31	0.00	4.20
Ce ppm	4010	0.50	1530.00	24.73	18.00	40.40	19.90	1529.50
Co ppm	4319	0.25	1090.00	28.30	18.00	46.19	20.30	1089.75
Cr ppm	4319	0.25	527.00	64.64	34.60	66.08	87.30	526.75
Ga ppm	4010	0.13	28.00	6.50	6.00	4.18	6.50	27.87
Hg ppm	3286	0.50	93.00	0.95	0.50	2.29	0.00	92.50
In ppm	4008	0.01	45.00	1.07	0.01	2.79	0.99	44.99
La ppm	4319	0.25	1100.00	12.47	8.00	27.58	8.50	1099.75
Li ppm	4317	0.05	81.00	14.87	13.00	10.34	12.25	80.95
Mn ppm	4317	0.50	5610.00	542.62	456.00	337.70	396.00	5609.50
Mo ppm	4319	0.13	5970.00	83.55	7.40	308.49	32.80	5969.87
Ni ppm	4257	0.25	397.00	40.55	32.00	33.01	39.85	396.75
P ppm	3595	5.00	4170.00	892.13	813.00	502.11	521.00	4165.00
Pb ppm	4319	0.01	231.00	4.47	2.52	7.86	4.20	231.00
Rb ppm	4010	0.05	83.00	14.52	14.00	11.73	17.50	82.95
Re ppm	722	0.00	9.19	0.10	0.00	0.61	0.02	9.19
Sb ppm	4317	0.04	966.00	9.07	4.00	37.65	8.00	965.96
Sc ppm	4319	0.25	40.50	7.98	5.80	6.02	7.20	40.25
Se ppm	4008	0.05	50.00	0.92	0.05	3.84	0.00	49.95
Sn ppm	4319	0.03	583.00	20.96	0.08	44.47	15.98	582.98
Sr ppm	4319	0.25	2580.00	123.94	92.50	132.58	94.20	2579.75

Table A-2 cont. Summary statistics of the Upper Beaver dataset

Element	Count Numeric	Max	Min	Mean	Median	Standard Deviation	Interqu- artile Range	Range
Ta ppm	4010	0.03	20.00	0.04	0.03	0.48	0.00	19.98
Te ppm	3636	0.01	21.00	0.12	0.01	0.94	0.00	20.99
Th ppm	4010	0.10	16.00	2.61	2.50	1.53	0.00	15.90
Tl ppm	4010	0.01	72.00	2.78	0.01	4.72	5.99	71.99
U ppm	4010	0.05	25.10	0.37	0.05	1.35	0.00	25.05
V ppm	4319	0.25	479.00	89.23	63.00	76.39	108.00	478.75
W ppm	4319	0.05	1180.00	6.92	0.05	43.23	2.35	1179.95
Y ppm	4319	0.50	85.40	7.21	6.00	4.45	5.00	84.90
Zn ppm	4312	0.05	183.00	27.72	23.80	17.54	19.58	182.95
Zr ppm	4319	0.80	112.00	8.34	7.00	6.34	8.50	111.20
Cs ppm	724	0.01	2.84	0.34	0.29	0.35	0.45	2.83
Dy ppm	724	0.10	7.32	1.38	1.12	0.73	0.91	7.22
Er ppm	724	0.10	3.50	0.67	0.50	0.38	0.50	3.40
Eu ppm	724	0.05	6.70	0.76	0.70	0.51	0.60	6.65
Hf ppm	724	0.05	3.00	0.15	0.05	0.21	0.15	2.95
Ho ppm	724	0.05	1.30	0.20	0.20	0.17	0.25	1.25
Lu ppm	724	0.05	0.50	0.07	0.05	0.04	0.00	0.45
Nb ppm	828	0.05	104.00	7.29	0.05	20.89	0.15	103.95
Nd ppm	724	0.66	413.00	14.00	9.25	19.75	9.52	412.34
Pr ppm	724	0.10	132.00	3.51	2.20	5.96	2.40	131.90
Tb ppm	1098	0.05	16.00	0.26	0.05	1.17	0.15	15.95
Sm ppm	724	0.10	36.40	2.50	1.90	2.21	1.40	36.30
Tm ppm	724	0.05	0.50	0.09	0.10	0.05	0.05	0.45
Yb ppm	724	0.10	2.90	0.56	0.50	0.31	0.30	2.80
Gd ppm	724	0.20	28.30	2.27	1.90	1.71	1.10	28.10
Ge ppm	722	0.05	1.20	0.12	0.05	0.12	0.15	1.15
AuBest g t UWO	4204	0.00	195.43	2.43	0.21	9.94	1.02	195.43
Cu pct UWO	4319	0.00	5.79	0.12	0.02	0.29	0.09	5.79
S pct	3595	0.00	18.10	0.49	0.18	0.91	0.41	18.10
Al pct	4317	0.01	6.27	1.56	1.41	0.90	1.18	6.27
Ca pct	4317	0.01	16.00	3.38	3.09	1.71	2.06	16.00
Fe pct	4317	0.01	31.00	4.44	3.78	2.99	3.41	31.00
K pct	4317	0.01	0.63	0.16	0.13	0.11	0.16	0.63
Mg pct	4317	0.01	8.39	1.66	1.36	1.05	1.48	8.39
Na pct	4317	0.00	0.23	0.05	0.04	0.03	0.03	0.23
P pct	3595	0.00	0.42	0.09	0.08	0.05	0.05	0.42
Ti pct	3595	0.01	1.00	0.11	0.05	0.13	0.18	1.00

**Appendix D: Geochemical Analysis Results for Mineralized Samples in the
Upper Beaver Deposit**

Table A-3. Geochemical analysis results for mineralized samples from the Upper Beaver deposit

	Au- AA23 Au ppm	Au- GRA21 Au ppm	ME- ICP41 Ag ppm	ME- ICP41 Al %	ME- ICP41 As ppm	ME- ICP41 B ppm	ME- ICP41 Ba ppm	ME- ICP41 Be ppm	ME- ICP41 Bi ppm	ME- ICP41 Ca %
UWO_2015_01	1.01		0.3	2.15	5	<10	60	<0.5	2	6.07
UWO_2015_02	>10.0	168	58.5	3.34	1360	<10	50	<0.5	4700	2.07
UWO_2015_03	>10.0	128	7.9	0.13	6	<10	40	<0.5	14	10.5
UWO_2015_04	>10.0	86.8	8	0.71	128	<10	10	<0.5	61	5.4
UWO_2015_05	>10.0	126	23.1	1.25	104	<10	70	0.8	<2	1.75
UWO_2015_06	>10.0	71.4	1.4	0.12	<2	<10	<10	<0.5	3	15.7
UWO_2015_07	>10.0	87.8	18.4	0.18	4	<10	<10	<0.5	<2	12.9
UWO_2015_08	>10.0	268	12.6	0.62	<2	<10	<10	<0.5	19	5.49
UWO_2015_09	>10.0	232	42	0.96	12	<10	<10	<0.5	16	13.3
UWO_2015_10	>10.0	28.4	13.7	0.27	13	<10	150	3.1	<2	3.31
UWO_2015_11	>10.0	51.3	23.4	0.85	7	<10	50	<0.5	<2	1.38
UWO_2015_12	>10.0	129.5	7.2	1.22	3	<10	40	<0.5	<2	2.36
UWO_2015_13	>10.0	39.9	11.7	0.83	8	20	20	<0.5	7	14.4
UWO_2015_14	7.82		1.7	2.46	4	<10	10	<0.5	6	4.18
UWO_2015_15	>10.0	31.8	0.9	1.14	3	<10	30	<0.5	2	3.49
UWO_2015_16	>10.0	25.8	3	0.61	10	<10	40	<0.5	7	3.01
UWO_2015_18	>10.0	42	2.5	2.58	110	<10	10	<0.5	5	7.5
UWO_2015_19	>10.0	21.8	2.4	0.79	19	<10	80	<0.5	6	2.72
UWO_2015_50	>10.0	146.5	39.1	0.48	206	<10	20	0.6	9	2.88

Table A-3 cont. Geochemical analysis results for mineralized samples from the Upper Beaver deposit

	ME- ICP41 Cd ppm	ME- ICP41 Co ppm	ME- ICP41 Cr ppm	ME- ICP41 Cu ppm	ME- ICP41 Fe %	ME- ICP41 Ga ppm	ME- ICP41 Hg ppm	ME- ICP41 K %	ME- ICP41 La Ppm	ME- ICP41 Mg %
UWO_2015_01	<0.5	27	152	3180	8.83	10	1	0.07	<10	2.39
UWO_2015_02	<0.5	2410	28	9420	19.35	10	3	0.14	<10	2.01
UWO_2015_03	<0.5	10	4	>10000	3.49	<10	3	<0.01	<10	0.13
UWO_2015_04	0.5	196	18	5950	11.05	<10	2	0.01	<10	0.65
UWO_2015_05	<0.5	51	4	>10000	29.9	10	12	0.13	<10	0.68
UWO_2015_06	<0.5	1	1	100	0.38	<10	1	<0.01	<10	0.14
UWO_2015_07	<0.5	87	1	>10000	7.62	<10	5	<0.01	10	0.21
UWO_2015_08	<0.5	3	11	154	1.41	<10	2	0.05	10	0.5
UWO_2015_09	<0.5	18	15	>10000	5.93	<10	7	0.01	10	1.08
UWO_2015_10	<0.5	86	4	>10000	39.7	<10	1	0.01	<10	0.24
UWO_2015_11	<0.5	11	12	9950	3.66	10	3	0.17	10	0.61
UWO_2015_12	<0.5	8	8	308	3.63	<10	2	0.14	20	0.86
UWO_2015_13	<0.5	36	28	>10000	6.85	<10	1	0.01	10	2.21
UWO_2015_14	<0.5	59	106	>10000	14.75	10	1	0.01	20	2.63
UWO_2015_15	<0.5	6	28	202	2.16	10	2	0.03	10	1.15
UWO_2015_16	<0.5	17	21	145	3.8	<10	4	0.18	120	1.09
UWO_2015_18	<0.5	31	82	4040	15.2	10	5	0.02	20	3.36
UWO_2015_19	<0.5	17	27	212	5.62	<10	2	0.34	10	1.19
UWO_2015_50	0.5	2120	31	>10000	21.1	<10	9	0.1	<10	1.18

Table A-3 cont. Geochemical analysis results for mineralized samples from the Upper Beaver deposit

	ME- ICP41 Mn ppm	ME- ICP41 Mo ppm	ME- ICP41 Na %	ME- ICP41 Ni ppm	ME- ICP41 P ppm	ME- ICP41 Pb ppm	ME- ICP41 S %	ME- ICP41 Sb ppm	ME- ICP41 Sc ppm	ME- ICP41 Ti ppm
UWO_2015_01	782	5	0.07	83	350	3	0.39	2	14	<10
UWO_2015_02	307	9	<0.01	78	1400	170	>10.0	<2	7	<10
UWO_2015_03	521	13	0.02	34	130	3	1.66	2	3	<10
UWO_2015_04	274	137	0.05	408	730	5	>10.0	18	3	<10
UWO_2015_05	272	91	<0.01	168	270	8	1.96	2	9	<10
UWO_2015_06	52	1165	<0.01	14	10	<2	>10.0	2	<1	<10
UWO_2015_07	67	228	<0.01	473	50	5	>10.0	<2	<1	<10
UWO_2015_08	451	>10000	0.02	25	310	12	1.38	4	2	<10
UWO_2015_09	1315	134	<0.01	52	50	3	2.41	3	3	<10
UWO_2015_10	213	29	0.02	184	110	10	2.82	<2	3	<10
UWO_2015_11	162	123	<0.01	28	650	6	1.03	3	5	<10
UWO_2015_12	286	3	0.07	28	670	<2	0.14	<2	3	<10
UWO_2015_13	1145	93	0.01	112	160	5	4.05	<2	5	<10
UWO_2015_14	381	21	0.03	124	1200	2	2.47	<2	14	<10
UWO_2015_15	257	1	0.06	32	830	<2	0.03	2	8	<10
UWO_2015_16	394	4840	0.01	49	1450	7	0.42	3	9	<10
UWO_2015_18	1145	42	<0.01	111	200	4	1.4	2	17	<10
UWO_2015_19	342	4160	0.01	42	620	4	0.35	2	3	<10
UWO_2015_50	396	54	0.01	94	960	12	>10.0	3	3	<10

Table A-3 cont. Geochemical analysis results for mineralized samples from the Upper Beaver deposit

	ME- ICP41 Sr ppm	ME- ICP41 Th ppm	ME- ICP41 Ti %	ME- ICP41 U ppm	ME- ICP41 V ppm	ME- ICP41 W ppm	ME- ICP41 Zn ppm	Cu- OG46 Cu %	Mo- OG46 Mo %	ME- ICP41 Te ppm
UWO_2015_01	238	<20	0.06	<10	237	<10	42			<10
UWO_2015_02	114	<20	0.01	<10	66	<10	80			10
UWO_2015_03	133	<20	<0.01	<10	7	<10	11	3.53		<10
UWO_2015_04	96	<20	<0.01	<10	63	<10	15			<10
UWO_2015_05	99	<20	<0.01	<10	184	50	28	3.86		<10
UWO_2015_06	659	<20	<0.01	<10	15	<10	4			<10
UWO_2015_07	680	<20	<0.01	<10	18	<10	11	6.92		<10
UWO_2015_08	42	<20	<0.01	<10	58	<10	12		1.95	<10
UWO_2015_09	289	<20	<0.01	<10	87	<10	19	4.67		<10
UWO_2015_10	903	<20	0.01	<10	151	590	15	7.82		<10
UWO_2015_11	145	<20	0.08	<10	49	10	14			<10
UWO_2015_12	69	<20	<0.01	<10	39	<10	20			<10
UWO_2015_13	143	<20	<0.01	<10	40	<10	14	3.59		<10
UWO_2015_14	104	<20	0.05	<10	162	<10	25	5.31		<10
UWO_2015_15	43	<20	0.01	<10	74	<10	19			<10
UWO_2015_16	137	<20	<0.01	<10	65	<10	17			<10
UWO_2015_18	47	<20	0.01	<10	198	80	25			<10
UWO_2015_19	180	<20	<0.01	<10	43	<10	19			<10
UWO_2015_50	298	<20	<0.01	<10	42	1160	20	1.865		<10

Table A-3 cont. Geochemical analysis results for mineralized samples from the Upper Beaver deposit

SAMPLE DESCRIPTION	ME-XRF26 Al ₂ O ₃ %	ME-XRF26 BaO %	ME-XRF26 CaO %	ME-XRF26 Cr ₂ O ₃ %	ME-XRF26 Fe ₂ O ₃ %	ME-XRF26 K ₂ O %	ME-XRF26 MgO %	ME-XRF26 MnO %	ME-XRF26 Na ₂ O %
UWO_2015_01	11.9	0.02	9.47	0.03	13.53	0.98	4.39	0.11	3.86
UWO_2015_02	9.61	0.05	3.18	0.01	29.03	1.28	3.96	0.05	0.05
UWO_2015_03	2.16	0.01	16.3	<0.01	5.5	0.04	0.23	0.09	1.16
UWO_2015_04	9.64	<0.01	8.05	<0.01	16.42	0.07	1.23	0.04	4.96
UWO_2015_05	4.88	0.04	2.84	<0.01	46.45	0.98	1.43	0.06	0.08
UWO_2015_06	0.28	0.01	39.9	<0.01	0.74	0.01	0.42	0.02	<0.01
UWO_2015_07	0.86	<0.01	28.2	<0.01	12.98	0.02	1.38	0.06	0.08
UWO_2015_09	1.95	<0.01	20.5	0.01	9.21	0.06	2.01	0.22	0.07
UWO_2015_10	1.27	0.67	5.61	<0.01	65.54	0.05	0.51	0.08	0.55
UWO_2015_11	14.06	0.23	4.57	<0.01	7.75	9.02	1.14	0.04	0.18
UWO_2015_14	9.64	<0.01	6.71	0.02	22.4	0.21	4.93	0.08	2.72
UWO_2015_15	13.38	0.01	5.02	<0.01	3.33	0.74	2.08	0.04	6.19
UWO_2015_16	7.42	0.09	4.45	0.01	6.03	4.93	2.03	0.06	0.07
UWO_2015_18	5.71	0.01	11.6	0.01	23.61	0.49	6.22	0.18	0.05
UWO_2015_19	13.46	0.1	3.99	0.01	10.13	5.14	2.73	0.05	1.28
UWO_2015_20	15.87	0.03	2.17	0.02	6.16	0.85	2.52	0.08	5.99
UWO_2015_21	11.6	0.04	1.54	<0.01	5.23	2.2	1.18	0.06	1.35
UWO_2015_22	3.41	0.02	22	<0.01	8.98	0.84	11.55	0.19	0.56
UWO_2015_23	10.62	0.09	0.39	<0.01	28.57	1.78	2.36	0.01	0.05
UWO_2015_24	17.45	0.32	4.83	0.01	2.87	5.88	1.16	0.02	0.07
UWO_2015_25	14.41	0.08	5.76	<0.01	8.47	4.06	0.95	0.05	2.81
UWO_2015_26	15.68	0.11	6.48	0.01	6.79	1.86	4.84	0.1	5.27
UWO_2015_27	18	0.08	3.95	0.01	4.98	2.35	2.27	0.05	5.18
UWO_2015_28	15.6	0.04	6.09	<0.01	5.4	2.89	2.71	0.06	3.86
UWO_2015_29	15.04	0.06	11.3	0.03	9.68	2.05	3	0.15	3.32
UWO_2015_30	13.58	0.02	6.73	0.01	6.36	0.46	3.88	0.1	4.95
UWO_2015_31	10.01	0.1	2.29	<0.01	0.71	2.73	0.48	0.01	1.32
UWO_2015_32	16.95	0.09	5.93	<0.01	3.27	2.07	0.49	0.05	5.33

Table A-3 cont. Geochemical analysis results for mineralized samples from the Upper Beaver deposit

SAMPLE DESCRIPTION	ME-XRF26 Al₂O₃ %	ME-XRF26 BaO %	ME-XRF26 CaO %	ME-XRF26 Cr₂O₃ %	ME-XRF26 Fe₂O₃ %	ME-XRF26 K₂O %	ME-XRF26 MgO %	ME-XRF26 MnO %	ME-XRF26 Na₂O %
UWO_2015_33	14.44	0.01	12.3	0.03	7.47	0.2	3.14	0.1	5.03
UWO_2015_34	14.93	0.06	6.65	0.02	11.5	3.11	2.44	0.07	2.92
UWO_2015_35	16.92	0.05	2.07	0.01	8.35	1.98	2.2	0.02	6.11
UWO_2015_36	14.17	0.04	6.21	0.01	14.33	2.4	2.54	0.07	4.82
UWO_2015_37	16.84	0.04	2.35	0.01	6.51	1.08	3.05	0.07	6.19
UWO_2015_38	7.35	0.05	2.13	0.01	28.79	1.8	1.18	0.03	0.11
UWO_2015_39	17.18	0.05	4.45	<0.01	4.32	2.54	1.04	0.02	3.4
UWO_2015_40	17.44	0.05	4.42	0.01	3.3	3.04	1.15	0.02	3.33
UWO_2015_41	13.32	0.01	8.47	0.03	10.48	0.13	6.46	0.16	2.79
UWO_2015_42	17.12	0.01	3.74	0.01	4.18	0.16	3.48	0.05	8.03
UWO_2015_43	15.48	0.02	8.88	0.01	9.34	0.82	4.26	0.09	5.64
UWO_2015_44	15.98	0.07	5.38	0.01	15.27	2.79	4.36	0.06	3.05
UWO_2015_45	14.01	0.09	6.41	0.02	8.85	2.92	6.07	0.09	3.07
UWO_2015_46	15.62	0.08	3.81	0.03	15.34	3.19	3.85	0.07	3.66
UWO_2015_47	15.2	0.06	3.43	0.03	14.44	2.46	4.61	0.09	3.11
UWO_2015_48	9.58	0.16	11.15	0.14	9.08	3.58	13.35	0.19	1.22
UWO_2015_49	15.75	0.02	7.24	0.03	9.76	0.41	4.41	0.26	5.27
UWO_2015_50	5.83	0.05	4.54	0.01	32.62	1.2	2.4	0.07	1.23

Table A-3 cont. Geochemical analysis results for mineralized samples from the Upper Beaver deposit

SAMPLE DESCRIPTION	ME-XRF26 P2O5 %	ME-XRF26 SO3 %	ME-XRF26 SiO2 %	ME-XRF26 SrO %	ME-XRF26 TiO2 %	ME-XRF26 Total %	OA-GRA05x LOI 1000 %
UWO_2015_01	0.08	1.02	44.51	0.03	1.08	100	8.48
UWO_2015_02	0.32	11.6	35.44	0.01	0.4	107.9	11.39
UWO_2015_03	0.03	9.62	59.57	0.02	0.05	109.55	9.9
UWO_2015_04	0.16	9.64	42.94	0.02	0.42	100.7	6.28
UWO_2015_05	0.07	9.37	31.94	0.02	0.16	108.6	5.03
UWO_2015_06	0.01	>34	3.24	0.12	0.02	99.93	0.54
UWO_2015_07	0.02	>34	8	0.12	0.02	>110	6.52
UWO_2015_09	0.02	12.35	41.56	0.04	0.08	103.15	8.8
UWO_2015_10	0.03	20.5	6.21	0.21	0.12	>110	2.5
UWO_2015_11	0.15	2.56	59.17	0.08	0.54	102.5	1.65
UWO_2015_14	0.27	12.95	36.43	0.03	0.5	108.65	4.52
UWO_2015_15	0.18	0.06	63.18	0.02	0.42	99.44	4.72
UWO_2015_16	0.37	1.12	66.49	0.02	0.42	100.05	6.45
UWO_2015_18	0.06	3.73	38.37	0.01	0.6	101.8	10.48
UWO_2015_19	0.15	0.92	54.27	0.03	0.38	99.55	6.79
UWO_2015_20	0.11	0.72	61.95	0.02	0.81	100.65	3.2
UWO_2015_21	0.14	0.26	73.49	0.01	0.42	100.3	2.7
UWO_2015_22	0.04	0.29	19.92	0.03	0.34	99.44	31.18
UWO_2015_23	0.16	15.35	43.17	<0.01	0.49	>110	11.45
UWO_2015_24	0.15	0.41	60.32	0.03	0.69	99.89	5.54
UWO_2015_25	0.13	0.84	56.4	0.03	0.58	100.7	6.02
UWO_2015_26	0.45	0.09	56.53	0.13	0.68	100.55	1.44
UWO_2015_27	0.23	0.21	58.45	0.03	0.88	100.2	3.44
UWO_2015_28	0.2	0.5	52.79	0.02	0.76	100.65	9.63
UWO_2015_29	0.09	2	41.93	0.05	1.04	100.6	10.7
UWO_2015_30	0.36	0.16	55.54	0.05	0.56	99.74	6.9

Table A-3 cont. Geochemical analysis results for mineralized samples from the Upper Beaver deposit

SAMPLE DESCRIPTION	ME-XRF26 P2O5 %	ME-XRF26 SO3 %	ME-XRF26 SiO2 %	ME-XRF26 SrO %	ME-XRF26 TiO2 %	ME-XRF26 Total %	OA-GRA05x LOI 1000 %
UWO_2015_31	0.08	0.02	79.96	0.02	0.22	100.2	2.23
UWO_2015_32	0.13	0.14	63.23	0.1	0.59	100.05	1.63
UWO_2015_33	0.08	1.98	46.71	0.07	0.98	101.25	8.58
UWO_2015_34	0.53	0.23	50.25	0.02	1.21	99.71	5.68
UWO_2015_35	0.32	0.11	57.62	0.02	1.48	100.3	2.93
UWO_2015_36	0.28	0.09	45	0.03	1.21	99.79	8.5
UWO_2015_37	0.15	3.99	58.15	0.03	0.71	103.35	4.07
UWO_2015_38	0.07	>34	41.02	0.02	0.25	>110	15.99
UWO_2015_39	0.14	3.21	62.84	0.03	0.64	102.75	2.83
UWO_2015_40	0.15	1.32	62.45	0.03	0.68	100.55	3.12
UWO_2015_41	0.06	0.36	52.22	0.03	0.82	99.45	3.98
UWO_2015_42	0.33	0.12	57.16	0.02	1.18	99.32	3.67
UWO_2015_43	0.27	1.69	45.27	0.02	1.04	101.8	8.87
UWO_2015_44	0.27	0.03	45.51	0.02	1.02	100.4	6.46
UWO_2015_45	0.46	0.45	49.4	0.04	0.66	99.77	7.06
UWO_2015_46	0.09	0.13	49.58	0.02	1.24	100.5	3.58
UWO_2015_47	0.1	1.38	50.62	0.02	1.14	101.15	4.34
UWO_2015_48	0.65	0.05	47.64	0.07	0.5	100.05	2.53
UWO_2015_49	0.1	1.64	51.55	0.06	1.08	101.5	3.73
UWO_2015_50	0.23	24.5	33.55	0.05	0.31	>110	15.04

Appendix E: Element Excitation Energies

Table A-4. Element excitation energies from “X-ray data booklet” Pub-490 Rev. 2, from the Technical Information Department, Lawrence Berkeley Laboratory, 1 Cyclotron Road, Berkeley, California 94720.

Element	K α 1	K α 2	K β 1	L α 1	L α 2	L β 1	L β 2	L γ 1	M α 1
3 Li	54.3								
4 Be	108.5								
5 B	183.3								
6 C	277								
7 N	392.4								
8 O	524.9								
9 F	678.8								
10 Ne	848.6	848.6							
11 Na	1,040.98	1,040.98	1,071.10						
12 Mg	1,253.60	1,253.60	1,302.20						
13 Al	1,486.70	1,486.27	1,557.45						
14 Si	1,739.98	1,739.38	1,835.94						
15 P	2,013.70	2,012.70	2,139.10						
16 S	2,307.84	2,306.64	2,464.04						
17 Cl	2,622.39	2,620.78	2,815.60						
18 Ar	2,957.70	2,955.63	3,190.50						
19 K	3,313.80	3,311.10	3,589.60						
20 Ca	3,691.68	3,688.09	4,012.70	341.30	341.30	344.90			
21 Sc	4,090.60	4,086.10	4,460.50	395.40	395.40	399.60			
22 Ti	4,510.84	4,504.86	4,931.81	452.20	452.20	458.40			
23 V	4,952.20	4,944.64	5,427.29	511.3	511.3	519.2			
24 Cr	5,414.72	5,405.51	5,946.71	572.8	572.8	582.8			
25 Mn	5,898.75	5,887.69	6,490.45	637.4	637.4	648.8			
26 Fe	6,403.84	6,390.84	7,057.98	705	705	718.5			
27 Co	6,930.32	6,915.30	7,649.43	776.2	776.2	791.4			

Table A-4 cont. Element excitation energies from “X-ray data booklet” Pub-490 Rev. 2, from the Technical Information Department, Lawrence Berkeley Laboratory, 1 Cyclotron Road, Berkeley, California 94720.

Element	K α 1	K α 2	K β 1	L α 1	L α 2	L β 1	L β 2	L γ 1	M α 1
28 Ni	7,478.15	7,460.89	8,264.66	851.5	851.5	868.8			
29 Cu	8,047.78	8,027.83	8,905.29	929.7	929.7	949.8			
30 Zn	8,638.86	8,615.78	9,572.00	1,011.70	1,011.70	1,034.70			
31 Ga	9,251.74	9,224.82	10,264.30	1,087.92	1,097.92	1,124.80			
32 Ge	9,886.42	9,855.32	10,982.10	1,188.00	1,188.00	1,218.50			
33 As	10,543.72	10,507.99	11,726.20	1,282.00	1,282.00	1,317.00			
34 Se	11,222.40	11,181.40	12,495.90	1,379.10	1,379.10	1,419.23			
35 Br	11,924.20	11,877.60	13,291.40	1,480.43	1,480.43	1,525.90			
36 Kr	12,649.00	12,598	14,112.00	1,568	1,586.00	1,636.60			
37 Rb	13,395.30	13,335.80	14,961.30	1,694.13	1,692.56	1,752.17			
38 Sr	14,165	14,097.90	15,835.70	1,806.56	1,804.74	1,871.72			
39 Y	14,958.40	14,882.90	16,737.80	1,922.56	1,920.47	1,995.84			
40 Zr	15,775	15,690.90	17,667.80	2,042.36	2,039.90	2,124.40	2,219.40	2,302.70	
41 Nb	16,615.10	16,521.00	18,622.50	2,165.89	2,163.00	2,257.40	2,367	2,461.80	
42 Mo	17,497.34	17,374.30	19,608.30	2,293.16	2,289.85	2,394.81	2,518.30	2,623.50	
43 Tc	18,367.10	18,250.80	20,619	2,424	2,420	2,538	2,674	2,792	
44 Ru	19,279.20	19,150.40	21,656.80	2,558.55	2,554.31	2,683.23	2,836.00	2,964.50	
45 Rh	20,216.10	20,073.70	22,723.60	2,696.74	2,692.05	2,834.41	3,001.30	3,143.80	
46 Pd	21,177.10	21,020.10	23,818.70	2,838.61	2,833.29	2,990.22	3,171.79	3,328.70	
47 Ag	22,162.92	21,990.30	24,942.40	2,984.31	2,978.21	3,150.94	3,347.81	3,519.59	
48 Cd	23,173.60	22,984.10	26,095.50	3,133.73	3,126.91	3,316.57	3,528.12	3,716.86	
49 In	24,209.70	24,002	27,275.90	3,286.94	3,279.29	3,487.21	3,713.81	3,920.81	
50 Sn	25,271.30	25,044	28,486	3,443.98	3,435.42	3,662.80	3,904.86	4,131.12	
51 Sb	26,359.10	26,110.80	29,725.60	3,604.72	3,595.32	3,843.57	4,100.78	4,347.79	
52 Te	27,472.30	27,201.70	30,995.70	3,769.33	3,758.80	4,029.58	4,301.70	4,570.90	

Table A-4 cont. Element excitation energies from "X-ray data booklet" Pub-490 Rev. 2, from the Technical Information Department, Lawrence Berkeley Laboratory, 1 Cyclotron Road, Berkeley, California 94720.

Element	K α 1	K α 2	K β 1	L α 1	L α 2	L β 1	L β 2	L γ 1	M α 1
53 I	28,612.00	28,317.20	32,294.70	3,937.65	3,926.40	4,220.72	4,507.50	4,800.90	
54 Xe	29,779	29,458	33,624	4,109.90	---	---	---	---	
55 Cs	30,972.80	30,625.10	34,986.90	4,286.50	4,727.20	4,619.80	4,935.90	5,280.40	
56 Ba	32,193.60	31,817.10	36,387.20	4,466.26	4,450.90	4,827.53	55,156.50	5,531.10	
57 La	33,441.80	33,034.10	37,801.00	4,650.97	4,634.23	5,042.10	5,383.50	5,788.50	833
58 Ce	34,719.70	34,278.90	39,257.30	4,840.20	4,823	5,262.20	5,613.40	6,052.00	883
59 Pr	36,026.30	35,550.20	40,748.20	5,033.70	5,013.50	5,488.90	5,850.00	6,322.10	929
60 Nd	37,361.00	36,847.40	42,271.30	5,230.40	5,207.70	5,721.60	6,089	6,602.10	978
61 Pm	38,724.70	38,171.20	43,826	5,432.50	5,407.80	5,961	6,339.00	6,892	
62 Sm	40,118.10	39,522.40	45,413	5,636.10	5,609.00	6,205.10	6,586	7,178	1,081
63 Eu	41,542.20	40,901.90	47,037.90	5,845.70	5,816.60	6,456.40	6,843.20	7,480.30	1,131
64 Gd	42,996.20	42,308.90	48,697	6,057.20	6,025	6,713.20	7,102.80	7,785.80	1,185
65 Tb	44,481.60	43,744.10	50,382	6,272.80	6,238	6,978	7,366.70	8,102	1,240
66 Dy	45,998.40	45,207.80	52,119	6,495.20	6,457.70	7,247.70	7,635.70	8,418.80	1,293
67 Ho	47,546.70	46,699.70	53,877	6,719.80	6,679.50	7,525.30	7,911	8,747	1,348
68 Er	49,127.70	48,221.10	55,681	6,948.70	6,905	7,810.90	8,189	9,089	1,406
69 Tm	50,741.60	49,772.60	57,517	7,179.90	7,133.10	8,101	8,468	9,426	1,462
70 Yb	52,388.90	51,354	59,370	7,415.60	7,367.30	8,401.80	8,758.80	9,780.10	1,521.40
71 Lu	54,069.80	52,965	61,283	7,655.50	7,604.90	8,709	9,048.90	10,143.40	1,581.30
72 Hf	55,790.20	54,611.40	63,234	7,899	7,844.60	9,022.70	9,347.30	10,515.80	1,644.60
73 Ta	57,532	56,277	65,223	8,146.10	8,087.90	9,343.10	9,651.80	10,895.20	1,710
74 W	59,318.24	57,981.70	67,244.30	8,397.60	8,335.20	9,672.35	9,961.50	11,285.90	1,775.40
75 Re	61,140.30	59,717.90	69,310	8,652.50	8,586.20	10,010	10,275.20	11,685.40	1,842.50
76 Os	63,000.50	61,486.70	71,413	8,911.70	8,841	10,355.30	10,598.50	12,095.30	1,910.20
77 Ir	64,895.60	63,286.70	73,560.80	9,175.10	9,099.50	10,708.30	10,920.30	12,512.60	1,979

Table A-4 cont. Element excitation energies from "X-ray data booklet" Pub-490 Rev. 2, from the Technical Information Department, Lawrence Berkeley Laboratory, 1 Cyclotron Road, Berkeley, California 94720.

Element	K α 1	K α 2	K β 1	L α 1	L α 2	L β 1	L β 2	L γ 1	M α 1
78 Pt	66,832	65,112	75,748	9,442.30	9,361.80	11,070.70	11,250.50	12,942.00	2,050.50
79 Au	68,803.70	66,989.50	77,984	9,713.30	9,628.00	11,442.30	11,584.70	13,381.70	2,122.90
80 Hg	70,819	68,895	80,253	9,988.80	9,897.60	11,822.60	11,924.10	13,830.10	2,195.30
81 Tl	72,871.50	70,831.90	82,576	10,268.80	10,172.80	12,213.30	12,271.50	14,291.50	2,270.60
82 Pb	74,969.40	72,804.20	84,936.60	10,551.50	10,449.50	12,613.70	12,622.60	14,764.40	2,345.50
83 Bi	77,107.90	74,814.80	87,343	10,838.80	10,730.91	13,023.50	12,979.90	15,247.70	2,422.60
84 Po	79,290	76,862	89,800	11,130.80	11,015.80	13,447	13,340.40	15,744	---
85 At	81,520	78,950	92,300	11,426.80	11,304.80	13,876	---	16,251	---
86 Rn	83,780	81,070	94,870	11,727.00	11,597.90	14,316	---	16,770	---
87 Fr	86,100	83,230	97,470	12,031.30	11,895	14,770	14,450	17,303	---
88 Ra	88,470	85,430	100,130	12,339.70	12,196.20	15,235.80	14,841.40	17,849	---
89 Ac	90,884	87,670	102,850	12,652	12,500.80	15,713	---	18,408	---
90 Th	93,350	89,953	105,609	12,968.70	12,809.60	16,202.20	15,623.70	18,982.50	2,996.10
91 Pa	95,868	92,287	108,427	13,290.70	13,122.20	16,702	16,024	19,568	3,082.30
92 U	98,439	94,665	111,300	13,614.70	13,438.80	17,220.00	16,428.30	20,167.10	3,170.80
93 Np	---	---	---	13,944.10	13,759.70	17,750.20	16,840	20,784.80	---
94 Pu	---	---	---	14,278.60	14,084.20	18,293.70	17,255.30	21,417.30	---
95 Am	---	---	---	14,617.20	14,411.90	18,852	17,676.50	22,065.20	---

Appendix F: Major Oxide Percents and Calculated CIPW Normative Values

Table A-5. Major oxide percents and calculated CIPW normative values for data from Feick (2015), DeAgazio (2012) and for select data from this study

Source	Sample ID	Lithology	SiO2 pct	Al2O3 pct	Fe2O3 pct	MnO pct	MgO pct	CaO pct	Na2O pct	K2O pct	TiO2 pct	P2O5 pct	Ba ppm	Sr ppm
Feick (2014)	KF01	Syenite Porphyry	62.39	15.95	3.51	0.04	1.81	3.76	5.29	2.47	0.39	0.19	676	402
Feick (2014)	KF02	Syenite Porphyry	59.81	15.60	4.57	0.05	1.60	4.58	6.14	1.62	0.36	0.19	422	361
Feick (2014)	KF03	Basalt	49.62	13.00	8.34	0.12	5.56	8.86	3.71	1.05	0.93	0.27	244	221
Feick (2014)	KF04	Basalt	62.97	11.38	8.11	0.05	1.49	4.56	4.61	1.28	1.75	0.11	232	163
Feick (2014)	KF05	Basalt	43.21	11.56	13.70	0.13	2.63	13.61	3.63	1.34	1.72	0.13	192	329
Feick (2014)	KF06	Basalt	50.35	11.62	9.30	0.14	4.31	10.00	1.75	1.49	0.64	0.50	278	348
Feick (2014)	KF07	Basalt	47.05	14.47	11.63	0.10	3.17	8.21	3.82	2.47	2.40	0.17	473	154
Feick (2014)	KF08	Basalt	52.80	12.57	8.14	0.07	2.93	7.68	0.87	7.66	1.95	0.13	1463	206
Feick (2014)	KF09	Basalt	41.99	16.37	13.83	0.11	3.31	14.98	1.91	1.36	2.48	0.15	281	782
Feick (2014)	KF10	Basalt	52.12	13.38	12.48	0.07	2.06	5.70	3.53	3.18	2.16	0.14	656	147
Feick (2014)	KF11	Basalt	47.27	15.36	13.99	0.11	3.01	7.48	2.98	2.43	2.45	0.16	421	350
Feick (2014)	KF12	Basalt	57.71	12.17	13.00	0.07	1.93	5.94	3.19	1.92	1.90	0.17	303	255
Feick (2014)	KF13	Basalt	48.55	15.38	12.21	0.12	3.78	8.45	2.54	2.11	2.41	0.14	422	508
Feick (2014)	KF14	Basalt	50.92	12.35	19.80	0.10	2.57	6.27	3.07	1.34	1.97	0.14	287	277
Feick (2014)	KF15	Basalt	53.64	13.49	15.06	0.08	1.50	6.51	3.18	2.03	2.15	0.16	462	329
Feick (2014)	KF16	Basalt	42.39	17.50	14.02	0.10	2.59	13.17	2.87	0.30	2.58	0.17	67	1069
Feick (2014)	KF17	Mafic Syenite	52.41	14.56	8.95	0.09	6.01	6.32	3.24	3.68	0.74	0.46	1333	561
Feick (2014)	KF18	Basalt	53.07	14.01	6.67	0.06	1.94	8.94	6.56	0.24	2.13	0.15	38	70
Feick (2014)	KF19	Volcaniclastic	50.91	14.89	9.57	0.10	3.67	8.02	4.44	0.73	1.00	0.09	124	419
Feick (2014)	KF20	Volcaniclastic	48.79	14.80	13.16	0.15	4.75	8.25	3.01	0.36	1.09	0.08	52	404
DeAgazio (2012)	273501.00	Spotted Feldspar Porphyry	64.30	13.00	4.84	0.04	3.25	3.08	5.47	0.34	0.43	0.24	385	286
DeAgazio (2012)	273504.00	Syenite Porphyry	67.30	14.10	3.04	0.03	1.48	2.83	4.42	1.58	0.28	0.12	788	249
DeAgazio (2012)	273508.00	Syenite Porphyry	61.00	14.70	2.89	0.03	1.65	5.29	6.48	0.72	0.36	0.16	153	498
DeAgazio (2012)	273509.00	Mafic Syenite Porphyry	59.30	16.60	2.92	0.05	1.21	4.34	6.76	1.36	0.74	0.18	104	154
DeAgazio (2012)	273511.00	Mafic Syenite	55.00	12.50	8.82	0.15	0.70	6.27	3.41	2.39	0.75	0.46	1108	396

Table A-5 cont. Major oxide percentss and calculated CIPW normative values for data from Feick (2015), DeAgazio (2012) and for select data from this study

Source	Sample ID	Lithology	SiO2 pct	Al2O3 pct	Fe2O3 pct	MnO pct	MgO pct	CaO pct	Na2O pct	K2O pct	TiO2 pct	P2O5 pct	Ba ppm	Sr ppm
DeAgazio (2012)	273513.00	Mafic Syenite Porphyry	57.80	17.50	5.43	0.07	1.92	4.68	2.42	3.52	0.79	0.19	1143	352
DeAgazio (2012)	273514.00	Syenite Porphyry	65.60	13.60	2.69	0.02	1.43	3.09	4.79	2.03	0.32	0.17	545	322
DeAgazio (2012)	273516.00	Tisdale Volcanic Tuff	54.80	12.80	8.86	0.05	1.50	6.73	1.30	2.75	0.98	0.25	340	88
DeAgazio (2012)	273518.00	Mafic Syenite	57.10	13.80	6.41	0.10	4.35	5.99	3.69	2.95	0.61	0.37	1415	747
DeAgazio (2012)	273519.00	Mafic Syenite Porphyry	60.60	15.30	4.78	0.05	1.57	3.72	3.95	2.39	0.65	0.16	318	176
DeAgazio (2012)	273520.00	Syenite Porphyry	64.40	14.20	4.99	0.02	1.77	3.36	3.85	2.17	0.36	0.17	188	256
DeAgazio (2012)	273521.00	Tisdale Volcanic Tuff	57.10	12.90	6.29	0.07	2.15	6.10	3.77	0.99	0.96	0.26	75	88
DeAgazio (2012)	273522.00	Syenite Porphyry	64.90	16.70	2.63	0.01	3.59	0.68	8.33	0.18	0.46	0.17	17	51
DeAgazio (2012)	273527.00	Tisdale Volcanic Tuff	55.30	15.40	5.92	0.11	2.71	4.47	2.07	3.13	1.32	0.41	672	103
DeAgazio (2012)	273532.00	Tisdale Volcanic Tuff	56.60	14.10	7.40	0.07	2.65	4.24	2.20	2.89	1.07	0.26	152	110
DeAgazio (2012)	273533.00	Spotted Feldspar Porphyry	59.80	12.90	5.20	0.07	3.81	3.85	5.35	0.21	0.47	0.25	352	374
DeAgazio (2012)	273534.00	Mafic Syenite	51.10	11.70	7.86	0.12	5.89	7.65	2.98	2.13	0.67	0.42	1182	366
DeAgazio (2012)	273538.00	Spotted Feldspar Porphyry	62.20	13.00	5.57	0.07	4.30	3.12	4.94	0.26	0.45	0.24	78	337
DeAgazio (2012)	273539.00	Spotted Feldspar Porphyry	60.60	12.50	4.93	0.09	3.66	5.05	3.97	1.26	0.43	0.24	179	176
DeAgazio (2012)	273542.00	Mafic Syenite	52.10	12.80	7.72	0.11	5.93	6.85	2.35	2.75	0.62	0.39	1564	593
DeAgazio (2012)	273545.00	Mafic Syenite Porphyry	65.00	13.70	3.83	0.17	1.57	2.59	6.32	0.81	0.74	0.14	242	154
DeAgazio (2012)	273546.00	Tisdale Volcanic Tuff	60.10	15.60	5.42	0.06	1.58	3.87	3.72	2.08	0.77	0.20	309	103
DeAgazio (2012)	273551.00	Spotted Feldspar Porphyry	59.60	13.00	4.87	0.09	3.51	0.42	4.78	1.56	0.44	0.24	258	256
DeAgazio (2012)	273553.00	Mafic Syenite Porphyry	66.60	14.10	5.02	0.06	1.36	4.01	5.02	0.55	0.60	0.15	276	249
DeAgazio	273555.00	Spotted Feldspar Porphyry	61.10	12.70	4.66	0.07	3.22	4.33	4.13	1.96	0.42	0.22	2732	271

(2012)

Table A-5 cont. Major oxide percents and calculated CIPW normative values for data from Feick (2015), DeAgazio (2012) and for select data from this study

Source	Sample ID	Lithology	SiO2 pct	Al2O3 pct	Fe2O3 pct	MnO pct	MgO pct	CaO pct	Na2O pct	K2O pct	TiO2 pct	P2O5 pct	Ba ppm	Sr ppm
DeAgazio (2012)	273556.00	Mafic Syenite	62.00	13.10	3.26	0.05	3.15	5.86	3.27	2.10	0.45	0.22	315	227
DeAgazio (2012)	283557.00	Mafic Syenite Porphyry	65.20	12.90	3.26	0.05	3.14	5.86	3.20	2.13	0.44	0.22	316	227
DeAgazio (2012)	273558.00	Syenite Porphyry	64.20	15.70	2.32	0.04	2.36	3.67	7.30	0.70	0.41	0.19	473	322
DeAgazio (2012)	273559.00	Tisdale Volcanic Tuff	57.60	13.90	5.33	0.07	1.71	5.97	1.61	3.53	1.05	0.27	536	168
DeAgazio (2012)	15819.00	Unknown	47.40	7.56	12.70	0.16	17.80	7.43		0.11	0.59	0.09		
DeAgazio (2012)	15822.00	Unknown	48.00	13.10	13.20	0.15	6.50	11.80	2.20	0.31	1.23	0.09	137	374
DeAgazio (2012)	15823.00	Unknown	53.00	12.70	12.20	0.08	4.27	5.28	4.30	0.63	1.24	0.11	382	110
DeAgazio (2012)	15824.00	Unknown	59.30	15.80	4.49	0.08	2.27	5.00	2.32	3.09	0.57	0.17	602	176
DeAgazio (2012)	JD12-51	Spotted Feldspar Porphyry	58.10	18.00	4.80	0.07	3.52	2.82	8.02	0.29	0.34	0.14	63	139
This Study	UWO_2015_20	Tisdale Cherty Sediments	61.95	15.87	6.16	0.08	2.52	2.17	5.99	0.85	0.81	0.11	300	
This Study	UWO_2015_21	Tisdale Cherty Sediments	73.49	11.60	5.23	0.06	1.18	1.54	1.35	2.20	0.42	0.14	400	
This Study	UWO_2015_22	Tisdale Greywacke	19.92	3.41	8.98	0.19	11.55	22.00	0.56	0.84	0.34	0.04	200	
This Study	UWO_2015_23	Graphitic Sediments	43.17	10.62	28.57	0.01	2.36	0.39	0.05	1.78	0.49	0.16	900	
This Study	UWO_2015_24	Cherty Sediments	60.32	17.45	2.87	0.02	1.16	4.83	0.07	5.88	0.69	0.15	3200	
This Study	UWO_2015_25	Volcaniclastics	56.40	14.41	8.47	0.05	0.95	5.76	2.81	4.06	0.58	0.13	800	
This Study	UWO_2015_26	Amphibole-rich Intrusive	56.53	15.68	6.79	0.10	4.84	6.48	5.27	1.86	0.68	0.45	1100	
This Study	UWO_2015_27	Microphyric Intrusive	58.45	18.00	4.98	0.05	2.27	3.95	5.18	2.35	0.88	0.23	800	
This Study	UWO_2015_28	Microphyric Intrusive	52.79	15.60	5.40	0.06	2.71	6.09	3.86	2.89	0.76	0.20	400	
This Study	UWO_2015_29	Volcaniclastics	41.93	15.04	9.68	0.15	3.00	11.30	3.32	2.05	1.04	0.09	600	
This Study	UWO_2015_30	Silty Arenite	55.54	13.58	6.36	0.10	3.88	6.73	4.95	0.46	0.56	0.36	200	
This Study	UWO_2015_31	Cherty Sediments	79.96	10.01	0.71	0.01	0.48	2.29	1.32	2.73	0.22	0.08	1000	
This Study	UWO_2015_32	Cherty Sediments	63.23	16.95	3.27	0.05	0.49	5.93	5.33	2.07	0.59	0.13	900	
This Study	UWO_2015_33	Conglomerate	46.71	14.44	7.47	0.10	3.14	12.30	5.03	0.20	0.98	0.08	100	
This Study	UWO_2015_34	Breccia (200 Zone)	50.25	14.93	11.50	0.07	2.44	6.65	2.92	3.11	1.21	0.53	600	

Table A-5 cont. Major oxide percents and calculated CIPW normative values for data from Feick (2015), DeAgazio (2012) and for select data from this study

Source	Sample ID	Lithology	SiO ₂ pct	Al ₂ O ₃ pct	Fe ₂ O ₃ pct	MnO pct	MgO pct	CaO pct	Na ₂ O pct	K ₂ O pct	TiO ₂ pct	P ₂ O ₅ pct	Ba ppm	Sr ppm
This Study	UWO_2015_35	Breccia (200 Zone)	57.62	16.92	8.35	0.02	2.20	2.07	6.11	1.98	1.48	0.32	500	
This Study	UWO_2015_36	Breccia (200 Zone)	45.00	14.17	14.33	0.07	2.54	6.21	4.82	2.40	1.21	0.28	400	
This Study	UWO_2015_37	Cherty Sediments	58.15	16.84	6.51	0.07	3.05	2.35	6.19	1.08	0.71	0.15	400	
This Study	UWO_2015_38	Graphitic Sediments	41.02	7.35	28.79	0.03	1.18	2.13	0.11	1.80	0.25	0.07	500	
This Study	UWO_2015_39	Conglomerate	62.84	17.18	4.32	0.02	1.04	4.45	3.40	2.54	0.64	0.14	500	
This Study	UWO_2015_40	Conglomerate/ Cherty Sediments	62.45	17.44	3.30	0.02	1.15	4.42	3.33	3.04	0.68	0.15	500	
This Study	UWO_2015_41	Brecciated Basalt	52.22	13.32	10.48	0.16	6.46	8.47	2.79	0.13	0.82	0.06	100	
This Study	UWO_2015_42	Breccia (Mafic Syenite) 1	57.16	17.12	4.18	0.05	3.48	3.74	8.03	0.16	1.18	0.33	100	
This Study	UWO_2015_43	Breccia (Mafic Syenite) 2	45.27	15.48	9.34	0.09	4.26	8.88	5.64	0.82	1.04	0.27	200	
This Study	UWO_2015_44	Breccia (Mafic Syenite) 3	45.51	15.98	15.27	0.06	4.36	5.38	3.05	2.79	1.02	0.27	700	
This Study	UWO_2015_45	Breccia (Mafic Syenite Porphyry) 1	49.40	14.01	8.85	0.09	6.07	6.41	3.07	2.92	0.66	0.46	900	
This Study	UWO_2015_46	Breccia (Mafic Syenite Porphyry) 2	49.58	15.62	15.34	0.07	3.85	3.81	3.66	3.19	1.24	0.09	800	
This Study	UWO_2015_47	Breccia (Mafic Syenite Porphyry) 3	50.62	15.20	14.44	0.09	4.61	3.43	3.11	2.46	1.14	0.10	600	
This Study	UWO_2015_48	Biotite-rich Intrusive	47.64	9.58	9.08	0.19	13.35	11.15	1.22	3.58	0.50	0.65	1600	
This Study	UWO_2015_49	Conglomerate	51.55	15.75	9.76	0.26	4.41	7.24	5.27	0.41	1.08	0.10	200	

Table A-5 cont. Major oxide percents and calculated CIPW normative values for data from Feick (2015), DeAgazio (2012) and for select data from this study

Source	Sample ID	Lithology	Quartz	Plagioclase	Orthoclase	Nepheline	Kalsilite	Corundum	Diopside	Hypersthene
Feick (2014)	KF01	Syenite Porphyry	12.36	61.24	16.89	0	0	0	3.64	4.16
Feick (2014)	KF02	Syenite Porphyry	7.58	68.5	11.33	0	0	0	8.2	2.32
Feick (2014)	KF03	Basalt	0.34	57.13	8.13	0	0	0	21.02	9.22
Feick (2014)	KF04	Basalt	23.06	50.89	8.98	0	0	0	11.22	1.52
Feick (2014)	KF05	Basalt	0	30.49	10.54	12.37	0	0	30.73	0
Feick (2014)	KF06	Basalt	12.96	41.8	11.64	0	0	0	21.83	6.84
Feick (2014)	KF07	Basalt	0	47.9	18.58	4.69	0	0	19.32	0
Feick (2014)	KF08	Basalt	2.84	16.25	54.45	0	0	0	18.82	0
Feick (2014)	KF09	Basalt	0	40.9	10.35	8.92	0	0	32.16	0
Feick (2014)	KF10	Basalt	5.14	47.65	23.34	0	0	0	12.47	4.78
Feick (2014)	KF11	Basalt	0	54.55	18.14	0	0	0	11.55	7.57
Feick (2014)	KF12	Basalt	17.99	45.29	13.59	0	0	0	11.33	5.8
Feick (2014)	KF13	Basalt	3.04	52.99	15.67	0	0	0	12.91	8.63
Feick (2014)	KF14	Basalt	8.61	49.3	10.01	0	0	0	11.18	12.83
Feick (2014)	KF15	Basalt	11.58	49.45	14.74	0	0	0	11.27	5.95
Feick (2014)	KF16	Basalt	0	59.24	2.31	5.48	0	0	23.89	0
Feick (2014)	KF17	Mafic Syenite	0	46.39	26.78	0	0	0	10.69	6.38
Feick (2014)	KF18	Basalt	0	70.56	1.69	1.68	0	0	14.04	0
Feick (2014)	KF19	Volcaniclastic	1.4	66.12	5.38	0	0	0	15.94	6.92
Feick (2014)	KF20	Volcaniclastic	5.18	60.85	2.74	0	0	0	11.46	13.82
DeAgazio (2012)	273501.00	Spotted Feldspar Porphyry	21.39	62.09	2.63	0	0	0	2.82	8.87
DeAgazio (2012)	273504.00	Syenite Porphyry	28.1	54.4	11.13	0	0	0.1	0	4.98
DeAgazio (2012)	273508.00	Syenite Porphyry	10.78	71.06	5.06	0	0	0	11.36	0
DeAgazio (2012)	273509.00	Mafic Syenite Porphyry	6.04	75.29	9.25	0	0	0	6.75	0.71

DeAgazio 273511.00 Mafic Syenite 15.13 47.75 18.51 0 0 0 13.19 1.09
(2012)

Table A-5 cont. Major oxide percents and calculated CIPW normative values for data from Feick (2015), DeAgazio (2012) and for select data from this study

Source	Sample ID	Lithology	Quartz	Plagioclase	Orthoclase	Nepheline	Kalsilite	Corundum	Diopside	Hypersthene
DeAgazio (2012)	273513.00	Mafic Syenite Porphyry	17.35	46.58	25.07	0	0	1.1	0	7.22
DeAgazio (2012)	273514.00	Syenite Porphyry	23.54	54.58	14.04	0	0	0	3.41	3.04
DeAgazio (2012)	273516.00	Tisdale Volcanic Tuff	24.07	37.53	20.65	0	0	0	8.63	4.93
DeAgazio (2012)	273518.00	Mafic Syenite	7.18	48.23	21.64	0	0	0	11.27	8.57
DeAgazio (2012)	273519.00	Mafic Syenite Porphyry	19	55.72	16.64	0	0	0	0.43	5.92
DeAgazio (2012)	273520.00	Syenite Porphyry	24.62	51.64	14.65	0	0	0	0.41	6.7
DeAgazio (2012)	273521.00	Tisdale Volcanic Tuff	19.76	55.54	7.25	0	0	0	10.18	3.83
DeAgazio (2012)	273522.00	Syenite Porphyry	9.19	77.78	1.17	0	0	1.39	0	9
DeAgazio (2012)	273527.00	Tisdale Volcanic Tuff	19.85	42.7	23.05	0	0	1.07	0	9.23
DeAgazio (2012)	273532.00	Tisdale Volcanic Tuff	21.07	43.7	20.84	0	0	0.19	0	10.38
DeAgazio (2012)	273533.00	Spotted Feldspar Porphyry	16.3	64.39	1.83	0	0	0	5.26	9.76
DeAgazio (2012)	273534.00	Mafic Syenite	3.95	45.07	17.15	0	0	0	18.54	11.3
DeAgazio (2012)	273538.00	Spotted Feldspar Porphyry	20.6	61.17	1.88	0	0	0	1.03	12.87
DeAgazio (2012)	273539.00	Spotted Feldspar Porphyry	20.11	52.61	8.99	0	0	0	8.14	7.85
DeAgazio (2012)	273542.00	Mafic Syenite	6.33	42.1	21.7	0	0	0	12.24	13.89
DeAgazio (2012)	273545.00	Mafic Syenite Porphyry	19.08	65.76	5.65	0	0	0	3.84	3.6
DeAgazio (2012)	273546.00	Tisdale Volcanic Tuff	20.83	54.99	14.53	0	0	0.47	0	6.49
DeAgazio (2012)	273551.00	Spotted Feldspar Porphyry	22.08	49.51	11.68	0	0	2.56	0	11.76
DeAgazio (2012)	273553.00	Mafic Syenite Porphyry	26.01	60.59	3.84	0	0	0	3.28	4.09

DeAgazio 273555.00 Spotted Feldspar 17.31 49.89 16.17 0 0 0 7.92 6.56
(2012) Porphyry

Table A-5 cont. Major oxide percents and calculated CIPW normative values for data from Feick (2015), DeAgazio (2012) and for select data from this study

Source	Sample ID	Lithology	Quartz	Plagioclase	Orthoclase	Nepheline	Kalsilite	Corundum	Diopside	Hypersthene
DeAgazio (2012)	273556.00	Mafic Syenite	22.26	47.21	14.74	0	0	0	9.34	4.63
DeAgazio (2012)	283557.00	Mafic Syenite Porphyry	25.43	44.72	14.47	0	0	0	9.27	4.37
DeAgazio (2012)	273558.00	Syenite Porphyry	9.84	74.27	4.94	0	0	0	6.26	3.3
DeAgazio (2012)	273559.00	Tisdale Volcanic Tuff	23.24	38.26	25.53	0	0	0	5.87	3.84
DeAgazio (2012)	15819.00	Unknown	4.28	25.49	0.88	0	0	0	13.46	51.17
DeAgazio (2012)	15822.00	Unknown	2.04	51.79	2.48	0	0	0	26.01	12.35
DeAgazio (2012)	15823.00	Unknown	7.73	59.35	4.97	0	0	0	9.44	13.46
DeAgazio (2012)	15824.00	Unknown	20.86	47.34	21.77	0	0	0	0.27	7.59
DeAgazio (2012)	JD12-51	Spotted Feldspar Porphyry	0	87.14	2	0	0	0	0.6	3.71
This Study	UWO_2015_20	Tisdale Cherty Sediments	18.36	61.16	5.91	0	0	1.66	0	8.89
This Study	UWO_2015_21	Tisdale Cherty Sediments	55.86	17.62	14.88	0	0	3.46	0	5.66
This Study	UWO_2015_22	Tisdale Greywacke	0	8.81	0	2.78	2.17	0	0	0
This Study	UWO_2015_23	Graphitic Sediments	22.23	0	12.38	0	0	6.06	0	23.14
This Study	UWO_2015_24	Cherty Sediments	5.85	45.47	42.17	0	0	1.88	0	3.71
This Study	UWO_2015_25	Volcaniclastics	15.37	39.62	28.8	0	0	0	7.73	3.72
This Study	UWO_2015_26	Amphibole-rich Intrusive	0	62.68	13.39	0	0	0	11.07	8.82
This Study	UWO_2015_27	Microphyric Intrusive	7.79	65.19	16.27	0	0	0.32	0	7.36
This Study	UWO_2015_28	Microphyric Intrusive	6.29	55.19	20.98	0	0	0	8.02	5.7
This Study	UWO_2015_29	Volcaniclastics	0	47.51	16.36	2.03	0	0	23.39	0
This Study	UWO_2015_30	Silty Arenite	9.12	63.83	3.46	0	0	0	12.9	7.22
This Study	UWO_2015_31	Cherty Sediments	57.44	22.18	18.02	0	0	0.54	0	1.23

Table A-5 cont. Major oxide percents and calculated CIPW normative values for data from Feick (2015), DeAgazio (2012) and for select data from this study

Source	Sample ID	Lithology	Quartz	Plagioclase	Orthoclase	Nepheline	Kalsilite	Corundum	Diopside	Hypersthene
This Study	UWO_2015_32	Cherty Sediments	13.7	63.19	14.04	0	0	0	5.34	0
This Study	UWO_2015_33	Conglomerate	0.46	62.59	1.56	0	0	0	25.73	0
This Study	UWO_2015_34	Breccia (200 Zone)	4.76	49.08	23.01	0	0	0	8.1	8.87
This Study	UWO_2015_35	Breccia (200 Zone)	6.1	65.32	13.81	0	0	1.31	0	8.81
This Study	UWO_2015_36	Breccia (200 Zone)	0	43.4	18.53	10.47	0	0	15.28	0
This Study	UWO_2015_37	Cherty Sediments	26.66	40.19	7.54	0	0	4.8	0	10.45
This Study	UWO_2015_38	Graphitic Sediments	23.63	16.41	17.66	0	0	1.47	0	30.38
This Study	UWO_2015_39	Conglomerate	37.5	29.74	16.89	0	0	3.58	0	4.32
This Study	UWO_2015_40	Conglomerate/ Cherty Sediments	27.15	42.49	20.3	0	0	1.84	0	3.9
This Study	UWO_2015_41	Brecciated Basalt	11.02	53.72	1.04	0	0	0	13.08	16.46
This Study	UWO_2015_42	Breccia (Mafic Syenite) 1	0	85.52	1.15	0	0	0	4.11	2.58
This Study	UWO_2015_43	Breccia (Mafic Syenite) 2	0	57.61	6.18	5.57	0	0	17.06	0
This Study	UWO_2015_44	Breccia (Mafic Syenite) 3	0	55.97	21.25	0	0	0	2.7	1.38
This Study	UWO_2015_45	Breccia (Mafic Syenite Porphyry) 1	0	47.36	22.24	0	0	0	9.1	15.51
This Study	UWO_2015_46	Breccia (Mafic Syenite Porphyry) 2	0	54.11	23.4	0	0	0	1.07	9.54
This Study	UWO_2015_47	Breccia (Mafic Syenite Porphyry) 3	11.62	39.1	18.35	0	0	2.42	0	20.24
This Study	UWO_2015_48	Biotite-rich Intrusive	0	14.87	27.59	4.48	0	0	31.7	0
This Study	UWO_2015_49	Conglomerate	4.38	64.76	3.02	0	0	0	8.5	12.1

Table A-5 cont. Major oxide percents and calculated CIPW normative values for data from Feick (2015), DeAgazio (2012) and for select data from this study

Source	Sample ID	Lithology	Wollastonite	Olivine	Larnite	Ilmenite	Magnetite	Apatite	Zircon	Pyrite	Anhydrite	Na ₂ SO ₄	Total
Feick (2014)	KF01	Syenite Porphyry	0	0	0	0.44	0.83	0.39	0.02	0.02	0	0	99.99
Feick (2014)	KF02	Syenite Porphyry	0	0	0	0.42	1.11	0.4	0.02	0.12	0	0	100
Feick (2014)	KF03	Basalt	0	0	0	1.2	2.26	0.63	0.02	0.06	0	0	100.01
Feick (2014)	KF04	Basalt	0	0	0	2.07	2	0.24	0.01	0.03	0	0	100.02
Feick (2014)	KF05	Basalt	8.87	0	0	2.3	3.83	0.31	0.01	0.54	0	0	99.99
Feick (2014)	KF06	Basalt	0	0	0	0.84	2.57	1.2	0.02	0.29	0	0	99.99
Feick (2014)	KF07	Basalt	0	2.89	0	3.05	3.09	0.39	0.01	0.07	0	0	99.99
Feick (2014)	KF08	Basalt	1.9	0	0	2.34	2.04	0.28	0.01	1.06	0	0	99.99
Feick (2014)	KF09	Basalt	0.29	0	0	3.18	3.72	0.35	0.01	0.12	0	0	100
Feick (2014)	KF10	Basalt	0	0	0	2.67	3.23	0.31	0.01	0.39	0	0	99.99
Feick (2014)	KF11	Basalt	0	0.84	0	3.09	3.69	0.37	0.01	0.2	0	0	100.01
Feick (2014)	KF12	Basalt	0	0	0	2.29	3.27	0.37	0.01	0.05	0	0	99.99
Feick (2014)	KF13	Basalt	0	0	0	3.01	3.19	0.32	0.01	0.24	0	0	100.01
Feick (2014)	KF14	Basalt	0	0	0	2.48	5.21	0.32	0.01	0.05	0	0	100
Feick (2014)	KF15	Basalt	0	0	0	2.62	3.85	0.35	0.01	0.18	0	0	100
Feick (2014)	KF16	Basalt	0	1.09	0	3.31	3.76	0.39	0.01	0.53	0	0	100.01
Feick (2014)	KF17	Mafic Syenite	0	5.58	0	0.89	2.25	1	0.02	0.03	0	0	100.01
Feick (2014)	KF18	Basalt	7.34	0	0	2.6	1.7	0.33	0.01	0.05	0	0	100
Feick (2014)	KF19	Volcaniclastic	0	0	0	1.26	2.51	0.2	0.01	0.25	0	0	99.99
Feick (2014)	KF20	Volcaniclastic	0	0	0	1.39	3.52	0.18	0.01	0.84	0	0	99.99
DeAgazio (2012)	273501.00	Spotted Feldspar Porphyry	0	0	0	0.5	1.18	0.51	0	0	0	0	99.99
DeAgazio (2012)	273504.00	Syenite Porphyry	0	0	0	0.32	0.72	0.25	0	0	0	0	100
DeAgazio (2012)	273508.00	Syenite Porphyry	0.25	0	0	0.42	0.71	0.34	0	0	0	0	99.98
DeAgazio (2012)	273509.00	Mafic Syenite Porphyry	0	0	0	0.86	0.72	0.38	0	0	0	0	100

Table A-5 cont. Major oxide percents and calculated CIPW normative values for data from Feick (2015), DeAgazio (2012) and for select data from this study

Source	Sample ID	Lithology	Wollastonite	Olivine	Larnite	Ilmenite	Magnetite	Apatite	Zircon	Pyrite	Anhydrite	Na ₂ SO ₄	Total
DeAgazio (2012)	273511.00	Mafic Syenite	0	0	0	0.95	2.33	1.05	0	0	0	0	100
DeAgazio (2012)	273513.00	Mafic Syenite Porphyry	0	0	0	0.93	1.34	0.41	0	0	0	0	100
DeAgazio (2012)	273514.00	Syenite Porphyry	0	0	0	0.37	0.65	0.36	0	0	0	0	99.99
DeAgazio (2012)	273516.00	Tisdale Volcanic Tuff	0	0	0	1.25	2.37	0.58	0	0	0	0	100.01
DeAgazio (2012)	273518.00	Mafic Syenite	0	0	0	0.73	1.59	0.8	0	0	0	0	100.01
DeAgazio (2012)	273519.00	Mafic Syenite Porphyry	0	0	0	0.77	1.18	0.34	0	0	0	0	100
DeAgazio (2012)	273520.00	Syenite Porphyry	0	0	0	0.42	1.21	0.36	0	0	0	0	100.01
DeAgazio (2012)	273521.00	Tisdale Volcanic Tuff	0	0	0	1.2	1.65	0.59	0	0	0	0	100
DeAgazio (2012)	273522.00	Syenite Porphyry	0	0	0	0.52	0.62	0.35	0	0	0	0	100.02
DeAgazio (2012)	273527.00	Tisdale Volcanic Tuff	0	0	0	1.64	1.54	0.92	0	0	0	0	100
DeAgazio (2012)	273532.00	Tisdale Volcanic Tuff	0	0	0	1.32	1.92	0.58	0	0	0	0	100
DeAgazio (2012)	273533.00	Spotted Feldspar Porphyry	0	0	0	0.57	1.33	0.55	0	0	0	0	99.99
DeAgazio (2012)	273534.00	Mafic Syenite	0	0	0	0.87	2.13	0.99	0	0	0	0	100
DeAgazio (2012)	273538.00	Spotted Feldspar Porphyry	0	0	0	0.54	1.39	0.52	0	0	0	0	100
DeAgazio (2012)	273539.00	Spotted Feldspar Porphyry	0	0	0	0.52	1.25	0.53	0	0	0	0	100
DeAgazio (2012)	273542.00	Mafic Syenite	0	0	0	0.79	2.05	0.9	0	0	0	0	100
DeAgazio (2012)	273545.00	Mafic Syenite Porphyry	0	0	0	0.85	0.93	0.29	0	0	0	0	100
DeAgazio (2012)	273546.00	Tisdale Volcanic Tuff	0	0	0	0.92	1.35	0.43	0	0	0	0	100.01
DeAgazio	273551.00	Spotted Feldspar Porphyry	0	0	0	0.56	1.29	0.55	0	0	0	0	99.99

(2012)													
DeAgazio	273553.00	Mafic Syenite Porphyry	0	0	0	0.68	1.19	0.31	0	0	0	0	99.99
(2012)													

Table A-5 cont. Major oxide percents and calculated CIPW normative values for data from Feick (2015), DeAgazio (2012) and for select data from this study

Source	Sample ID	Lithology	Wollastonite	Olivine	Larnite	Ilmenite	Magnetite	Apatite	Zircon	Pyrite	Anhydrite	Na ₂ SO ₄	Total
DeAgazio (2012)	273555.00	Spotted Feldspar Porphyry	0	0	0	0.5	1.17	0.48	0	0	0	0	100
DeAgazio (2012)	273556.00	Mafic Syenite	0	0	0	0.53	0.81	0.47	0	0	0	0	99.99
DeAgazio (2012)	283557.00	Mafic Syenite Porphyry	0	0	0	0.51	0.79	0.46	0	0	0	0	100.02
DeAgazio (2012)	273558.00	Syenite Porphyry	0	0	0	0.46	0.55	0.39	0	0	0	0	100.01
DeAgazio (2012)	273559.00	Tisdale Volcanic Tuff	0	0	0	1.29	1.37	0.6	0	0	0	0	100
DeAgazio (2012)	15819.00	Unknown	0	0	0	0.82	3.68	0.23	0	0	0	0	100.01
DeAgazio (2012)	15822.00	Unknown	0	0	0	1.58	3.55	0.21	0	0	0	0	100.01
DeAgazio (2012)	15823.00	Unknown	0	0	0	1.57	3.23	0.25	0	0	0	0	100
DeAgazio (2012)	15824.00	Unknown	0	0	0	0.68	1.12	0.37	0	0	0	0	100
DeAgazio (2012)	JD12-51	Spotted Feldspar Porphyry	0	4.71	0	0.39	1.15	0.29	0	0	0	0	99.99
This Study	UWO_2015_2 0	Tisdale Cherty Sediments	0	0	0	0.93	1.49	0.23	0	0	0	1.38	100.01
This Study	UWO_2015_2 1	Tisdale Cherty Sediments	0	0	0	0.48	1.25	0.29	0	0	0	0.49	99.99
This Study	UWO_2015_2 2	Tisdale Greywacke	0	35.62	45.48	0.63	3.48	0.13	0	0	0	0.89	99.99
This Study	UWO_2015_2 3	Graphitic Sediments	0	0	0	0.55	6.73	0.33	0	0	0.41	28.16	99.99
This Study	UWO_2015_2 4	Cherty Sediments	0	0	0	0.8	0.69	0.31	0	0	10.98	-11.87	99.99
This Study	UWO_2015_2 5	Volcaniclastics	0	0	0	0.69	2.12	0.28	0	0	0	1.66	99.99
This Study	UWO_2015_2 6	Amphibole-rich Intrusive	0	0.49	0	0.79	1.64	0.94	0	0	0	0.17	99.99
This Study	UWO_2015_2 7	Microphyric Intrusive	0	0	0	1.01	1.19	0.48	0	0	0	0.4	100.01
This Study	UWO_2015_2 8	Microphyric Intrusive	0	0	0	0.94	1.4	0.45	0	0	0	1.02	99.99

This Study	UWO_2015_2 9	Volcaniclastics	0	2.03	0	1.38	2.68	0.22	0	0	0	4.39	99.99
------------	-----------------	-----------------	---	------	---	------	------	------	---	---	---	------	-------

Table A-5 cont. Major oxide percents and calculated CIPW normative values for data from Feick (2015), DeAgazio (2012) and for select data from this study

Source	Sample ID	Lithology	Wollastonite	Olivine	Larnite	Ilmenite	Magnetite	Apatite	Zircon	Pyrite	Anhydrite	Na ₂ SO ₄	Total
This Study	UWO_2015_3 0	Silty Arenite	0	0	0	0.69	1.65	0.81	0	0	0	0.33	100.01
This Study	UWO_2015_3 1	Cherty Sediments	0	0	0	0.24	0.16	0.16	0	0	0	0.04	100.01
This Study	UWO_2015_3 2	Cherty Sediments	1.8	0	0	0.65	0.76	0.26	0	0	0	0.26	100
This Study	UWO_2015_3 3	Conglomerate	2.06	0	0	1.25	1.99	0.18	0	0	0	4.17	99.99
This Study	UWO_2015_3 4	Breccia (200 Zone)	0	0	0	1.51	3	1.2	0	0	0	0.47	100
This Study	UWO_2015_3 5	Breccia (200 Zone)	0	0	0	1.72	2.04	0.67	0	0	0	0.21	99.99
This Study	UWO_2015_3 6	Breccia (200 Zone)	0	5.94	0	1.59	3.93	0.66	0	0	0	0.2	100
This Study	UWO_2015_3 7	Cherty Sediments	0	0	0	0.82	1.57	0.31	0	0	0	7.65	99.99
This Study	UWO_2015_3 8	Graphitic Sediments	0	0	0	0.41	9.84	0.21	0	0	0	0	100.01
This Study	UWO_2015_3 9	Conglomerate	0	0	0	0.72	1.01	0.28	0	0	0	5.95	99.99
This Study	UWO_2015_4 0	Conglomerate/ Cherty Sediments	0	0	0	0.77	0.78	0.31	0	0	0	2.47	100.01
This Study	UWO_2015_4 1	Brecciated Basalt	0	0	0	1.03	2.76	0.14	0	0	0	0.75	100
This Study	UWO_2015_4 2	Breccia (Mafic Syenite) 1	0	3.34	0	1.37	1.01	0.69	0	0	0	0.23	100
This Study	UWO_2015_4 3	Breccia (Mafic Syenite) 2	0	5.62	0	1.32	2.47	0.62	0	0	0	3.55	100
This Study	UWO_2015_4 4	Breccia (Mafic Syenite) 3	0	12.65	0	1.3	4.07	0.62	0	0	0	0.06	100
This Study	UWO_2015_4 5	Breccia (Mafic Syenite Porphyry) 1	0	0.61	0	0.84	2.35	1.05	0	0	0	0.94	100
This Study	UWO_2015_4 6	Breccia (Mafic Syenite Porphyry) 2	0	5.95	0	1.52	3.94	0.2	0	0	0	0.26	99.99
This Study	UWO_2015_4 7	Breccia (Mafic Syenite Porphyry) 3	0	0	0	1.42	3.77	0.23	0	0	0	2.85	100
This Study	UWO_2015_4 8	Biotite-rich Intrusive	0	16.77	0	0.63	2.38	1.48	0	0	0	0.1	100
This Study	UWO_2015_4	Conglomerate	0	0	0	1.3	2.46	0.22	0	0	0	3.27	100.1

Appendix G: APS Standard Operating Procedures

**Advanced Photon Source Standard Operating Procedure for Beamline 20 I-D
for this Project**

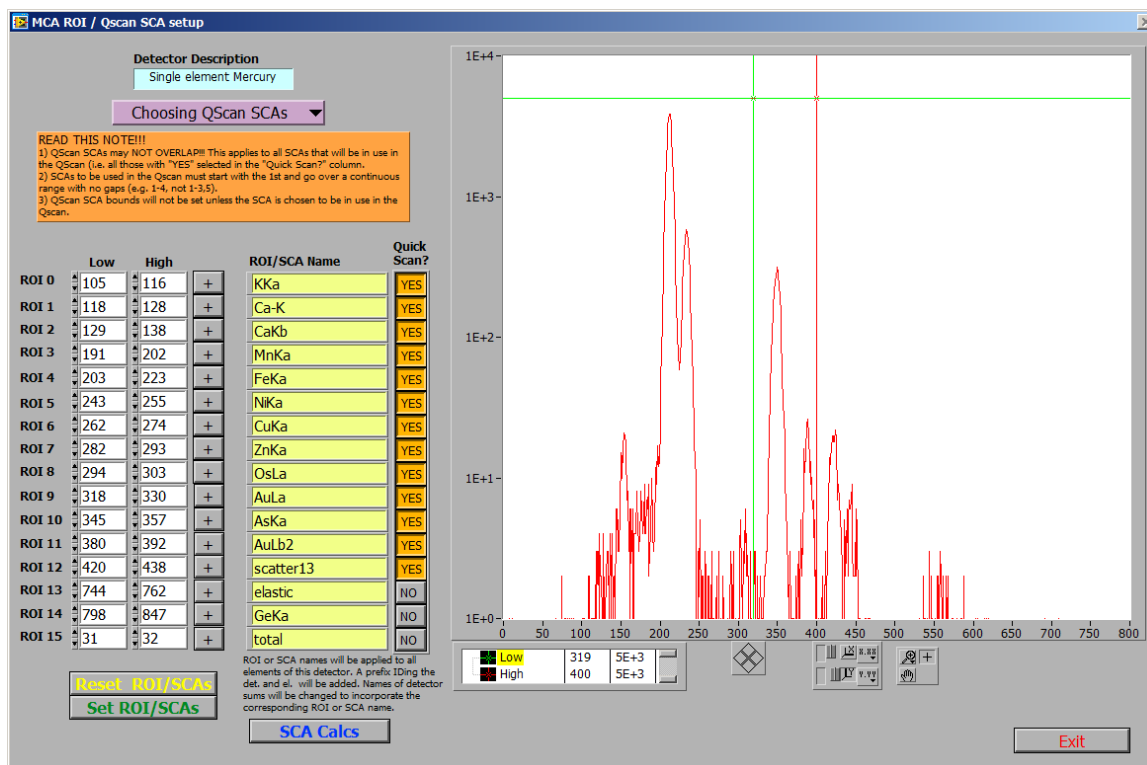
Prior to Arrival and Experiment Setup

Prior to arriving at the beam,

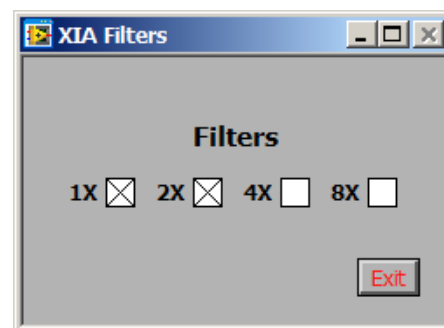
- Take pictures of your samples. Pictures should include
 - A photo of the thin section with the grains of interest circled and labeled accordingly. Circles should not be redrawn or changed after pictures are printed
 - A number of photos getting progressively closer to the grains of interest so that the grains are very easy to find.
 - If possible have both microscope photos as well as reflective light photos and label the grains if any further analysis has been done on them and the composition is known
 - A list of the thin sections and areas you would like to get a scan of in order of priority
 - All your online training complete

Setting up your samples

- Record the approximate numbers for the PreSlip, PreKB_IO, mini-IO, BPM Sum for (horizontal and vertical) after the technician adjusts the numbers for your samples. If you notice the numbers change drastically then consult your technician
- On the MCA Display v12 you must enter all of the ROIs that you are interested in collecting along with their appropriate photon energy ranges. Ensure that the energies don't overlap each other
 - The ROIs and their regions will need to be changed on both the MCA ROIs and the QScan SCA ROIs Tabs



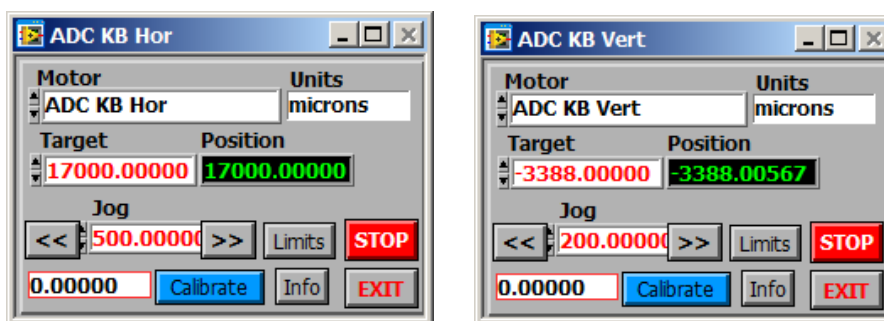
- When loading your first sample onto the sample holder, make sure that you are aware of the limitations going horizontally and vertically. This will help so you don't end up getting part of the way through your scan sequence and then you realize that your other sample is too far away
- Adjust the ADC focus by first removing all filters. Look for mineral grain boundaries and to get them as sharp as possible. The beam should appear as a bright light in roughly the middle of the computer screen. Adjust ADC KB Focus accordingly (beginning with a jog of about 50 and moving down to 10 for finer adjustments) until satisfied. Ensure that you put all filters back on prior to running any scans or you may oversaturate the motor and any tests completed after may not complete properly
- When adding or removing filters, remember that if you have the 1X and 2X checked off, the total is 3X. If you wanted to increase the filters in this case, you must uncheck the 1X and 2X and check off the 4X. Increase filter amounts until MCA counts are within range.
- To set up the motors, choose a location between two grains or in the center of a grain. Set the fine motors to zero (the motor will move) and use the coarse motors to move to the midpoint between two grains/ samples or the center of the grain. Record the coarse motor setting. Record X_1Y_1 and X_2Y_2 for the area of interest



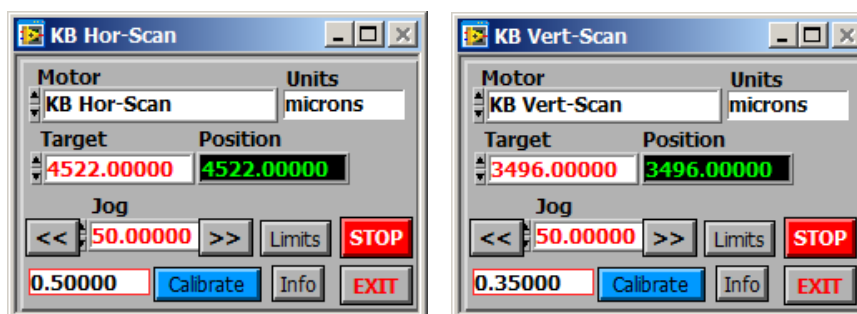
- Make sure the Mono Control target eV is correct. When changing the beam energy, always wait until the Energy Position is roughly settled and close to the target eV
- Before you run any coarse scans you must do a few MCAs (no need to save them) to make sure counts are below 100,000. Move the motor over the most mineralized sections of the area(s) of interest to check for variation
 - Check to see what the values for PreKB_I0 are to ensure that the number of filters is appropriate for your sample. The value of PreKB should be just under 1
- Before beginning a sequence or scan make sure your coarse motors are set to the correct position

Setting up the location of your scans

Find locations of scans by using the fine/coarse motors. Also known as ADC KB (coarse)/KB (fine). Coarse Motors:

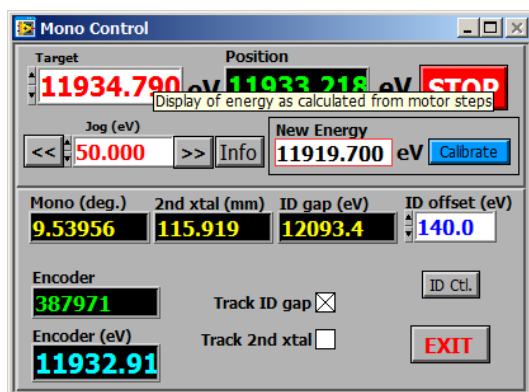


Fine Motors:



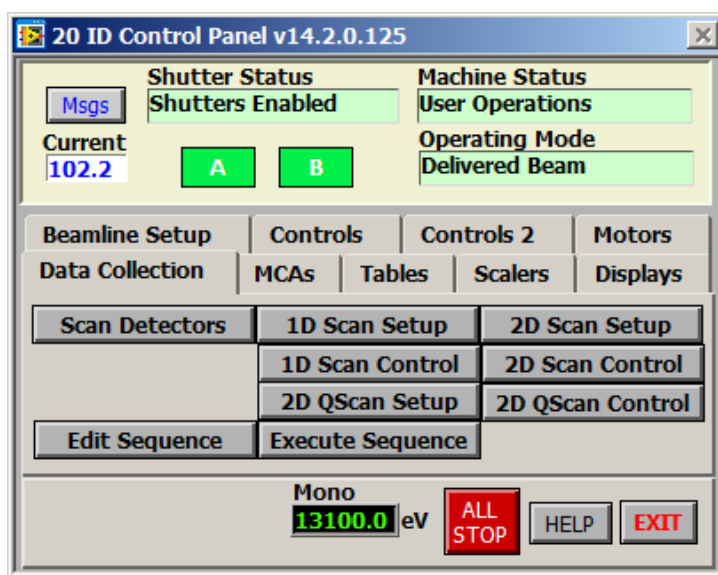
Beam width

Ensure that your beam width is appropriate for the tests you are running. Beam width is the energy that you want to run scans at. It can be viewed in the “Mono Control” dialogue box. For samples in this thesis, the beam was largely at 13.1 KeV or 31.1 KeV.

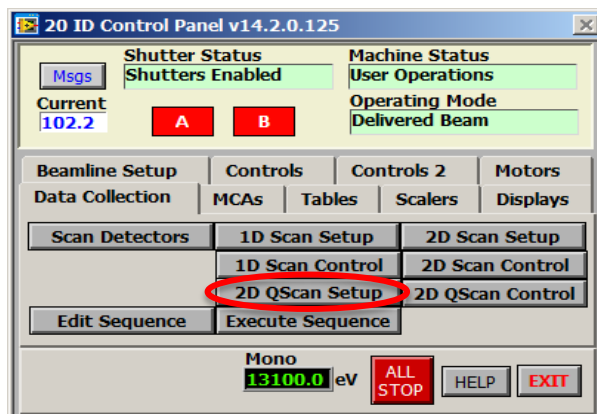


Additional Panels of Interest:

Main Control Panel



2D QSCAN Scan Maps (Fine and Coarse)



Set up For Fine Maps

Enter the fine motor location (double check that your coarse motors are set to the appropriate area). Open the 2-D Quick Scan Setup dialogue box. Enter desired step size. For coarse maps we used a step size of 20, and for fine maps we used a step size of 2. Note: if you zero out the number of points then enter your start and end coordinates as well as desired step size it will prevent the computer from adjusting your numbers. Enter desired integration time / pt. For coarse maps we used 100msec, while for fine maps we used 400msec. Make sure bi-directional scanning is on and that the positioner Mode is set to absolute. Record all entered numbers in your notes for reference later.

2-D Quick Scan Setup

Lead (Scanning) Dimension - "X"

Number of Pts: 121

Positioner: KB Hor-Scan

Start: -1730.000

End: -1490.000

Step Size: 2.000000 microns

Positioner Mode: Absolute

NOTE: Selection of this motor is not arbitrary. Beamline hardware has to be set up to use a particular motor.

2nd Dimension - "Y"

Number of Pts: 161

Positioner: KB Vert-Scan

Start: -90.000000

End: 230.000000

Step Size: 2.000000 microns

Positioner Mode: Absolute

NOTE: When new scan parameters are entered, other parameters will be adjusted to make sure scan steps are integral multiples of the motor resolution. Integration time will also be adjusted to make sure the resulting speed of the X motor is within the minimum and maximum speed limits. Click the info button to get info about the selected motor.

Integration Time / pt: 400 msec

Estimated Scan Time: 2 Hrs 9 Min 52 Sec

(Doesn't include time to move Y positioner)

After Scan: Return to previous position

Use Bi-directional Scanning:

Buttons: Restore & Apply, Apply & Save, Select Detectors

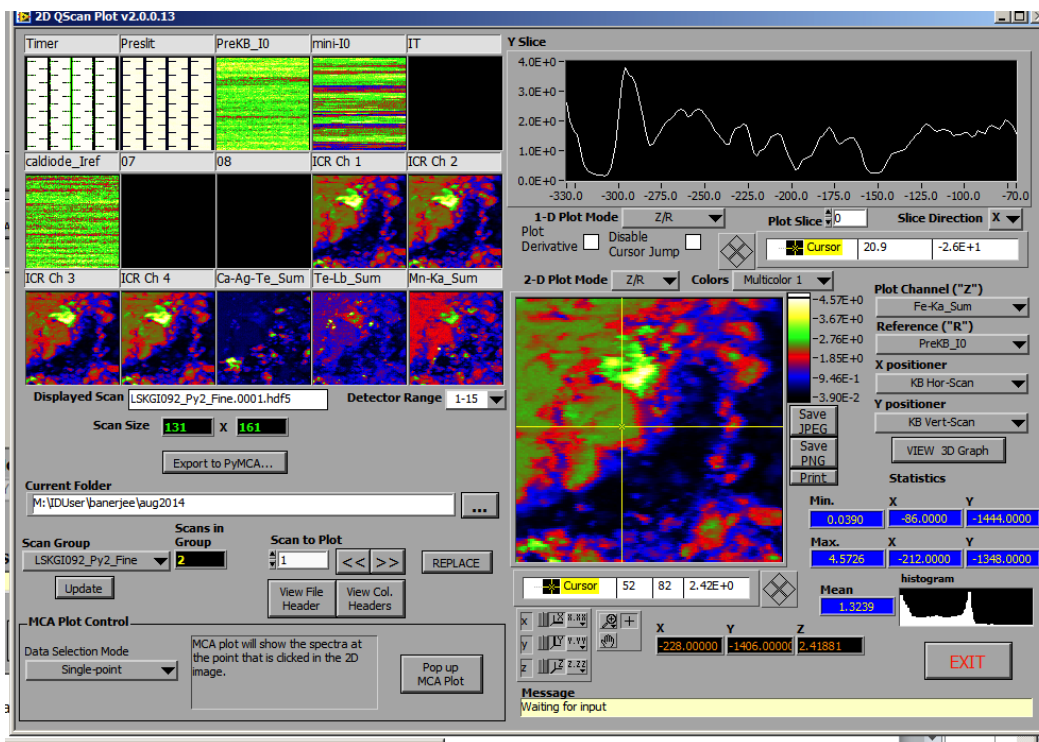
Qscanning MCA: xMap 4 element

Configure SCAs in the MCA ROI/SCA setup

Buttons: Apply, EXIT, Set up sums...

Finished Map

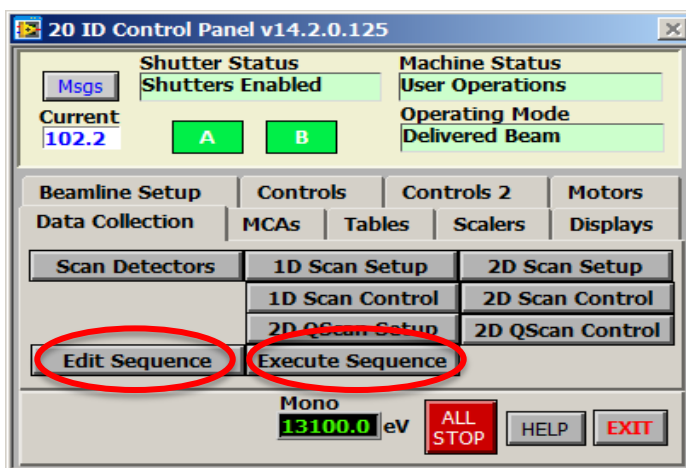
The most recently run map can be seen on the computer that you set the scan up on, while any maps that you ran prior to the most recent map can be seen on the adjacent computer. Adjust the plot channel to see the distribution of the different elements

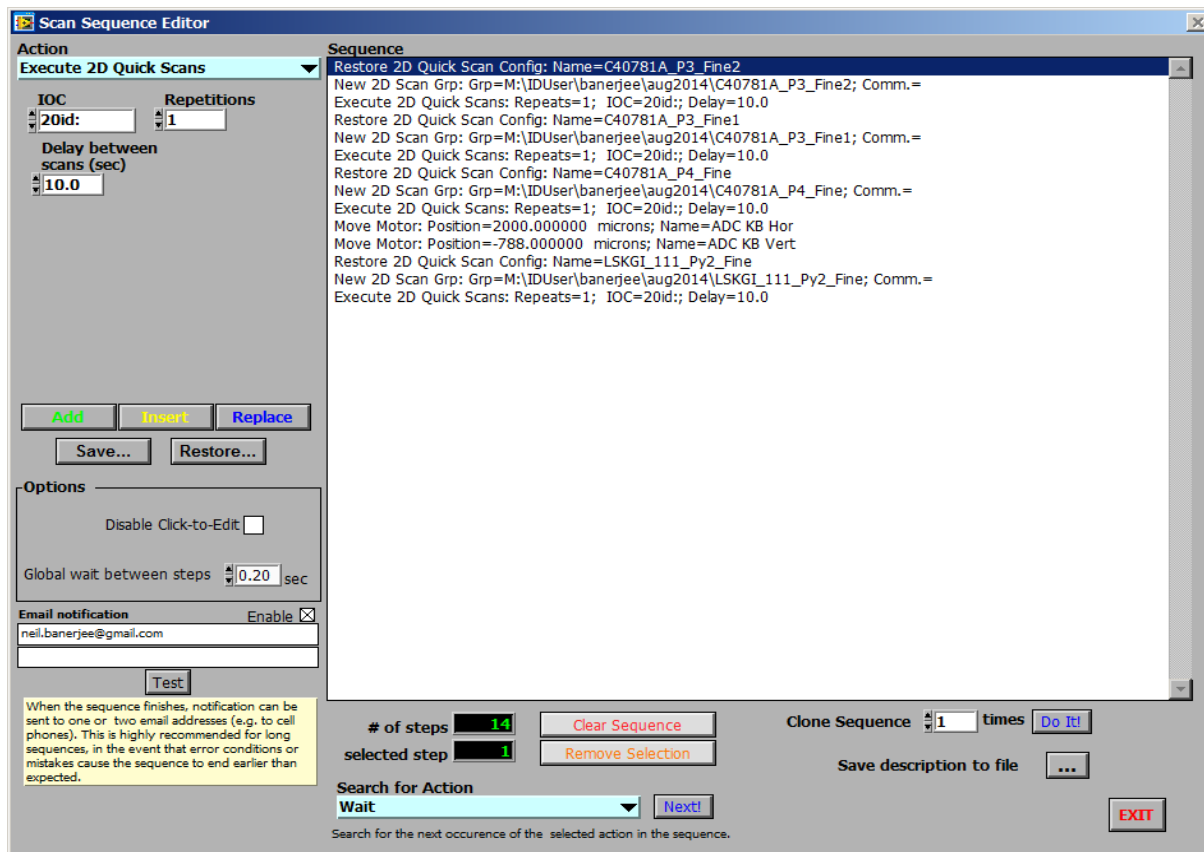


Note- if you run multiple scans under the same name, “scans in group” will be a number above 1, and you can use the arrows to the right under the “Scans to plot” title to switch the map you’re viewing (just press replace)

Running Multiple Scans

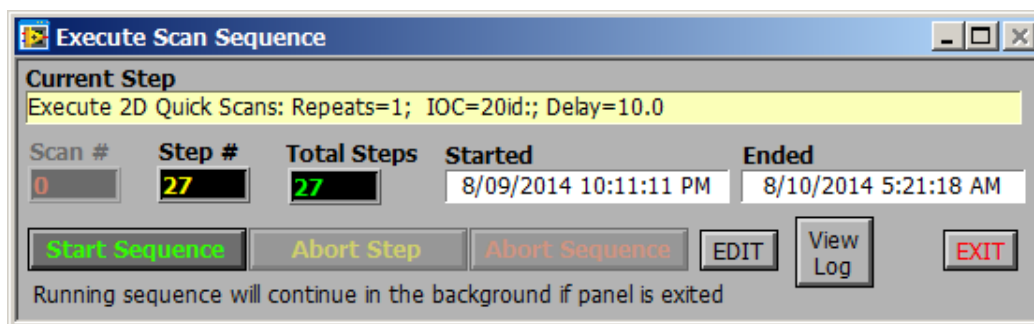
In the 20 ID Control Panel, Go to “edit sequence”. Follow the screenshot below for the proper experimental setup. Remember to always start with “restore” and end with “execute”.





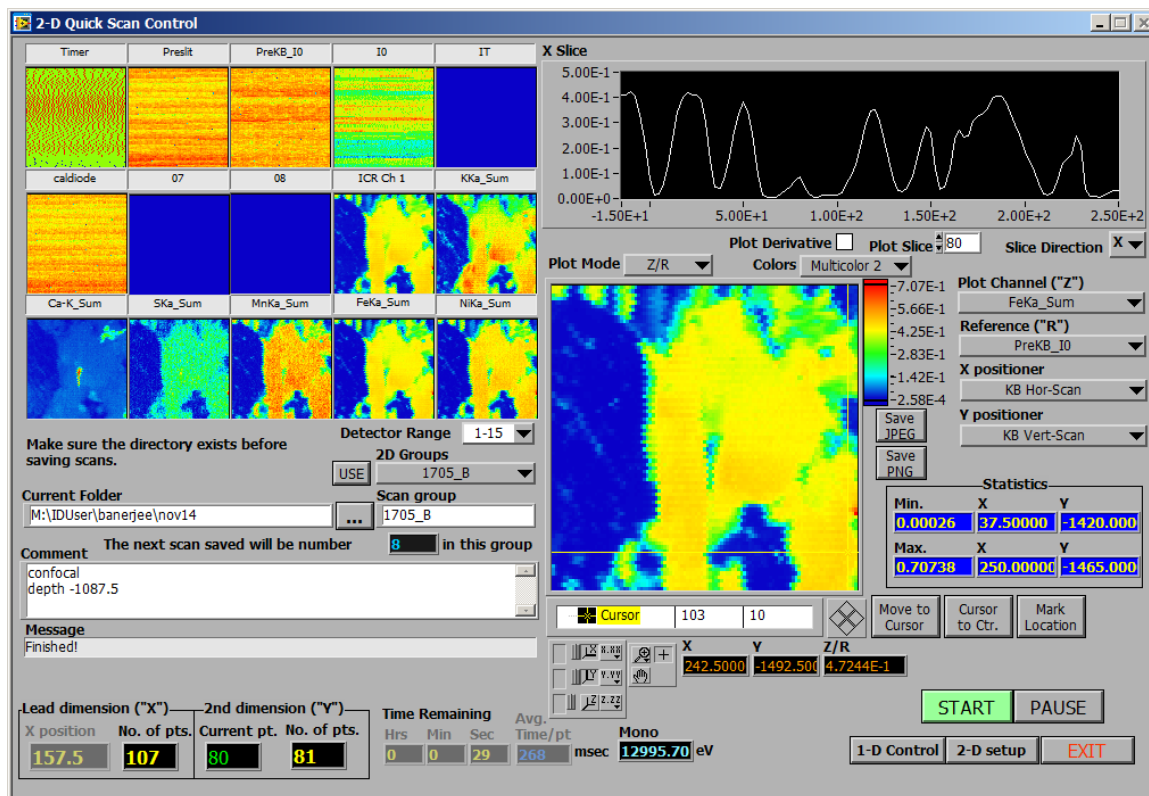
Note: Enabling email notification is a great feature to use for receiving an email when sequence is complete.

When finished set up, go to “Execute Sequence” on the main control panel, as shown below. Do not be alarmed if the Total Steps do not correlate with the number of steps on the Editor screen, this will update once you start the sequence



MCA ROI Scanning Instructions

MCA ROIs are typically completed after coarse or fine scans are complete. Mini quick maps may need to be completed to ensure that the beam is exactly where you expect it to be. The main computer must be used to run MCA scans (MCA Display v12 screen). Use the mouse to click on an area of interest on the 2D quick scan window, and select “Move to cursor” to move the beam to the spot of interest.

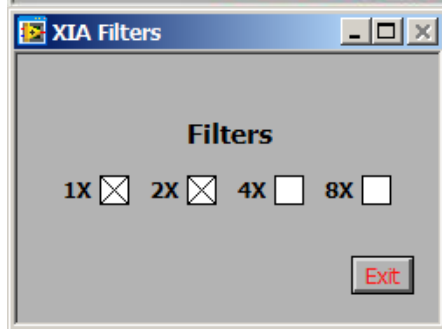
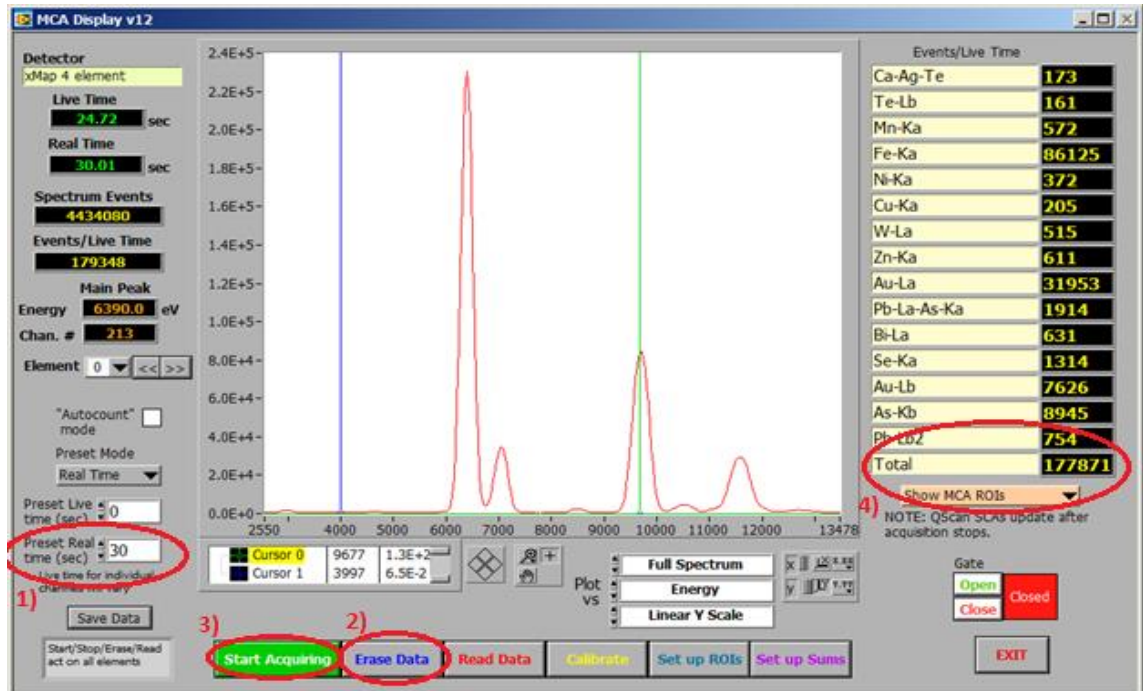


Open the MCA display v12 window from the main control panel.

Once the spot is chosen, a quick scan can be done to check the total counts by setting the Preset Real time (sec) to 5. Click “Erase Data” to clear remaining data from memory (screen won’t change but data is being erased). Click “Start Acquiring” to begin quick scan. The total counts must be monitored. ****Counts must be under 200 000**** (ideally around 100,000)

If counts are within range, the Preset Real time can be increased to 30 seconds for a full MCA scan.

If counts are not within range, filters must be added to lower the counts. (See screenshot of XIA Filters)

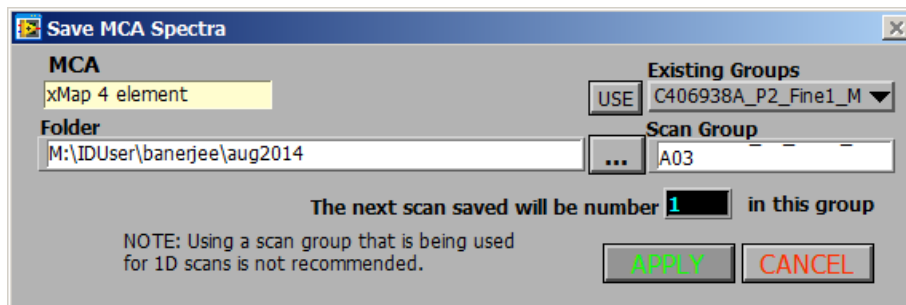


When adding or removing filters, remember that if you have the 1X and 2X checked off, the total is 3X. If you wanted to increase the filters in this case, you must uncheck the 1X and 2X and check off the 4X. Increase filter amounts until MCA counts are within range.

After scan has been run at 30 sec, save the data. Press the save data button located in the bottom

left corner of the MCA display screen.

To save the data, make sure the folder is the correct one that you would like to save your file to and that the “existing groups” title is the correct name of the current scan/slide. If you’re doing multiple scans to the same group (eg. Two separate areas on the same fine scan) then you will need to adjust the “Scan Group” and label accordingly.



Appendix H: GeoPIXE Standard Operating Procedures

Geopixe Standard Operating Procedure

Processing of synchrotron X-ray fluorescence data is a dynamic and iterative process that involves correcting images to account for chemical concentration gradients, differential absorption effects, and pileup effects (Ryan et al., 2015). Data processing for this project was achieved using GeoPIXE, a well-established software designed for quantitative particle induced X-ray emission (PIXE) and synchrotron X-ray fluorescence (SXRF) trace element imaging and analysis (Pallon et al., 2009; Cohen et al., 2015; Ryan et al., 2015). GeoPIXE automatically accounts for significant non-linear distortion of spectra and provides support for image generation, analysis, and validation (Woll, 2014). GeoPIXE has built-in routines for data corrections, as described by Pallon et al., (2009), and briefly summarized here.

GeoPIXE has built-in routines for data corrections, as described by Pallon et al., (2009), and briefly summarized here. Raw data begins starts as an event-file with coordinates and detector events sorted into a “master spectra”. The spectrum is selected, calibrated, and stored. It must also be “cut” so that the energy range spans all transmitted events without including background noise. The event data is then used to produce an energy map to assist with the next stages of data processing. The event-file is stored using the dynamic analysis (DA) projection for spectral deconvolution, which allows for new PIXE spectra and image reconstruction from event data (Ryan et al., 2015). New PIXE spectra can then be fitted and stored.

Routine data analysis workflow for this project followed five main steps: (1) energy and charge calibration; (2) spectrum fitting, yields calculation (which takes into account experiment geometry, detector information, and sample information), and individualized DA matrix generation for each sample; (3) production of energy concentration images; (4) image validation; and (5) qualitative and quantitative image analysis.

Element identification works by using the synchrotron-sourced hard x-rays to excite electrons on the surface of samples and measuring the full-spectrum emitted (i.e., the wavelengths and relative emission strengths of energy released by test materials) (Buffiere and Baruchel, 2015). It is based on the characteristic secondary x-ray energy released when individual atoms of different elements are excited by an external energy source (Rollinson, 1993).

Prior to and During Data Collection

Decide what energy to scan samples

Use the characteristic K and L edge excitation energies to determine what energy to perform scans at. To get Au we typically performed scans at 13.1 KeV just above the Au L edge. However, to collect information about other elements of interest such as Mo and Ag, which have higher excitation energies, we also performed scans at 31 KeV.

Plan ahead of time how to get the maximum amount of useful data effectively given strict time constraints

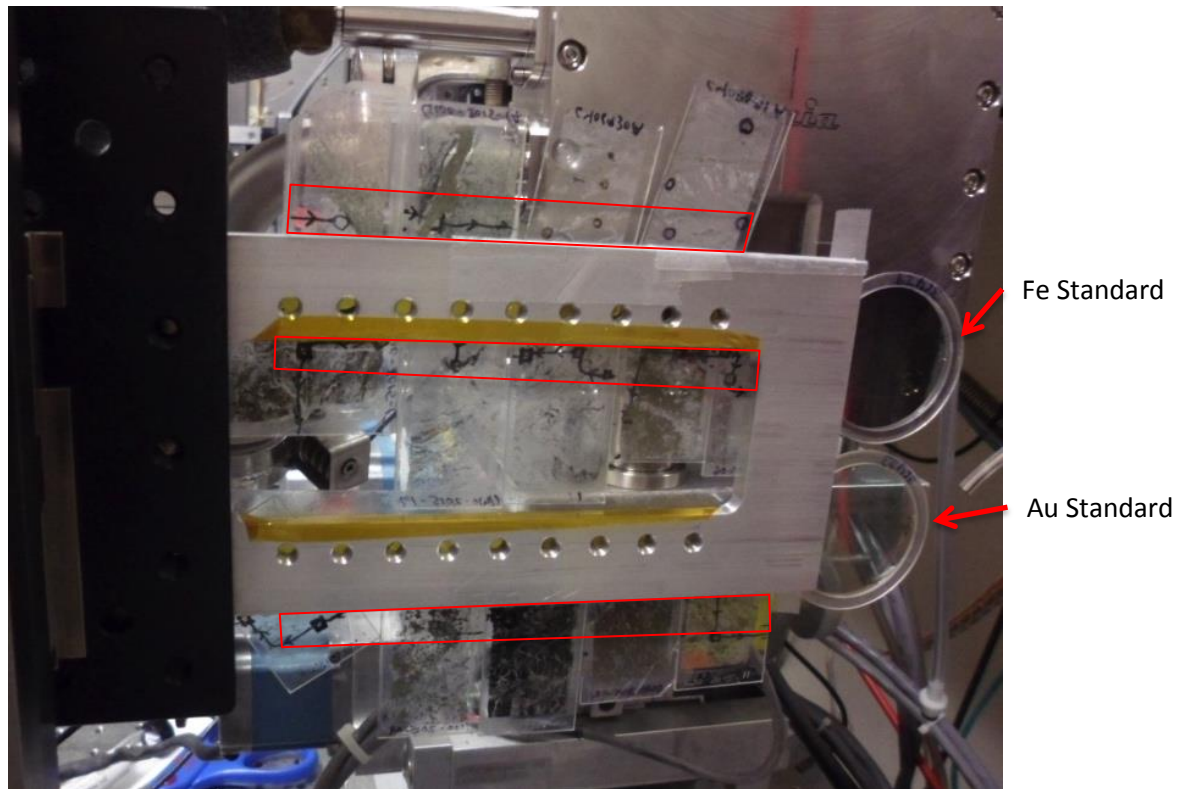
Circle the specific areas of interest either using a hand lens or microscope prior to data collection using a thin marker such as a sharpie or a dry erase marker. This ensures that areas of interest can be found quickly.



At Cornell data can be collected fastest in the x direction, while data collection in the y direction takes more time. Try to set up your samples in a way that takes advantage of the fast horizontal data collection time. Take measurements of your thin sections so that you know how far in the x and y direction you need to go to collect the data you need.

At this time only one scan can be run. You have to come in to set up all additional scans so it's a really good idea to choose a reference point (such as the bottom or top corner of the rock master) that can easily be found and then know from that reference point what you need to enter to run the scans you need to run.

In the picture below the Rock Master 3000 was used to mount 14 samples at the same time for analysis. Sample areas were approximately 20cm x 1cm. The bottom right edge of the Rock Master was used as a reference point when setting up maps. The bottom map was at [(reference point x)+1cm], [(reference point y)-1cm].



Collect data for appropriate standards

This is essential for performing charge calibrations and flux calibrations when processing data so that quantitative data can be extracted from the spectra.

Keep a chart in your notes with the following information for standards:

Run Number	Date	Energy	Scan Name	Scan Number	Step size	Dwell time	Serial Number	Concentration and material
9614	Nov 17, 2015	13.1KeV	Au_Cal	1	0.02x0.02 microns	10	36433	19.2 on 6.3 um mylar
9615	Nov 17, 2015	13.1KeV	Fe_Cal	1	0.02x0.02 microns	10	26429	18.3 on 6.3 um mylar

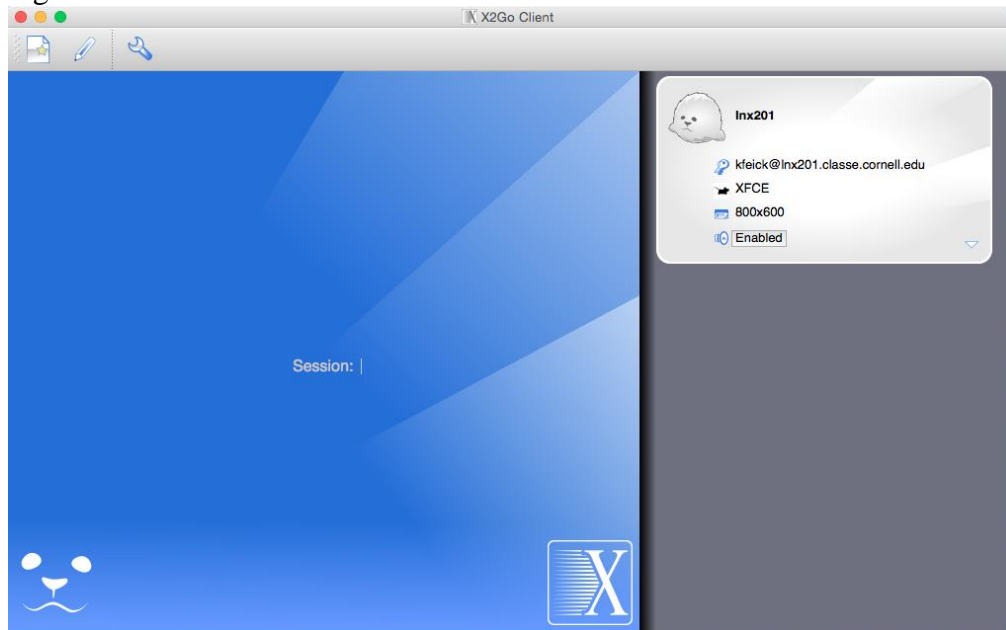
Take note of the following information for each Scan:

- Sensitivity
- Channel
- Units
- Dwell
- Conversion Factor

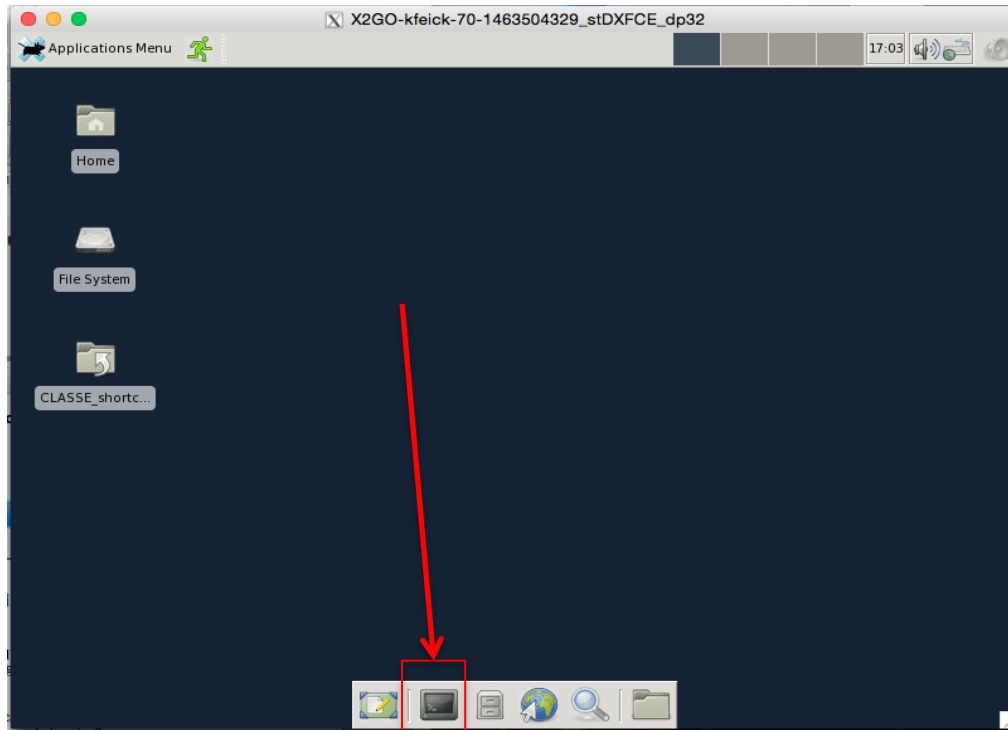
Logging on to GeoPixe

Download and open the appropriate software (x2goclient and xquartz)

A new window should open. In the top right corner you can click on the user name to log in



Use the XFCE Connection and your assigned username and password to login. Once logged in, press the terminal button at the bottom of the screen, as shown below.



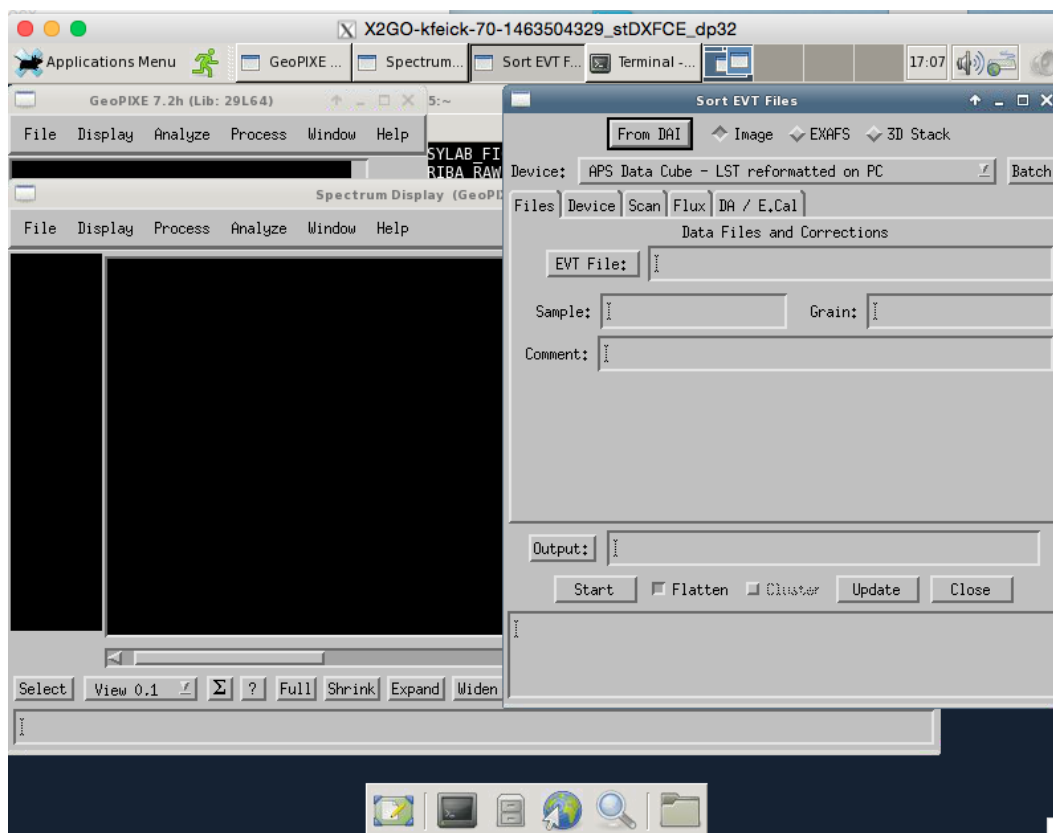
When the terminal opens type “qint” to connect directly to a Cornell computer then press enter. It may ask you to enter your password, if so, do that and press enter again. A few lines of text will follow as the computer processes your command.

```

Terminal - kfeick@lnx335:~
File Edit View Terminal Go Help
[kfeick@lnx201 ~]$ qint
Password for kfeick@CLASSE.CORNELL.EDU:
Warning: Permanently added '[lnx335.lns.cornell.edu]:58537,[172.16.5.135]:58537'
(RSA) to the list of known hosts.
Please login using your CLASSE credentials.
Last login: Mon Mar 14 09:03:22 2016 from lnx201.classe.cornell.edu
*****
This is a 64-bit SL6 system. Please be conscious of what
architecture and OS you are compiling for.

Please see the following for information on 64-bit computing
and Scientific Linux 6.
https://wiki.classe.cornell.edu/Computing/ScientificLinux6
https://wiki.classe.cornell.edu/Computing/Lnx64Bit
*****
[kfeick@lnx335 ~]$ █
  
```


Next type “geopixe and” to start the program (if you get an error then make sure you typed it correctly). Press enter



Your main windows include the following:

- Sort EVT Files – for entering parameters to create new images
- Spectrum Display – for viewing the spectrums associated with each map
- GeoPIXE – for viewing images that you create

Charge Calibration

Dynamic analysis generally includes the fitting of K, L, and M characteristic X-ray lines to a background and the use of primary fitted $K\alpha$, $L\alpha$, or $M\alpha$ line area to determine the elemental concentration (Cohen et al., 2015). Characteristic energies emitted by select trace elements are presented in Table 21, below

Table 3. Characteristic emission lines of select trace elements. Energies highlighted in red were measured during data acquisition at 13.1 KeV, while energies highlighted in blue were measured during data acquisition at higher energies. Energies from “X-ray Data Booklet”

Element	K α 1	K α 2	K β 1	L α 1	L α 2	L β 1	L β 2	L γ 1	M α 1
22 Ti	4,510.84	4,504.86	4,931.81	452.20	452.20	458.40			
23 V	4,952.20	4,944.64	5,427.29	511.3	511.3	519.2			
24 Cr	5,414.72	5,405.51	5,946.71	572.8	572.8	582.8			
25 Mn	5,898.75	5,887.69	6,490.45	637.4	637.4	648.8			
26 Fe	6,403.84	6,390.84	7,057.98	705	705	718.5			
27 Co	6,930.32	6,915.30	7,649.43	776.2	776.2	791.4			
28 Ni	7,478.15	7,460.89	8,264.66	851.5	851.5	868.8			
29 Cu	8,047.78	8,027.83	8,905.29	929.7	929.7	949.8			
30 Zn	8,638.86	8,615.78	9,572.00	1,011.70	1,011.70	1,034.70			
33 As	10,543.72	10,507.99	11,726.20	1,282.00	1,282.00	1,317.00			
42 Mo	17,497.34	17,374.30	19,608.30	2,293.16	2,289.85	2,394.81	2,518.30	2,623.50	
47 Ag	22,162.92	21,990.30	24,942.40	2,984.31	2,978.21	3,150.94	3,347.81	3,519.59	
52 Te	27,472.30	27,201.70	30,995.70	3,769.33	3,758.80	4,029.58	4,301.70	4,570.90	
78 Pt	66,832	65,112	75,748	9,442.30	9,361.80	11,070.70	11,250.50	12,942.00	2,050.50
79 Au	68,803.70	66,989.50	77,984	9,713.30	9,628.00	11,442.30	11,584.70	13,381.70	2,122.90
80 Hg	70,819	68,895	80,253	9,988.80	9,897.60	11,822.60	11,924.10	13,830.10	2,195.30
82 Pb	74,969.40	72,804.20	84,936.60	10,551.50	10,449.50	12,613.70	12,622.60	14,764.40	2,345.50
83 Bi	77,107.90	74,814.80	87,343	10,838.80	10,730.91	13,023.50	12,979.90	15,247.70	2,422.60
92 U	98,439	94,665	111,300	13,614.70	13,438.80	17,220.00	16,428.30	20,167.10	3,170.80

An example of full-spectrum data is provided below. The figure includes full spectrum data for the entire region analyzed, as well as for sub regions (as identified). Key characteristic energy lines for elements in the sample have also been identified

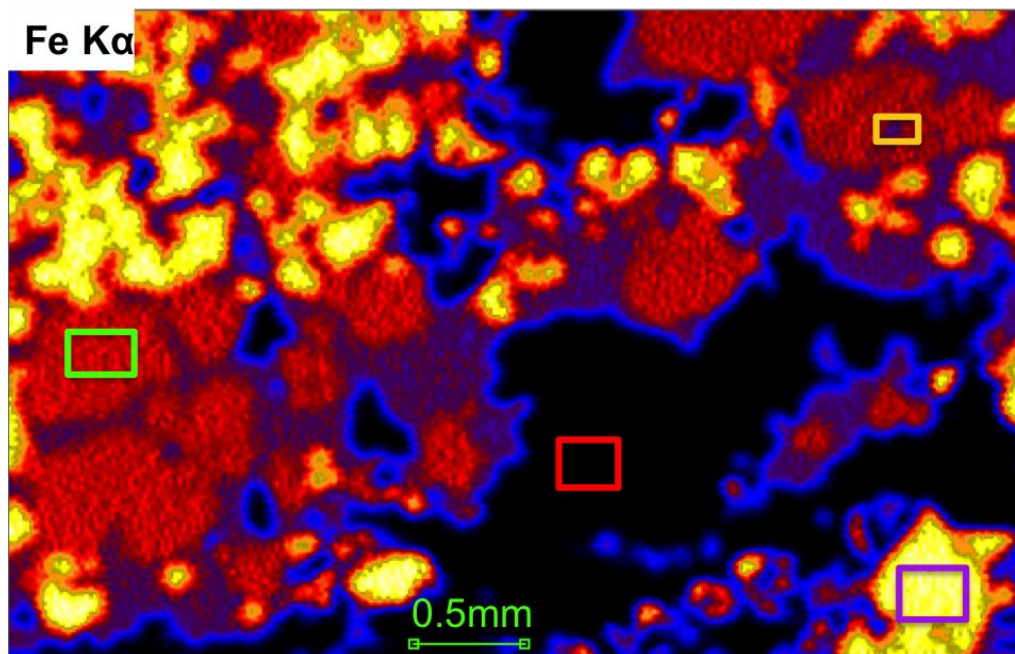
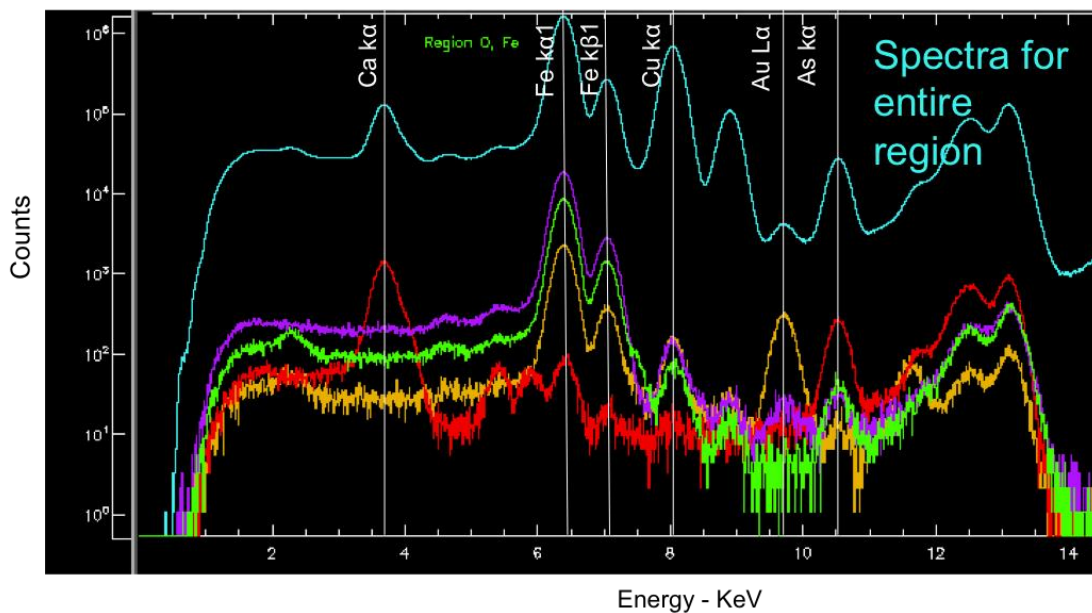
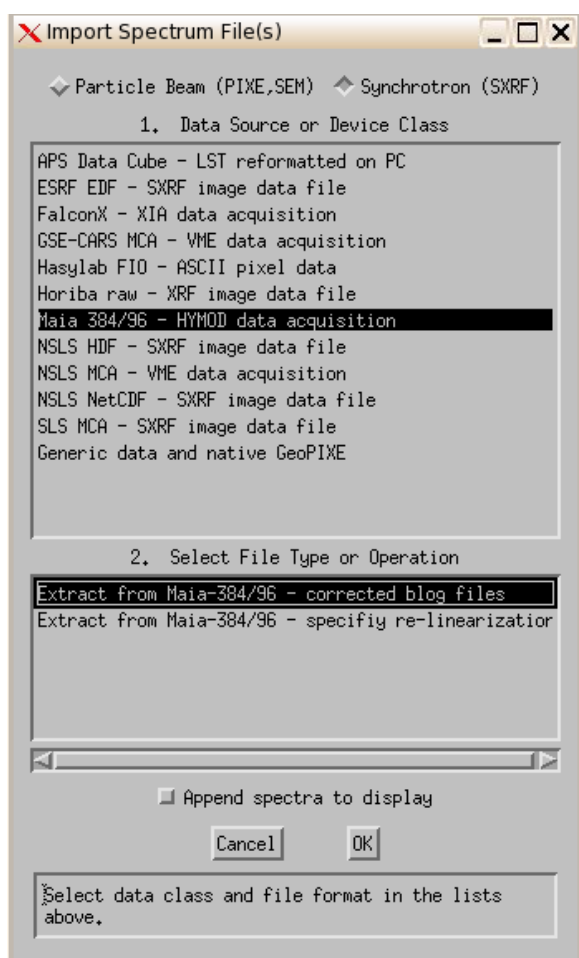


Figure A-H1. (Top) Example of full XRF spectrum data obtained at CHESS including select identified peaks that correspond to elements of interest in the sample for the entire region as well as for sub-regions (as colour coded). (Bottom) Fe $K\alpha$ energy map showing regions of interest included in the spectrum above.

Calculating the Charge Calibration

A charge calibration is a conversion factor that is typically close to $1\text{E-}9$. To perform a charge calibration first import the spectra from a calibration foil using the Spectrum Display window. To do this, under the “File” drop down menu, select Import → spectra. You will be prompted for additional information about the scan. Select the following:

- Synchrotron (SXRF)
- Data Source or Device Class: Maia 384/96-HYMOD data acquisition
- File Type or Operation: Extract from Maia-384/96 – corrected blog files
- Select “Ok”



Select the file or range of files that were run for the calibration standard. At 13.1 KeV we ran both Au and Fe calibration standards, while at 30.1 KeV we ran a Bi calibration standard. Select an appropriate output path and name it accordingly. Once the file has loaded, in the “window” dropdown select “Spectrum Select”. Once the dialogue box opens, press “Delete all: XY and T”. Back in the spectrum display window, from the “process” drop down menu, select “Add (re-map cal)”. Save the new spectrum.

In the Spectrum Display window, from the “Process” dropdown menu, select “Get all energy calcs” and navigate to load a recent energy-calibrated spectrum with similar counts to the one you want to calibrate your samples to.

Open the X-ray spectrum fit window by selecting it from the “window” dropdown menu in spectrum display. Load a recent calibration .pcm file by pressing “load” at the top of the window beside Set-up. Typically these are stored in the setup directory and are titled something like “rock-13.1 keV.pcm”. Any file will fit, you will change the important parameters.

In the X-ray spectrum fit window load a yield file. Typically, foils work best. To do this, press “new” beside where it says “Yields:” and select the appropriate foil. Once the file has been loaded, change the beam energy to the energy the scan was run at and any other appropriate parameters. Make sure you enter the appropriate density for the scan you completed. The yields file will be used to determine what “100%” of your sample means. Save the new yields file.

In the spectrum display window, use the view cursors to isolate the region of interest. Use “fit one” to check the fit. Adjust the elements that have been fit until you are satisfied. In the X-ray spectrum fit window make sure that you’re using the appropriate filter. For a foil 1.5mm away from the detector the filter should be 5mm of air + 6.5 um Mylar. Once you are happy with the results, under the “window” drop down menu select “fit results”. Load the most recent fit and write down the concentration of the foil element in ng/cm². This number is your “C fit”. In the X-ray spectrum window, record the number that shows up in the “Q” box.

Perform the following calculation = $\frac{C_{Fit}}{C_{Foil}} * Q$ (note – C Foil is the concentration of your foil element). Now replace the Q value in the X-ray spectrum fit window with the calculated value and redo the fit. In the fit results window your foil element should now show up with the proper concentration (C Foil).

In the X-ray spectrum fit window press “?” by the Q button. Record the number in the upper right box, which should be on the order of 1 E-9. This is the new flux conversion factor. Write it down and use it for the flux/ Q conversion factor in the Sort EVT window and the Flux PV window when it comes up.

Loading a new Spectrum File

In the Spectrum display window select File → Import → spectra. You will be prompted for additional information about the scan. Select the following:

- Synchrotron (SXRF)
- Data Source or Device Class: Maia 384/96-HYMOD data acquisition
- File Type or Operation: Extract from Maia-384/96 – corrected blog files
- Select “Ok”

Next, navigate to the appropriate files and press “open”. This will bring up the Flux PV Select window. Use “Indirect using Ion Chamber (Synchrotron, with PV)” and then enter the appropriate information for the scan. Press “ok”. Use the conversion factor that you calculated previously.

Flux PV Select

Beam Flux / Charge Set-up

Indirect using Ion Chamber (Synchrotron, with PV)

Ion Chamber Parameters

IC Scaler channel: Maia:scaler,FC0

Preamp Sensitivity: 500.

Preamp Scale Units: pA/V

Dwell time (ms): 4.

Scan data for PVs Conversion (Q/IC): 1.1e-9

Maia Option Parameters

Off

DT cal A: 33.4 B: 0.

Slowest motor axis (for YLUT): 1

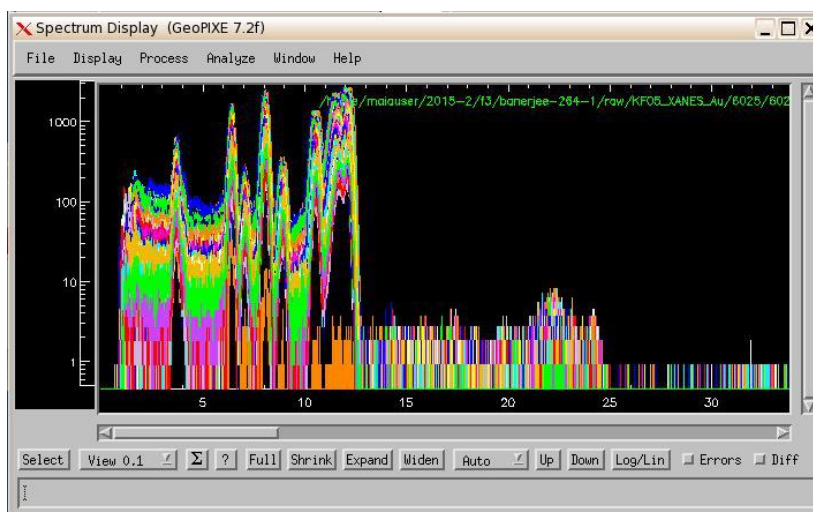
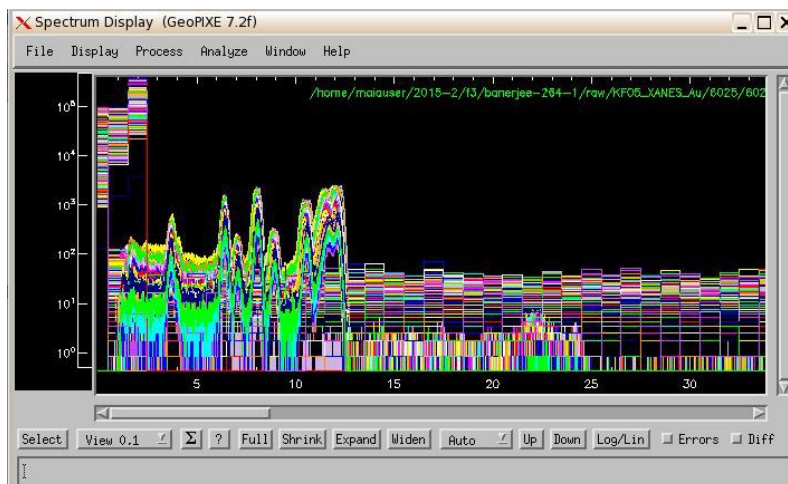
Select Motor Axis Indices for XYZ

X axis: 0 Y axis: 1 Z axis: 2

Clear Axis Border X: 1 Y: 0 Z: 2

From: SPEC DAI Cluster OK

Once the file has loaded, in the “window” dropdown list select “Spectrum Select”. Once the dialogue box opens, press “Delete all: XY and T”



Spectrum Fitting and Yield Calculations (Loading and modifying a DA Matrix)

Yield Calculation

In the X-ray Spectrum Fit window, beside where it says “yields” press the “New” button to bring up the PIXE/SXRF Yield Calculation window.

In the new PIXE/SXRF Yield Calculation window, press “load” to load an appropriate pre-existing yield calibration file. These are typically stored in the setup folder. Change the appropriate parameters (the title, the energy the scan was run at, geometric parameters (theta should be 180 and phi should be 0 unless these parameters were changed for the experiment), Thin sections typically have a thickness of 30 microns and a density of 3. The formula that was entered for this experiment was $(\text{SiO}_2)_{70}(\text{FeO})_{20}(\text{Al}_2\text{O}_3)_{10}$. Save the adjusted parameters using the “Save” button at the top of the screen. Press “Calculate Yields” at the bottom of the

window. Save the new yield calculation using an appropriate name. Press “exit” to close the window.

PIXE/SXRF Yield Calculation

Set-up: ee-264-2/setup/rock-7-177keV-10mm.lc Load Save

Title: rock, 7.177 keV

Beam Particle
 Photons (mono) Z: 0 A: 0
 Energy: 7.177 Charge: 1.

Energy Range
 E min: 1.5
 E max: 48.

Detector
 Theta: 180. Phi: 0. ?
 Array NewChessMaia384B-10mm

Target
 Alpha: 0.
 Beta: 0.

Target Layer Selection
 # Layers: 1 Define Layer: 1

Target Layer Details
 Thick: One 30. micror Density: 3.
 Formula Mode: Type in formula Atomic Fraction

Formula: (SiO2)70(FeO)20(Al2O3)10

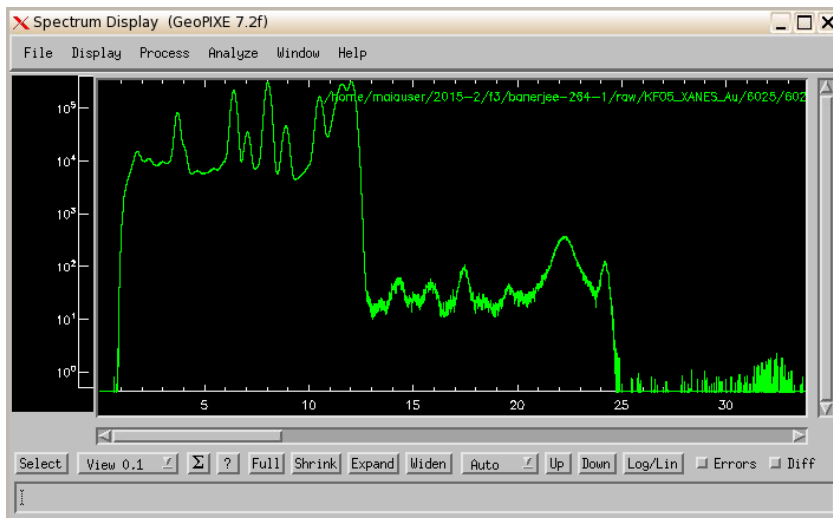
Output: /home/maiauser/2015-3/f3/banerjee-264-2/setup/roc

Calculate Yields Plot Yields Export Close

In the X-Ray Spectrum Fit window press “Fit: One” to fit the spectra.

Spectrum Fitting

In the “Spectrum Display” window, from the “Process” dropdown menu, select “Add (re-map calibration)” to produce one smooth spectrum.



Now under the “window” dropdown menu, press “X-ray spectrum Fit”

In the new X-Ray spectrum fit window, press Load (at the top of the window) and select a pre-existing PCM Parameter file. Pcm files are typically stored in the setup directory. This file will be used to create the DA Matrix. Once the file has been loaded, save it under a new name to avoid overwriting the initial file. Select elements should now be highlighted. Press Fit: “one” to fit the elements to your spectrum.

In the spectrum display window, on the bottom left beside “select” button, choose “View 0,1” from the dropdown menu. Now right click on the spectrum display window the upper limit of where you want to fit the spectrum. Choose a spot that is below the energy you ran the scan at, and after the peaks that you want to fit. Similarly, left click at the lower limit of where you want to fit the spectrum immediately before the characteristic energy peaks begin.

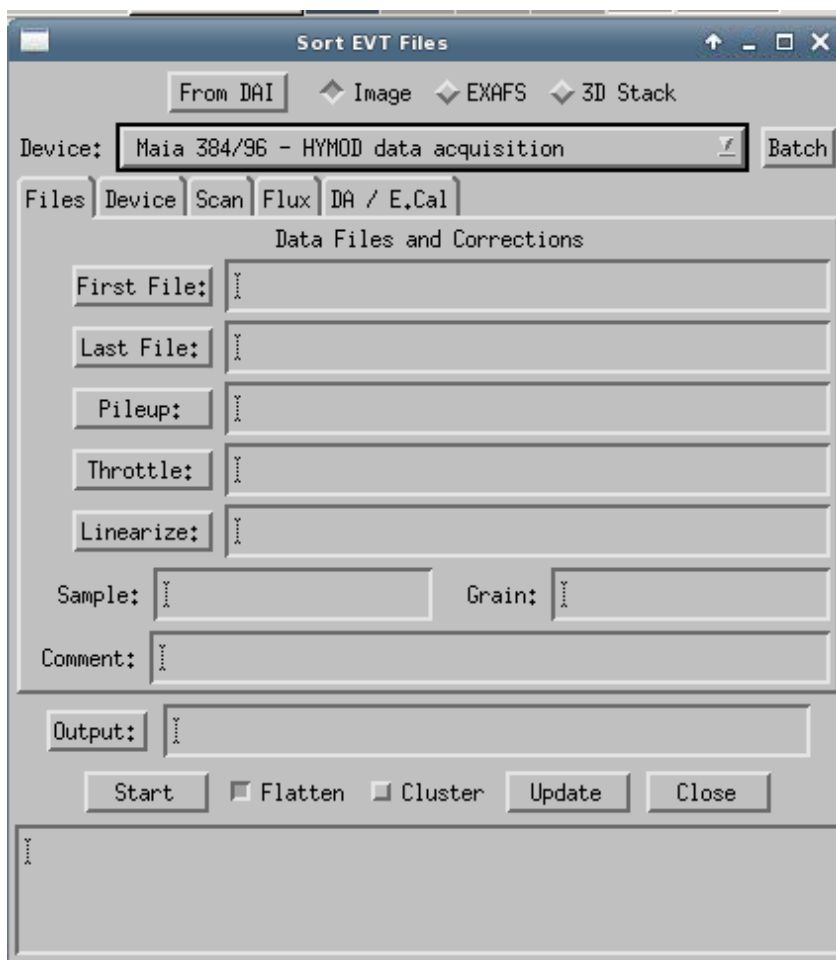
Now, in the X-ray spectrum fit window, press “use view”, ensure that “Cal on” is on (looks like it’s pushed in), and press “Fit: One” to re-fit the spectrum. Note – if you get an error message you likely need to add more elements or less in the X-ray spectrum fit spectrum to make the fit match the spectrum you measured. Continue experimenting with different elements until you get an appropriate fit. In the “X-ray spectrum fit” window, press “save spectrum” (it’s usually also a good idea to save as you test out different elements to make sure that work is not lost). Remember that only elements that have characteristic excitation energies below the energy you ran the scan at will be recorded. A very helpful feature is the “Identify line” feature. Try selecting it from the dropdown menu that you selected “use view” from on the spectrum display window. In the “window” dropdown menu select “identify line” to

open the corresponding window that will allow you to identify what elements are present.

Once the fit is satisfactory, press “generate DA matrix” in the “X-ray spectrum fit” window. Save the file with an appropriate name.

Producing Energy Concentration Images

In Sort EVT Files window, ensure that you’re creating an image file by ensuring that “image” has been checked off. Select “Maia 384/96 –MYMOD data acquisition” as the “Device”.



In the Files Tab - To fill out the necessary standard information, press “From DAI” and navigate to select a pre-existing file. It doesn’t matter which file you select, as long as it’s one that was run by the research group before. All important parameters will be changed.

Once the pre-existing file has been loaded, select the appropriate first file by pressing “first file” and navigating to the appropriate file. Once you press enter, you will be asked: “Do you want to set the detector calibration parameters based on the values loaded along with the list-mode header?” Select “No” (it’s preferential to keep those from the pre-existing DAI that you loaded). It will also ask: “Do you want to use these to set the ‘pileup’ and ‘Throttle’ fields?”. Select “Yes”. Next, select the appropriate “last file”.

Remember to change the “Output” to the appropriate directory and re-name the file to something that you will remember.

In the Device Tab - Change “DT cal A:” to 33.4

In the Scan Tab - In this tab we can trim the size of the image. We will come back to this later.

In the Flux Tab - Enter the conversion factor calculated in 1.0. The equivalent charge will update accordingly.

In the DA/E.Cal Tab - Change the data type to SXRF. Select an appropriate DA Matrix by pressing “File:” and navigating to the file of choice. The file of interest is typically stored in the setup folder.

Before Pressing Start - Ensure that the “cluster” button at the bottom of the screen is turned on

Press Start.

This process usually takes a long time to complete. A loading bar will appear to tell you how long until the image is loaded. For larger images, often the image will take a minute or so to open even after the loading bar is complete.

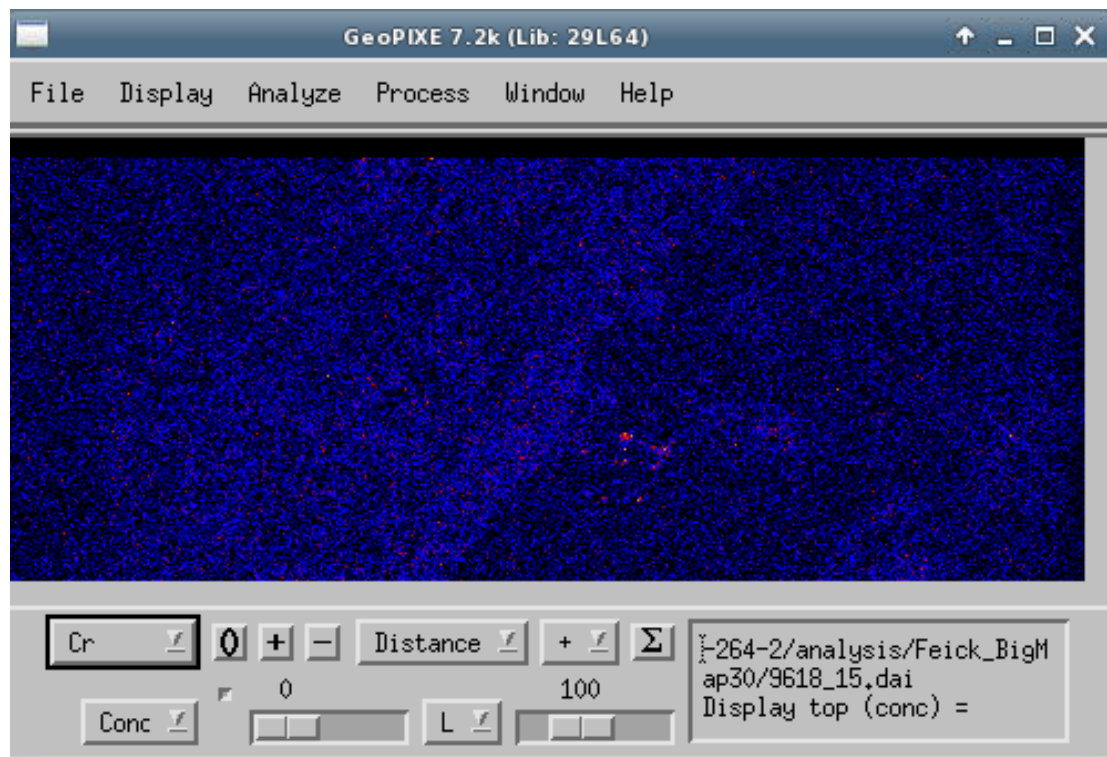
Your image should load in the GeoPixe 7.2 main image window once it’s done processing.

Image Validation

In the “sort EVT Files” window, press “from DAI” to load the file of interest that you just created a DA matrix for. This will fill out all appropriate information. Now in the “DA/ E.Cal” tab, select the appropriate DA Matrix. Ensure that “cluster” is on, and change the “output:” name if desired to avoid writing over the pre-existing file. Then press “Start”.

Once the image has been generated, confirm the presence of various elements. If an elements appears to be universally spread out across the thin section, e.g., in the

figure below, then it indicates that the element is not actually present and should be taken out of the DA Matrix.



Similarly, you will want to make sure that the presence of certain elements of interest. To do this, in the dropdown box that says “Distance” select “Box” and use your mouse to draw a box around the area of interest. Next, under the “window” dropdown menu select “image regions”. This will open a new window. Where it says “individual”, click it and select “array”. You now want to press the Σ button in the “Geopixe 7.2k” window (the window that has the image) to populate a row in the Image Regions window. Now press “EVT” in the Image Regions window to save the region and export a spectrum. Save it with an appropriate name.

Once the spectrum has been exported for the smaller region, open it in the “Spectrum Display” window. There’s no need to import the spectrum as you did before, it pulls the appropriate data from the pre-existing image. Now make sure the element(s) of interest in the region correspond to the appropriate energy peaks.

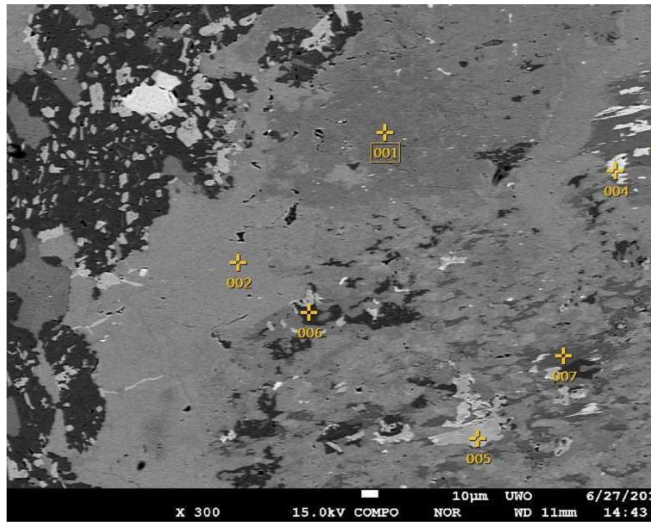
Qualitative and Quantitative Image Analysis

Open the energy map of interest. Draw a box around the area you would like to obtain quantitative information from. To do this, in the dropdown box that says “Distance” select “Box” and use your mouse to draw a box around the area of interest. Next, under the “window” dropdown menu select “image regions”. This will open a new window. Where it says “individual”, click it and select “array”. You now want to press the Σ button in the “Geopixe 7.2k” window (the window that has the

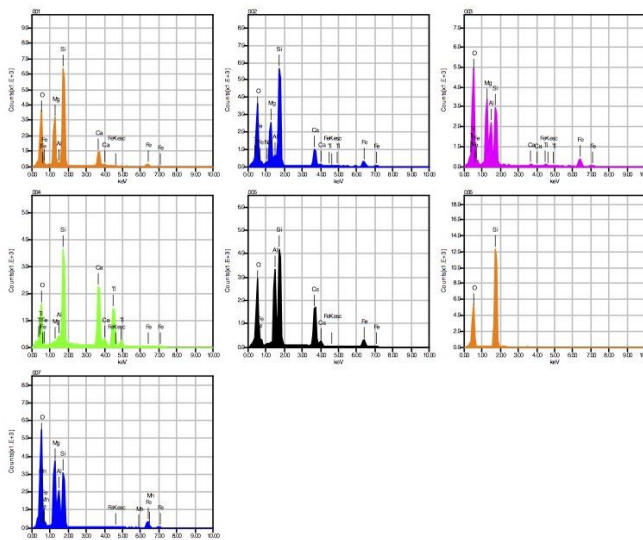
image) to populate a row in the Image Regions window. This row will contain all details regarding the concentration of various elements in your sample. This technique was used to calculate the Au:Ag ratio in Au-rich hot spots in this thesis.

Appendix I: Microprobe Results

26_amphibole



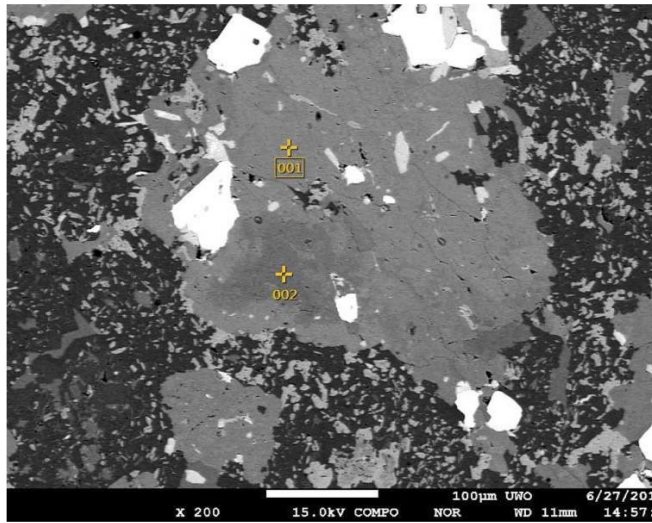
Volt : 15.00 kV
 Mag. : x 300
 Date : 2016/06/
 Pixel : 1280 x 9



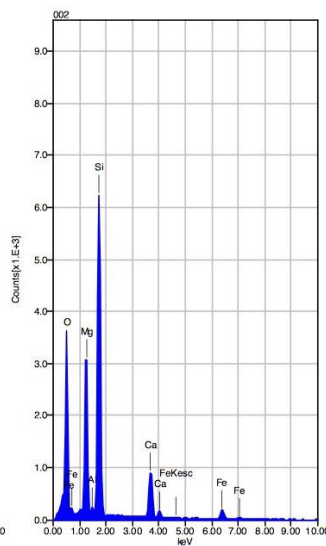
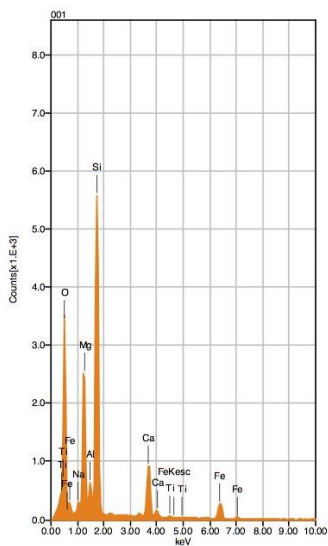
Acquisition Condition
 Instrument : 8530F
 Volt : 15.00 kV
 Current : ---
 Process Time : T2
 Live time : 10.00 se
 Real Time : 11.02 se
 DeadTime : 9.00 %
 Count Rate : 19258.00

	Fe	O	Na	Mg	Al	Si	Ca	Ti	Mn
001	6.36	43.15		12.65	0.49	28.05	9.31		
002	10.48	41.28	0.78	10.29	2.26	25.22	9.19	0.50	
003	14.73	44.76		14.09	9.80	14.51	0.96	1.14	
004	1.79	37.40		0.40	1.17	14.63	21.16	23.44	
005	11.43	40.14			12.46	18.37	17.60		
006		52.05				47.95			
007	13.84	45.75		15.67	9.44	14.82			0.49

26_amphibole2



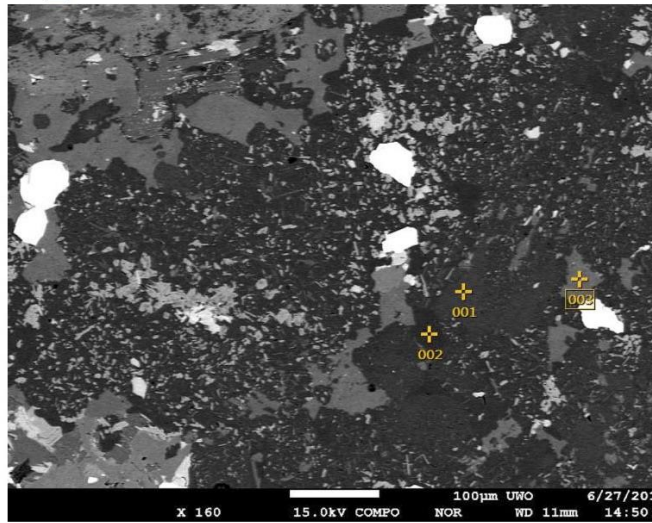
Volt : 15.00 kV
 Mag. : x 200
 Date : 2016/06/
 Pixel : 1280 x 9



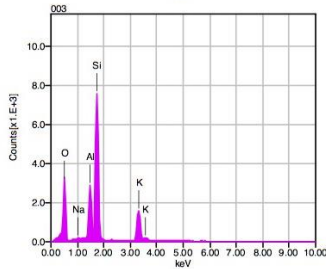
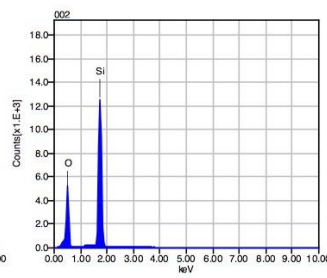
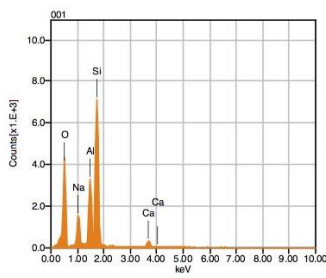
Acquisition Condition
 Instrument : 8530F
 Volt : 15.00 kV
 Current : ---
 Process Time : T2
 Live time : 10.00 se
 Real Time : 11.00 se
 DeadTime : 9.00 %
 Count Rate : 18848.00

	Fe	O	Na	Mg	Al	Si	Ca	Ti
001	10.63	41.51	0.85	10.05	2.27	25.18	9.08	0.43
002	7.01	42.61		12.34	0.50	28.04	9.50	
Average	8.82	42.06	0.85	11.20	1.38	26.61	9.29	0.43
Deviation	2.56	0.77	0.00	1.62	1.25	2.03	0.30	0.00

26_groundmass



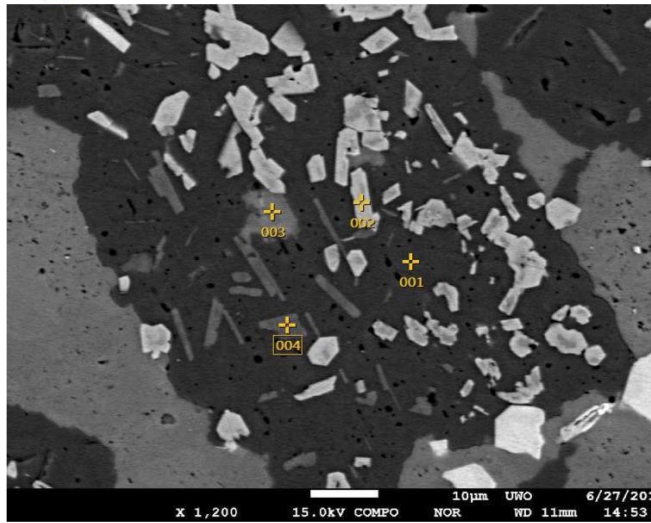
Volt : 15.00 kV
 Mag. : x 160
 Date : 2016/06/
 Pixel : 1280 x 9



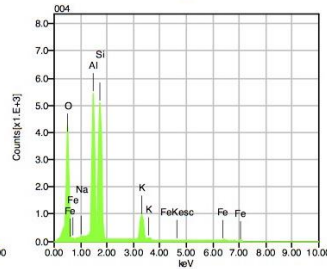
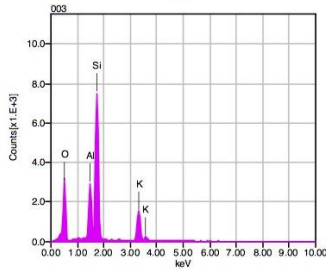
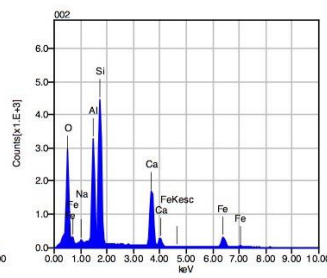
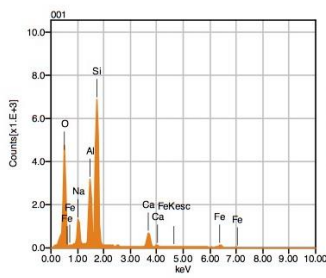
Acquisition Condition
 Instrument : 8530F
 Volt : 15.00 kV
 Current : ---
 Process Time : T2
 Live time : 10.00 se
 Real Time : 11.08 se
 DeadTime : 10.00 %
 Count Rate : 20131.00

	K	O	Na	Al	Si	Ca
001		46.05	6.25	12.33	32.34	3.03
002		50.93			49.07	
003	14.60	43.29	0.22	10.13	31.76	
Average	14.60	46.76	3.24	11.23	37.72	3.03
Deviation	0.00	3.87	4.26	1.55	9.83	0.00

26_groundmass2



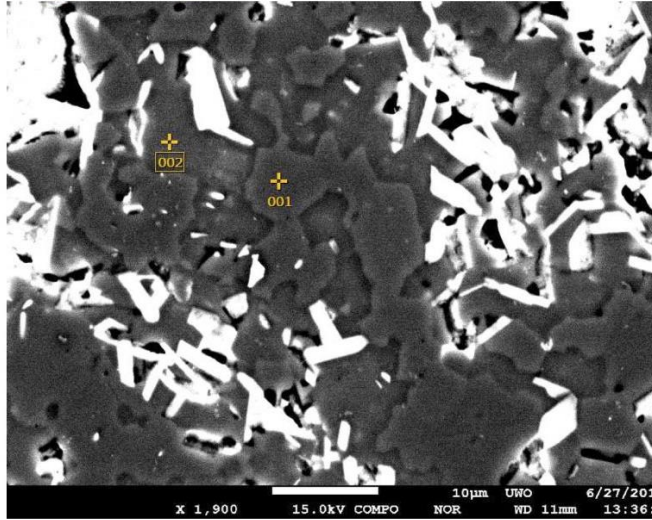
Volt : 15.00 kV
 Mag. : x 1,200
 Date : 2016/06/
 Pixel : 1280 x 9



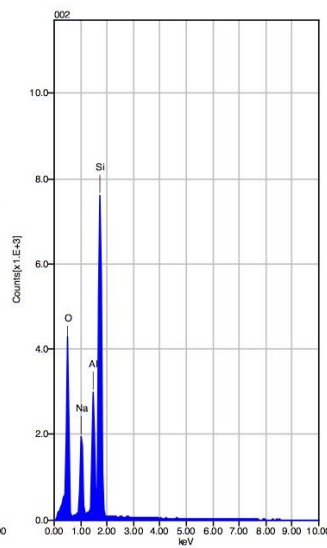
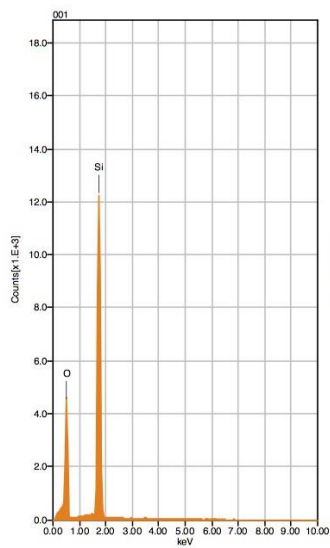
Acquisition Condition
 Instrument : 8530F
 Volt : 15.00 kV
 Current : ---
 Process Time : T2
 Live time : 10.00 se
 Real Time : 11.07 se
 DeadTime : 10.00 %
 Count Rate : 20580.00

	Fe	K	O	Na	Al	Si	Ca
001	3.08		46.90	5.10	10.98	28.03	5.91
002	11.56		39.51	0.46	12.04	19.25	17.18
003		14.48	42.93		10.36	32.23	
004	1.98	8.50	46.63	0.21	19.35	23.33	
Average	5.54	11.49	43.99	1.93	13.18	25.71	11.55
Deviation	5.24	4.23	3.49	2.75	4.17	5.64	7.97

27_quartz_albite



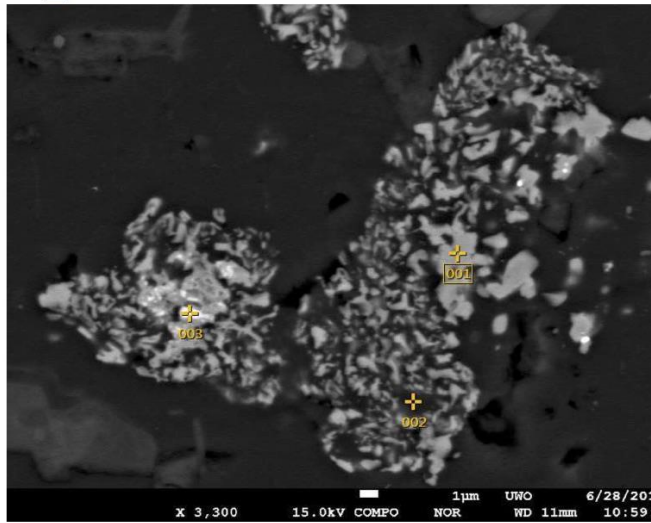
Volt : 15.00 kV
 Mag. : x 1,900
 Date : 2016/06/
 Pixel : 1280 x 9



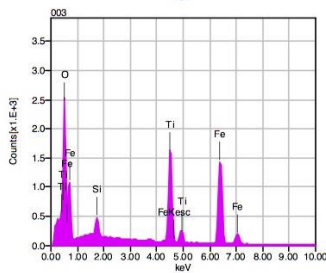
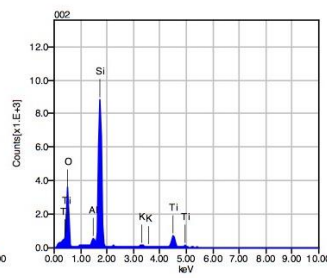
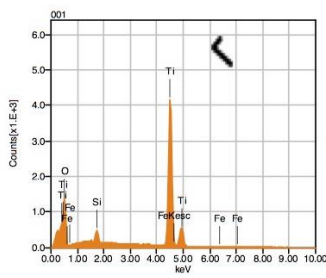
Acquisition Condition
 Instrument : 8530F
 Volt : 15.00 kV
 Current : ---
 Process Time : T2
 Live time : 10.00 se
 Real Time : 11.08 se
 DeadTime : 10.00 %
 Count Rate : 20430.00

	O	Na	Al	Si
001	49.71			50.29
002	44.41	8.22	11.45	35.93
Average	47.06	8.22	11.45	43.11
Deviation	3.75	0.00	0.00	10.16

28_Rim



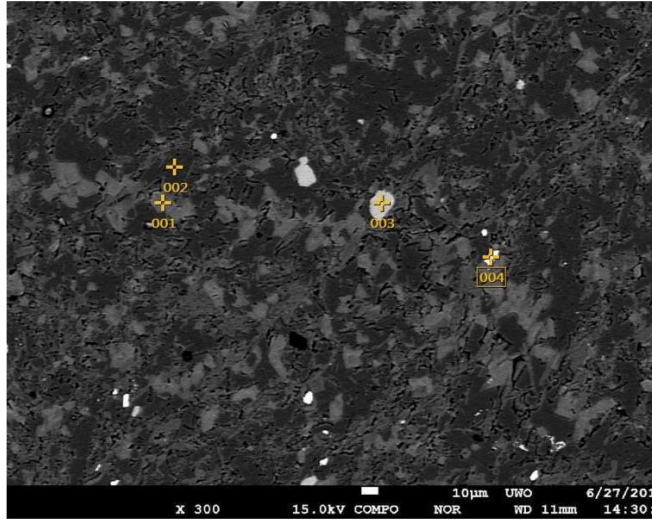
Volt : 15.00 kV
 Mag. : x 3,300
 Date : 2016/06/
 Pixel : 1280 x 9



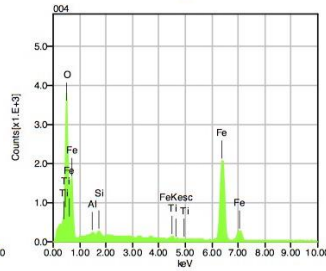
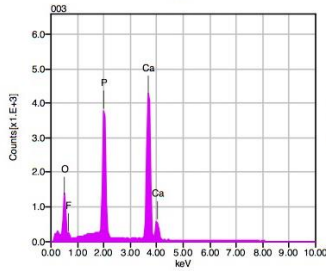
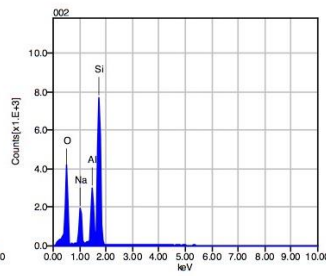
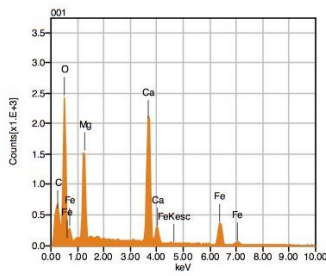
Acquisition Condition
 Instrument : 8530F
 Volt : 15.00 kV
 Current : ---
 Process Time : T2
 Live time : 10.00 se
 Real Time : 10.83 se
 DeadTime : 8.00 %
 Count Rate : 15599.00

	Fe	K	O	Al	Si	Ti
001	0.74		35.14		1.22	62.89
002		0.84	48.89	1.57	37.17	11.53
003	48.69		28.03		1.33	21.95
Average	24.72	0.84	37.36	1.57	13.24	32.12
Deviation	33.91	0.00	10.60	0.00	20.72	27.15

28_wave



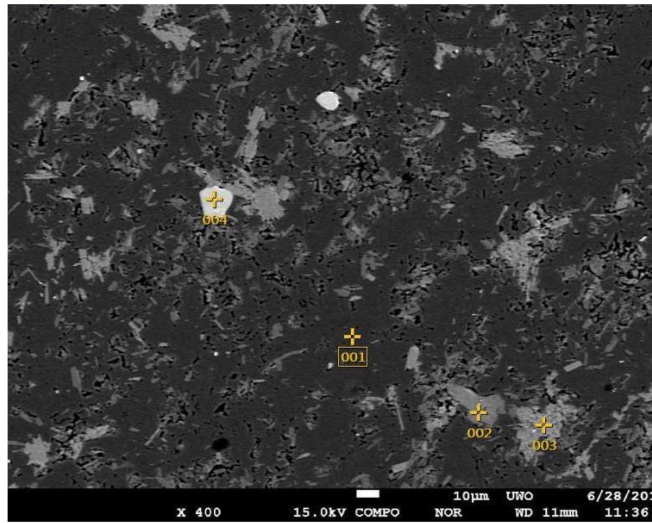
Volt : 15.00 kV
 Mag. : x 300
 Date : 2016/06/
 Pixel : 1280 x 9



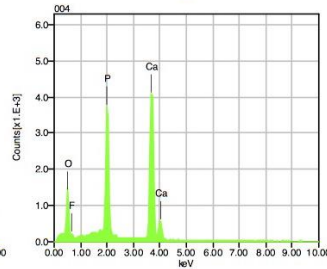
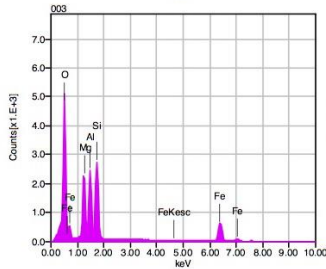
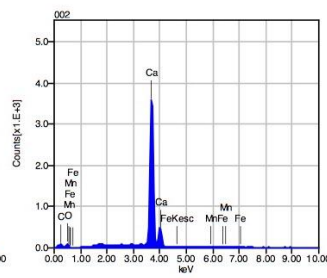
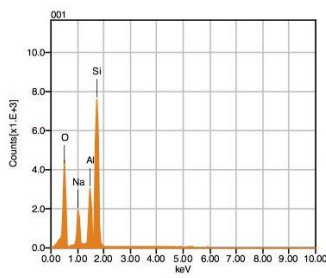
Acquisition Condition
 Instrument : 8530F
 Volt : 15.00 kV
 Current : ---
 Process Time : T2
 Live time : 10.00 se
 Real Time : 10.91 se
 DeadTime : 8.00 %
 Count Rate : 16995.00

	P	Fe	O	C	F	Na	Mg	Al	Si	Ca	Ti
001		16.75	45.40	4.57			7.97			25.30	
002			44.48			8.34		11.41	35.77		
003	19.54	74.24	32.98		3.40					44.18	
004			24.28					0.35	0.49		0.63
Average	19.54	45.50	36.76	4.57	3.40	8.34	7.97	5.88	18.13	34.74	0.63
Deviation	0.00	40.65	10.08	0.00	0.00	0.00	0.00	7.82	24.95	13.35	0.00

30_groundmass



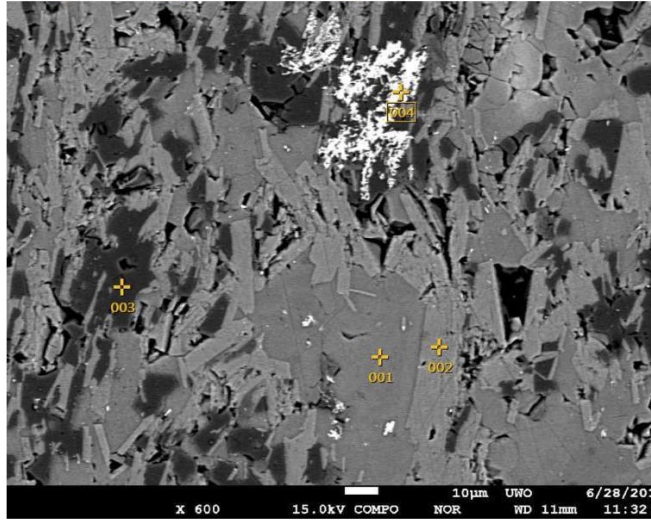
Volt : 15.00 kV
 Mag. : x 400
 Date : 2016/06/
 Pixel : 1280 x 9



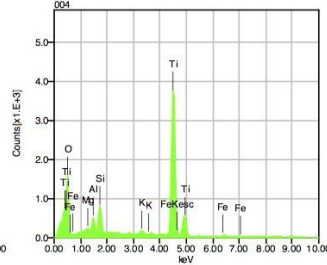
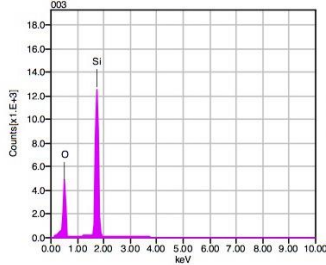
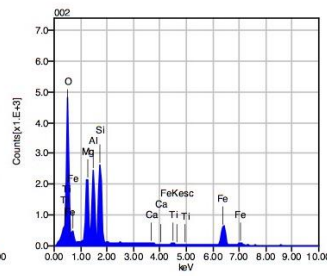
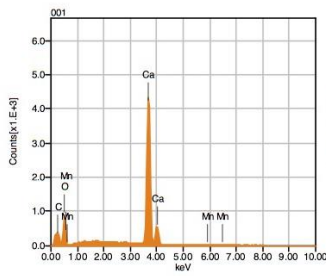
Acquisition Condition
 Instrument : 8530F
 Volt : 15.00 kV
 Current : ---
 Process Time : T2
 Live time : 10.00 se
 Real Time : 11.09 se
 DeadTime : 9.00 %
 Count Rate : 20607.00

	P	Fe	O	C	F	Na	Mg	Al	Si	Ca
001			45.23			7.67				
002		1.90	9.33	1.11						81
003		23.97	41.92				9.86	11.07	13.18	
004	19.31		34.00		3.27					41
Average	19.31	12.94	32.62	1.11	3.27	7.67	9.86	11.21	24.47	61
Deviation	0.00	15.61	16.23	0.00	0.00	0.00	0.00	0.20	15.96	31

30_large_replaced_grain



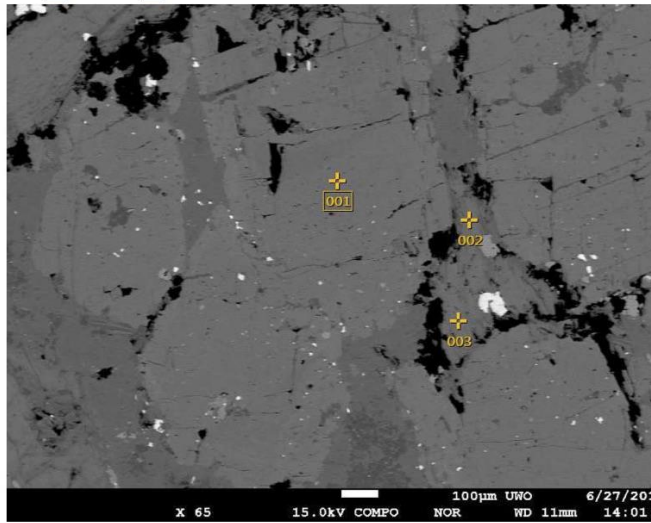
Volt : 15.00 kV
 Mag. : x 600
 Date : 2016/06/
 Pixel : 1280 x 9



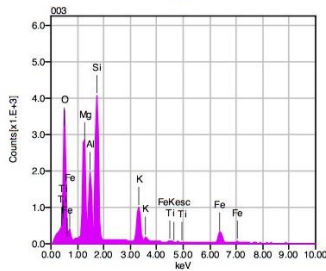
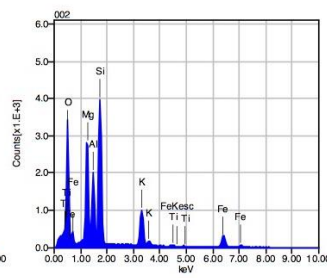
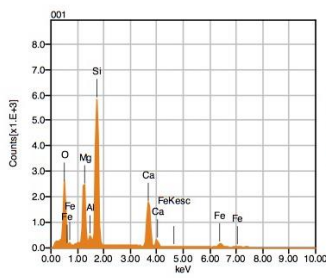
Acquisition Condition
 Instrument : 8530F
 Volt : 15.00 kV
 Current : ---
 Process Time : T2
 Live time : 10.00 se
 Real Time : 10.85 se
 DeadTime : 8.00 %
 Count Rate : 15738.00

	Fe	K	O	C	Mg	Al	Si	Ca	Ti	Mn
001			36.45	2.69				60.04		0
002	24.63		40.72		9.49	11.05	13.13	0.31	0.68	
003			50.28				49.72			
004	1.19	0.68	37.27		0.29	1.37	2.47		56.73	
Average	12.91	0.68	41.18	2.69	4.89	6.21	21.77	30.17	28.70	0
Deviation	16.57	0.00	6.34	0.00	6.50	6.84	24.78	42.24	39.63	0

48_amph_biotite



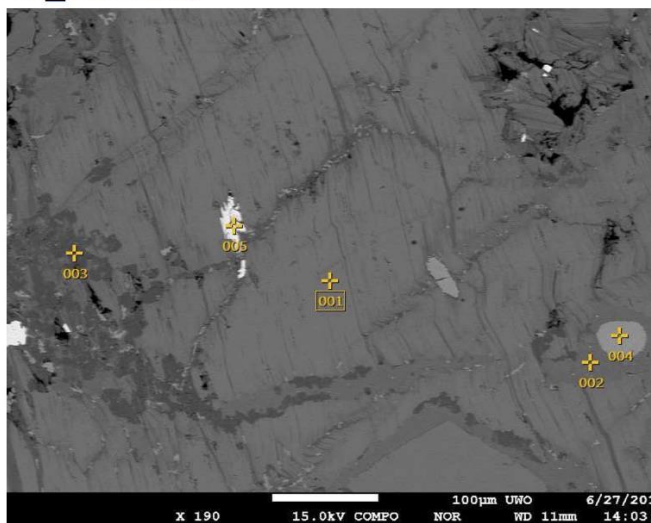
Volt : 15.00 kV
 Mag. : x 65
 Date : 2016/06/
 Pixel : 1280 x 9



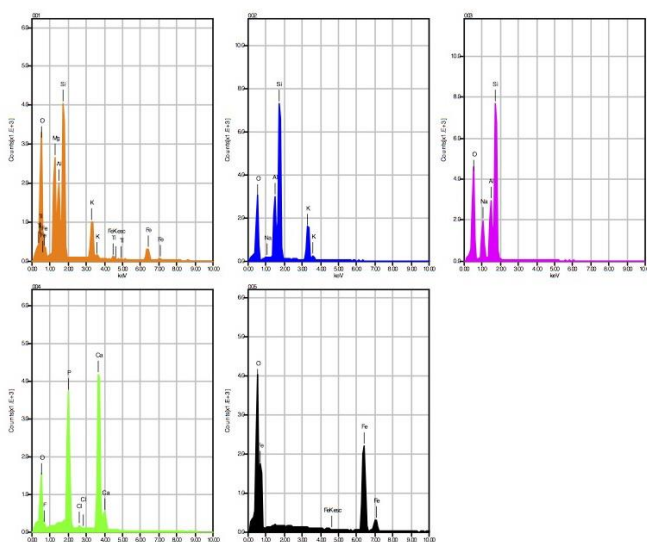
Acquisition Condition
 Instrument : 8530F
 Volt : 15.00 kV
 Current : ---
 Process Time : T2
 Live time : 10.00 se
 Real Time : 11.00 se
 DeadTime : 9.00 %
 Count Rate : 18639.00

	Fe	K	O	Mg	Al	Si	Ca	Ti
001	5.12		39.68	9.57	1.40	25.64	18.59	
002	12.10	9.37	38.88	11.40	8.44	19.15		0.66
003	11.74	9.18	39.75	11.36	8.21	19.15		0.61
Average	9.65	9.28	39.44	10.78	6.02	21.31	18.59	0.64
Deviation	3.93	0.14	0.49	1.05	4.00	3.75	0.00	0.03

48_biotite



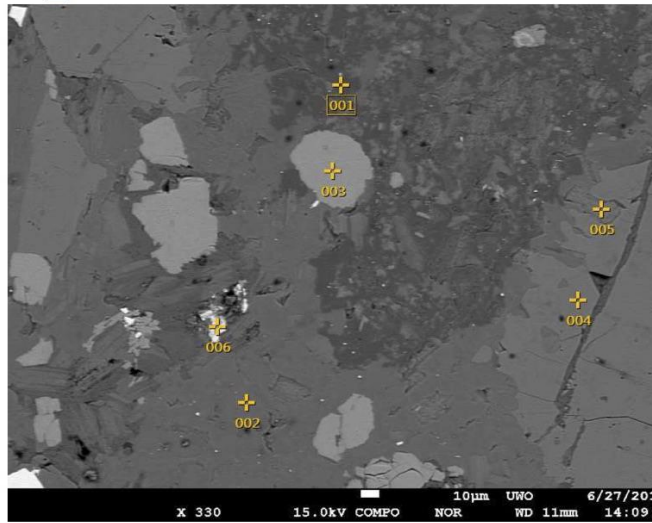
Volt : 15.00 kV
 Mag. : x 190
 Date : 2016/06/
 Pixel : 1280 x 9



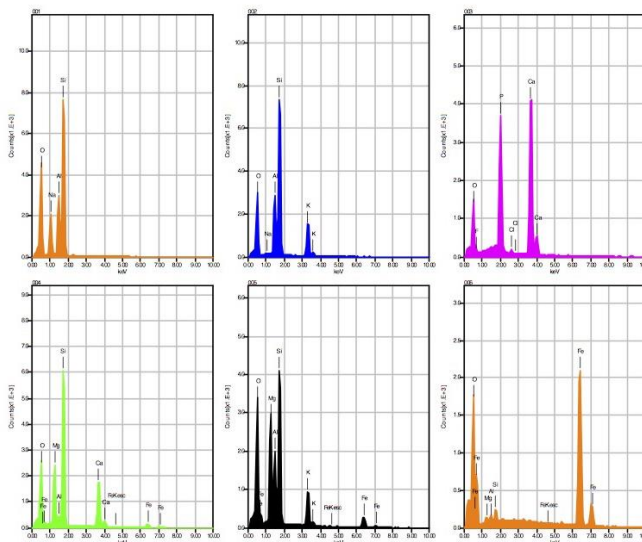
Acquisition Condition
 Instrument : 8530F
 Volt : 15.00 kV
 Current : ---
 Process Time : T2
 Live time : 10.00 se
 Real Time : 10.98 se
 DeadTime : 9.00 %
 Count Rate : 18588.00

	P	Fe	K	O	F	Na	Mg	Al	Si	Cl	Ca	Ti
001		12.91	9.06	38.09			10.87	8.66	19.17			1.24
002			15.35	42.25		0.29		10.27	31.83			
003				45.83		8.19		10.84	35.14			
004	19.05			34.76	3.55					0.51	42.13	
005		75.65		24.35								
Average	19.05	44.28	12.20	37.06	3.55	4.24	10.87	9.92	28.71	0.51	42.13	1.24
Deviation	0.00	44.36	4.45	8.24	0.00	5.58	0.00	1.14	8.43	0.00	0.00	0.00

48_groundmass



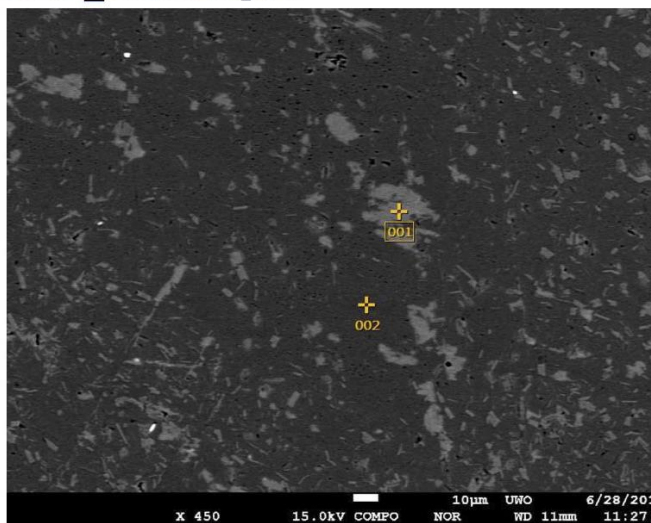
Volt : 15.00 kV
 Mag. : x 330
 Date : 2016/06/
 Pixel : 1280 x 9



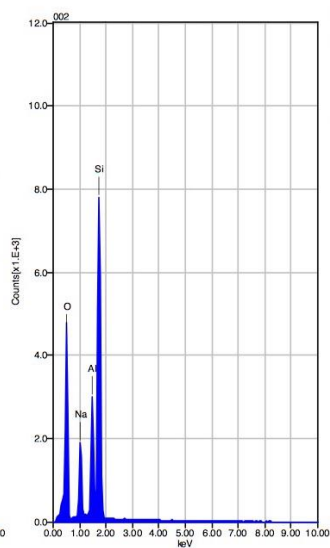
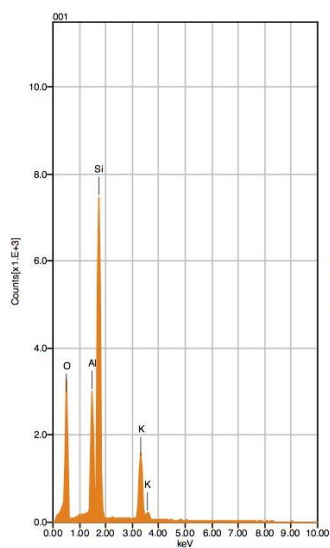
Acquisition Condition
 Instrument : 8530F
 Volt : 15.00 kV
 Current : ---
 Process Time : T2
 Live time : 10.00 se
 Real Time : 11.11 se
 DeadTime : 10.00 %
 Count Rate : 20718.00

	P	Fe	K	O	F	Na	Mg	Al	Si	Cl	Ca
001				45.10		8.54		11.28	35.08		
002			14.94	42.02		0.16		10.53	32.34		
003	19.11	5.10		34.48	2.81					0.62	42.99
004		5.10		39.04			9.34	1.41	26.17		
005		11.77	8.89	39.19			12.11	8.43	19.61		
006		84.34		13.88			0.55	0.43	0.80		
Average	19.11	33.74	11.91	35.62	2.81	4.35	7.33	6.42	22.80	0.62	30.97
Deviation	0.00	43.95	4.28	11.22	0.00	5.92	6.04	5.14	13.67	0.00	17.00

KF02_Phenocryst



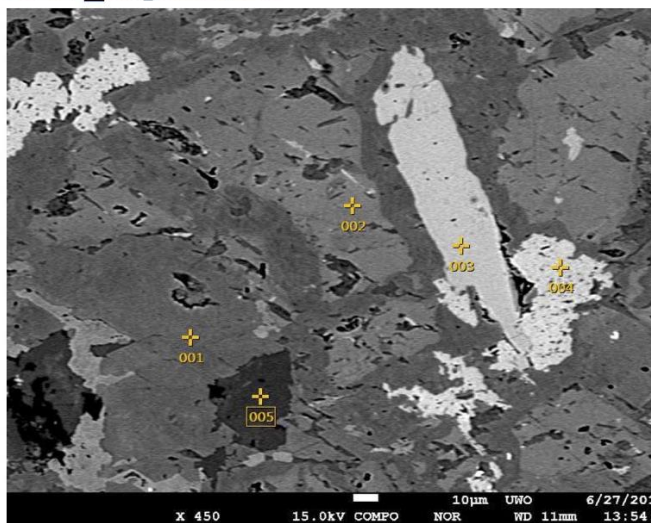
Volt : 15.00 kV
 Mag. : x 450
 Date : 2016/06/
 Pixel : 1280 x 9



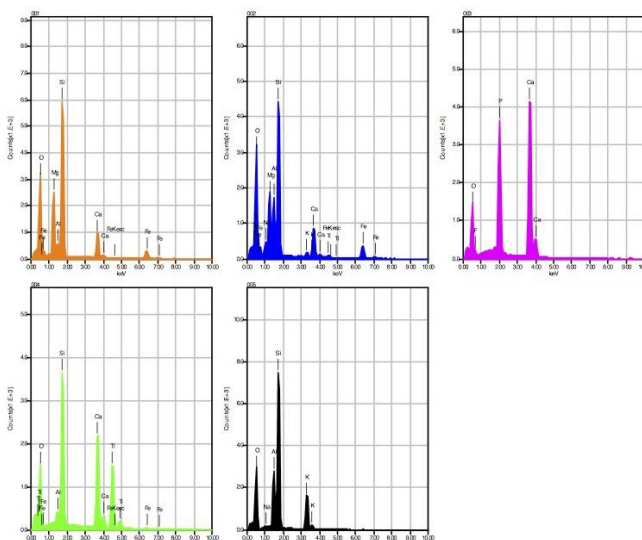
Acquisition Condition
 Instrument : 8530F
 Volt : 15.00 kV
 Current : ---
 Process Time : T2
 Live time : 10.00 se
 Real Time : 11.08 se
 DeadTime : 10.00 %
 Count Rate : 20143.00

	K	O	Na	Al	Si
001	14.34	42.68		10.44	32.54
002		46.34	7.59	10.86	35.21
Average	14.34	44.51	7.59	10.65	33.87
Deviation	0.00	2.58	0.00	0.30	1.89

KF17_amphibole



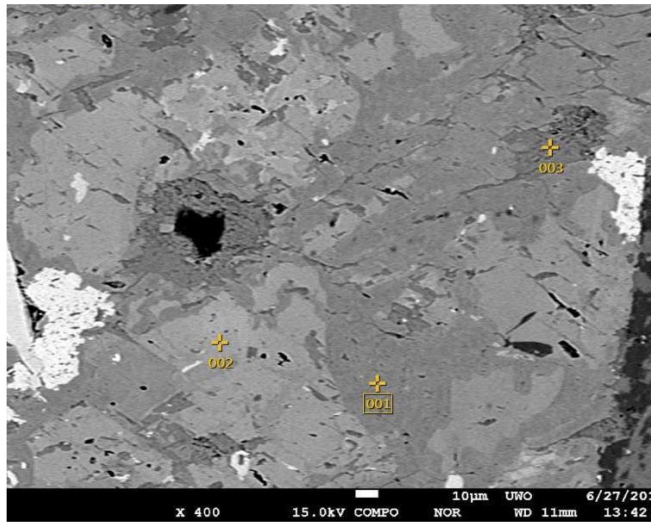
Volt : 15.00 kV
 Mag. : x 450
 Date : 2016/06/
 Pixel : 1280 x 9



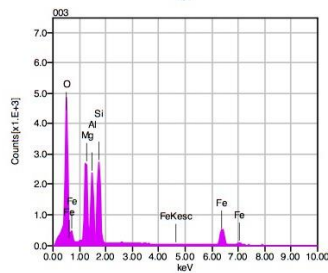
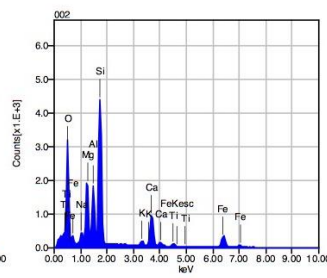
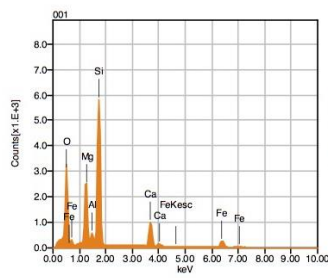
Acquisition Condition
 Instrument : 8530F
 Volt : 15.00 kV
 Current : ---
 Process Time : T2
 Live time : 10.00 se
 Real Time : 11.08 se
 DeadTime : 10.00 %
 Count Rate : 20240.00

	P	Fe	K	O	F	Na	Mg	Al	Si	Ca	Ti
001		11.03		39.80					26.77	10.20	
002		13.33	1.15	38.62		1.67	7.64	7.02	20.52	8.79	1.25
003	19.08			34.81	3.35					42.76	
004		1.07		37.19				1.10	14.58	21.66	24.41
005			15.39	42.02		0.22		10.02	32.35		
Average	19.08	8.48	8.27	38.49	3.35	0.94	8.88	5.06	23.56	20.85	12.83
Deviation	0.00	6.52	10.07	2.71	0.00	1.03	1.75	4.20	7.69	15.70	16.38

KF17_amphibole1



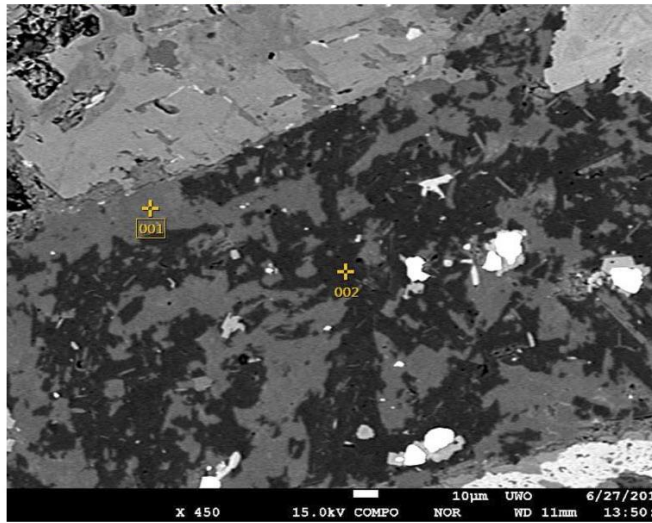
Volt : 15.00 kV
 Mag. : x 400
 Date : 2016/06/
 Pixel : 1280 x 9



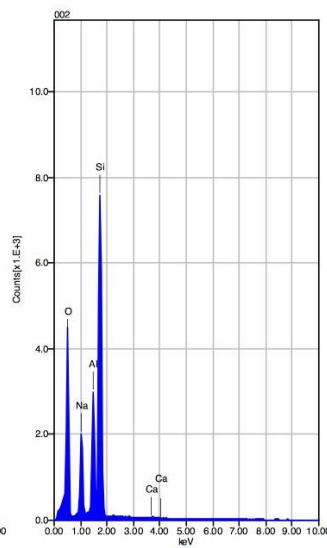
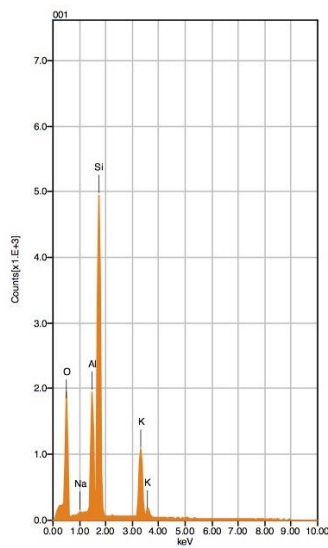
Acquisition Condition
 Instrument : 8530F
 Volt : 15.00 kV
 Current : ---
 Process Time : T2
 Live time : 10.00 se
 Real Time : 11.00 se
 DeadTime : 9.00 %
 Count Rate : 18917.00

	Fe	K	O	Na	Mg	Al	Si	Ca	Ti
001	10.74		40.17		10.39	1.77	26.50	10.43	
002	13.39	1.24	38.38	1.54	7.69	7.26	20.25	9.09	1.15
003	20.89		41.85		12.20	10.78	14.28		
Average	15.01	1.24	40.13	1.54	10.09	6.60	20.34	9.76	1.15
Deviation	5.27	0.00	1.73	0.00	2.27	4.54	6.11	0.95	0.00

KF17_k-spar_albite



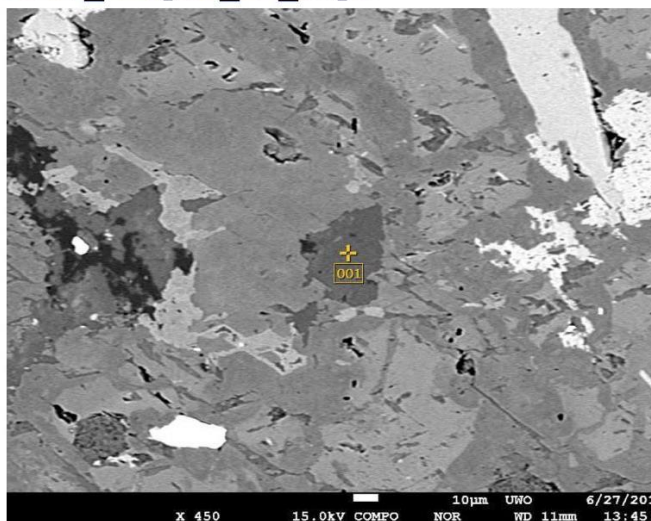
Volt : 15.00 kV
 Mag. : x 450
 Date : 2016/06/
 Pixel : 1280 x 9



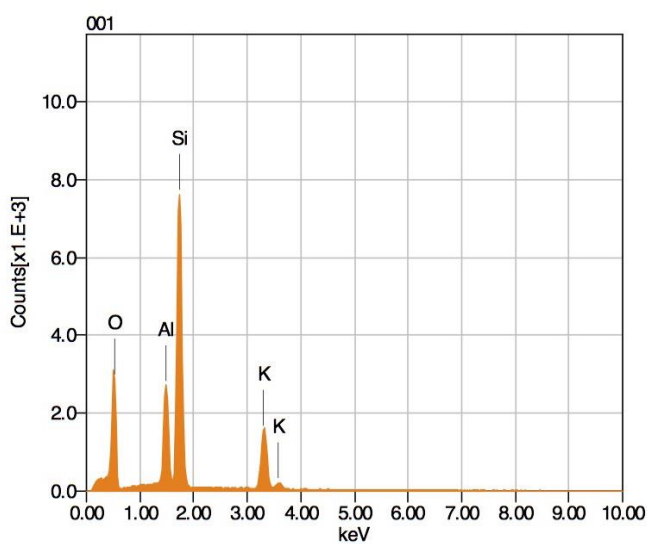
Acquisition Condition
 Instrument : 8530F
 Volt : 15.00 kV
 Current : ---
 Process Time : T2
 Live time : 6.56 sec
 Real Time : 7.26 sec
 DeadTime : 10.00 %
 Count Rate : 19995.00

	K	O	Na	Al	Si	Ca
001	15.59	41.02	0.29	10.44	32.66	
002		45.32	8.15	11.12	35.12	0.30
Average	15.59	43.17	4.22	10.78	33.89	0.30
Deviation	0.00	3.04	5.56	0.48	1.74	0.00

KF17_k-spar_in_amph



Volt : 15.00 kV
Mag. : x 450
Date : 2016/06/
Pixel : 1280 x 9



Acquisition Condition
Instrument : 8530F
Volt : 15.00 kV
Current : ---
Process Time : T2
Live time : 10.00 se
Real Time : 11.08 se
DeadTime : 10.00 %
Count Rate : 20272.00

Formula	mass%	Atom%	Sigma	Net	K ratio	Line
O	42.23	57.89	0.13	617374	3.5402460	K
Al	9.67	7.86	0.06	725682	1.4004859	K
Si	33.03	25.79	0.12	2281703	4.9252876	K
K	15.08	8.46	0.08	630633	2.4756299	K
Total	100.00	100.00				

Curriculum Vitae

Name: Katherine Feick

Post-secondary Education and Degrees: University of Waterloo
Waterloo, Ontario, Canada
2009-2014 B.Sc.

The University of Western Ontario
London, Ontario, Canada
2014-2016 M.Sc.

Honours and Awards: Province of Ontario Graduate Scholarship
2015-2016

AER Global Opportunities Award in Environmental and Sustainable Studies
2015

Related Work Experience Graduate Teaching Assistant
The University of Western Ontario
2014-2015

Geologist-in-Training
Canadian Malartic Corporation
2013

Undergraduate Teaching Assistant
The University of Waterloo
2014